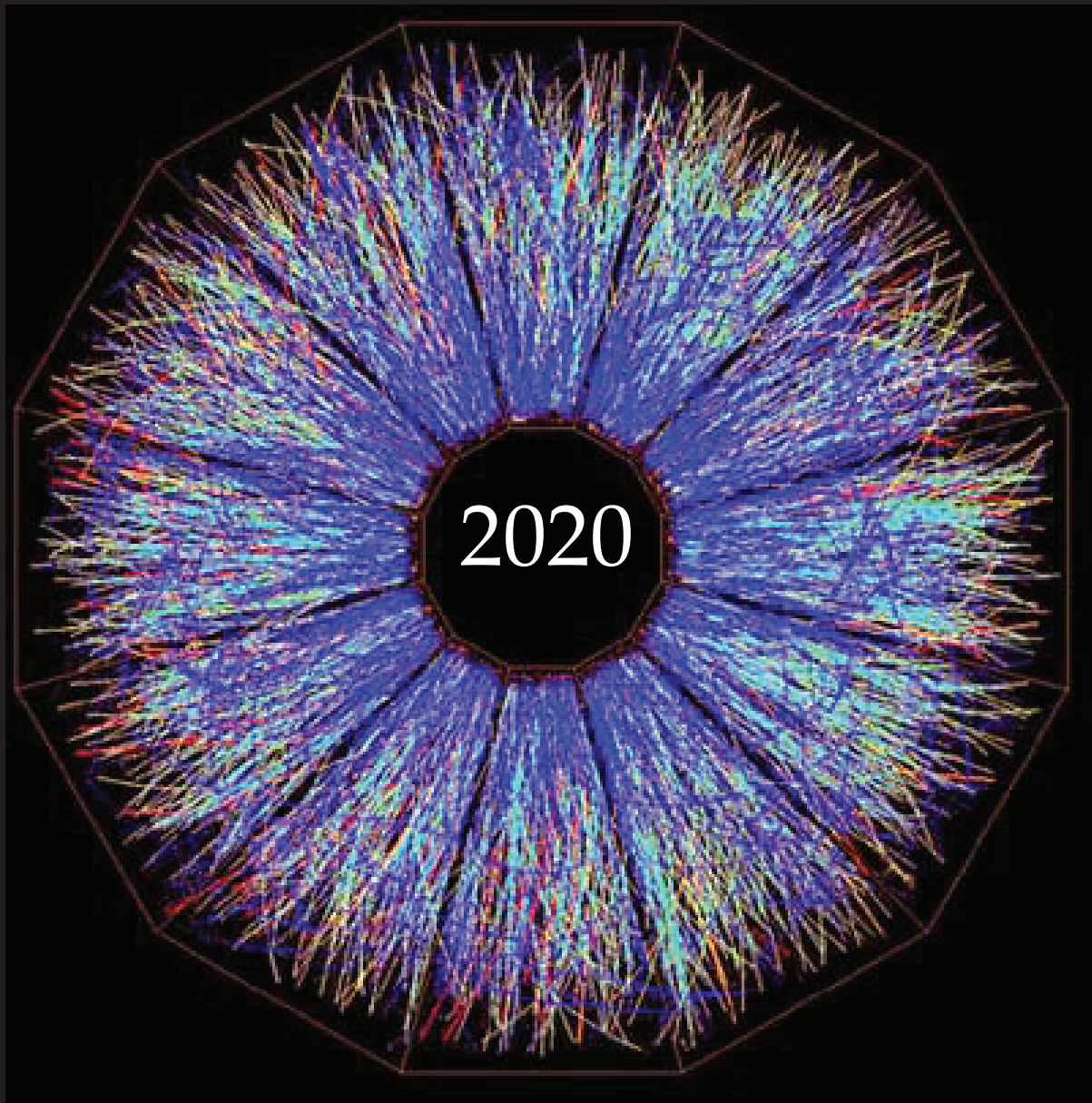


A Compilation of Internship Reports



Prepared for The Office of Educational Programs
Brookhaven National Laboratory
Office of Educational Programs

DISCLAIMER

This work was prepared as an account of work sponsored by an agency of the United States Government. Neither the United States Government nor any agency thereof, nor any of their employees, nor any of their contractors, subcontractors or their employees, makes any warranty, express or implied, or assumes any legal liability or responsibility for the accuracy, completeness, or any third party's use or the results of such use of any information, apparatus, product, or process disclosed, or represents that its use would not infringe privately owned rights. Reference herein to any specific commercial product, process, or service by trade name, trademark, manufacturer, or otherwise, does not necessarily constitute or imply its endorsement, recommendation, or favoring by the United States Government or any agency thereof or its contractors or subcontractors. The views and opinions of authors expressed herein do not necessarily state or reflect those of the United States Government or any agency thereof.



BROOKHAVEN
NATIONAL LABORATORY

Table of Contents

FeynGraphGen: a QGRAF-based Feynman diagram generator for lattice QCD code generation	1
<i>Ryan Abbott</i>	
Thermal analysis of the Electron-Ion Collider Hadron Ring SC magnet bellows	7
<i>Andrew Abdala</i>	
Development of a novel algorithm for RSA factorization based upon algorithmic entropy reduction in sequenced binary quadratic forms	22
<i>Alpha Bah and Emma Ryan</i>	
Design studies for the laser calibration system for the sPHENIX time projection chamber	35
<i>Salvatore Baldinucci</i>	
Effects of I-131 on the thyroid	40
<i>Deonna Beard</i>	
Developing a two-layer HTS conductor on round core superconducting coil design for quench studies	47
<i>Michael Bianco</i>	
Real-time dashboard for monitoring performance of the general parallel file system.....	55
<i>Matthew Broadbent</i>	
Radiophobia: how fearing radiation impacts mental and physical health.....	65
<i>Mecca Brooks</i>	
How automation is helping us stay safe during COVID-19: Pi based dewar controller to reduce staff overhead for the MX beamlines at NSLS-II	73
<i>Andrew Campbell</i>	
Controls solutions and integration for dynamic equipment at the National Synchrotron Light Source II..	77
<i>Brandon Catalano</i>	
Rack interlock systems interface.....	94
<i>Michael Charumaneeroj</i>	
Quantifying frost formation on frozen-hydrated biological samples with computer vision	103
<i>Holdy Chauvette</i>	
Hydrogen intensity mapping simulator: Interpolation improvements and radio point source compatibility with application to the GaLactic and Extragalactic All-Sky MWA Survey dataset	115
<i>Zhi Chen</i>	
Logic design of rack interlock system for detector infrastructure	122
<i>Jason Cheung</i>	
Modeling of software-defined radio for National Synchrotron Light Source II radio frequency control	140
<i>Jade Hayan Chun</i>	
Investigation of the structural sensitivity of theoretical XANES spectra in dilute PdAu alloy nanoparticles	157
<i>Phillip Comer and Jennifer LaPoff</i>	
Simulating the space charge effect inside the ICARUS liquid argon time projection chamber at Fermilab	166
<i>Elijah D. S. Courtney</i>	

Preparation for and prevention of radiological events.....	181
<i>John Cummings</i>	
Optimization of calibration analysis tools for the light detection system in the ICARUS neutrino detector.....	183
<i>Austin DeMurley and Douglas Howell</i>	
The International Safeguards Project Office information system upgrade	189
<i>Nathaly Diaz</i>	
Identifying source of excess noise in the BMX testbed intensity mapping instrument	196
<i>Josie Fenske</i>	
Analysis of x-rays using electron multiplying charge coupled devices	207
<i>James Flemings</i>	
Comparative genomics of arsenic detoxification in <i>S. cerevisiae</i> and <i>C. reinhardtii</i>	223
<i>Garret Genco</i>	
A comprehensive literature study of SARS-CoV-2's morphology, pathogenesis and drug targets	244
<i>Sonali George</i>	
Engineering challenges of sPHENIX inner HCAL installation	248
<i>Carter Godin</i>	
Quantum entanglement and non-locality measures at high energy colliders.....	251
<i>Wenjie Gong</i>	
Examination of aerosol optical properties at a rural continental site	274
<i>Brian Hambel</i>	
Literature analysis of COVID-19 drug and vaccine development.....	279
<i>Emma Hert</i>	
Nuclear scattering code python interface.....	295
<i>Nicholas Holfester</i>	
Classifying neutron resonances with decision tree algorithms	306
<i>Sophia Hollick and Pedro Rodríguez</i>	
Automation of the nsls2forge conda infrastructure.....	317
<i>Thomas Hopkins</i>	
Scintillation waveform fitting in the ICARUS detector's photomultiplier array	329
<i>Douglas Howell</i>	
The Analysis of ARM data related to cloud droplet activation and the study of Köhler theory.....	334
<i>Marcus Johnson</i>	
Far-forward neutrinos at the Large Hadron Collider	341
<i>Karan Kumar</i>	
TCAD Simulations of AC-LGADs.....	348
<i>Sean King</i>	
Data acquisition with frame programmable grid arrays.....	352
<i>Matthew D. Leone</i>	
Promoting the selective CO ₂ activation to methanol: Catalyst optimization using density functional theory	361
<i>Zhuoying Lin</i>	
Testing anomalies with provenance in high performance computing.....	372
<i>Allen Liu</i>	
Direct measurement of trapped ion micromotion	377
<i>Maverick Millican</i>	
X-ray spectromicroscopy and comparison of minerals and materials	382
<i>Shivani Mishra</i>	

Making machines into masterminds: machine learning applications in image segmentation and analysis.....	391
<i>Ethan Mulle</i>	
Optimizing data processing procedures and data analysis in the BMX experiment.....	401
<i>Jesse Osborn</i>	
Investigating radiation at RHIC access road using Monte Carlo simulation	409
<i>Z. S. Rechav</i>	
Development of mobile applications for medical isotope reference.....	420
<i>Vanessa E. Rodriguez</i>	
Ventrecycle	430
<i>Russell Rohan</i>	
Analyzing utility systems at Brookhaven National Laboratory to maintain infrastructure more efficiently	437
<i>Carmine Romano</i>	
A novel factorization algorithm for Rivest-Shamir-Adleman composites: algorithmic entropy reduction in sequenced binary quadratic forms	447
<i>Emma Ryan and Alpha Bah</i>	
Photo recognition for the 4-poster tick management system®	461
<i>Coral Salort</i>	
Analysis of charge diffusion in EMCCD.....	479
<i>John Santucci</i>	
Universal winding machine upgrade and EIC IR magnet B1APF endplate analysis	485
<i>Calvin Schmalzle</i>	
Effect of a copper chelator on zinc levels in A β deposits in Cerebral Amyloid Angiopathy	495
<i>Andrea Sprague-Getsy</i>	
InvenioRDM user interface and DOI enhancements	506
<i>Cole Swartz</i>	
Development of target database for the Quantitative Plant Science Initiative (QPSI)	520
<i>Michelle Tapia</i>	
Drone calibration of the Baryon Mapping Experiment.....	525
<i>Gregory Troiani</i>	
Variability on precipitable water vapor in the Houston, TX metropolitan region	536
<i>James Turner and Brian Wittemann</i>	
Comparison of Gamma Spectrum between simulation and evaluation for ⁵⁵ Mn	542
<i>Josselyn Velasquez Ocaris</i>	
Designing high-pressure vessel system to transport CO ₂ laser.....	547
<i>Thea Vijaya Kumar</i>	
The Design of the Electron Ion Collider RF Systems Power Supply Building	568
<i>Oksana Vysochanska</i>	
Monitoring facility services with ELK stack	584
<i>Brandon Weindorf</i>	
Identifying sea/bay breeze circulations in the Houston, TX region using a surface meteorology network	597
<i>Brian Wittemann and James Turner</i>	
The civil engineering development of the Electron Ion Collider support infrastructure	607
<i>Angela Zavala Yanes</i>	

FeynGraphGen: a QGRAF-based Feynman diagram generator for Lattice QCD code generation

Ryan Abbott¹ and Peter Boyle²

¹Department of Physics, Columbia University, New York, New York 10027

²Department of Physics, Brookhaven National Laboratory, Upton, New York 11973

Abstract—Calculations in Quantum Field theory typically utilize Feynman diagrams as a combinatorial tool to help organize calculations. Generating all such diagrams satisfying certain conditions is a crucial but tedious and error-prone step in any such calculation, and thus it is desirable to have automated tools to enumerate all Feynman diagrams of a given type. Current tools for this purpose include FeynArts and QGRAF which, while effective tools for their intended purposes, have functionality limited primarily to perturbative calculations. Extending these tools to nonperturbative lattice gauge theory calculations presents some nontrivial difficulties. We present an alternative to QGRAF, a program FeynGraphGen that replicates the functionality of QGRAF in a C++ program. We also present a Python interface to FeynGraphGen and provide examples showing how this could be used to facilitate code-generation for lattice gauge theory.

I. Introduction

As the size and complexity of Lattice QCD calculations grow, so does the complexity of generating the required diagrams and translating them into code. While presently diagram generation is typically done by hand, for future calculations with hundreds or even thousands of diagrams this may no longer be feasible. Current tools for Feynman graph generation include FeynArts, a Mathematica package aimed at low order (1 & 2 loop) phenomenological calculations[4] and QGRAF, a fast and efficient Fortran program that works better for higher-order calculations.[7] Both of these programs are insufficient for lattice QCD purposes due to their lack of support for disconnected diagrams, and modifying either of these programs for Lattice QCD code generation would present several difficulties, so instead we have built FeynGraphGen, an extensible C++ program which replicates much of the behavior of QGRAF and provides a scriptable Python interface that should enable FeynGraphGen to be used for code generation if future Lattice QCD projects.

II. Conventions and Definitions

A. Graphs

For Feynman diagram generation there are two types of graphs of interest. The first are undirected multigraphs, which are graphs that allow any number of undirected edges between any two nodes, including loops. The second type of graph is the Feynman diagrams themselves, which can be considered multigraphs with possibly directed colors (i.e. propagators) assigned to each edge.

We always represent graphs in an adjacency matrix format, so a graph G is represented by entries G_{ij} which correspond to the set of edges from i to j . We will say two graphs G and G' are equal if $G_{ij} = G'_{ij}$ for all i and j , while two graphs are isomorphic if their adjacency matrices are similar by permutations matrices (see Section II-B). We denote equality by $G = G'$, while we denote isomorphism by $G \cong G'$.

B. Permutations

We consider a permutation $\sigma \in S_n$ as a function $\sigma : \{0, \dots, n-1\} \rightarrow \{0, \dots, n-1\}$. The set of all permutations on n vertices forms a group under function composition, which we will refer to as S_n . Our primary concern with permutations will be how they act on graphs by relabelling:

Definition 1. We define an right action of S_n on the set of all n -vertex labelled graphs by

$$(G^\sigma)_{ij} = G_{\sigma(i)\sigma(j)} \quad (1)$$

for all $\sigma \in S_n$.

One can easily check that this a right action, so $(G^\sigma)^\tau = G^{\sigma\tau}$. Using this notation, we may reword the definition of isomorphism to say that $G \cong G'$ if and only if $G' = G^\sigma$ for some $\sigma \in S_n$.

C. Symmetry Groups

Given a Feynman graph G , there are three symmetry groups relevant for our graph generation algorithms:[7]

- $\Gamma_P(G) = \text{Aut}(G)$, the automorphism group of the underlying multigraph of G
- $\Gamma_I(G)$, the subgroup of $\text{Aut}(G)$ fixing all external legs
- $\Gamma_F(G)$, the symmetry group of the full Feynman diagram

We consider all of these as subgroups of S_n ,¹ note that by definition we have $S_n \supset \Gamma_P(G) \supset \Gamma_I(G) \supset \Gamma_F(G)$.

D. Partitions

A partition P of a set X is a collection of disjoint subsets P_1, \dots, P_k of X whose union constitutes the whole of X . For our purposes the set X will typically be $\{0, \dots, n-1\}$, and the relevant subsets P_1, \dots, P_n will be contiguous sets of integers. Such a partition can be determined by integers x_0, \dots, x_k such that $0 = x_0 < x_1 < \dots < x_k = n$, with $P_i = \{p_{i-1}, \dots, p_i - 1\}$; this is how we represent partitions within FeynGraphGen.

Given a partition $P = \{P_1, \dots, P_k\}$ of a set X , and an action of S_n on X , we say that σ respects P if $\sigma P_i = P_i$ for all i . The set of all permutation respecting P forms a subgroup of S_n which we denote by S_n^P .

Given a graph G we can partition the vertices of G by their degrees, so the vertices of degree 1 fall in one class, the vertices of degree 2 in another, and so on. We denote this partition by $P(G)$. Note that since automorphisms must carry a vertex v to a vertex of the same degree, any $\sigma \in \text{Aut}(G)$ must respect $P(G)$, and hence $\text{Aut}(G) \subset S_n^{P(G)}$.

E. Canonicalization

A common problem in graph generation is the generation of isomorphic diagrams whose adjacency matrices are not equal. This means we might generate a pair of graphs $G \neq G'$ so that $G' = G^\sigma$ for some permutation σ . In order to prevent such redundancy, we require that generated graphs satisfy a canonicity condition that selects a unique labelling of the given graph, i.e. function $C(G)$ such that

- 1) $C(G) = G^\tau$ for some $\tau \in S_n$
- 2) $C(G^\sigma) = C(G)$ for all $\sigma \in S_n$

For multigraphs we use the C library nauty which implements the canonicalization function defined

¹See [7] for a discussion of how this aligns with the usual definition of symmetries of Feynman diagrams.

in [6], while for Feynman diagrams we require that (1) the underlying multigraph G is canonical, (2) the labelling of the endnodes is canonical under the action of $\text{Aut}(G)$ (see Section III-B), and (3) the coloring of internal propagators is canonical under the action of the elements of $\Gamma_I(G)$ (see Section III-C), following the conventions of [7].

There are two applications of canonicalization which are relevant for FeynGraphGen. The first is that requiring our graphs be canonical reduces the problem of graph isomorphism to graph equality (though in practice this simply pushes the complexity from determining graph isomorphisms to producing canonical labellings). The second is that canonicity checks allow us to avoid isomorphism testing entirely by iterating over all graphs and keeping only the graphs which are in their canonical forms.[7], [8]

III. Diagram generation algorithms

The general procedure FeynGraphGen uses for Feynman diagram generation follows the same steps as QGRAF:[7]

- 1) Generation of all undirected multigraphs satisfying certain conditions
- 2) Associating each external vertex with an external state
- 3) Coloring the internal edges to produce a full Feynman diagram

As discussed in (II-E) we check for canonicity graphs at each stage so that we only have one copy of any given graph.

A. Multigraph generation

1) Determining vertex degrees: Following QGRAF, the first step FeynGraphGen takes in generating multigraphs is to determine the degrees of the vertices of the multigraphs it will generate. In particular for the case of replicating QGRAF we must convert the specified loop order and number of external states into a set of possible vertex degrees. The key formula needed for this is the following formula which one may prove by induction:²

$$V - E + L = 1 \quad (2)$$

where V is the number of vertices, E is the number of edges, and L is the number of loops in a given multigraph. For a graph G let n_k denote the number

²Alternatively one could also prove this formula by noting that (using cellular homology) we have $V = \dim C_0(G)$, $E = \dim C_1(G)$, $L = \dim H_1(G)$, and $\dim H_0(G) = 1$, so

$$\chi(G) = V - E + L = 1 - L$$

where $\chi(G)$ is the Euler characteristic of G .

of vertices of degree k . Then we have $V = \sum_k n_k$ and $E = \frac{1}{2} \sum_k k n_k$; if we substitute this into (2) and rearrange we find

$$2L - 2 + n_1 = \sum_{k \geq 2} (k - 2)n_k \quad (3)$$

Note that n_1 is the number of external vertices, so the left hand side is fixed. Assuming $n_2 = 0$ (i.e. there are no degree-2 vertices) all the terms on the right-hand side are positive, so there are finitely many solutions to this equation which can be found through a direct search, yielding the desired degree sequences.

2) Graph generation: For multigraph generation we use the algorithms described in [5] adapted to generate multigraphs with vertices of the desired degrees. Beginning with the algorithm for triangle-free graphs, we modify the definitions of lower and upper objects appropriately for multigraphs. This gives a search tree for all possible multigraphs, which we then prune to only consider the multigraphs which could be augmented to obtain the desired degree sequence

Strictly speaking the above is a slight oversimplification. The algorithm implemented might better be considered to generate all colored multigraphs of a given size, where the colors correspond to the target vertex degree. This means, for instance, if the desired degree sequence was $(3, 3, 2, 2)$, then this graph:



would not be considered isomorphic to this graph:



Note that this does not change the output of the algorithm, since any isomorphism of graphs must send a vertex of a given degree to another vertex of the same degree.

B. External state labelling

For external state labelling we follow QGRAF and generate all possible external state labellings, keeping only those that we consider canonical. In order to define what we mean by canonical, suppose we have external states E_1, \dots, E_k , and we want to assign them to a graph G with external vertices e_1, \dots, e_k . Given $\tau \in S_k$ we can obtain an assignment of external states by assigning E_i to $e_{\tau(i)}$ for all i (and vice versa we can obtain $\tau \in S_k$ from such an assignment). Now let $\sigma \in \text{Aut}(G)$, and let $\gamma \in S_k$ be defined by $\sigma(e_i) = e_{\gamma(i)}$. We can obtain an assignment equivalent to $E_i \mapsto e_{\tau(i)}$ by applying σ^{-1} to G ; in this case one obtains the assignment $E_i \mapsto e_{\gamma\tau(i)}$. This tells us that τ and $\gamma\tau$ are equivalent for the purposes of assigning external states, so we

ought only to choose one of these for our purposes. We arbitrarily make the choice to take which of τ or $\gamma\tau$ is greater lexicographically. This choice defines a canonical element within the action of $\text{Aut}(G)$ on the external state assignments

C. Graph coloring

For assigning propagators we follow QGRAF and color each graph in every possible way, recursively coloring each edge every possible color. Throughout the algorithm we are careful to check which interaction vertices each graph vertex could be, and we exit early if it becomes impossible to finish coloring the graph. Once we've fully colored the diagram we accept only canonical diagrams; a Feynman diagram G is considered canonical if it is maximal under the action of $\Gamma_I(G)$ on the graph, where the ordering is some arbitrarily-defined ordering on Feynman diagrams (the exact ordering depends on the details of how the diagrams are represented in code, though the choice of ordering does not change the end result).

IV. Comparison to QGRAF

A. Correctness checking

In order to check FeynGraphGen for correctness and to provide an independent verification of QGRAF, we performed several comparisons between FeynGraphGen's output and QGRAF's. The first and most basic check is simply comparing the number of diagrams generated under a range of inputs.

Beyond diagram-counting, we also performed deeper comparisons to ensure that the diagrams generated by FeynGraphGen match those generated by QGRAF exactly. Towards this purpose we implemented the ability to read QGRAF's output in certain conditions³ and compare the generated graphs themselves. Note that we cannot compare the graphs for equality directly, as we have different canonicity conditions and methods, so we must canonicalize QGRAF's output before comparison is possible.

We have shown some comparison results in Table I – note that the last 3 columns are all 0, which indicates that QGRAF and FeynGraphGen agree exactly on all of the given inputs.

B. Performance comparison

Performance varies from application to application, but in general we have found FeynGraphGen

³In particular we implemented the ability to read the output when QGRAF used the style file "form.sty" which comes by default with QGRAF.

File	Graphs	Mismatches		
		Diagram	Symm.	Sign
complex_1loop	16	0	0	0
complex_2loop	4544	0	0	0
phi3_scatter_1loop	39	0	0	0
phi3_scatter_2loop	399	0	0	0
phi3_scatter_3loop	5625	0	0	0
phi3_vertex_1loop	7	0	0	0
phi3_vertex_2loop	58	0	0	0
phi3_vertex_3loop	535	0	0	0
phi3_vertex_4loop	5427	0	0	0
phi4_vertex_1loop	7	0	0	0
phi4_vertex_2loop	42	0	0	0
phi4_vertex_3loop	255	0	0	0
phi4_vertex_4loop	1592	0	0	0
phi4_vertex_5loop	10441	0	0	0
qed_bridge_2loop	2	0	0	0
qed_bridge_3loop	43	0	0	0
qed_bridge_4loop	798	0	0	0
qed_onshell_1loop	1	0	0	0
qed_onshell_2loop	11	0	0	0
qed_onshell_3loop	143	0	0	0
qed_onshell_4loop	2121	0	0	0
qed_scatter_1loop	156	0	0	0
qed_scatter_2loop	2640	0	0	0
qed_vertex_1loop	6	0	0	0
qed_vertex_2loop	50	0	0	0
qed_vertex_3loop	518	0	0	0
qed_vertex_4loop	6354	0	0	0

TABLE I

Example output from comparing against QGRAF. The columns “Symm.”, and “Sign” refer to the number of diagrams for which FeynGraphGen and QGRAF disagree with respect to the symmetry factor and sign of the diagram, respectively.

to be faster than QGRAF on very small inputs (e.g. 1-loop QED or ϕ^3 calculations), but QGRAF performs better for large input. Looking at the time per diagram we find that in higher loop calculations both FeynGraphGen and QGRAF have an approximately constant time per diagram generated, but FeynGraphGen is 40-50 times slower. We believe this is a result of two factors:

- 1) Our choice to prefer simpler and more understandable code to highly optimized but difficult to understand code.
- 2) Our use of adjacency matrices rather than, for instance, an edge list as QGRAF uses.

Ultimately we consider point 1 to be an intentional design decision that should make future modifications to FeynGraphGen easier, while point 2 could be the subject of future usage. In any case FeynGraphGen is currently performant enough for most lattice QCD calculations, generating approximately 5000 diagrams/second in our tests, so we do not consider these performance issues to be a priority for future development.

C. Unimplemented features of QGRAF

The following features of QGRAF have not been implemented in FeynGraphGen:

- The propagator options notadpole, external
- The options topol, nosigma, sigma, notadpole, tadpole, floop
- Constants associated with propagators and vertices
- Several printing options/keywords are untested, incomplete, or missing
- No features beyond QGRAF version 3.0 have been implemented

There are also a number of other inconsistencies between FeynGraphGen and QGRAF, primarily relating to handling of strings and files. For instance, QGRAF requires that the input file has its parameters in a specified order, while FeynGraphGen has no such restriction.

V. Extensions

A. Insertion-based diagram generation

When generating diagrams for use in Lattice QCD, the model of specifying a particular loop order for a calculation is no longer applicable. The analysis in Section III-A1 does not hold for disconnected diagrams (in particular (2) is no longer true), and in any case typically one does not specify a lattice calculation by giving external states in a loop order; instead one typically specifies which insertions/operators appear in the diagram. So we created a new method of generating diagrams where specify the number and types of vertices present in the diagram; we call this insertion-based diagram generation.

Beyond the simple description given above, we also considered the scenario that one might have a number of interchangeable vertices that could also be inserted. For instance, if we wanted to compute the QED corrections to a particular process by considering QED perturbatively (i.e. not including photon fields in the generation of gauge configurations) then to compute the order- α corrections we would want two insertions of QED vertices, either $\bar{u}A_\mu u$, $\bar{d}A_\mu d$, or $\bar{s}A_\mu s$. We could specify first two insertions of $\bar{u}A_\mu u$, and then specify $(\bar{u}A_\mu u)(\bar{d}A_\mu d)$, and then $(\bar{u}A_\mu u)(\bar{s}A_\mu s)$, and so on, but this would be quite inefficient since we would be re-generating the same topologies for every calculation. Instead we allow the specification of some number of “model vertices,” and allow the user to specify the number of model vertices to insert into the final diagram. So for the order- α corrections to some process, one would add model vertices $\bar{u}A_\mu u$, $\bar{d}A_\mu d$, and $\bar{s}A_\mu s$ and specify that two model vertices should be inserted. This also

has the benefit that computing to higher order, say α^2 , is quite simple – we just specify 4 model vertices instead of 2.

B. Python Interface

In order to provide a more scriptable interface to FeynGraphGen than the interface provided by QGRAF, we have constructed a Python interface using Cython[1] for both the typical perturbative calculations of QGRAF and the new insertion-based interface. A Python interface also has the benefit that it does not tie FeynGraphGen to any particular method or library for calculating the diagrams, so users are free to use whatever methods are most applicable to their particular calculation.

The interface is perhaps best explained by an example:

```
from feyngraphgen import Model, run_perturbative,
    Filter

model = Model()
model.add_particle("photon")
model.add_particle("electron", "positron",
    is_fermionic=True)

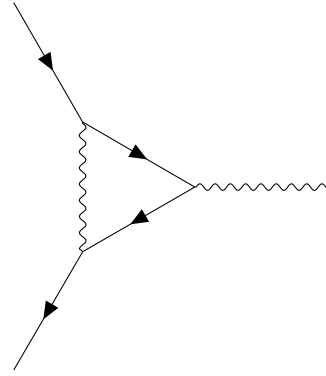
model.add_vertex(["positron", "electron", "photon"])

external_in = ["electron", "positron"]
external_out = ["photon"]

filters = [Filter("connected"), Filter("onshell")]

diagrams = run_perturbative(model, external_in,
    external_out, num_loops=1, filters=filters)
```

This code generates all of the necessary diagrams for the QED vertex function at 1 loop. In order to create a QED model we first construct a model containing a two propagators, namely “photon” and the “electron”, with the electron having the antiparticle of “positron.” We then add the standard interaction vertex $\bar{\psi}\psi A_\mu$, and specify an incoming electron and positron and an outgoing photon. The first filter (“connected”) specifies that the diagram is connected, and the second (“onshell”) specifies that there are no self-energy insertions on the legs of the diagram. By changing the “num_loops” parameter this can easily be extended to an arbitrary order calculation. The output of this script (at one loop) is exactly one diagram:



The diagrams output by the Python interface are MultiDiGraph’s from the Python library NetworkX[3] with an additional attribute “propagator” on each edge indicating the name of the propagator. Keeping the diagrams in such a format should be useful in that it opens the possibility of using the extensive Python ecosystem to aid in working with and manipulating graphs. For instance, we have already had some success in sketching generated diagrams using a combination of NetworkX’s `spring_layout` functionality for layout and TikZ-Feynman[2] for drawing.

Here is an example of using the insertion-based interface to generate the diagrams needed for all order- α QED corrections for the $K \rightarrow \pi\pi$ decay:

```
from feyngraphgen import Model, Filter, run_insertion

model = Model()
model.add_particle("photon")
model.add_particle("Q")

for q in ["1", "s"]:
    qbar = q + "bar"
    model.add_particle(q, qbar, is_fermionic=True)
    model.add_vertex([qbar, q, "photon"])

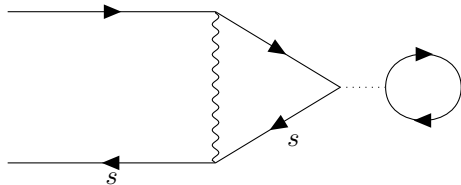
external_in = ["sbar", "1"]
external_out = ["lbar", "1", "lbar", "1"]

insertions = [{"s", "lbar", "Q"}, {"1", "lbar", "Q"}]

filters = []

diagrams = run_insertion(model, external_in,
    external_out, insertions, num_model_vertices=2,
    filters=filters)
```

The two primary differences here are the parameters “insertions” and “num_model_vertices,” which match the description of the interface given in V-A. Here the propagator “Q” represents the contraction of a 4-quark operator, or alternatively one can think of Q as the integrated-out W -boson. This procedure generates 600 diagrams; here is an example of one such diagram:



VI. Future Work

A. Implementing QGRAF Features

In general, implementing any individual QGRAF feature mentioned in Section IV-C should not present too much difficulty; however, implementing and testing all of these features would in total be a fairly time-consuming task. Instead we have decided to wait and see which features, if any, are desired and implement only features which are required for calculations of interest.

B. Performance improvements

The algorithms and data structures in FeynGraphGen were chosen primarily for their simplicity and ease of implementation; however, as our comparison with QGRAF shows there is much room improvement. Some investment in terms of optimizing the data structures and algorithms in FeynGraphGen could potentially yield an order of magnitude improvement. Furthermore we could also parallelize the generation of multigraphs (see [5]) and their subsequent coloring, which would give an additional performance benefits. We should note, however, that for most physics applications performance is not an issue for graph generation (for instance, FeynGraphGen can generate the graphs for a 5-loop QED vertex-function calculation in a matter of seconds), so such improvements would likely be low-priority unless current physics applications reach a point at which the FeynGraphGen's performance becomes a bottle-neck.

VII. Conclusion

We have presented a program FeynGraphGen, a C++ program with a Python interface for generating Feynman diagrams for use in Lattice QCD calculations. By providing a generic interface to

FeynGraphGen we ensure that the program is not tied to any particular method of calculating the resulting diagrams, and hence FeynGraphGen ought to be useful for a variety of different computational methods and libraries. Moving forward we expect FeynGraphGen to provide a strong basis on which to build future calculations utilizing the ability to automatically generate and programmatically work with Feynman diagrams, increasing the complexity and accuracy of future Lattice QCD calculations.

VIII. Acknowledgements

This project was supported in part by the Brookhaven National Laboratory (BNL), Department of Physics under the BNL Supplemental Undergraduate Research Program (SURP).

References

- [1] Stefan Behnel, Robert Bradshaw, Craig Citro, Lisandro Dalcin, Dag Sverre Seljebotn, and Kurt Smith. Cython: The best of both worlds. *Computing in Science & Engineering*, 13(2):31–39, 2011.
- [2] Joshua P. Ellis. TikZ-Feynman: Feynman diagrams with TikZ. *Computer Physics Communications*, 210:103 – 123, 2017.
- [3] Aric A. Hagberg, Daniel A. Schult, and Pieter J. Swart. Exploring network structure, dynamics, and function using networkx. In Gaël Varoquaux, Travis Vaught, and Jarrod Millman, editors, *Proceedings of the 7th Python in Science Conference*, pages 11 – 15, Pasadena, CA USA, 2008.
- [4] Thomas Hahn. Generating Feynman diagrams and amplitudes with FeynArts 3. *Computer Physics Communications*, 140(3):418 – 431, 2001.
- [5] Brendan D McKay. Isomorph-free exhaustive generation. *Journal of Algorithms*, 26(2):306 – 324, 1998.
- [6] Brendan D. McKay and Adolfo Piperno. Practical graph isomorphism, II. *Journal of Symbolic Computation*, 60(0):94 – 112, 2014.
- [7] P. Nogueira. Automatic Feynman graph generation. *Journal of Computational Physics*, 105(2):279 – 289, 1993.
- [8] Ronald C. Read. Every one a winner or how to avoid isomorphism search when cataloguing combinatorial configurations*. In B. Alspach, P. Hell, and D.J. Miller, editors, *Algorithmic Aspects of Combinatorics*, volume 2 of *Annals of Discrete Mathematics*, pages 107 – 120. Elsevier, 1978.

Thermal Analysis of the Electron-Ion Collider Hardon Ring SC Magnet Bellows

Andrew Abdala

Engineering Department, SUNY University at Buffalo, Buffalo, NY, 14260

Joseph Tuozzolo

Collider Accelerator Department, Brookhaven National Laboratory, Upton,
NY 11973

Contents

I Abstract	1
II Introduction	2
III Scope & Objective	3
IV Methods & Process	3
V Conclusion	6
VI Appendix A	9

I Abstract

The conversion of Relativistic Heavy Ion Collider (RHIC) to Electron-Ion Collider (EIC) is the next step in Nuclear Physics Research at Brookhaven National Laboratory. The EIC will have the ability to collide electrons with ions (protons to gold) which will lead to a better understanding of subatomic

particles. When electron collide, at such high energy and momentum, they are able to probe deeply into protons and neutrons and explore the quarks and gluons within..There are many challenges for the EIC because it will run at record beam currents for , one of which is to overcome the heating of bellows in the superconducting magnet beam-line. The high-intensity Hardon beam will excite electrons in the copper-plated surface on the nonmagnetic stainless steel bellows shield in the bellows assembly. The copper has very high conductivity at the cryogenic operating temperature. The Hardon beam will generate an induced current on the walls of the shield that will increase its temperature. This will raise the temperature of the shield could reduce the copper conductivity to the point where it can affect the EIC's performance. The temperature must be as low to keep the copper conductivity high which will prevent this from happening. The goal of this project is to generate a thermal analysis simulation of the bellows shield heating and then develop a better method to carry away that heat to keep the copper temperature below 15K.

II Introduction

Electron -Ion Collider (EIC) is a complex machine that will use most of RHIC (Relativistic Heavy Ion Collider) as its base foundation. The EIC will use collisions between electrons and ions to investigate the sub-atomic particles and their properties. One of the problems is that the material used for the beam tube in RHIC is not suitable for the EIC. Since EIC runs at higher beam currents than RHIC the current beam tube, which is made of stainless steel, is a problem. Stainless steel has a poor electrical conductivity, which will increase the temperature of the beam tube which is very close to the RHIC superconducting (SC) magnet coils. The beam tube temperature must be as low as possible for the magnets to work. To mitigate this, the decision is made to cover the beam tube with a copper plated stainless-steel nonmagnetic sleeve. Copper has a very high electrical conductivity at the 4.5K magnet operating temperature. Its thermal conductivity is very high close to $1000 \text{ W/K}^4.m^2$

at those temperatures as well. The sleeve will be coated with 1 mm copper due to its high conductivity and low resistivity at low temperature. Due the complexity of the project, multiple conduction and radiation thermal simulations and hand calculations were made to verify the temperature distribution inside the beam tube and its effect of the project.

III Scope & Objective

This project is consisting of three stages. The first stage is functionally modeling and connecting the bellow parts. The bellow parts are designed in 2D designs that must be integrated into the 3D designs and connected for further analysis. The second part is applying thermal analysis on the bellow assembly based on 0.5 W/m input flux on the bellow inner surface. A 0.5 W/m is the flux generated when the beamline excites the copper sleeve inside the bellow, which free the electors on the copper surface. This is the highest heating expected should the copper temperature stay below 25K. The Second part is applying radiation analysis to see if radiation transfer will help at these temperatures. The third part is conducting a conduction analysis and verify the results of the thermal simulation with the Engineering calculation to verify the thermal simulation of the below assembly is as expected. Part of the thermal analysis is applying a hand calculation with a comparison with the computer simulation for accuracy. Simplifying the design, adjusting the bellow thickness, and adding coating copper sleeve for more accurate simulation. The target simulation result is to make the temperature inside the bellow assembly below 25K for the project to work properly.

IV Methods & Process

The first part of this project is to combine the bellow assembly parts from the 2D drawing that was designed in the previous years into 3D designs. After gathering all the drawings and reconstructing the parts piece by piece, obstacles start to manifest in the form of design changes and dimensions incompatibility. Some of these designs were unclear and required more details. Some dimensions were missing and had to be looked up in other parts. Due to these complications, the parts designing time was a little longer than expected. After designing the parts, the next step is to specify the material

used in the designs. These materials were stainless steel 316L and copper 1000. The physical material properties were defined in neither the simulation nor the 3D designing program, which required manual input to the physical properties of the material. The exact physical properties required an online extensive search in multiple website sources to ensure the accuracy of the numbers at cryogenic temperatures where they are very different. Once the material properties were determined, manual input of the numbers that are related to the stress, strain, thermal conductivity, resistivity, elasticity, and emissivity was inputted into the system.

When the design process was completed. The assembly process started, which included functionally combining all parts into one bellow tube. This process included the material assigning to each part with its specific material. Most of the bellow made of stainless steel 316 and only the inner face of the copper non-magnetic stainless steel coated with a layer of copper 1000. The copper coating must not exceed 2 mm thickness as per the physicist, or it will affect the magnetic field. The copper coating applied to the sleeve inside the bellow assembly (Figure 2,3 Appendix A). The assembly of the parts has some challenges due to the small gaps between the parts. After the assembly process was completed the bellow tube was ready for the thermal radiation analysis (Figure 4, 5 Appendix A).

The next step is to apply thermal analysis on the bellow tube assembly. The first thermal simulation is radiation analysis. By determining the temperature of the copper sleeve from the heat flux generated from the beam-line due to beam heating it is seen whether the copper is still in its high electrical conductivity temperature. For radiation calculations, the tube was modified to be in the form of concentric cylinders. The purpose of this calculation is to determine the flux and the heat generated on the outer surface of the beam tube, which is assumed to be at 5K. This calculation defined the flux the inner surface to the outer magnet assembly surface as Q_{12} . The emissivity of the stainless steel for both surfaces defined as $\epsilon_1 = \epsilon_2 = 0.32$. The tube outer surface of the bellow was inside a the larger tube magnet assembly surface. The temperature of the big tube was assumed 10K. The flux goal was estimated at $0.5W/m$ as per the physicists. Stefan-Boltzmann constant $\sigma = 6.78E - 8W/m^2.K^4$. Using this flux to calculate the temperature of the outer surface of the beam tube. The area between the inner surface and the outer surface of the beam tube is determined by $A_1 = 2\pi r_1 L$ where r_1 is the radius of the inner surface and L is the length of the tube. $T_2=5K$, by using

Equation (1) we determine that the temperature inside the inner surface of the tube is between $T_1 = 174 - 128K$ with a flux between $0.5 - 1W/m$.

$$Q_{12} = \frac{\sigma A_1(T_1^4 - T_2^4)}{\frac{1}{\epsilon_1} + \frac{A_1}{A_2}(\frac{1}{\epsilon_2} - 1)} \quad (1)$$

The more we spread outwards to the outer surface of the tunnel the less flux we get. For further verification of the results we determine the outer tube surface at $10K$ and calculated the flux, then use this flux to calculate the inner temperature again by readjusting the radius. The hand calculation was a little different than the simulation due to the changes made (Figure 6,7 Appendix A).

The final step in the thermal analysis is the conduction simulation. This process is to measure the heat on the inner surface of the copper sleeve generated from $0.5W/m$ flux. In this process, the conductivity of the copper adjusted from $410W/m^2.K^4$ to a better copper conductivity of $1000W/m^2.k^4$. The stainless steel conductivity also adjusted to $50W/m^2.k^4$. However, before the conductivity simulation applied, a hand calculation on a test design tube with the same material and the same length applied for calculation verification. The $0.5W/m$ adjusted to $2.6W/m^2$ by dividing over the diameter for the bellow tube. The thickness of the copper in the computer simulation is different that the actual value which required a proportional change in the thermal conductivity constant. The difference in the test tube was not important as the purpose of this simulation is to test the accuracy of the result comparing to the hand calculation and then applying the same method on the bellow tube. The hand calculation starts by taking fiber from the test tube and treat it as a small box with a length of the tube . The calculation results were $238W/m^2$ and a temperature of $T_1 = 13.15K$ (Figure 8,9 Appendix A) . By using the flux from surface one to surface two Q_{12} , $T_2 = 5K$, $dx = 0.5m$ the length of the tube, which is equal to the distance from surface one to surface two, and K as the conductivity of the stainless steel. Using equation(2) we are able to determine $T_1 = 13.15K$ as a result of $238W/m^2$. These hand calculations were confirmed by the thermal simulation on the test tube design(Figure 10, Appendix A). The test of the simulation accuracy of the program proven reliable from this method.

$$Q_{12} = \frac{K(T_1 - T_2)}{dx} \quad (2)$$

After the accuracy test, the thickness of the coating copper sleeve determined by 0.075mm . However, the system cannot mesh the bellow with a thickness less than 1mm , so 1mm thickness added on the sleeve. The calculation adjusted to compensate the added thickness. Since the thickness changes so the calculation adjusted to calculate the flux and $T - 1$ (Figure 11, Appendix A). The same calculation made on 0.075mm without the adjustment in the calculation and the temperature was the same $T_1 = 5.0012\text{K}$. The thermal analysis indicate that the bellow thermal conduction simulation $T_1 = 6.376\text{K}$ (Figure 12, Appendix A). The slightly difference is due to the difference in thickness and shapes across the parts of the bellow assembly.

V Conclusion

The thermal analysis revealed that the radiation results from the beam-line excited the copper sleeve, has no insignificant effect on the temperature change. The calculation of the Engineers and the physicists confirmed the hand calculation analysis and the simulation results. This calculation confirmed that to have a 0.5 W/m flux, the temperature difference resulting from only radiation has to be significantly higher. The temperature difference has to exceed 150K , so it would affect the bellow shield to generate a flux of 0.5 W/m . The conduction simulation has a direct effect on the bellow shield as it would affect the shield more than the radiation. By applying a flux 2.6w/m^2 which is equivalent of 0.5w/m , which is calculated due to the coating thickness of the copper sleeve, and 5K on the outside of the bellow as an effect of liquid helium. The temperature would increase to 13.6K based on our copper conduction of $410\text{W/m}^2.\text{K}^4$. The high temperature generated from the process was alerting because the copper conductivity is very high at low temperatures, but when the temperature increases the resistivity of the copper increases. To verify the results of the calculation and the simulation, a test tube designed with the exact dimensions and thickness as the bellow design. The tube designed to test the thermal conduction analysis. The tube designed to be 0.5m simple cylinder made of stainless steel and due to the simulation limitation 1 mm thickness of copper coating instead of 0.075 mm . The hand calculation made on the 1 mm with consideration of the change in thickness, but the temperature was relatively high above 10K and we need it as low as possible. Switching to a better copper material with a higher conductivity of $1000\text{W/m}^2.\text{K}^4$. The temperature from simulation decreased

to $6.3K$ which is very good for the project. A graph generated to determine the relationship between the temperature and the distance from the heat source(Figure 1).

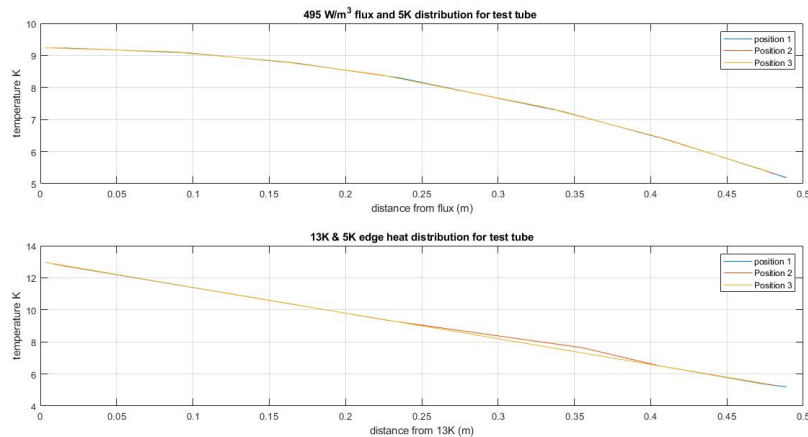


Figure 1: Tube test design for heat and flux distribution over the surface area Top graph Indicate case 1 by applying internal heat of $495W/m^3$ and $5K$ temperature from one end measure the temperature across the tube, bottom graph represent case 2 by applying $13K$ and $5K$ from both sides of the tube and measure the change in temperature over the length of the tube

This graph indicates that the temperature distribution decreased as it goes away from the heat source. The applying temperature indicated that the flux over the volume is fixed across the test tube. By reversing the process, the temperature would increase slightly to reach $6.3K$, which indicated that the simulation accuracy verified. The exact simulation on the bellow would indicate that the bellow would increase in temperature if there is $0.5W/m$ applying on it. The temperature would increase slightly to $6.7K$ due to the very high conductivity of the copper coating layer. When the hand calculation made to $1mm$ taking on consideration the increase in thickness in the equation, and comparing this result with the real thickness it would match the temperature of $6.7K$. The results of this project proved that the simulation verified the hand calculation made by the physicist and engineers for conduction and radiation heat transfer distribution. The project would work properly due to the high conductivity of the copper that would prevent the temperature from increasing.

VI Appendix A

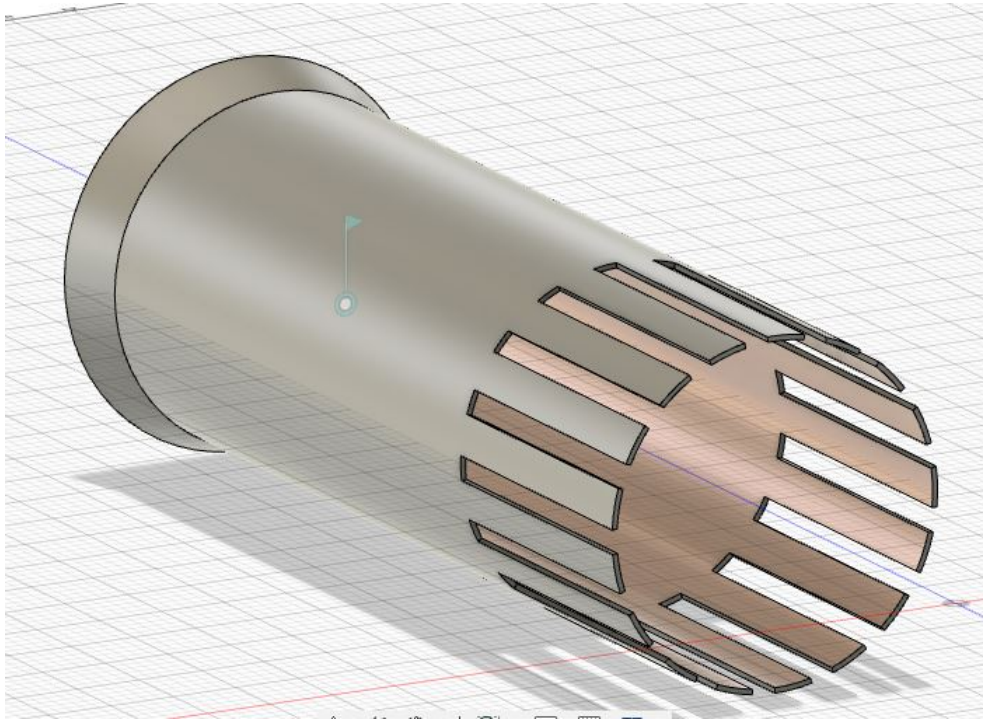


Figure 2: Front view of Copper coating on inner surface of the sleeve

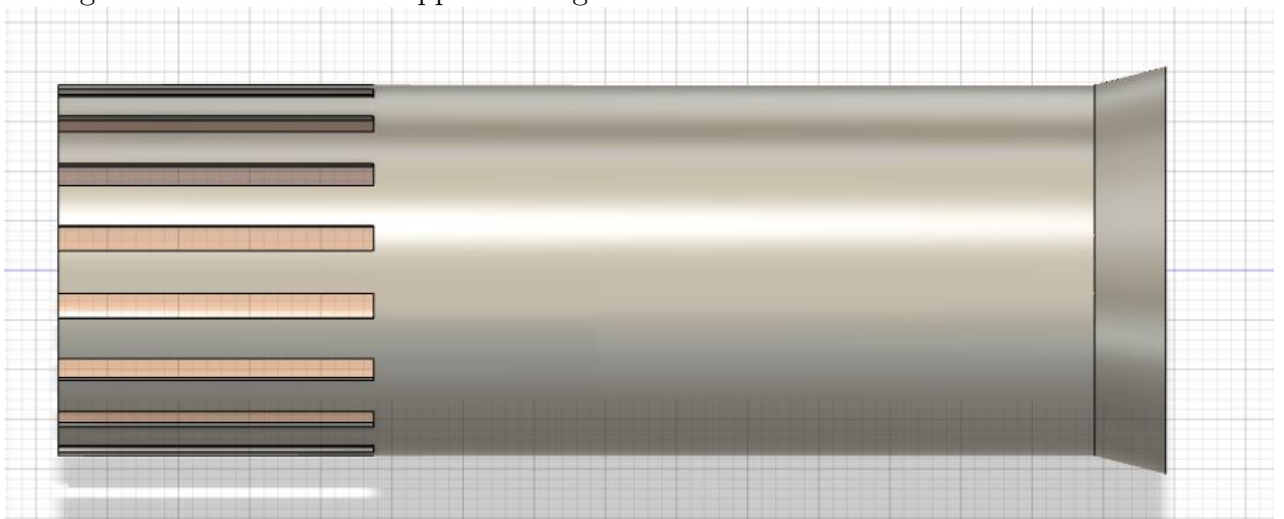


Figure 3: Side view of copper coating on inner surface of the sleeve

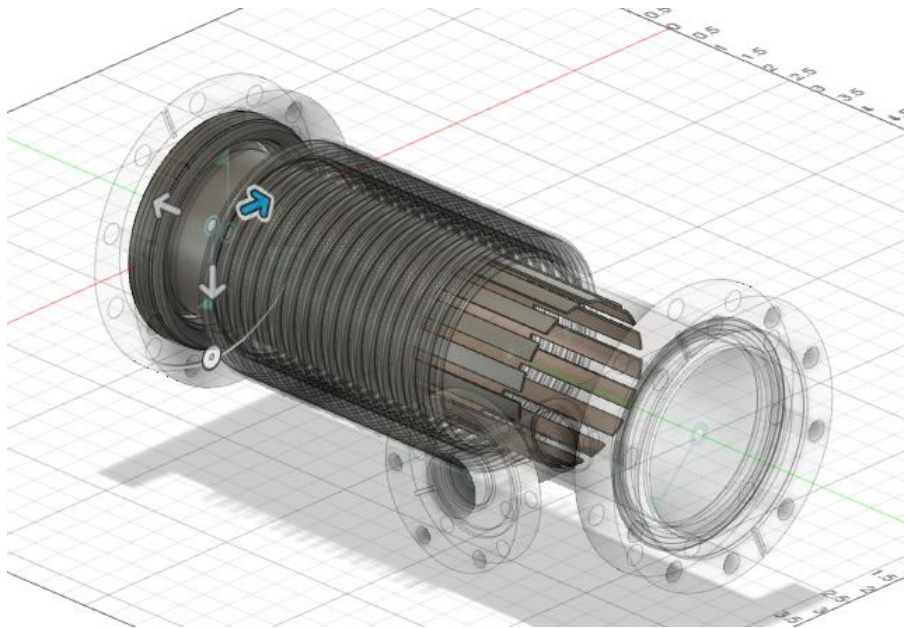


Figure 4: Complete bellow tube with inside component

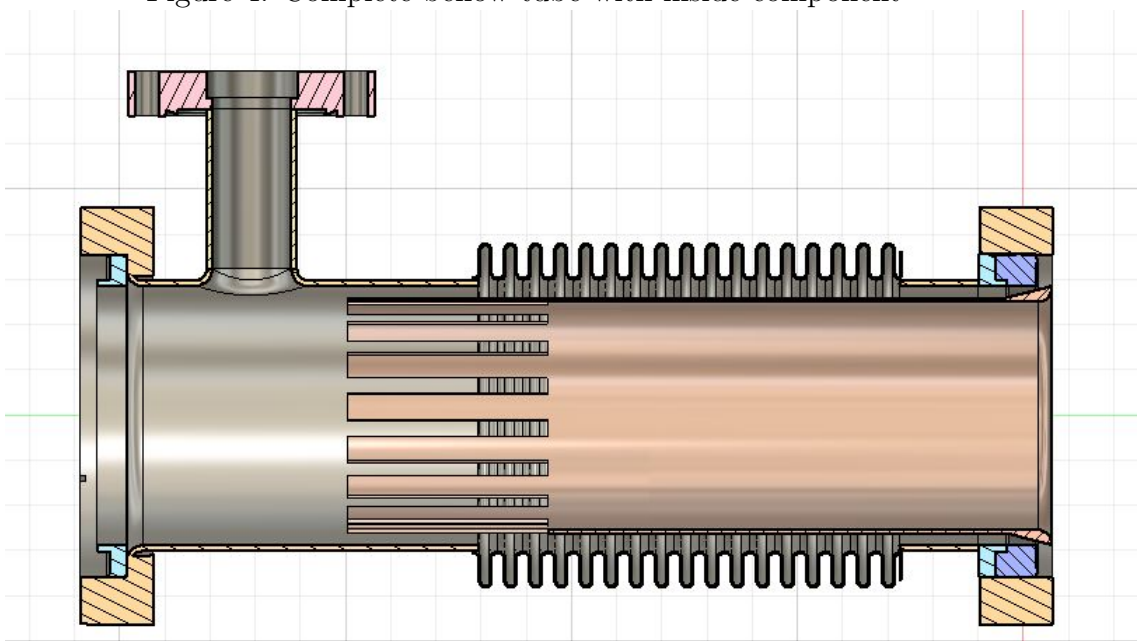


Figure 5: Cross sectional view of the bellow tube

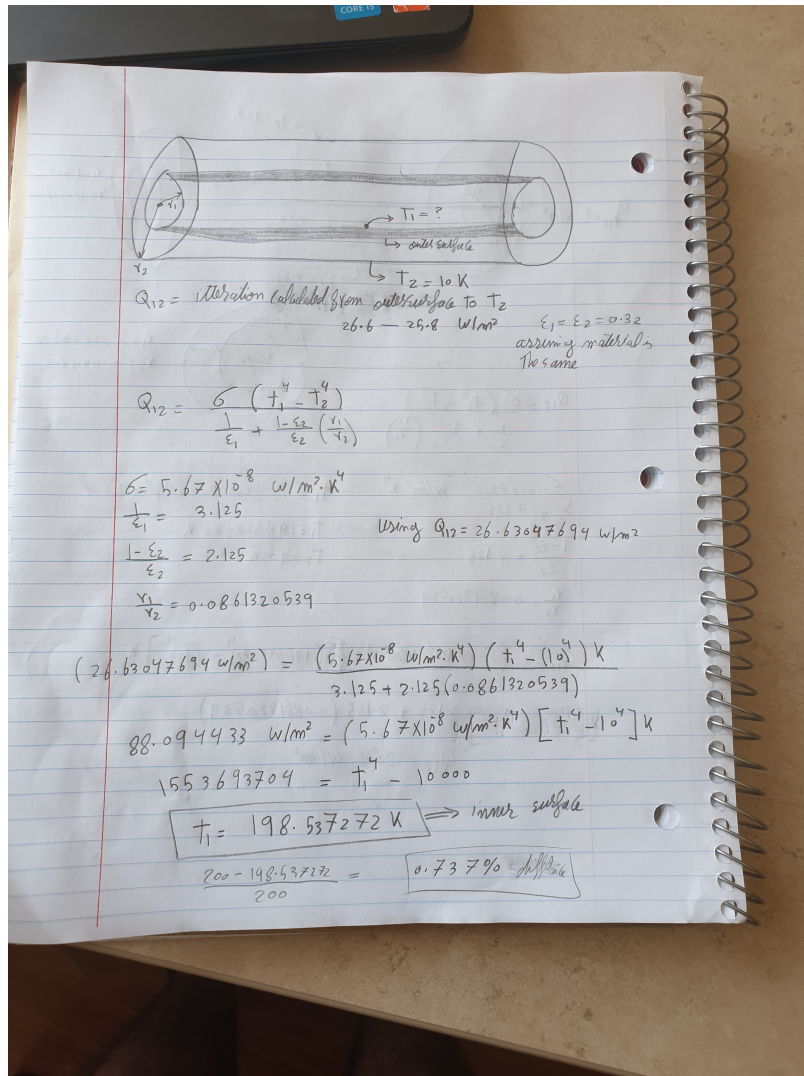


Figure 6: Radiation hand calculation for inner surface temperature of the bellow tube

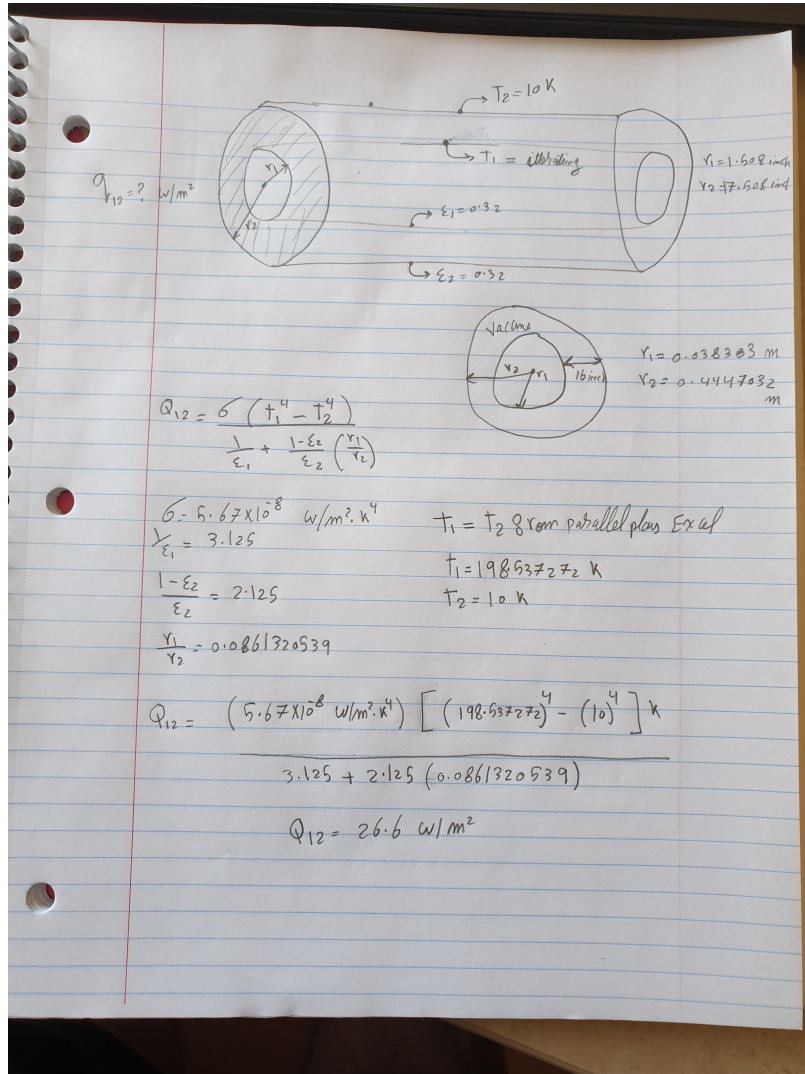


Figure 7: Radiation hand calculation for the flux of bellow tube based on outer surface 10K

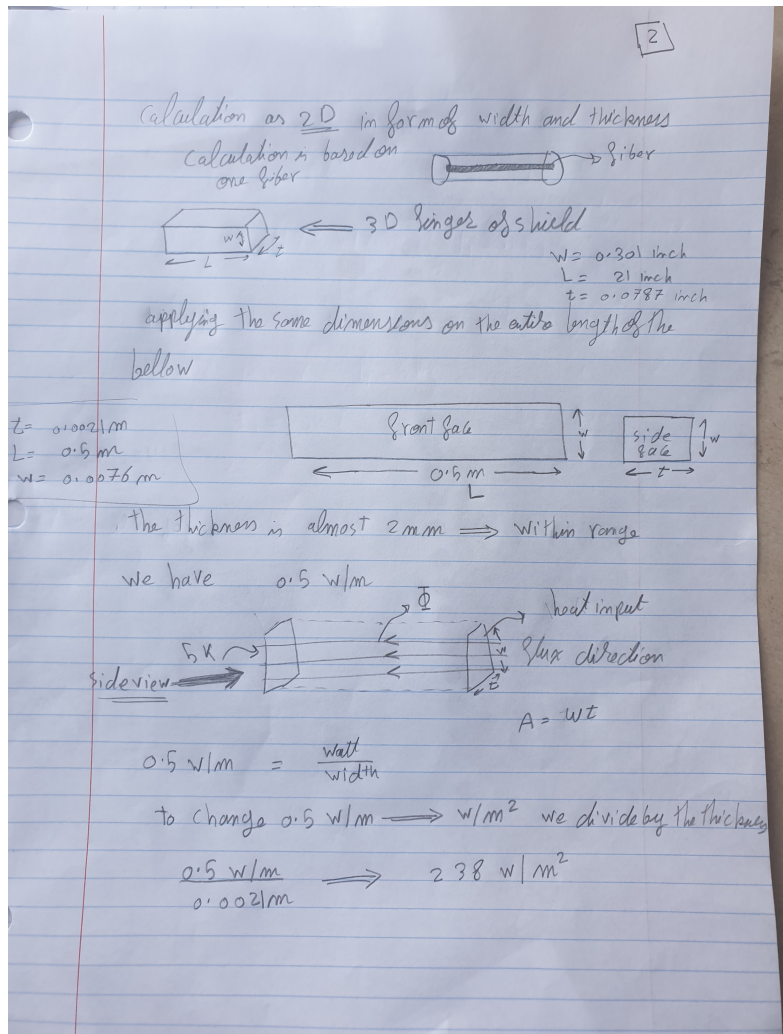


Figure 8: Conduction hand calculation of fiber test tube with length of 0.5 m and thickness of 2 mm

3

using 2D equation for heat transfer
and treating the surfaces as wall problem

$$q = \frac{k (T_1 - T_2)}{dx}$$

$dx = \text{distance between the 2 surfaces (side view)}$

$$238 \text{ w/m}^2 = \frac{(14.6 \text{ w/k}\cdot\text{m}) (T_1 - 5\text{K})}{0.5 \text{ m}}$$

$$119 \text{ w/m} = (14.6 \text{ w/k}\cdot\text{m}) (T_1 - 5\text{K})$$

$$T_1 - 5\text{K} = 8.2 \text{ K}$$

$T_2 = 13.15\text{K}$

Figure 9: Conduction hand calculation for inner surface of test tube 13.15K

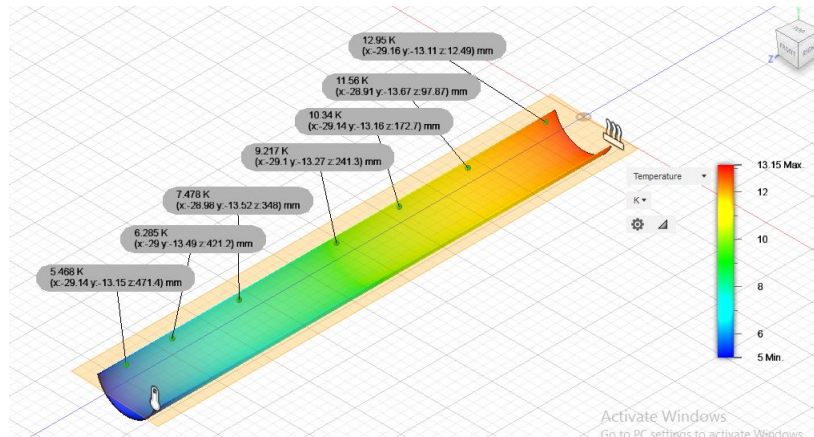


Figure 10: Conduction test tube simulation from $238\text{W}/\text{m}^2$

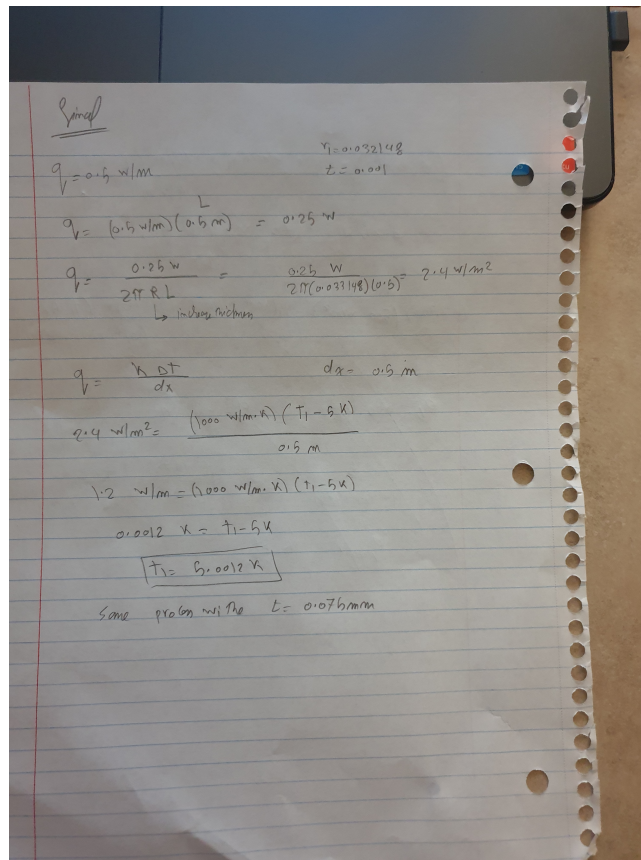


Figure 11: Hand calculation for 1mm copper coating flux and temperature

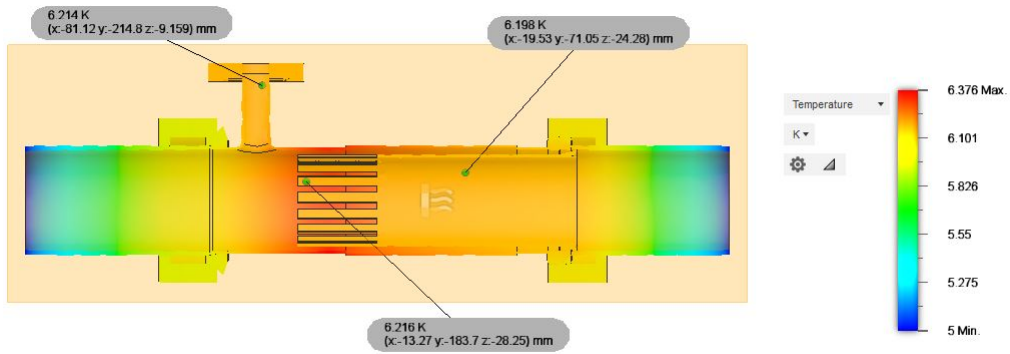


Figure 12: Conduction Thermal simulation on bellow tube due to $2.5W/m^2$ and $5K$ from the edges

Development of a novel algorithm for RSA factorization based upon algorithmic entropy reduction in sequenced binary quadratic forms (AERISBQ).

Alpha Bah, Department of Electrical Engineering, Hostos Community College, Bronx, NY, 10451

Emma Ryan, Department of Biology, Adelphi University, Garden City, NY, 11530

David Biersach, Department of Information Technology, Brookhaven National Laboratory, Upton, NY, 11973

Abstract

A quantum algorithm published in 1994 by Peter Shor can break the RSA encryption scheme used to secure sensitive information sent over the public Internet. However, even 26 years after the initial discovery, it is believed that a quantum computer powerful enough to implement Shor's algorithm and break RSA encryption cannot be constructed using even the most cutting-edge technology. However, if someone were to find an efficient way to factor exceptionally large composite numbers, then all electronic commerce over the Internet would grind to a halt, as nothing would be secure. The algorithm under investigation is the Algorithmic Entropy Reduction in Sequenced Binary Quadratic forms (AERISBQ). Unlike traditional factoring algorithms based upon modular forms, this approach seeks to restore the information lost during the original multiplication of the two primes that generate that RSA composite. We worked manually through the four steps of the AERISBQ and during my project with the existing AERISBQ algorithm implemented an algorithm in the programming language Python using a classical (procedural/imperative) approach. This research problem has an enormous social significance, and crucial military applications as well. Understanding how the AERISBQ algorithm performs on a quantum computer may help encryption researchers develop a stronger algorithm than RSA, to continue to keep the internet safe from hackers.

I. Introduction

Since decades, the game of primes factorization has greatly evolved. In 1970, it became hardly possible to factor a 20-digit number. Ten years later, the Billhart-Morrison continued factoring algorithm made easy factoring a 50-digit number in 1980. In 1990, Carl Pomerance's quadratic sieve factoring algorithm factored a 116 digits number. The quadratic sieve method had factored the 126-digits RSA challenge number that was believed to take 40 quadrillion years to factor. With all the success of the quadratic sieve method, the Pollard's number field sieve showed more efficiency in 1996 than the quadratic sieve method. Primes factorization becomes extremely hard as the bit length of the number N becomes important. That is due to the entropy gained during the original multiplication because multiplication is a lossy compression.

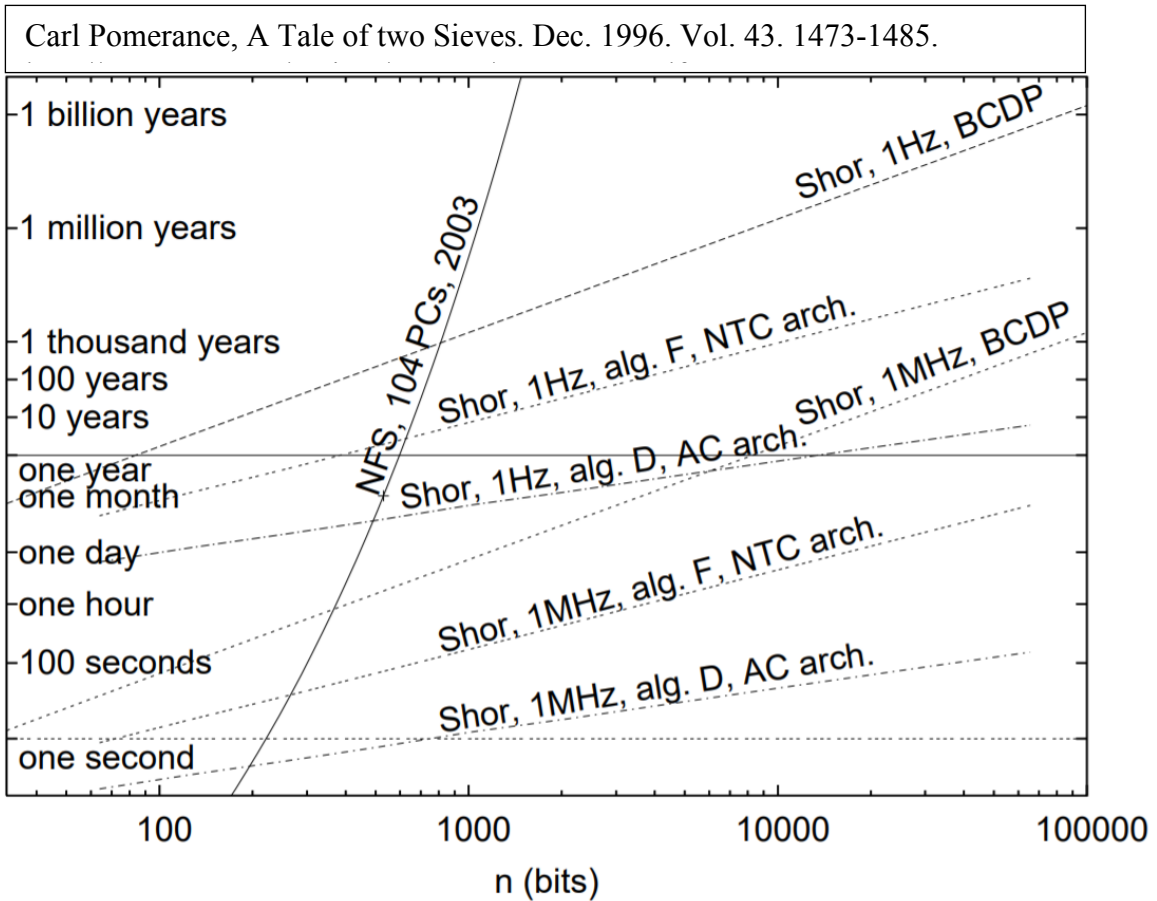


Fig. 1. Showed the bit length of the number N versus the time required to factor N

The RSA encryption uses a public (e, n) key to encrypt the original message “m” into a cyphertext “c” and uses a private key (d) to decrypt the cyphertext “c” into the original message “m”.



The RSA strength lies in the powerlessness of humans to factor the modulo N into its original primes p and q which is a good thing. But as scientists, we ask ourselves what if someone overcome this powerless and become able to factor the RSA composites N . This concern led us to think about investigating RSA weaknesses to improve it or find an alternative of the RSA.

The AERISBQ under investigation in this research uses a different approach than the traditional known algorithms. It aims to reduce the entropy gained during the multiplication of the two primes. It is based upon the factorization of the two primes using only one bit at a time. Currently, the AERISBQ algorithm has four steps that their main goals are – trivially reject invalid BQF, or reduce the value of N .

II. Method

In the AERISBQ method, the binary quadratic form was used to represent the factors p and q of the RSA composite N where the two unknown variables are x and y .

$$[A_l x + B_l + r][A_l y + C_l + s] = N \quad (1)$$

Where:

- $A_l = 2^{a+l}$ (a is the round number)
- $B_l, C_l \in \{0, 2^a\}$

A. Step 1: Trivial Rejection (TR)

In step 1, we expanded the binary representation of the product of p and q in Eq (1). All constants were moved to the right-hand side of the equation. Then the right-hand side was divided by the coefficient A. The BQF is valid only if the right-hand side is divisible by A. If so, we moved to the next step with that BQF; Otherwise, that BQF is trivially rejected.

$$A_1^2xy + A_1C_1x + A_1sx + A_1B_1y + B_1C_1 + B_1s + A_1r + C_1r + rs = N$$
$$A_1xy + (C_1 + s)x + (B_1 + r)y = \left[\frac{N - rs - B_1C_1 - B_1s - C_1r}{A_1} \right] \quad (2)$$

The validity of the current BQF depends on the divisibility of the right-hand side of Eq. (2). If the division of the numerator by the denominator on the right-hand side yields to an integer, we proceed to the next step with this BQF where:

- $A_1 = A_2$
- $C_1 + s = B_2$
- $B_1 + r = C_2$
- $n_2 = \left[\frac{N - rs - B_1C_1 - B_1s - C_1r}{A_1} \right]$

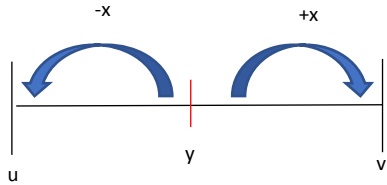
A_2, B_2, C_2 and n_2 are the coefficients in step 2. The main goal of step 1 is to reject invalid BQFs.

B. Step 2: uv-substitution

The *uv-substitution* aims to get rid of the xy non-linear term. Considering y as the origin or the midpoint, the left side of y would be $-x$ represented by u while the right side of y is $+x$ represented by v .

Then x would be the half distance between the two ends u and v , and y would be the average between the two ends u and v .

$$A_2xy + B_2x + C_2y = n_2 \quad (3)$$



$$x = \frac{v-u}{2}$$

half distance

$$y = \frac{v+u}{2}$$

average of u & v

In Eq. (3), x and y were replaced by their values, thus Eq. (3) yield to the following equation. In addition, for x and y to be integers, u and v must have the same parity.

$$-A_2u^2 + A_2v^2 - 2(B_2 - C_2)u + 2(B_2 + C_2)v = 4n_2$$

- $A_3 = A_2$
- $B_3 = A_2$
- $C_3 = -2(B_2 + C_2)$
- $D_3 = 2(B_2 + C_2)$
- $n_3 = 4n_2$

$$A_3u^2 + B_3v^2 + C_3u + D_3v = n_3 \quad (4)$$

C. Step 3: l -substitution

Step 3 is the l -substitution where we tried to get rid of the v^2 term. Knowing that u and v have the same parity, we can set:

$$u-v = 2l \quad \text{therefore } u = v+2l$$

Substituting u in Eq. (4) by $v+2l$, Eq. (4) becomes

$$4A_3l^2 - 4A_3lv + [A_3 + B_3]v^2 - 2C_3l + [C_3 + D_3]v = n_3 \quad (5)$$

We proceed to another change of variable:

$$x = l, \quad y = v$$

Hence, Eq. (5) becomes:

$$4A_3x^2 - 4A_3xy + [A_3 + B_3]v^2 - 2C_3l + [C_3 + D_3]y = n_3$$

But $B_3 = -A_3$ so $A_3 + B_3 = 0$, thus the v^2 term disappears.

Finally Eq. (5) becomes:

$$4A_3x^2 - 4A_3xy - 2C_3x + [C_3 + D_3]y = n_3 \quad (5)$$

- $A_4 = 4A_3$
- $B_4 = -4A_3$
- $C_4 = -2C_3$
- $D_4 = C_3 + D_3$

D. Step 4: Reduction

Note that Eq. (6) below obtained at step 3 does not have the term y^2 , therefore, we can move all x terms to the right-hand side and solve for y .

$$A_4x^2 + B_4xy - C_4x + D_4y = n_3 \quad (6)$$

$$y = \frac{n^4 - A^4x^2 - C^4x}{B^4x + D^4} \quad (7)$$

E. Step 5: Reduction (Future study)

III. Results and discussions:

After running the AERISBQ algorithm using the last two hundred of the first three hundred primes, we studied the efficiency of the AERISBQ by dividing the bit length of the number N by the bit length of the number of BQF, the outcome showed that the AERISBQ has higher efficiency when the binary expansion of p or q has a contiguous of “0s” digits close to the Less Significant Bit (LSB) and a contiguous of “1s” close to the Most Significant bit (MSB). On the other hand, the lowest efficiency of our AERISBQ were noticed when p or q has a contiguous of “0s” close to the MSB and a contiguous of “1s” close to the LSB.

Table 1 and 2 show these two categories of numbers:

Table was obtained from Dr. Biersach AERISBQ code implementation

N	p	q	# of BQFs	Efficiency	p Base2	q Base2
1528003	769	1987	130	2.9208	1100000001	11111000011
1631419	1019	1601	133	2.92067	1111111011	11001000001
1521851	769	1979	130	2.91997	1100000001	11110111011
1500319	769	1951	130	2.91705	1100000001	11110011111
1634621	1021	1601	134	2.91664	1111111101	11001000001
1924891	1019	1889	142	2.91574	1111111011	11101100001
1621813	1013	1601	134	2.91504	1111110101	11001000001
1586591	991	1601	133	2.91498	1111011111	11001000001
1484939	769	1931	130	2.91494	1100000001	11110001011
1517237	769	1973	131	2.9148	1100000001	11110110101
1838491	929	1979	140	2.91476	1110100001	11110111011
1573783	983	1601	133	2.91332	1111010111	11001000001
1466483	769	1907	130	2.91237	1100000001	11101110011
1498781	769	1949	131	2.9123	1100000001	11110011101
1928669	1021	1889	143	2.91205	1111111101	11101100001
1812479	929	1951	140	2.91188	1110100001	11110011111
1596197	997	1601	134	2.91179	1111100101	11001000001
1554571	971	1601	133	2.91082	1111001011	11001000001
1486477	769	1933	131	2.91061	1100000001	11110001101
1913557	1013	1889	143	2.91047	1111110101	11101100001

Table 1. Depicts Ns that could be easily break by AERISBQ

p or q	Binary Expansion
1051	10000011011
1087	10000111111
1039	10000001111
1103	10001001111
1151	10001111111
1063	10000100111
1069	10000101101
1117	10001011101
1031	10000000111
1231	10011001111

Table was obtained from Dr. Biersach
AERISBQ code implementation

Table 1. Shows the factors p or q hard to break by the AERISBQ

IV. Conclusion

As a special purpose factoring algorithm, AERISBQ efficiency is more related to the nature of the factor p and q that made N than merely the bit length of N . A weak N is made of factors p and q that have either a large contiguous series of “0s” digits in the right half of their binary representation (close to the LSB) or have a large contiguous series of “1s” digits in the left half of their binary representation (close to the MSB). This is a newly discovered qualification for proper choices of the random primes that are multiplied to generate the RSA composite N and hence the public and private key used for encryption.

V. Acknowledgments:

I am incredibly grateful to my mentor Dr. David Biersach for his expertise professionalism and patience, who even though we cannot meet in person, managed to accommodate us. He has been always available to us and very supportive, and most

importantly, Dr. Biersach introduced us to one of the most interesting current topics of study. I would like also to thank my partner Emma Ryan, who provided me tremendous help. Also, I want to thank the Brookhaven National Laboratory for their incredible work. This project was supported in part by the U.S. Department of Energy, Office of Science, Office of Workforce Development for Teachers and Scientists (WDTS) under the Community College Internship Program (CCI)

VI. References:

[1] Jongmin Baek, And Deopurkar, Katherine Redfield. Points on Conics Modulo p.

<https://cs.stanford.edu/people/jbaek/18.821.paper3.pdf>

[2] Carl Pomerance, A Tale of two Sieves. Dec. 1996. Vol. 43. 1473-1485.

<http://www.ams.org/notices/199612/pomerance.pdf>

[3] Rodney M. Van, Kohei Itoh, Thaddeus Ladd, Architecture-Dependent Execution Time of Shor's Algorithm. Mar. 2005.

[4] Gordon Pall. Discriminantal Divisors of Binary Quadratic Forms. Jan 1969.

Design Studies for the Laser Calibration System for the sPHENIX Time Projection Chamber

Salvatore Baldinucci ¹, Bob Azmoun ², Craig Woody ²
Physics Department, Stony Brook University, Stony Brook, NY 11794 ¹
Physics Department, Brookhaven National Laboratory, Upton, NY 11973 ²
(Dated: August 19, 2020)

Using the ray tracing program TracePro, and the CAD software Inventor, a model of the sPHENIX Time Projection Chamber (TPC) involving the inner/outer field cages, central membrane, and photocathode strips was created. Within TracePro, the proposed laser calibration system was implemented with its diffuse and straight beam lasers. The light from the diffuse lasers incident upon photocathode strips on the central membrane was analyzed. It was found that a 15 percent decrease in the width of the central strips will ensure a similar photon yield per unit length for different strips. The peak irradiance from the straight beam laser was analyzed at various angles/distances within the TPC volume. Simulations found there was little to no effect on peak irradiance for angles less than 60 degrees entering the volume, while the ratio of peak irradiance between distances 0.001m and 1m away from the exit of the light pipe never reached above 2.5 inside the volume.

I. INTRODUCTION

The sPHENIX experiment at the Relativistic Heavy Ion Collider (RHIC) at Brookhaven National Lab (BNL) will have a Time Projection Chamber as its main particle tracking detector. A novel laser calibration system is currently being developed for the TPC and the objective here is to simulate the performance of this system under different configurations.

In particular, a diffuse laser source will be simulated to determine the number of expected photons on an array of aluminum photocathode strips placed on the central membrane. The signals produced on the strips will be used to calibrate the TPC in the presence of space charge produced by the large number of ionizing particles in the detector. As the diffuse laser light will not be perfectly uniform on the central membrane; one must determine how to scale the size of photocathode strips in order to get similar photon yields per unit length from each strip.

The laser calibration system also involves a straight beam laser that produces lines of ionization to mimic infinite momentum particle tracks in the TPC volume at various angles. The laser beam ionizes trace organic materials in the gas via two photon absorption. The resulting ionization yield goes as the beam intensity squared. Therefore, one must also look at the beam profile/peak irradiance at various points within the volume to make sure there is enough intensity to ionize the impurities within the gas and the ionization yield at all points is matched to the dynamic range of the front end electronics. These questions involving the two different laser systems were investigated using the ray tracing program TracePro.

II. TRACEPRO

The software TracePro is a ray tracing program developed by Lambda Research Corporation for simulating optical systems. TracePro was an integral part of these simulations as we can visualize the light rays and generate irradiance maps at various surfaces. We were also able to include various surface and optical properties such as wavelength, spatial and angular profiles of the lasers, as well as surface coatings and the index of refraction for surfaces. This allowed us to create a much more accurate simulation of the laser calibration system.

III. METHOD

A. TPC Model

In order to see the effects of the lasers from the laser calibration system within the TPC, a model for the TPC must be created first as seen in FIG 1. This was done initially using the CAD software Inventor and later moved and finished in TracePro. First the inner and outer field cages were created with an inner diameter of the outer field cage of 60.2 in, and the outer diameter of the inner field cage of 17 in. Both with a length of 83.1 in. Then the central membrane was implemented directly in the middle of this length with a width of 0.22 in, to represent the 5.6mm honeycomb and the 8.9 micron thick Cu layer on both sides. Finally, the aluminum photocathode strips were placed 1 mm above the surface of the central membrane according to predetermined center locations and surface areas. The photocathode strips were replicated four times at angles of 20 degrees around the central membrane to represent more pad sectors and to

generate more data. All surfaces were made to be perfect absorbers to ensure we did not double count rays. Once this geometry was in place, studies involving the two types of lasers could be explored.

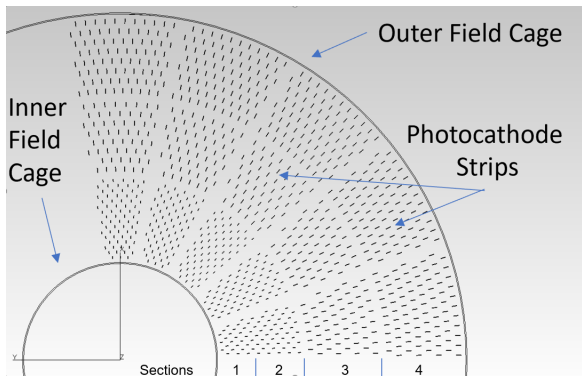


FIG. 1: TPC model with photocathode strips and sections for those strips.

B. Diffuse laser

The diffuse laser source used was coded in ROOT and transferred to TracePro. It consists of a Gaussian beam with a sigma of 1 cm on a focal plane 11 cm away convoluted with two diffusers. The process of integration into the TPC model involved replicating the laser source file twelve times, placing them 16 in radially outward from the center of the inner field cage, and applying a tilt angle of 15 degrees outwards. Once this was done, ray tracing of the source files with a total of 12 million rays were performed and the power per unit length on the photocathode strips was analyzed and compared to each other. Many configurations with different laser sources, tilts, and number of diffusers were analyzed as the laser calibration system design evolved.

C. Straight beam laser

The straight beam laser travels through an apparatus involving a beam energy monitor, beam shaping optics, and various steering mirrors as seen in FIG 2. This system, along with the grid source for the laser, was integrated into the TPC model in TracePro. Specifically, the center of the light pipe was placed 22.8 in radially outward from the center of the inner field cage while having it protrude 1.25 in into the TPC volume. We then looked at the laser beam coming out of the light pipe and into the TPC volume at angles between 0 and 60 degrees from the normal of the end of the light pipe. We analyzed the cross sectional peak irradiance at distances from 1 mm

to 1 m away from the exit of the light pipe and inside the TPC volume with these different angles using 10 mm x 10 mm thin surfaces.

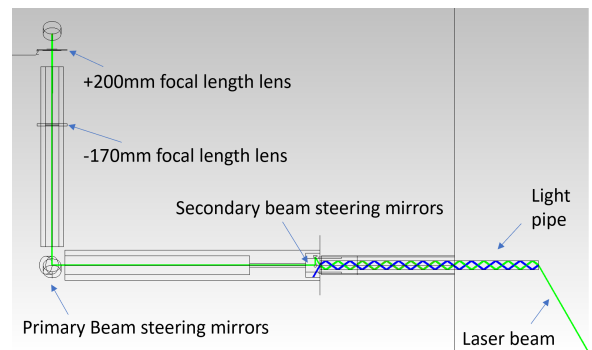


FIG. 2: Straight line laser entering the TPC volume at an angle of 60 degrees from the exit of the light pipe.

IV. SIMULATION RESULTS

A. Diffuse laser

Initial data for the power per individual strip showed a steep drop in power for the smaller length strips. After dividing each strip's incident power by their respective lengths, the distribution became much more uniform and seems to correlate with the light distribution upon the central membrane as shown in FIG 3.

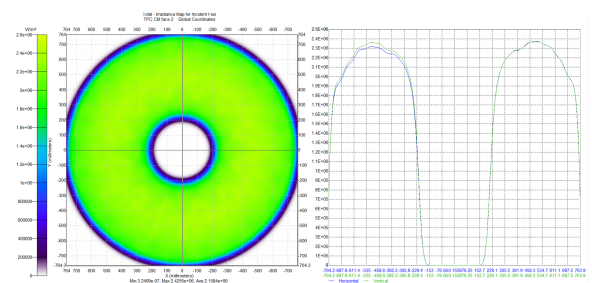


FIG. 3: Irradiance map of light from the diffuse laser on the central membrane

FIG. 4 shows the power per unit length for each of the strips going radially outward from the inner field cage. The average of each of the four sections of the pad plane (see Fig. 1) were taken and found to be similar within a factor of 1.3, with sections 2 and 3 (center most strips) having the highest averages of $2.34W/mm$ and $2.39W/mm$ respectively compared to sections 1 and 4 which had averages of $1.99W/mm$ and $2.04W/mm$ respectively. This tells us that the center most strips are receiving disproportionately more incident light than the

outer strips. This study of the incident rays on the photocathode strips was repeated with different strip sizes in order to find the optimal strip sizes that produced the most uniform power per unit length. Sections 2 and 3 of the strips were decreased in width from 1mm to 0.85mm. With this decrease in width, we were able to get the different sections of strips average power per unit length similar to within a factor of 1.027. Specifically, the averages for sections 2 and 3 fell to $1.99W/mm$ and $2.02W/mm$ respectively. FIG 5. shows the power per unit length for the modified strips. Since the photocath-

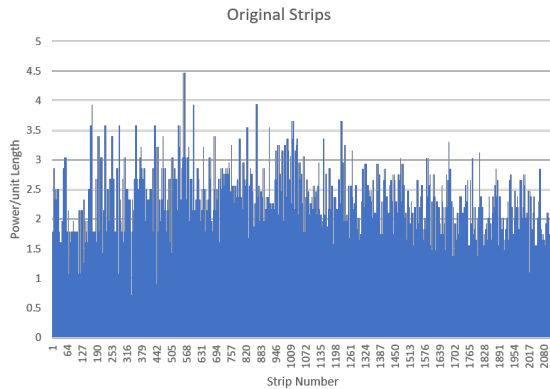


FIG. 4: Power per unit length of the original photocathode strips vs individual strip number going radially outward from the inner field cage.

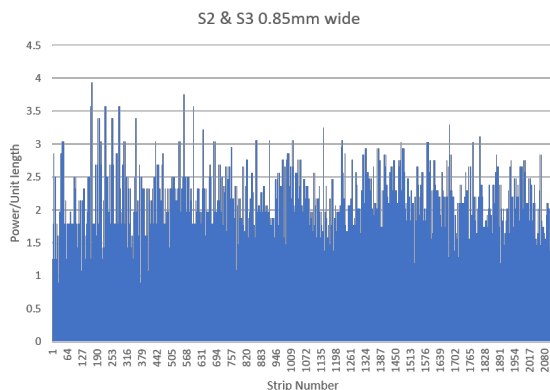


FIG. 5: Power per unit length of the modified photocathode strips vs individual strip number going radially outward from the inner field cage.

ode strips that are in the same row (the same distance radially from the inner field cage) tend to have similar photon yields, we averaged the power per unit length for each row to effectively increase the statistics per bin in the histograms. FIG 6. shows the average power per unit length for all 31 rows of the original strips. The higher yields are evident in this graph. FIG 7. shows the more uniform photon yields per unit length with the reduction

in width of rows 9 through 24.

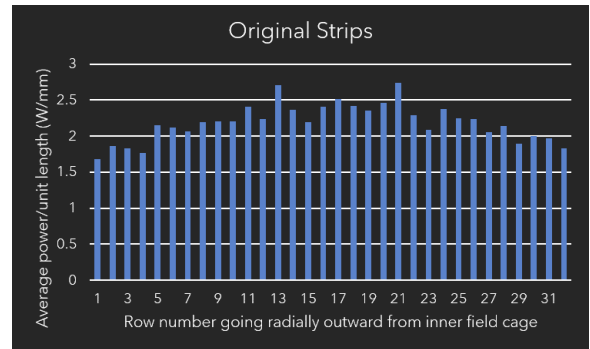


FIG. 6: average power per unit length of the original photocathode strips by row vs row number going radially outward from the inner field cage.

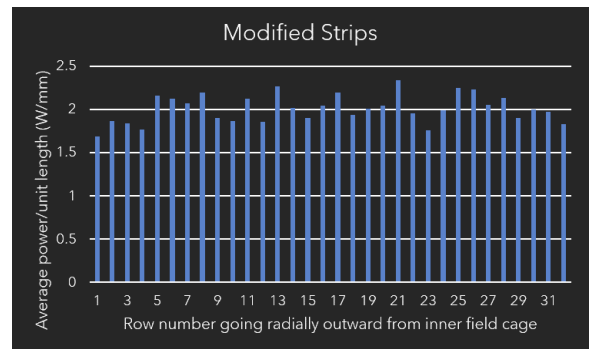


FIG. 7: average power per unit length of the modified photocathode strips by row vs row number going radially outward from the inner field cage.

B. Straight beam laser

The straight beam laser was simulated coming out of the light pipe at different angles. The peak irradiance did not seem to depend significantly on the angle, but extreme angles above 60 degrees ran into problems with the light pipe and a loss of rays. As the straight-line laser entered farther into the TPC volume the beam width continued to expand more due to the beam's 0.5 mrad full angle divergence, resulting in a smaller peak intensity. FIG 8 and 9 show a 15 and 50 degree exit from the light pipe and the peak irradiance at intervals of 5cm away. It should be noted that the laser hits the outer field cage at 0.65 m for the 50 degree case. The outer field cage was removed and the study continued to compare to the 15 degree case. It can be seen that the maximum peak irradiance occurs directly outside the light pipe while the minimum occurs at the farthest distance away. The ratio between these two were found to be 2.32 and 2.33 for the 15 and 50 degree case respectively. Similar results were

found for all angles between 0 and 60 degrees.

B. Straight beam laser

The beam profile from the straight-line laser source was found to have peak irradiances which varied within a factor of 2.5 for all angles and distances within the TPC volume tested. However, the angular profile of the beam seems quite important in determining the peak irradiance at different distances. While we tried to stay conservative with a 0.3 mrad half angle divergence, a change in this property of the laser significantly affects the final results. This study also revealed a discrepancy with the model used for the lenses in the beam shaping optics that simulated the beam waist inside the TPC volume which was later resolved by contacting the laser manufacturer. Further studies could explore moving the beam in all three dimensions within the volume and finalizing the angular profile of the beam to get a more accurate simulation.

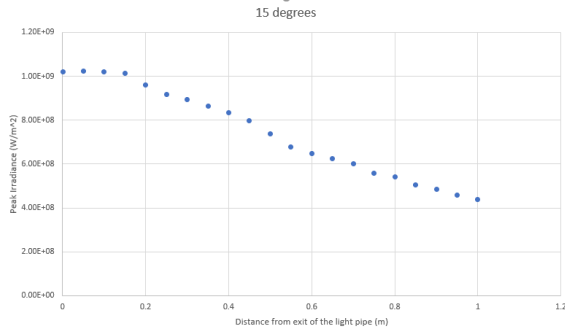


FIG. 8: Distance from the exit of the light pipe vs peak irradiance for a 15 degree exit from the normal of the light pipe.

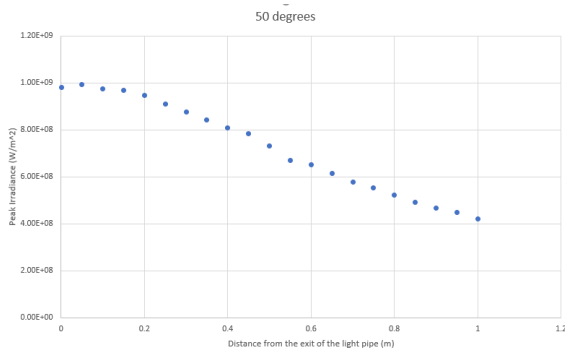


FIG. 9: Distance from the exit of the light pipe vs peak irradiance for a 50 degree exit from the normal of the light pipe.

V. DISCUSSION AND CONCLUSIONS

A. Diffuse laser

The photon yield per unit length of the aluminum photocathode strips on the central membrane was shown to be similar within a factor of 1.5 that is required by the dynamic range available in the front-end electronics for the different strip sections. Through this simulation, we were able to improve that factor to 1.027 with a 15 percent decrease in sections 2 and 3 of the strips. One could also improve this further by looking at smaller groups of strips and modify them accordingly to get even more uniformity among all the photocathode strips. However the illumination of these strips are heavily dependent upon the light distribution from the diffuse laser, which is still being investigated. This study should be repeated with the final and more accurate diffuse laser source.

VI. ACKNOWLEDGMENTS

I sincerely thank my mentors Bob Azmoun and Craig Woody for their willingness to help me throughout this project. Without their time, patience, and vast knowledge they bestowed upon me this would not have been possible. I'd also like to thank Kristina Finnelli and

Nikhil Kumar from Stony Brook University for their work on the laser calibration system as many of their designs were implemented in this project. This project was supported in part by the U.S. Department of Energy, Office of Science, Office of Workforce Development for Teachers and Scientists (WDTS) under the Science Undergraduate Laboratory Internships Program (SULI).

Effects of I-131 on the thyroid

Deonna Beard

Biology Dpt., Delaware State University, Dover, DE 19901

Susan Pepper

Nonproliferation and National Security Department, Brookhaven Nation Laboratory,
Upton, NY, 11973

Abstract:

This research project focuses on understanding how radioactive iodine mutates thyroid proto-oncogenes into oncogenes. As an intern at BNL, I have been collaborating with researchers who are familiar with radiation and others who are familiar with genetics to interpret this phenomenon. I have learned how to use BNL databases to conduct literature reviews. To understand the impact of I-131 on DNA, I have focused on the Chernobyl incident which dispersed 50 tons of radioactive hazardous material into the atmosphere; including I-131 which is said to have increased thyroid cancer in children.⁶ As for the experimental process, we will review published data associated with the genetic outcomes of this incident including the molecular analysis of exposed cells from the incident to comprehend how the DNA was altered. My hypothesis is that if one is exposed to the I-131 isotope and develops thyroid cancer, then there must be one specific mechanism responsible for this mutation. One such published discovery concludes that the homodimerization of the RET gene and PTC gene on chromosome 10, due to radioactive iodine, is primarily responsible for the link to thyroid cancer. Overall, this experience has allowed me to become more familiarized with BNL's research library and databases as I've done in-depth research like never before. This skill is necessary for me moving forward in my education and into graduate school. I've also cultivated the power of networking and communication as I have been able to discuss and utilize the expertise of scientists in the lab.

Introduction:

Genetic mutations acquire a few defining characteristics encompassing originality, copious random causes, and a plethora of outcomes.⁴ Upon further research, the mechanism behind how the genetic mutation of thyroid cancer arises from radiation exposure was targeted. More specifically, the I-131 isotope and how it meticulously mutates genetic material. The

effects of I-131 have been apparent in “the worst nuclear disaster in history,” known as Chernobyl. On April 26th, 1986 unauthorized testing at the Chernobyl Nuclear Power Plant in Ukraine resulted in an explosion on reactor four due to the system running on an insufficient amount of power. The outcome of the explosion spread 50 tons of mixed nuclear particles into the atmosphere spanning from; the 19 mile exclusion zone around where the incident had occurred, all throughout Belarus, and into parts of Russia.⁵ This event was one of three monumental disasters that shaped the way the public views radiation to this day (the others being Three Mile Island and Fukoshima). So why Chernobyl? Simple. The incident report depicts a clear link between the radiation released and a genetic mutation, unlike the other two disasters.⁶ This study focuses on what creates that link.



Figure 1A. The Chernobyl nuclear power plant incident

Methods & Materials:

For the research process, access to BNL resources has been useful for recovering reliable information, more specifically the research library has provided great insight. Google Scholar has been an additional source used to acquire published works to conduct literature reviews, which was the bulk of this project. Another method utilized has been discussions with experts from the lab in various fields to contribute to the focal topics.

Discussion:

Further dissecting Chernobyl, many first responders from Ukraine, Belarus, and parts of Russia died due to acute radiation poisoning. Of the 800,000 volunteers who tried to clean up the mess, somewhere between those 90,000-200,000 survivors acquired long term health implications from the incident. While at the break of the incident, the Soviet Union tried to downplay its severity. However, it is since reported that in high exposure zones, even plants and animals that inhabit the area suffered from reproductive loss.⁶

The relationship between I-131 consumption and thyroid complications was evident. Many children were reported to have ingested large amounts of I-131 through the consumption of contaminated cow milk in the first year following the incident.⁴ In the grand scheme of things, from 1996-2005 there were 6,848 cases reported of childhood thyroid cancer of those in affected areas.⁴ This number increased to 11,000 cases by 2016. While the I-131 isotope can even be used for thyroid treatment at the appropriate dosage, the amount that some 5,000,000 residents were exposed to was far beyond the level the body can tolerate in such a short period of time.⁵ In the focus of this study, excess radioactive iodine collected in the thyroid is responsible for converting normal functioning cells into cancerous ones.

Genetic mutations can be categorized by the type of cell they mutate. If they occur in germ cells this results in heritable changes. On the other hand, if they occur in somatic cells this results in cancer. The excess I-131 naturally deposits into the thyroid because that's where it's typically absorbed. However, while the oncogenesis of these cells does not result in apoptosis

(cell death), it does alter the blueprint of the cell, essentially changing its DNA and normal function.

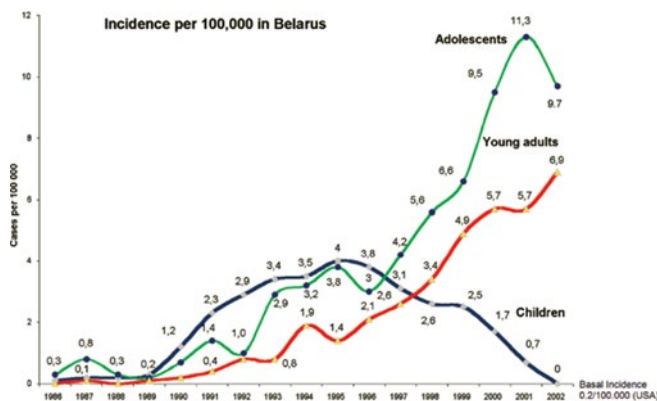


Figure 1B. Graph depicting rise in thyroid cancer among affected areas

Results:

Additionally, upon analyzing incident reports, published data, and deep researching, the mechanism was made clear. The driver mutation of thyroid cancer by I-131 occurs when the RET gene and a PTC1 or PTC3 gene come into contact on chromosome 10.² When the 3' end of the RET gene fuses with the 5' end of a PTC gene, it is referred to as homodimerization.¹ Although this is the primary cause observed, all mutations are random and other rearrangements are possible.³ For example, there is another type of gene mutation that we see occur less frequency, less than 10% of the time for these cases, which is a point mutation in the BRAF gene.¹ All things considered; the RET/PTC mutation is the main focus. This mutation results in an unscheduled expression of kinases in the thyroid, which normally play a role in the rate of cell division. This link between the two is clear because cancer is defined as uncontrolled and rapid cell division. The rate of naturally occurring child thyroid cancer is 1/1,000,000 while this

mutation is responsible for a 4,000 case spike directly linked to the fallout from Chernobyl.³

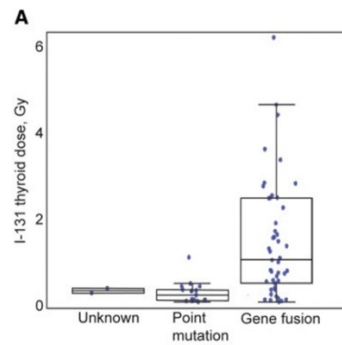


Figure 1C. Primary mechanism of this type of thyroid cancer is gene fusion

Conclusion:

Understanding the most common mechanism can allow for alternative treatment options. Other than conventional methods, knowing the two genes in question can allow treatment that targets either one of those genes, if detected in early stages. Not only can these findings provide a basis for dealing with radiation-based illnesses, but also can contribute to cancer treatment.

References:

1. Abend, M., Pfeiffer, R., Ruf, C., Hatch, M., Bogdanova, T., Tronko, M., . . . Brenner, A. (2012). Iodine-131 dose dependent gene expression in thyroid cancers and corresponding normal tissues following the Chernobyl accident. Retrieved August 19, 2020, from <https://www.ncbi.nlm.nih.gov/pmc/articles/PMC3405097/>
2. Suzuki, K., Saenko, V., Yamashita, S., & Mitsutake, N. (2019, September 2). Radiation-Induced Thyroid Cancers: Overview of Molecular Signatures. Retrieved July 19, 2020, from <https://www.ncbi.nlm.nih.gov/pmc/articles/PMC6770066/>
3. Efanov AA;Brenner AV;Bogdanova TI;Kelly LM;Liu P;Little MP;Wald AI;Hatch M;Zurnadzy LY;Nikiforova MN;Drozdovitch V;Leeman-Neill R;Mabuchi K;Tronko MD;Chanock SJ;Nikiforov YE;. (n.d.). Investigation of the Relationship Between Radiation Dose and Gene Mutations and Fusions in Post-Chernobyl Thyroid Cancer. Retrieved July 29, 2020, from <https://pubmed.ncbi.nlm.nih.gov/29165687/>
4. How Does Radiation Affect Humans. (2019, May). Retrieved July 7, 2020, from https://bioethicsarchive.georgetown.edu/achre/final/intro_9_5.html
5. Chernobyl: The true scale of the accident. (2018, December 27). Retrieved June/July, 2020, from <https://www.who.int/mediacentre/news/releases/2005/pr38/en/index1.html>
6. All That's Interesting. (2020, June 11). Inside The Post-Apocalyptic Yet Oddly Flourishing Chernobyl Of Today. Retrieved July 2, 2020, from <https://allthatsinteresting.com/chernobyl-today>

Pictures-

Figure 1A. . Lallanilla, M. (2019, June 20). Chernobyl: Facts About the Nuclear Disaster. Retrieved August 11, 2020, from <https://www.livescience.com/39961-chernobyl.html>

Figure 1B. . Reiners, C. (1970, January 01). Figure 1 from Radioactivity and thyroid cancer: Semantic Scholar. Retrieved August 11, 2020, from <https://www.semanticscholar.org/paper/Radioactivity-and-thyroid-cancer-Reiners/e749c55a27b7db55aa43b6dde4c03fa95d2d038b/figure/1>

Figure 1C. Efanov, Alexey A et al. "Investigation of the Relationship Between Radiation Dose and Gene Mutations and Fusions in Post-Chernobyl Thyroid Cancer." Journal of the National Cancer Institute vol. 110,4 (2018): 371-378. doi:10.1093/jnci/djx20

Acknowledgements:

Brookhaven National Laboratory Supplemental Undergraduate Research Program (SURP)

This project was supported in part by the Brookhaven National Laboratory (BNL), (Name of Department) , under the BNL Supplemental Undergraduate Research Program (SURP).

Developing a two-layer *HTS Conductor on Round Core (CORC)* superconducting coil design for quench studies

Michael Bianco

Mechanical Engineering Department, State University of New York at New Paltz, New Paltz, New York 12561

Michael Anerella & Jesse Schmalzle

Program Mentors, Superconducting Magnet Division, Brookhaven National Laboratory, Upton, NY 11973

Abstract

The Superconducting Magnet Division (SMD) at Brookhaven National Laboratory in partnership with the Magnet Design Program (MDP) needs a new two (2) layer four (4) turn coil design. The coil design is to be reminiscent of a racetrack with 4 turns in both layers. The turns are of different radii and centers of the turns are offset by a value. The goal of this research project is to demonstrate a proof of principle dipole with a new novel high temperature superconductor, “Conductor on Round Core cable (CORC)”. This design utilizes HTS CORC insert coils installed in the aperture of and powered in series with an existing Nb₃Sn Common coil dipole, which provides a 10 tesla background field for the CORC coils. In addition to designing the two (2) layer coil, various hardware were developed in order to hold the overall structure in place and aid in the coil winding process. This hardware included spacers which would lay in between coils, end and filler plates, and nonpermanent fasteners to fasten components together; all designs were done on Creo Parametric. With approval from MDP, the coil will be wound according to the desired geometry. The coil and its hardware will then be situated inside the common coil magnet for quench studies. A quench refers to the sudden loss of superconductivity when a coil’s temperature is raised above its critical temperature. In the superconducting state, the resistance of the magnet coil windings is zero and hence no energy is required to maintain current flow. If the coil temperature rises above the critical temperature (T_c), the windings suddenly develop a finite resistance. After the summer, it is the hope of MDP to obtain data regarding the new coil design through quench studies. In addition to the current carrying capability of the HTS, other important factors in the performance of the coil are the mechanical support from spacers and other hardware, as excessive motion may result in quenching due to frictional heat generated. As a result of this summer, I have added important design skills necessary for engineering. Additionally, I am familiar with Creo Parametric (CAD Program).

Introduction

A “superconductor” is a material that can conduct electricity or transport electrons from one atom to another with no resistance. Hence, no heat would be released from the material when it is cooled below its "critical temperature" (T_c), or the temperature at which the material becomes

superconductive. There are two types of superconductors; the low temperatures superconductor (LTS) and the high temperature superconductor (HTS). The most commonly used superconductor, niobium titanium (NbTi), begins behaving in this manner at temperatures close to 10K (with zero magnetic field; critical temperature is lowered with increasing field and NbTi magnet are routinely operated at liquid helium temperature, 4.2K); however HTS materials begin behaving as such at a temperature of roughly 90K. Figures 1 & 2 highlight the temperatures at which LTS & HTS materials become superconducting.

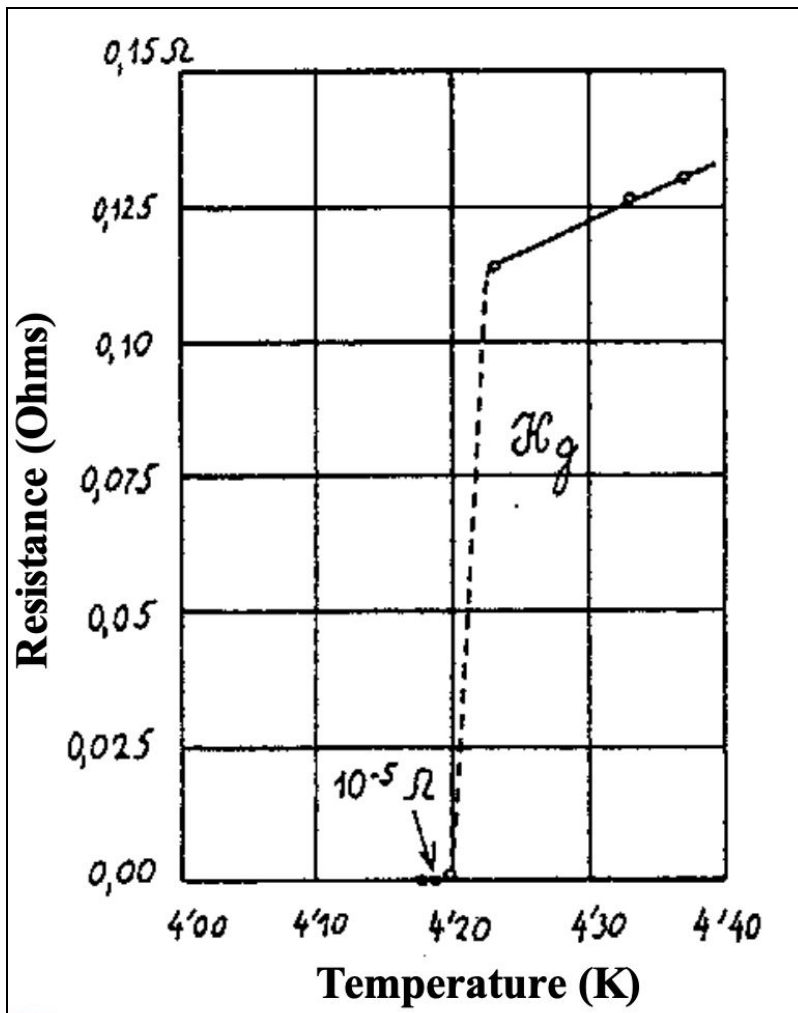


Figure 1: Typical electrical resistance behavior of a Low Temperature Superconductor [1].

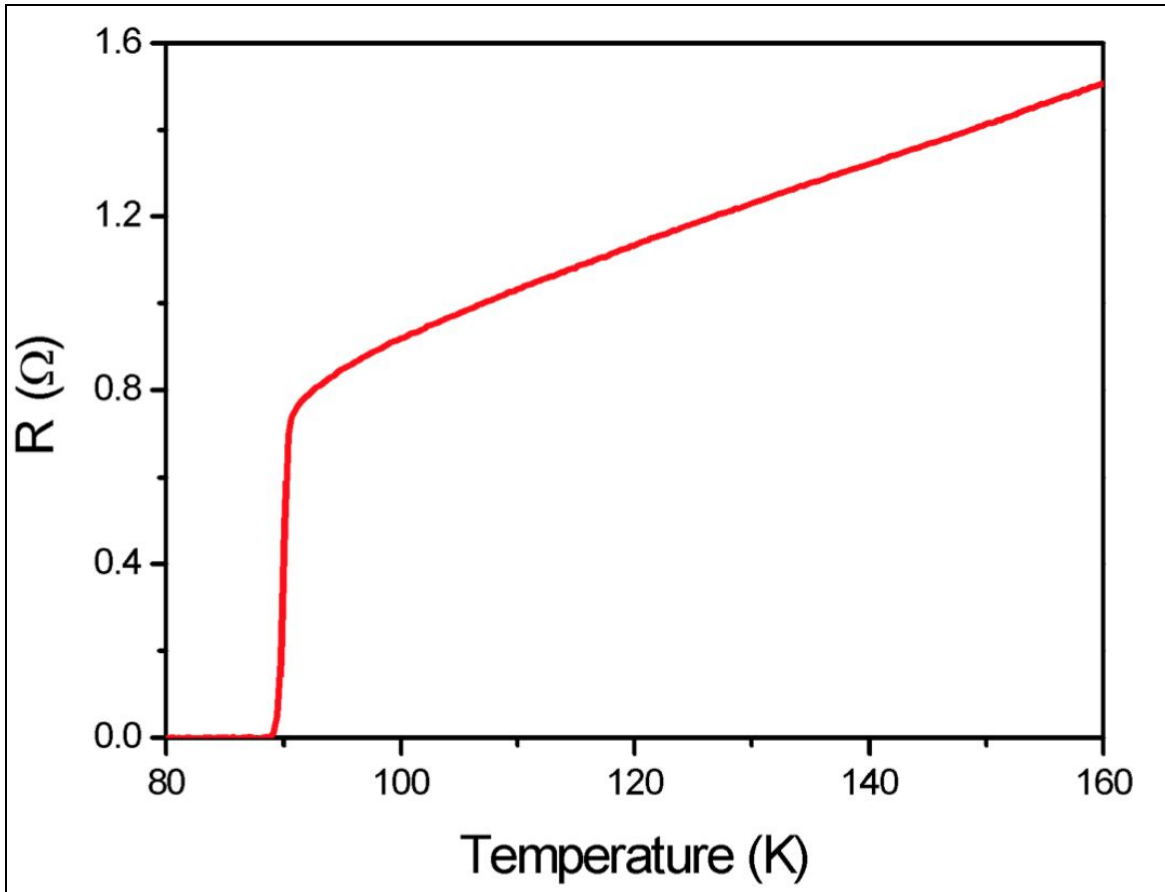


Figure 2: Typical electrical resistance behavior of a High Temperature Superconductor [1].

Typically, most materials are cooled to their critical temperatures via liquid nitrogen. The issue with LTS materials is with the drastic temperatures they must be cooled to - approximately 4.2 degrees above absolute zero [2]. HTS materials only require their surface temperatures to be cooled to 90 degrees above absolute zero, thus making this a less involved, and costly task. As a result, HTS are being investigated more frequently to be used in place and in conjunction with LTS.

Project Scope & Description

The goal of this project is to demonstrate a proof of principle dipole with a new novel high temperature superconductor, “Conductor on Round Core cable (CORC)”. This design utilizes HTS CORC insert coils installed in the aperture of and powered in series with an existing Nb₃Sn Common coil dipole, which provides a 10 tesla background field for the CORC coils. Once proof of principle is established, the designs will be implemented and the coil will be wound and other hardware will be machined. All designs were created via Creo Parametric 6.0 CAD software. Figures 3 & 4 show the “Conductor on Round Cable (CORC)” being investigated in this research project.

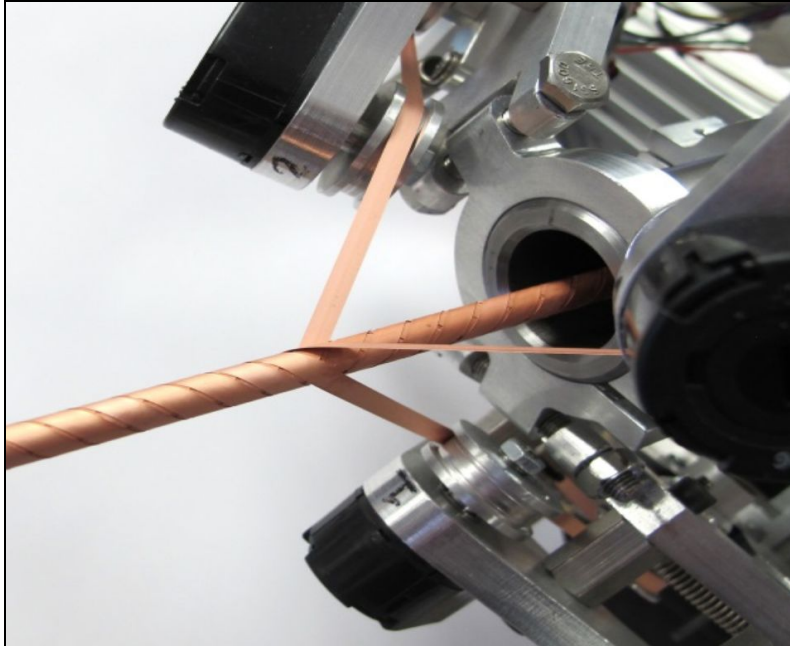


Figure 3: CORC being wound.



Figure 4: HTS Conductor on Round Cable.

Methods & Results

All designs were created on Creo Parametric 6.0. There are three (3) main components associated with the project; 2 different coil layers and a coil ramp. The first coil layer differs from the second coil layers very slightly; on both sides of the first coil layer there are four (4) turns, however there are four (4) turns on only 1 side of the second coil layer. The remaining side of the second coil layer has only 3 sides - this is so the coil ramp may be incorporated in the design. The transition, referred to as the “s” layer, is particularly important because it allows for the 2-layer coil to be fabricated from a single length of conductor, and the continued electric current to transfer from coil to coil without the need for a splice in the conductor. Figures 5 - 7 shows the two different coil layers, and the “s” layer in their separate part files.



Figure 5: Coil Layer 1.

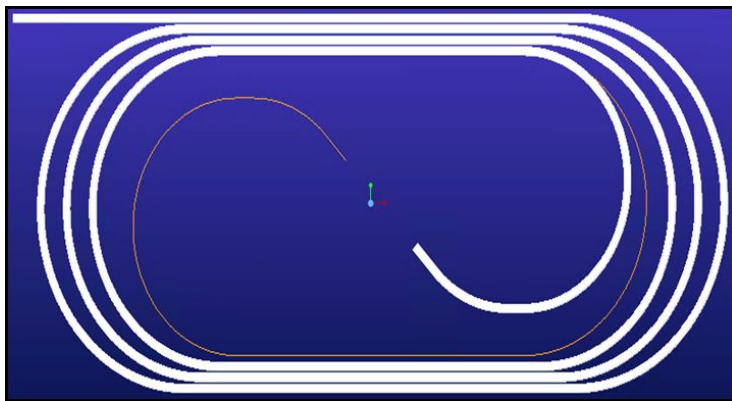


Figure 6: Coil Layer 2.

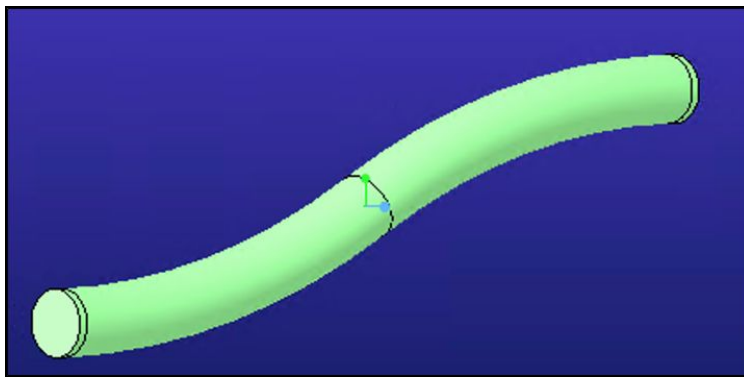


Figure 7: "s" layer transition.

The dimensions for the accompanying figures can be found in appendix A. The minimum bend radius used to model the CORC is 90mm and the largest bend radius used in the design is 130mm. The aperture of the common coil magnet, which is where this assembly gets inserted, is 31mm wide and 335mm in length, thus these are the constraints in which the design was held to. In addition to developing designs for the coils, other hardware was also developed. Spacers, end plates, and filler plates were also created to help hold the entire assembly together and aid during the winding process. The full packaged assembly (without end plates) can be seen in Figure 8.

The packaged assembly with end plates can be seen in Figure 9. Not shown, are the fasteners needed in order to hold the overall structure together.

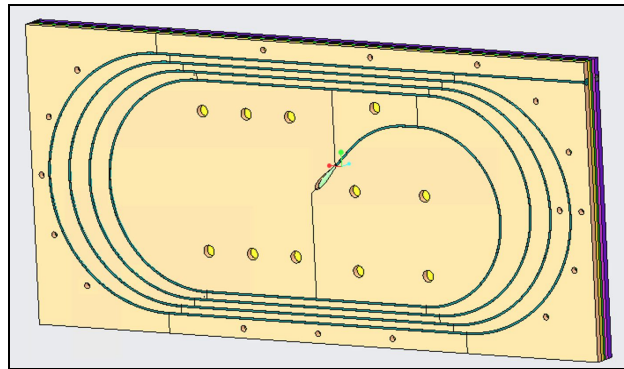


Figure 8: Packaged assembly no endplates.

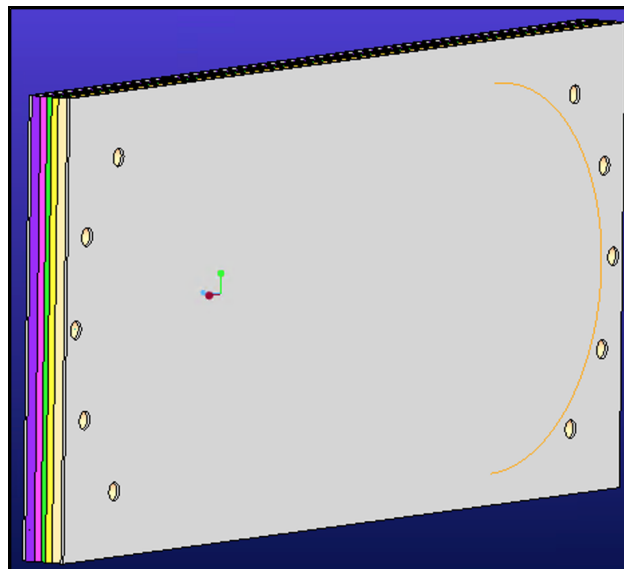


Figure 9: Packaged assembly with endplates.

Conclusion

In terms of aspects of the design that still need to be completed, there are two main components. A bolt has already been found which will aid in holding the assembly together, and to bolt down the spacers while winding. However, the holes for the bolt must still be appropriately threaded in order for the bolts to be properly held. Additionally, once these threads are created, the geometry as a whole must be brought into ANSYS Workbench. When the common coil magnet is powered on, there are forces produced called Lorentz magnetic forces; these forces produce normal stresses on the plates. By simulating these normal forces in ANSYS Workbench we can see how the plates and spacers react in terms of internal stresses and deformations. These guidelines are very important in determining an effective engineering design - one in which internal stresses and deformations remain low.

Acknowledgements

This project was supported in part by the U.S. Department of Energy, Office of Science, Office of Workforce Development for Teachers and Scientists (WDTS) under the Science Undergraduate Laboratory Internships Program (SULI). Additionally, I wish to thank my mentors Michael Anerella and Jesse Schmalzle, for their professionalism and generosity during the SULI program. Also, a special thanks to everyone who helped introduce and familiarize me with how to use Creo Parametric. The project would not have gone so smoothly without that help.

Citations

[1] Gupta, Ramesh. Introduction to the Design and Construction of CORC Coils. June 2020, PowerPoint Presentation.

[2] “Low-Temperature Superconductors - MagLab.” *The National High Magnetic Field Laboratory*, nationalmaglab.org/magnet-development/applied-superconductivity-center/research-areas/low-temperature-superconductivity.

Appendix A:

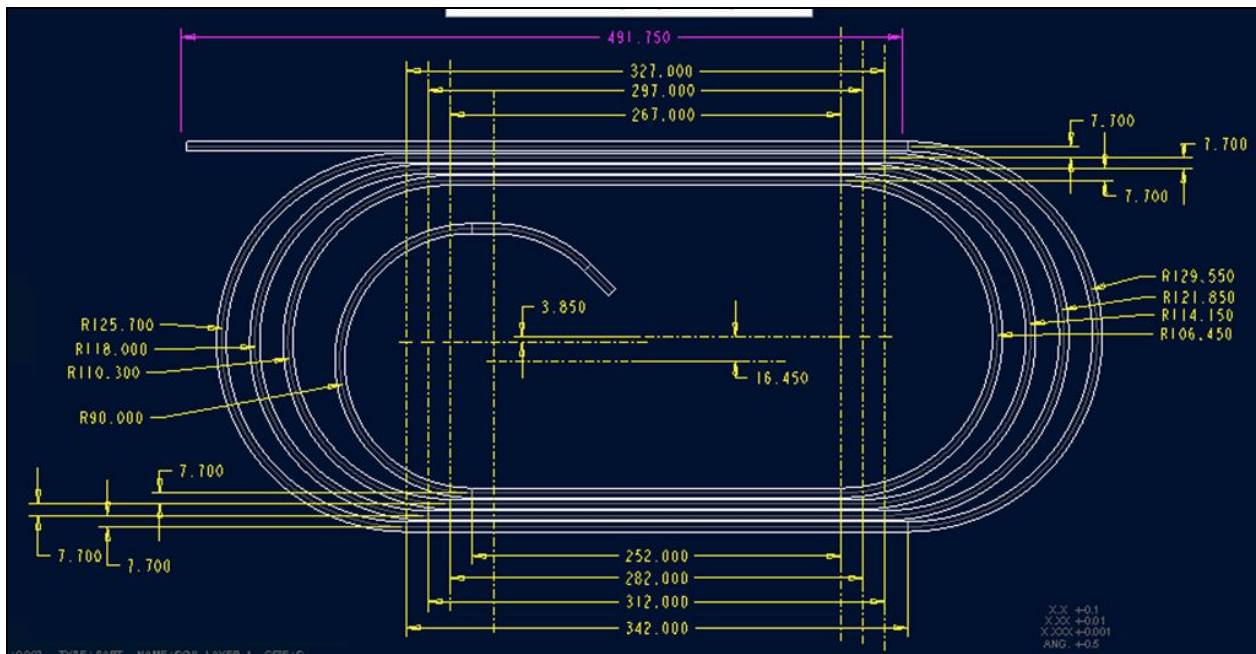


Figure A1: Dimensioned 1st Coil Layer.

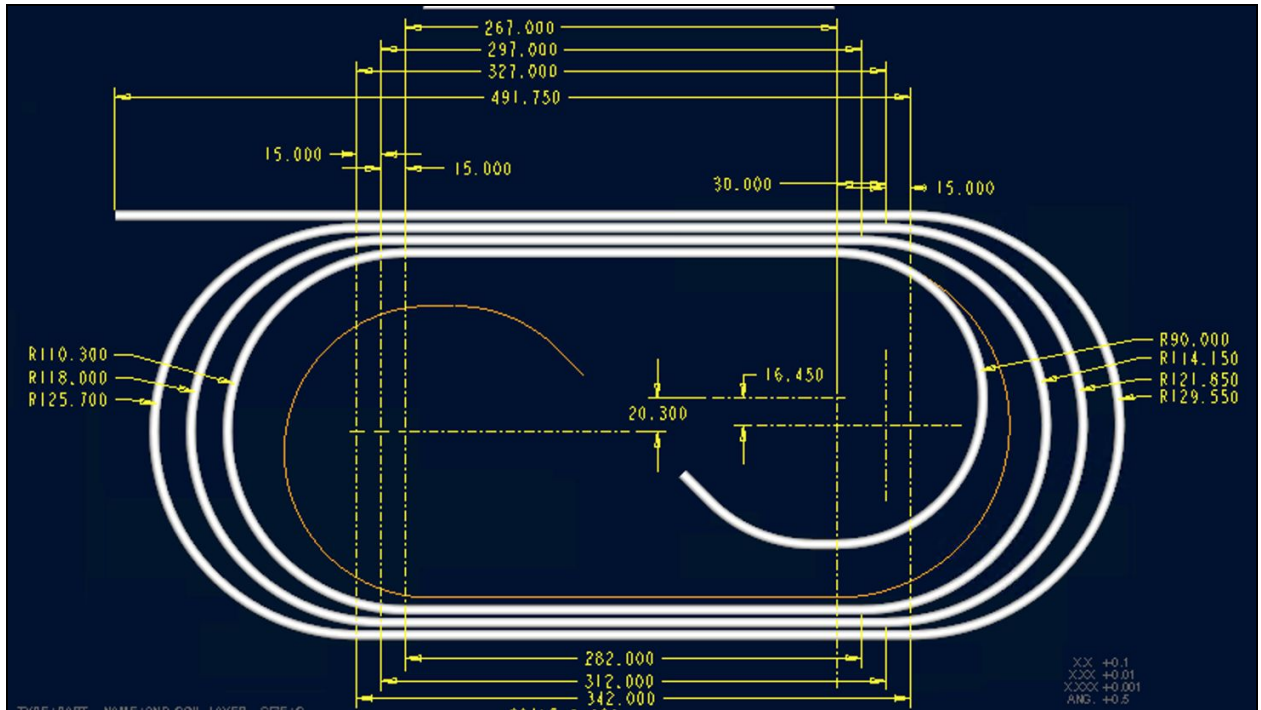


Figure A2: Dimensioned 2nd Coil Layer.

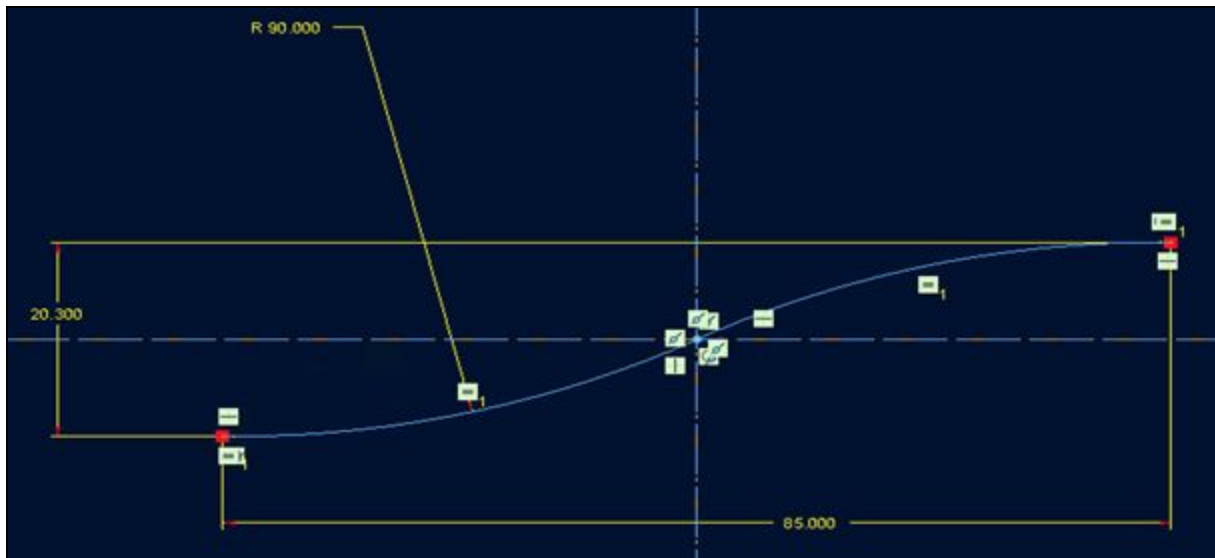


Figure A3: Dimensioned transition layer.

Real-time dashboard for monitoring performance of the general parallel file system

Matthew Broadbent

Computer Science, Stony Brook University, Stony Brook, New York 11733

Thomas Smith

NSLS-II, Brookhaven National Laboratory, Upton, NY 11973

Abstract

The National Synchrotron Light Source II (NSLS-II) at Brookhaven National Laboratory uses IBM's General Parallel File System (GPFS) to handle large amounts of data that is accumulated from beamline experiments at the facility. The GPFS infrastructure is different across experiments depending on each experiment's specific needs. It is important that the scientists operating these experiments can be able to quickly digest information regarding the status of the GPFS infrastructure used for their needs. For instance, a common occurrence includes a GPFS solid state disk nearing its maximum capacity; this would be important for a scientist to know so that the storage can be cleared. Because of this need, my project involves using the analytics visualization platform Grafana to create dashboards that monitor GPFS to provide relevant information for both the scientists at the facility and the controls groups that maintain GPFS. There are many different metrics of data collected that give insight into the status of GPFS, so it was important to determine which of these metrics provide useful information. The approach we used consisted of creating a main dashboard that highlights a wide array of important metrics on a general level. In addition to the main dashboard, we worked to create secondary dashboards that give a more detailed analysis of specific areas such as network, server vitals and capacity and throughput. Hopefully, these dashboards will be displayed on monitors inside NSLS-II to give scientists a clear look at the current status of the file system at their beamline.

I. Introduction

Given the significance of large amounts of data in conducting experiments at NSLS-II, it is important that scientists and controls engineers can easily monitor the status of the file systems that allow for the storage and transfer of this data. These dashboards aim to give scientists and controls engineers a digestible and concise way of viewing the key information regarding the status of the GPFS infrastructure at a given beamline so that downtime issues are minimized as much as possible.

Prior to coming onto this project, there already existed dashboards to fulfill this same purpose that had been created by the system administrators. This project aimed to create a more condensed set of dashboards that would be more useful to beamline scientists. In addition, some of the old dashboards are dysfunctional and would have needed to be updated.



Figure 1. Example of a dysfunctional dashboard that measures Pool Capacity for the LIX beamline.

Ideally, this project's dashboards would be easily transferrable to other beamlines. Additionally, some data can be broken down more specifically in order to be useful to control's engineers, so that they can more easily identify sources of error. These dashboards need to provide key information without being overwhelming or too elaborate.

II. Methods

These dashboards were created using Grafana, a web-based statistics visualization platform. Dashboards are not shared amongst beamlines- each beamline has its own Grafana domain. In Grafana, the data source OpenTSDB had already been configured so that the data can be queried.

In the query interface for OpenTSDB, as shown in Figure 2, the most important components are the metric and the filters. The metric dictates which statistic will be pulled from the database, and the filters constrain the metric to specific components in the file system. For instance, filters can allow the user to measure data throughput for only a specific disk drive.

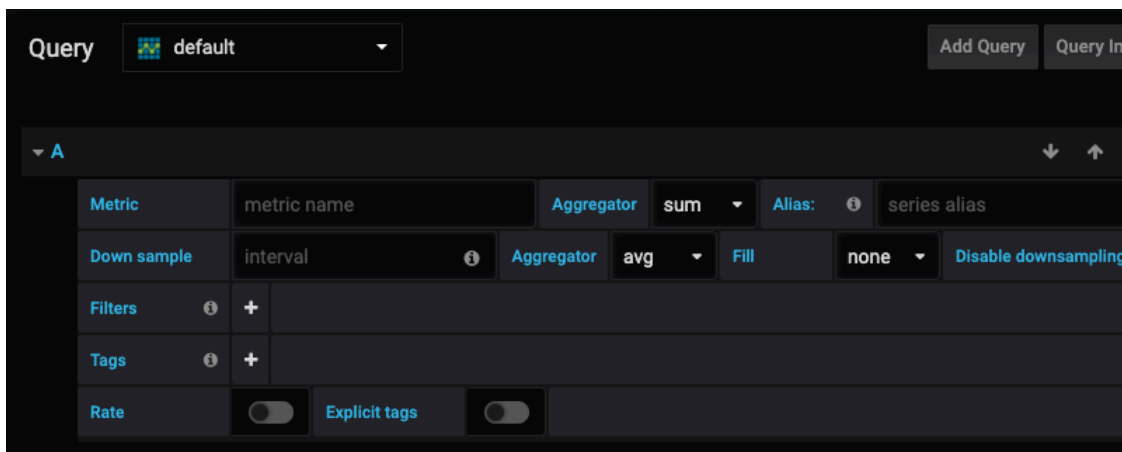


Figure 2. Example of the Grafana interface for queries. Notice the options for metric and filters.

Secure shell (SSH) is used in the terminal to gain access to beamline servers in order to obtain a list of all possible metrics and filters for a specific beamline using the `mmpfermon` command as depicted in Figures 3 and 4.

```
mbroadben@xf18id-srv1:~$ sudo /usr/lpp/mmfs/bin/mmpperfmon query --list filters
[sudo] password for mbroadben:

Available Filters:

node
  xf18id-ca1
  xf18id-srv1
  xf18id-srv2
  xf18ida-ioc1
gpfs_cluster_name
  XF18ID1.cs.nsls2.local
gpfs_disk_name
  FXIGPFSSSD
  FXIGPFSSSD1CA1
  FXIGPFSSSD2
  FXIGPFV1
  FXIGPFV2
  FXIGPFV3v1
  FXIGPFV3v2
  FXIGPFSSSD1SRV1
```

Figure 3. List of filters available for FXI beamline using mmpperfmon query.

```
mbroadben@xf18id-srv1:~$ sudo /usr/lpp/mmfs/bin/mmpperfmon query --list all
[sudo] password for mbroadben:

Available Metrics:

cpu_interrupts
  Number of interrupts serviced.
cpu_contexts
  Number of context switches across all CPU cores.
cpu_user [%]
  Percentage of total CPU time spent in normal priority user processes.
cpu_nice [%]
  Percentage of total CPU time spent in lowest-priority user processes.
cpu_system [%]
  Percentage of total CPU time spent in kernel mode.
cpu_idle [%]
  Percentage of total CPU spent idling
```

Figure 4. List of metrics available for FXI beamline using mmpperfmon query.

When creating the first test dashboard, it was important to identify which metrics should be displayed. General metrics that would be useful for beamline scientists at NSLS-II include: storage capacity, data throughput and input/output per second, and network traffic. It was necessary to decide how the dashboards would be organized. Ultimately, it made the most sense to create a main (home) dashboard, primarily for scientists, that gives a general overview of GPFS monitoring for that beamline. In addition, secondary dashboards would be created that are broken down with more specific filters so that points of failure can be more easily identified. These secondary dashboards would likely prove more useful for controls engineers. Users would also be able to navigate from the home dashboard to the secondary ones using a dashboard navigation panel.

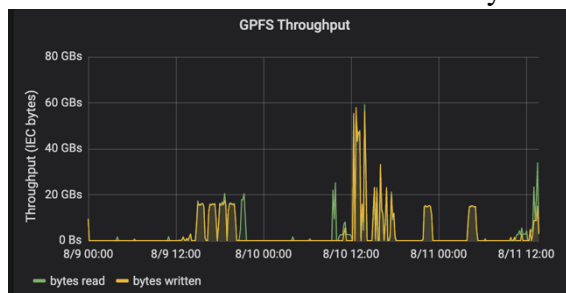


Figure 5. Data throughput panel.

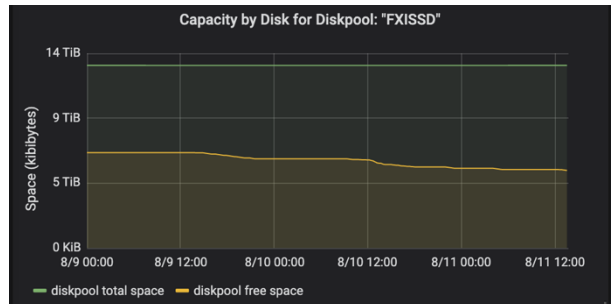
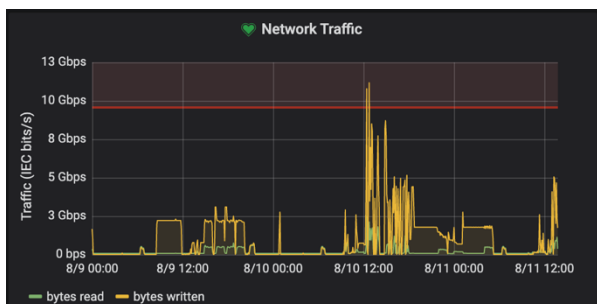


Figure 7. Storage capacity panel

For the secondary dashboards, it made sense to place panels into one of three dashboards. One dashboard would include any panels related to data storage or transfer rates. Another dashboard would surround panels with non-GPFS specific metrics related to the beamline servers. The last dashboard would have panels measuring network traffic per interface.

Grafana also includes a certain functionality that would be useful for this project known as alerts. Alerts provide an easy way to notify a user when a metric value reaches a certain threshold. For this project, it made sense to trigger an alert if storage for a disk drive fell below 15%, or if network traffic exceeded 90% of the maximum link speed. Alerts can also notify users by email, which is a function that was included after finishing the dashboards.

III. Results

Depicted below are screenshots of the four aforementioned dashboards configured for the FXI beamline.

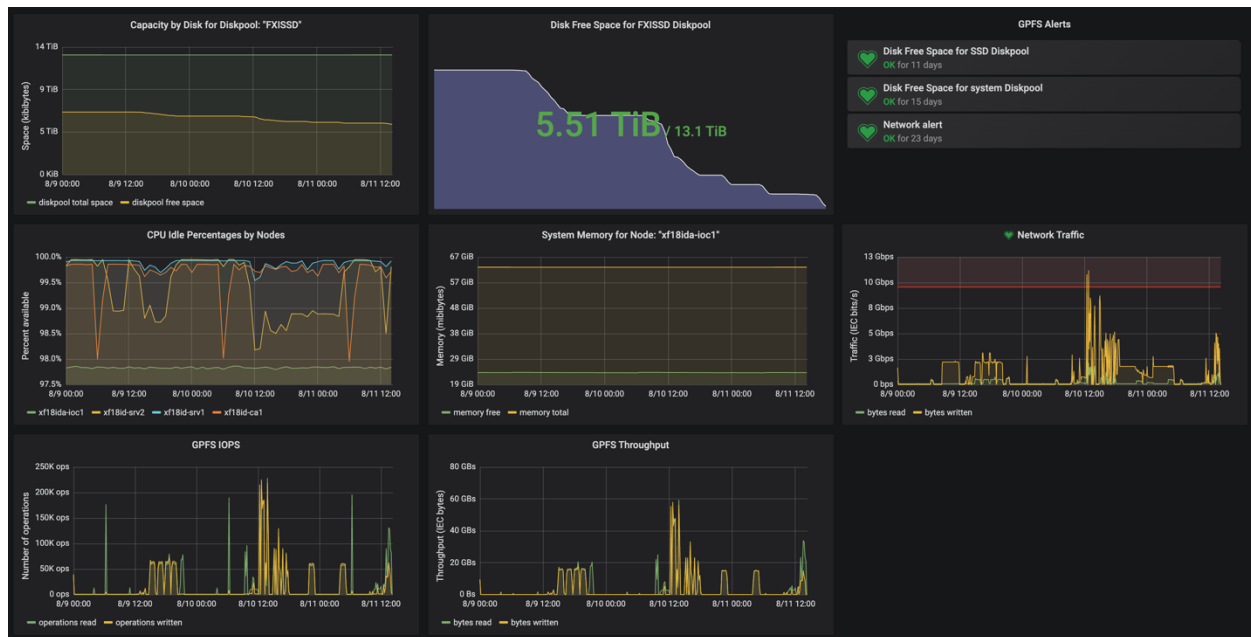


Figure 8. FXI Home dashboard



Figure 9. FXI Network dashboard

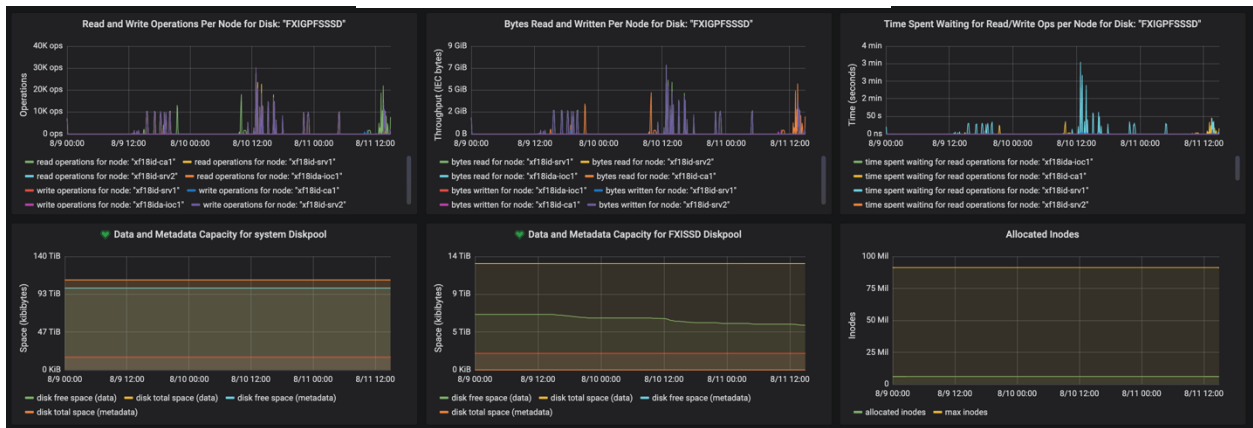


Figure 10. FXI Capacity, IOPS, and throughput dashboard

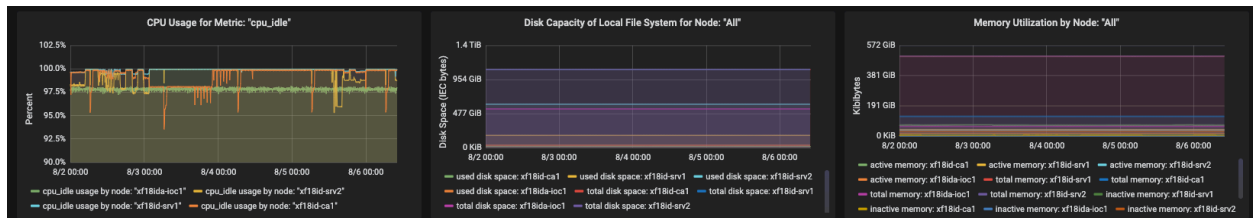


Figure 11. FXI Server dashboard

In Figures 9, 10, and 11, it can be seen that the data displayed is more filtered out than the data on the main dashboard (Figure 8). There exists more series in the legend, with each one corresponding to a different filter, like nodes or interfaces.

Once the dashboards were finished on the ISS beamline Grafana page, they were copied to many other beamline's Grafana domains. These include, but are not limited to FXI, LIX, and CHX. Templates provide a simple solution for being able to easily redeploy these dashboards for

other beamlines in the future. Fortunately, templates are possible in the form of JavaScript Object Notation (JSON) files, which is given as an option for creating dashboards with. Ideally, everything specific to a beamline in the dashboards would be written with variables so that the templates would automatically configure themselves to each beamline's filters, but unfortunately that is not possible. Variables were used where it was possible, and everything else was indicated in a text panel that was included in the template. The text panel has detailed instructions on everything that may need to be changed manually.

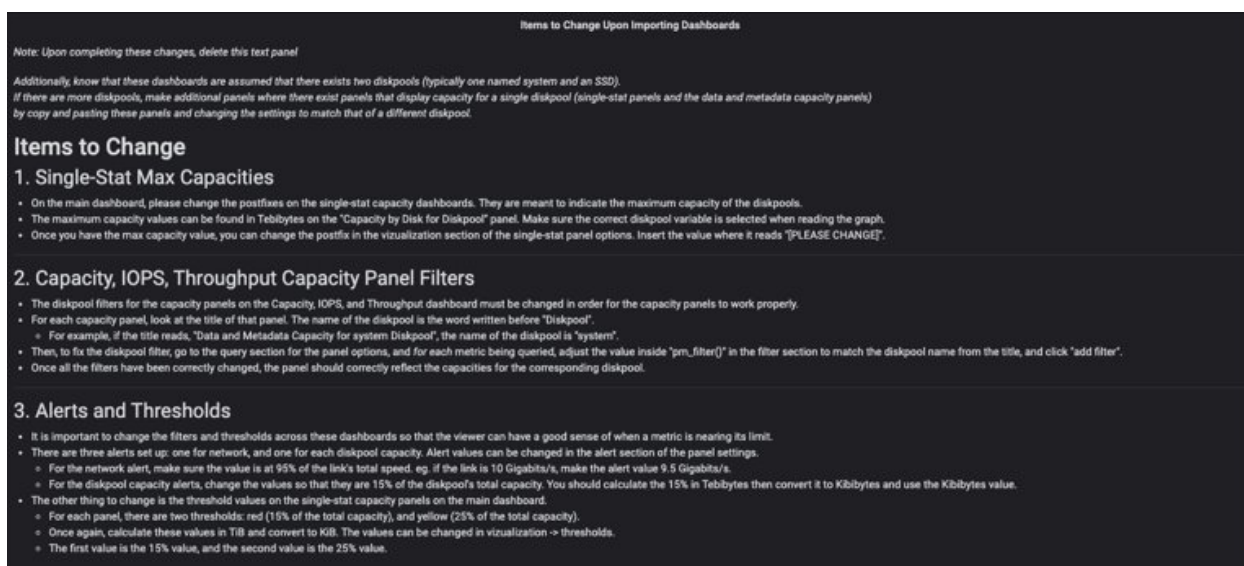


Figure 12. Template dashboard text panel including “items to change”

IV. Discussion

These dashboards can provide useful information to both beamline scientists and controls engineers. Given that some of the old dashboards measured metrics that I did not include in this project's dashboards, we decided to link those old dashboards in the dashboard navigation panel. Dashboards pertaining to active file management metrics were included here, for instance. However, given that these older dashboards have not been modified for some time, they may need to be updated to work properly with the current infrastructure.



Figure 13. FXI Active file management dashboard

While the dashboards have been pushed to several beamline Grafana domains, they have not yet been pushed to every domain. However, finishing that in the future would not be a difficult task given the templates that were created as discussed above. Additionally, the dashboards are only just beginning to roll out to be used by the scientists at NSLS-II. Just recently my mentor has introduced a few scientists to the new dashboards with positive reception. There is still a lot of work to do in rolling out the dashboards, both in setting them up in NSLS-II and providing the dashboards for more beamline domains, before they are fully put to use by beamline scientists.

V. References

[1] Grafana <https://grafana.com/>

[2] IBM Spectrum Scale Documentation

https://www.ibm.com/support/knowledgecenter/en/STXKQY_5.0.0/com.ibm.spectrum.scale.v5r00.doc/bllins_intro.htm

[3] OpenTSDB <http://opentsdb.net/>

VI. Acknowledgements

This project was sponsored in part by the Brookhaven National Laboratory (BNL) Photon Sciences Department under the BNL Supplemental Undergraduate Research Program (SURP). I would like to thank my mentor, Tom Smith, for giving me the opportunity to complete this project, as well as Matt Cowan, Leon Flaks, and Robert Petkus for also giving me advice on the dashboards. Thank you to the OEP for making all these internship programs possible in the first place.

Radiophobia: how fearing radiation impacts mental and physical health
Mecca Brooks, Department of Psychology, State University of New York at Albany, Albany,
NY, 12222

Susan Pepper, Nonproliferation and National Security Department, Brookhaven National
Laboratory, Upton, NY, 11973

Abstract:

Radiophobia, is the fear elicited from radiation and nuclear technology. This fear first became realized after atomic bombs were used on Hiroshima and Nagasaki and has deepened during the past forty years with the three major nuclear mishaps: Three Mile Island, Chernobyl, and Fukushima. After reviewing several articles, I constructed the research question: How widespread is radiophobia and what impact does it have on health, psychologically and physiologically? To investigate this question, I am taking a two-method approach. The first method uses a survey that seeks to test if, and to what extent, radiophobia exists in my immediate community. The survey is to be distributed among my fellow interns and will include six questions that seek to understand the intern's past and current knowledge and concern regarding radiation and nuclear technology. For the second part of my research question, one that seeks to assess the health implications of radiophobia, I turn to a literature review to assess how radiophobia may effect individuals psychologically and physically. With this study I expected to see that the more stress an individual finds themselves in, the more damage it will do to their mental and physical health. I also expected to find that those who are not aware of the risk and research involved with nuclear technology and radiation will perceive it as more concerning. Results from this study showed the opposite, as it appears that with more knowledge increases slightly more concern, however wording with the survey may need more clarification. Understanding the fear and apprehension surrounding nuclear technology and radiation among the public can assist in implementing better communication between scientists and the general public. Improved communication can lead to more education and, in turn, will build more trust, cooperation and interest. This internship has allowed me to build investigative skills and critical thinking that I will be able to carry with me throughout my career. I also received the opportunity to gain experience in proposal writing and the study review processes.

Introduction:

In the past few decades major nuclear accidents such as Three Mile Island, Chernobyl, and Fukushima, have produced great caution and, understandably, fear. But, at what point does this fear become unhealthy? It is thus my intention to investigate the consequence of the fear surrounding nuclear technology and radiation, or radiophobia. More specifically I sought to find out how widespread radiophobia is and what impact it has on health, psychologically and physiologically. To get the full picture, a literature review has been conducted to gather more insight on how health is impacted by radiophobia. According to the literature, 15% of adult evacuees after the Fukushima Daiichi nuclear power plant accident experienced extreme stress and 20% experienced trauma (Brumfiel). Evacuations, themselves contribute to this stress as the pressures of being uprooted from familiarity is combined with the worry of being exposed to radiation. According to Ropeik, 1,656 died during these evacuations at Fukushima. At a quick glance, individuals attribute the large number to the radiation exposure. However, a closer look at the situation expresses that the deaths are attributed to the decrease in medical assistance for the most vulnerable within the population. The majority of these deaths were individuals who were elderly and others with health conditions (Hasegawa, *et al*). Medical assistance was not provided during the mass evacuations, thus when issues arose, there was inadequate care to respond to them. Despite this fact, individuals still look at the number of deaths and view that they, too, are in danger due to the radiation exposure. There has been only one confirmed death due to radiation exposure after the nuclear accident of a worker at the Fukushima Daiichi power plant who developed lung cancer (Sheldrick). Similarly, evacuees in Chernobyl experienced chronic stress due to the fear they felt from the aftermath of the event. The likelihood of these individuals to develop cardiovascular disease, diabetes, high blood pressure, and report being clinically depressed increased significantly after the nuclear accident (Ropeik). Health of children in the area of Fukushima was also negatively impacted by fear of radiation exposure even when levels were deemed too low to impact health. Parents of these children as well as the schools in which they attended kept them indoors with the intention to protecting them, however, this action cut down on their physical activity. Obesity in the children of Fukushima increased by 20% in the aftermath of the nuclear power accident due to radiophobia (Ropeik). Even five years after the nuclear accident in Fukushima, 100,000 people refused to return to their homes despite the areas being deemed habitable. This serves to show that radiophobia lingers, allowing for the health impacts to continue. The literature makes it clear that individuals do face much stress when it comes to fearing radiation and nuclear technology.

Miscommunication of knowledge between the science and the general public is the main issue that allows radiophobia to flourish and impact health. As expressed in the aftermath of the Chernobyl accident, individuals found themselves with added stress when they did not receive adequate information about the event and its effects (Ropeik). Those in authority provided dishonest and unreliable information with the expectation of lessening fear, however, the opposite occurred. This sparked feeling of mistrust and a great fear. The consequences of miscommunication can also be seen in the aftermath of the accident that took place at the

Fukushima Daiichi nuclear power plant. The surrounding area was assessed to determine how much radiation exposure the evacuated residents received during the accident. It has been reported by the World Health Organization that individuals near the area received between 12 to 25 millisieverts (mSv) of radiation exposure (Normile). As noted by Brumfiel, these levels of exposure are significantly lower than the 100 mSv radiation exposure level that has been associated with increasing the likelihood of developing cancer. However, misinformed fear that the radiation was significant enough to increase cancer cases lead to the authorities in Fukushima to provide increased ultrasound screening technology to detect radiation-induced thyroid cancer in children. According to Ropeik, this technology has the ability to detect the finest thyroidal abnormalities, most of which appear to be non-cancer-causing abnormalities. In the case after the nuclear accident at Fukushima, 450,000 children were assessed using this advanced technology and about half were found to have abnormalities (Ropeik). However, children who resided in other areas in Japan and were not exposed to the radiation from the accident also showed similar abnormalities in their thyroid assessments tested with the same ultrasound screening technology. This serves to express that officials failed to understand that the abnormalities may have arisen from other factors, or combinations of factors, in the lives of these children other than just focusing on the radiation exposure. Despite the abnormalities being widespread throughout Japan, the report itself sparked such radiophobia that families opted to have the thyroid of 100 children removed as a preventative measure to avoid preserved risk of thyroid cancer development, against the judgment from the experts (Ropeik). Sutou offers more insight on the actuality of the situation. Patients after the nuclear accident at Fukushima who were diagnosed with having thyroid cancer were more advanced in age than those who were diagnosed prior to the event (Sutou). This suggests that the cancer began to develop before the nuclear accident, lessening the likelihood of radiation exposure being the leading factor in cancer diagnosis rates. Looking at these examples of how miscommunication leads to fear and mistrust, it is important that we consider working to better improve communication between specialist and the public. As I have seen through the literature, the public have genuine concerns and the science has very advanced ways of possibly providing relief to these concerns, however, there is a great divide between these two groups. By studying to understand how radiophobia impacts health and decisions made about health, it could perhaps promote new and effective ways to provide the general public with information about radiation and nuclear technology. This is important in the broader view, as public trust may be restored and strengthened in the science.

Previous research has focused on investigating the radiophobia that comes out of areas where accidents occurred: Three Mile Island, Chernobyl, and Fukushima. With the second part of my study, I sought to gather more information into whether radiophobia exists outside of these zones. I issued my survey to the current community of interns at the Brookhaven National Laboratory Summer Internship program to gain more insight into radiophobia. I suspected to find that those who are more concerned with radiation and nuclear technology and radiation nuclear technology also report to not having much knowledge on the subject and have been influenced by hearing about the events when things went wrong with it (Three Mile Island, Chernobyl, and

Fukushima). I looked to compare this with the intern's time after becoming an intern at the Laboratory, as I suspected to find that after interning and becoming more familiar with nuclear technology and radiation individuals would be less worried about it. As noted above, when people do not receive proper information, there are dire consequences. It is my belief that the more informed people are, the less fearful they will be, the better the condition of health is.

Methods:

To study how widespread is radiophobia and what impact does it have on health, psychologically and physiologically, I selected a two-method approach that consisted of breaking down this question into two parts. The first half of the question, *how widespread is radiophobia*, was evaluated by a survey sent to interns in the college Brookhaven National Laboratory Summer Internship program. With this survey, I sought to test whether radiophobia was present in my intern community, and if learning more information about radiation helped to decrease any pressing concerns they may have had. I chose to survey this group because of the broad range of educational backgrounds of the interns who, at Brookhaven, were attending lectures and talks regarding the Laboratory's involvement with radiation research and past involvement with nuclear technology. This survey was constructed on the internal network of Brookhaven National Laboratory, so only individuals with Brookhaven National Laboratory's virtual private network could access the survey, which all current interns had access to at the time. The survey included six questions that assessed the intern's concern with nuclear technology before and after interning, how much their research projects involved study in nuclear technology or radiation, and how much knowledge they have on the three major radiation accidents (Three Mile Island, Chernobyl, and Fukushima) before and after interning. The responses were completely anonymous and recorded on a scoring scale of 1 (least) and 5 (most). Once the responses were collected analysis was conducted to test the data against my research question.

The second half of my research question, *what impact does [radiophobia] have on health, psychologically and physiologically*, I turned to a literature review to assist me. At the beginning of my internship, I met with Edward Sierra, an employee at Brookhaven National Laboratory and member of the local chapter of the American Nuclear Society, to learn more about the real risk involved with radiation and nuclear technology and to see how warranted the fear was surrounding the topic. Sierra provided me with several sources, including a virtual textbook, *Sustainable Solutions for Our World*, that details the uses of nuclear technology in our environment. They also provided me with resources that allowed me to gather more information on radiation dosage, what are considered dangerous levels, and to what extent are we normally exposed to various sources of radiation in our daily lives. After I gathered this background information, I began to look for articles that could provide me with more information on radiophobia and its impacts on mental and physical health. I came across the article "*The dangers of radiophobia*" by David Ropeik after conducting an online search. This article provided me with the greatest insight on the health impacts of radiophobia as it breaks down the aftermath of the three major nuclear accidents Three Mile Island, Chernobyl, and Fukushima).

After reading this article, I furthered my search with the references provided in the Ropeik article. From there I built collection of background articles discussing mental health and physical health issues that arise as a result of radiophobia. I contacted Elizabeth Ricard-McCutchan, researcher in the Nuclear Science and Technology Department, to further assist me in finding articles for my literature review. They were able to find an article, “*Risk perception and anxiety regarding radiation after the 2011 Fukushima Nuclear Power Plant accident*” (Yoshitake Takebayashi, et al) that I used as a basis to further my understanding of how risk is perceived and impacts mental health. In all, my literature review led me to draw a variety of articles that allowed me to understand the role that fear plays in health issues. Where I am limited to test the impact myself, the existing literature has helped to fill in the gaps in my study, so that I could draw accurate and informed conclusions.

Results:

Reviewing the literature has provided me with much insight on the health impacts of radiophobia. According to studies taken after the Fukushima Daiichi nuclear power plant accident, reports of individuals feeling high levels of anxiety about radiation in Japan increased from 38% before the nuclear accident to 83% after the nuclear accident (Takebayashi, *et al*). This anxiety continued to be expressed a year after the events of the nuclear accident as the number of people who were anxious about the event increased (from 49.8% the year of the accident to 70.8% one year later) (Takebayashi, *et al*). This is further shown in the 100,000 people who refuse to return to their homes in and around the Fukushima even after officials and experts deemed it safe (Ropeik). Additionally, 79% of individuals in Japan feared that food that come from areas in and around Fukushima was contaminated despite the scientific experts stating otherwise (Brumfiel). There appears to be mistrust and misinformation lingering among the evacuees that continues to raise anxiety about the nuclear event. Similarly, after the nuclear accident at Chernobyl, anxiety and unsureness about the nuclear accident placed the population with chronic stress. Chronic stress places the body in constant fear response that negatively impacts mental health. After the Chernobyl nuclear accident, the population saw doubled rates of depression, increased instances of widespread alcoholism and suicidal tendencies as well as Post Traumatic Stress Disorder brought on by fear of radiation and its perceived consequences (Ropeik). As supported by studies in Fukushima, concern by mothers about the negative consequences of radiation was associated with depressive symptoms (Takebayashi, *et al*). Correspondingly, medical workers who were deployed to the Fukushima Daiichi nuclear power plant site after the accident, who were concerned about being exposed to radiation, was associated with depression, psychological distress, and PTSD (Takebayashi, *et al*). Being exposed to chronic stress also does damage to physical health as well. Ongoing stress places a strain on the heart and makes them more at risk for cardiovascular disease and increased blood pressure rates. The immune system activity is slowed, allowing individuals to be exposed to infectious diseases. The likelihood of developing type two diabetes is also noted as part of the physical toll stress takes on the body (Ropeik). Considering the amount of stress and the clearly

shown lingering fears regarding radiation, it is logical to connect these physical health consequences of chronic stress to those who experienced strenuous circumstances in Chernobyl and Fukushima.

My survey was available from August 3rd to August 8th and received 22 response from interns. To the first question on the survey, *how concerned were you with nuclear technology and radiation before interning at BNL*, most respondents (twelve) reported a score of 2 (between no concern and moderate concern), six reported being moderately concerned and four reported being not concerned (1). The second question, *how concerned are you are with nuclear technology and radiation after interning at BNL*, saw that most respondents (twelve) reported again a score of 2 and four reported being not concerned (1). Four respondents reported moderately concerned (3), one respondent reported a score of 4 (between moderate concern and much concern) and one reported much concern with nuclear technology and radiation (5). These results suggest that, overall, learning about nuclear technology and radiation may have increased, slightly, the concern with nuclear technology and radiation, however an improvement that could be made to this study in the future would need to offer a definition of the concept of “concern”. The increase in concern may just reflect genuine interest or awareness that has been gained from the while at the program. Clearer wording in the future will provide better insight going forward. Also, the results still saw that the majority still remained unconcerned. Responses to question three, *how much experience with nuclear research did you have prior to interning*, showed that the majority of interns (thirteen) did not have any experience (1), four responded with a score of 2 (between moderate experience and no experience), three reported having moderate experience, and two responded with a score of 4 (between much experience and moderate experience). This serves to show that respondents reflected how generally, the population has a lack of knowledge and experience regarding nuclear technology and radiation. This has the potential to confirm that, given the fact that the public does not necessarily have the opportunity to get directly involved in research, the science has to find its way more efficiently to our communities. Question four, *how well did you know about the three radiation accidents (Chernobyl, Three mile island, and Fukushima) prior to interning*, resulted in most respondents (nine) reporting having moderate knowledge (3), six reporting a score of 4 (between moderate knowledge and much knowledge), three reporting having much knowledge (5), three also reported a score of 2 (between having moderate knowledge and having no knowledge, and one person reported that they did not have much knowledge. The responses to the fifth, *how well did you know about the three radiation accidents (Chernobyl, Three mile island, and Fukushima) after interning*, had a shift in the majority rating as more participants (seven) reported a score of 4 (between moderate knowledge and much knowledge). Four respondents reported having much knowledge on the nuclear accidents (5), six reported moderate knowledge (3), four reported a score of 2 (between moderate knowledge and no knowledge), and 1 respondent reported no knowledge (1). The shift from before and after interning shows that participants had the opportunity to learn more about nuclear technology and radiation, or, at the very least, when it goes wrong. To connect these questions with the previous before and after questions (questions one and two), perhaps the

increase in concern for nuclear technology and radiation is related to knowing more and being more aware of the topic, the opposite of what was originally expected. The final question, *how much (if at all) does your current projects deal with researching nuclear technology and radiation*, responses were polymodal, as the majority of participants (fourteen) reported that their current intern projects did not involve nuclear technology and radiation (1), three respondents reported a score of 2 (between moderate involvement and no involvement), three respondents reported a score of 4 (between moderate involvement and much involvement), two respondents reported having much involvement (5). This serves to reflect that the shift that occurred between question four and five may be due to the lectures and talks given during the Brookhaven National Laboratory's events may have assisted in raising "concern", whether taken to mean interest or awareness for nuclear technology and radiation. In all, these results represent only a fraction of the intern community, however, given more time and responses for a deeper study, may provide a greater view of how radiophobia impacts our immediate community.

Conclusion:

Radiophobia is impactful to health, mentally and physically. With this study I expected to see that the more stress an individual finds themselves in, the more damage it will do to their mental and physical health. The literature review portion of my study has provided me with great insight on how radiophobia has led to mental strain on individuals and contributed to feelings of depression. To further this research, there would need to be a broader research to seek other areas outside of Three Mile Island, Chernobyl, and Fukushima to investigate how radiophobia impacts the health there. This will allow researchers to understand the broader attitudes and possible misconceptions surrounding radiation and nuclear technology in the various regions of the world and look to develop meaningful ways to better educate the public and build trust.

Secondly, I expected to find that those who are not aware of the risk and research involved with nuclear technology and radiation will perceive it as more concerning. However, the opposite was supported. The data collected from the surveys express that when individuals learned more about the three major nuclear accidents, there was also a slight shift toward more concern, however the majority still reported little concern overall. More research would need to be given to better understand if radiophobia occurs less in our community, to what extent, and what other factors contribute to our perceptions of nuclear technology and radiation.

It seems that radiophobia is a consequence of when the general public is disconnected from the science, so much so that when they are provided with information from the experts, they tend to mistrust it. Here lies the opportunity to improve communication between these two groups for the sake of protecting the mental, emotional, and physical health of our communities.

Acknowledgements:

This project was supported in part by the U.S. Department of Energy, Office of Science, Office of Workforce Development for Teachers and Scientists (WDTS) under the Science Undergraduate Laboratory Internships Program (SULI). My mentor, Susan Pepper has been a

great assistance to the advancement of my project. Others who have helped me with my survey construction and distribution, understanding the science behind radiation and nuclear technology, and those who have supported my project overall include Christopher Weaver at ITD, Salvador Gonzalez, Noel Blackburn, Edward Sierra, the African- American Advancement Group (AAAG), and the interns who took the time to participate in my study.

References:

Brumfiel, Geoff. "Fallout of fear: after the Fukushima nuclear disaster, Japan kept people safe from the physical effects of radiation--but not from the psychological impacts." *Nature* 493.7432 (2013): 290-294.

Hasegawa, A., et al. "Emergency responses and health consequences after the Fukushima accident; evacuation and relocation." *Clinical Oncology* 28.4 (2016): 237-244.

Normille, D. "Mystery cancers are cropping up in children in aftermath of Fukushima." *Science* (2016).

Ropeik, David. "The dangers of radiophobia." *Bulletin of the Atomic Scientists* 72.5 (2016): 311-317.

Sheldrick, Aron. "Japan acknowledges first radiation death among Fukushima workers." *Reuters*. (2018)

Sutou, Shizuyo. "A message to Fukushima: nothing to fear but fear itself." *Genes and Environment* 38.1 (2016): 12.

Takebayashi, Yoshitake, et al. "Risk perception and anxiety regarding radiation after the 2011 Fukushima nuclear power plant accident: A systematic qualitative review." *International journal of environmental research and public health* 14.11 (2017): 1306.

How automation is helping us stay safe during COVID-19: Pi based dewar controller to reduce staff overhead for the MX beamlines at NSLS-II

Andrew Campbell, Watson School of Engineering, Binghamton University, Binghamton, New York, 13902

Edwin Lazo, NSLS-II, Brookhaven National Laboratory, Upton New York, 11973

Abstract

Experiments run at the AMX and FMX beamlines at the National Synchrotron Light Source II at Brookhaven National Laboratory are carried out within experimental hutches, where protein crystals are exposed to an x-ray beam and data is obtained. Protein crystals are kept at cryogenic temperatures in a dewar inside the hutch throughout the experiment to mitigate radiation damage while in the x-ray beam. Sample transfers are done via a robotic sample changer. When fully loaded twenty-four Unipucks (sample holder that can hold up to 16 samples) can be placed on the motorized platform within the dewar. This platform needs to be rotated at least eight times to fully load the dewar. Currently, the only way to rotate the dewar is from workstations located outside of the experimental hutch, which increases overhead time and risk of equipment damage. Given the new restrictions on the number of staff per beamline due to COVID-19, more pressures are put on the staff supporting users due to the absence of support staff. To mitigate this issue, a Raspberry Pi with an associated touchscreen will be mounted within the experimental hutch to enable dewar

control within the hutch. The Raspberry Pi will be running Control System Studio and will allow staff to rotate the dewar from within the hutch. The Raspberry Pi can also move the detector to a defined location, control the smart magnet boost, and place the end-station into the sample exchange state. This device has enable staff to more efficiently setup the beamlines for user experiments despite the absence of support staff. This has resulted in less stress and pressure on staff supporting users during the COVID-19 restrictions.

I. Introduction

At NSLS-II, the Frontier Microfocusing Macromolecular Crystallography (FMX), and Highly Automated micro focus Macromolecular Crystallography (AMX) beamlines are constantly working towards higher throughput. Reducing staff overhead for repetitive tasks is one of many methods that increase throughput. The project I worked on aims to achieve this by integrating a Raspberry Pi with an associated touch screen into the experimental hutch where

staff members perform various tasks. I have built a graphical user interface (GUI) using Control Systems Studio (CSS) for both the AMX and FMX beamlines, to achieve this. The GUI will allow a staff member to control dewar rotation while in the experimental hutch. This will reduce the time it takes to load samples, since prior to this implementation a staff member was required to exit the hutch and go to a workstation computer to rotate the dewar, which generally, needs to be done 8 times to fully load the dewar.



Figure 1.

Currently, staffing levels at NSLS-II are reduced due to Covid-19 restrictions, which has led to an increased workload for staff members when they are on site. Automating tasks in a manner that leads to more efficient operation is very important during this time. A controller that can be mounted within the experimental hutch reduces the time it takes staff to load the dewar and perform maintenance, freeing up time for on site staff. The dewar at both the AMX and FMX beamlines have 8 plates each holding 3 Unipucks which each hold 16 samples, for a total of 384 samples (Edwin Lazo et al. in preparation). Staff members would generally be required to move in and out of the experimental hutch 8 times while loading the dewar. The controller will allow staff to stay in the hutch and quickly rotate the dewar which will decrease the loading time for both beamlines subsequently increasing throughput.

II. Methods

To create the controller a Raspberry Pi model 3 B+ and Raspberry Pi Touch Display were utilized. The Raspberry Pi was booted with Raspberry Pi OS, from there Phoebus (the version of CSS used). After CSS was running on the Pi's they were configured for connection to the FMX and AMX networks. This gave CSS access to the process variables associated with the beamlines. These process variables are what control the various functions the controller performs at the beamline. Once, CSS could communicate with the process variables a graphical user interface (GUI) was created using the display editor in CSS. This editor allows for buttons, text, and various other graphical features to read and write to process variables. To rotate the dewar 8 buttons were created and each writes to the process variable responsible for controlling the dewar's position. Each button writes a different value that corresponds to one of the defined plate positions. The buttons also display "LEDS" as shown in figure one, these LEDs indicate whether there is currently a puck at the specific position on the said plate. The indicators were placed inside the buttons to maintain a sleek design and save space on the display. The display also reads out the current position of the dewar in degrees. It also makes use of rules in CSS to interpret the position of the dewar and print out what plate it is at. Relational and logical operators were used to determine when the dewar was at a specific plate.



Figure 2.

The displays also can move the Eiger detectors to a predefined position for both AMX and FMX. This moves the detector back to a position that allows for maintenance to be performed on the end-stations, as seen in figure three. The button named “Park Det”, as seen in figure one was created to perform this function. The button writes the position value to the process variable that controls the position of the detector. Another feature of the display is unlocking the touchscreen as shown in figure two that is part of the dewar. This touchscreen gets locked out during certain beamline operations, and requires a command be sent to Life Science Data Collection (LSDC) server to unlock. The button created in CSS uses a process variable and the LSDC command name for enabling the touchscreen and can unlock this touchscreen. The button named “SE” as shown in figure one stands for Sample Exchange which is a governor state for both the AMX and FMX beamlines. This moves several pieces of equipment into a state that allows for robot access for beamline staff (Schneider et al., in preparation). The “SE” button utilizes whatever the motor positions are defined as in the governor CSS file from the beamline workstations. The last button named “BOOST OFF” is a Boolean button and toggles the smart magnet boost on and off. When the boost is on it increases the

smart magnets voltage form 2.5V to 5V (Lazo et al., in preparation).

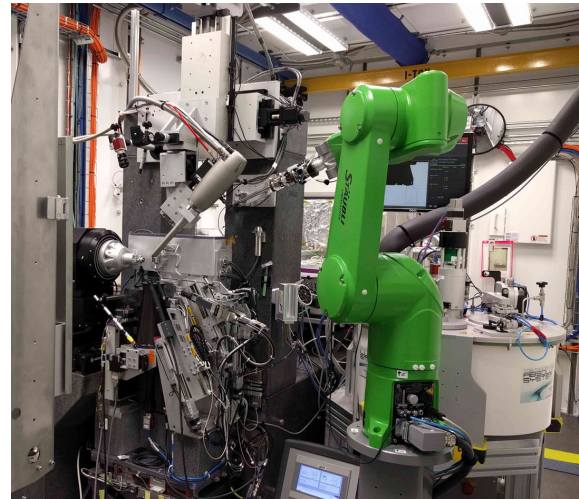


Figure 3.

The controllers created are placed inside cases as seen in figure four, these cases allow for simple and sturdy mounting of the controller within the hutch. The controllers will be mounted along the hutch walls where staff members can easily access them when needed. The cases also feature a built-in fan for cooling the Raspberry Pi. This prevents the Pi from slowing down due to overheating, increasing its usability. The controller also makes use of a shell script that resets CSS once a day when it is not being used. This was done because it was noticed that after extended periods without resetting, CSS would occasionally freeze. This is a relatively uncommon event, nevertheless adding a script that resets CSS once a day at 2:10AM will prevent the issue. These features were added to make the controllers robust and hassle free.

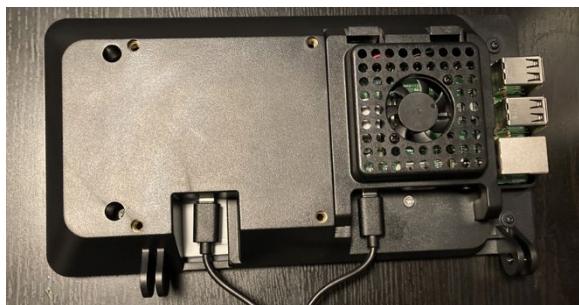


Figure 4.

III. Conclusion

The Raspberry Pi based controllers can now rotate the dewar, place the end-station into the sample exchange state, move the detector, toggle liquid nitrogen boost, and unlock the touchscreen that is part of the dewar. All these processes would have previously required a staff member to move to a workstation computer outside of the experimental hutch. These controllers have an important role in reducing staff overhead time and will allow staff to work more efficiently at the AMX and FMX beamlines. Throughout the Covid-19 pandemic these controllers will allow the onsite staff to work in a more efficient manner, thus allowing for higher levels of productivity at the AMX and FMX beamlines. It is very important to continually automate processes to work towards higher throughput, and the Raspberry Pi based controllers created help contribute to this cause.

IV. References

[1] Edwin Lazo, Stephen Antonelli, Herbert J. Bernstein, Dileep Bhogadi, Martin R. Fuchs, Nicolas Guichard, Sean McSweeney, Stuart Myers, Kun Qian, Grace Shea-McCarthy, Lin Yang and Jean Jakoncic., “A Robotic Sample changer for Macromolecular X-ray Crystallography and Biological Small-Angle X-ray Scattering at the National Synchrotron Light Source II: ASEN”. National Synchrotron Light Source

II, Brookhaven National Laboratory, Upton, NEW YORK, 11973, USA (In preparation)

[2] Dieter K. Schneider, Wuxian Shi, Babak Andi, Jean Jakoncic, Yuan Gao, Dileep K. Bhogadi, Stuart F. Myers, Bruno Martins, John M. Skinner, Herbert J. Bernstein, Edwin O. Lazo, Thomas Langdon, John Lara , Mourad Idir, Lei Huang , Oleg Chubar, Robert M. Sweet , Lonny E. Berman , Sean McSweeney and Martin R. Fuchs., “FMX – the Frontier Microfocusing Macromolecular Crystallography Beamline at the National Synchrotron Light Source II”. Photon Sciences, Brookhaven National Laboratory, Upton, NY, 11973, United States. (In preparation)

V. Acknowledgements

I would like to give a special thanks to my mentor Edwin Lazo for his support and knowledge on this project. I would also like to thank the additional members of Structural Biology Program for their insight and assistance. This project was supported in part by the U.S. Department of Energy, Office of Science, Office of Workforce Development for Teachers and Scientists (WDTS) under the Science Undergraduate Laboratory Internships Program (SULI).

Controls solutions and integration for dynamic equipment at national synchrotron light source II

Brandon Catalano
Electrical Engineering, Stony Brook University, New York, 11794

Nathanael Maytan
Photon Sciences Division, Brookhaven National Laboratory, Upton, NY, 11973

Abstract

There are currently two major controller-based systems in use at each beamline at the National Synchrotron Light Source II at Brookhaven National Laboratory: the Equipment Protection System, and the Personnel Protection System. A third controller-based solution, DIODE (Distributed I/O for Dynamic Equipment) has been designed to further enhance the reliability and maintainability of the beamline subsystems. Since its inception, DIODE has been rolled out to several beamlines with more on the way. As the number of adopters grows, so does the need for new features and add on solutions which can expand DIODE's capabilities. This project aimed to plan, design, and implement new reusable controls features for DIODE that will help contribute to the capabilities of the beamlines at NSLS-II. Efforts were focused on developing support for new PLC (Programmable Logic Controller) modules which expand the I/O available from DIODE. The project was accomplished using various tools including EPICS (Experimental Physics and Industrial Control System), Control System Studio, and Rockwell Automation Studio 5000. New EPICS databases were developed for generating module specific process variables (PVs), which control their associated module by writing to module defined tags (taken from Studio 5000). New operator interfaces were created in CS Studio to provide a user-friendly interface to the new PVs. As a result of this project, module support for the 5069-OW4I, 1734-IE2V, and 1734-OE2V modules was completed. These modules add digital relay outputs, analog voltage inputs, and analog voltage outputs respectively which can be used to integrate new dynamic

equipment. With these new features, NSLS II now has additional tools and capabilities which can be deployed at any beamline.

I. Background

A. Why DIODE is Needed

DIODE stands for Distributed I/O for Dynamic Equipment. Dynamic equipment refers to a class of equipment that is integrated into a beamline but does not serve any function to one of the two controller-based safety systems traditionally found at NSLS-II: the EPS and PPS.¹ DIODE acts as a third controller-based system that increases the reliability and maintainability of beamline subsystems. It fundamentally acts to decouple dynamic equipment from the EPS and PPS that also requires full scale integration at a given beamline, things such as mass flow controllers, sample heaters, general I/O, or PID loops for example. Traditionally, dynamic equipment has simply been lumped into the EPS since it was much more evenly distributed and configurable than the PPS. While this may work for certain circumstances, this has the unfortunate consequences of adding increased complexity to the EPS while making documentation significantly more difficult, causing troubleshooting difficulty, increased installation time, and overloading of I/O boxes. Thus, DIODE helps to subvert these issues altogether by providing a robust, reusable, and readily expandable platform to add dynamic equipment to.

B. Scope

DIODE has the convenient capability to work on an individual beamline basis. Each beamline contains a PLC that communicates with the dynamic equipment at the beamline using the Distributed I/O protocol. Communication with the EPS is also possible but EPS (or PPS) functions will not be performed. Additionally, previously integrated dynamic equipment can easily be migrated to DIODE, which helps to mitigate some of the previously discussed issues with the EPS housing dynamic equipment.

C. Summary of Core DIODE Hardware and Software Components

As mentioned, DIODE is a controller-based system. DIODE makes use of the Allen Bradley (A-B) CompactLogix 5380 series PLCs and the corresponding software suite Rockwell Automation Studio 5000 (referred to as Studio 5000 from here on out). DIODE specifically makes use of the 5069-L310ER PLC, which supports up to 8 local expansion modules, 24 remote I/O nodes, 1MB of programmable memory, and an embedded power supply.² Expansion modules are at the core of DIODE and this project in general since they perform the functions needed to integrate dynamic equipment to a beamline. The PLC communicates with input output controllers (IOCs), programs on the NSLS-II I/O network that act as I/O servers for communicating with a PLC. At NSLS-II, we tend to use host-based software IOCs or softIOCs (though some VME based hardware IOCs do exist) that reside on a dedicated IOC server at each beamline

for communication with the DIODE PLC through a proprietary Allen-Bradley driver. These IOCs are written in control systems software suite called EPICS and contain smaller files called databases. These databases dictate the behavior of the module by allowing the PLC to communicate with fundamental units called process variables, or PVs. These PVs can be accessed through a powerful subset of instructions called records (similar to functions in other text-based languages) such as analog in/out, binary in/out, or calculations to name a few.³ These PVs communicate with the PLC hardware through module defined tags at the controller level. The databases can be specifically written to communicate with these module tags to affect changes in the modules.

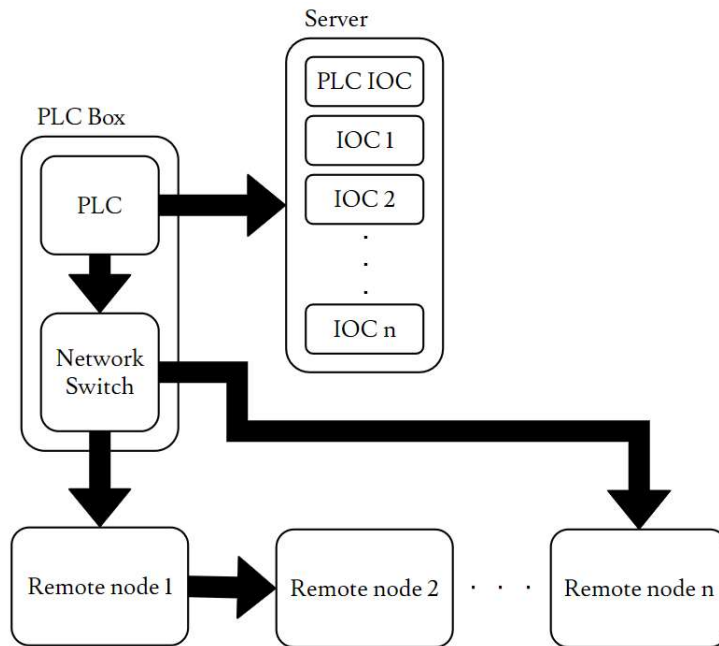


Figure 1. Typical interconnection of hardware components within a DIODE system.

The databases in a running IOC can be used to leverage control of expansion modules in a variety of ways, but the most useful is through Control System Studio (CSS or CS-Studio). CSS allows for creation of operator interfaces (OPIs), GUI based front panels that allow for graphical communication and modification of the process variables contained within the EPICS databases of an IOC. This completely obfuscates the low-level software from the individual controlling the hardware and leads to a much more user-friendly experience for implementing dynamic equipment at their beamline which at the end of the day, leads to easier adoption of DIODE. While dynamic equipment could theoretically be controlled through the deployment of Studio 5000 at beamlines, implementation of an EPICS IOC and CS-Studio solution allows for much greater customization of what the end user sees and interacts with. Moreover, it allows for the potential addition of supplementary database logic that can add enhanced functionality or readability to the given module.

D. Objectives

It becomes clear that DIODE is a powerful platform for beamlines to implement. Consequently, while DIODE has already been deployed to several beamlines at NSLS-II, there is still significant demand for the implementation at others. Therefore, as the number of adopters increases, so does the need for the novel features and expansion solutions to heighten DIODE's capabilities. The objectives of this project aimed to accomplish the following:

- Write custom EPICS databases that bring module support to DIODE for both the CompactLogix 5000 series and POINT I/O expansion modules
- Design user friendly OPI pages in CS Studio for module control
- Verify the function of these databases and OPIs
- Version control code using Gitlab. Databases and OPIs will be production ready for NSLS II
- Deploy new module support for use at a production beamline.

Thus, the design, implementation, testing, and integration of these databases and OPIs for the purposes of having production ready module support was the fundamental objective for this project.

II. Methods

A. System Preparation

Based on the dynamic equipment requirements of the ISS-8ID beamline, we decided that the ideal modules to support would be the Compact 5000 5069-OW4I 4 channel digital output relay, the POINT I/O 1734-IE2V 2 channel analog voltage input module and 1734-OE2V 2 channel analog voltage output module. Documentation for each module was carefully consulted to determine the data type, range, and module tags for each system. In the case of the POINT I/O series modules, the module tags could not be determined from the documentation, and consultation with Studio 5000 was

necessary. Connection to a valid PLC and population of the expansion slots allowed for visualization of the module tags within the program. These module tags could later be used for creation of process variables that communicate with the PLC and affect given changes on the expansion module.

An important step was to design a module schematic for connection of dynamic equipment using Microsoft Visio. This allows for technicians or individuals responsible for installation of hardware to explicitly understand the system. In this case, only the 5069-OW4I was used to create a schematic. The dynamic equipment selected for connection to the OW4I was a normally open SPDT load relay and a solenoid (which would likely represent some sort of solenoid valve in a true physical beamline system). In addition, a 12 VDC power supply to energize the load, two flyback diodes and a 2 amp fuse were included. An important feature of the schematic was inclusion of a cutout in the upper right corner which visualized the internal function of the 5069-OW4I. While this isn't crucial to understanding the system, it's useful to anyone who desires to comprehend the overall electrical function.

B. Creating the IOC and Databases

For the purposes of DIODE module support, an already existing IOC was used that allowed for rapid addition of databases for expansion modules. However, this IOC still required some conditioning since it was already deployed to a production beamline. To begin, EPICS 3.15.6-3.1 was installed using the NSLS-II Debian packaging on a

Linux Debian 10 remote workstation. The following packages were also installed: autosave, caputlog, catools, ether-ip, iocstats, sys-rc-softioc, and their corresponding libraries. The directory `~/EPICS/IOCs` was created to house the IOCs, and it is recommended to follow this structure as well. At this point, the installation of EPICS was verified by using `makeBaseApp.pl` to create a barebones IOC called “sampleIOC”:

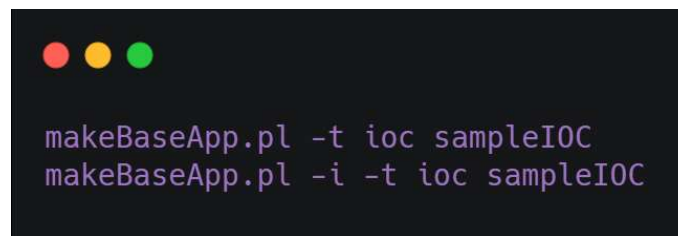
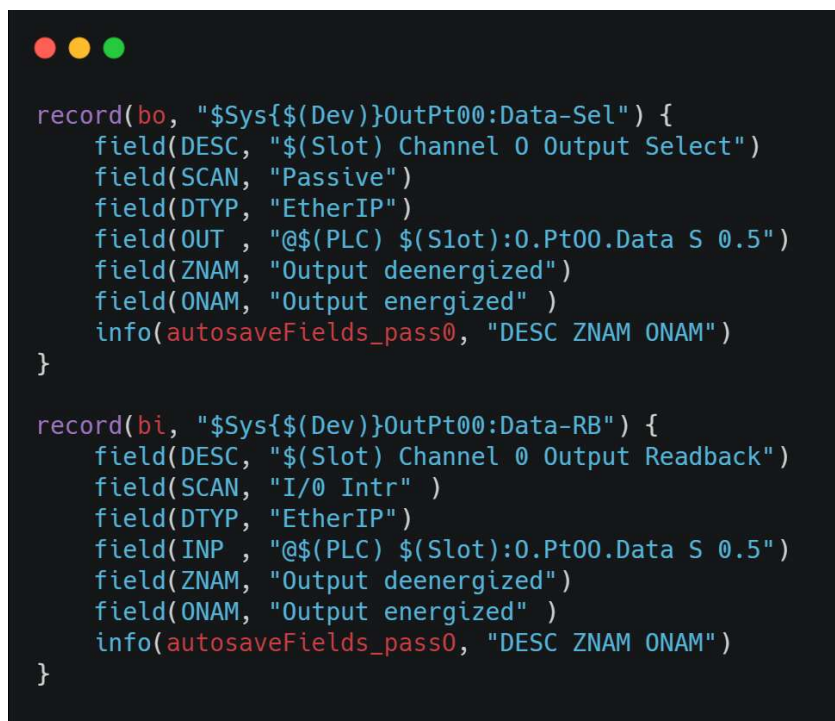
A terminal window with a dark background and three colored window control buttons (red, yellow, green) in the top left corner. The terminal displays two lines of purple text: `makeBaseApp.pl -t ioc sampleIOC` on the first line and `makeBaseApp.pl -i -t ioc sampleIOC` on the second line.

Figure 2. Instructions to create a sample IOC in the top-level directory.

With the sample IOC successfully created, the startup script `st.cmd` and `envPaths` were both moved to the top directory of `sampleIOC`. The shebang at the top of the startup script was also updated to account for the change in location of the IOC shell.

GNUMake (or simply `make` depending on the Linux installation) was run to compile the IOC from the top-level directory. Running `./st.cmd` started the IOC within the command line, and typing `dbl` in the EPICS shell listed all of the records available. Once this compiled with no errors, it was determined that the EPICS installation was successful and the pre-configured DIODE IOC could be run with slight modification.

To get the DIODE IOC working, the PLC IP address had to be specified in the startup script, as well as the engineer name. While a `caputlog` server should be specified, in the case of this project we did not have access to one so it was commented out in the startup script. `make distclean` was run to decompile the IOC from its previously deployed state and clean the directory. Rebuilding the IOC using `make` once again left us with a fresh DIODE IOC ready for deployment on the workstation we were working from. At this point, databases could be written following EPICS conventions and syntax.



```
record(bo, "$Sys{$(Dev)}OutPt00:Data-Sel") {
  field(DESC, "$$(Slot) Channel 0 Output Select")
  field(SCAN, "Passive")
  field(DTYP, "EtherIP")
  field(OUT, "@$(PLC) $(Slot):0.Pt00.Data S 0.5")
  field(ZNAM, "Output deenergized")
  field(ONAM, "Output energized")
  info(autosaveFields_pass0, "DESC ZNAM ONAM")
}

record(bi, "$Sys{$(Dev)}OutPt00:Data-RB") {
  field(DESC, "$$(Slot) Channel 0 Output Readback")
  field(SCAN, "I/O Intr")
  field(DTYP, "EtherIP")
  field(INP, "@$(PLC) $(Slot):0.Pt00.Data S 0.5")
  field(ZNAM, "Output deenergized")
  field(ONAM, "Output energized")
  info(autosaveFields_pass0, "DESC ZNAM ONAM")
}
```

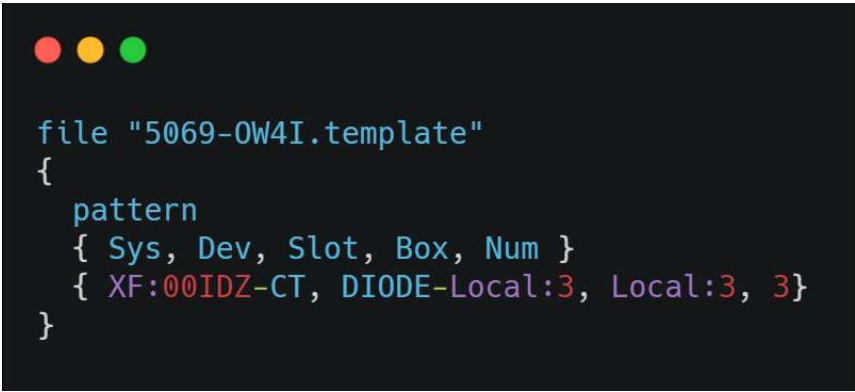
Figure 3. Example database for output toggle and readback on the first channel of the 5069-OW4I. Note the naming convention for NSLS-II includes environment variables for Sys, Dev, PLC, and Slot and a signal type suffix.

DIODE is deployed using SNACK which allows for dynamic inclusion of databases and OPIs without having to rewrite the entire database. This is why in Figure 3, it can be seen that there are multiple environment variables corresponding to various system components. The database was saved as a `.template` file to go with a corresponding `.substitution` file. When a substitution file exists for a given template, the respective database will automatically be added to the IOC with the specified variables within the substitution file as defined in the makefile within the Db folder:

A terminal window with a dark background and three colored window control buttons (red, yellow, green) at the top left. The terminal displays a Makefile snippet with the following text:

```
ifneq (, $(wildcard ../5069-0W4I.substitutions))
    DB += 5069-0W4I.db
endif
```

Figure 4. Snippet of code that would add the 5069-0W4I database to the IOC. There would be corresponding `ifneq` statements for each module that needs support.

A terminal window with a dark background and three colored window control buttons (red, yellow, green) at the top left. The terminal displays a substitution file with the following text:

```
file "5069-0W4I.template"
{
    pattern
    { Sys, Dev, Slot, Box, Num }
    { XF:00IDZ-CT, DIODE-Local:3, Local:3, 3 }
}
```

Figure 5. Substitution file that would specify PLC, device, slot, box, and number for template file.

Finally, the startup script was simply updated using `dbLoadRecords()` to specify the name of the newly implemented database(s). On IOC start, the records in this new database would have their PVs successfully initiated for communication with.

C. OPI Design

OPIs were designed making use of Control System Studio. Previous DIODE OPI deployments had created a library of pre-defined OPI parts that could be used to make user-friendly OPIs, much like a function library in certain programming languages. Thus, OPIs were designed using these previously created parts to mimic the function and appearance of previously supported modules which support the module's core functionality, PV editing and configuration of database fields. When custom OPI parts were needed, they were designed using the templates as reference for style and function. Special consideration was taken to implement linking and grouping containers to finalize the design of the OPI. Parent macros were used to specify the environment variables from the substitution files (PLC, Slot, etc.) so that OPIs could also dynamically be deployed without having to rewrite the interface.

D. Verification and Version Control

Once the OPIs were successfully created, they were verified by connecting them to the physical system that included both the 5069-L310ER PLC and the given expansion module(s). Verification could be performed for modules such as the OW4I by

toggling the OPI components and simply listening for the audible clicks of the relay on the physical device, and for the POINT I/O, Studio 5000 could be used to verify the given input and output values being seen by the module. The EPICS shell was also closely observed to confirm that the given write operations had occurred and there were no communication errors between the IOC and hardware. Any debugging was performed if the system did not behave as expected, and the code was then version controlled. Git, and more specifically an NSLS-II DIODE repo on Gitlab, was utilized to version control the databases newly developed for the IOC. OPI changes had to manually be contributed as credentials for the OPI branch of the repo were difficult to obtain within the SULI timeframe. The rule of thumb was to commit changes to the testing branch whenever new functionality had been added. Special consideration was taken to document changes in significant detail when making commit messages so that other individuals would be able to track the changes most effectively.

III. Results

Development of a system schematic, connection and configuration of the physical system, and development of an easily controllable OPI for the 5069-OW4I were performed. Successful communication with the 5069-L310ER was achieved, and while OPIs were not developed for the POINT I/O modules, verification of their function was performed using the DIODE remote box pictured below with their databases properly version controlled in the DIODE repo on Gitlab.

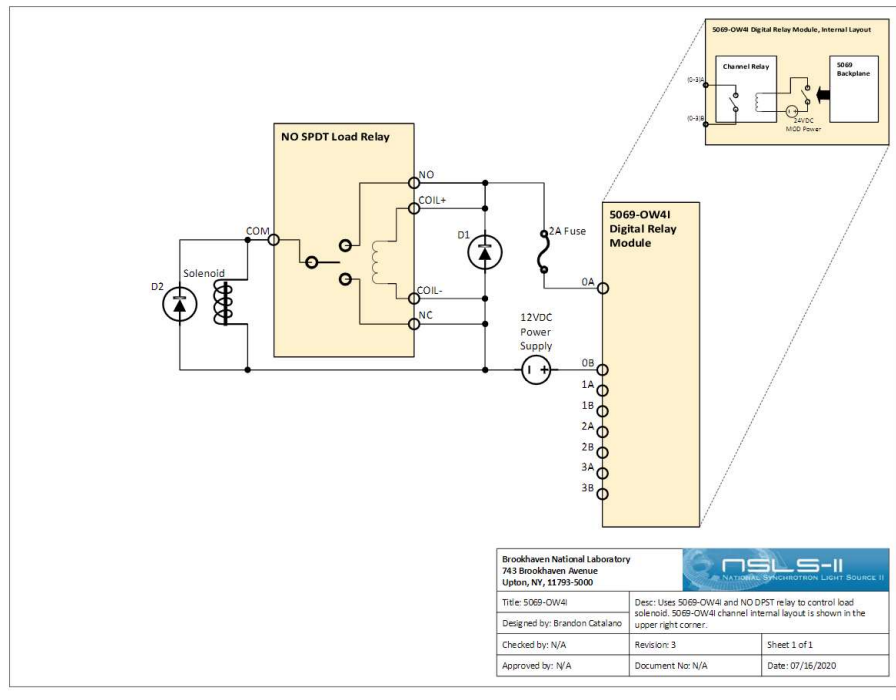


Figure 6. Schematic for connection of a load relay and solenoid to the output channel of the 5069-OW4I.

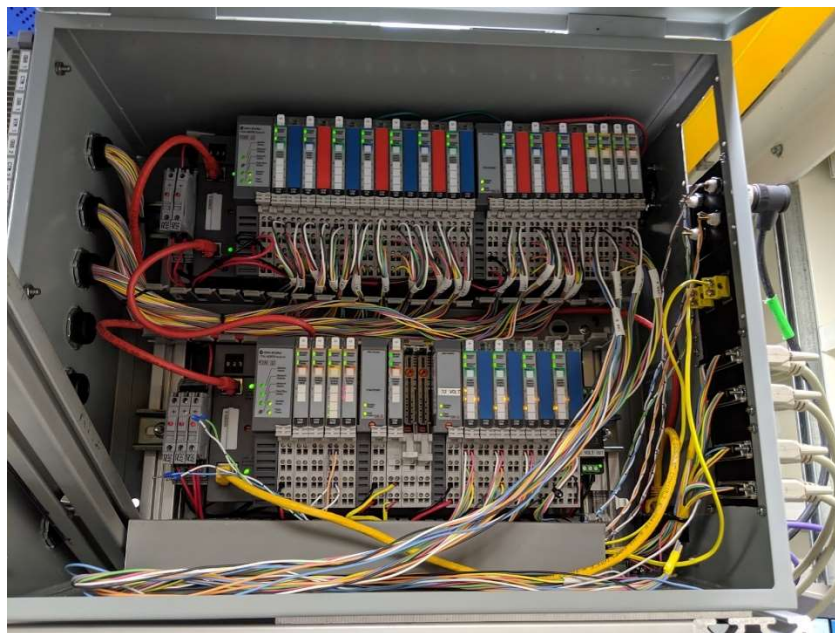


Figure 7. Remote box for implementation of POINT I/O at ISS-8ID beamline.

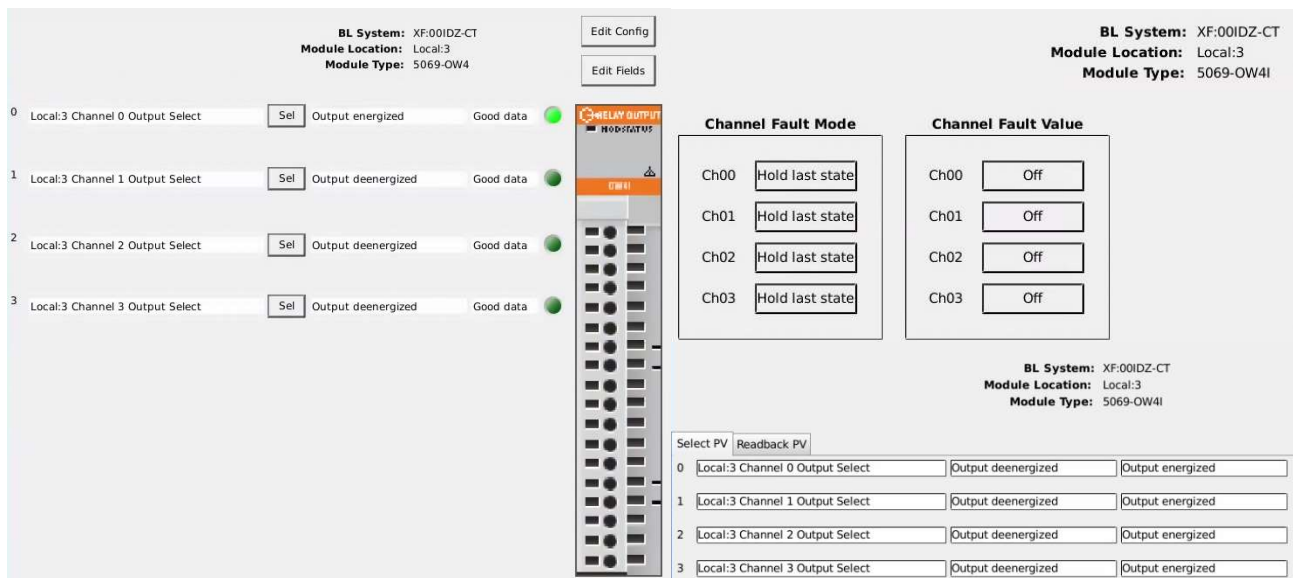


Figure 8. OPI pages for the control of the 5069-OW4I. The main page (left) is used for interaction with the module. The configuration page (upper right) allows the user to modify the configuration tags for fault detection. The page on the bottom left allows the user to modify certain PVs such as description and output names.

```
epics> tag 3 'Local:3:0.Pt00.Data' (write): 31 (0x1F), 4 (0x4)
```

Figure 9. Output from the EPICS shell denoting successful communication with the PLC and energization of the 5069-OW4I first channel output relay.

IV. Conclusion

Module support development resulted in the addition of 3 new modules to the DIODE database library including the 5069-OW4I, 1734-IE2V and 1734-OE2V. This means that beamlines will now have a much wider array of modules to choose from for their dynamic equipment, including digital output relay and analog I/O functionality, respectively. For modules such as the 5069-OW4I where peripheral features such as fault detection are available, it is not clear how this functionality can be harnessed by

beamline scientists within the OPI. Testing of various fault conditions such as short circuit, no load, and power loss still revealed no change in the fault readback process variables from the normal no fault condition. It is likely that fault detection on modules that do not outright support no load, short circuit, or power loss module tags is an internal diagnostic that is not of use at NSLS-II beamlines, at least not with our current understanding. Thus, module support should still stick to implementation of core functionality for the time being until more fault conditions can be tested. Beamlines can transition away from using the EPS for general I/O and add dynamic equipment such as sampler heaters, solenoid valves, mass flow controllers, and more through DIODE. Implementation of DIODE and its expansion modules adds new tools, convenience and capabilities for experimentation at NSLS II.

V. Acknowledgements

I would like to take the time to deeply thank my mentor, Nathanael Maytan, for his unending patience and teaching ability. There is no way I would have been able to complete this project without his assistance and have learned so much as a result. Especially in an unprecedented situation for SULI in which we went entirely remote, he found a way to salvage an experience that was comparable to a fully in person one. I would also like to extend a big thank you to the Core Controls Group whose insight was instrumental. This project was supported in part by the U.S. Department of Energy,

Office of Science, Office of Workforce Development for Teachers and Scientists (WDTS) under the Science Undergraduate Laboratory Internships Program (SULI).

VI. References

1. “CompactLogix 5380 Controllers: Allen-Bradley.” *Rockwell Automation*, Allen-Bradley, May 2020, www.rockwellautomation.com/en-us/products/hardware/allen-bradley/programmable-controllers/small-controllers/compactlogix-family/compactlogix-5380-controllers.html.
2. “EPICS Overview.” *EPICS Overview - EPICS Documentation Documentation*, EPICS Controls, 2019, docs.epics-controls.org/en/latest/guides/EPICS_Intro.html.
3. Maytan, Nate, and Anton Derbenev. “Distributed I/O for Dynamic Equipment (DIODE).” Brookhaven National Lab, June 2019.

Rack interlock systems interface

Michael Charumaneeroj, Department of Electrical and Computer Engineering, Stony Brook University, Stony Brook, NY 11794

Joel Vasquez, Physics Department, Brookhaven National Laboratory, Upton, NY 11973

Abstract

The sPHENIX (super Pioneering High Energy Nuclear Interaction eXperiment) is an upgrade to the former PHENIX. Along with the STAR (Solenoidal Tracker At RHIC), these two detectors monitor collisions of particles at the RHIC (Relativistic Heavy Ion Collider). The sPHENIX is expected to be completed in 2023 and will be able to collect more information regarding the initial conditions following the Big Bang than its predecessor. On the sPHENIX, there will be 36 individual racks that will collect data about nucleic collisions. On each rack, there will be a system of sensors that will monitor the rack's temperature and look for smoke or water leaks. Should one of these sensors trigger, the corresponding rack would turn off. This logic is programmed with ladder logic for PLC (Programmable Logic Controller) and will be accessible through an HMI (Human Machine Interface) display. In layman's terms, the PLC acts as the brains of the system while the HMI allows the users to access key information regarding the sPHENIX. My role in the project is to create the display that users would see. This display includes graphics, banners and indicators that

will all help the operators ensure the system is okay. From measuring out icon dimensions to picking the correct colors, it is important to think of the user when designing a display. By the end of the summer we created the full system with four racks that can communicate with input and output cards.

Introduction

The sPHENIX will collect data about quark gluon plasma (QGP), which will allow scientists to better understand the conditions of the universe directly following the Big Bang. QGPs are a fundamental state of matter that existed one microsecond after the Big Bang. The RHIC assists this process by colliding the nuclei of atoms at nearly the speed of light. This data will be collected by the support racks of the sPHENIX. Our project deals with the interlocks of these support racks and the design of displays for operator use.

PLC Logic is vital in the creation of HMI Displays. The project revolves around the basic logic that will turn an output on or off based on the inputs. Inputs consist of a status bit which can be represented by a “normally open” (NO) or “normally closed” (NC) contact. These names represent a bit’s resting state; if a NO contact is TRUE, the contact will close – conversely if a NC contact is TRUE, the contact will open. Inputs can also be arranged sequentially after each other (AND gate) or on top of each other (OR gate). In the case of the former, all inputs must have a closed contact for the output to turn on, and in the ladder only one input must be closed in order for the output to turn on. Outputs can also be “stored” through the use of a latch. This is very helpful in the logic as it helps give the program more structure; the only way a latch can be cleared is by asserting a reset bit. Using these simple concepts, the basis of the project’s logic can be seen in Figure 1.

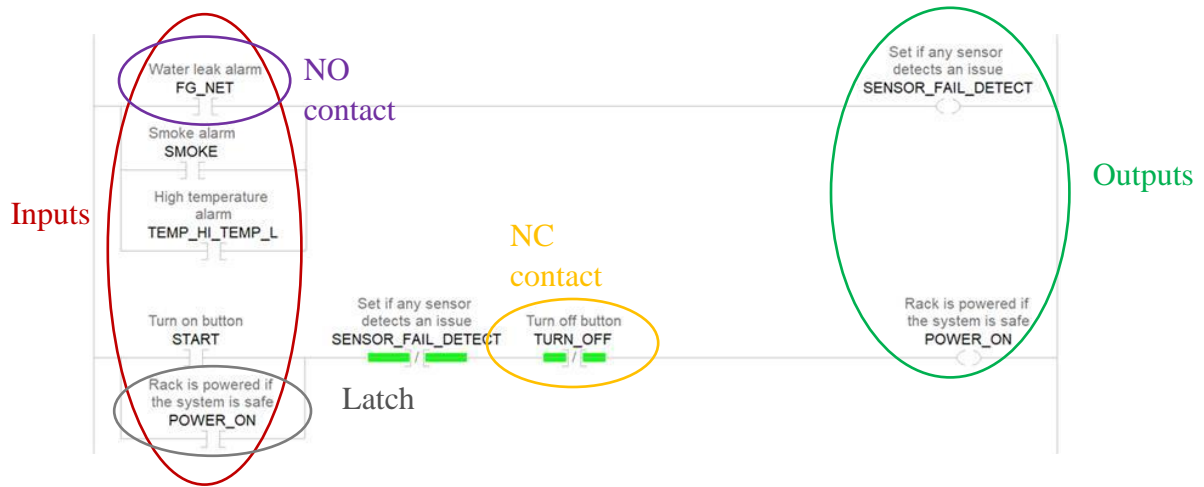


Figure 1. Basic ladder logic for powering on racks

The HMI display communicates closely with the PLC through tags. Tags are associated with contacts, inputs and outputs from the PLC's logic. The HMI displays are created from scratch using polygons, text boxes, images, buttons, other objects and animations. These objects link with PLC tags to display key information and animations use tags to develop Boolean statements which will only occur when the Boolean statements are true. An example of one of these animations can be seen in Figure 2. In this case, when the Boolean statement is true, the object will become visible on the display. Otherwise, it is invisible.

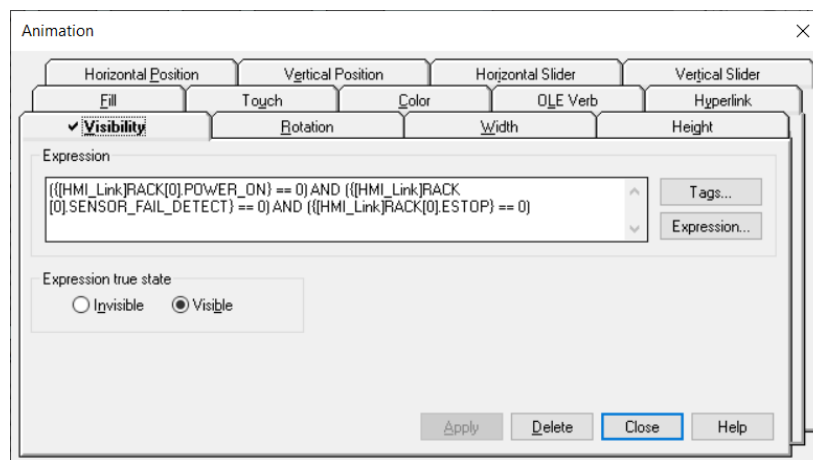


Figure 2. Boolean expression for an object's visibility

The Project

The objective of this project is to combine the PLC and HMI to create a program that will allow operators to examine, identify and address problems on the system. The PLC would obtain data from the inputs and set up the logic that gives the correct outputs, and the HMI would work as a device that reads and writes to the PLC. As the sPHENIX is in the early stages of development it should also be well-structure and flexible for any future changes that are proposed. By the end of the summer, a preliminary system should be able to communicate inputs and outputs through cards on the PLC and the HMI should be able to display information for operators.

The most difficult part of creating the display is getting started; from deciding on colors for backgrounds and titles to creating indicators for each alarm detected the amount of work to be done was daunting. However, once the design choices were made, the project kicked into a high gear. Creating a display that would show off key information for a system of 36 racks with four statuses and was pleasing to the eye was a tedious task; layers needed to be added, pixels needed to be counted and dimensions needed to be calculated. A concept was created evolved into the display depicted in Figure 3. This display includes navigation to a level overview display, a rack control display, an alarm history and status display, and an individual rack display. Each rack includes four led lights that can toggle between on and off with a key on the bottom right of the display. The background of each rack also mirrors the status of that rack, with green symbolizing that the system is on and OK, orange is the system has an alarm, red is the estop button on the rack has been triggered and grey showing the rack is off. This display makes it very easy for an operator to see the system and identify problems.

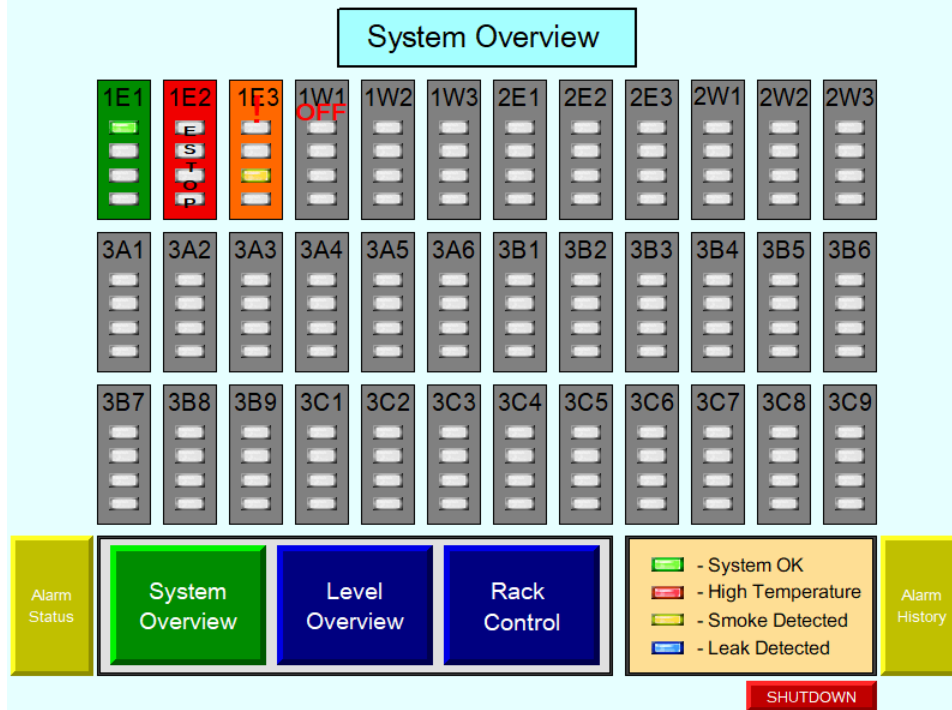


Figure 3. Displays the System Overview page of the HMI display with an example of the four states a rack can be in

An individual rack’s page displays greater information about each rack such as the temperature of the rack, smoke detector power and status, and water controller alarms. It also includes an image of a rack with indicators of each alarm, should one go off. The level overview display allows users to see a top-down view of the sPHENIX and its platforms. If a rack encounters an issue, the corresponding rack on this display will show an indicator. The rack control page, depicted by figure 4, allows operators to turn a rack on or off; this action is preceded by a caution page confirming the operator’s actions. A rack will not power on if there are alarms active or the rack has not been reset, and the rack control display depicts that as well.

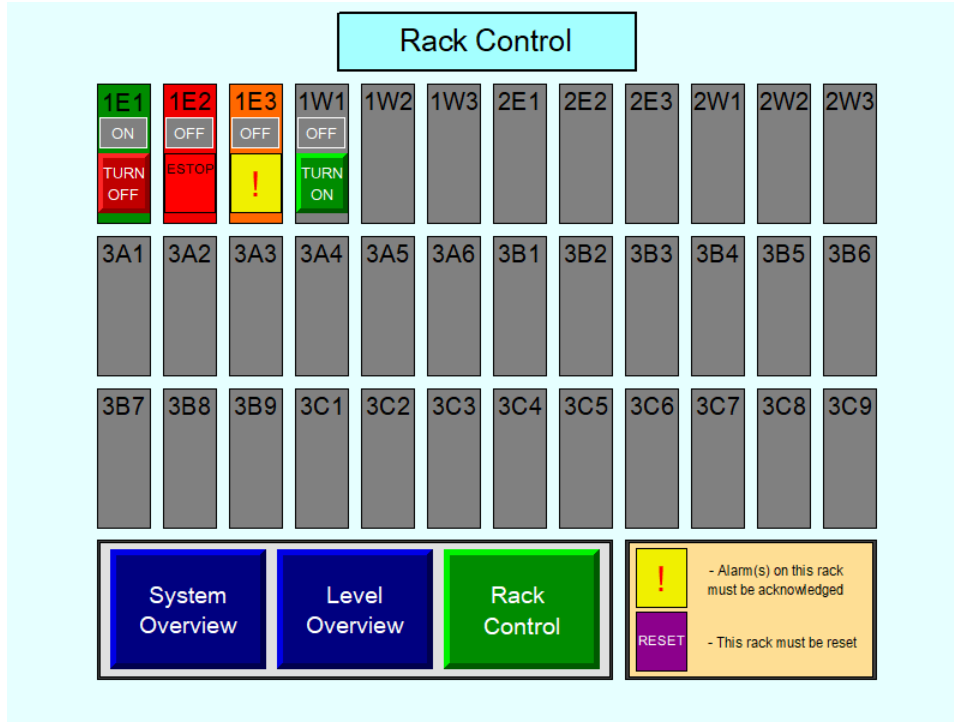


Figure 4. Rack Control display showing corresponding four states a rack can be in

Alarms on the racks are handled by the HMI program as well. Each alarm handles a PLC tag and will trigger if that tag reaches a certain value (the trigger value). Alarms like such as the High Temperature, Smoke Detected and Leak Detected alarms among others will show up on the alarm status page depicted in figure 5.

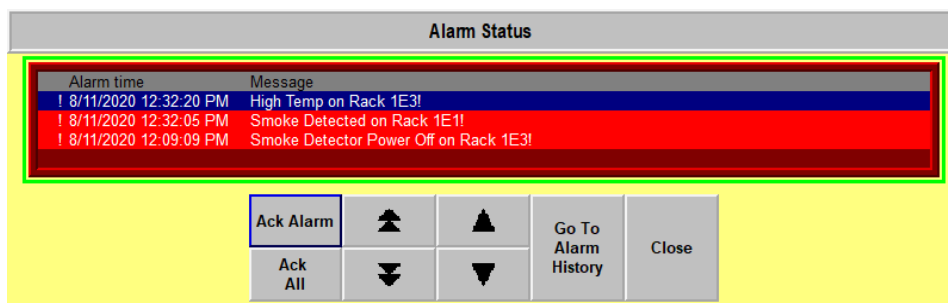


Figure 5. Alarm Status page showing active alarms on three racks

On the alarm history page (depicted in figure 6), informative banners will appear with timestamps showing important events such as alarms clearing, system resetting, or racks being powered on. Operators will be able to use this page to help diagnose and address triggered

alarms. Should an alarm trip, an operator would be able to see the alarm on the display's System Overview page. They would then be able to acknowledge the alarm on the Alarm Status page and address the source of the problem at the support rack. Once the problem is believed to be fixed, the reset button would be pressed. As long as the problem is fixed, the button press would go through the system and be recognized by the PLC and HMI.

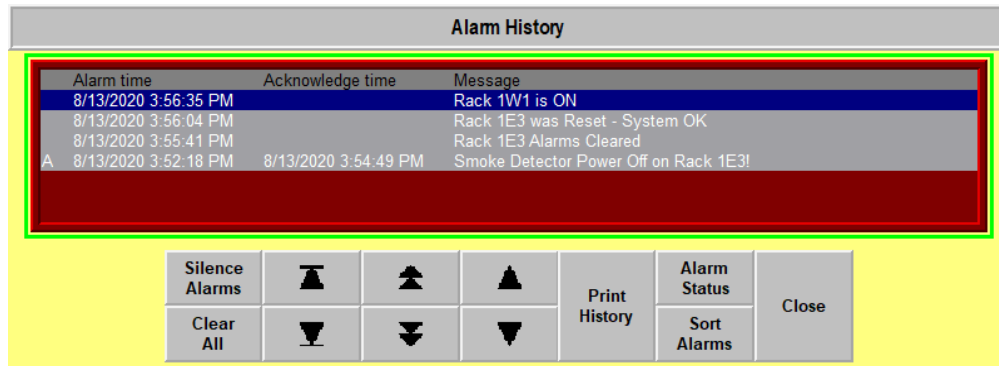


Figure 6. Alarm History page with alarm, acknowledgement and information banners for a rack

Sample Scenario

We can understand the capability of the HMI displays through a sample scenario. An operator would be in the operating room and notice that one of the racks on the HMI changed color from green to orange. Upon further examination, the operator sees a yellow LED on the Rack 1E1. The operator pressed the iPad like display on Rack 1E1 and an overview page of Rack 1E1 appears. From this page the operator is able to see that the smoke detector is not powered. Now that the operator understands what the problem on the support rack is, he navigates to the Alarm Status page and presses “Ack Alarm” to acknowledge the alarm. The operator then goes to Rack 1E1 and addresses the problem. After fixing the problem the operator pushes the Reset button located on the support rack and sees a light turn on. The operator understands that this means the rack was successfully reset and the rack can be powered on. The operator then walks back to the operating room and navigates on the HMI to the Rack Control page. They would look

to Rack 1E1 and see that the background is grey, the indicator shows the rack is off and there is a green button that says “TURN ON”. The operator presses the button and is brought to a caution page where they are prompted: “You are about to turn ON Rack 1E1”. Under this there is a red “GO BACK” button and a grey “YES” button. The operator presses the “YES” button and the button is replaced by a green indicator that says, “RACK IS ON”. The operator presses the “GO BACK” button and is taken back to the Rack Control page where they can confirm that the rack is on. The operator finally returns to the System Overview page to see all of the racks have a green background and a green LED, signaling that all systems are on and OK. It’s easy to see that this program will give a great amount of information for operators to work with and is very easy to follow.

Conclusion

The development of the HMI displays throughout the summer ended with a program that is very easy for operators to follow and understand. While the HMI could not have performed without the PLC, another incredibly important device of this project is the EWON VPN device. With a remote internship as this, it would have been very difficult for this project to have been completed to the point where it is now. The EWON VPN device allowed us to work on the software from our homes and see how it would communicate with each other and the hardware through a remote connection.

For the future, support for multiple languages and a connection to an external database for the alarm history page will be added. This design has the ability to be adjusted and changed with additional requests by operators, technicians and scientists.

Acknowledgements

I would like to express my sincerest thanks to Joel Vasquez and Peter Hamblen for all of their help and guidance through the project. Additionally, I would like to thank Jason Cheung, Robert Benkov, Roland Wimmer, the sPHENIX team and the SULI team for their endless support through the project. This project was supported in part by the U.S. Department of Energy, Office of Science, Office of Workforce Development for Teachers and Scientists (WDTS) under the Science Undergraduate Laboratory Internships Program (SULI).

Quantifying frost formation on frozen-hydrated biological samples with computer vision

Holdy Chauvette

Department of Mechanical Engineering Technology, Farmingdale State College, Farmingdale,
NY, 11735

Adam Lowery

Department of Mechanical Engineering, Virginia Tech, Blacksburg, VA 24060

Ashwin Ambi

Department of Chemistry, Stony Brook University, Stony Brook, NY, 11794

Tiffany Victor and Lisa Miller

NSLS-II, Brookhaven National Laboratory, Upton, NY 11973

Abstract

The National Synchrotron Light Source II (NSLS-II) at Brookhaven National Laboratory utilizes x-ray light to conduct x-ray based imaging and spectroscopy techniques on many types of samples, including frozen-hydrated biological specimen. A cryostage is used to prevent hydrated samples from being damaged by x-ray radiation. However, residual water vapor in the sample environment condenses onto the surface of the frozen sample and deteriorates the visibility of the specimen and data quality over time. Our objective was to develop a software program using Python and OpenCV to measure frost formation by evaluating an image supplied by the user and quantifying the monochromatic intensity of the pixels at specific regions of the sample and outputs the pixel value (0 - 255). To test the program, we used an image of a silicon nitride window located within a cryogenic stage that was accumulating frost over time. Our results showed that frost formation can be observed and analyzed through pixel intensity as a function of time. As the frost develops in a specific area, the pixel intensity increases from 0 to 255. Using the intensity values, the average was calculated and plotted to visualize dot array intensity overtime. For the cryostage we tested, we found an 89 % increase in frost over one hour. In summary, the changes in the image intensities permitted us to compute the rate of frost formation and hence, it will assist in determining the best process to slow the rate of frost formation.

I. Introduction

X-ray fluorescence microscopy and spectroscopy are techniques used to study the elemental and chemical composition of a sample, respectively (Shen, 2015). The x-rays provide valuable information, but they can also damage hydrated, biological samples (Beetz, 2003; Gianoncelli,

2015). To combat this issue, cryogenic stages can be used to freeze the hydrated, biological samples at cryogenic temperature (-150°C and lower) (Maser, 2000). Freezing the sample will stop all metabolic activities (Kaufmann, 2014). Although this is helpful to fight against ionizing radiation, residual water vapor in the sample environment nucleates on the cold sample surface, leading to condensation frosting. The frost progression compromises the visibility and transparency of regions of interest in biological samples for cryo-microscopy (Walker, 2019). As the integrity of the sample deteriorates, the data quality is affected. Therefore, frost development on the samples needs to be controlled. Scientists have tried all sorts of frost mitigation techniques, from dry nitrogen gas purge to vacuum environments, but with limited success. After finding a method to reduce the frost progression, it's necessary to have a way to verify the efficacy of the method. So, we developed a software program through OpenCV using Python to create a numerical assessment of the frost formation on the surface of the sample.

II. Methods

To conduct the experiment, a four-dot array sample, each dot 500 microns in diameter, was printed on a sheet of paper. The printed paper with the dots was adhered to the bottom side of a 2x2 mm silicon nitride window, so that the sample was observable through the transparent silicon nitride membrane (Deborah, 2013). A nitrogen purged cryostage was employed to freeze the nitride window at cryogenic temperature (-150°C and lower). Nitrogen purged was preferred over vacuum because it does not freeze dry the sample. Also, the cryostage window is made out of Ultralene, so it is not strong enough to hold against a sufficiently strong vacuum. The cooling block of the cryostage was programmed to reach cryogenic temperature within five minutes. Images of the frozen hydrated biological sample were taken under a Nikon Eclipse LVDIA-N light microscope over three hours to evaluate the frost formation at specified intervals. A pseudo-code

was written representing all the steps needed to reach the ultimate goal of quantifying the frost formation (Figure 1).

Pseudo-Code	
•	Locate/Import Image
•	Convert Image to Gray Scale
•	Draw ROI on Specific Area
•	Find Intensity Value inside of ROI
•	Data Analysis
•	Save Data in Text-file

Fig1: The schematic that was followed to create the code.

The code was written in Python with imported libraries: *OpenCV*, *NumPy*, *SciPy* and *Matplotlib*. Python was the programming language used due to its accessibility, extensive range of libraries, and frameworks (Sandeep, 2020). The first task was to locate and import images of the sample within the directory, which in this case were the images of the silicon nitride window at different periods in the cryogenic stage. After locating and importing the image from a directory on the computer, it was converted into *grayscale* (Szeliski, 2011). Measuring grayscale was the most straightforward method that allows one to follow how the pixel intensities are changing over time (Figure 2) (Sandeep, 2020). Intensity values ranged from 0 (for black) to 255 (for white) (Figure 2). Converting the image from RGB to grayscale gave the opportunity to use the region of interest (ROI) function to separate the foreground from the background.

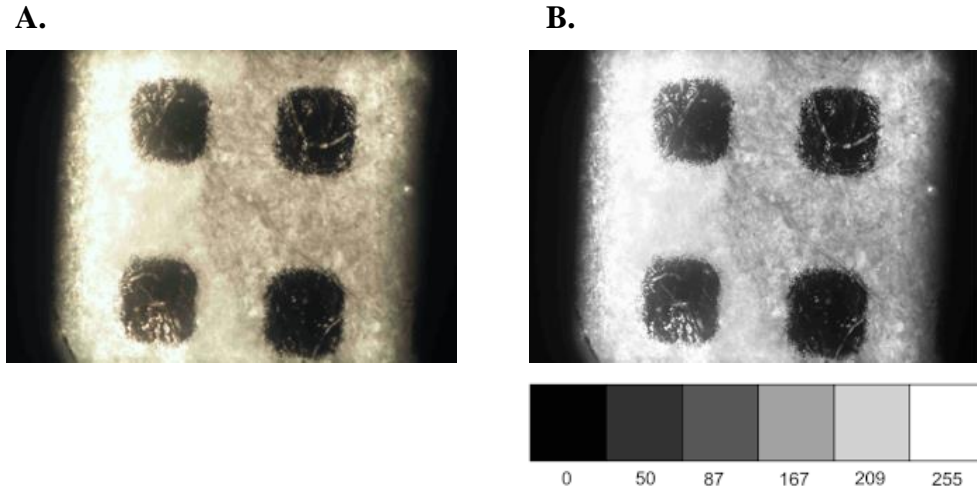


Fig 2: A.) RGB Image of silicon nitride window at room temperature. B.) Grayscale image of silicon nitride window at room temperature with scale.

The foreground was the four black dots, while the unwanted region was the background surrounding the dots. Therefore, four rectangular ROIs were drawn. After identifying those four ROIs, their vertices were used to calculate the bounds (Figure 3). The coordinate for the top left vertex of each region was identified by the ROI function, but the coordinate for the bottom right vertex was unknown. The height of the rectangular ROI was added to the y-point of the top left vertex to find the y coordinate for the bottom right vertex. Then, the x-point was added to the width to determine the x coordinate for the bottom right vertex (Figure 3). Doing that simple operation gave the coordinates for the bottom right vertex. Followed by that, the x and y ranges were established.

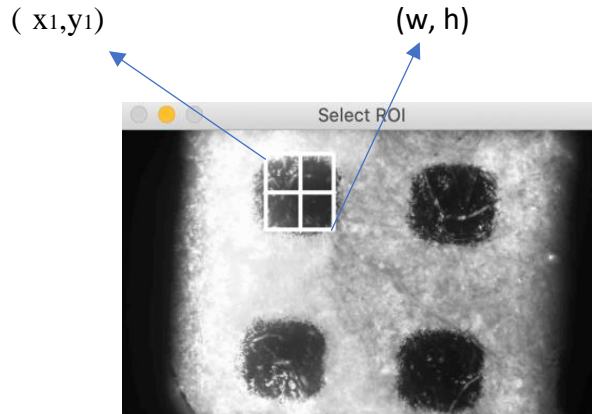
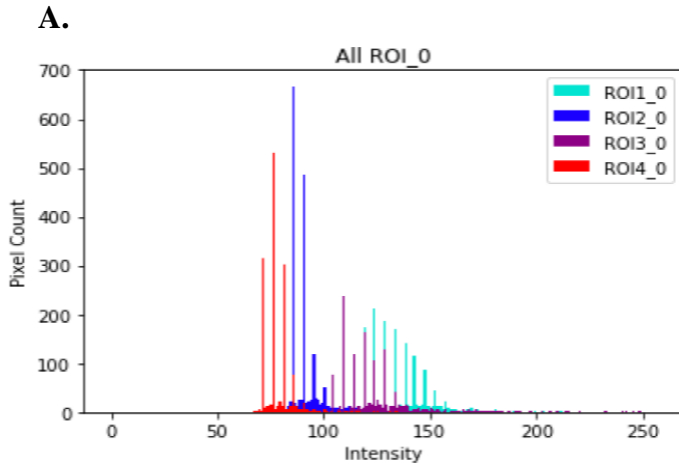


Fig 3: Silicon nitride window at room temperature with ROI and vertices/coordinates.

Those coordinates set a boundary to find all the intensity values bounded by each ROI (Region of Interest) or each black dot (Figure 4). The intensity values were plotted in a histogram to view the intensity distribution (Figure 4). Using the same intensity values, the mean, median, mode, and standard deviation were calculated for each region. The intensities for all ROIs were averaged together. The same operation was done for the median and mode pixel values (Figure 7). After generating the bounds for each ROI, the mean, median, and mode for each picture, were then stored in a text file outside of the Python program. The code was first run on an image of the sample at room temperature and repeated on seven other images at cryogenic temperature for timestamps of 30 minutes, 60 minutes, 90 minutes, 120 minutes, 150 minutes, and 180 minutes. After examining all images of the frozen sample, the change in the sample's visibility was established through a percent difference in pixel intensity between room temperature and cryogenic temperature.



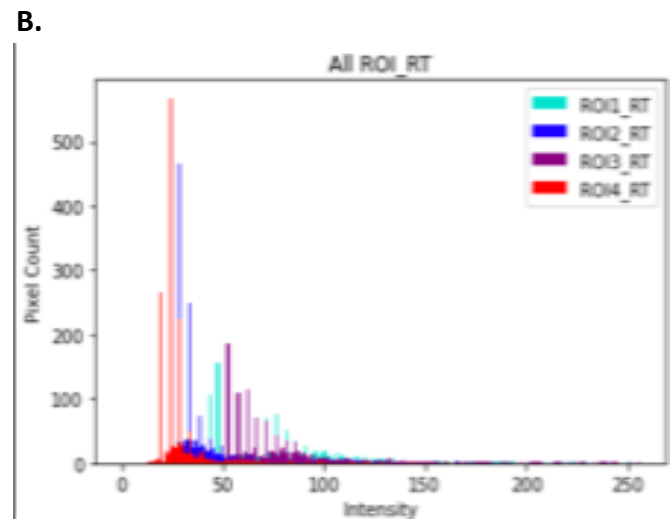
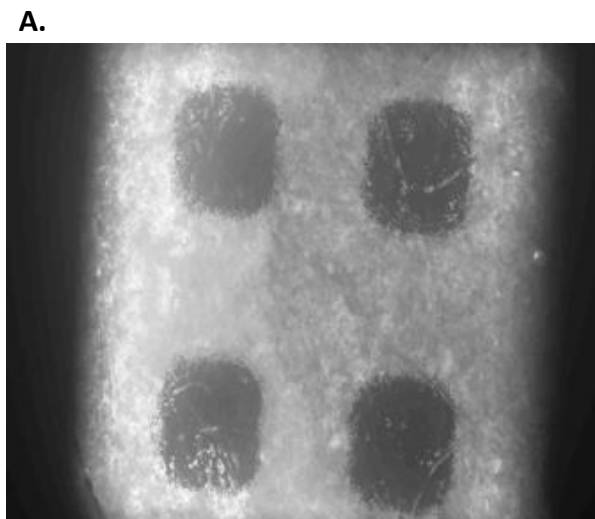
B.

	0	1	2	3	4	5
0	252	252	252	252	252	252
1	252	252	252	252	252	252
2	252	252	252	253	221	239
3	232	240	238	252	225	253
4	246	216	240	252	221	203
5	241	196	196	205	154	195
6	229	223	201	150	142	199
7	190	191	152	153	136	138
8	188	137	134	140	133	124

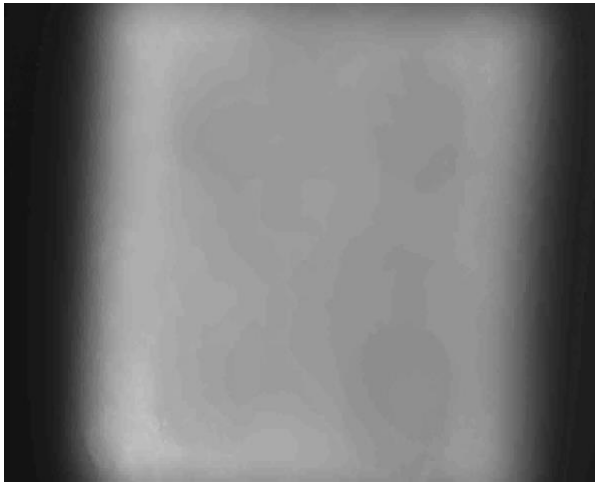
Fig 4: A.) Histogram of distributed intensity value B.) Intensity values inside of ROI

III. Results

The code showed success, demonstrating how the frost gradually developed in numerical values. The histograms show that, at room temperature, most of the intensities of each ROI are close to 0. Once the temperature was changed to cryogenic temperature, the intensity of each ROI moved closer to 255 (Figure 5). This overall change in intensity means that, as frost builds up on the sample, the intensity values increased.



C.



D.

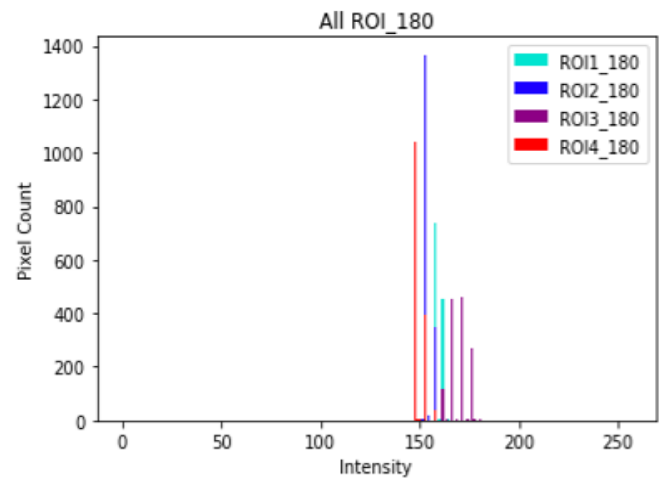


Fig 5: A.) Image of nitride window at room temperature B.) Histogram of distributed intensity value at room temperature. C.) Image of silicon nitride window at 180 minutes in cryogenic stage D.) Histogram of distributed intensity value at 180 minutes in cryogenic stage.

The average mean for each image was found and plotted on a line graph against time with the standard deviation of the mean for each ROI (Figure 6).

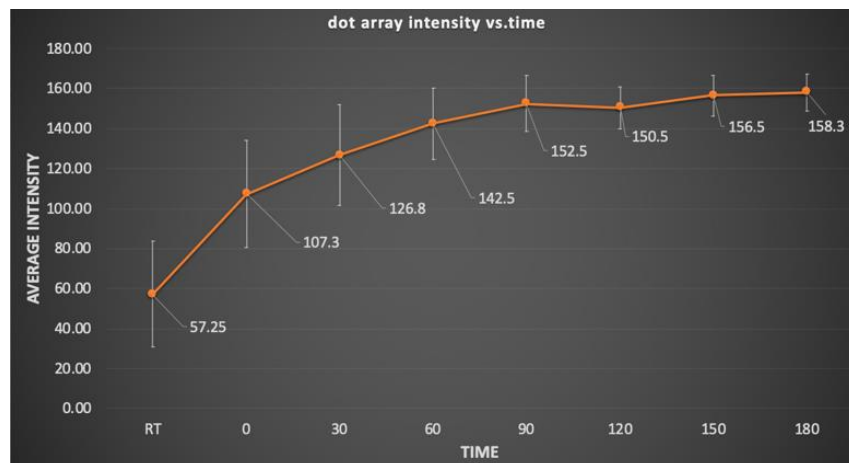


Fig 6: Line graph of average intensity over time with standard deviation.

The dot array intensity vs. time graph implies that frost build ups faster going from RT to 60 mins compared to going from 120 mins to 180 mins (Figure 6). The data was carefully analyzed and demonstrated after 90 minutes the dots were covered in frost, making it difficult for the code to read the intensity values. Using the average intensities at room temperature and cryogenic temperature, a 61% increase in frost was calculated. The sample was held at cryogenic temperature for 60 minutes in the cryogenic stage and a 28% increase in frost was found. In general, there was an 89% increase in frost starting from room temperature and holding the sample at cryogenic temperature for 60 minutes in the cryogenic stage. The sample was close to being fully covered with frost and cryo-microscopy, imaging, and/or spectroscopy studies should be conducted before the 90-minute time point for valid results.

Time	MEAN	STDV	MODE	MEDIAN	
RT		57.25	26.35	37.75	49.75
0	107.3	26.70	98.3	104.5	
30	126.8	25.02	123.5	124.8	
60	142.5	17.94	138.8	142.3	
90	152.5	14.15	150.5	151.8	
120	150.5	10.66	148.5	149.5	
150	156.5	10.25	155.5	156.5	
180	158.3	9.287	156.8	157.8	

Fig 7: Data chart used to quantify frost formation

IV. Conclusions

After a careful analysis, it was determined that the slow progression of frost between 120 to 180 minutes was due to the dot arrays being sufficiently covered in frost after 90 minutes (Figure 6). There was also a strong increase in pixel counts as the frost progresses over time (Figure 5). Based on the fluctuation of the averaged intensities, imaging and spectroscopy techniques would have to be done on the sample before 90 minutes.

The code proved capable of quantifying the frost formation over time, although the performance of the code can be improved. For future iterations, instead of using a rectangular ROI, the user should be able to change the geometry of the ROI selector tool to better fit the geometry of the image. The printer paper affected the intensity values of the black dot array due to its non-uniform texture diffusing the background illumination unevenly. A transparent film or a substrate with a more Lambertian texture would be a better choice going forward. In the future, this code could be used as a tool to compare how frost mitigation methods, such as dry gas purge and vacuum, perform against each other.

V. References

1. Beetz T, Jacobsen C. (2003) “Soft X-ray radiation-damage studies in PMMA using a cryo-STXM.” *J Synchrotron Radiation*. 10(Pt 3):280-283.
2. Deborah, Kelly F., et al. (2013) “Cryo-SiN – An Alternative Substrate to Visualize Active Viral Assemblies.” *Journal of Analytical & Molecular Techniques*, vol. 1, no. 1
3. Gianoncelli, A., Vaccari, L., Kourousias, G. *et al.* (2015) “Soft X-Ray Microscopy Radiation Damage on Fixed Cells Investigated with Synchrotron Radiation FTIR Microscopy.” *Scientific Reports* **5**, 10250.
4. Kaufmann R, Hagen C, Grünewald K. (2014) “Fluorescence cryo-microscopy: current challenges and prospects.” *Current Opinions Chemical Biology*. 20(100):86-91.
5. Maser J, Osanna A, Wang Y, et al. (2000) “Soft X-ray microscopy with a cryo scanning transmission X-ray microscope: I. Instrumentation, imaging and spectroscopy.” *Journal of Microscopy*. 197(Pt 1):68-79.
6. Sandeep, J. (2020, January 30). OpenCV Python Tutorial
7. Shen, F. (2015, November 4). Synchrotron X-ray Techniques for Scientific Research.
8. Szeliski, R. (2011). *Computer Vision Algorithms and Applications*. London: Springer.
9. Walker, Christopher, et al. (2019) “Transparent Metasurfaces Counteracting Fogging by Harnessing Sunlight.” *Nano Letters*, vol. 19, no. 3, pp. 1595–1604.

VI. Acknowledgements

I would like to express my sincere thanks to my mentors Dr. Lisa Miller and Adam Lowery for their guidance and knowledge on this project. I would like to thank the valued team members of the Miller Research Group and BNL's DAMA group for their awareness and help. The completion of this project could not have been possible without the assistance and hospitality of Brookhaven National Lab. This project was supported in part by the U.S. Department of Energy, Office of Science, Office of Workforce Development for Teachers and Scientists (WDTS) under the Science Undergraduate Laboratory Internships Program (SULI).

Hydrogen Intensity Mapping Simulator: interpolation improvements and radio point source compatibility with application to GaLactic and Extragalactic All-Sky MWA Survey dataset

Zhi Chen, Physics, Stony Brook University, Stony Brook, NY 11794
Anze Slosar, Physics, Brookhaven National Laboratory, Upton, NY 11973

Summer 2020

Abstract

BMX is a radio telescope built at Brookhaven National Laboratory to serve as a prototype to experiment with methods for mapping the structure of the Universe by detecting 21cm hydrogen emission lines. The biggest challenge of this technique is the presence of galactic foreground. Galactic foreground are radio frequency signals emitted from galaxies that contaminate hydrogen signals, so an effective filtering method is necessary for this technique. The development of BMX will eventually lead to the construction of the Packed Ultrawide Mapping Array (PUMA), which is a large radio transit interferometric telescope designed to explore the large scale of the Universe through hydrogen intensity mapping. My role in this project is to improve a simulator that simulates complex visibility given mock data collected by a simulated telescope looking at a fixed sky. I have successfully implemented Lanczos interpolation which significantly improves the complex visibility curve as it generates a theoretically smooth curve for the foreground data set. In addition, an implementation of calculating complex visibility for radio point sources also helped to examine radio point source datasets, which can be compared with hydrogen and foreground signal data. The goal of this simulator is to decontaminate real datasets by removing signals other than hydrogen signals. Along with the technique, hydrogen intensity mapping, we will explore different aspects of cosmology such as cosmic inflation and the growth of the cosmic structure.

1 Introduction

For decades, cosmologists are trying to model the general structure of the Universe through variety of methods. One of the relatively new but very promising method is hydrogen intensity mapping. Neutral hydrogen has two energy states, which correspond to two different spin configurations. The state where electron and proton spin in the same direction has slightly higher energy compared to the one where they spin in the opposite direction. Once the electron experiences a spin flip, a photon with rest wavelength of 21cm will be emitted. The wavelength will be stretched once it reaches Earth since the signal will be redshifted due to Universe expanding. Once the signal's redshift is determined, it is straightforward to infer the position and time period of the signal emission. Since there are countless neutral hydrogen clouds floating in the Universe, there should be sufficient amounts of signals coming from all directions for us to map out the general structure of the Universe. However, there are many obstacles making it difficult to measure these signals. One of the major challenge is the galactic foreground, which are radio signals emitted by galaxies. These signals are many orders of magnitude higher than the hydrogen signal making it extremely difficult to separate the two. Scientists can still investigate and study properties of hydrogen intensity mapping by running simulations with mock data since its currently not possible to completely decontaminate the signals. The simulator called *imcurio* is

seeking to find an effective filtering method by analyzing different data types including foreground, radio point sources, and hydrogen signals.

2 Objectives and Scope

The simulator had one minor issue. Even though it is extremely complicated to filter out foreground signal from the cosmological signal for real datasets, the simulated datasets already separated the two. The theoretical complex visibility curve for solely foreground signal will be smooth across all frequency range. However, it is not the case for the existing linear interpolation. The way to approach this issue to have a better interpolation method called Lanczos interpolation. The first objective is to implement and prove that Lanczos interpolation is better a presenting the dataset by generating a much smoother curve.

The simulator depends on the fast fourier transform (FFT) module in python to fourier transform sky brightness distribution into complex visibility. However, it is not an ideal method to do the transform for radio point sources due to the nature of dirac-delta functions. Instead of using FFT, direct calculation is a more efficient and accurate way to calculate complex visibility. Therefore, the second objective is to expand the simulator such that it is capable of calculating complex visibility for point sources. Lastly, we want to apply this technique to analyze GaLactic and Extragalactic All-sky MWA Survey (GLEAM) dataset.

3 Methods & Results

3.1 Lanczos Interpolation

Lanczos interpolation uses a normalized sinc function as a kernel function to interpolate data points. a in the kernel function, equation(1), is an integer that defines the size of the kernel. a is usually chosen to be 2 or 3, while higher window length might result in slightly better results in exchange for time consumption. The interpolation equation is given by equation 2. s_i refers to the data in the i th index of the data set. x refers to the point that you want to interpolate and $[x]$ is the floor function.

$$L(x) = \begin{cases} 1 & \text{if } x = 0 \\ \frac{a \sin(\pi x) \sin(\pi x/a)}{\pi^2 x^2} & \text{if } -a \leq x < a \text{ \& } x \neq 0 \\ 0 & \text{otherwise} \end{cases} \quad (1)$$

$$S(x) = \sum_{i=[x]-a+1}^{[x]+a} s_i L(x-i) \quad (2)$$

By applying this sinc filter, the data that is closer to the interpolation point will be weighted more while data further away will be weighted less. One thing to note is that the interpolated point is in data index space. This means that if we choose $x = 1$, then the interpolated data will be exactly the same as s_1 . One convenient property of this technique is that this filter can be easily expanded to higher dimension, which is described in equation(3).

$$L(x, y) = L(x)L(y) \quad (3)$$

The way to approach this is to first write a code for 1D interpolation and generalize this to 2D using equation (3). In order to check the validity of the code, mock data generated by using a known function, such as a sine function is desired. The implementation for the actual simulator will begin after confirming that the code works for both 1D and 2D sine functions.

After successfully implementation of Lanczos interpolation, a comparison should be made between the existing linear interpolation and Lanczos, shown in figure(1).

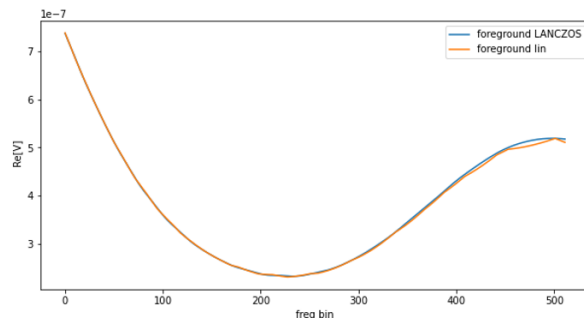


Figure 1: This plot compares the difference between 2 different interpolation method. This plot shows the real part of complex visibility for some specific baseline as a function of frequency bins. Baseline refers to the set of telescope with some position (u,v) observing the signal. Clearly, the linear interpolation has some jagged lines in the end while Lanczos interpolation is a lot smoother.

3.2 Point source compatibility

Radio telescope surveys over the sky collecting spectral flux density over a wide range of frequencies. In order to analyze the data, complex visibility is often calculated, which is simply the fourier transform of the spectral flux density.

$$V(u, v) = \iint I(l, m) e^{-2\pi i(ul+vm)} dl dm \quad (4)$$

In equation(4), $V(u, v)$ is the complex visibility as a function of u and v , which are the spatial frequency having units in wavelength, i.e. $u = x/\lambda$ and $v = y/\lambda$. $I(l, m)$ is the spectral flux density as a function of l and m , which are the position of the radio point source in the sky's plane. Even though the equation for complex visibility is given by equation(4), it is still necessary to include the antenna beam size of the telescope since it roughly determines how sensitive the telescope picks up the data. The beam of most radio telescope is approximately gaussian, which is what we used in the simulator, (equation 5) where the σ is the angular resolution of the telescope.

$$B(l, m) = e^{-\frac{(l^2+m^2)}{2\sigma^2}} \quad (5)$$

After considering antenna beam size, the equation for the complex visibility becomes equation(6). By multiplying the spectral flux density by the gaussian, signals further away from

center of the beam will be weighted less compare to the ones closer to the center.

$$V(u, v) = \iint I(l, m)B(l, m)^2 e^{-2\pi i(ul+vm)} dldm \quad (6)$$

The unit for spectral flux density is energy per unit area of receiver per unit frequency, i.e Jansky = $10^{-26} W/m^2/Hz$. However, it is often convenient to describe the flux in the unit of temperature or Kelvin, which is described in expression 7. λ is the wavelength at which telescope is observing, F_{ν} is the spectral flux density, k_b is the boltzmann constant, and Ω is the beam area in steradian. After the transformation, the complex visibility will have a unit of $[T\Omega]$. In order to eliminate the steradian, it is a good practice to normalize the complex visibility by dividing the complex visibility by the sum of the beam area, which is in steradian.

$$T = \frac{\lambda^2 F_{\nu}}{2k_b \Omega} \quad (7)$$

FFT is the ideal module that optimizes efficiency when calculating fourier transforms. However, it is not the case for point sources. Point sources can be described by using dirac-delta functions. Due to the integral property of dirac-delta function, equation(8), direct calculation of complex visibility by dropping the integral is more efficient and accurate if we were to compare it with the result of FFT.

$$\int_c^d f(x)\delta(x-a)dx = \begin{cases} f(a), & a \in (c, d) \\ 0, & \text{otherwise} \end{cases} \quad (8)$$

We can define the spectral flux density of point sources to be $I(l, m)_{ps} = F(l, m)\delta^2(l, m)$, then the equation(6) becomes equation(10), where l' and m' refer to the position of the point source on the sky plane.

$$V(u, v) = \iint F(l, m)B(l, m)^2 \delta^2(l-l', m-m') e^{-2\pi i(ul+vm)} dldm \quad (9)$$

$$V(u, v) = F(l', m')B(l', m')^2 e^{-2\pi i(ul'+vm')} \quad (10)$$

The way to verify the validity of the code is to compare it with the result from using the usual FFT method. The way to do it is to let all spectral flux density on the sky to be equal to 0 except for one small area and the position that region is specified using spherical coordinate system, θ and ϕ . In order to mimic the point source, all values in this small area should have the same value. For example, 1 Jansky. For the direct calculation route, I will place the point source at the same location using θ and ϕ , and set the flux to 1 Jansky just like the FFT method. The result is similar as shown in plot 2 just as expected.

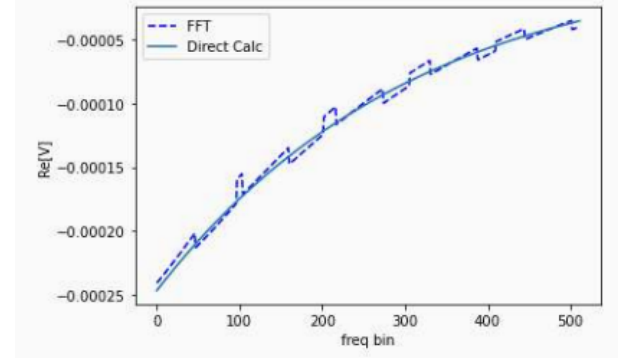


Figure 2: The plot shows the real part of the complex visibility vs. different frequency bins for a specific baseline. The jagged blue curve is from FFT calculation while the smooth curve is from direct calculation. Both curves look extremely similar. The result from direct calculation produces a much better and cleaner result compare to a jagged curve produced by the FFT, which is expected.

3.3 Application to GLEAM

The next step read in the GLEAM dataset which contains 200,000+ radio point sources with their corresponding position, flux density, and spectral index. The position of the sources are measured in declination and right ascension with unit in degrees. It is more convenient to convert this system to spherical coordinate (sph), $\theta_{sph} = 90 - \theta_{dec}$ and $\phi_{sph} = \phi_{RA}$. Flux density is measured in Jansky and the spectral index is the measure of the dependence of flux density on frequency. The equation for the relationship between the two is given by $S_{\nu} \propto \frac{\nu}{\nu_0}^{\alpha}$, where α is the spectral index and $\nu_0 = 200 MHz$. Therefore the actual flux density observed at different frequency

will be $S'_\nu = S_\nu \times \frac{\nu}{\nu_0}^a$.

One thing to consider is that it is very inefficient to load all data points. First, it takes around 4-5 hours to load all data points because there are just too many of them. Second, most data points don't contribute much since they are far away from the center of the beam that we defined earlier. Data points away from the center will be suppressed heavily especially when they are outside the Gaussian lobe. Now, the idea is to find the angle pointing away from the center of the beam such that the results would converge. Telescope will now only consider a disk region right above it defined by that angle as the radius. This angle is the same as theta if the position of the telescope is defined to be at the north pole. However, it generates some minor issues due to how GLEAM surveyed over the sky.

$$R_y(\theta) = \begin{bmatrix} \cos \theta & 0 & \sin \theta \\ 0 & 1 & 0 \\ -\sin \theta & 0 & \cos \theta \end{bmatrix} \quad (11)$$

GLEAM surveyed from 30° to -90° declination, which is not covering the entire sky. This causes a little trouble since the default position of the telescope is defined using the gaussian beam equation 5, which is $(l, m) = (0, 0)$ or directly at the north pole. This is obviously not in the range of all the data points. Therefore, it is necessary to relocate the telescope by rotating all data points such that it appears at different position. Since $\theta \in (60^\circ, 180^\circ)$, its reasonable to choose the position at the midpoint, $\theta = 120^\circ$. Next, we simply apply rotation matrix, equation(11), around y-axis to rotation the telescope at $\theta = 120^\circ$ to the north pole. Last step is to try out different θ values to find the convergent angle, which happens to be around 10° .

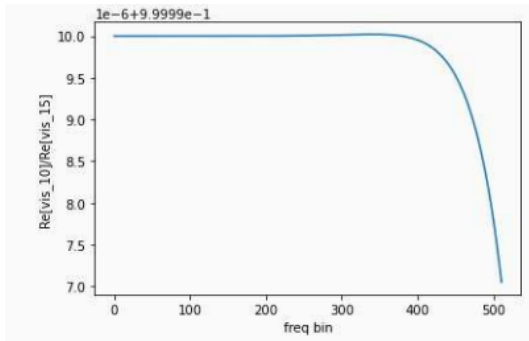


Figure 3: This plot shows the ratio of complex visibility between two theta for a specific baseline. For $\theta = 10^\circ$ and $\theta = 15^\circ$. Its clear to see that there is no difference the two, which means $\theta > 10^\circ$ is not going to affect anything.

3.4 Comparison

Next step compare all three different types of signals: galactic foreground, radio point sources, and hydrogen signals. The main objective for this simulator is to find a way to filter out foreground and radio point sources. The real and complex part of the visibility for three different data types are shown below in figure 4.

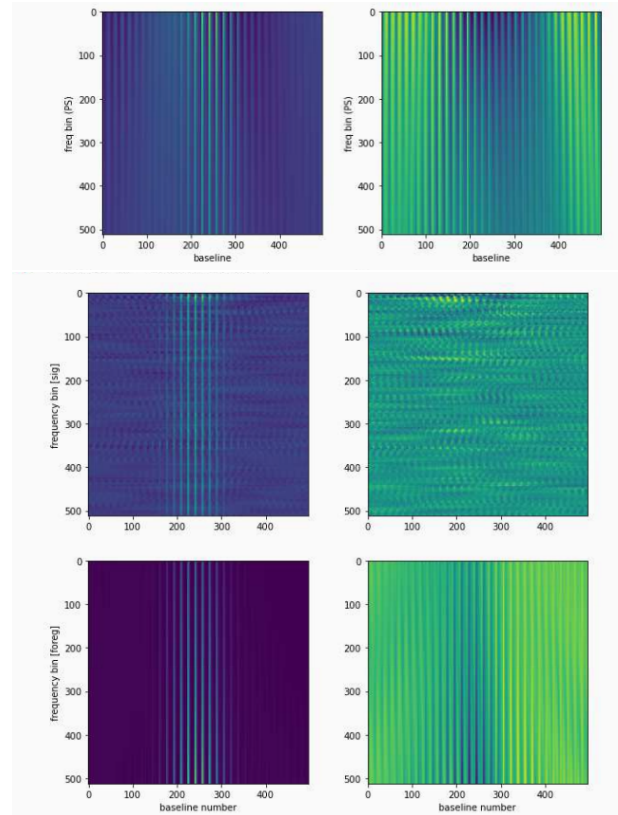


Figure 4: This shows the image plot for different signals. This is plotted as frequency bin vs. baseline. The magnitude of the complex visibility is determined by the color. The one on the left shows the real part of the complex visibility while the one on the right shows the complex part. The set on the first row is radio point sources, second row is for hydrogen signals, and the last row is for foreground.

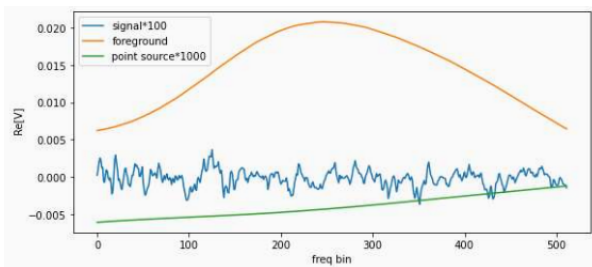


Figure 5: This shows a more quantitative comparison between three different data points. It shows the real part of visibility for some baseline. Both point source and foreground data are smooth across frequencies, while the signals have many edges. Note that the magnitude for signal is multiplied by 100 while for point source it is multiplied by 1000. The magnitude for the foreground is significantly larger than other 2 signals, and surprisingly the point sources have smaller magnitude than the hydrogen signal.

4 Discussions

4.1 Interpolation and Point Source

In figure 1, we see that there is a noticeable improvement between the linear interpolation and lanczos interpolation. Galactic foreground data is supposed to be smooth in frequency space(REF 1), which means it should not have any jagged lines which are produced in linear interpolation. Even though lanczos interpolation always outperforms linear interpolation, visibility curves for some baseline is still not very smooth. Nonetheless, this is still a major improvement for correctly simulating the galactic foreground. In terms of efficient, lanczos interpolation takes about 120% of the process time needed compare to the linear interpolation, so it is slightly slower. The processing time can be improved by optimizing the code, but I think it is good for now.

In figure 2, both curves obtained from FFT and direct calculation are extremely similar. FFT has its limitation when calculating point sources, since point sources are in theory infinitely small pixels. FFT will put data points on a grid line which includes unwanted data points for point sources, and the jagged lines in the complex visibility curve also reflect this. On the other hand, directly calculate complex visibility curve by using the property of dirac-delta function gives the

exact answer.

In figure 5, it shows the magnitude and shape for all three different data types. Foreground has largest magnitude as expected. Surprisingly, the radio point sources appear to have smaller magnitude compare to the hydrogen signal, this could be a mistake in the code. However if this is true, it suggests that we can probably ignore the flux emitted by point sources since its significantly smaller than hydrogen signals. In terms of the general shape, foreground and point sources are both smooth in the frequency space while the signal is not.

4.2 Next Step

In figure 4, we can see image plots for complex visibility with different frequency bins and baselines. By implementing point source compatibility, the simulator is now capable of producing visibility curves with three different types of data. Since the radio signals that BMX collect will be a mixture of different signals, filtering is an essential part for data analysis. The next step is look for filtering methods such that we can successfully obtain only the hydrogen signals by removing the rest. The current idea is to look at the power spectrum for different data types. In theory, the power spectrum for the foreground should vary slowly in frequency so it will dominate at low k power or large scale, while the signal should dominate at high k power or small scale. The idea is to perform some filtering so that the foreground part is heavily suppressed so that its smaller than the signal, and one possible method is to weight the spectra by some ν , frequency.

5 Conclusion

Hydrogen intensity mapping is proven to have the potential to map out the general structure of Universe. In order to resolve the issue of data contamination from galactic foreground, simulators are developed to seek for effective filtering methods. Incurio now utilizes lanczos interpolation which outperforms linear interpolation. The foreground visibility curve generates a much smoother curve by using lanczos interpolation. Another accomplishment is point source compatibility. Since FFT doesn't work well with point sources, it

is necessary to calculate their complex visibility separately. With the addition of point source compatibility, Imcurio is able to analyze a real dataset called GLEAM that contains 200,000+ radio point source signals. In the future, the development of an effective filtering method is needed so that real datasets collected by the radio telescope can be successfully decontaminated.

6 Acknowledgement

This project was supported in part by the U.S. Department of Energy, Office of Science, Office of Workforce Development for Teachers and Scientists (WDTS) under the Science Undergraduate Laboratory Internships Program (SULI).

I also want to thank my mentor, Anze Slosar, for his teaching and guidance on the project

Logic design of rack interlock system for detector infrastructure

Jason Cheung, Department of Electrical and Computer Engineering, Stony Brook University,
Stony Brook, NY 11794

Joel Vasquez, Physics Department, Brookhaven National Laboratory, Upton, NY 11973

1. Abstract

The Super Pioneering High Energy Nuclear Interaction eXperiment (sPHENIX) is a proposed upgrade to the former PHENIX detector at the Relativistic Heavy Ion Collider (RHIC). sPHENIX's upgraded readout electronics will be able to collect new data on the quark-gluon plasma (QGP), a fundamental state of matter. A supervisory system is necessary to ensure the electronics operate in a normal range. This project proposes a design for an interlock system that monitors racks carrying the electronics. Each rack is equipped with temperature, smoke, and water leakage sensors. A programmable logic controller (PLC) is programmed in ladder logic to continuously poll the sensors and automatically power off racks with detected hazards. The ladder program also triggers corresponding alarms and displays them on a touchscreen panel called a human machine interface (HMI). The project is a starting point for a centralized control system, and more infrastructure will be added to maintain safe operation of the detector.

2. Introduction

QGP is a state of matter that existed under the extreme conditions one microsecond after the Big Bang. Remarkable for being the most perfect fluid ever observed, its properties may unlock new insights on the theory of quantum chromodynamics (QCD) that defines the strong force. To study QGP, the RHIC recreates it by colliding heavy ions near the speed of light. Collisions occur at the heart of a detector, and data is collected by readout electronics located on racks. A CAD model of sPHENIX is shown in Figure 1.

The sPHENIX upgrade is expected to be complete by 2023. Although sPHENIX will reuse some existing equipment, the original PHENIX has been dismantled, and new support infrastructure is needed. A supervisory system should be sensitive to environmental hazards that can damage the machinery. Racks are immediately powered off in the presence of high temperature, smoke, or water leakage. This safeguard is called an interlock.

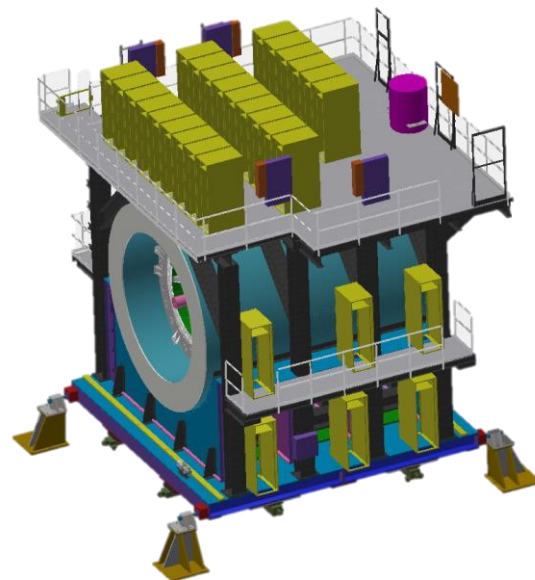


Figure 1. CAD model of sPHENIX detector. The detector is 3 stories tall and has several support racks on each level (in yellow)

3. Methods and Materials

PLCs are specialized digital computers used to automate industrial processes, such as assembly lines. External modules such as input/output (I/O) cards make them flexible as ports can be added to fit the needs of a system. A PLC and its modules are mounted together on a rack, as shown in Figure 2. This project uses a CompactLogix PLC from the popular industrial automation supplier Allen Bradley, owned by Rockwell Automation. Sensors are connected to the input ports, and output ports are used to power the racks. For a complete list of the specific products that are discussed in this paper, see Appendix A.



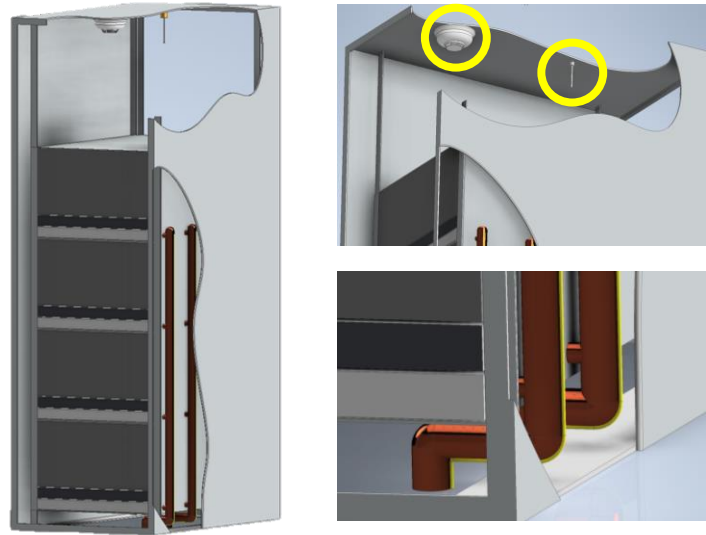
Figure 2. (Left) Ewon VPN router (Right) PLC and modules mounted together

To adjust to the challenges of a remote internship, remote access to hardware is made possible by an Ewon VPN router. Connecting the PLC to a VPN allows it to be remotely programmed. More details on the PLC program is discussed in a later section.

The PLC provides power to 36 total racks. While each rack carries varying support electronics depending on its function, they share identical supporting infrastructure. A CAD model for a single rack is shown in Figure 3. A resistance temperature detector (RTD) sensor and

a smoke sensor are located at the top of the rack. The water leakage sensor is a cable wrapped around water cooling pipes on the side.

Figure 3.
 (Left) Full CAD model of a rack
 (Top right) Close-up smoke and temperature sensors
 (Bottom right) Close-up cooling pipe



Models for the temperature and smoke sensor are still undecided. The leak cable is provided by the company TTK Leak Detection. Each leak cable has an embedded microprocessor that communicates with TTK’s FG-NET leak detection unit to report the location of a leak. The cables are connected in series to the unit, as shown in Figure 4. The FG-NET then sends data to the PLC.

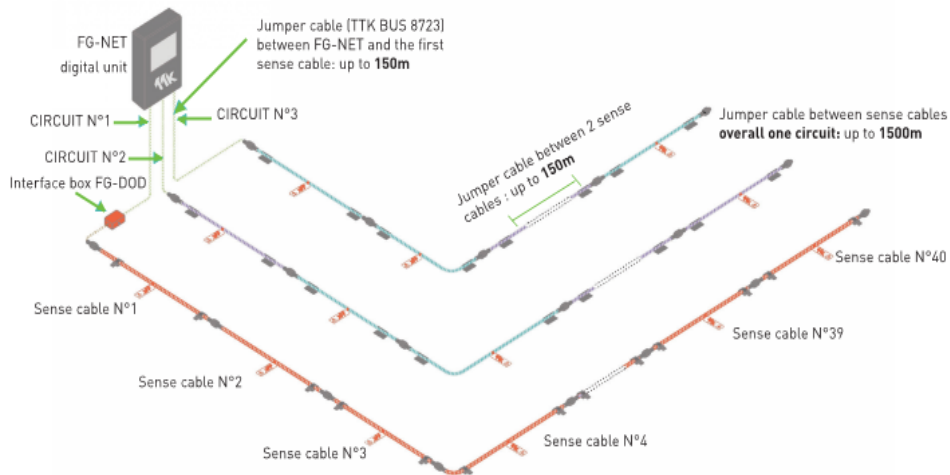


Figure 4. Leak detection unit and leak cables circuit from FG-NET User Manual ^[1]

4. PLC program

4.1 Ladder Logic Basics

The PLC is programmed in ladder logic with Rockwell Automation's Studio 5000 Logix Designer software environment. Aptly named, ladder programs are graphic diagrams that look like ladder rungs. Ladder programs are infinite loops that execute instructions on each rung sequentially. A very simple ladder program is shown in Figure 5.

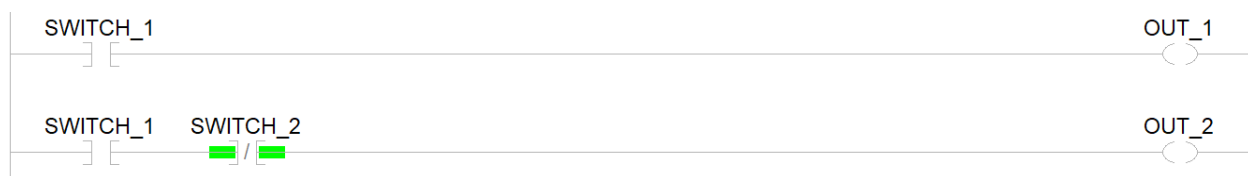


Figure 5. A very simple ladder program

Each rung of the ladder program has a physical interpretation as a circuit with relays. Relays are electromagnetic switches that open and close based on the value of a control bit. In Figure 5, SWITCH_1 and SWITCH_2 are bits called tags that control the switches. Tags can be values from physical I/O or internally defined variables. SWITCH_1 controls a normally open switch (represented by the] [block), meaning that a value of 1 closes the switch, and a 0 opens the switch. Conversely, SWITCH_2 controls a normally closed switch (represented by the] / [block), meaning that a value of 0 closes the switch, and a 1 opens the switch.

The left rail of the ladder is power, while the right rail of the ladder is ground. Power can flow through a rung and energize outputs (represented by the () block) if there is a closed path through the switches. In Figure 6, OUT_2 requires SWITCH_1 = 1 and SWITCH_2 = 0. Thus, while ladder logic has a nice circuit interpretation, analogous to other programming languages, it

can also be understood in terms of Boolean algebra. Switches in series implement an AND gate, while switches in parallel implement an OR gate.

One commonly used ladder logic construct called a latch is shown in Figure 5.

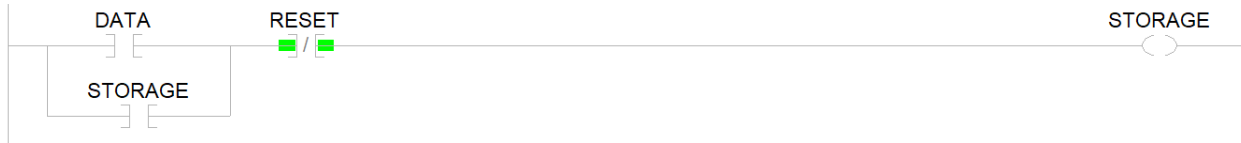


Figure 6. Logic for a latch

Latches are memory circuits used to store the value of an input. The value of DATA is stored in the bit STORAGE. When DATA = 1, there is a closed path to the output and STORAGE = 1. Notice that STORAGE also controls a switch parallel to DATA. Because of this parallel connection, even after DATA changes to 0, STORAGE will still hold a 1. In order to reset, or clear, the STORAGE bit, the RESET input must be asserted. This is because RESET controls a normally closed switch, and when it is 1, the circuit is open. STORAGE will remain a 0 until DATA returns to 1.

4.2 Program Overview

Even with only basic understanding of ladder logic components, the code to automatically power off racks with detected hazards is straightforward. Figure 7 shows a sample implementation.

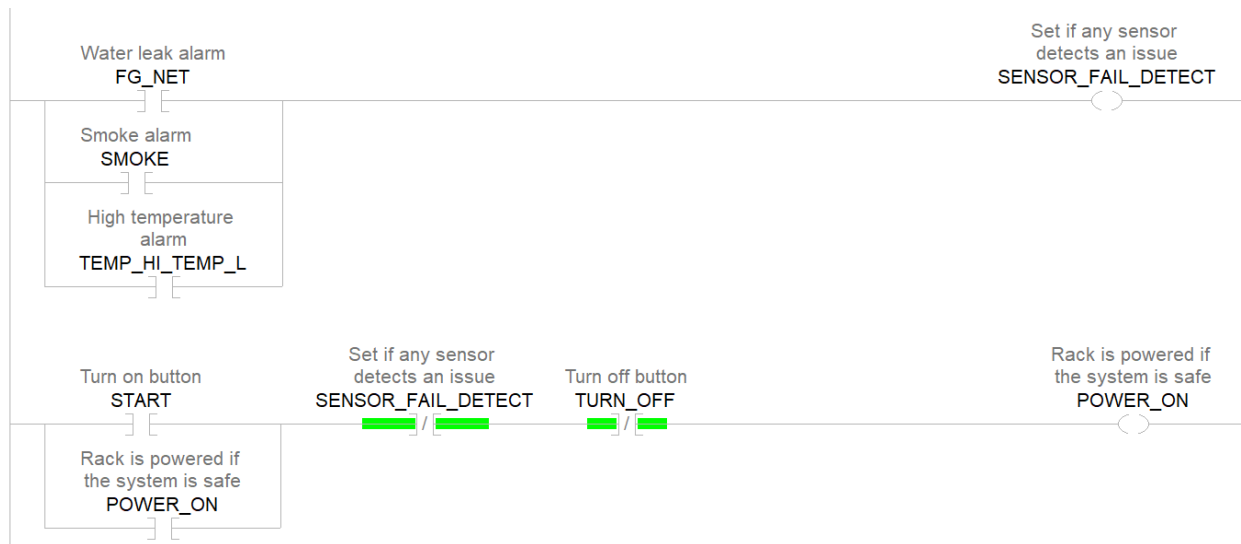


Figure 7. Logic for powering racks

There are three sources of hazards, high temperature, smoke, and water leakage, and any combination of hazards triggers a shutdown. The three hazards can be connected in parallel to energize an output `SENSOR_FAIL_DETECT` that represents any problem at the rack. This tag is then used as the reset input to a latch whose output provides power to a rack. In ladder logic, powering a device is often done with a latch because a device is turned on with a momentary button press, and the storage bit holds onto that signal. Interlocks can naturally be added as reset inputs that clear the latch and power off the device.

An important consideration for writing a program is scalability. All 36 racks share the same logic, but it would be inefficient to create new tags and copy and paste the same logic 36 times. Studio 5000 enables user-defined functions called Add-on Instructions (AOI) that can be executed to reuse logic in multiple places. Defining functions for commonly used code is good practice and greatly improves readability. An AOI named `RACK` is defined by the logic in Figure 7, and the logic for 2 racks is implemented with AOIs in Figure 8.

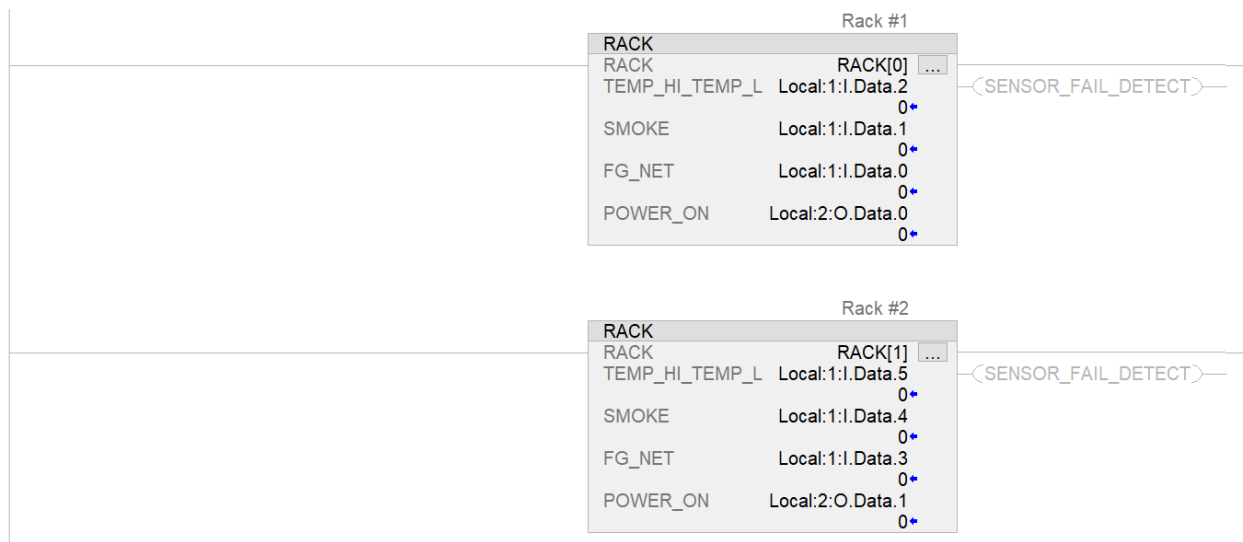


Figure 8. Logic for 2 racks using Add-on Instructions

The functions blocks are always energized and will always execute. However, parameters must be passed to each block. Since the tags for the sensors correspond to input ports, and each rack uses different ports, the input ports must be passed as parameters. Similarly, since racks are powered by different output ports, the output ports must also be passed as parameters.

Although this program could work, the wiring between the sensors and PLC is more sophisticated than what is shown. The following sections discuss the actual connections between the sensor and PLC in more depth.

4.3 Temperature sensor

An RTD sensor does not produce an output on its own. It is simply a variable resistor. An external transmitter measures the resistance of the RTD by applying a voltage across it, and the transmitter's 4 to 20 mA current output is measured by the PLC.

Logic in the PLC is needed to convert the current value to an interpretable temperature. The PLC reads the current as a value between 3200 to 21000. Since a transmitter has a specified

temperature output range in its data sheet, the current value can be scaled linearly by the following expression.

$$Temp = \frac{TempMax - TempMin}{21000 - 3200} (RawVal - 3200) + TempMin$$

This expression is derived from the equation of a line connecting the points (3200, TempMin) and (21000, TempMax). To implement it in ladder logic, a CPT instruction is used, as shown in the first rung of Figure 9. The next rung checks the temperature against a threshold and sets a flag when the temperature becomes too high. The exact values of the constants in the program are still undecided but can be easily changed.

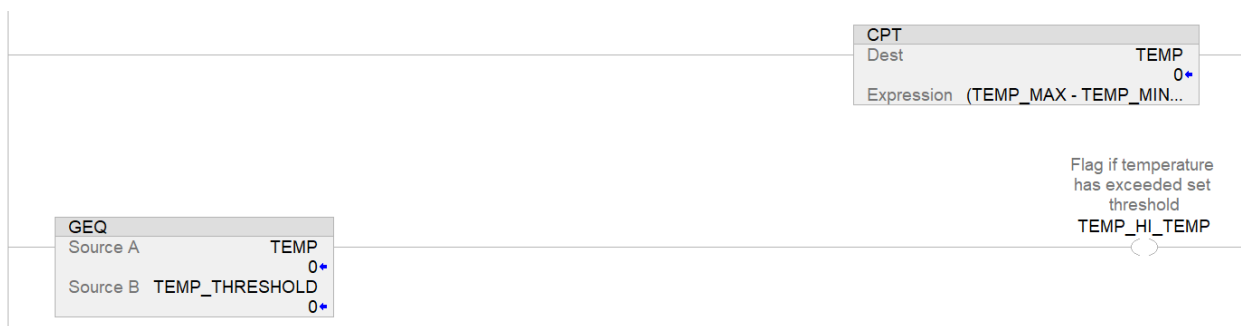


Figure 9. Calculation of temperature from current input value

Although the TEMP_HI_TEMP flag can be used, it is important to consider the event in which the temperature exceeds the threshold for a brief moment and then cools down. Technicians do not watch the system all the time, and it is possible for them to miss this event. Even if the hazard corrects itself, we would like to inform technicians that it had occurred. For this reason, the signal is latched with the logic in Figure 10.

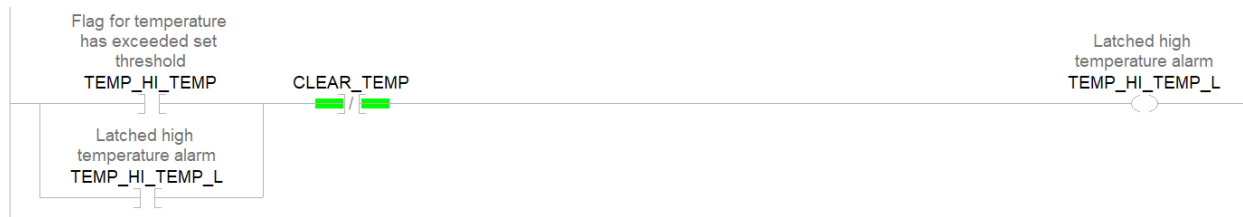


Figure 10. Latching logic for temperature sensor

4.3 Smoke sensor

The smoke sensor has two outputs: one to signal the presence of smoke, and another to signal the sensor is powered. The power supervision output is useful because it reports whether the sensor is functional. The presence of smoke and power is both given by a 1. Since the outputs are simple bits, they are directly connected to two input ports of the PLC. As shown in Figure 11, the signals are latched for the same reasons as previously discussed.

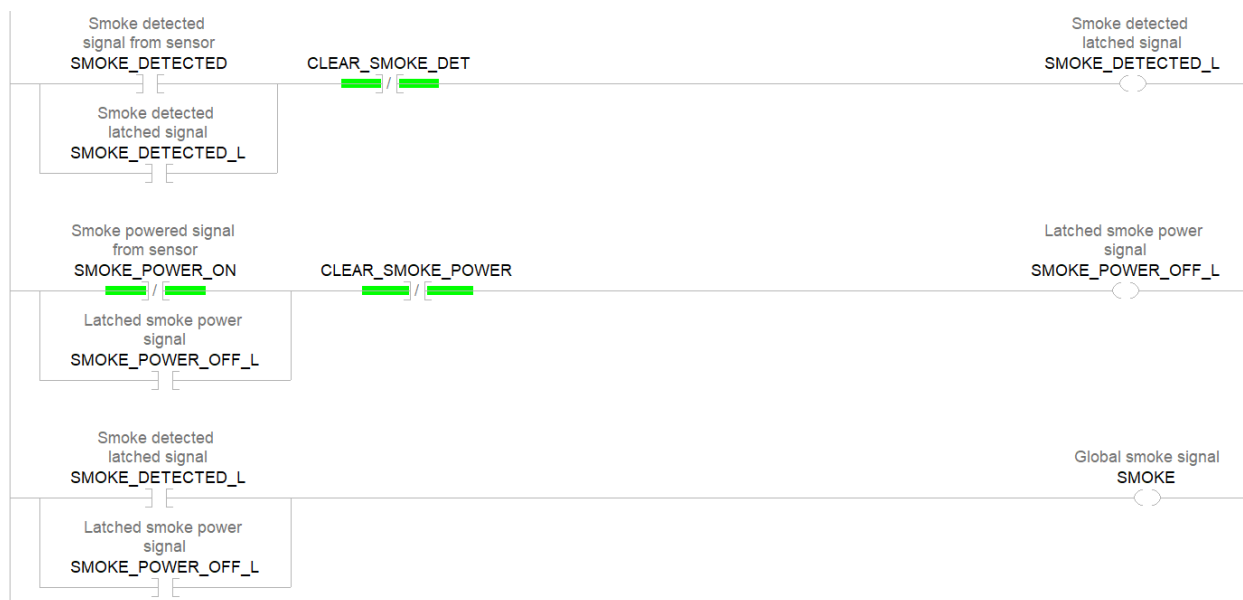


Figure 11. Latching logic for smoke detector and definition of global SMOKE tag

A small detail is that the smoke power latch checks for `SMOKE_POWER_ON = 0`. This is accomplished by using a normally closed switch for the input. The third rung in Figure 10

energizes the SMOKE tag seen in Figure 7. This tag is now understood as a global signal for any hazard that can be detected by the smoke detector.

4.4 Water leak sensor

As mentioned previously, the leak cables first communicate with the FG-NET leak detection unit, which then sends data to the PLC. The difference between the PLC and the FG-NET from other sensors is that communication is accomplished through an internet network, and not a hardwired connection. The PLC communicates through an MVI69-MNET Modbus TCP/IP communication module. In short, this protocol transfers contiguous blocks of data, known as arrays, from the leak detection unit to the PLC. A data transfer from the PLC to the leak unit is a read, and the converse direction is a write. A diagram is shown in Figure 12

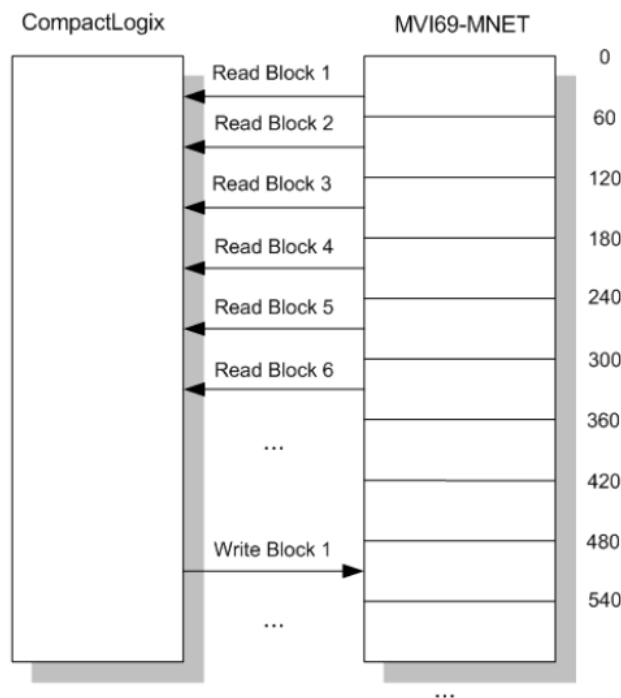


Figure 12. Modbus communication diagram from MVI69-MNET user manual ^[2]

We now describe what is contained in a block of data. Each cable use 3 registers in the leak detection unit to signal status information. Only 2 of the registers are important for this project. The first register has bits that signal the presence of leak or a break in the cable. The second register holds the location of the leak along the cable. Specific details are shown in Figure 13. Pictorially, a block of data consists of all the registers for every cable stacked on top of each other.

		TYPE INFORMATION					LOCATION (m)	
CABLE NUMBER	DESCRIPTION	TYPE REGISTER ADDRESS	TYPE BIT POSITION				LOCATION REGISTER ADDRESS	LOCATION BIT POSITION
			LEAK	CABLE BREAK BUS	CABLE BREAK SENSOR	CABLE BREAK END PLUG		LOCATION (m)
CIRCUIT 1 (up to 40 cables from 1_01 to 1_40)								
1_01	CABLE_1_01	7101	bit 4	bits 0+7	bits 1+7	N/A	9101	bits 0 to 15
1_02	CABLE_1_02	7102	bit 4	bits 0+7	bits 1+7	N/A	9102	bits 0 to 15
1_03	CABLE_1_03	7103	bit 4	bits 0+7	bits 1+7	N/A	9103	bits 0 to 15
1_04	CABLE_1_04	7104	bit 4	bits 0+7	bits 1+7	N/A	9104	bits 0 to 15
1_05	CABLE_1_05	7105	bit 4	bits 0+7	bits 1+7	N/A	9105	bits 0 to 15
1_06	CABLE_1_06	7106	bit 4	bits 0+7	bits 1+7	N/A	9106	bits 0 to 15
1_07	End Plug	7107	N/A	N/A	N/A	bits 2+7	9107	N/A

Figure 13. Leak cable register information from FG-NET user manual

The PLC continuously reads from the leak detection unit and copies the data into an array in internal memory. Now that the PLC has a copy of all the registers, the specific registers corresponding to a cable can be passed as parameters to the rack with that cable. As usual, the status bits are latched. The logic that drives the FG_NET tag from Figure 7 is shown in Figure 14.

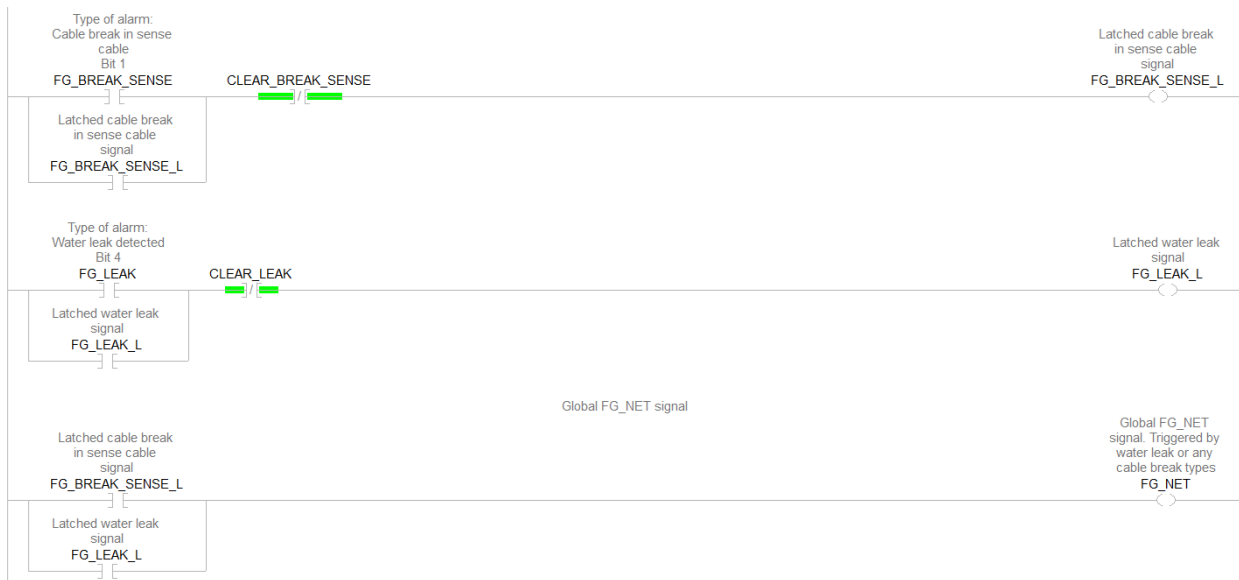


Figure 14. Latching logic for leak sensor and definition of global FG-NET tag

5. Other Features

5.1 HMI panel

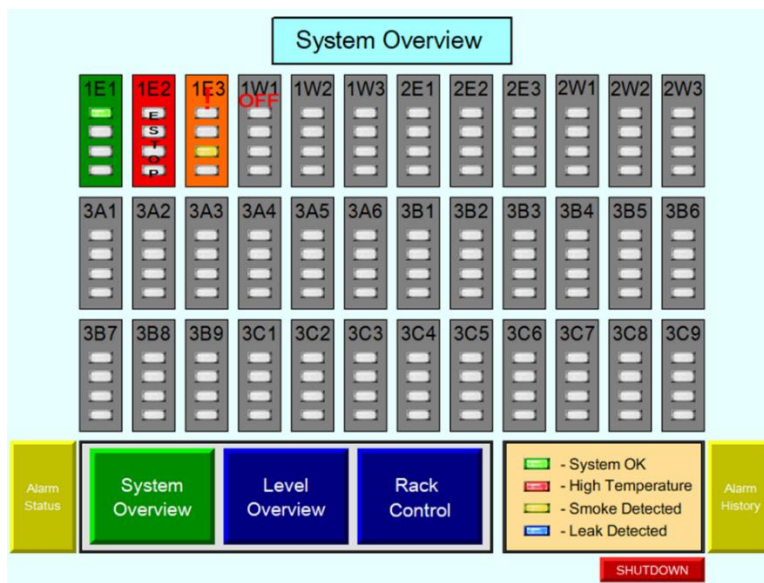


Figure 15. HMI rack overview display page. Rack 1E1 is ON and safe. Rack 1E2 is in emergency stop mode. Rack 1E3 has a smoke alarm. Rack 1W1 is OFF and safe.

For a technician to observe the status of a rack, it would be very inconvenient to read the values of bits. Instead, an HMI control panel reads tags from the PLC and displays them as color coded alarms on a screen. 4 of the racks are properly configured in Figure 15. In the figure, since rack 1E3's smoke bit is a 1, a yellow LED is lit up.

The HMI can also write to tags with buttons. When buttons are pressed, a 1 is sent to a linked tag. The most important buttons are used for turning on and off racks, and for acknowledging alarms. The turn on and off buttons control the tags START and TURN_OFF in Figure 7, and the acknowledge alarm buttons control reset inputs of the latches seen throughout this paper. More details on the HMI are explained in a partner SULI project "Rack interlocks system interface" by Michael Charumoneeroj.

5.2 Local Reset Button

An alarm is cleared if the acknowledge button is pressed and the sensor no longer detects a problem. However, as discussed previously, a problem can clear on its own. The temperature threshold can be exceeded by a rack, but it may cool down by itself. A technician can clear the alarm by pressing the button on the HMI, but we would like to ensure that they went out to the field and made sure everything is safe. To accomplish this, after a hazard is fixed, a physical reset button is set up at each rack. Pushing the button lights up a light at the top of the rack, and this light is required to turn the rack back on.

5.3 Emergency stop button (ESTOP)

In case of some other emergency, a second physical button, an emergency stop mushroom button, is placed at each rack. An ESTOP button is shown in Figure 16. The emergency stop button is a latching button,



Figure 16.
ESTOP button

meaning it holds its position after being pressed. When the button is pressed, the rack immediately shuts off. The button is reset by pressing it again.

6. Finalized Code

After discussing these details, the previously shown code in Figure 7 and 8 need a few modifications. Each rack uses 5 physical inputs: 1 by the temperature sensor, 2 by the smoke detector, and 2 by the Reset and ESTOP buttons. The leak detection unit sends data through an internet network and does not use a physical port. Modifications to the power logic and parameters of the AOI are shown Figure 17.

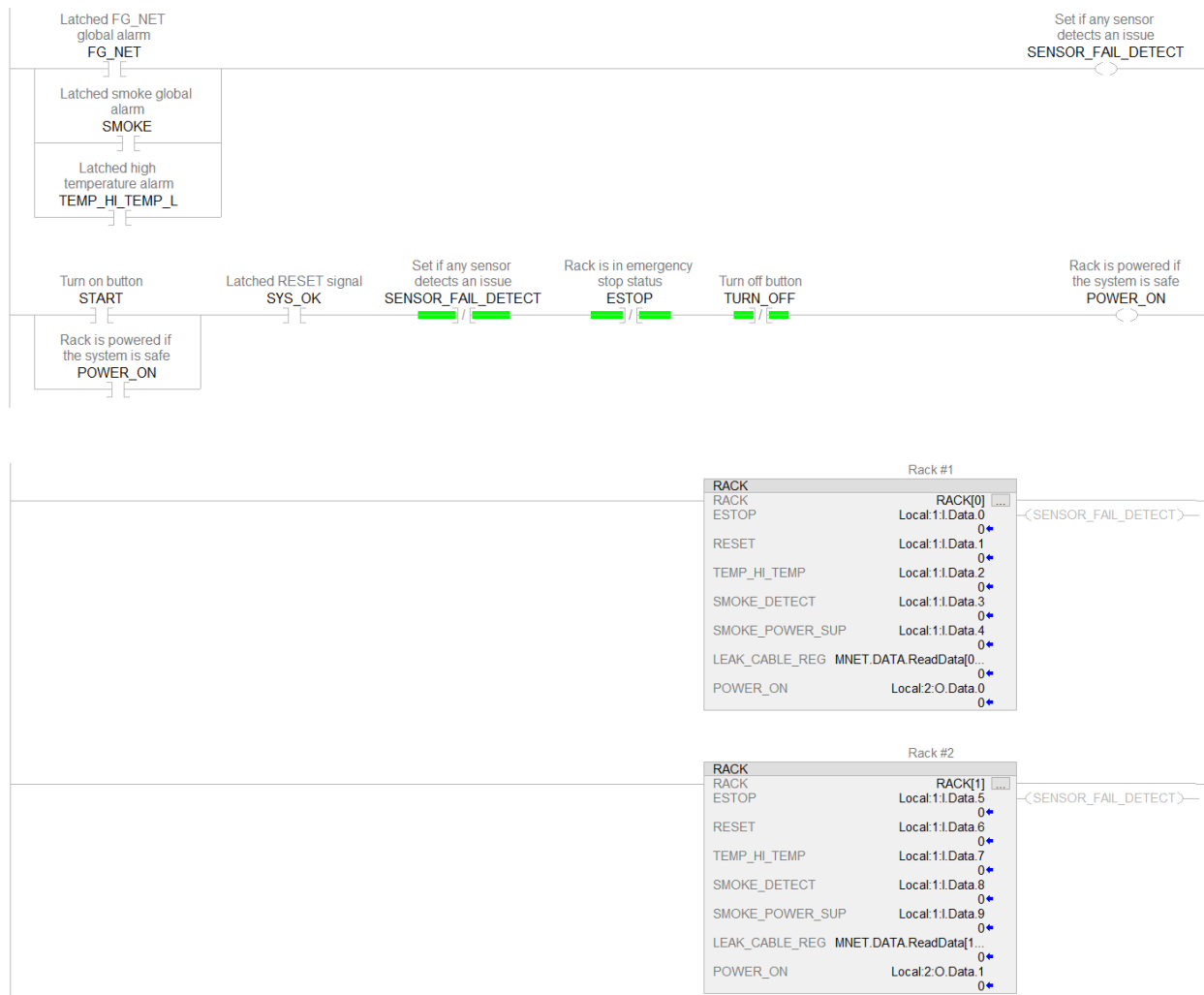


Figure 17. (Top) Finalized power logic (Bottom) Finalized AOI parameters

6. Discussion and Conclusion

This project is a starting point for a centralized control system. The structure of the code is well-organized and flexible to changes. In the future, the HMI will support multiple languages, and the alarm history page will be able to be exported to an external database. Additional requests by scientists for specific racks can also be implemented with ease.

7. Acknowledgements

I express my sincerest thanks to Joel Vasquez, Michael Charumaneeroj, Peter Hamblen, Rob Benkov, Roland Wimmer, and the SULI team for supporting me tremendously with this project. Using a VPN for the hardware was a brilliant idea to make this remote internship successful.

Science Undergraduate Laboratory Internships (SULI)

This project was supported in part by the U.S. Department of Energy, Office of Science, Office of Workforce Development for Teachers and Scientists (WDTS) under the Science Undergraduate Laboratory Internships Program (SULI).

8. References

- [1] TTK Leak Detection, "Operation & Installation Manual Digital Unit: FG-NET," FG-NET User Manual, Sep. 2018
- [2] Prosoft Technology, "Modbus TCP/IP Communication Module for CompactLogix MVI69-MNET User Manual," MVI69-MNET User Manual, Oct. 2011

10. Appendix A

List of products :

1. Allen Bradley 1769-L30ER PLC
2. Allen Bradley 2711P-T10C21D8S 10.4" HMI Touchscreen
3. Rockwell Automation Studio 5000 Logix Designer (PLC programming)
4. Rockwell Automation Factory View Studio (HMI Programming)
5. Allen Bradley 1769-IQ16 DC Input Module
6. Allen Bradley 1769-IF8 Analog Input Module
7. Allen Bradley 1769-OW16 DC Output Module
8. Prosoft Technologies MVI69-MNET Modbus TCP/IP Communication Module
9. (Undecided) RTD sensor
10. (Undecided) RTD transmitter
11. (Undecided) Smoke detector
12. TTK Leak Detection FG-EC sense cables
13. TTK Leak Detection FG-NET leak detection unit
14. TTK Leak Detection FG-NC Jumper Cables

Modeling of software-defined radio for National Synchrotron Light Source II radio frequency control

Jade Hayan Chun, School of Applied & Engineering Physics, Cornell University College of Engineering, Ithaca, NY 14853

Hengjie Ma, National Synchrotron Light Source II, Brookhaven National Laboratory, Upton, NY 11973

The National Synchrotron Light Source II (NSLS-II) at Brookhaven National Lab (BNL) is currently developing a new 500 MHz / 3 GHz software-defined radio (SDR) for the linear accelerator (LINAC). By definition, SDR is a radio transceiver in which all or a part of its functions, both its hardware and functionalities, is reconfigurable by software. SDR for the LINAC RF control applications is composed of an RF receiver digital front-end (Rx FE), an RF transmitter digital front-end (Tx FE), as well as a baseband data processor back-end. We used MATLAB and Simulink as a tool to: mathematically describe the basic RF signals in both the time and frequency domains, simulate the process of digital baseband signal demodulation from their input RF carriers, simulate the process of digital synthesis of the output RF signals, and model the signal processing in Rx FE. As a result of this summer, I have added experiment simulation with Simulink to my repository of laboratory skills and developed further understanding of signals processing applications in particle accelerators.

I. INTRODUCTION

A typical SDR system is comprised of a Tx FE, Rx FE, and a baseband data processor back-end. By definition, SDR is a radio transceiver in which all or a part of its functions, both their hardware and functionalities, is reconfigurable by software.¹ The SDR technology developed over the past decades has been widely used in wireless telecommunication infrastructure. The same SDR technology has also found applications in the low-level RF (LLRF) controls of large-scale particle accelerators. Examples include the Spallation Neutron Source² (SNS), NSLS-II Light Source, and the European XFEL.

The block diagrams in Figure 1.1 show the typical SDR architecture of a wireless network base-station of a cellular communication system and that of the digital LLRF controller of an accelerator. Both architectures appear very similar, comprised of a digital radio Rx FE in the Rx path, a digital radio Tx Fe in the Tx path, and a baseband processor back-end. While a cellular base-station SDR is typically implemented with a combination of the mixed-signal processing application-specific integrated circuit (ASIC), digital signal processing (DSP), and field programmable gate array (FPGA) technologies, the SDR for accelerator RF control is primarily implemented with FPGA due to its limitation in production quantities. This project is focused on the modeling and simulation of mixed RF signal processing in the SDR Rx and Tx path.

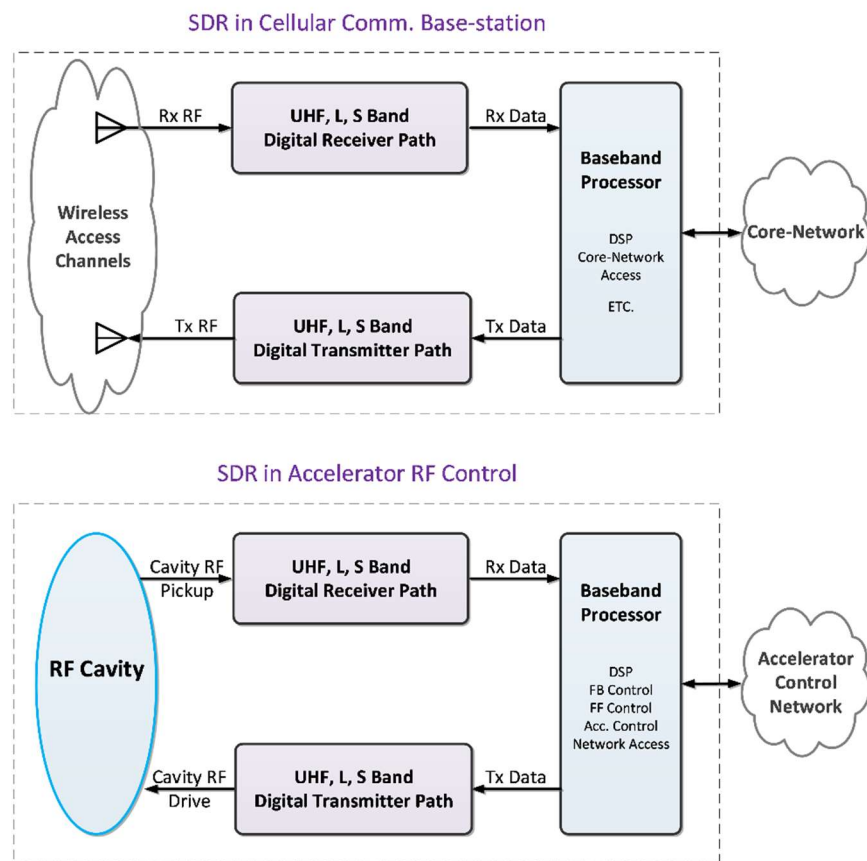


Figure 1.1: Block diagrams showing the typical SDR architecture in a cellular communication system versus in accelerator RF control.

The DSP in the Rx FE involves RF signal spectrum down-shifting with RF quadrature direct sampling, baseband data demodulation and smoothing with digital down-conversion (DDC), and optional error analysis for the data quantization jitter in the analog-to-digital converter (ADC) sampling clock. The DSP in the Tx FE involves baseband data interpolation filtering, digital quadrature modulation of the baseband data, digital intermediate frequency (IF) to RF frequency up-conversion, and optional signal noise analysis for the data quantization and digital-to-analog converter (DAC) clock jitter.

II. OBJECTIVES

Through this project, we aim to give a technology overview of SDR and the specific system design for its application in BNL's LINAC RF. We model the signal processing in both the Rx FE and Tx FE with MATLAB/Simulink, showing how the DSP can be done with computer simulation.

III. METHODS

A. Frequency down-conversion in the Rx path

Frequency translations to lower IFs are essential in many RF applications.³ An ideal mixer is usually represented by a multiplier symbol with two input ports and one output port, as shown in Figure 3.1. The signal at the output port is the vector multiplication of the signals at the two input ports. One of the input signals is the reference signal, the local oscillator (LO). Using some trigonometric product-to-sum identities and assuming two sinusoidal input signals with amplitudes A_{RF} , A_{LO} and frequencies f_{RF} , f_{LO} , the multiplied output signal y_{IF} can be represented as

$$\begin{aligned}
 y_{IF}(t) &= y_{RF}(t) \cdot y_{LO}(t) \\
 &= \frac{1}{2} A_{LO} A_{RF} \cdot (\sin[(\omega_{RF} - \omega_{LO})t + (\phi_{RF} - \phi_{LO})] + \sin[(\omega_{RF} + \omega_{LO})t + (\phi_{RF} + \phi_{LO})])
 \end{aligned}$$

The input signal is translated to two output frequencies, the upper ($f_{RF} + f_{LO}$) and the lower ($f_{RF} - f_{LO}$) sideband signals. In the case of down-conversion, the RF and LO signals are high-frequency inputs while the resulting output signal is the IF signal, as shown in Figure 3.2. The lower sideband of the mixing process is selected by filtering the output signal. For receiver applications, the lower sideband is extracted by low-pass filtering. This yields for the IF signal

$$y_{IF}(t) = \frac{1}{2} A_{LO} A_{RF} \cdot \sin[(\omega_{RF} - \omega_{LO})t + (\phi_{RF} - \phi_{LO})]$$

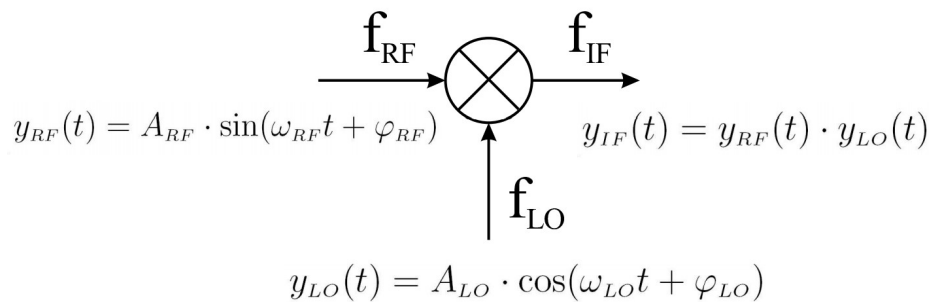


Figure 3.1: An ideal mixer.

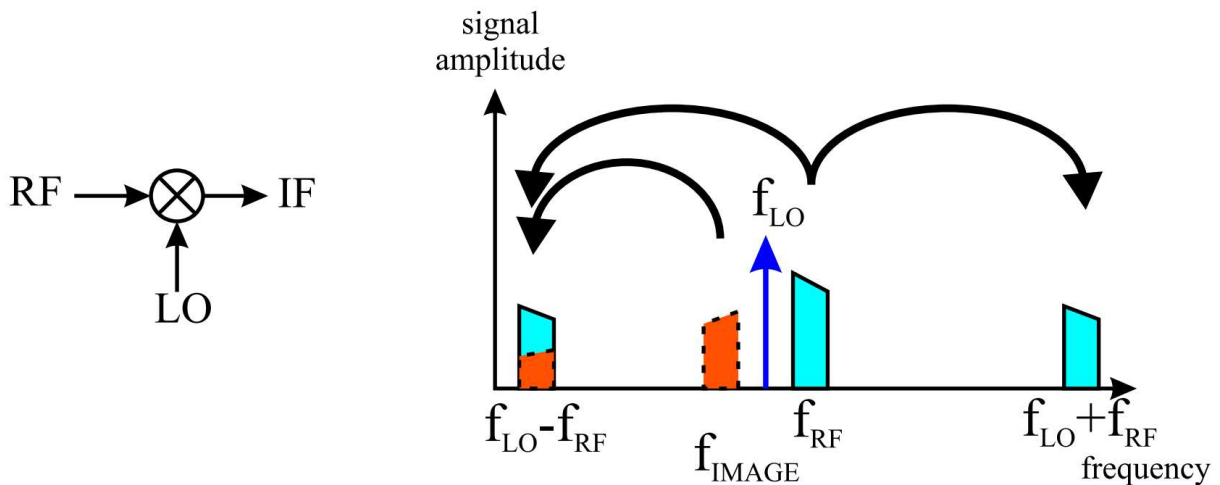


Figure 3.2: Down-conversion scheme for an RF mixer.

Using Simulink, this ideal frequency down-conversion can be modeled in a block diagram. Simulink provides signal source blocks, a vector product block, and scopes for signal analysis.

B. I/Q sampling

The terminology I/Q originates from the representation of an RF signal which can be in either polar (amplitude/phase representation) or in Cartesian coordinates.³ An RF signal with amplitude A , frequency ω , and an initial phase ϕ_0 can be modelled as a rotating phasor:

$$y(t) = A \cdot \sin(\omega t + \phi_0)$$

This expression can be reformatted using basic trigonometric functions:

$$y(t) = A \cos \phi_0 \sin \omega t + A \sin \phi_0 \cos \omega t$$

The amplitude of the sine component can be defined as the in-phase component (I), while the amplitude of the cosine component is called the quadrature-phase component (Q). This phasor representation is graphically displayed in Figure 3.3. If I/Q of the rotating phasor is known initially and measured again later at a well-defined time, a comparison of the two measurements can reveal whether the incoming RF signal has changed its amplitude and phase. Figure 3.4 shows the I/Q sampling at a sampling frequency of 4 times the IF.

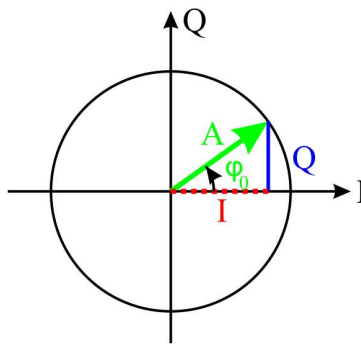


Figure 3.3: Phasor representation of an RF signal.

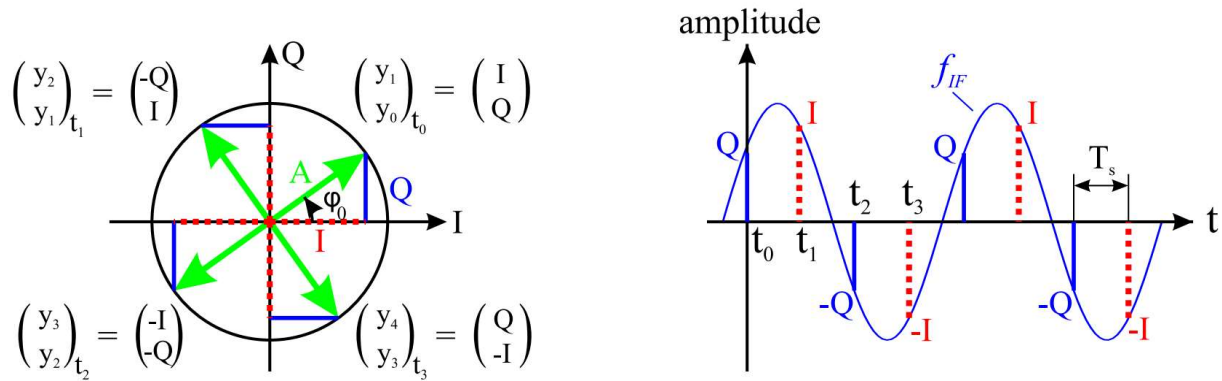


Figure 3.4: I/Q sampling with 90 degrees phase advance between consecutive samples.

This is the basic concept behind I/Q sampling, which we used in our Simulink model of DDC. With DDC, the I/Q information is extracted from samples in a purely digital way.

C. DDC

Another possible way of extracting amplitude and phase information from a sampled carrier is by DDC.³ DDC is a technique which takes a band-limited high-sample rate digital signal, shifts the band of interest to a lower frequency and reduces the sample rate while retaining all the information. The basic function of DDC is shown in Figure 3.5.

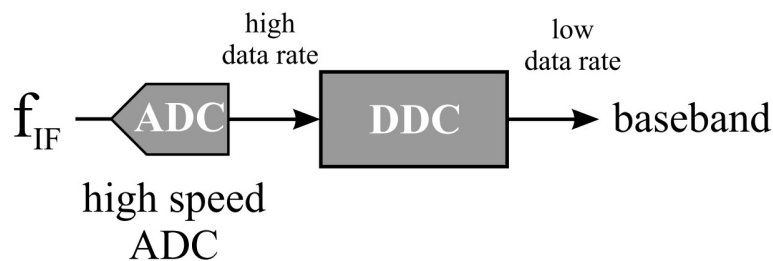


Figure 3.5: Basic principle of DDC.

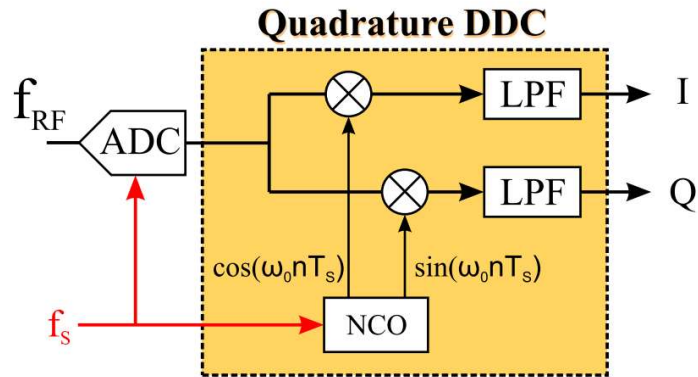


Figure 3.6: Main building blocks of DDC.

There are three major DDC building blocks: a digital mixer, an LO, and a low-pass filter (LPF). Figure 3.6 displays these main building blocks in a block diagram format. The digital mixers convert the incoming digitized RF signal down to baseband as ideal multipliers. The resulting output consists of the sum and the difference frequency with respect to the input frequency. The LPF then suppresses the sum frequency component and provides anti-aliasing filtering.

IV. RESULTS

Figure 4.1 shows the entire block diagram for the Rx FE Simulink model. The virtual simulation of the aforementioned DSP techniques was done in Simulink using NSLS-II RF parameters. This meant utilizing a 500 MHz RF and a 550 MHz LO to produce a 50 MHz IF. To accurately reflect the noisy RF signal from the cavity pickup in practical applications, 10% white noise is added to the RF input prior to the frequency mixing stage. Figure 4.2 shows the subsystem within the Simulink model where noise was added to the input RF.

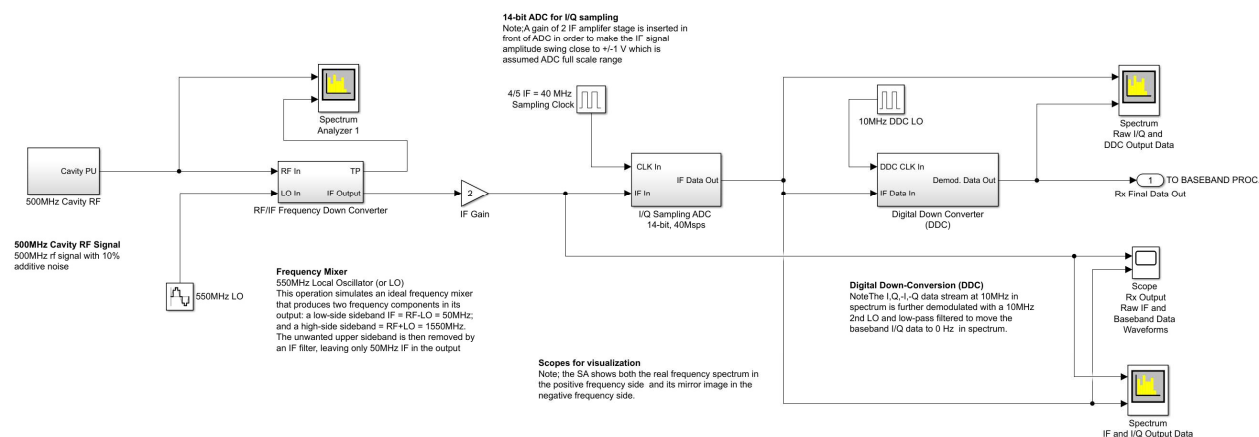


Figure 4.1: NSLS-II SDR Rx FE Simulink model block diagram with annotations.

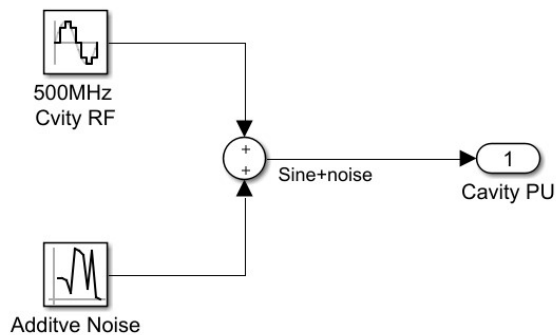


Figure 4.2: Subsystem for adding white noise to the input RF signal.

A. Frequency mixer Simulink model

The noisy RF is mixed with the 550 MHz LO using a double-sideband frequency mixer (DSB). The mixer output is then filtered by a properly designed IF filter to remove the unwanted sideband frequency, keeping only the desired 50 MHz IF for the following digitization. Figure 4.3

shows the subsystem for frequency mixing. Figure 4.4 shows the filter design parameters using Simulink's Filter Designer dialog window.

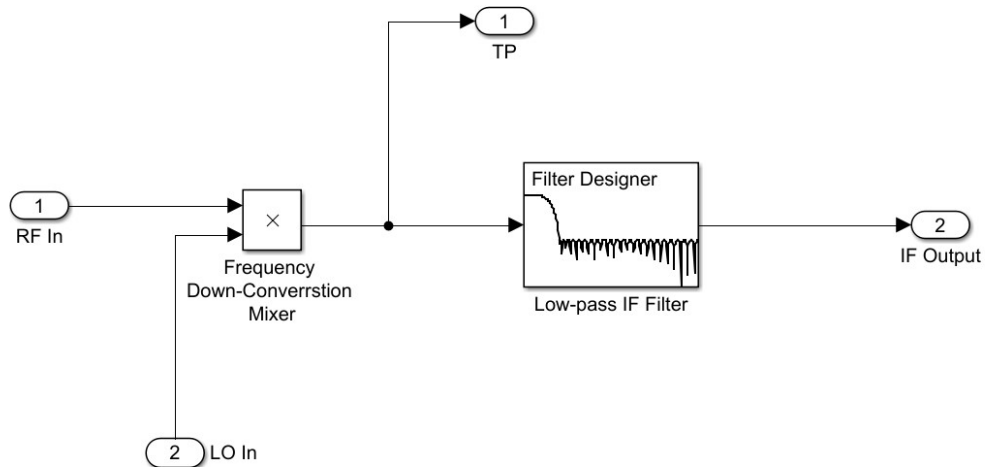


Figure 4.3: Frequency mixing subsystem.

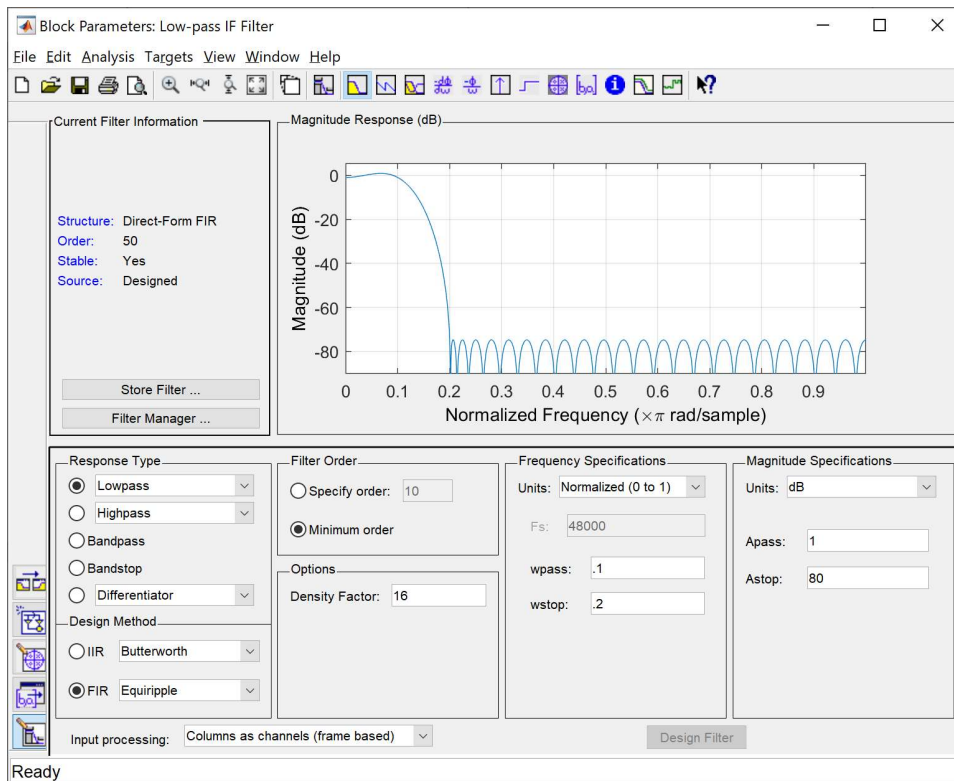


Figure 4.3: Filter Designer dialog window for low-pass filtering.

The simulation spectrum analyzer (SA) screen in Figure 4.4 shows the spectrum of the 500 MHz RF carrier going into the mixer as a yellow trace and the spectrum of the mixer output as a blue trace. As the yellow trace demonstrates, the RF spectrum before mixing is simply a spectral line of the carrier frequency at ± 500 MHz. In contrast, the blue trace for the DSB mixer output is missing the ± 500 MHz spectral line and instead has two sideband frequencies. One is at $f_{RF} + f_{LO} = 1550$ MHz, and the other is at $f_{IF} = f_{LO} - f_{RF} = 50$ MHz. Note the mirrored spectrum on both the positive and negative sides due to the DSP effect. In order for the downstream digitizer and signal processing to work properly, the unwanted sideband at 1550 MHz must be removed by an IF filter. The cutoff frequency of the IF LPF at the output side of the mixer should be placed far below the RF and LO frequency, but sufficiently above the 50 MHz IF. Thus, the passband frequency was set to 100 MHz and the stopband frequency was set to 200 MHz. The simulation SA screen in Figure 4.5 shows the spectrum of the filter input as a yellow trace and that of the output as a blue trace. The unwanted 1550 MHz sideband is completely removed in the filter output, leaving only the 50 MHz IF. The filter also reduced the noise floor in the stop band.

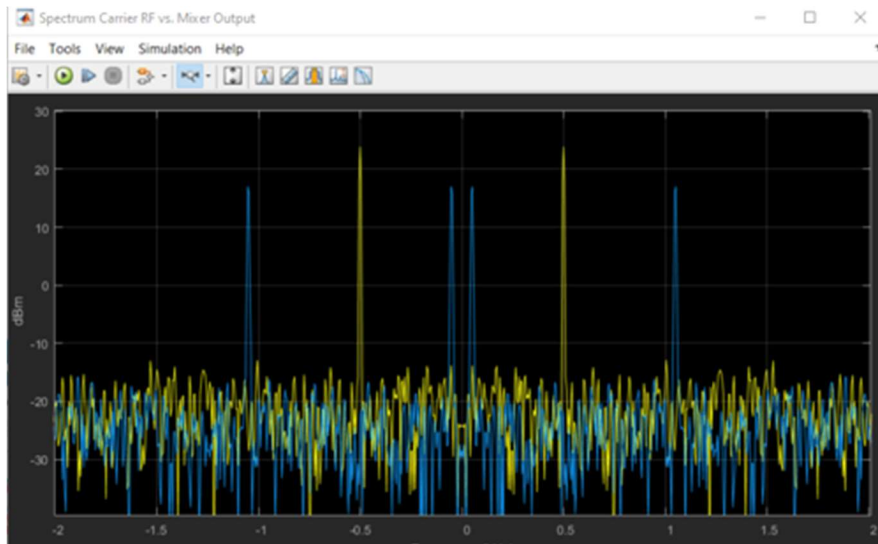


Figure 4.4: SA screen showing the unmixed carrier spectrum (yellow trace) and the DSB output spectrum (blue trace).

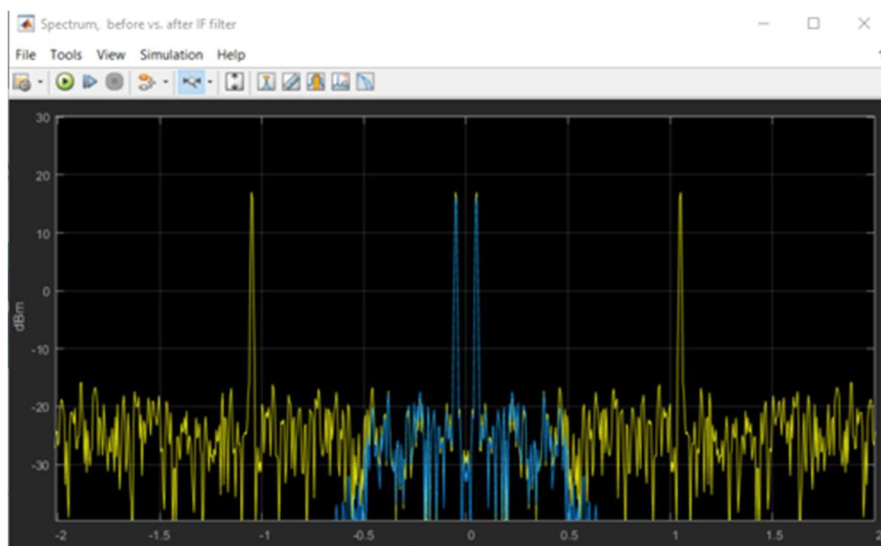


Figure 4.5: SA screen showing the unfiltered DSB spectrum (yellow trace) and the DSB spectrum after passing through an LPF (blue trace).

B. I/Q sampling Simulink model

Figure 4.6 shows the subsystem for I/Q sampling in the Simulink model. I/Q sampling of the 50 MHz IF was done with an under-sampling rate of four-fifths that of the IF frequency, or 40 Msp/s. The 40 Msp/s sampling in time was modeled with a Sample/Hold block (S/H) triggered by an IF-synchronous 40 MHz clock. The output of the S/H was then fed through a ± 8091 step quantizer to simulate the effect of a 14-bit ADC. The range limiter at the end finishes the model of the ADC for I/Q sampling. Figure 4.7 is the scope display for I/Q sampling of the IF signal with the under-sampling clock.

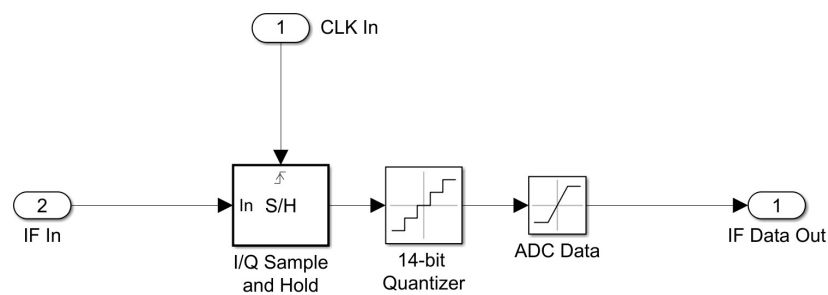


Figure 4.6: I/Q sampling subsystem.

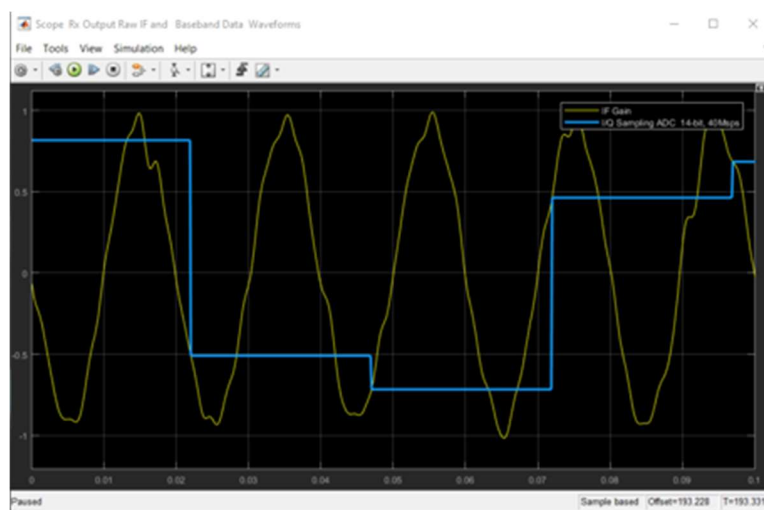


Figure 4.7: Scope output displaying I/Q sampling of the IF at an under-sampling frequency.

Before quadrature sampling, the IF spectral lines were at ± 50 MHz, as indicated by the yellow trace on the SA screen in Figure 4.8. After the 40 MHz quadrature sampling, the output data of the ADC is a sequence of the baseband data $\{I, Q, -I, -Q; I, Q, -I, -Q; \dots\}$, repeating in groups of four data points. Due to the sign alternation on the I/Q data at a rate of 40 MHz divided by 4, or 10 MHz, the $\{I, Q, -I, -Q; \dots\}$ data was at 10 MHz in the spectrum instead of 0 Hz as it should have been for baseband data. A DDC in the DSP chain is necessary to bring the demodulated I/Q data spectrum to the baseband.

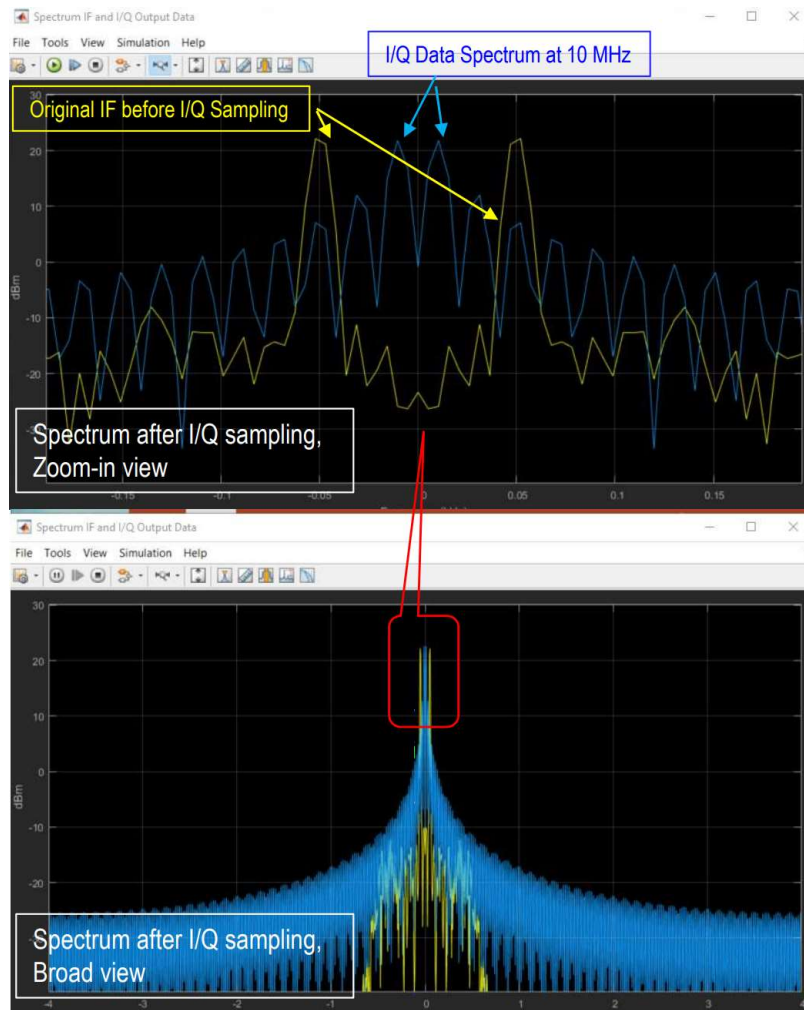


Figure 4.8: IF and I/Q output data SA screen, with annotations.

C. DDC Simulink model

Figure 4.9 shows the subsystem for DDC in the Simulink model. The DSP of the DDC after I/Q sampling was straight-forward. It consisted of a procedure that removed the sign alternation from the original $\{I, Q, -I, -Q; \dots\}$ data sequence to produce the final baseband data of $\{I, Q, I, Q; \dots\}$. To emulate this data processing procedure, the Simulink model was constructed with the raw I/Q data multiplied by a 10 MHz synchronous ± 1 square wave DDC clock. The output of the multiplier was further smoothed by a LPF. As for the SA result, before the DDC, the spectral line of the raw I/Q data was at 10 MHz, as indicated by the yellow trace in the first SA screen of Figure 4.10. After the DDC, the spectra of the I/Q data was down-shifted to the baseband at 0 Hz, as indicated by the blue trace and arrow in the first SA screen of Figure 4.10.

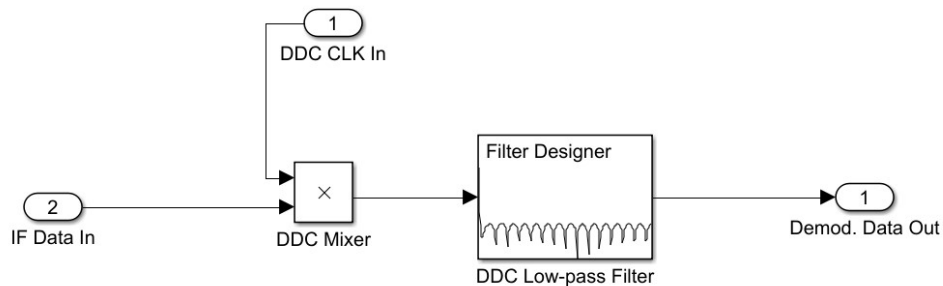


Figure 4.9: DDC subsystem.

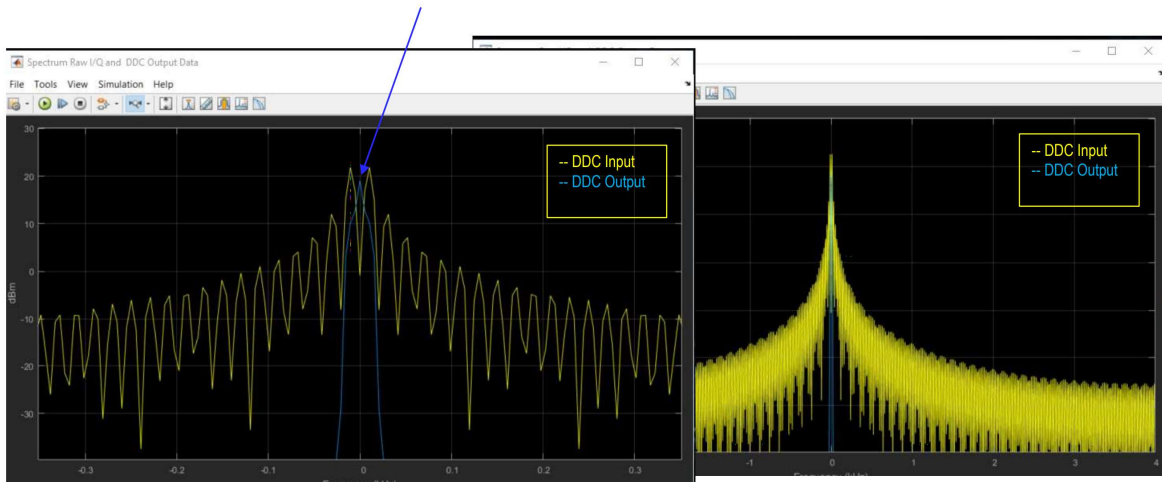


Figure 4.10: SA screens displaying the effect of DDC; the first screen is a zoomed-in view, while the second screen is a zoomed-out view.

V. CONCLUSION

We were successfully able to simulate the Rx FE DSP for SDR in accelerator applications using Simulink blocks from the basic signals processing libraries available. This project highlights Simulink's attractiveness as a virtual laboratory for DSP. It is a step up from hard-coded MATLAB plot outputs, as Simulink emulates a digital oscilloscope screen and spectrum analyzer without additional effort. Subsequently, the block diagram nature of coding within Simulink lends itself well to signals processing applications, especially for that in experimental accelerator RF control with SDR. As the NSLS-II looks towards the future, this sort of virtual laboratory experimentation would allow for better estimates on power and current requirements for upgrades. The next step in this project would be the simulate the Tx FE to complete the SDR system.

VI. ACKNOWLEDGEMENTS

This project was supported in part by the U.S. Department of Energy, Office of Science, Office of Workforce Development for Teachers and Scientists (WDTS) under the Science Undergraduate Laboratory Internships Program (SULI).

I give special thanks to my mentor Hengjie Ma, who was very helpful and enthusiastic in assisting my learning throughout the entirety of this internship.

Lastly, I highly appreciate Tom Schilcher's excellent reference on RF signals processing, of which most of this text is based upon.

VII. REFERENCES

- [1] Simic, I.S. (2007, June). Evolution of Mobile Base Station Architectures. *Microwave Review*, 29-34.
- [2] Holtkamp, N.R. (2005, May). *The Spallation Neutron Source*. Seminar presented at Teacher's Day at the Particle Accelerator Conference, Knoxville, TN.
- [3] Schilcher, T. (2008). RF applications in digital signal processing.

Investigation of Structural Sensitivity of Theoretical XANES Spectra in Dilute PdAu Alloy Nanoparticles

Phillip Comer

Department of Mechanical Engineering, Manhattan College, Riverdale, NY 10471

Jing Liu

Department of Physics, Manhattan College, Riverdale, NY 10471

Jennifer LaPoff

Department of Chemistry and Biochemistry, Manhattan College, Riverdale, NY 10471

Nicholas Marcella

Department of Materials Science and Chemical Engineering, Stony Brook University, NY 11794

Anatoly I. Frenkel

Department of Materials Science and Chemical Engineering, Stony Brook University, Stony Brook, NY 11794

Chemistry Division, Brookhaven National Laboratory, Upton, NY 11973

Abstract

Bimetallic alloy nanoparticles as catalysts have attracted much attention in research because of their enhanced activity and selectivity. Their catalytic properties are highly related to the atomic arrangement and local structure of the metals. X-ray absorption fine spectroscopy (XAFS), including x-ray absorption near edge structure (XANES) and extended x-ray absorption fine structure (EXAFS), is widely used to study the electronic structure and local structure of bulk and nanomaterials. Monitoring the changes of working materials during the reaction and structural transformation in real time by using in situ/operando XAFS facilitates the understanding of catalytic reaction mechanisms. Recently, the progress in developing the machine learning approach offers new opportunities for XANES quantitative analysis to extract structural descriptors which was challenging using conventional approach due to the limitations of data quality, experimental or theoretical complexity. This idea is based on the association between XANES spectral features and structural descriptors. To investigate such association in the dilute PdAu alloy system, we performed a series of ab initio theoretical simulations of XANES spectra at Pd K-edge for dilute PdAu nanoparticles (Pd concentration less than 5%) using JFEFF (FEFF9 code) by systematically varying the structural parameters such as structure, size, Pd location, interatomic distance and so on. We focused on the cuboctahedral and icosahedral structures and used their geometries to generate templates containing only non-equivalent Pd sites. This method makes our work in theoretical calculations more efficiently and less time-consuming. We observed strong correlation between structural descriptors (interatomic distance, Pd location...) and the XANES spectra. The completion of our work as a theoretical proof of principle will assist the identification of active site structure from XANES spectra in the process of understanding the reaction mechanisms in catalysis, and it can also directly lead to the construction of the training data set of dilute PdAu alloy in neural network based XANES analysis approach.

Introduction

Bimetallic alloy nanoparticles (NPs) exhibit unique catalytic activities different from the monometallic metals [1,2]. The knowledge of their atomic structures and active sites during the reactions is critical to understand the reaction mechanisms and to future optimize and design the bimetallic alloy NPs catalysts. Our study places the focus on the dilute PdAu alloy NPs (low Pd loading) which have been reported to be very active and selective in various catalytic reactions, e.g. low-temperature CO oxidation [3,4], selective oxidation of 2-propanol to acetone in the presence of H₂ and O₂ [5], vinyl acetate formation [6], hydrogenation of cyclohexene and butadiene [4,7], aerobic oxidation of benzyl alcohol [8], and hydrogenation of 1-hexyne [9–11]. It's been also demonstrated that the isolated Pd on the surface of Au NPs plays a crucial role for O₂ or H₂ dissociation to activate the reaction [12,13].

Many efforts have been made to seek for the optimized active structure and composition of dilute PdAu alloys with high stability and enhanced catalytic performance using a comprehensive experimental and theoretical probes [3,5,9,14]. Among the available characterization tools, x-ray absorption fine spectroscopy (XAFS) as an element specific technique is commonly used to provide the atomic structure and electronic structure information of materials from bulk to nanomaterials [15]. XAFS consists of two regions: x-ray absorption near edge structure (XANES) and extended x-ray absorption fine structure (EXAFS). The spectral features in XANES are sensitive to the electronic structure and less sensitive to the disorder, while EXAFS is mainly attributed by how the neighbors arranged around the absorbing atom which is so-called local structure and is sensitive to the disorder in local structure [16,17]. In recent years, the development of time-resolved, in situ and in operando XAFS measurements enables the researchers to monitor the changes of working materials during the reaction and structural transformation in real time [16,18–20]. The employment of in situ and in operando XAFS did facilitate the studies of material growth mechanism, reaction kinetics and the understanding of structure-property relationship of catalysts. However, the low metal loading, nanoscale size, the harsh reaction conditions, heterogeneous sizes compositions and the large amount of data can pose complexity and challenges to the data collections and the quantitative data analysis of XAFS (particularly EXAFS). In addition, although a lot of structural information coded in XANES spectra, they were used mostly in qualitative analysis (energy shift, finger print features) in over a few decades. Such qualitative analysis is highly relied on the available standard materials. In recent two decades, the development of computational codes and software in the theoretical calculation has brought the XANES analysis to a new level [21–25].

Driven by the data-discovery techniques, the supervised machine learning (SML) method opens a path for fast and accurate extraction of quantitative structural parameters from XANES that complements the conventional analysis methods [11,26–28]. The basis of this method is the association between the XANES spectral features and structural descriptors. In order to get a theoretical proof of principle and finally develop supervised machine learning (SML) method of XANES in dilute PdAu alloy system, in this work we performed the theoretical Pd K-edge XANES spectra for a series of site-specific dilute PdAu NPs models to systematically examine the sensitivity of XANES spectra to different generalized structural descriptors (such as structure, size, lattice constant, Pd location...). The results from this work could assist the identification of active site structure of dilute PdAu NPs using XANES spectra and could be used to construct the training data set for developing the machine learning based analysis approach for dilute PdAu alloy.

Progress

I. Methods

In this project, we focused on establishing the association between the calculated theoretical Pd K-edge XANES spectral features and structural descriptors in dilute PdAu alloy NPs.

To systematically examine the sensitivity of theoretical XANES spectra to different structural descriptors, we performed the theoretical calculations of Pd K-edge XANES spectra for a series of models of dilute PdAu alloy NPs. First of all, we designed a series of dilute PdAu NPs models for XANES simulation. Examples of dilute PdAu alloy models are presented in Figure 1(a). We varied a few structure parameters in the models including structure, size, lattice constant, Pd location and so on. The icosahedral and cuboctahedral structures with the total number of atoms ranging from 13-561 are constructed. In each model, there is only one Pd site on surface or subsurface of Au nanoparticle to ensure the atomic dispersion of Pd in dilute PdAu. The lattice constant (interatomic distance) in the range of 90% - 110% of bulk Au lattice constant is also varied to account for possible change in interatomic distance between Pd and gold atoms in dilute PdAu alloy NPs. For each structure model, site specific Pd K-edge XANES spectrum is calculated for non-equivalent Pd sites. Then, we calculated the theoretical XANES spectra from all these PdAu NPs models via ab initio FEFF9 code. FEFF program is a very popular and time efficient codes for ab initio multiple scattering calculations of XAFS and XANES [29]. The theoretical XANES spectrum of bulk Pd metal calculated with FEFF9 code (with a correction of Fermi level) has a good agreement with the experimental data (Figure 1(b)). The obtained optimized parameters of theoretical calculation are used for all XANES calculations in this work. For each structure model, site specific XANES spectrum is calculated for non-equivalent Pd sites. It enabled us to obtain the high-quality theoretical XANES spectra in a reasonable amount of computational time. The theoretical XANES spectra for non-equivalent Pd atom sites in PdAu alloy models are different and reflect the local environment of specific site.

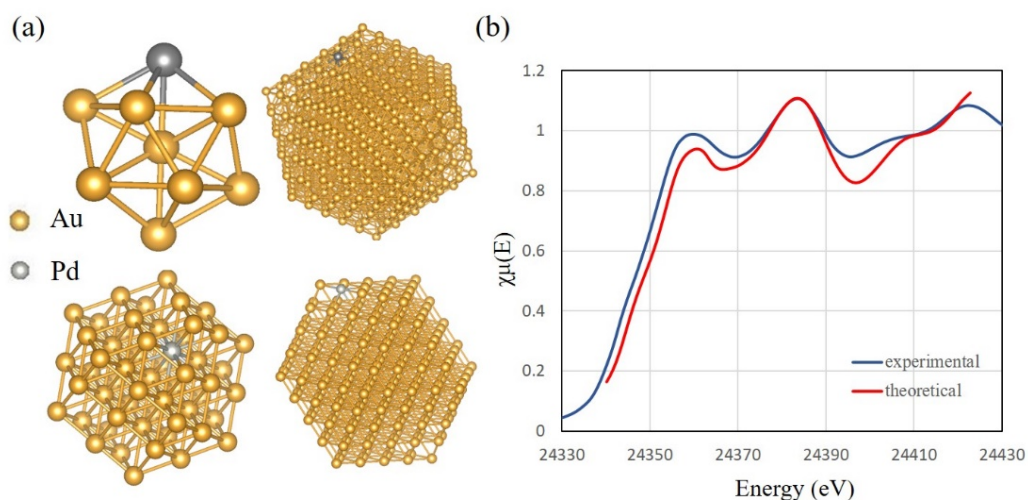


Figure 1. (a) Examples of dilute PdAu alloy models in icosahedral and cuboctahedral structures. (Generated by VESTA) (b) Comparison of the experimental and theoretical XANES spectra of bulk Pd at the Pd K-edge.

II. Results and Discussion

We observed strong correlations between the theoretical Pd K-edge XANES spectral features and the generalized structural descriptors including atomistic structure, lattice constant and Pd location, whereas the size effect is not very significant for the surface sites between the models with the total number of atoms 55-561.

First, the atomistic structure (icosahedron and cuboctahedron) significantly affect the calculated spectra. Using the structure with 309 atoms as one example, as shown in Figure 2(a)-(c), the major features beyond the white line in the calculated spectra of all icosahedral structure models with one Pd atom at corner, edge or face site shift to the left of the spectra of the corresponding cuboctahedral structure models. Meanwhile, the intensity of the white line in the spectra of icosahedral structure with one Pd atom at edge or face site are slightly dampened. When the lattice constant changes from 90% to 110% of the value of bulk Au, there is a clear shift of the spectrum to lower energy in both icosahedral and cuboctahedral structures. A comparison of the calculated XANES spectra of the icosahedral models with Pd located at the corner site, as an example, is shown in Figure 2(d). In addition, the location of Pd is an important structural descriptor, which is related to the catalytic performance of dilute PdAu alloy. Thus, the corner, edge and face sites on both the surface and subsurface are evaluated. The results from the models with Pd sites on the surface or subsurface can be distinguished since the theoretical XANES spectra of the models with the Pd on the subsurface sites possess higher intensities relative to those with Pd on the surface sites. The Pd at different surface sites are also compared. For instance, some differences exist in the theoretical XANES spectra of icosahedral structure

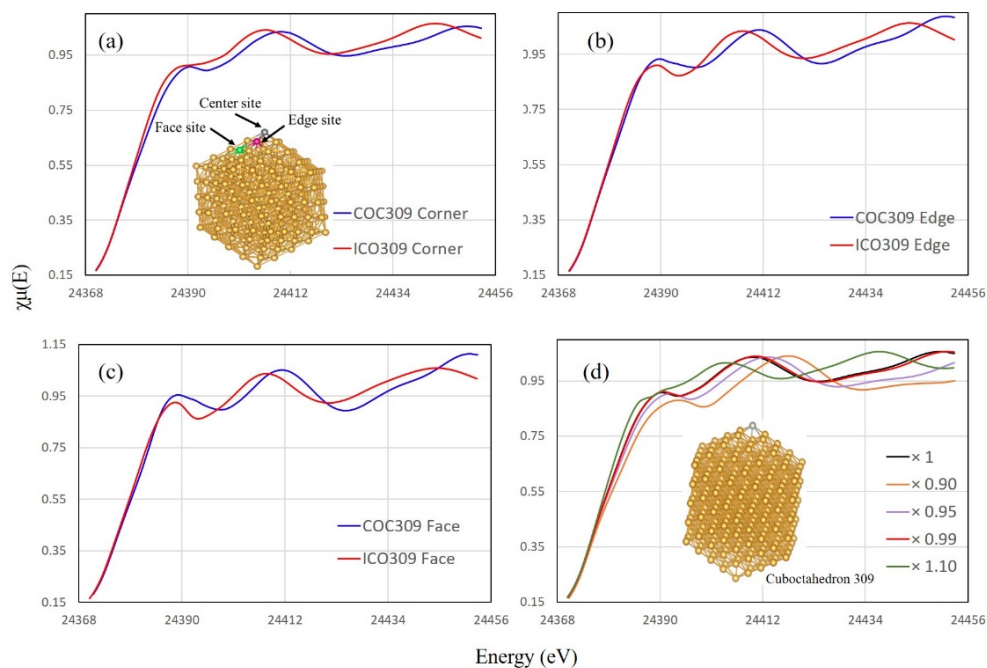


Figure 2. Theoretical Pd K-edge XANES spectra of cuboctahedral (309 atoms) (COC309) and icosahedral (309 atoms) (ICO309) structural models with one Pd atom at (a) corner site, (b) face site and (c) edge site on the surface. (d) Theoretical Pd K-edge XANES spectra of cuboctahedral structures (309 atoms) with one Pd at the corner site with changes to the lattice constant from 90%-110% of the value of bulk Au.

models consisting of 561 atoms with different Pd location on the surface (Figure 3(a)). The

spectrum with Pd located at corner is most distinct from the spectra with Pd at other locations. Similar trend is observed in other models with different total numbers of atoms. However, we observed very small variations in the calculated XANES spectra for the surface sites when only the total number of atoms changes which is unlike the size effect observed in monometallic cases. In Figure 3(b), as an example, among all of the obtained spectra corresponding corner site of Pd, only the structure model with 13 atoms is different from others by visual observation.

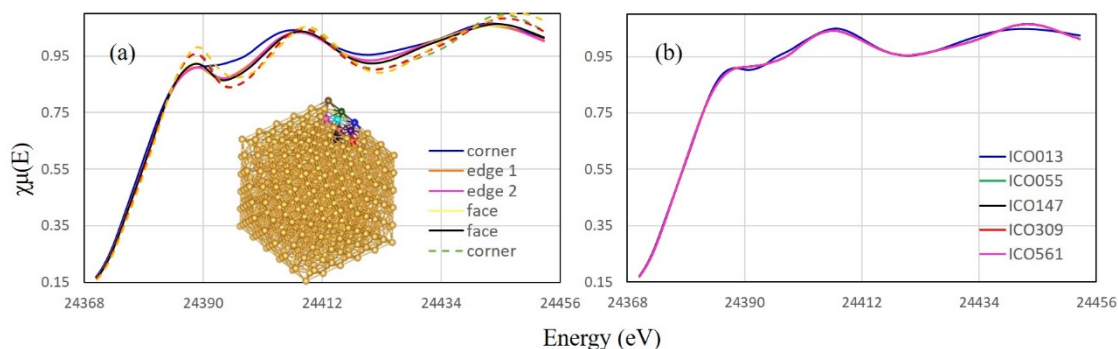


Figure 3. Theoretical Pd K-edge XANES spectra of (a) icosahedral structure (561 atoms) models with unique equivalent sites on surface (solid lines) and subsurface (dashed lines), (b) icosahedral (ICO) structure models (corner site) consisting of a varying total numbers of atoms (13, 55, 1147, 309 and 561).

Future Work

The faculty and one student will continue the collaboration with the BNL host in this program and will work on this project after summer. We plan to construct more models of different atomistic structures with varied structural parameters to get a more complete understanding of the generalized structure effects on the theoretical XANES. The structures will extend to hemispherical cuboctadron, octahedron, hexagonal closest packed (hcp) and so on. Based on the analysis of all the data from theoretical calculations, we will start to work on the construction of training data set for neural network (NN) training, similar to the previous reports [26,27]. We will use the site-specific theoretical data obtained from ab initio XANES simulations instead of using limited available experimental data and do linear combination of the unique site specific spectra to obtain a large representative data set. NN is a composite nonlinear function that is trained to make a nonlinear relationship between the input and output vectors. We will take the preprocessed and discretized theoretical XANES spectra as input and the generalized structural descriptors as output. In the training process, 80% of theoretical XANES data set will be used for training and the rest used for testing. The NN will be optimized to minimize the difference between the predicted and true coordination numbers of training and testing data. The validation of NN will be performed as well using both available theoretical and experimental XANES data of dilute PdAu alloy.

We will give presentations about our work in this project at Manhattan College and/or national, international conferences. The constructed NN will be shared to enrich the library of NNs. Furthermore, the investigators expect to extend the knowledge and experience obtained from this SML based NN approach obtained to other metal and bimetallic metal nanoparticles systems/projects that will result in the further publications and funding proposals.

Impact on Laboratory or National Missions

This collaborative project has been greatly benefited from the computational research and education resources at Brookhaven National Laboratory (BNL). The work done in this project could contribute to the development of NN for dilute PdAu alloy NPs that will be shared and enrich the library of NNs that will contribute to the BNL's efforts in "Machine Learning Assisted Material Discovery" [32]. In addition, BNL is developing arrays of in situ characterization techniques at National Synchrotron Light Source II (NSLS-II) and Center for Functional Nanomaterials for users. The knowledge learned from this project could be used by users from these facilities and even the broader science community to interpret XANES data of dilute PdAu alloy.

Conclusions

In summary, we have successfully calculated the theoretical Pd K-edge XANES spectra of dilute PdAu alloy NPs in icosahedral and cuboctahedral (13-561 atoms) structures with different generalized structure parameters. It is observed that the Pd K-edge theoretical XANES spectra of dilute PdAu in icosahedral and cuboctahedral structures are significantly affected by lattice constant, location of Pd, while the size effect for the surface sites is very small when the total number of atoms in the particles from 55 to 561. The theoretical Pd K-edge XANES spectra have a good sensitivity to distinguish the surface and subsurface locations of Pd, particularly in icosahedral structure. We will continue this project to construct more different structure models to obtain a more complete picture of the XANES-generalized structural descriptors association. Our findings could be used in identifying active site structure from XANES spectra to understand reaction mechanisms in catalysis. They could also lead to developing the training data set of low concentration PdAu alloy NPs in machine learning based XANES analysis approach.

References

- [1] D. M. Alonso, S. G. Wettstein, and J. A. Dumesic, *Chem. Soc. Rev.* **41**, 8075 (2012).
- [2] M. Sankar, N. Dimitratos, P. J. Miedziak, P. P. Wells, C. J. Kiely, and G. J. Hutchings, *Chem. Soc. Rev.* **41**, 8099 (2012).
- [3] M. Luneau, T. Shirman, A. Filie, J. Timoshenko, W. Chen, A. Trimpalis, M. Flytzani-Stephanopoulos, E. Kaxiras, A. I. Frenkel, J. Aizenberg, C. M. Friend, and R. J. Madix, *Chem. Mater.* **31**, 5759 (2019).
- [4] T. Ward, L. Delannoy, R. Hahn, S. Kendell, C. J. Pursell, C. Louis, and B. D. Chandler, *ACS Catal.* **3**, 2644 (2013).
- [5] C. J. Wrasman, A. Boubnov, A. R. Riscoe, A. S. Hoffman, S. R. Bare, and M. Cargnello, *J. Am. Chem. Soc.* **140**, 12930 (2018).
- [6] M. Chen, D. Kumar, C.-W. Yi, and D. W. Goodman, *Science* **310**, 291 (2005).
- [7] A. Hugon, L. Delannoy, J.-M. Krafft, and C. Louis, *J. Phys. Chem. C* **114**, 10823 (2010).
- [8] S. Hayashi, R. Ishida, S. Hasegawa, S. Yamazoe, and T. Tsukuda, *Top. Catal.* **61**, 136 (2018).
- [9] M. Luneau, T. Shirman, A. C. Foucher, K. Duanmu, D. M. A. Verbart, P. Sautet, E. A. Stach, J. Aizenberg, R. J. Madix, and C. M. Friend, *ACS Catal.* **10**, 441 (2020).
- [10] M. Luneau, E. Guan, W. Chen, A. C. Foucher, N. Marcella, T. Shirman, D. M. A. Verbart, J. Aizenberg, M. Aizenberg, E. A. Stach, R. J. Madix, A. I. Frenkel, and C. M. Friend, *Commun. Chem.* **3**, 46 (2020).
- [11] Y. Liu, N. Marcella, J. Timoshenko, A. Halder, B. Yang, L. Kolipaka, M. J. Pellin, S.

- Seifert, S. Vajda, P. Liu, and A. I. Frenkel, *J. Chem. Phys.* **151**, 164201 (2019).
- [12] W.-Y. Yu, L. Zhang, G. M. Mullen, G. Henkelman, and C. B. Mullins, *J. Phys. Chem. C* **119**, 11754 (2015).
- [13] W.-Y. Yu, G. M. Mullen, and C. B. Mullins, *J. Phys. Chem. C* **117**, 19535 (2013).
- [14] F. Gao and D. W. Goodman, *Chem. Soc. Rev.* **41**, 8009 (2012).
- [15] B. Roldan Cuenya, *Acc. Chem. Res.* **46**, 1682 (2013).
- [16] A. I. Frenkel, J. A. Rodriguez, and J. G. Chen, *ACS Catal.* **2**, 2269 (2012).
- [17] A. Bugaev, A. Guda, A. Lazzarini, K. Lomachenko, E. Groppo, R. Pellegrini, A. Piovano, H. Emerich, A. Soldatov, L. Bugaev, V. P. Dmitriev, J. Bokhoven, and C. Lamberti, *Catal. Today* **283**, 119 (2017).
- [18] X. Teng, Q. Wang, P. Liu, W. Han, A. I. Frenkel, W. Wen, N. Marinkovic, J. C. Hanson, and J. A. Rodriguez, *J. Am. Chem. Soc.* **130**, 1093—1101 (2008).
- [19] M. S. Nashner, A. I. Frenkel, D. L. Adler, J. R. Shapley, and R. G. Nuzzo, *J. Am. Chem. Soc.* **119**, 7760 (1997).
- [20] A. Piovano, G. Agostini, A. I. Frenkel, T. Bertier, C. Prestipino, M. Ceretti, W. Paulus, and C. Lamberti, *J. Phys. Chem. C* **115**, 1311 (2011).
- [21] A. L. Ankudinov, B. Ravel, J. J. Rehr, and S. D. Conradson, *Phys. Rev. B* **58**, 7565 (1998).
- [22] J. J. Rehr and A. L. Ankudinov, *Coord. Chem. Rev.* **249**, 131 (2005).
- [23] R. W. Strange, L. Alagna, P. Durham, and S. S. Hasnain, *J. Am. Chem. Soc.* **112**, 4265 (1990).
- [24] K. Gilmore, J. Vinson, E. L. Shirley, D. Prendergast, C. D. Pemmaraju, J. J. Kas, F. D. Vila, and J. J. Rehr, *Comput. Phys. Commun.* **197**, 109 (2015).
- [25] J. Vinson, J. J. Rehr, J. J. Kas, and E. L. Shirley, *Phys. Rev. B* **83**, 115106 (2011).
- [26] J. Timoshenko, D. Lu, Y. Lin, and A. I. Frenkel, *J. Phys. Chem. Lett.* **8**, 5091 (2017).
- [27] N. Marcella, Y. Liu, J. Timoshenko, E. Guan, M. Luneau, T. Shirman, A. M. Plonka, J. E. S. van der Hoeven, J. Aizenberg, C. M. Friend, and A. I. Frenkel, *Phys. Chem. Chem. Phys.* (2020).
- [28] J. Timoshenko and A. I. Frenkel, *ACS Catal.* **9**, 10192 (2019).
- [29] J. J. Rehr, J. J. Kas, F. D. Vila, M. P. Prange, and K. Jorissen, *Phys. Chem. Chem. Phys.* **12**, 5503 (2010).

Appendix:

Participants

Name	Institution	Role
Jing Liu	Department of Physics, Manhattan College	Faculty participant, Principal Investigator
Jennifer LaPoff	Department of Chemistry and Biochemistry, Manhattan College	Student participant
Phillip Comer	Department of Mechanical Engineering, Manhattan College	Student participant
Anatoly I. Frenkel	Department of Materials Science and Chemical Engineering, Stony Brook University Chemistry Division, Brookhaven National Laboratory	Collaborating staff member, co-Principal Investigator
Nicholas Marcella	Department of Materials Science and Chemical Engineering, Stony Brook University	Graduate student Collaborator

Notable Outcomes

A presentation titled as “Interpretation of Structure Evolution of Metallic and Bimetallic Nanoparticles Using X-ray Absorption Spectroscopy and Neural Network” was given at Faculty Colloquium at Brookhaven National Laboratory on July 20th, 2020.

Research Vibrancy

The VPF faculty participant plans to return to visit Brookhaven National Laboratory to use the on-site facilities at Center for Functional Nanomaterials and NSLS-II as well as the computational resources at Center for Functional Nanomaterials. The proposals to NSLS-II and Center for Functional Nanomaterials to perform experiments have been submitted. The VPF faculty participant also plans to return BNL under VFP or other possible funding resources.

Connection to Programs at Home Academic Institution

This program provided a very precious opportunity to both VPF faculty and student participants to carry out the research in the field of theoretical simulations during the current pandemic. This unique experience expanded the horizon of research and skills of the faculty participant and students. Thus, the faculty will be able to use these knowledge and skills to apply to future research in functional bimetallic alloy materials and to establish new and more competitive collaborated projects within home institution. Also, one of the undergraduate student participant expressed great interest and will continue the project that will further enrich the student’s research experience and assist the student’s pursuit of education in graduate school. The knowledge of bimetallic alloy and supervised machine learning-spectroscopy approach could be incorporated into teaching to introduce undergraduate students to the prestigious development in this multidisciplinary research field.

Simulating the space charge effect inside the ICARUS liquid argon time projection chamber at Fermilab

Elijah D. S. Courtney

*Department of Physics and Astronomy and the Center for Simulational Physics,
University of Georgia, Athens, GA 30602*

Haiwang Yu and Milind Diwan

*Electronic Detectors Group, Physics Department,
Brookhaven National Laboratory, Upton, NY 11973*

Abstract

Fermilab's Imaging Cosmic and Rare Underground Signals (ICARUS) detector is a Liquid Argon Time-Projection Chamber (LArTPC) used to measure oscillations between neutrino flavors to explore the limits of the Standard Model as part of the Short-Baseline Neutrino Program. Neutrino interactions inside ICARUS emit charged particles, which ionize neutral atoms and produce free electrons to be drifted by an external electric field toward three parallel planes of angled wires. Free charges moving near the wires induce a current, which is amplified, digitized, and analyzed to detect the initial neutrino event. A high level of noise is associated with these measurements, calling for accurate simulations of the detector to refine analytical techniques and train neural networks to recognize and correctly describe neutrino events. My project independently simulated the space charge in ICARUS from first principles, calculating the path distorting effect of the ionic charge densities that result from the cosmic muon flux. Although the simulation can be improved, we report agreement with previously simulated and measured results for other LArTPCs, estimating a maximum distortion of the external electric field of approximately 0.8%, a peak electron drift time delay of approximately 2%, and a peak radial drift of approximately 8 mm, well above the 1 mm spatial resolution and the 3 mm wire pitch of ICARUS, indicating that existing simulations of the current ICARUS installation at Fermilab should consider space charge effects.

I. INTRODUCTION

In LArTPC detectors, after a neutrino event generates a charged particle, the charged particle ionizes atoms and creates an ionization track formed of newly freed electrons. In order to separate the newly formed ions from the free electrons, a constant external electric field is applied, drifting the positive ions toward the cathode and the electrons toward the anode, formed of three parallel planes of wires. When the electrons pass through these planes, they induce a current, which is then amplified, digitized, and recorded to reconstruct the path and energy of the original ionizing charge. However, the cosmic muon flux constantly produces argon ions throughout the LArTPC by dissociating neutral argon atoms into a free electrons and positive ions³. The presence of positive ions enables drifting electrons to recombine, forming neutral argon at a rate proportional to the argon ion density. Although ions and electrons are both drifted out by the external electric field, argon ions drift $\approx 200,000$ times slower than electrons, and a net positive charge density accumulates inside the detector. Additionally, drifting electrons can form anions from impurities in the argon, forming a negative charge density over time. These charge densities produce a net electric field, introducing a distorting factor into the recorded data that should be characterized in order to understand how it may distort drifting ionization tracks.

Previous studies of the space charge distortion within TPCs has often made simplifying assumptions: that electrons are not captured by positive ions once they have dissociated^{1,3,5}, that the anion density is negligible^{3,5}, and that the muon flux is constant through the medium^{1,3}. This work accounts for the depth dependence of muon flux, anion density, recombination, and the shielding effect of the 3 m overburden above the TPC. However, this study does not account for the bulk motion of the liquid argon due to thermal convection or recirculation via pumps.

II. METHOD

Inside liquid argon at 87 K, argon cations have a drift velocity of approximately 8 mm/s (v_{Ar}), and thus linger in the larger neutral argon fluid for longer than their corresponding electrons, which drift at approximately 1648 m/s ($v_e l$). Cation and anion drift velocities are assumed to be the same, based on the mobility of ions inside argon¹. I propose the

following method for calculating the number density of free electrons, anions, and argon cations formed as a result of the muon flux, allowing for an accurate estimate of the average charge density within the ICARUS LArTPC, the resultant electric field, and the radial shift and time delay on ionization tracks in the medium. This calculation assumes that the charge density of ICARUS is in a steady state, and that the 50,000 V/m external field is applied in the negative x-direction. First, the muon flux as a function of depth was determined according to the approximate Gaisser's formula^{2,5}.

$$J(z) = \frac{dE}{dx} \frac{2\pi}{W_1} \int_0^{\pi/2} \int_{\frac{E_T(z)}{\cos(\theta)}}^{\infty} f(E, \theta) \cos(\theta) \sin(\theta) dE d\theta \quad (1)$$

$$f(E, \theta) = \frac{0.14}{\text{cm}^2 \cdot \text{s} \cdot \text{sr} \cdot \text{GeV}} \left[E \left(1 + \frac{3.64 \text{GeV}}{E(\cos(\theta^*))^{1.29}} \right) \right]^{-2.7} \left(\frac{1}{1 + \frac{1.1E\cos(\theta^*)}{115 \text{GeV}}} + \frac{0.054}{1 + \frac{1.1E\cos(\theta^*)}{850 \text{GeV}}} \right) \quad (2)$$

$$\cos(\theta^*) = \sqrt{\frac{(\cos(\theta))^2 + P_1^2 + P_2(\cos(\theta))^{P_3} + P_4(\cos(\theta))^{P_5}}{1 + P_1^2 + P_2 + P_4}} \quad (3)$$

In the above equations, $J(z)$ is the depth dependent ion formation rate, with units of $n/m^3/s$, calculated from the cosmic muon flux through the 3 m concrete shield above ICARUS at Fermilab⁵. The threshold energy $E_T(z)$ was determined in GeV from previously reported data⁵ for the threshold energy at sea level beneath 3 m of overburden, fit to a linear function, $E_T(z) = 0.2337z + 1.5764$. Parameters P_1, \dots, P_5 are given in Table I, $\frac{dE}{dx} = 2.1$ MeV/cm is the rate at which energy is lost by muons inside liquid argon, and $W_1 = 23.6$ eV/ion pair.

Parameter	Value
P_1	0.102573
P_2	-0.068287
P_3	0.958633
P_4	0.0407253
P_5	0.817285

TABLE I: Parameters of the $\cos(\theta^*)$ function.

From this, an analytical estimate of the cation and anion densities is easily formed. Neglecting recombination, the rate of change of density of cations at a point in the steady

state is determined by Eq. 4.

$$\frac{\partial \rho_{Ar}(x, z)}{\partial t} = J(z) - \frac{\partial \rho_{Ar}(x, z)}{\partial x} v_i = 0 \quad (4)$$

Since $J(z)$ is known from Eqs. 1-3, solving for $\rho_{Ar}(x, z)$ is trivial. Setting the cathode at the origin,

$$\rho_{Ar}(x, z) = \int_0^{W-x} \frac{J(z)}{v_i} dx = (W-x) \frac{J(z)}{v_i}, \quad (5)$$

where W is the drift distance of the TPC. A similar estimate can be obtained for the anion density, based on the probability density for an electron to form an anion as a function of distance, $\frac{1}{v_e \tau} e^{-x/v_e \tau}$

where τ is the electron lifetime and v_e is the electron drift velocity:

$$\frac{\partial \rho_{an}(x, z)}{\partial t} = R_{an}(x, z) - \frac{\partial \rho_{an}(x, z)}{\partial x} v_i = 0 \quad (6)$$

We perform the calculation in two steps. In the first step we calculate the source of anions from electron attachment.

$$R_{an}(x', z) = J(z) \int_0^{x'} \frac{1}{v_e \tau} e^{-(x'-t)/v_e \tau} dt = J(z)(1 - e^{-x'/v_e \tau}). \quad (7)$$

And in the second step we calculate the anion density after it has stabilized in the external field.

$$\rho_{an}(x, z) = \int_0^x \frac{R_{an}(x', z)}{v_i} dx' = \frac{J(z)}{v_i} (x - v_e \tau (1 - e^{-x/v_e \tau})) \quad (8)$$

In order to account for the recombination of electron-cation pairs, as well as the space charge field rendering velocity an unknown function of position, a numerical model was also devised to calculate anion, cation, and electron densities.

Consider the detector as being made up of a large number of arbitrary box of volumes V , each with length L , height Δz , and width Δx , where $\Delta x, \Delta z \ll L$. The argon ions are considered to flow only through the plane faces of V , as length $L = 19m$ is chosen to equal the full dimension of the ICARUS detector.

The net cation flux in V can be described as

$$R_{Ar,in} - R_{Ar,cap} + R_{Ar,cre} = R_{Ar,out}, \quad (9)$$

where $R_{Ar,in}$ is the flux of cations into the volume, $R_{Ar,out}$ is the outward cation flux, $R_{Ar,cre}$

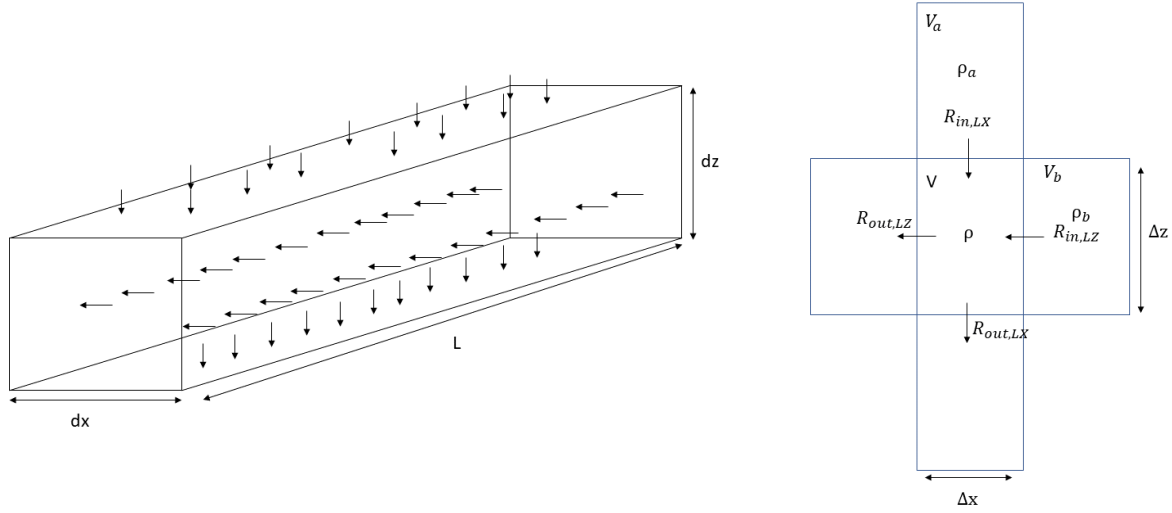


FIG. 1: Diagrams of the inward and outward flux through V.

is the total number of cations created by cosmic muons inside the volume, and $R_{Ar,cap}$ is the number of cations within the volume that have recombined with available free electrons to form neutral atoms, effectively removed as space charges. By taking small enough steps $\Delta x, \Delta z$, density in a given volume can be assumed to be approximately constant, and the fluxes can be described as follows:

$$R_{Ar,in} = R_{in,LX} + R_{in,LZ} = \rho_a v_{Ar,\perp} L \Delta x + \rho_b v_{Ar,\parallel} L \Delta z \quad (10)$$

$$R_{Ar,out} = R_{out,LX} + R_{out,LZ} = \rho v_{Ar,\perp} L \Delta x + \rho v_{Ar,\parallel} L \Delta z \quad (11)$$

$$R_{Ar,cre} = L \Delta x \Delta z J(z) \quad (12)$$

$$R_{Ar,cap} = [\rho_{el} \pi r_c^2 L] \left(\rho_a v_{\perp} \Delta x \frac{\Delta x}{2} + \rho_b v_{\parallel} \Delta x \Delta z \right) \quad (13)$$

Densities ρ_a and ρ_b are the number densities of argon ions at the boundaries LX_1 and LZ_1 , respectively. Densities ρ and ρ_{el} are the number densities of argon cations and electrons within volume V, while v_{rel} is the relative velocity of the argon cations and electrons, in order to account for relative flux. The radius r_c is the Onsager radius, calculated as $r_c = \frac{e^2}{4\pi\epsilon_0\epsilon kT}$. This gives the radius at which an electron with thermal energy kT will be captured by a cation with a single net positive charge, where e is the proton charge, ϵ_0 is the vacuum permittivity, and ϵ is the dielectric constant of liquid argon at 87 K (1.505).

By substituting Eqs. 10-13 into Eq. 9, accounting for the capture of newly created cations, and solving for density, we obtain Eq. 14,

$$\rho_{Ar} = \frac{\mathcal{P}_a^{Ar} + \mathcal{P}_b^{Ar} + \Delta z \Delta x J(z) - [\rho_{el} \pi r_c^2 \Delta x] \left(\frac{\mathcal{P}_a^{Ar}}{2} + \mathcal{P}_b^{Ar} + J(z) \Delta z \frac{\Delta x}{2} \right)}{v_{Ar,\parallel} \Delta z + v_{Ar,\perp} \Delta x}, \quad (14)$$

where $\mathcal{J}(z) = J(z) \Delta x \Delta z$, $\mathcal{P}_a^{Ar} = \rho_{Ar,a} v_{Ar,\perp} \Delta x$, and $\mathcal{P}_b^{Ar} = \rho_{Ar,b} v_{Ar,\parallel} \Delta z$. With the insight that, because no ions flow from outside the detector, $\rho_{Ar,a}$ is zero at the top ($z=0$ m) and bottom ($z=3.8$ m) of the detector, while $\rho_{Ar,b}$ is zero at the anode ($x=1.6$ m), this method can be iteratively applied to find the argon ion density at any point x, z , by first finding the density at $(0,0)$, then $(0, \Delta z) \dots (0, 3.8)$, then $(\Delta x, 0), (\Delta x, \Delta z) \dots$ and iterating until the density in all partial volumes is known. However, this method requires that the electron density be known as a function of x and z .

Using similar reasoning as above, we can obtain an analogous formula for the electron density, though an additional term must be added. Although the argon anion is both unstable and difficult to form, the liquid argon inside the detector contains certain impurities, primarily O_2 , CO_2 , and H_2O ¹. These molecules can capture electrons with relative ease, forming persistent negative ions in the medium that then drift toward the anode. The proportion of electrons that form ions in this way over a single volume slice can be estimated from the electron lifetime in the medium, $\tau_e \approx 3ms$, and the electron drift velocity. The electron lifetime is an experimental variable that can change during the experiment as the Ar is purified. For the purposes of this paper, we have set it to a nominal value of $3ms$.

$$\frac{N_{e,ion}}{N_e} = \frac{\Delta x}{\tau_e v_e} \quad (15)$$

Thus, the rate at which these ions form in a volume slice is

$$R_{anion,create} = (\rho_{e,b} v_{e,\parallel} L \Delta z) \frac{\Delta x}{\tau_e v_e} + (\rho_{e,a} v_{e,\perp} L \Delta x + J(z) L \Delta z \Delta x) \frac{\Delta x}{2 \tau_e v_e}, \quad (16)$$

where $J(z) L \Delta x \Delta z$ has been introduced to account for increased density of electrons formed inside the step.

$$\rho_e = \frac{\mathcal{P}_a^{el} + \mathcal{P}_b^{el} + \mathcal{J}(z) - [\rho_{Ar} \pi r_c^2 \Delta x] \left(\frac{\mathcal{P}_a^{el}}{2} + \mathcal{P}_b^{el} + \frac{\mathcal{J}(z)}{2} \right) - (\mathcal{P}_b^{el}) \frac{\Delta x}{\tau_e v_e} + (\mathcal{P}_a^{el} + \mathcal{J}(z)) \frac{\Delta x}{2 \tau_e v_e}}{v_{e,\parallel} \Delta z + v_{e,\perp} \Delta x}, \quad (17)$$

where $\mathcal{J}(z) = J(z)\Delta x\Delta z$, $\mathcal{P}_a^{el} = \rho_{e,a}v_{e,\perp}\Delta x$, and $\mathcal{P}_b^{el} = \rho_{e,b}v_{e,\parallel}\Delta z$.

In addition to cations and electrons, a third charge density contributes to the space charge effect. The equivalent expressions to Eqs. 9 and 14 for anions are Eqs. 18 and 19,

$$R_{anion,in} + R_{anion,create} = R_{anion,out}. \quad (18)$$

$$\rho_{an} = \frac{\mathcal{P}_b^{an} + \mathcal{P}_a^{an} + (\rho_{e,b}v_{e,\parallel}\Delta z)\frac{\Delta x}{\tau_e v_e} + (\rho_{e,a}v_{e,\perp}\Delta x + J(z)\Delta x\Delta z)\frac{\Delta x}{2\tau_e v_e}}{v_{an,\parallel}\Delta z + v_{an,\perp}\Delta x}, \quad (19)$$

where $\mathcal{J}(z) = J(z)\Delta x\Delta z$, $\mathcal{P}_a^{an} = \rho_{an,a}v_{an,\perp}\Delta x$, and $\mathcal{P}_b^{an} = \rho_{an,b}v_{an,\parallel}\Delta z$. However, each of these expressions relies on knowing the electron or cation density; it seems that one cannot precisely calculate one density without previously knowing another. This dilemma is easily resolved by estimating the fraction of electrons that will recombine or form anions. We used the width of the ICARUS LArTPC (1.6 m) and drift velocity⁴ of argon (8 mm/s) to estimate the average time required for a randomly selected cation to be drifted out as 100 seconds. Multiplying by the formation rate -approximated as $6 \times 10^8/m^3/s$ from Eq. 1 over the depth of ICARUS-, one obtains an average number density of $6 \times 10^{10}/m^3$. By calculating the mean free path L of a free electron in this density before it recombines with an argon ion from the Onsager capture radius of 127 nm, it becomes clear that an electron encounters approximately 0.003 cations/m, and over an average drift distance of 0.8m, thus approximately 0.25% of all free electrons will recombine with the argon cations before being drifted out. This estimate assumes that cation density is constant throughout the medium; as both electron and cation densities are roughly linear with slopes of opposite signs, and recombination rate is related to the product of the densities, the recombination rate is approximately quadratic in position with a maximum value at the center and minima at $x=0$ and $x=1.6$ m. With a lifetime $\tau_e \approx 3ms$ and velocity $v_{el} \approx 1648m/s$, the average electron travels approximately 4.9m before forming an anion, and thus forms approximately 0.2 anions/meter, or 0.16 anions over the average drift length. Thus, while only 0.3% of electrons will neutralize existing cations, approximately 16% of electrons will form new anions. Thus, the electron density can be initially approximated as the original density multiplied by a constant, linearly increasing with distance. That is, $\rho_{el}(x, z) \approx 0.84\frac{xJ(z)}{v_{el}}$.

Using this initial estimate for electron density, Eqs. 13 and 19 can be iteratively applied using small steps $\Delta x = 10^{-3}m$ and $\Delta z = 0.1m$ over the width of the detector to obtain

an approximation of cation and anion densities as functions of position. These values were chosen because over any $\Delta z = 0.1\text{m}$ step, the ion creation rate $J(z)$ varies by less than 1%, and $\Delta x = 10^{-3}\text{m}$ allows for 1600 steps to be taken over the drift distance, allowing for a good approximation of continuous values by a fit function.

The cation and anion densities enable use of Eq. 17 to recalculate the electron density, which can then be used with Eqs. 14 and 19 to recalculate the ion densities; this process can be repeated until desired, but should quickly approach the stable state assumed to be in the detector. With a reasonable estimate of initial electron density, density values tended to converge to their final values within 4 iterations.

Once electron and ion densities have been numerically obtained as functions of position, calculating charge density is trivial, as shown in Eq. 20.

$$\rho_{ch}(x, z) = (\rho_{Ar}(x, z) - \rho_{el}(x, z) - \rho_{anion}(x, z))e \quad (20)$$

We have made a fit to the numerically evaluated function $\rho_{ch}(x, z)$; the fit results in an explicit function of position and depth of the form $A + Bx + Cz + Dx^2 + Exz + Fz^2 + Gx^2z + Hxz^2 + Iz^3$. Once the charge density has converged to a final result, the space charge electric field is calculated. Coefficients A,...,I are reported in Appendix A for the final charge densities under the external field and five subsequent calculations of the electric field. Stability is reached after only a few recalculations of the electric field.

The electric field produced by the space charge can be calculated from the dimensions of the ICARUS detector.

Although solving for the space charge electric field at an arbitrary point inside a rectangular volume of non-uniform charge density with dielectric constant ϵ is simple conceptually, it is somewhat difficult analytically, due to the non-negligible terms $\frac{E_y}{dy} + \frac{E_z}{dz}$ in Eq. 21 and lack of convenient symmetry in the charge density.

$$\nabla \cdot \bar{E} = \frac{E_x}{dx} + \frac{E_y}{dy} + \frac{E_z}{dz} = \frac{\rho_{ch}(x, z)}{\epsilon_0\epsilon} \quad (21)$$

or equivalently,

$$\bar{E}(\bar{r}) = \frac{1}{4\pi\epsilon_0} \iiint_{V \setminus \bar{r}} \frac{\hat{r} \rho_{ch}(x, z) dx dy dz}{\epsilon |\bar{r}|^2}, \quad (22)$$

However, it can easily be solved numerically for a given point at $\bar{r}(t)$ by approximating the constant distribution as a large number of point charges, each representing the charge

contained in an arbitrarily small rectangular volume ΔV centered at $\bar{r}_{i,j,k}(t)$. By summing over 64^3 such volumes contained in the LArTPC, excluding only the single volume containing the point of interest, a reasonable estimate can be obtained for the electric field at any point.

$$\bar{\mathcal{R}}_{i,j,k}(\bar{r}) = [x_i, y_j, z_k] - [x, y, z] = \bar{r}_{i,j,k} - \bar{r} \quad (23)$$

$$[x_{i+1}, y_{j+1}, z_{k+1}] = [x_i, y_j, z_k] + [\Delta x, \Delta y, \Delta z] \quad (24)$$

$$\bar{E}_{i,j,k}(\bar{r}) = \frac{1}{4\pi\epsilon_0\epsilon} \frac{\rho_{ch}(x_i, z_k)\Delta x\Delta y\Delta z}{|\bar{\mathcal{R}}_{i,j,k}(\bar{r})|^2} \hat{\mathcal{R}}_{i,j,k}(\bar{r}) \quad (25)$$

$$\bar{E}(\bar{r}) = \bar{E}_{ext} + \sum_{i=1}^{64} \sum_{j=1}^{64} \sum_{k=1}^{64} \bar{E}_{i,j,k}(\bar{r}) \quad (26)$$

The electric field was calculated in this way at 17^3 points, with trilinear interpolation used to obtain continuous values for recalculation of charge density. The calculated electric field was then used to recalculate the drift velocities in Eqs. 14, 17, and 19 for further iterations of charge density. The electric field was recalculated every four iterations of the charge density calculation, as the charge density comfortably converged within this span. This process was iterated until all components of the space charge electric field remained constant to the sixth significant digit.

The drift speed of the electron can be well-approximated if the temperature and magnitude of the field at a given point is known, as shown by Eq. 27.

$$F(|E|) = |V(|E|)| = |E \frac{a_0 + a_1 E + a_2 E^{3/2} + a_3 E^{5/2}}{1 + \frac{a_1}{a_0} E + a_4 E^2 + a_5 E^3} (\frac{87}{89})^{-\frac{3}{2}}|, \quad (27)$$

where $a_0 = 551.6$, $a_1 = 7953.7$, $a_2 = 4440.43$, $a_3 = 4.29$, $a_4 = 43.63$, and $a_5 = 0.2053$; a_0 , a_1 , a_2 , and a_3 have units to give their term dimensions of $\text{cm}^2/\text{kV/s}$, while a_4 and a_5 have units to make their term dimensionless. Equation 27 is easily formed to produce drift velocity in m/s as a function of the electric field in units of V/m by replacing E with $E * 10^{-5}$, and multiplying the entire expression by an overall factor of 10. In order to quantify the effect of the space charge electric field on drifting electrons, a simple model was run to calculate the drift path and time of a single electron given its initial position.

$$|\bar{V}_i(t)| = F(|\bar{E}(r_i(t))|) \quad (28)$$

$$\bar{V}_i(t) = -|\bar{V}_i(t)| \frac{\bar{E}(r_i(t))}{|\bar{E}(r_i(t))|} \quad (29)$$

$$\bar{r}_i(t + dt) = \bar{r}_i(t) + \bar{V}_i(t)dt \quad (30)$$

From this model, both the final radial displacement δr and the time delay δt were calculated for a range of initial positions within the volume and averaged over the y-coordinate, where δr is the radial distance from the ideal drift path at the anode ($x=1.6$ m) and δt is the difference in the times taken to reach the anode from the initial position under the near-physical (including space charge) and ideal electric fields.

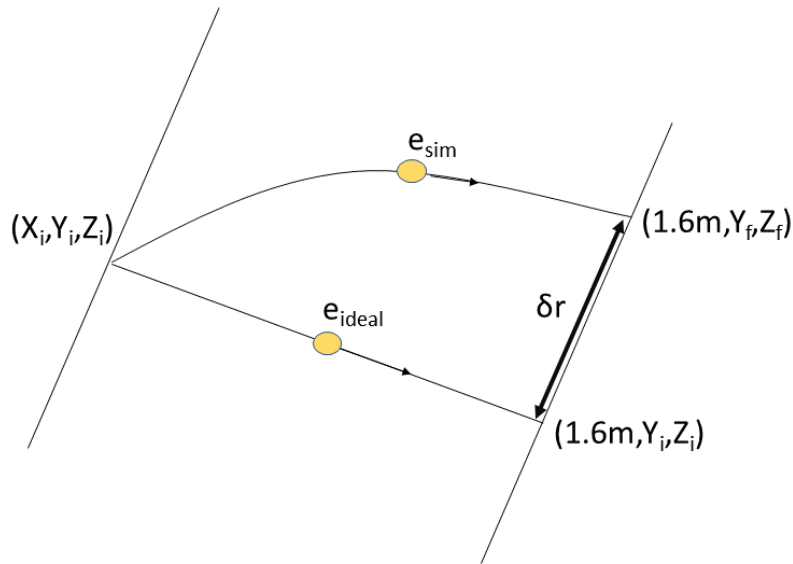


FIG. 2: The definition of radial shift δr .

III. RESULTS

As shown in Figure 3, the number density of ions was much higher than that of electrons; this is expected, as the electron drift velocity is 200,000 times larger than that of the ions, and $\approx 16\%$ of electrons will form anions. A visual inspection of Figure 3 confirms that $\rho_e \approx \frac{0.84}{200,000} \rho_{Ar}$, affirming the initial estimate for electron density based on the formation and capture rates.

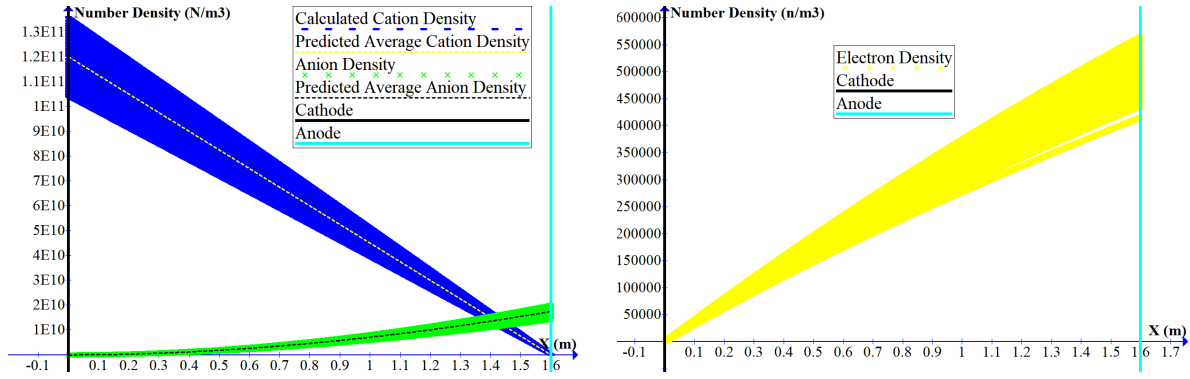


FIG. 3: Simulated ion and electron densities for all depths as a function of position. Also shown are the predicted cation and anion densities, based on Eqs. 5 & 8 with the muon flux averaged over depth.

Figure 4 follows from Eq. 20 and Figure 3, showing a positive charge density in most of the LArTPC volume with a small region of negative charge.

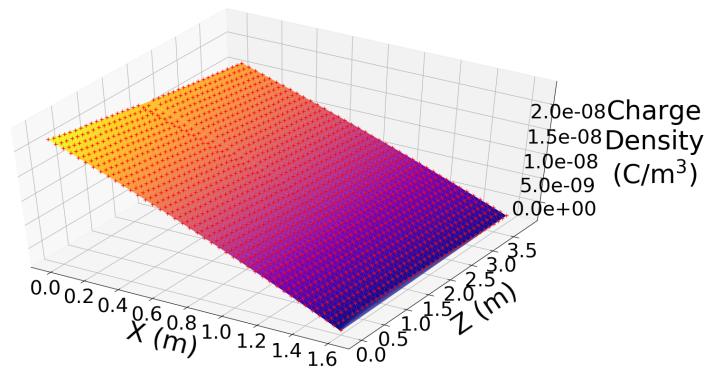


FIG. 4: Charge density as a function of position; note that charge density is assumed constant as a function of y .

After 24 iterations of the charge density calculation, with the electric field recalculated every fourth iteration, it was found that the maximum magnitude of any component of the space charge electric field is approximately 380 V/m, less than 0.8% of the external electric field, and will typically reduce the x-component of the total field. Accounting for the methodological differences in the value of drift velocity and muon flux, this is in good agreement with estimates from previous calculations³.

Shown in Figure 5 are the components of the electric field halfway along the drift axis x , the horizontal transverse axis y , and the vertical transverse axis z of the LArTPC, with

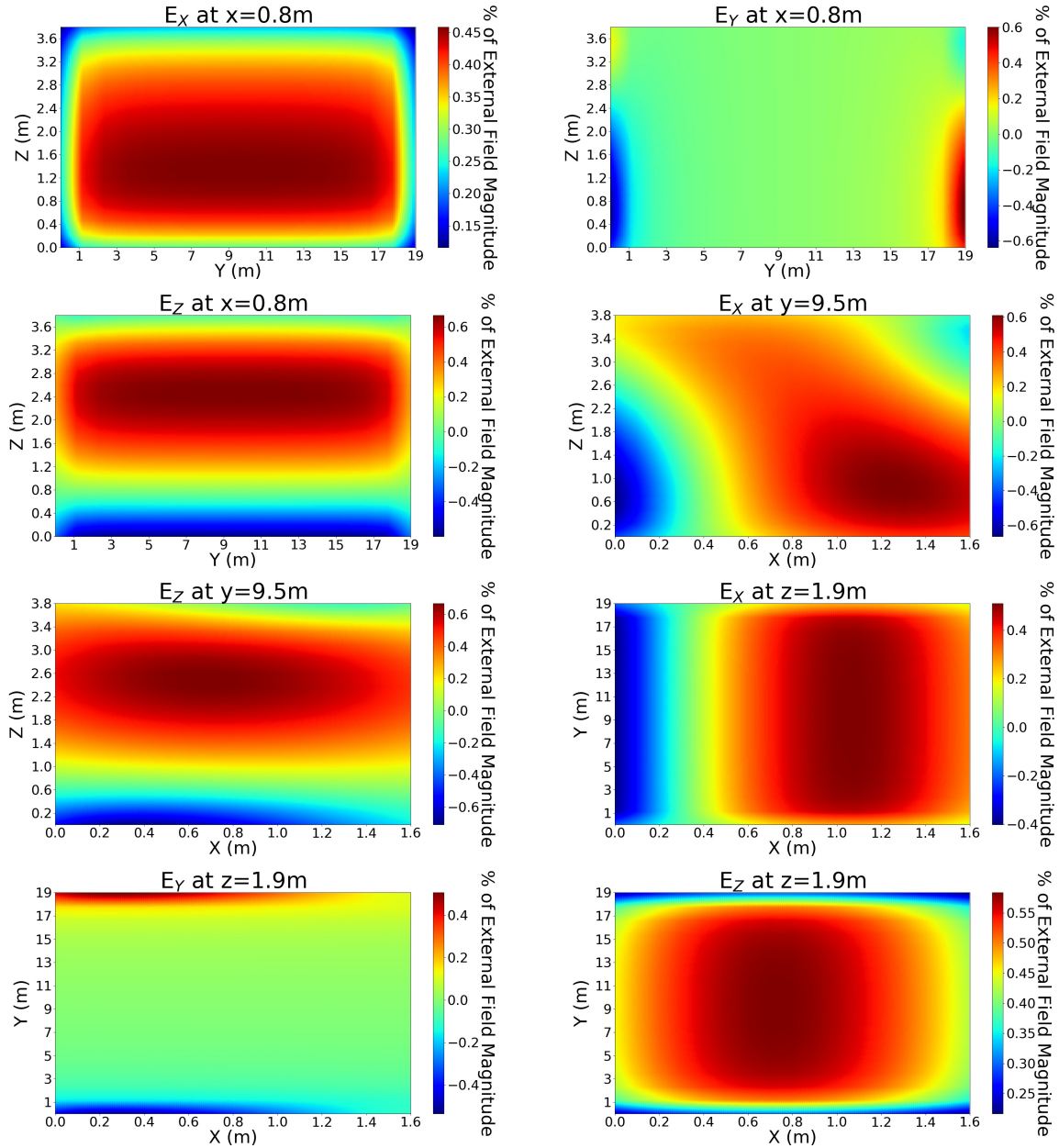


FIG. 5: Electric field components halfway along each axis. Note that the external electric field is considered equal to $-50,000\text{ V/m}$, and thus a negative space charge field increases the total field magnitude.

the exception of the E_y at $y=9.5\text{m}$, as it is zero by the assumption that charge density is uniform with respect to the y -axis.

From this electric field, the radial shift and delay of a drifting electron were calculated, according to Eqs. 27-30. Naturally, the radial shift and time delay decrease as the anode at

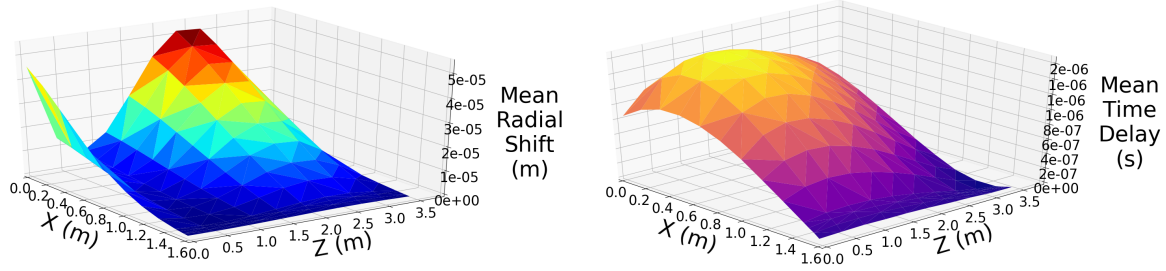


FIG. 6: Mean displacement and delay over the width and depth of the detector.

$x=1.6$ m is approached, as the electron's total drift distance decreases.

As shown in Figure 6, the peak radial shift, averaged over all y -values at each (x,z) , was approximately 8 mm, and the total drift time differed from that of the external field by a maximum of $\approx 1.6 \mu s$, with both varying with initial position. Because the spatial reconstruction resolution of ICARUS is 1 mm and the wire pitch is 3 mm, the space charge effect should be considered in simulations and data analysis.

Future simulations of this kind will consider the charge induced on the conducting sides of the TPC by the charge density, likely using the method of image charges. It is anticipated that inclusion of this effect will increase the electric field distortion.

IV. CONCLUSION

Overall, the charge density is significant, even after accounting for the depth dependence of muon flux beneath 3 m of shielding. The anion density formed is a significant fraction of the cation density over much of the volume, even exceeding the cation density in the final centimeters before the anode, and must be considered for an accurate calculation of the electric field.

This initial study shows that the depth-dependent muon flux yields non-negligible distortions of the field and electron drift, which may account for previously observed discrepancies between previous models and recorded data for surface detectors¹. However, this work's simplifying assumption of a steady state does not account for the bulk motion of the liquid argon due to thermal convection or recirculation via pumps.

Although the magnitude of the space charge electric field is a small fraction of the external

field, reaching a maximum value of $\approx 0.8\%$, even this small fraction will result in non-negligible distortions, drifting electrons by as much as 8 mm compared to those in the external field alone. Accurate measurements of ion drift velocity and electron lifetime within ICARUS are necessary, as they are both inversely proportional to components of the space charge density. Because of the magnitude of distortion predicted by this model, future simulations and analysis of data from ICARUS must account for the space charge density.

- ¹ Antonello, M., Baibussinov, B., Bellini, V., et al. 2020, Study of space charge in the ICARUS T600 detector. <https://arxiv.org/abs/2001.08934>
- ² Gaisser, T. K., Engel, R., & Resconi, E. 2016, Cosmic Rays and Particle Physics, second edition (Cambridge University Press), doi: <https://doi.org/10.1017/CB09781139192194>
- ³ Mooney, M. 2015, The MicroBooNE Experiment and the Impact of Space Charge Effects. <https://arxiv.org/abs/1511.01563>
- ⁴ Thorn, C. 1984, Catalogue of Liquid Argon Properties. <https://microboone-docdb.fnal.gov/cgi-bin/private/ShowDocument?docid=412>
- ⁵ Yu, B. 2012, Estimate of the Space Charge Effect in the 5kton FD. <https://lbne2-docdb.fnal.gov/cgi-bin/ShowDocument?docid=6471>

V. APPENDIX A

Iteration	A	B	C	D
1	2.19155E-8±8E-13	-1.3809E-8±2E-12	-1.658E-9±1E-12	-1.173E-9±1E-12
2	2.1724E-8±4E-12	-1.3438E-8±9E-12	-1.594E-9±5E-12	-1.324E-9±5E-12
3	2.1725E-8±4E-12	-1.3439E-8±9E-12	-1.594E-9±5E-12	-1.323E-9±5E-12
4	2.177E-8±2E-11	-1.350E-8±4E-11	-1.61E-9±2E-11	-1.32E-9±2E-11
5	2.177E-8±1E-11	-1.350E-8±4E-11	-1.61E-9±2E-11	-1.32E-9±2E-11
6	2.177E-8±1E-11	-1.350E-8±4E-11	-1.61E-9±2E-11	-1.32E-9±2E-11
E	F	G	H	I
1.053E-9±1E-12	8.49E-11±6E-13	7.47E-11±5E-13	-5.28E-11±2E-13	-1.6E-12±1E-13
9.47E-10±5E-12	7.7E-11±3E-12	9.2E-11±2E-12	-3.6E-11±1E-12	-2.41E-12±5E-13
9.89E-10±5E-12	7.7E-11±3E-12	9.2E-11±2E-12	-3.6E-11±1E-12	-2.40E-12±5E-13
9.9E-10±2E-11	7E-11±1E-11	1.2E-10±1E-11	-6.5E-11±4E-12	4E-12±2E-12
9.9E-10±2E-11	7E-11±1E-11	1.2E-10±1E-11	-6.5E-11±4E-12	4E-12±2E-12
9.9E-10±2E-11	7E-11±1E-11	1.2E-10±1E-11	-6.5E-11±4E-12	4E-12±2E-12

TABLE II: The fit coefficients to the charge density, over six iterations of the total electric field.

Preparation for and prevention of radiological events

Introduction: In Harborview, Washington, there was a leakage of C-137 at the Harborview Research and Training Building. A contractor was hired to remove and safely transport for disposal a capsule of radioactive C-137. The contractor inexplicably tried to separate the pipes with the electric cutter which was not authorized. Unbeknownst to him, this led to the capsule to leak. The vicinity was shut down for investigating and decontaminating. Investigators believed that this entire ordeal could have been prevented if there was tighter supervision and higher regard for safety. In Goiânia, an abandoned hospital left behind old machines and supplies because they were not needed in the new location. Two men found a teletherapy unit with C-137 while rummaging and sold it to a junkyard. The junkyard employees took the machine apart and released the substance. They did not know what it was, so the workers distributed it to others. As a result, a widespread of people got ill from radiation poisoning. But the situation was eventually taken care of, with the help of other countries.

Method: In order to accomplish my task, I had research many different articles and sites that discuss these topics. I used the REAC/TS website, which was suggested to me by BNL scientist Steve Musolino, to find out important safety precautions when around radioactive material. I used news sites to find more information on these incidents. I then compared both incidents in order to find the root cause of radioactive incidents. By doing that, I will be able to develop a solution to these problems. But that was not enough, I needed more information. I needed to get a different opinion on these incidents. My mentor suggested that I reach out to the principal scientific adviser at NYC Department of Health, Mark Maiello. When I met with him, he gave information that I was not able to find in news reports. He revealed to me what he believed to be the root cause for Harborview was the focus of money. He explained that they purposely cut corners and did not think of safety because saving money was their main priority. This was very useful information because Maiello and my mentor told me that in Goiania, they left the medical machines because it was too expensive to properly dispose of them, so they believed that the best solution is to leave the equipment there, unguarded and unprotected. This is when I knew what the root causes of these accidents were.

Results: By carefully analyzing these incidents, I was able to determine that the root causes are human error and the focus of money. I came to this conclusion because in Harborview, the reason why there was a leakage was because of the contractor, who did not act safely and did not carefully inspect the capsule. In Goiânia, the people who left the hospital did not make sure to dispose of their old machines or prevent them from ending up in someone else's possession. In both scenarios, they were more concerned with money than the safety of others. The most pressing issue appears to be people not being cautious around radioactive material and putting all concern for safety behind finances. In order to prevent these incidents from happening, we need to be more attentive when it comes to radiation and show more concern for lives of others, even if it is expensive.

Acknowledgments: I would like to thank my mentor Susan Pepper for helping me find radiological incidents to analyze. I would also like to thank the mentors of the African American

Advancement Group (AAAG): Karl Clarke, Juanita McKinney, etc. who gave me great feedback on my project.

References: Oak Ridge Institute For Science and Education: Radiation Emergency Assistance Center/Training Site; Capitol Hill Seattle Blog; NBC KING5; Joint Investigation Report: Sealed Source Recovery at the University of Washington Harborview Training and Research Facility Results in Release of Cesium-137 on May 2, 2019; Goiania Nuclear Accident, Brazil 1987 Meg Gerli March 24, 2018

Optimization of calibration analysis tools for the light detection system in the ICARUS neutrino detector

Austin DeMurley
*Department of Physics,
Columbia University, New York, NY, 10027*

Amelia Camino
*Department of Physics and Astronomy,
Stony Brook University, Stony Brook, NY 11790*

Douglas Howell
*Department of Physics,
Penn State University, University Park, PA, 16802*

Andrea Scarpelli and Milind Diwan
*Electronic Detectors Group, Physics Department
Brookhaven National Laboratory, Upton, NY 11973*

(Dated: August 11, 2020)

The ICARUS (Imaging Cosmic and Rare Underground Signals) detector at Fermilab is a Liquid Argon Time-Projection Chamber (LArTPC) that can detect neutrinos from the Booster Neutrino Beamline as the far detector of the Short Baseline Neutrino (SBN) program. The detector was commissioned to measure oscillations between neutrino flavors in search of sterile neutrinos beyond the standard model. ICARUS consists of an array of 360 photomultiplier tubes (PMTs) and a time projection chamber. The PMTs detect scintillation light from neutrino interactions with liquid Argon (LAr). Data was collected in February 2020 from all PMTs with a laser system before LAr was filled, in vacuum at room temperature, using CAEN digitizers. Data was taken from each PMT at three High Voltages (HV) to produce gain curves. Charge distributions were created by taking the integral of the pulse waveforms over 100ns. Statistical fits for charge distributions have been developed. These were used to measure the intensity of light pulses as well as the gain of the PMT for a single photo-electron. An optimization study was conducted to determine the stability of the fit and correlation between parameters. The effect of binning size and the number of detection events necessary for an accurate calibration were explored. The intense laser light used for HV calibrations created a degeneracy between the mean number of photo-electrons produced at the photo-cathode, and the amplification provided by the PMTs. A joint fit of the charge distribution for all three HV points of any given PMT was developed to constrain the mean number of photo-electrons; the effect on the degeneracy is explored.

I. INTRODUCTION AND BACKGROUND

The standard model of particle physics predicts three “flavors” of Neutrino to correspond with the three types of charged Lepton: Electron Neutrinos ν_e and Electrons, Muon Neutrinos ν_μ and Muons, and Tau Neutrinos ν_τ and Taus (in addition to their antiparticles). Neutrinos are now known to have very small but nonzero masses, and can oscillate between flavors.[1] These Neutrinos produce the lepton they correspond with upon interactions, predicting precise ratios of any lepton observed based on the interactions and type of incident Neutrino.

Experiments in recent years have cast some uncertainty into this model, with some experiments like MiniBooNE[2] measuring discrepancies such as strong oscillation signals evidenced by an excess detection of Electrons. This behavior is beyond the predictions of the standard model of particle physics, possibly hinting at previously unknown physics. Some have explained this with a model including a low mass and non-interacting or “sterile” Neutrino. Other experiments like IceCube have fit within the known models, and further study is necessary. The ICARUS detector in Fermilab’s Short-Baseline Neutrino (SBN) program was commissioned to shed new light on this dilemma.

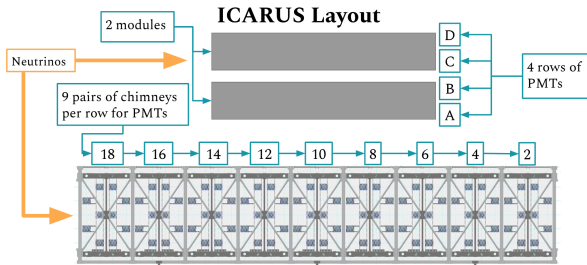


FIG. 1: Layout of the ICARUS detector. Top view shown from top, side view shown on bottom.

The ICARUS (Imaging Cosmic and Rare Underground Signals) detector [Figure 1], as the far detector of the SBN program, is a ~ 760 -ton Liquid Argon Time Projection Chamber (LAr-TPC) that can detect Muon Neutrinos generated by the Booster Neutrino Beamline. Neutrinos rarely interact with molecular Argon, but the abundant quantity present in the detector allows for sufficient collisions, referred to as events, to be measured. These interactions produce abundant leptons and antileptons which ionize the liquid Argon along the path of the incident Neutrino. These are then detected by the TPC, two induction planes and one collection plane of parallel wire electrodes. Each lepton has a characteristic path through the liquid Argon, which can

be projected in two dimensions.

The interactions with these leptons also ionize the molecular Argon, thereby emitting UV photons (peaked at ~ 128 nm) in a process known as scintillation. The walls of the liquid Argon tanks are lined with 360 Hamamatsu R5912-20Mod PMTs coated with tetraphenyl butadiene (TPB), which converts the colliding UV photons into detectable green photons by the PMTs.[3] These photons hit the bialkali photocathode within nanoseconds and, via the photoelectric effect, are converted into Photoelectrons (PE). The PMT is a sophisticated circuit that steps up the gain (number of Electrons released between dynodes) until a measurable signal is released.

The calibration of these PMTs is a sensitive process that must be done with a high degree of precision to report accurate and quality results, and this calibration is the focus of our analysis. PMTs have internal noise (dark pulses) as part of their inherent background which must be characterized and subtracted from the data. The entire array must be calibrated so all PMTs remain at the same gain. PMT gain “drifts” over time, so calibrations must be done on a regular basis. To this end, we have begun development of a robust and modular analysis framework to streamline these calibrations.

II. PROGRESS

II.1. Analysis Framework

The basic physical and mathematical tools from previous analyses were maintained for the current analysis: a streamlined and standardized analysis framework using the object-oriented class structure of C++. This framework brings all of the analysis within the same structure, and is a much more powerful tool in conducting the various analyses necessary for the PMT calibrations.

Replacing individual analysis software with a centralized framework allows for object-oriented development. The software tools are standardized and modular to allow for future inclusions, including analysis of noise, dark rates, and afterpulsing. This framework is the first step in creating a larger framework [Figure 4]. The tools demonstrated here make up a part of the Main PMT Analysis Code.

There is currently a decoder used for the previous data, but a wrapper will be needed due to different potential input formats. The software should also include input for mapping information. The current framework does not discriminate between which PMTs are which, and instead shows 30 across two digitizer boards. The full framework must map their locations within the experiment in all necessary

hardware modes (module, row, flange, position, digitizer, ... etc).

This framework was designed because the PMTs will need to be calibrated weekly for the lifetime of the experiment to maintain the quality of the data due to the sensitivity of the equipment. Therefore, part of the input will not just be new calibration data, but also the current HV setting as determined by the previous calibration.

In addition to all ROOT analysis files, including the plots presented here, the framework will also need to output a Weekly Calibration File. This will include the Current Gain of each PMT as well as the Future HV to which they must each be set to be 10^7 gain. This Weekly Calibration File will be the input to a different software that will append it to all the previous Weekly Calibration Files. This will create an updated Master Calibration File, as well as plots to show how the gain in each PMT is changing or "drifting" over time.

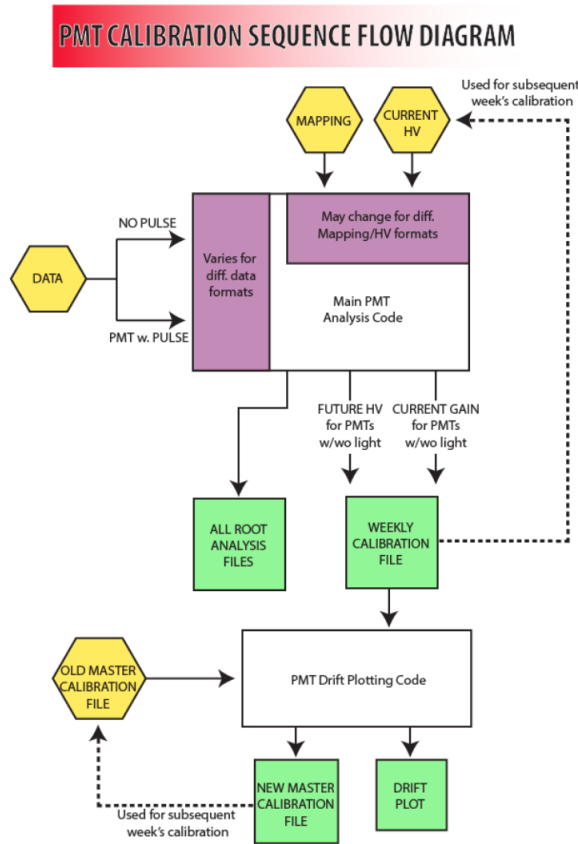


FIG. 2: Framework of the software being developed, including all necessary dependencies. New Data comes in two forms, which must both be preprocessed for input into the main PMT Analysis code.

One of the macros is for charge analysis, providing

the fitting of charge distributions and the development of gain curves. First the software processes the runs and subruns (3 runs at a time for any number of subruns in its current structure), and then creates waveform objects to load the decoded data into. The baseline, or inherent noise fluctuations are subtracted here and the waveforms processed. Once this has been completed, histograms of overall charge distribution are produced by integrating the waveforms.

In order to extract the gain from this data, first we fit these charge distributions corresponding to histograms for each PMT in the three runs processed assuming ideal PMT response:

$$S(x) = A \sum_{n=1}^{100} \frac{1}{\sqrt{2\pi n\sigma}} \frac{\mu^n e^{-\mu}}{n!} \exp\left(\frac{-(x - Qn)^2}{2n\sigma^2}\right) \quad (1)$$

where μ = mean number of PE, Q = gain in terms of charge, A = normalization, σ = std dev of single PE charge distribution, and n = number of PE. This is traditionally an infinite sum, but with the LED kept at a low enough intensity that the chances of generating a high number of PE was negligible, and the terms could be capped at 100. [4]

The mean number of PEs should not change over the 3 HV points measured for each PMT if the laser intensity is kept constant. Under this key assumption, a "global fit" could be performed where μ is kept constant and the other parameters are allowed to vary. To determine the global fit, we define the following χ^2 :

$$\chi^2 = \sum_{m=1}^{N_{hist}} \sum_{j=1}^{N_{bin}} \frac{(N_{ij} - P_{ij}(\mu, q_i, \sigma_i, a_i))^2}{N_{ij}} \quad (2)$$

where N_{hist} = number of charge distributions (3), N_{bin} = number of bins in the charge distributions, N_{ij} = number of events in the j -th bin in the i -th distribution, and $P_{ij}(\mu, q_i, \sigma_i, a_i)$ = the calculation based on the ideal response for charge distribution, with parameters μ, q_i, σ_i, a_i . We then present χ^2 per degree of freedom, χ^2/ndf , to quantify the quality of the fit. This is used to determine goodness of fit, with a $\chi^2/ndf=1$ being an ideal fit, >1 indicating an overfitting, <1 indicating a poor fit or underestimation of the error variance. Now the gain can be extracted with the determined Q through the relationship:

$$g = \frac{10^7}{1.6} Q \quad (3)$$

which uses the ratio to convert Q to be in terms of number of Electrons rather than charge. With gain determined at 3 separate points for each HV

per PMT, we can fit the gain to a power law:

$$g(V) = aV^b \quad (4)$$

with parameters a, b to determine each PMT's gain curve. For gain of $10^7 V$, we use these in the above equation to solve for $V = HV$ setting.[5]

II.2. Data Collection

For the calibration, all 360 PMTs were tested at room temperature and in vacuum. A laser was used to pulse light to the PMTs through the fiber connected in each flange (groups of 10 PMTs). A Tektronix oscilloscope was used to collect waveforms of 10 μs window (with 2 ns sample intervals, 5000 samples) were taken. During each run, 10 PMTs on the same digitizer board were tested with HV and input light, and the other 5 turned off. Each run had 16-20 subruns of different trials with 1000 events each in order to obtain ≥ 15000 events for statistical significance. Over the course of the data collection each PMT was tested at 3 different HV points: the nominal Voltage from November calibration, -50V from nominal, and +30V from nominal.

II.3. Optimization Preliminary Results

The calibration of the photomultipliers is a delicate convolution of many parameters. In our setup, the intense laser light creates a degeneracy between the mean number of photoelectrons produced at the photocathode (expected to be independent from the amplification provided), and the amplification provided by the phototubes(depend on the voltage applied). A joint fit of all the three charge distributions has been introduced to constrain the mean number of photons and help break the degeneracy between parameters. To ensure these analysis tools are fine tuned to best interpret our data, binning size needed to be optimized to ensure the bins were fine enough to see all necessary structure in the charge distributions, but not so overbinned that structure was lost.

Using data from all runs, we produced plots for the gain and charge distribution for each PMT. Fits of charge distribution for 2 PMTs are shown in [Figure 2] for each of the 3 HV points for a given PMT. Initial runs yield quality fits for high charge, and quality fits for low charge with a clearly defined pedestal. Initial optimization has improved χ^2/ndf through adjustment of binning size and constraining the number of photoelectrons. The quality of the low charge fits still shows room for improvement. Corresponding gain curves for these two PMTs are shown

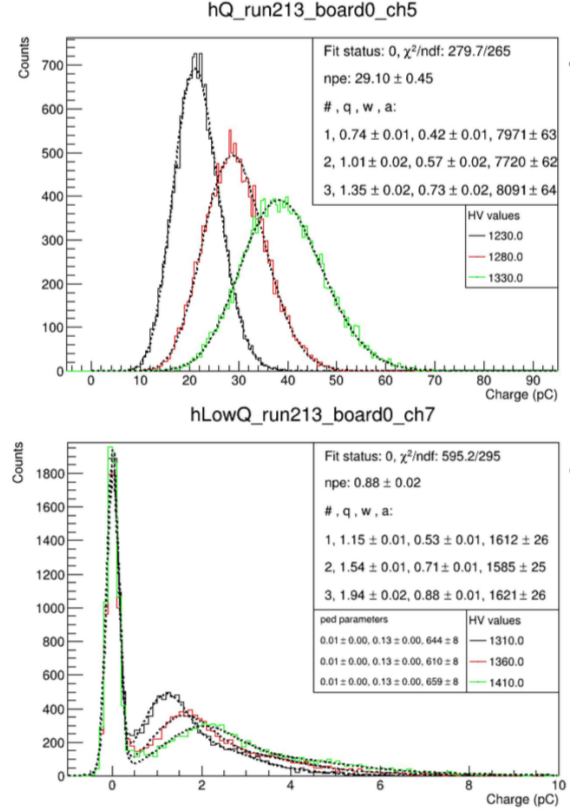


FIG. 3: Charge distributions for two sample PMTs, with high charge (top) and low charge (bottom) shown.

in figure 3. Both of these fits were determined to be highly accurate for this data set. The analysis framework as a tool has been successfully used to perform an initial gain calibration. Further tuning is expected as the methods for producing the fit and quantifying the statistics are further tested and optimized, including trials over new runs of data, but the initial results presented are promising.

III. FUTURE WORK

Initial testing has been promising, with strong fits produced and successful gain calculations. It is essential to characterize how much data needs to be taken to make a highly accurate calibration. This work is currently underway, by modifying the number of subruns used in the calibration to see the effects on the statistics, we can determine the minimum number of events needed for a successful calibration.

The optimization results for February data must be finalized, we aim for a precision of 10%. This will be followed by the development of standardized

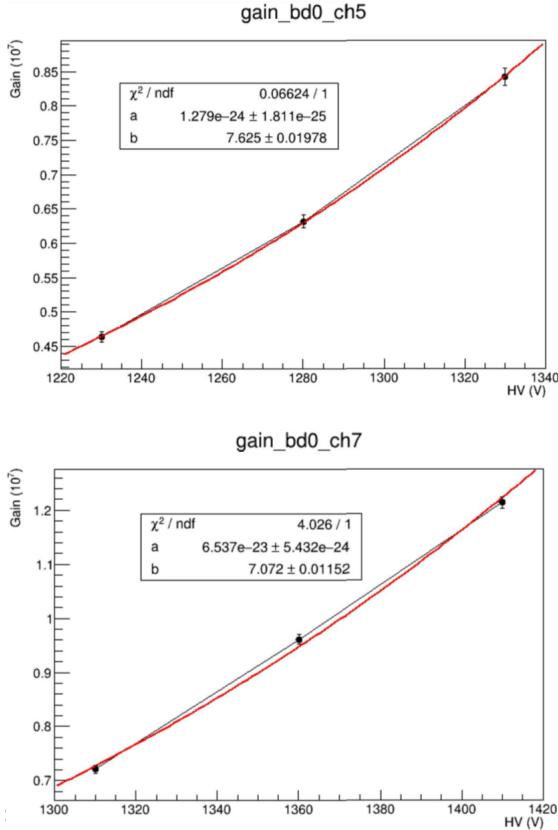


FIG. 4: Charge distributions for two sample PMTs, with high charge (top) and low charge (bottom) shown.

optimization procedures. Initial optimization must be repeated for future data, including with lAr. Fitting a scintillation pulse is different from fitting a laser pulse, this must be optimized as well. Another area of exploration is a comparison between the direct light calibrations presented here and indirect reflected light measured on the dark PMTs? Indirect light measurements naturally reduce the parameter degeneracy, but are very sensitive to background noise and dark rates. The large number of parameters necessitates the use of individual fits rather than the global fit presented. A comparison between the two calibration methods must be made to ensure confidence in the statistical techniques and particle measurements for the beginning of the experiment.

IV. IMPACT ON LABORATORY/DOE MISSION

This project was carried out in full collaboration with the local BNL ICARUS collaboration in the Electronic Detectors group of the Physics Depart-

ment. As a part of the ICARUS experiment, the photomultiplier tubes must be fully calibrated, a task taken up by the BNL group. The efforts demonstrated here are directly applicable to this task. The goal of a standard calibration protocol was established, and the development of the diagram in Figure 4 was a concrete step in visualizing the basic form the requisite software would take, including inputs, outputs, and dependencies. Optimization of this rudimentary framework is underway.

We first conducted several preliminary analyses. These were done by developing a series of individual pieces of software in C++, Python and shell scripting individually applied through ROOT. Advancing the utility of the previously developed framework, various statistics were studied in an effort to better understand the interplay between parameters and the confidence in the results.

V. CONCLUSION

The standard model of particle physics is one of the best models physicists have ever developed, with powerful predictive and descriptive power. Irregularities in Neutrino oscillations might hint at the existence of new physics beyond the standard model, and the ICARUS detector was commissioned to shed light on this. The calibration of the sensitive PMTs is of vital importance to ensure this research is done accurately. For this purpose we have used our software framework to calibrate the detectors, and are undergoing analysis of the statistics used.

We demonstrate the effectiveness of this tool with fits of charge distributions and gain curves, representing a successful gain calibration. There are several areas still under investigation for the quality of the gain analysis. The effect on the statistics of the number of events necessary and the optimal binning strategy must be further understood to achieve the 10% precision threshold, and progress thus far is promising. Further analysis is required on the status of the global fit and whether the variance in the mean number of PEs is high enough to warrant using indirect light calibration procedures. The sensitivity and statistics of these two methods must be compared.

Once this work is complete, the software will be prepared for production. In preparation for being used in the regular calibration of all PMTs during the experiment lifetime, the calibration software has demonstrated quality results and reliable progress is being made to prepare for when ICARUS begins collecting data in Autumn 2020.

-
- [1] K. Walsh and M. Diwan, Detecting ghostlike neutrinos: Tiny messengers from the universe, (J. Frontiers for Young Minds: ID 506458, 2019).
- [2] H.-C. Oliver Fischer and T. Schwetz, Explaining the MiniBooNE excess by a decaying sterile neutrino with mass in the 250 MeV range, (Phys. Rev. D 101, 075045, 2020).
- [3] A. Falcone, *on behalf of ICARUS Collaboration*, Performance study of the new light collection system for the ICARUS T600 detector, (J. Phys.: Conf. Ser. 888 012093, 2017).
- [4] E. Bellamy, G. Bellettini, J. Budagov, F. Cervelli, I. Chirikov-Zorin, M. Incagli, D. Lucchesi, C. Pagliarone, S. Tokar, , and F. Zetti, Absolute calibration and monitoring of a spectrometric channel using a photomultiplier, (Nucl. Instrum. Meth. A 339, 468, 1994).
- [5] Hamamatsu Photonics, *Photomultiplier Tubes: Basics and Applications* (3rd Edition, 2007).

Appendix A: Acknowledgments

I would like to thank my mentor Milind Diwan, advisor Andrea Scarpelli, Brett Viren, and the rest of the BNL Electronic Detectors Group for their guidance, support, and expertise on this project. This work was supported in part by the U.S. Department of Energy, Office of Science, Office of Workforce Development for Teachers and Scientists (WDTS) under the Community College Internships Program (CCI).

The International Safeguards Project Office Information System Upgrade

Nathaly Diaz, College of Engineering and Applied Sciences, Stony Brook University, Stony Brook, NY 11794

Mentor: Raymond Diaz, International Safeguards Project Office, Brookhaven National Laboratory (BNL), Upton NY 11973

Teresa Montuori, International Safeguards Project Office, Brookhaven National Laboratory (BNL), Upton NY 11973

Abstract

As a 2020 BNL Summer Intern, I have been assigned to assist the International Safeguards Project Office (ISPO) in the Non-Proliferation and National Security Department (NN) in their pursuit of an upgrade to their information system. ISPO is a vital part of the United States Support Program (USSP) to the International Atomic Energy Agency (IAEA) Department of Safeguards. The focus of my assignment is reviewing and assisting in writing the statement of work (SOW) for the upgrade of the ISPO Information System (IIS) website. IIS is used by ISPO to track USSP financial activities, produce a quarterly capsule summary of active USSP work Tasks for the IAEA, and produce the capsule digest of completed USSP Tasks. In my time working with and learning from the ISPO team members, I have acquired a better understanding of the work ISPO does for the IAEA Department of Safeguards. I have spoken individually to ISPO team members to get a better idea of how each person contributes to the team and how each team member uses the IIS website. Gaining this insight from each team member provided me with a better understanding of the need for the IIS upgrade. I contributed my ideas to a list of IIS enhancements detailed in the SOW for the upgrade. The ISPO team requested permission to pull data that resides in the IAEA Safeguards Support Programme Information and Communication System (SPRICS) since this data also resides in IIS. This testing is complete and was successful. The purpose of pulling this data from SPRICS is to reduce the manual effort required to keep IIS up to date, as well as to ensure its accuracy. This will allow ISPO to have a more robust website to input and retrieve data from. In the process, I have learned a lot about teamwork and communication in a professional work environment.

Background

The need for the IIS upgrade originated from ISPOs government sponsor's request during the 2015 ISPO Program Review meeting to streamline ISPO operations in order to reduce manual effort and increase efficiency. Over the years, ISPO has identified and implemented improvements. The ISPO team is currently finalizing a SOW for the upgrade. ISPO uses the IIS for tracking financial activity, producing quarterly capsule summaries of active Tasks, the digest of completed Tasks. ISPO team members have recognized that SPRICS has improved tremendously in recent years. Both systems track the status of pending USSP requests and active Tasks. SPRICS contains much more easily accessible information and has a more user-friendly interface. ISPO reviews and manually inputs IAEA financial information into IIS. In January 2020, the IAEA agreed to, and began implementing, all ISPO's enhancement suggestions for SPRICS. There is a great deal of identical data that resides in IIS and SPRICS. The IAEA informed ISPO that any information the ISPO team has access to in SPRICS can be pulled into the IIS via an Application Program Interface (API). The Project Office Head, Raymond Diaz, delayed the upgrade in order to avoid recreating the existing system without identifying improvements that will make the IIS more efficient. The IIS upgrade has the potential to be the most significant contributor to the streamlining of ISPO's operations.

My Contribution

At the start of my assignment, I scheduled meetings with each of the members of ISPO in order to get to know everyone and understand how each individual uses the IIS website. I spoke to the Task Monitors and learned that not all use IIS frequently, apart from when a Capsule Summary is being created or finalized. IIS was created with certain functions in mind to help the ISPO team carry out their operations. In addition, I also had an in-depth look into the IIS website with ISPO's Financial Assistant, Deborah Johnson. She and I walked through her daily use of IIS

and reviewed what functions are currently available. This was when I discovered some of the tabs were not functioning. ISPO decided in the past to not use the pending request tab as it involved too much manual input to keep it current. The system uses an outdated programming language called Lotus Script. This language is being phased out. In maintaining the IIS, Lotus Script requires much effort resulting in higher maintenance costs. I made note of all their concerns and ideas regarding the IIS upgrade and then relayed the information to my mentor, Raymond Diaz. In addition to the ISPO team members' input, I did some research and provided my own feedback for the completion of the SOW. ISPO has identified a prioritized list of all suggested enhancements for the IIS upgrade. This list was presented and approved by their government sponsors.

Recommendations

After completing this review, it was determined that the core items that must be addressed include the IIS financials, the capsule summary, and the digest of completed Tasks capabilities. ISPO also included a prioritized list of IIS enhancements. At the top of that list, is the ability to pull select IAEA request data from SPRICS into IIS. This modification will allow ISPO to track pending IAEA requests without manually entering the data. The IIS was designed to have ISPO manually input this information. Creating an Outstanding Request List (ORL) in IIS is ranked as the second priority enhancement. The plan is to create an ORL template in the IIS that will extract selected data from SPRICS and provide the option for ISPO to update select Task status fields. Next on the list is streamlining the production of final Capsule Summary publications. This enhancement would include the development of a report writing tool that would enable the IIS to compile the entire capsule for ISPO final review with all the correct formatting. Most data contained in the final Capsule Summary already resides in the IIS. Fourth on the list of enhancements is the capability to import SPRICS data related to Cost-Free Expert

(CFE) and Junior Project Officer (JPO) Tasks directly into IIS for ISPO Task Monitor final review, eliminating manual input of data. Approximately 30% of ISPO's Capsule Summary entries include this data, therefore, it is crucial that it also be automatically added to the IIS. The fifth item on this list is improving the digest of completed Tasks by making it mandatory for Task Monitors to enter final Task summary information upon Task closeout, and then automating the process of producing a fully formatted downloadable report. Priority number six is adding the ability of autogenerating Task and Subtask numbers when Tasks are approved in IIS. This action presently requires discussions between Task Monitors to determine the next available Task or Subtask number. The seventh item on the list is having funding approvals and expenditures for the USSP Tasks and Subtasks with the U.S. national laboratories and contractors pulled into IIS from the BNL's PeopleSoft financial system. ISPO's Financial Assistant, Deborah Johnson, reconciles the PeopleSoft financial data to IIS's financial data to ensure that all entries are accurate. The final item on the list of requested IIS enhancements is minimizing the manual input of data the IAEA's monthly financial report. That information is currently transmitted by the IAEA to Ms. Johnson in an Excel spreadsheet. She compares this data to IIS information prior to manually entering the monthly expenditures into the IIS. The main obstacle for this item is that the information ISPO wishes to automatically extract is not currently contained in the SPRICS database.

Summary

The IIS upgrade has the potential to have the greatest impact on the streamlining of ISPO operations. The Statement of Work for the IIS upgrade details both the existing core functions and a prioritized list of all the desired IIS enhancements. ISPO presented their IIS upgrade plan to their government sponsors, the Subgroup on Safeguards Technical Support (SSTS), who then approved the plan. This upgrade will leverage off the IIS data that already resides in SPRICS by

pulling this data into the IIS via an Application Program Interface (API), which was recently tested successfully. Unfortunately, the upgrade will not be completed within the ten weeks of my internship. However, many steps have been taken to in order to advance the process of the IIS upgrade during my time with ISPO. I have learned a great deal about teamwork from ISPO and the way they organize their operations. This assignment focused heavily on my main area of study, which is information systems and finance. Not only was I fortunate enough to have worked with incredible people and get exposure to the type of field I am planning to work in once I graduate, I also learned about subjects outside of my major. For example, I was not familiar with Nuclear Safeguards, but I leave my internship with a better understanding and wider knowledge of Nonproliferation and National Security.

Acknowledgments

African-American Advancement Group (AAAG)

Thank you to the wonderful people in the AAAG for your guidance and assistance throughout my internship.

Brookhaven National Laboratory Supplemental Undergraduate Research Program (SURP)

This project was supported in part by the Brookhaven National Laboratory (BNL), Department of Energy under the BNL Supplemental Undergraduate Research Program (SURP).

International Safeguards Project Office (ISPO)

I would like to give a special thanks to Raymond Diaz and Teresa Montuori, in addition to the rest of the ISPO team, for their help and kindness throughout my internship.

Identifying source of excess noise in the BMX testbed intensity mapping instrument

Josie Fenske, Physics/Astronomy, Central Washington University, Ellensburg, WA 98926

Anže Slosar, Physics Department, Brookhaven National Laboratory, Upton, NY 11973

ABSTRACT

Scientists at Brookhaven National Laboratory have proposed the implementation of a large-scale intensity mapping survey instrument that will use radio interferometry to measure the redshift of galaxies. Radio interferometry is a highly effective way of mapping the structure of the universe using the light emissions from galaxies. The Baryon Mapping Experiment (BMX), a small array of 4 dishes, is the prototype for the proposed large-scale intensity mapping survey which will eventually consist of 32,000 dishes. Data analysis and calibration must first be done on the prototype in order to work out any bugs in preparation for implementation of the larger array. A necessary step in data analysis is identifying the source of the noise in the frequency signal from BMX. Possible sources are the internal fan that works to regulate the internal temperature of the instrument, or the position of the sun relative to BMX. I wrote a Python script that compared

the patterns in the signal to patterns of the fan and sun to identify a possible correlation. The results indicate that neither the internal fan, nor the position of the sun, is the source of the noise. Ruling out these factors as possible source of the noise puts us one step closer to identifying the real cause and correcting for it, as well as encourages further investigation into factors such as weather conditions and unidentified celestial sources.

I. INTRODUCTION

In 1925 Edwin Hubble proved that the universe is expanding by observing the motion of distant galaxies. Galaxies emit light at low radio frequency wavelengths, particularly the 21cm line of neutral hydrogen, which comes from the hyper-fine transition of electrons from the triplet to the singlet spin state¹. The 21cm line, equivalent to a frequency of 1420 MHz, is important to cosmologists because it can be used as a tracer of early universe structure and is easily distinguishable in a galaxy's radio emission spectrum. As a galaxy travels with the expanding universe and moves away from an observer, the wavelength of the emitted light is stretched and the entire emission spectrum, including the unique 21cm line, is shifted to a lower frequency. This is known as measuring a galaxy's redshift, and is fundamental to understanding the structure and expansion of the universe. Different redshift measurements are indicators of different times in the universe's history, with a larger redshift being linked to periods closer to the big bang. Previous intensity mapping surveys have targeted the higher redshift range $z \sim 7 - 20$, also known as the Epoch of Reionization¹. The proposed stage II 21cm intensity mapping survey will target the low redshift, post-reionization era, $z \sim 2 - 6$, which scientists currently know the least about.

Before the full-scale intensity mapping survey can be realized, a prototype must be built and calibrated. The Baryon Mapping Experiment (BMX) is a small-scale array of 4 radio dishes and is the prototype for the proposed large-scale array that will eventually consist of 32,000 dishes². BMX has been collecting data since October 2019, and currently the team is working on data analysis and calibration. There are some bugs that need to be worked out before implementation of the larger array can begin, one of them being noise analysis. Background noise is expected as many different sources of radio frequencies can interfere with the telescope and taint the data. My project this summer was to analyze data from BMX and identify the source of the noise in the signal so that it can be corrected for. I investigated the possibilities that the source is the internal fan switching on and off, or the position of the sun relative to BMX. I also examined cross correlation data in order to identify any calibration factors that need to be accounted for.

II. OBSERVATIONS

BMX, which consists of 4 dishes and 8 channels, continuously collects data in 28 hour cycles. It observes in two frequency bands: the galactic cut, which refers to frequencies in the range 1100 – 1650 MHz, as well as a smaller cut centered around the 21cm line in the range 1419.5 – 1422.0 MHz. Figure 1 shows one cycle's worth of data as a waterfall plot, showing right ascension (RA) versus frequency in the smaller cut near the 21cm line. The obvious bright spots at RA -1 and 5 are detection of the galaxy Cygnus-A, and the smear from RA -1 to 1 is the detection of the Milky Way galaxy as it passes over BMX. Fairly obvious are the streaks that run

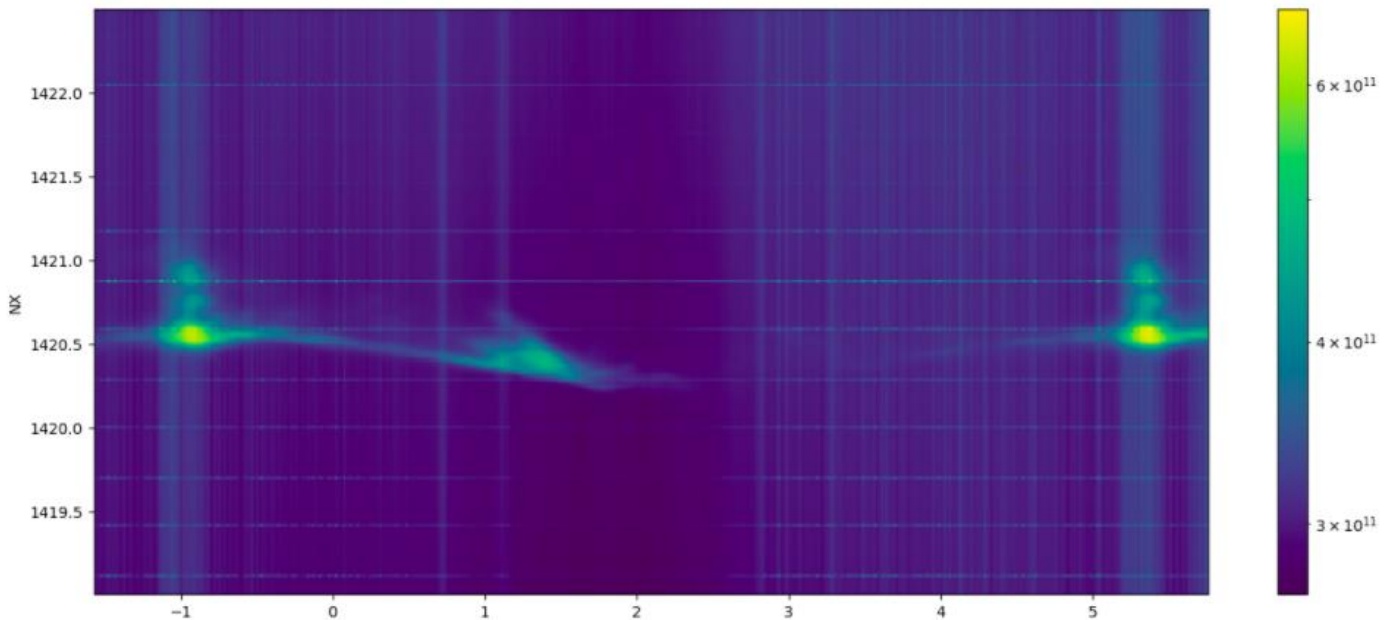


FIG. 1. One cycle of data showing frequency versus right ascension. The brightest spots at -1 and 5 are detection of the galaxy Cygnus-A, and the smear from -1 to 2 is the detection of the galaxy. The apparent streaks running vertically are indicating noise coming from an unknown source.

vertically along the RA axis, these are detection of noise from an unknown source. It is important to note that there are also horizontal streaks throughout the data, however these are a result of comb filtering, a consequence of constructive and destructive interference in the frequency detection, and are not the noise that I refer to in this paper.

III. METHODS

In order to perform my noise analysis, I first averaged the data over time in order to produce a plot showing time versus signal amplitude (Figure 2). For this particular cycle of data, the noise appears as the jagged hash from 500 – 700. In the database of cycles collected by BMX there are hundreds of days worth of data, however, I focused on the datasets that have the most apparent noise in them which gave me a sample size of 24 days.

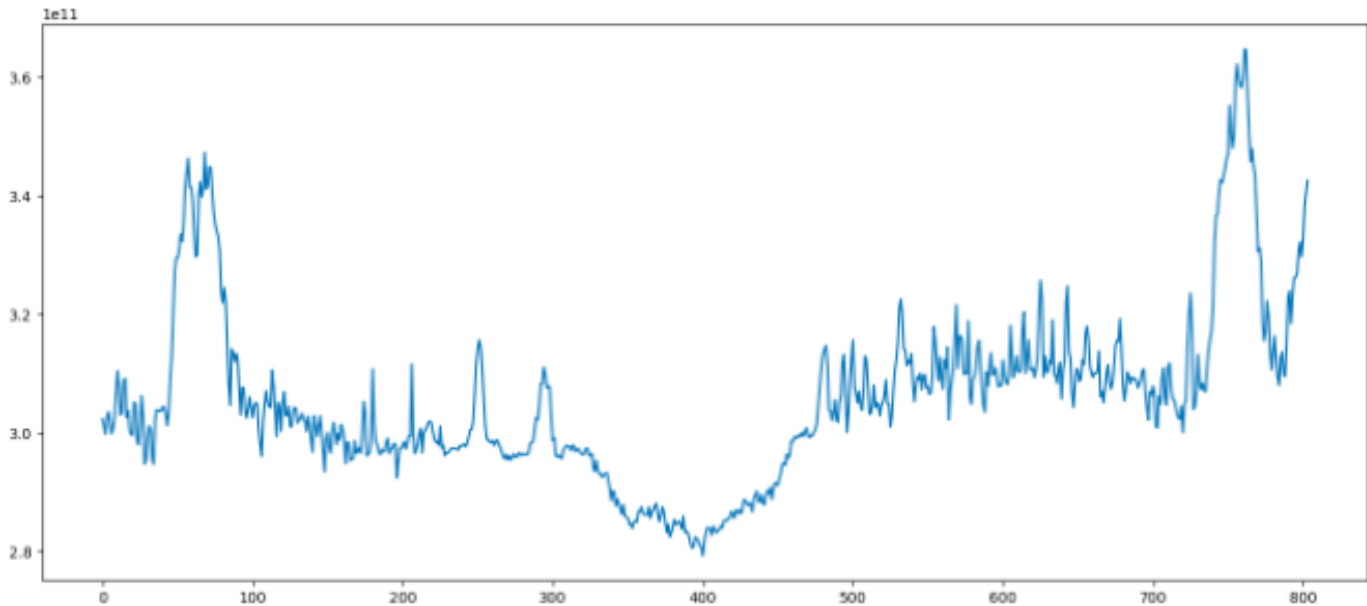


FIG. 2. One cycle of data (same as in Figure 1) that has been averaged over time. X-axis is iteration number, y-axis is signal amplitude. The large spikes on the left and right side of the plot are detection of Cygnus-A. The jagged hash from 500 to 700 is noise from an unknown source.

A. Fan Analysis

My first task was to investigate the possibility that the internal fan is causing the noise due to it continuously switching on and off. I first pulled the fan state data from the BMX database, which contains timestamps for the internal fan activity. Given a cycle's start and end times, I can see whether the fan was on or off for any given time during that cycle. After selecting which dataset to analyze the fan state for, I found a "clean" range of frequencies that was purely noise and did not contain any important data. For 2020-05-14, this range was 1421.3 – 1422.0 MHz. I selected a 2-hour period that was particularly abundant in noise, averaged the signal over time, and plotted it on the same plot as the fan state (Figure 3). If the fan is causing the noise, I would expect to see a correlation between the fan switching on and the jumps in the signal. This analysis was done for multiple 2-hour time periods, and for multiple days.

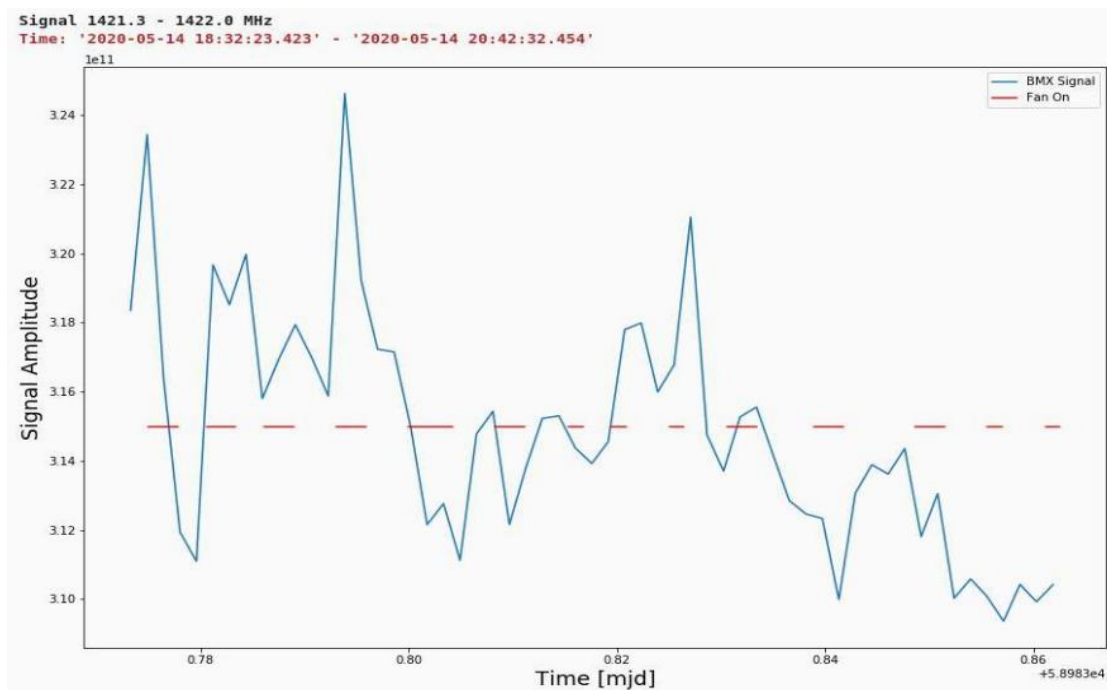


FIG.3. Signal data gathered over 2-hour time period in the specific frequency range of 1421.3 - 1422.0 MHz plotted against the fan state. X-axis is time (mjd), y-axis is signal amplitude. The red lines indicate the time when the fan is on.

B. Sun Position

A common characteristic throughout the data was that the noise seemed to begin at around the same time every day when looking at consecutive cycles. This suggests that the position of the sun might be correlated with the noise. A high intensity beam of sunlight may be passing into the tent, in which the instrumentation is located, at the same time every day and interfering with the sensors, causing the signal to become noisy.

To investigate this possibility, I took my sample of 24 days and separated them into categories based on general trend of data and similarities in noise. I wanted to see if the trends in the noisy signal were more dependent on the position of the sun, or on RA. Figure 4 shows one group of data that demonstrates the same trend in noise. It can be seen that at the same point in the cycle, the general trend in data shifts and the signal becomes noisy. Figure 5 illustrates the

same characteristic but for a different group of days. The signal in this group is very noisy, and then, at roughly the same point in each cycle, shifts and becomes less noisy.

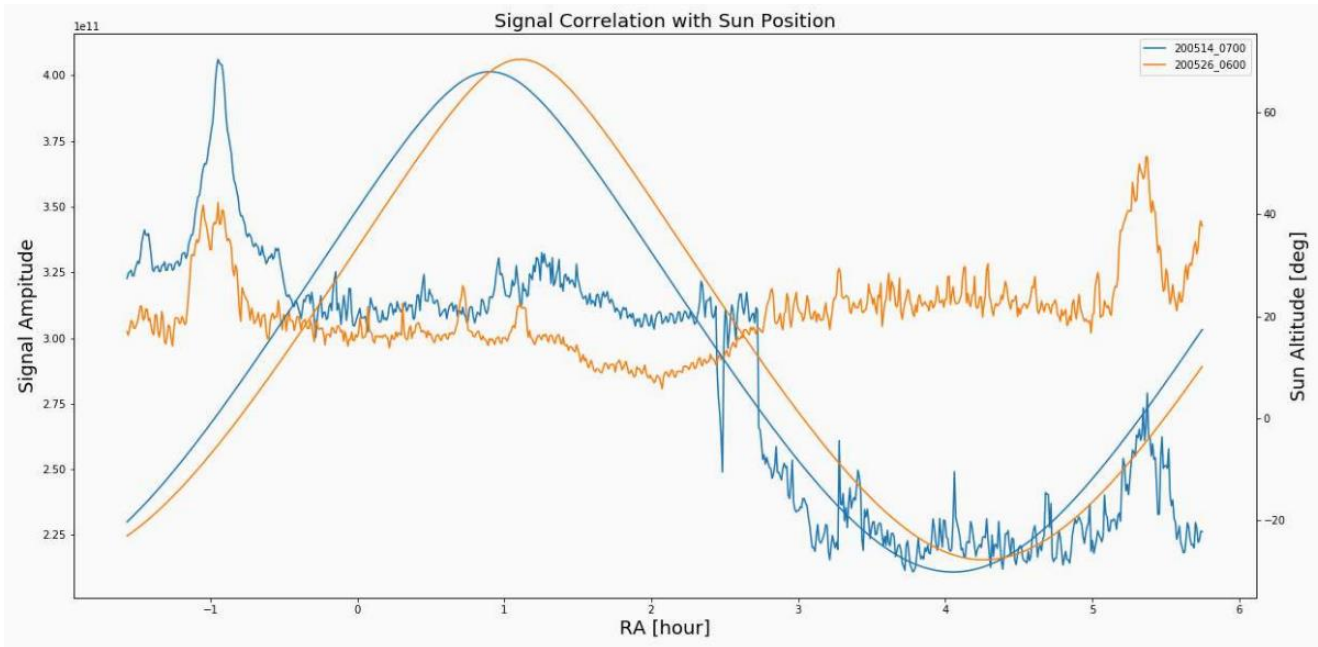


FIG. 4. Signal data for 2 days, that follow a similar trend, plotted with the sun position for corresponding days.

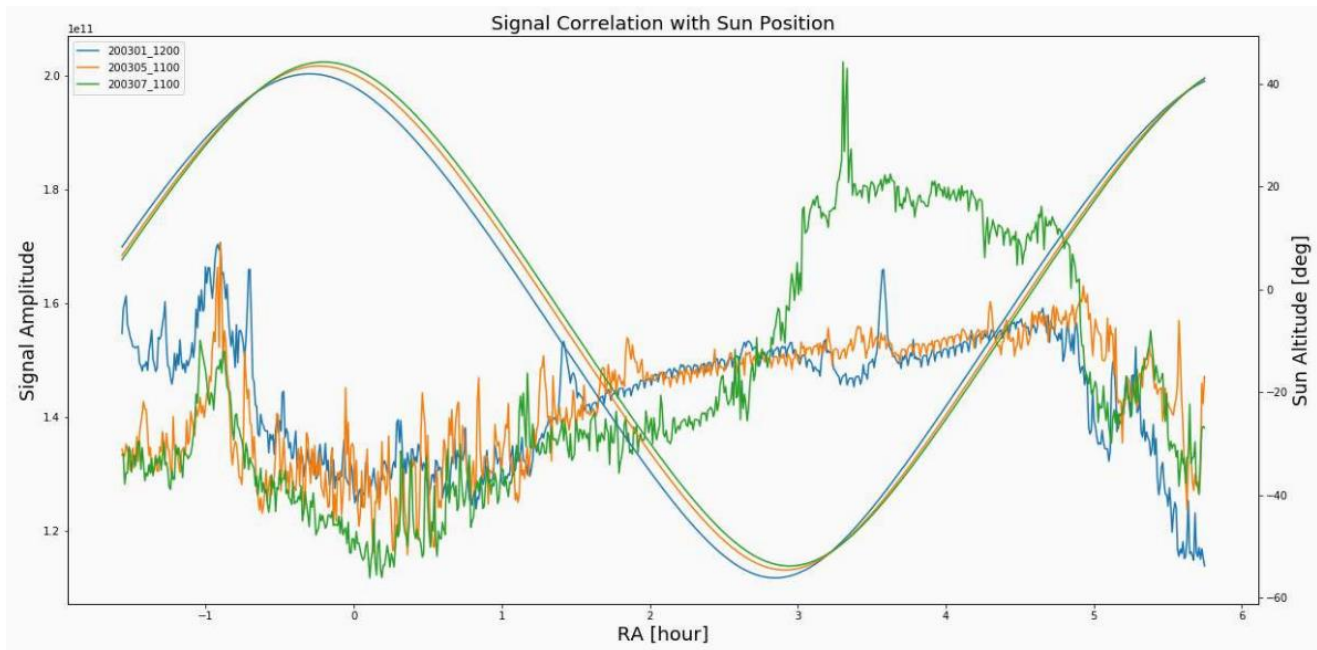


FIG. 5. Signal data for 3 days, that follow a similar trend, plotted with the sun position for corresponding days.

C. Calibration Factors

The last task of my project was to cross correlate the signal between multiple days, multiple channels, and multiple frequency ranges by looking at ratios. By doing this, I hoped to determine the intrinsic repeatability of the data and identify any calibration factors that need to be accounted for. The telescope is equipped with an amplifier that makes even the smallest of detections easily identifiable. However, the amplification factor is not consistent from cycle to cycle, so comparing signals across days, channels, and frequencies is difficult. By instead looking at the ratio between two signals, this amplification becomes negligible. Through this method I was able determine if the telescope was seeing the same thing from cycle to cycle after correcting for the gain. If I were to find inconsistencies, I would then be able to pin point the intrinsic factor that lead to the variations in the signal.

I isolated the data from one of the eight channels into two different frequency ranges that contained an abundance of noise. I averaged one cycle's worth of data over the frequencies 1400 – 1415 MHz and 1430 – 1445 MHz. I then took the ratio of these two datasets and plotted it versus RA, doing so for two consecutive days. What I hoped to see was a ratio close to one between the two frequency bands, as well as a similar trend in ratio between the two days. Figure 6 shows the plots for 2020-05-26 and 2020-05-27, specifically for channel 1.

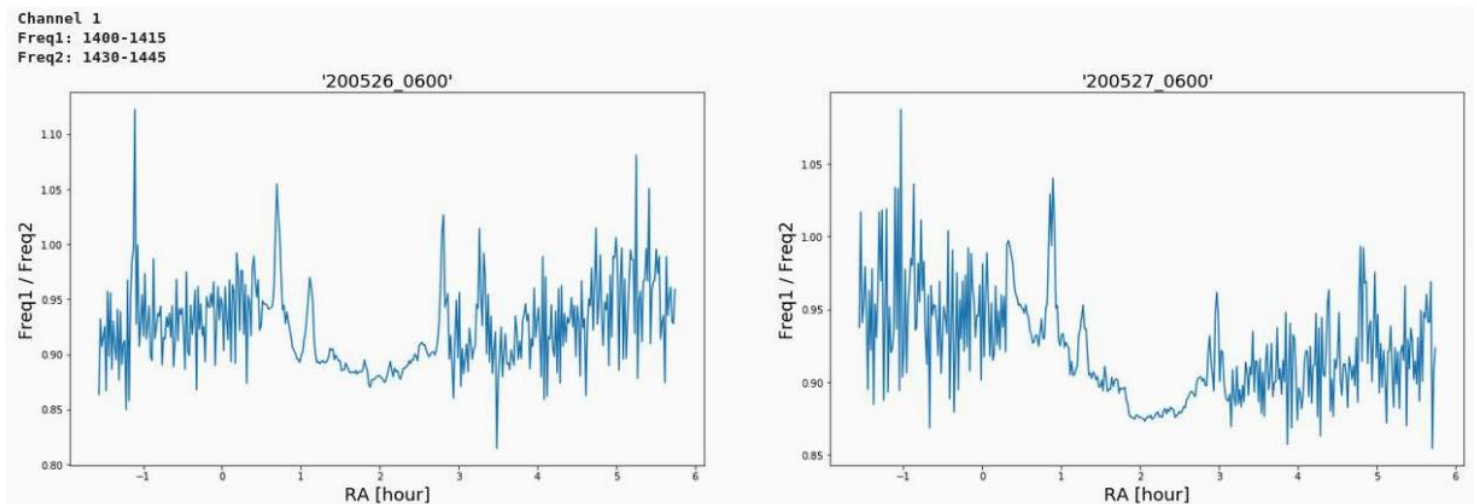


FIG. 6. Ratio of signal from a single channel averaged over two frequency ranges, for two consecutive days.

IV. RESULTS

Through analysis of the fan state, in comparison to the noise in the signal, I was able to conclude that the two are not correlated. Looking at Figure 3, there is no discernable pattern in the jumps in the signal in relation to the fan switching on and off. In fact, the noise in the signal appears to be completely random in when it spikes and falls. The same result of fan state analysis was consistent across all 2-hour time periods, as well as across all days. Thus, I conclude that the instrument's internal fan activity is not the source of the noise.

When investigating the sun position as a possible source of noise, at first it seemed promising. At first glance of Figures 4 and 5, it appears as if the noise in the signal is correlated to the sun setting i.e. altitude < 0 . But upon closer inspection, this trend is not consistent for all days. This can be seen best in Figure 4 when looking at the signal data for 2020-05-26. The signal becomes noisy and jagged slightly *before* the sun reaches altitude 0. However, it does appear that the signal becomes noisier at a specific RA for both cycles. Figure 4 shows that the signal is consistent up until RA ~ 2.7 , at which it becomes jagged for both days. Similarly, Figure 5 shows that the signal for all three days is noisy and jagged up until RA ~ 1.5 , after which it is smoother and more defined. This indicates that the noise in the signal is more closely related to the position in the sky at which BMX is collecting data from, rather than the position of the sun.

Calibration factor analysis indicates that the telescope is seeing the same data from cycle to cycle after correcting for gain. Figure 6 illustrates this claim by revealing the similar trends in ratios over two consecutive days. The ratios between the two frequency bands varies by $\pm 15\%$ or less, demonstrating the intrinsic repeatability of the data. While the percentage of variation is relatively small, the wild fluctuations of the ratio in the early and late parts of the cycle indicate

the telescope is detecting more noise in one of the frequency bands during these time periods. Thus, further investigation into the cause of this is highly encouraged.

V. CONCLUSION

This project has brought BMX one step closer to implementation of the large-scale, 32,000 dish, array. By ruling out factors, such as fan activity and sun position, that could be causing the source of the noise in the signal, the team can focus on investigating other possible sources. Further investigation into the weather activity at the location of BMX would be useful in determining if wind or rain is causing the noise. Also, identifying any unknown celestial objects that could be causing the spikes in the signal is encouraged.

By working out these bugs in the prototype, we can prepare for a highly accurate and effective large-sale array that can significantly improve precision on standard cosmological parameters. In addition, characterization of redshift, dark energy, and new physics will be powerfully enhanced by multiple cross-correlations with previous surveys and cosmic microwave background measurements. As a result of this summer, I have largely improved my coding skills, as well as my understanding of cosmology and radio interferometry.

VI. REFERENCES

¹Cosmic Visions 21 cm Collaboration et al., 2018, arXiv e-prints, p. arXiv:1810.09572v3

²Packed Ultra-wideband Mapping Array (PUMA): Astro2020 RFI Response et al., 2020, arXiv e-prints, p. arXiv:2002.05072v2

VII. ACKNOWLEDGEMENTS

This project was supported in part by the U.S. Department of Energy, Office of Science, Office of Workforce Development for Teachers and Scientists (WDTS) under the Science Undergraduate Laboratory Internships Program (SULI). I would also like to thank my mentors Anže Slosar and Paul O'Connor for their patience and resourcefulness.

Analysis of x-rays using electron multiplying charge coupled devices

James Flemings, Computer Science & Engineering, University of Alaska Anchorage,
Anchorage, Ak 99508

Ivan Kotov, Instrument Division, Brookhaven National Laboratory, Upton, NY 11973

I Abstract

The National Synchrotron Light Source II (NSLS-II) Soft Inelastic X-ray Scattering (SIX) beam line uses Electron Multiplying Charge Coupled Devices (EMCCDs) to detect x-rays by using a spectrometer to beam x-rays onto EMCCDs. The number of generated electron-hole pairs is proportional to the x-ray energy. Electrons diffuse and drift towards pixel gates where it ultimately reaches an amplifier and is converted into a voltage. These voltages are read out to create images that contain the corresponding x-rays that struck the surface of the EMCCD. A program developed in the ROOT framework uses these images to produce useful information about pixel amplitudes and x-ray distributions. Our study develops further functionality to the existing code and explores contemporary methods to uncover the radial distribution of the charge. One new aspect is to study the noise sources presented in these devices. The Fast Fourier Transform (FFT) is used to reveal harmonics present in the image before and after baseline subtraction. Also, noise amplitude distributions are produced for detailed noise analysis. Methods explored to describe the radial charge distribution involves solutions of the diffusion equation and Monte Carlo simulations. Our findings show that noise distributions roughly follow the Gaussian distribution, but distortions caused by traps, dark currents, etc. Our Monte Carlo simulations reveal that the charge distribution along pixel gates is non-gaussian. This research project has improved my software skills by working with large programs and converting raw data into human-understandable figures. I've also gained a deeper understanding of the physics behind silicon devices, i.e EMCCDs.

II Introduction

Charge Coupled Devices (CCDs) are integrated circuits that contain metal-oxide-silicon structures (MOS) that are closely linked. This allows charges to move from one structure to another. Eventually, this charge reaches an amplifier where it converts the charge into a voltage. EMCCDs are CCDs with the added function of multiplying electrons by impact

ionization. For our EMCCDs, the serial register has 536 multiplication elements. The advantage of EMCCDs is making readout noise negligible.

The e2v CCD207-40 sensors located in the SIX beam line are n-channel, partially depleted, and back-illuminated with 16 μm pixel size. The imaging area is 1632(columns) x 1608(rows). A spectrometer in the SIX beam line beams x-rays with an energy range between 0.23 keV and 2.6 keV. For most of the x-rays, the conversion point is in the field-free region. The charge diffuses in this region, creating an electron cloud approximated by a Gaussian shape. The exact shape can be obtained by solving the diffusion equation written as

$$D\nabla^2\rho(\mathbf{r}, z, t) = \frac{\partial\rho(r, z, t)}{\partial t} \quad (1)$$

where $\rho(\mathbf{r}, z, t)$ is the charge density, \mathbf{r} is the two-dimensional radius vector in the plane parallel to the chip surface, z is the depth, D is the diffusion coefficient, and ∇^2 is the Laplacian. From this equation, we can derive a solution that satisfies the required initial condition and boundary conditions.[1]

Another method involves using a Monte Carlo simulation to model the motion of an electron in a silicon environment. Using data from the literature,[2] we can probabilistically assign values to an electron's direction and magnitude, then look at the r, x, and y profiles of electrons as they reach the exit boundary.

The average x-ray cluster method is also used to analyze the shape distribution of the charge. Our x-ray cluster is a 5 x 5 zone around a pixel with maximum amplitude.

The code inherited for this project uses the images produced from the EMCCDs to construct figures and histograms. Several new additions to the code involve applying FFT to pixels before and after applying baseline subtraction, calculating the total number of pixels that contain signals and no signals, and experimentally changing the cluster seed candidates of the pixels. The baseline value was estimated using pixels without signals in them then taking the average and subtracting it off.[3]

III Data and Analysis

Each data set contains 120 images from EMCCDs at 532 eV taken with approximately one second integration time. Each image contains roughly 100 x-rays. Figure 1 displays the pixel amplitude distribution with cluster seed candidates larger than $10 * \sigma_{noise}$ while Figure 2 is with $30 * \sigma_{noise}$. The horizontal axis is the pixel amplitude and the vertical axis is the number of pixels. Pixels with amplitude around zero represent empty pixels. One interesting observation to note is the behavior of the right tail of the no signal distribution when the cluster seed is increased.

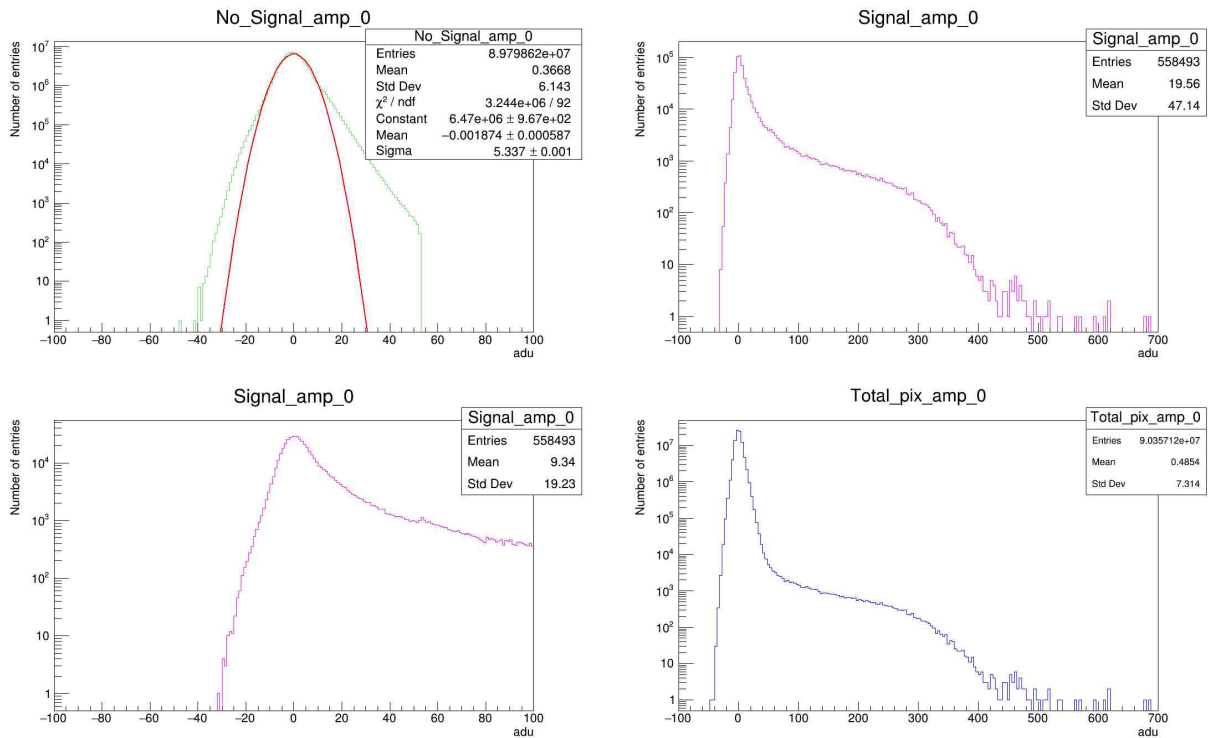


Figure 1: Pixel amplitude distribution with cluster seed candidates larger than $10 * \sigma_{noise}$

Applying FFT to rows and columns, the Power Spectral Density (PSD) was obtained before and after baseline subtraction. Figure 3 shows the PSD before baseline subtraction on the left plots and after baseline subtraction on the right plots.

A couple of observations can be made about the plots:

- The magnitude of the PSD is less after baseline subtraction than before baseline sub-

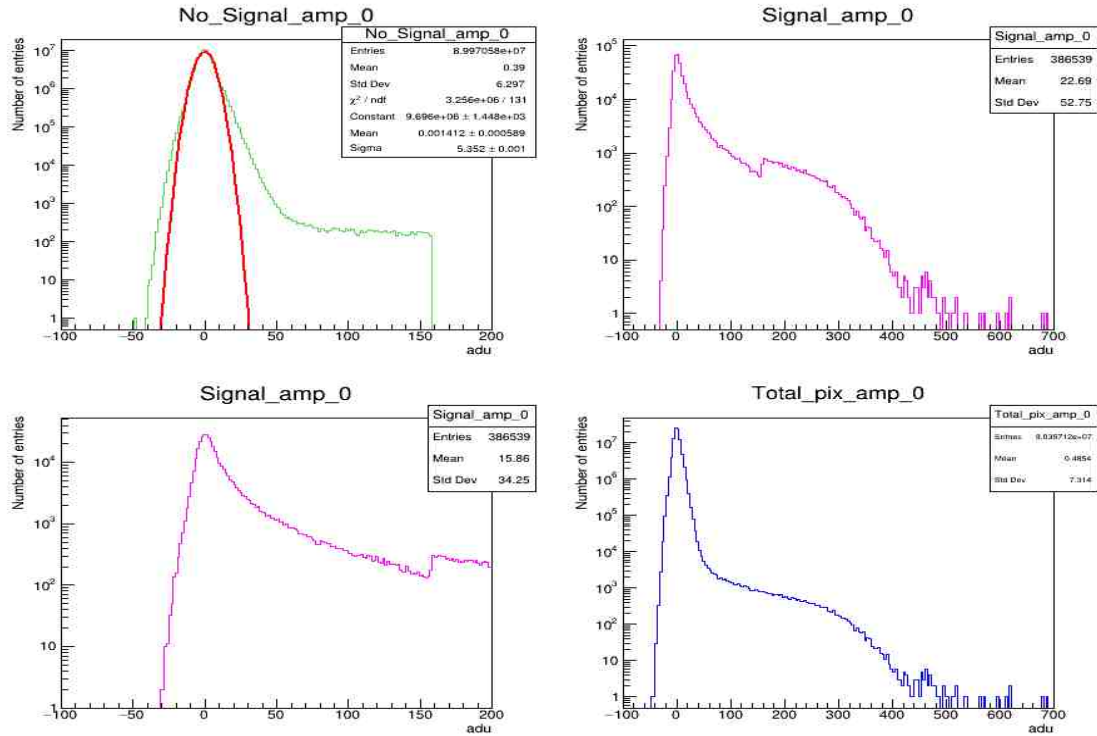


Figure 2: Pixel amplitude distribution with cluster seed candidates larger than $30 * \sigma_{noise}$

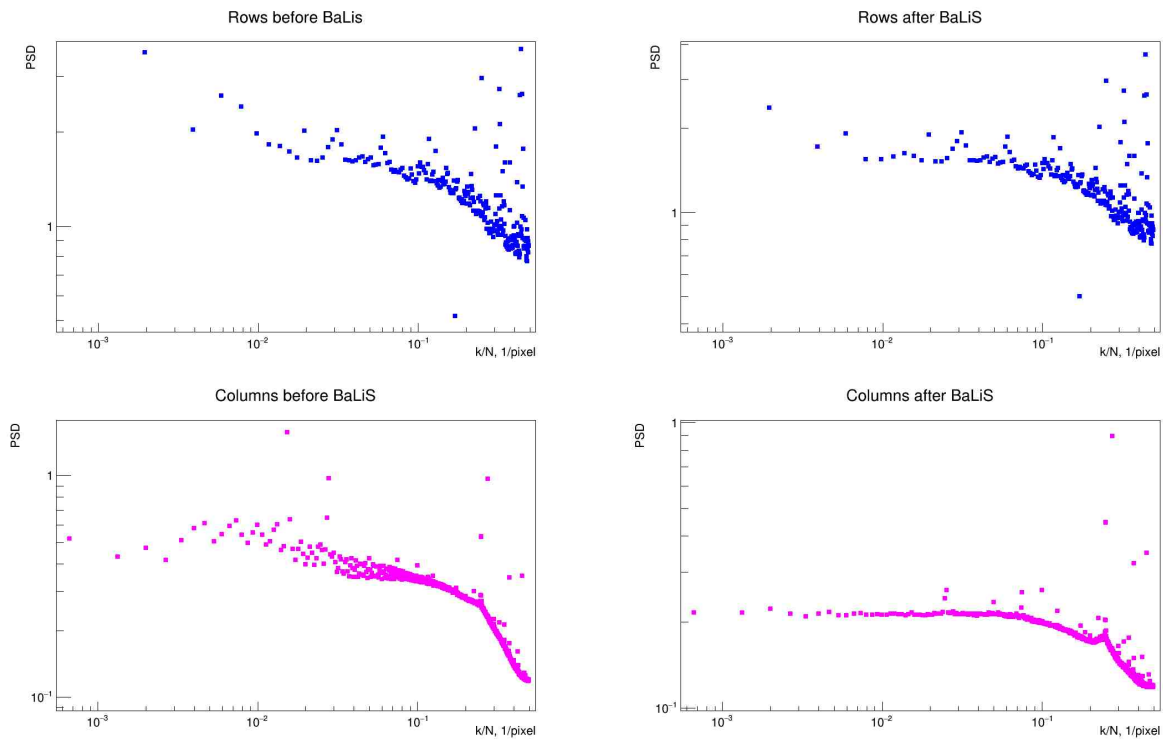


Figure 3: Plots of rows and columns using FFT before and after baseline subtraction

traction.

- Two peaks around $10^{-2}k/N$ frequency in PSD for columns before baseline subtraction disappear after baseline subtraction.

Two images are shown in in figure 4. The right image is raw data before baseline subtraction. The left image is the same data after baseline subtraction. The banding in the vertical direction has disappeared after baseline subtraction.

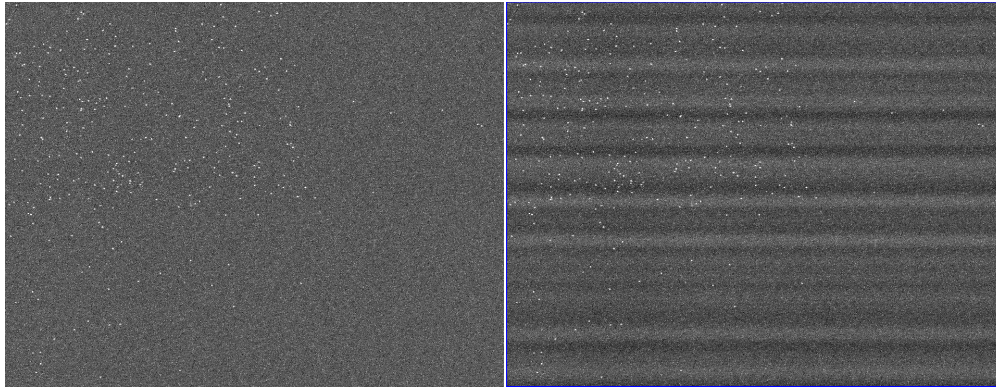


Figure 4: Fit images. The right is raw data before baseline subtraction. The left is after baseline subtraction

IV Monte Carlo

Our Monte Carlo method uses both cartesian and spherical coordinates to record the location of an electron in the field-free region, and to calculate the trajectory of an electron after each step in the simulation. Figure 5 shows relationship between spherical coordinates and cartesian coordinates.

The field-free region is constrained in the z direction. The upper boundary acts as a wall that reflects electrons when they reach the boundary. The lower boundary is a door that allows electrons to exit the volume. The size of the field-free region is $8 \mu\text{m}$, so the upper and lower boundary will be at 4000 nm and -4000 nm .

The Monte Carlo procedure is an event-by-event scheme with electron-phonon interactions. In each event, either energy is lost by the electron due to emission of phonons or energy is gained by the electron from the lattice through phonon absorption. Each one of these two interactions dictate the mean free path of the current step, the distance an electron will travel before another electron-phonon interaction occurs.[2]

The Monte Carlo simulation was written in both Python and C++. A noteworthy technique that was used is parallel processing. For large data sets, uniprocessing became too inefficient when using Python. When the number of electrons equaled 10000, the run time was a little over 30 minutes. After changing the code to utilize parallel processing, the runtime was 10 minutes with 2 computer processing unit cores, a two-thirds reduction. When C++ was used, however, the runtime for 10000 electrons was below 10 seconds. Clearly, C++ is the ideal language to use for runtime optimization.

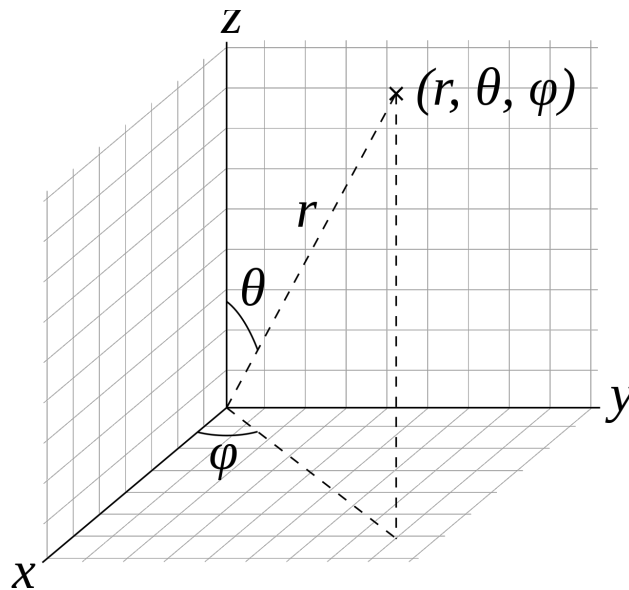


Figure 5: sphericals coordinates

The following steps describes the Monte Carlo method in detail.

1. Place an electron at cartersian coordinates $(0, 0, z_0)$, where z_0 is the initial coordinate along the z axis.

2. Set the electron energy ε by randomly selecting a value from the Boltzmann distribution

$$\frac{1}{k_B T} e^{-\frac{\varepsilon}{k_B T}}. \quad (2)$$

3. Assign a probability p from a uniform distribution $[0, 1]$. Use p to determine if an electron at ε emits or absorbs phonons, then assign the mean free path value ℓ .
4. Set the direction by randomly selecting values from a uniform distribution $[0, \pi]$ and $[0, 2\pi]$ for angles θ and ϕ .
5. Set the distance r by randomly selecting a value from an exponential distribution

$$\frac{1}{\ell} e^{-\frac{r}{\ell}}, \quad (3)$$

with the average equal to ℓ .

6. Calculate the new location (x_n, y_n, z_n) using

$$x_n = r * \sin \theta * \cos \phi + x_{n-1} \quad (4)$$

$$y_n = r * \sin \theta * \sin \phi + y_{n-1} \quad (5)$$

$$z_n = r * \cos \theta + z_{n-1}. \quad (6)$$

7. Check if z_n is above the upper boundary condition, which is 4000 nm. If so, the electron should reflect the boundary to a new location. First, we find the magnitude r' when the electron reaches the boundary, $z_n = 4000$ nm, using

$$4000 = r' * \cos \theta + z_{n-1} \quad (7)$$

$$r' = \frac{4000 - z_{n-1}}{\cos \theta}. \quad (8)$$

Second, we calculate the cartesian coordinate (x', y', z') when the electron hits the upper boundary using equations 4, 5, and 6 with $x = x''$, $y = y''$, $z = z''$, and $r = r''$. In this case, $z' = 4000$. Next, we must find (β, θ', ϕ) , which is the spherical coordinate after being reflected with (x', y', z') as the origin. The magnitude β is

$$\beta = r - r'. \quad (9)$$

The angle θ' is calculated using figure 6.

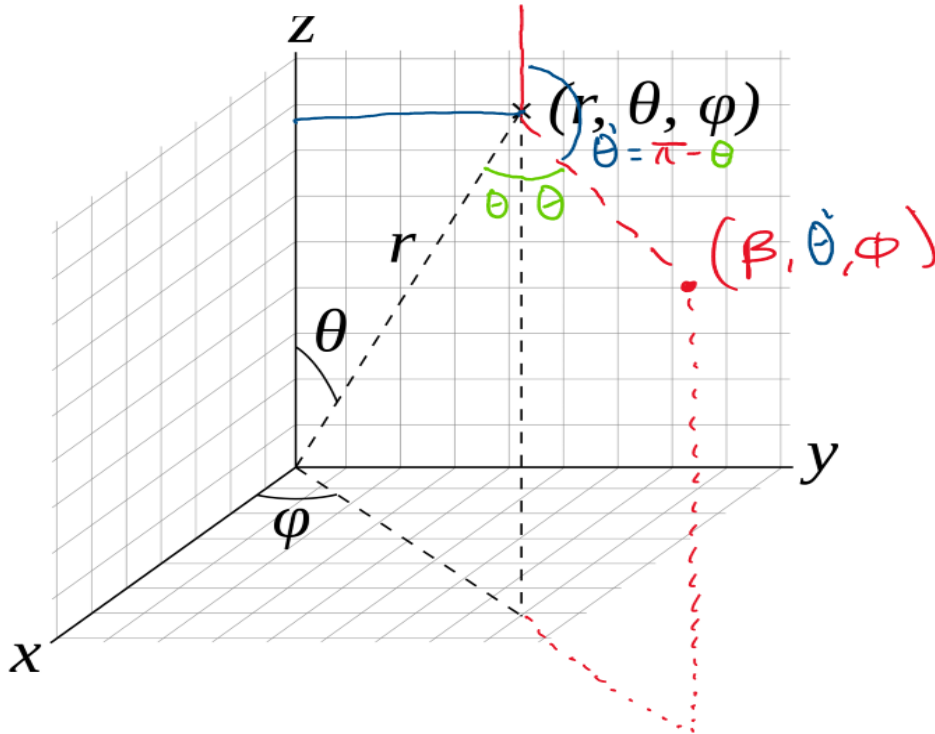


Figure 6: Reflection in spherical coordinates

$$\theta' = \pi - \theta. \quad (10)$$

ϕ isn't transformed during the reflection, so ϕ is used before and during reflection. Finally, we calculate the new cartesian coordinate

$$x_n = x' + \beta * \sin \theta' * \cos \phi \quad (11)$$

$$y_n = y' + \beta * \sin \theta' * \sin \phi \quad (12)$$

$$z_n = z' + \beta * \cos \theta'. \quad (13)$$

8. If z_n is below the lower(exit) boundary condition, which is -4000 nm, then record the exit coordinates and proceed to step 1. If there are no more electrons, then exit program.
9. Repeat to step 2.

Figure 7 shows the distribution of ε , which follow the boltzmann distribution. In both figures, the total number of entries is 1000.

Figure 8 shows two graphs and scatter plots of the x vs y and y vs z displacement of an electron in a typical simulation. The electron is diffusing in the field-free region, reflecting at the upper boundary, and exiting at the lower boundary.

A test was ran with $z_0 = 0$ and the number of electrons equal to 200000. Figures 9, 10, and 11 show the exit coordinates of the electrons for r, x, and y. The mean μ and root mean squared RMS are shown in the figures. For r, the $\mu_r = 0.7605$ and $RMS_r = 0.9695$. For x, the $\mu_x = 0.0006$ and $RMS_x = 0.6842$. For y, $\mu_y = 0.001$ and $RMS_y = 0.6869$. Figures 10 and 11 also show the log scale of the x and y exit coordinates.

More simulations were ran by varying the value of z_0 and setting the number of electrons equal to 10000. Figures 12, 13, and 14 show the r, x, and y exit coordinates. Table 1 shows

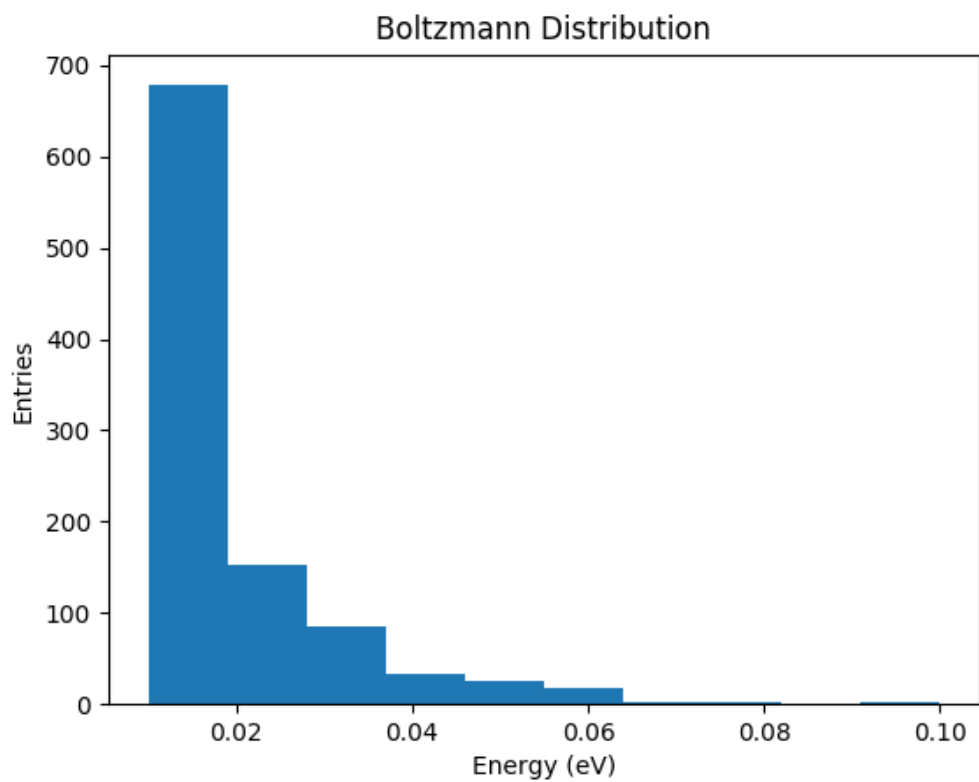


Figure 7: Distribution of ϵ .

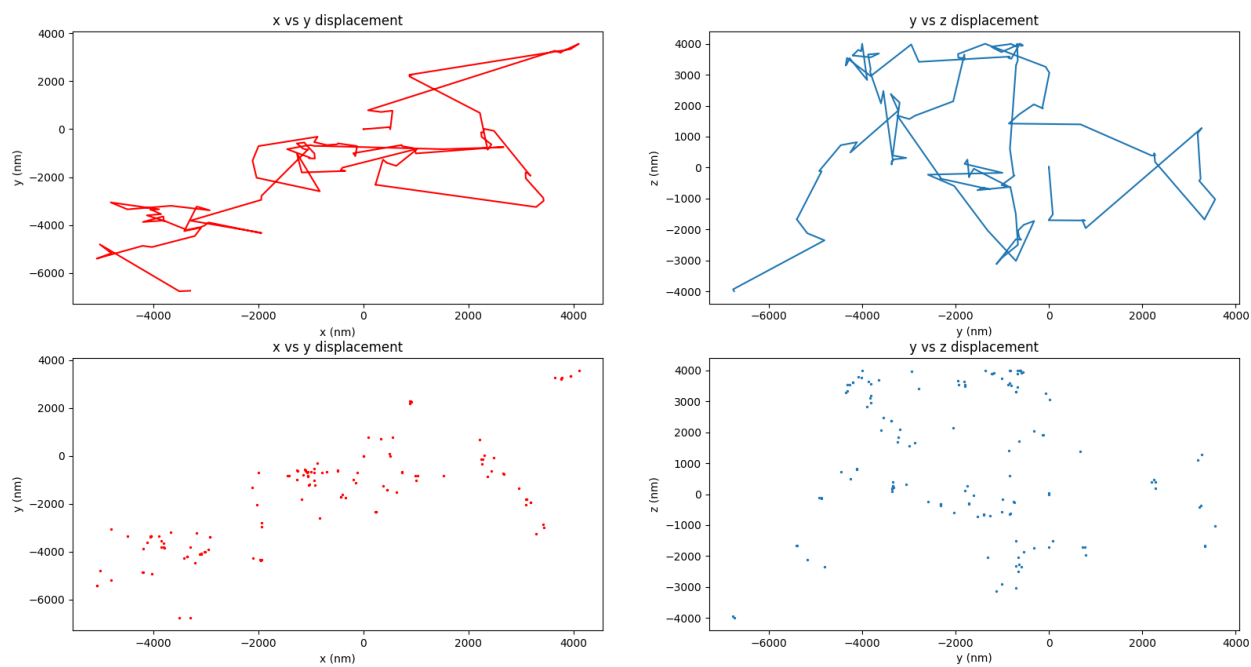


Figure 8: Graphs and scatter plots of the x vs y and y vs z displacement of an electron

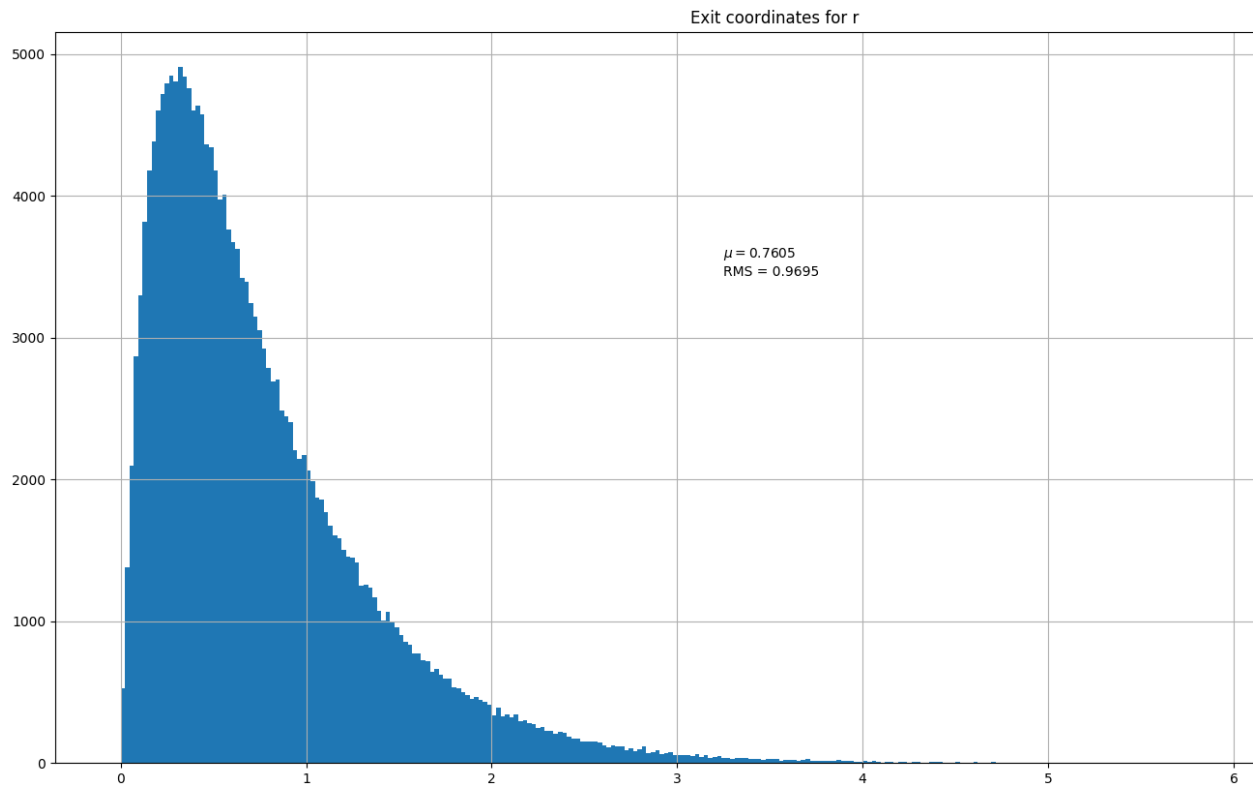


Figure 9: Exit coordinates of electrons for r.

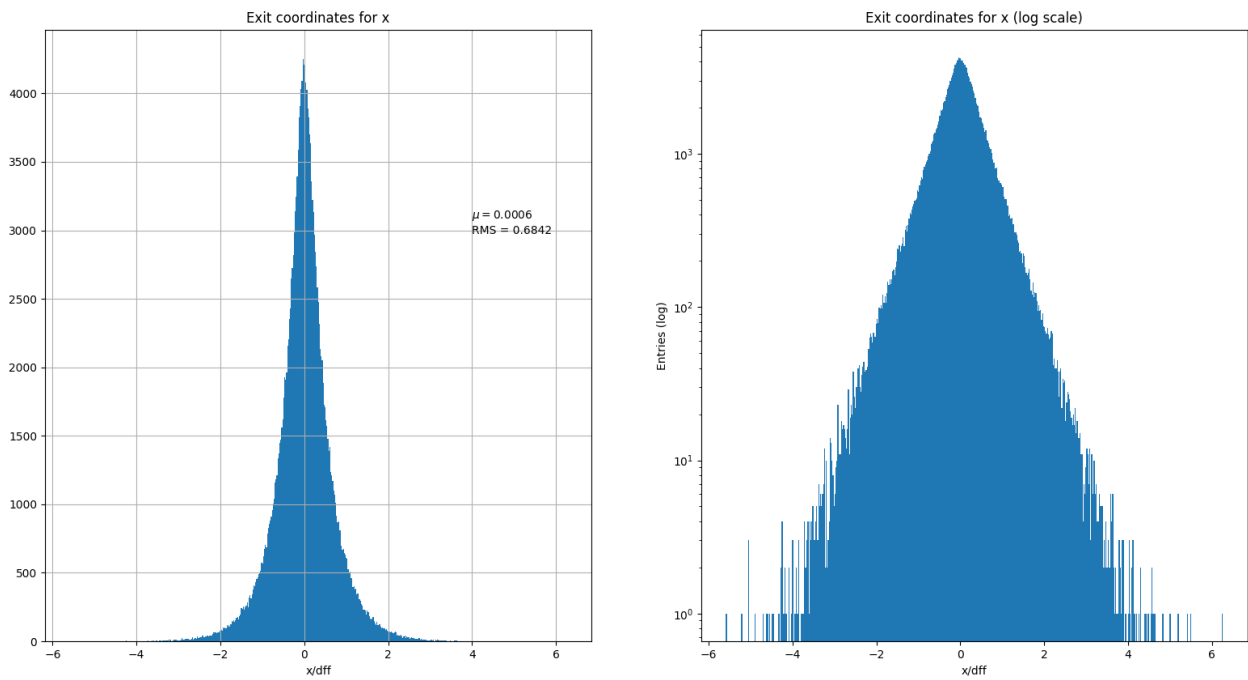


Figure 10: Exit coordinates of electrons for x.

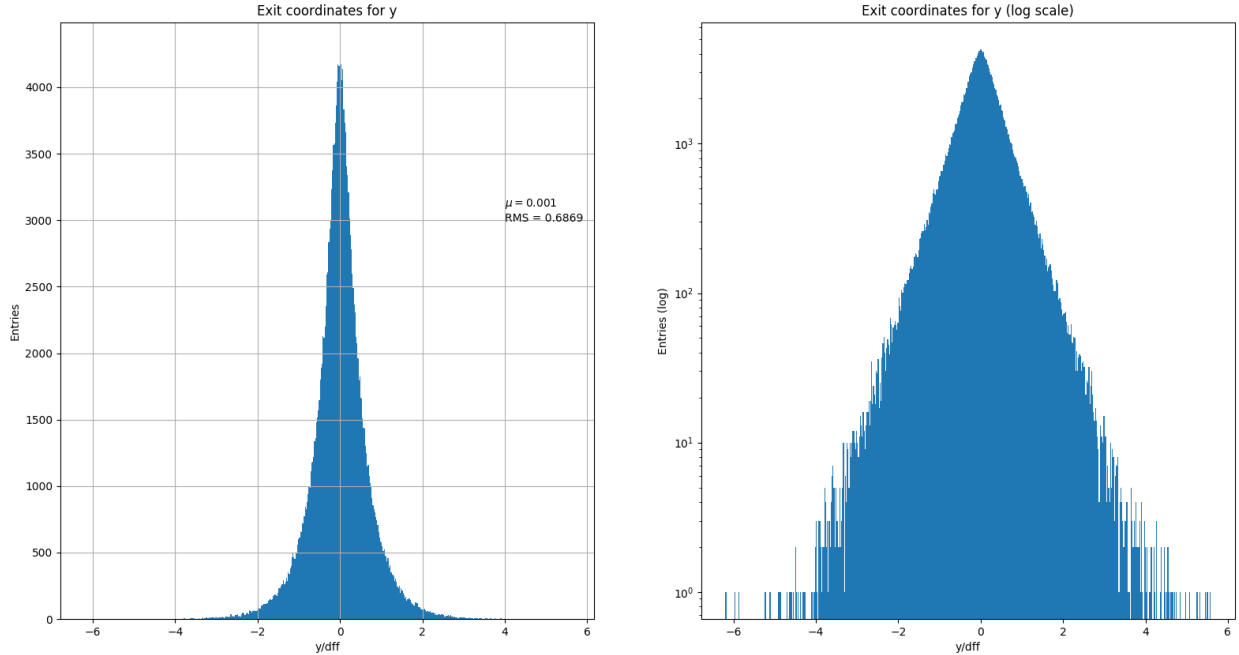


Figure 11: Exit coordinates of electrons for y.

the mean and rms of exit coordinates r, x, and y.

z_0	μ_r	RMS_r	μ_x	RMS_x	μ_y	RMS_y
-3500	0.3228	0.5559	0.005	0.3867	0.0015	0.3993
-1500	0.6248	0.8439	-0.0009	0.6003	-0.0083	0.5931
0	0.7689	0.9784	0.0081	0.6922	0.0025	0.6915
1500	0.8510	1.0555	-0.0003	0.7481	-0.005	0.7446
3500	0.9013	1.1036	-0.0126	0.7843	0.0024	0.7764

Table 1: Mean and RMS of exit coordinates r, x, and y for varying z_0

V Conclusion

The code added to the EMCCD analysis program reveals the noise amplitude distribution of the different cluster seed candidates and highlights how the power spectral density of the image changes after baseline subtraction. Using the Monte Carlo simulation, we can better understand the charge distribution of electrons using parameters that accurately reflect our silicon environment. It also serves as an equivalent comparison to the analytical solution of the diffusion equation.

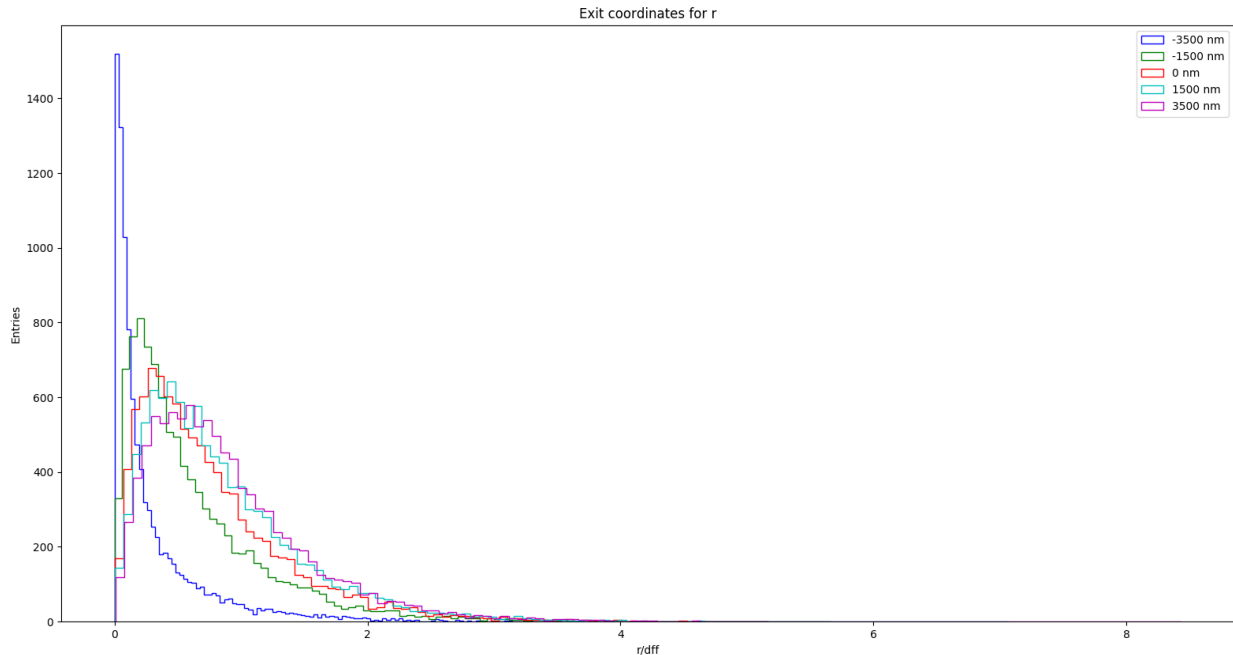


Figure 12: Exit coordinates of electrons for r with varying z_0 .

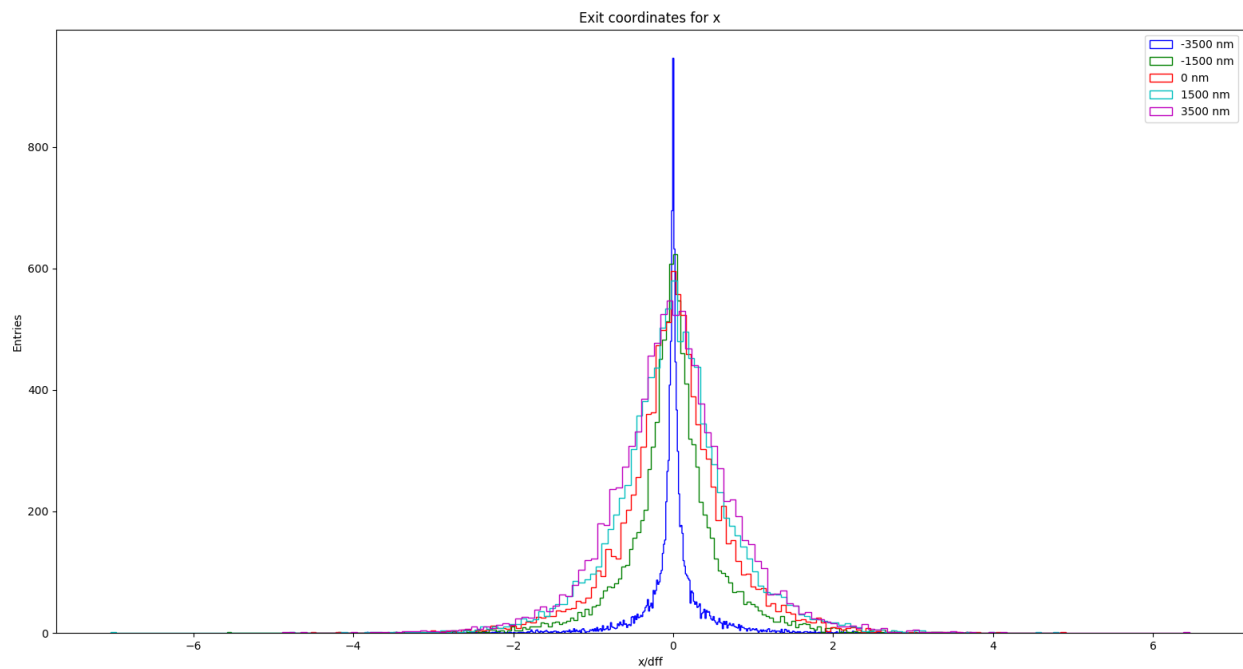


Figure 13: Exit coordinates of electrons for x with varying z_0 .

VI Acknowledgements

This project was supported in part by the U.S. Department of Energy, Office of Science, Office of Workforce Development for Teachers and Scientists (WDTS) under the Science

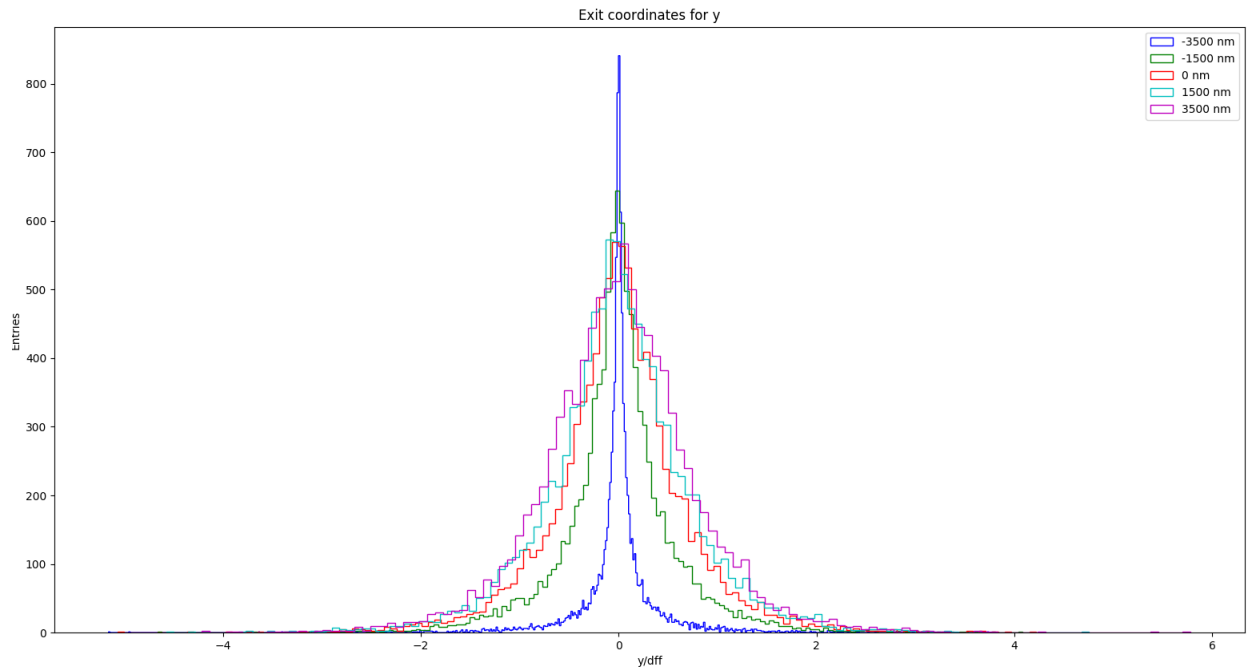


Figure 14: Exit coordinates of electrons for y with varying y_0 .

Undergraduate Laboratory Internships Program (SULI). I want to thank my mentor, Dr. Ivan Kotov, for sharing his vast knowledge, providing tremendous guidance, and giving me the opportunity to attend the SULI program. Also, I want to thank all the Brookhaven National Laboratory staff involved in SULI for making the virtual internship experience incredible with the given circumstances.

References

- [1] G.G. Pavlov and J.A. Nousek, "Charge diffusion in CCD x-ray detectors," *Nuclear Instruments and Methods in Physics Research A* 428, pp. 348-366, 1999.
- [2] A. Akkerman and M. Murat, "Electron-phonon interactions in silicon: Mean free paths, related distributions and transport characteristics," *Nuclear Instruments and Methods in Physics Research B* 350, pp. 49-54, 2015.
- [3] I.V. Kotov, A.I. Kotov, J. Frank, P. O'Connor, V. Perevoztchikov, P. Takacs, "CCD Base Line Subtraction Algorithms," *IEEE Transactions on Nuclear Science*, Vol. 57, No. 4, 2010.
- [4] T.S. Ursell, "The Diffusion Equation A Multi-dimensional Tutorial," *Department of Physics, University of Oregon*, 2016.

Comparative genomics of arsenic detoxification in *S. cerevisiae* and *C. reinhardtii*

Garret Genco, Biology Department, Colby College, Waterville, ME 04901

Crysten Blaby, Biology Department, Brookhaven National Laboratory, Upton, NY 11973

I. Abstract

Arsenic is a pervasive, heavily toxic, naturally occurring metalloid that poses significant health risks through contamination of water sources, air-born particulate matter and soil-derived matter. Arsenic interferes with multiple metabolic pathways producing a plethora of cytotoxic effects that inhibit gene function and induce apoptosis. In response to the ubiquitous presence of arsenic, organisms have developed a myriad of genomic detoxification mechanisms, including metalloid expulsion, compartmentalization and detoxification. To understand the gene functions controlling these mechanisms, this study focused on two microbial model organisms – *Saccharomyces cerevisiae* and *Chlamydomonas reinhardtii*, a fungus and green alga respectively. A comprehensive literature review and comparative genomics analyses generated testable hypotheses for characterizing unknown gene and protein functions involved in arsenic detoxification. In *S. cerevisiae*, the up regulation of Yap1 and Yap8 primarily control the transcription of genes encoding antioxidant, compartmentalization, and regulatory properties. In *C. reinhardtii*, the over-expression of PTA and PTB gene family members act as phosphate transporters and arsenate regulation factors. Furthermore, in both species, the arsenate reductase (ACR2 and CRACR2.1/2) increases the efflux potential of arsenic in cells. To determine whether the identified protein functions are

shared between these species or novel, sequence similarity networks and phylogenetic trees will be constructed in EFI-EST. Arsenic is an extensive carcinogen to humans, thus studying the various genomic mechanisms used to detoxify arsenic toxicity are vital to reducing hazardous exposures to humans. This project has developed my understanding of phylogenetic relationships between species and across protein families through hands-on experience with bioinformatic and gene databases, such as Uniprot, the Saccharomyces Genome Database, NCBI and EFI.

II. Introduction

The ability of plants to efficiently harvest sunlight, water and carbon dioxide to generate carbon-based products and other fuels represent their immense potential as green energy systems, especially in areas decimated by climate change. A better understanding of plant genome biology is foundational to transitioning to a more bio-based economy, which has led to the recent surge in plant genomics research. The establishment of the Quantitative Plant Science Initiative (QPSI) by Brookhaven National Laboratory is one such example. The program aims to accelerate the development of strategies to improve current and emerging bioenergy/bioproduct crops, by leveraging genomic and post-genomic data to address the gap between plant genomes and the function encoded within them (Genomic Science Program 2019). The initiative strives to utilize synthetic research that integrates new and/or existing genomes to address topics including plant genome organization, evolution, function, and manipulation.

The genome contains all the genes needed to build cells, tissues, and reproduce, providing a comprehensive understanding of the organism's physiology. However, a conservative study estimated that approximately 50% of the proteins identified in genome projects have unknown, uncertain, or incorrect functional annotations (Gerlt et al. 2015). These sequences with no precise function are known as 'dark matter', and with the number of genomic sequences doubling every

2.5 years, the extent of ‘dark matter’ is expanding (Zallot et al. 2019). This shortcoming limits interpretation of genome-based data and strategies for synthetic biology approaches. Thus, the challenge encountered by many experimentalists is developing methods to interrogate the plethora of ‘dark matter’ data, so hypotheses can be generated to predict sequence to function of uncharacterized enzymes (Gerlt 2017).

Many genes have relatives across the tree of life, which can be identified by protein sequence similarity and used to understand different gene functions. Assuming there is a gene relationship, gene function information from one species can be used to understand the function of genes in a different species, and the opposite is also true (Zallot et al. 2018). Two microbial model organisms of such an approach are the yeast *Saccharomyces cerevisiae* and green alga *Chlamydomonas reinhardtii*. These two microbes are generally regarded as the most well understood eukaryotic organism in the stress response field (Kaise et al. 1999; Rodrigues-Pousada et al. 2019).

One pertinent stress to bioenergy crops is arsenic, which is a ubiquitous toxic pollutant that universally exists in the environment and contaminates water sources, air and soil derived matter (Chung et al. 2014). When ingested by organisms, arsenic can inhibit gene function (i.e. photosynthesis, nutrient uptake and respiration) and induce apoptosis (Kobayashi et al. 2003; Rodrigues-Pousada et al. 2019). Thus, it is imperative to understand the different gene functions in response to arsenic toxicity.

This project aims to leverage phylogenetic relationships across protein families of *S. cerevisiae* and *C. reinhardtii* and contextualize functional inferences to understand and predict protein function in response to arsenic stress. Furthermore, in accordance with the QPSI’s purpose, this project seeks to describe uncharacterized ‘dark matter’ and accelerate bio-designing strategies to improve emerging bioproduct and bioenergy crops.

III. Experimental Design

A. Literature Review

To ascertain the known protein functions of *S. cerevisiae* and *C. reinhardtii* a comprehensive literature review was conducted using Google Scholar and SCOPUS, with a particular emphasis on bioinformatic studies. From the readings, a list of proteins that directly and indirectly affected intracellular arsenic concentrations and effects were recorded.

B. Comparative Genome Analyses

Using the recorded proteins involved in arsenic detoxification, a comparative genome analyses concentrated on identifying shared and novel gene functions were constructed. For both species, the comparative analyses involved listing every proteins' name, locus ID, function and experimental evidence for the function (see Appendix for full table). If protein locus IDs were not classified by the according study, then genome databases including Uniprot, National Center for Biotechnology Information (NCBI), and Saccharomyces Genome Database (SGD) were used to identify the IDs. Not all locus IDs could be identified.

C. Sequence Similarity Networks (SSNs)

Finally, the Enzyme Function Initiative (EFI) website will be utilized to investigate testable hypotheses for characterizing roles of proteins involved in arsenic detoxification. Specifically, the Enzyme Function Initiative Enzyme Similarity Tool (EFI-EST) web tool will allow experimentalists to segregate protein families into isofunctional groups – those with the same substrate and reaction. The objective is to place uncharacterized enzymes in sequence–function context with those for which reliable experiment-based functions are available. Identification of isofunctional clusters is the first step in exploring sequence–function space in enzyme families and devising strategies to determine the unexplored functions (Gerlt et al. 2015)

IV. Results and Discussion

Table 1. *S. cerevisiae* proteins that are directly involved in arsenic detoxification. The name, gene locus ID and function are described for each protein.

Protein	Gene Locus	Function
Fps1	SGD ID: SGD:S000003966	Bidirectional channel that constitutes major uptake and efflux route for As(III). Repressed by arsenite exposure. Inactivation of the uptake system improves cellular tolerance to As(III) salts
Yap1	SGD ID: SGD:S000004466	Induced by the presence of As(III). (1) Controls transcription of genes encoding proteins with antioxidant properties. (2) Induce sulfur/GSH pathway genes with Met4. (3) Regulates expression of the vacuolar transporter of metal-glutathione conjugates (Ycf1).
Yap8	SGD ID: SGD:S000006403	Induced by the presence of As(III). Master regulator of arsenic detoxification that couples metalloid sensing to detoxification by regulating the levels of Acr2 and Acr3
Met4	SGD ID: SGD:S000005047	Induced by the presence of As(III). Yap1 and Met4 contribute to As(III)-stimulated expression of sulfur/GSH pathway genes, which help repress ROS.
Ycf1	SGD ID: SGD:S000002542	Induced by the presence of arsenic. Major pathway for vacuolar sequestration of GSH-conjugated As
Acr2	SGD ID: SGD:S000006404	Induced by the presence of arsenic. Arsenate reductase that converts As(V) to As(III)
Acr3	SGD ID: SGD:S000006405	Induced by the presence of arsenic. Increases efflux of As(III), reducing arsenic toxicity

Table 2. *C. reinhardtii* proteins that are directly involved in arsenic detoxification. The name, gene locus ID and function are described for each protein.

Protein	Gene Locus	Function
PTB1	Accession # = AB074880	The gene product may play as a regulation factor for P uptake. When its gene activity was inhibited, arsenate resistance increased
PTB2	Accession # = AB074881	Is a high affinity P transporter that is up-regulated by P deprivation. Similarity with Na ⁺ /P cotransporters that encode a derepressible high affinity P transporter; compensatory transport activity in presence of As
PTB3	Uniprot Accession Number = A8JH07	High affinity P transporter that is up-regulated by P deprivation; compensatory transport activity in presence of As
PTB4	Uniprot Accession Number = A8J0U4	
PTB5	Uniprot Accession Number = A8J0U2	
PTA1	Accession # = AB074874	Low affinity P transporter that is down regulated by P deprivation
PTA2	Accession # = AB074875	Low affinity P transporter that is neither up- nor down- regulated by P deprivation
PTA3	Accession # = AB074876	
PTA4	Uniprot Accession Number = A8ISD7	High affinity P transporter that is up-regulated by P deprivation; compensatory transport activity in presence of As
CrACR2.1	Uniprot Accession Number = A8HQ36	Acts as arsenate reductases; has the stronger ability for arsenate reduction. Possible homology to <i>S. cerevisiae</i> ACR2
CrACR2.2	Uniprot Accession Number = A8IUB5	Acts as arsenate reductases; has the weaker ability for arsenate reduction. Possible homology to <i>S. cerevisiae</i> ACR2

The predominant arsenic detoxification mechanisms in both species include sequester, efflux, regulator, and reductase proteins. Upon further analysis, *S. cerevisiae* regulates – induce and suppress – several more arsenic detoxification proteins than *C. reinhardtii*, however, this may be the result of substantially more genome research on *S. cerevisiae* than *C. reinhardtii*. Regardless of the quantitative difference in arsenic detoxification proteins, though, experimental computation approaches specifically emphasized the importance of some proteins.

In *S. cerevisiae*, the up regulation of Yap1 and Yap8 primarily control the transcription of genes encoding antioxidant, compartmentalization, and uptake regulatory properties (Table 1). Due to sensitivity of the yap8 mutant and array of regulated proteins, the over-expression of Yap8 was suggested as the main line of defense to arsenic detoxification (Thorsen et al. 2007). In *C. reinhardtii*, the over-expression of PTA and PTB gene family members act as phosphate transporters and arsenate regulation factors (Table 2). The enhanced arsenic resistance and phosphate uptake induced by the PTA and PTB gene family members, is an important regulatory pathway for maintaining photosynthetic rates in the presence of arsenic (Murota et al. 2012). Furthermore, in both species, the arsenate reductase proteins increase the efflux potential of arsenic in cells. *S. cerevisiae* and *C. reinhardtii* may share a possible efflux protein homology, ACR2 and CrACR2.1/2, respectively (Mukhopadhyay et al. 2000; Yin et al. 2011).

Before conclusions can be inferred, further research is required to examine the functional relationship between protein families of *S. cerevisiae* and *C. reinhardtii*. To determine whether the identified proteins share common functions or unique functions to arsenic presence, sequence similarity networks for each of the identified protein families will be created and phylogenetic trees/profiles from the sequence similarity networks will also be generated.

V. Acknowledgements

I wish to thank my mentor, Dr. Crysten Blaby, for inviting me to join her project and for her professionalism, guidance and support during the SURP program. I would also like to thank the laboratory team for their suggestions and critique during lab meetings. Further, I would like to express my gratitude to the Office of Science Education, and all who helped plan and prepare this virtual internship. Finally, I wish to acknowledge the virtual accommodation and kindness of Ms. Diana Murphy, Brookhaven National Laboratory and the Biology Department

VI. References

- Chung, Jin-Yong, Seung-Do Yu and Young-Seoub Hong. Environmental Source of Arsenic Exposure. *Journal of Preventive Medicine and Public Health* no. 47 (2014): 253-257.
- Gerlt, John A., Jason T. Bouvier, Daniel B. Davidson, Heidi J. Imker, Boris Sadkhin, David R. Slater and Katie L. Whalen. Enzyme Function Initiative-Enzyme Similarity Tool (EFI-EST): A web tool for generating protein sequence similarity networks. *Biochimica et Biophysica Acta* no. 1854 (2015): 1019 – 1037.
- Gerlt, John A. Genomic Enzymology: Web Tools for Leveraging Protein Family Sequence–Function Space and Genome Context to Discover Novel Functions. *Biochemistry* no. 56 (2017), 4293–4308
- Kaise, Toshikazu, Shoko Fujiwara, Mikio Tsuzuki, Teruaki Sakurai, Tohru Saitoh and Chiyo Mastubara. Accumulation of Arsenic in a Unicellular Alga *Chlamydomonas reinhardtii*. *Applied Organometallic Chemistry* no. 13 (1999): 107-111.
- Kobayashi, Isao, Shoko Fujiwara, Kosuke Shimogawara, Toshikazu Kaise, Hideaki Usuda and Mikio Tsuzuki. Insertional Mutagenesis in a Homologue of a Pi Transporter Gene Confers Arsenate Resistance on *Chlamydomonas*. *Plant Cell Physiology* 44, no. 6 (2003): 597-606.
- Mukhopadhyay, Rita, Jin Shi and Barry P. Rosen. Purification and Characterization of Acr2p, the *Saccharomyces cerevisiae* Arsenate Reductase. *The Journal of Biological Chemistry* 275, no. 28 (2000): 211149 – 21157.
- Murota, Chisato, Hiroko Matsumoto, Shoko Fujiwara, Yosuke Hiruta, Shinichi Miyashita, Masahito Shimoya, Isao Kobayashi, Margaret O. Hudock, Robert K. Togasaki, Norihiro Sato and Mikio Tsuzuki. Arsenic tolerance in a *Chlamydomonas* photosynthetic mutant is due to reduced arsenic uptake even in light conditions. *Planta* no. 236 (2012): 1395-1403.

“Quantitative Plant Science Initiative (QPSI),” Genomic Science Program, U.S. Department of Energy, last modified December 18, 2019, <https://genomicscience.energy.gov/research/sfas/bnlqpsi.shtml>

Rodrigues-Pousada, Claudina, Frédéric Devaux, Soraia M. Caetano, Catarina Pimentel, Sofia da Silva, Ana Carolina Cordeiro and Catarina Amaral. Yeast AP-1 like transcription factors (Yap) and stress response: a current overview. *Microbial Cell* 6, no. 6 (2019): 267-285.

Thorsen, Michael, Gilles Lagniel, Erik Krisiansson, Christophe Junot, Olle Nerman, Jean Labarre and Markus J. Tamas. Quantitative transcriptome, proteome, and sulfur metabolite profiling of the *Saccharomyces cerevisiae* response to arsenite. *Physiology Genomics* no. 30 (2007): 35-43.

Yin, Xixiang, Lihong Wang, Guilan Duan and Guoxin Sun. Characterization of arsenate transformation and identification of arsenate reductase in a green alga *Chlamydomonas reinhardtii*. *Journal of Environmental Sciences* 23, no. 7 (2011): 1186-1193.

Zallot, Remi, Nils Oberg and John A. Gerlt. ‘Democratized’ genomic enzymology web tools for functional assignment. *Current Opinion in Chemical Biology* no. 47 (2018): 77–85

Zallot, Remi, Nils Oberg and John A. Gerlt (2019). The EFI Web Resource for Genomic Enzymology Tools: Leveraging Protein, Genome, and Metagenome Databases to Discover Novel Enzymes and Metabolic Pathways. *Biochemistry* no. 58 (2019): 4169-4182.

VII. Appendix

Table 1. All *S. cerevisiae* proteins that are directly and indirectly involved in arsenic detoxification. The name, gene locus ID, function, and experimental evidence for the function are described for each protein.

Protein	Gene Locus	Function	Evidence
Msn2	Saccharomyces Gene Database ID: SGD:S000004640	Up-regulated by arsenic exposure. Zinc-finger transcription factor that largely mediate HSF-independent mechanisms, which acts as its environmental stress response to As	A RNA isolation, cDNA synthesis, and microarray hybridization experiment was used to analyze gene expression. To measure phosphorylation of Msn2, a Western Blot was performed. Green fluorescent microscopy was also used to localize nuclei and record cell counts under treatment conditions
Msn4	Saccharomyces Gene Database ID: SGD:S000001545	Up-regulated by arsenic exposure. Zinc-finger transcription factor that largely mediate HSF-independent mechanisms, which acts as its environmental stress response to As	A RNA isolation, cDNA synthesis, and microarray hybridization experiment was used to analyze gene expression. Green fluorescent microscopy was also used to localize nuclei and record cell counts under treatment conditions
Fps1	Saccharomyces Gene Database ID: SGD:S000003966	Aquaglyceroporin that is a bidirectional channel which mediates transport of substrates down the concentration gradient. Constitutes a major uptake and efflux route for As(III). Activity is repressed by arsenite exposure. Inactivation or limitation of the uptake system improves cellular tolerance to As(III) salts	To analyze gene expression, the study used a RNA isolation, cDNA synthesis, and microarray hybridization experiment. To quantify transcript levels, at least two independent Northern blot analyses were performed for each growth condition and transcript. A proteome analysis of protein extraction, two-dimensional gel electrophoresis, and gel analysis were conducted to rapidly identify proteins. Metabolite measurements and metabolic flux analysis were then determined by GSH and protein synthesis rates

Pho84; Pho86; Pho87; Pho88	Saccharomyces Gene Database ID: SGD:S000004592; SGD:S000003653; SGD:S000000633; SGD:S000000310	Phosphate transporters that uptake As(V). Regulation (inhibition) of them increased As(V) tolerance	In multiple phosphate concentrations, phosphate uptake was measured. Then to monitor the activity of the different phosphate permease transporters, fluorescent microscopy was used to photograph the activity of the live cells
Hog1	Saccharomyces Gene Database ID: SGD:S000004103	Induced by As(III). Regulates As(III) transport through Fps1p: (1) Hog1p phosphorylates Fps1p on Thr231 and this phosphorylation reduces Fps1p-mediated transport OR (2) indirectly by downregulating the positive regulators of Fps1p activity	Measured arsenate uptake and efflux. Then a rabbit polyclonal IgG antibody against dually phosphorylated p38, was used to detect phosphorylated Hog1p whereas a goat polyclonal IgG antibody was used to detect total Hog1p. Fluorescent microscopy was used to analyze the distribution of Hog1p. A RNA isolation, cDNA synthesis, and microarray hybridization experiment was used to analyze gene expression
Yap1	Saccharomyces Gene Database ID: SGD:S000004466	Induced by the presence of As(III). (1) Controls transcription of genes encoding proteins with antioxidant properties. (2) With Met4, they contribute to As(III)-stimulated expression of sulfur/GSH pathway genes. (3) Regulates expression of the vacuolar transporter of metal-glutathione conjugates (Ycf1).	To analyze gene expression, the study used a RNA isolation, cDNA synthesis, and microarray hybridization experiment. To quantify transcript levels, at least two independent Northern blot analyses were performed for each growth condition and transcript. A proteome analysis of protein extraction, two-dimensional gel electrophoresis, and gel analysis were conducted to rapidly identify proteins. Metabolite measurements and metabolic flux analysis were then determined by GSH and protein synthesis rates. Analysis of the capacity of <i>S. cerevisiae</i> mutant and wild type cells to absorb and accumulate As(III) was determined using atomic-absorption spectrophotometry
Yap8	Saccharomyces Gene Database ID: SGD:S000006403	Induced by the presence of As(III). Master regulator of arsenic detoxification that binds the promoter region located between ACR2 and ACR3. Couples metalloid sensing to detoxification by regulating the levels of Acr2p and Acr3p	As(III) was determined using atomic-absorption spectrophotometry

Met4	Saccharomyces Gene Database ID: SGD:S000005047	Induced by the presence of As(III). Yap1 and Met4 contribute to As(III)-stimulated expression of sulfur/GSH pathway genes, which help repress ROS.	
Rpn4	Saccharomyces Gene Database ID: SGD:S000002178	Expression is enhanced by As(III). Might control the transcriptional response to As(III), specifically controlling As(III)-stimulated expression of proteasome gene. This assists in increasing tolerance to build-up of protein degradation by As(III)	
Rgc1	Saccharomyces Gene Database ID: SGD:S000006319	Positive regulators of Fps1. Deletion of them inactivates Fps1 and increases As(III) tolerance	Three different genomic clones of FPS1 were isolated from a high-copy genomic library in pRS202 as suppressors of the temperature-sensitivity of a rgc1/2D mutant. The screen was conducted in the rgc1/2D mutant. Plasmids for each gene was then generated and used to (1) measure zymolyase sensitivity, cell wall stress reporter assays, intracellular glycerol concentrations, and glycerol efflux; (2) identify the number of cells, activity and distribution via Fluorescence microscopic detection
Rgc2/ASK10	Saccharomyces Gene Database ID: SGD:S000003329		
Ycf1	Saccharomyces Gene Database ID: SGD:S000002542	Induced by the presence of arsenic. Through the ATP binding cassette (ABC) transporter Ycf1p, glutathione conjugated As(III) in the vacuole is sequestered. This represents a major pathway for vacuolar sequestration of GSH-conjugated metals	To analyze gene expression, the study used a RNA isolation, cDNA synthesis, and microarray hybridization experiment. To quantify transcript levels, at least two independent Northern blot analyses were performed for each growth condition and transcript. A proteome analysis of protein extraction, two-dimensional gel electrophoresis, and gel analysis were conducted to rapidly identify proteins. Metabolite measurements and metabolic flux

			analysis were then determined by GSH and protein synthesis rates
Acr2/Arr2	Saccharomyces Gene Database ID: SGD:S000006404	Induced by the presence of arsenic. Is an arsenate reductase that converts As(V) to As(III) for subsequent export out of the cell	Isolated the gene from <i>S. cerevisiae</i> into <i>E. coli</i> , purified the proteins and then conducted an assay of arsenate reductase activity
Acr3/Arr3	Saccharomyces Gene Database ID: SGD:S000006405	Induced by the presence of arsenic. The plasma membrane protein Acr3p can increase efflux of trivalent As(III), reducing arsenic toxicity	To analyze gene expression, the study used a RNA isolation, cDNA synthesis, and microarray hybridization experiment. To quantify transcript levels, at least two independent Northern blot analyses were performed for each growth condition and transcript. A proteome analysis of protein extraction, two-dimensional gel electrophoresis, and gel analysis were conducted to rapidly identify proteins. Metabolite measurements and metabolic flux analysis were then determined by GSH and protein synthesis rates
Fhl1	Saccharomyces Gene Database ID: SGD:S000006308		
Ifh1	Saccharomyces Gene Database ID: SGD:S000004213	The forkhead-like protein Fhl1 and an interacting factor Ifh1 constitute one axis of ribosomal proteins (RP) gene regulation.	A RNA isolation, cDNA synthesis, and microarray hybridization experiment was used to analyze gene expression
Sfp1	Saccharomyces Gene Database ID: SGD:S000004395	Localized to the nucleus, where it binds to target-gene promoters and promotes the expression of ribosomal proteins under optimal growth conditions. Phosphorylation was decreased and localization shifted from nuclear	A RNA isolation, cDNA synthesis, and microarray hybridization experiment was used to analyze gene expression. To measure phosphorylation of Sfp1, a Western Blot was performed. Green fluorescent microscopy was also used to localize nuclei and record cell counts under treatment conditions

		to a more cytoplasmic distribution in response to As(III) exposure	
Snf3	Saccharomyces Gene Database ID: SGD:S000002353	They are necessary for cells to induce the expression of HXT (P/As transporter). The Snf3 protein is expressed at very low level and involved in the induction of high-affinity glucose transporters, while the Rgt2 protein is induced under glucose-replete conditions and has no relationship with the expression of HXT2 and HXT4 which are induced under glucose-deprived conditions.	Disruption strains and mutants were developed in the study. Beta-Galactosidase (beta-Gal) Assays were run on permeabilized cells. The DNA sequences for the gene were identified and constructed for analysis and comparison to Rgt2
Rgt2	Saccharomyces Gene Database ID: SGD:S000002297		Disruption strains and mutants were developed in the study. Beta-Galactosidase (beta-Gal) Assays were run on permeabilized cells. The DNA sequences for the gene were identified and constructed for analysis and comparison to Snf3
Sch9	Saccharomyces Gene Database ID: SGD:S000001248	Major and direct downstream target of TORC1 for control of both stress-and growth-related transcription. Phosphorylation status was rapidly reduced upon exposure As(III) stress. Absence rendered cells more sensitive to As	A RNA isolation, cDNA synthesis, and microarray hybridization experiment was used to analyze gene expression. Chemical fragmentation using the Antibody 12CA5 was used to detect the gene
FTR1	Saccharomyces Gene Database ID: SGD:S000000947	In combination with Fet4 and Fet3, the permease Ftr1 is one of three genes that operate the reductive pathways of low- and high- affinity Fe uptake systems. The Fet3-Ftr1 complex is specific for Fe. Upon As(V) exposure, mRNA levels were significantly decreased, which causes defective high affinity Fe uptake and eventual Fe deficiency but high As resistance	Conducted a genome-wide mRNA profiling of the <i>S. cerevisiae</i> response to As(V). This include a DNA microarray analysis, RNA blot analysis, RT-PCR

FET3	Saccharomyces Gene Database ID: SGD:S000004662	In combination with Fet4 and Ftr1, the protein complex composed of the multicopper ferroxidase Fet3 is one of three genes that operate the reductive pathways of low- and high- affinity Fe uptake systems. The Fet3-Ftr1 complex is specific for Fe. Upon As(V) and As(III) exposure, mRNA levels were significantly decreased, which causes defective high affinity Fe uptake and eventual Fe deficiency but high As resistance	analysis, beta-Galactosidase assay, measurement of total arsenic and iron, protein analysis and fluorescent microscopy (ends at CTH2/TIS11)
Xrn1	Saccharomyces Gene Database ID: SGD:S000003141	Is up-regulated by As(V) exposure, and causes the FET3 mRNA degradation, which causes defective high affinity Fe uptake and eventual Fe deficiency but high As resistance	
CTH1	Saccharomyces Gene Database ID: SGD:S000002558	In response to Fe deficiency and after Fet3 repression, the gene was up-regulated and mRNA started to increase. The activation of this gene under the aft1 regulon offset the Fe deficiency and increase Fe uptake. Activating the Aft1/2-dependent Fe regulon is a corrective measure to Fe deficiency	
CTH2/TIS11	Saccharomyces Gene Database ID: SGD:S000004126	In response to Fe deficiency and after Fet3 repression, the gene was up-regulated and mRNA started to increase. The activation of this gene under the aft2 regulon offset the Fe deficiency and increase Fe uptake. Activating the Aft1/2-dependent Fe regulon is a corrective measure to Fe deficiency	

Aco1/ISC (mitochondrial)	Saccharomyces Gene Database ID: SGD:S000004295	In response to As(V), overexpression of this gene was observed, which alleviated growth defects stimulated by arsenate that increase Fe toxicity. To overcome Fe toxicity, synthesis of Fe-S proteins that have been damaged by As (and ROS) is increased, thus buffering displaced iron from Fe-S clusters by As (And ROS)	Analyzed the trnascriptomic profile of the yap1 and yap8 mutant strains in response to arsenate treatment. This was performed by using flow cytometry, DNA microarrays, quantitative RT-PCR analyses, measurements of total arsenic, iron and phosphate, and activity measurements of isopropylmalate isomerase (Leu1) and aconitase (Aco1)
CIA (Cytolsolic) /Leu1	Saccharomyces Gene Database ID: SGD:S000002977	In response to As(V), overexpression of this gene was observed, which alleviated growth defects stimulated by arsenate that increase Fe toxicity. To overcome Fe toxicity, synthesis of Fe-S proteins that have been damaged by As (and ROS) is increased, thus buffering displaced iron from Fe-S clusters by As (And ROS)	

Table 2. All *C. reinhardtii* proteins that are directly and indirectly involved in arsenic detoxification. The name, gene locus ID, function, and experimental evidence for the function are described for each protein.

Protein	Gene Locus	Function	Evidence
PTB1	Accession # = AB074880	Instead of acting as a transporter, the gene product may play as a regulation factor for P uptake. When its gene activity was inhibited, arsenate resistance increased	Cloned the gene responsible for the arsenate-resistant phenotype of AR3. (1) Described the kinetics of Pi uptake and (2) measured the intracellular P and As content of the AR mutant. (3) In addition, also discussed the relationships between PTB1 disruption and Pi uptake of AR3 by first measuring mRNA levels and then Sequence alignment with other Na ⁺ /Pi transporters. (N-

			terminal domains of Na ⁺ /Pi co-transporters & between PTB2, PHO89, PHO4, A. thaliana, M. crystallinum, T. brucei, Nostoc sp.)
PTB2	Accession # = AB074881	Is a high affinity Pi transporter that is up-regulated by Pi deprivation. Similarity with Na ⁺ /Pi cotransporters that encode a derepressible high affinity Pi transporter; compensatory transport activity in presence of As	Using the AR3 mutant, the following methods were used. (1) Described the kinetics of Pi uptake and (2) measured the intracellular P and As content of the AR mutant. (3) In addition, also discussed the relationships between PTB1 disruption and Pi uptake of AR3 by first measuring mRNA levels and then Sequence alignment with other Na ⁺ /Pi transporters. (N-terminal domains of Na ⁺ /Pi co-transporters & between PTB2, PHO89, PHO4, A. thaliana, M. crystallinum, T. brucei, Nostoc sp.)
PTB3	Uniprot Accession Number = A8JH07		Measured As(V) and Pi uptake with the photosynthetic mutant CC981 under light and dark conditions and compared it to the wild type. Also elucidated the photosynthetic and respiratory activity. Then sequenced and ran a RT-PCR to investigate the expression and characteristics of the Pi transporters
PTB4	Uniprot Accession Number = A8J0U4		
PTB5	Uniprot Accession Number = A8J0U2	High affinity Pi transporter that is up-regulated by Pi deprivation	
PTA1	Accession # = AB074874	Low affinity Pi transporter that was down regulated by Pi deprivation	

PTA2	Accession # = AB074875		
PTA3	Accession # = AB074876	Low affinity Pi transporter that was neither up- or down- regulated by Pi deprivation	
PTA4	Uniprot Accession Number = A8ISD7	High affinity Pi transporter that is up-regulated by Pi deprivation	
CrACR2.1	Uniprot Accession Number = A8HQ36	Act as arsenate reductases; has the stronger ability for arsenate reduction	To investigate As accumulation, transformation and efflux, <i>C. reinhardtii</i> cells were grown in various As concentrations, and samples were harvested and frozen to determine As species. Two potential arsenate reductase genes were cloned and characterized in vivo. Finally, sequence alignment of the predicted green alga ACR2 compared with some identified ACR2 was conducted (<i>O. sativa</i> ; <i>S. cerevisiae</i> ; <i>A. thaliana</i> ; <i>H. lanatus</i> ; <i>P. vittata</i> ; <i>Z. mays</i> ; <i>L. major</i> ; <i>P. patens</i> ; <i>C. reinhardtii</i>) and then used to build a phylogenetic tree.
CrACR2.2	Uniprot Accession Number = A8IUB5	Act as arsenate reductases; has the weaker ability for arsenate reduction	
Grx	N/A	Involved in the reduction of arsenate to arsenite (provides the reducing agent)	Determined the draft genome sequence of the <i>Chlamydomonas eustigma</i> and performed comparative genome and transcriptome analyses between <i>C. eustigma</i> and its neutrophilic relative <i>Chlamydomonas reinhardtii</i> (which had already been fully sequenced)

20S proteasome (alpha) subunit D type 7	C. reinhardtii v4.0 Acc No = 183620	Responsible for the removal of short-lived or abnormal intracellular proteins. An increase of the 20S core unit appears to result in an increase in protein degradation of oxidized proteins and so enhances tolerance towards oxidative stress. Might also be increased in the As-treated cells in order to remove proteins that are damaged by exposure to arsenate	First measured the effect of arsenate on cellular growth. Protein extracts from control and arsenic treated C. reinhardtii cells were then compared to determine differential responses to As stress. Ran a gel electrophoresis, and only the spots that were over expressed were investigated (remained visible and did not decrease in intensity)
Superoxide dismutase [Mn]	Accession Number = 193511	Catalyzes the reduction of superoxide anions to hydrogen peroxide. Increase of this enzyme might be to reduce oxidative stress (ROS)	
Superoxide dismutase [Fe]	Accession Number = 182933	An increase in antioxidant capacity --> improved tolerance to arsenic	
Peptidyl-prolyl cis-trans isomerase	Accession Number = 34270	Catalyzes the interconversion of peptidyl-prolyl imide bonds in peptides and proteins. It is also expressed in response to oxidative stress. May also act together with chaperonins, and protein disulfide isomerases that are involved in protein folding	
14-3-3 Multifunctional chaperone protein	Accession Number = 187228	Appear to have diverse functions including protein synthesis, folding, and posttranslational modification. During metal stress they are able to prevent irreversible protein denaturation or help channel proteins for proteolytic degradation	
Rubisco small subunit 1	Accession Number = 82986	Major enzyme that catalyzes carbon assimilation, hence controls photosynthetic rate and thus has a major effect on plant growth. Could be to compensate for damage to the photosynthesis system	

Glyceraldehyde 3-phosphate dehydrogenase (GAPDH3)	Accession Number = 140618	Pleiotropic protein involved in various stresses, programmed cell death, DNA damage repair and DNA replication. May support the possible increase in gluconeogenesis. Also catalyzes arsenylation of G3P to form 1As3PGA to be transported out of the cell by ArsJ	
Oxygen evolving enhancer protein 1	Accession Number = 130316	Major catalytic in photosynthetic oxygen evolution in green plants, and is associated with the photosystem II complex, the site of oxygen evolution. Shown to exhibit thioredoxin activity in cells exposed to high light and low CO2 concentrations. Helps maintain proper redox state	
Heat shock protein 90B	Accession Number = 97057	Chaperonin protein reported to be expressed under metal stress	
Alpha-amylase	Accession Numbers = 173725 & 58178	Increase of expression is indicative of an increase in energy requirement; maybe the result of damage to the alga's photosynthetic capacity	
ArsJ	N/A	A bacterial organoarsenical efflux permease that extrudes 1-arseno-3-phosphoglycerate from the cell. The formation of 1-arseno-3-phosphoglycerate is catalyzed from arsenate and Glyceraldehyde 3-phosphate by the putative transporter belonging to the Major Facilitator Superfamily (MFS). MFS and ArsJ most likely related	
PGK3	N/A	Formation of 1As3PGA by GAPDH3 is unstable and may spontaneously hydrolyze into As(V) and 3PGA before 1As3PGA can be transported out of the cell by	To identify conserved gene neighborhoods, they compared gene proximity in the nuclear genomes of 10 green algae that have high-quality publicly accessible genome assemblies and gene models. Then neighborhoods were manually annotated and inspected for potential functional relevance. Mutant screens and resequencing of <i>C. reinhardtii</i> mutants and wildtype cells were conducted. Using the Enzyme Function Initiative Enzyme Similarity Tool

		algal ArsJ. Thus, PGK3 could function in concert with GAPDH3 to recycle the resulting 3PGA producing G3P, and avoid 3PGA build-up	(EFI-EST), sequence similarity networks and family-specific phylogenetic analyses were constructed.
ArsB	N/A	Acts as an efflux of arsenite that was produced by an arsenate reductase. Functions similarly to ACR3	
ArsM	Uniprot Accession Number = K0BVM7	Part of a two step process whereby arsenite is methylated by ArsM, and could be oxidized by ArsH to a less toxic pentavalent form of methylated arsenate	

A comprehensive literature study of SARS-CoV-2's morphology, pathogenesis and drug targets

Sonali George

Biology, Stony Brook University, Stony Brook, NY, 11794

Desigan Kumaran

Structural Biology, Brookhaven National Laboratory, Upton, NY 11973

ABSTRACT

Severe acute respiratory syndrome coronavirus 2 (SARS-CoV-2) is the virus that has been declared to have created this global pandemic of the coronavirus disease 2019 (COVID-19). This literature study is part of a greater project to develop a summary of research papers into a literature review. My approach was to create a slide of the morphology of SARS-CoV-2 with its basic proteins, to develop a video with animations that aims to clarify the replication cycle and lastly create an overview of the replication cycle to situated popular drug targets within the overview. This review on the basic sciences aims to describe the replication cycle that the virus undergoes within the host with greater biological bases than popular media and news outlets. By combining visual presentations and clear explanations through videography, I hope to create a classic classroom environment in which concepts are sketched out so that the research can be understood by a broader and general audience.

I. INTRODUCTION

At the end of 2019, the World Health Organization was informed about an outbreak of pneumonia cases due to an unknown cause in Wuhan, China. The infectious virus behind this novel pandemic is now called SARS-CoV-2 and the resulting disease is called COVID-19. SARS-CoV-2 is essentially a virus pathogen that covers its genetic material, encoded in a single-stranded RNA, with an envelope made of proteins. It has several proteins but the name *corona* (Latin for crown) was termed because of its spike protein that has crown-like morphology. Since the CoV-2 outbreak, researchers around the world have made great progress in studying this virus and have created an enormous reservoir of information. However, a hindrance in greater development and awareness of SARS-CoV-2 is the lack of access to accredited, scientifically sound information to the general public. This literature study seeks to elucidate the virology hidden

within the scientific research jargon. Mainly, by clarifying the viral structure, replication cycle, epidemiology and possible drug targets in a simpler way, a greater understanding of the virus will result in those not in the scientific realm. We aim to go beyond the superficial understanding popular media provides, to give the general audience a deeper understanding of the virology behind this unprecedented pandemic.

II. METHODS

References for this study were identified through searches on PubMed, Ovid MEDLINE, and NCBI from June 15, 2020 to 24 July 2020. I began by formulating questions like “How and what does this virus do to enter into the host cell?” and “How can I explain these processes that the virus undergoes?”. Using keywords like “COVID”, “SARS-CoV-2”, “CoV”, etc. to search science databases to find accredited articles. Then curating these 15- 20 peer reviewed articles into the virus's background, replication cycle, how the virus enters the host and potential drug targets I was able to create a script that was four minutes long for the animation. The software I used to create the animation were Autodesk Sketchbook (with an external tablet) and iMovie, for the audio I used Audacity. One of the essential components of the animation/video was to be able to preface the replication cycle by including the events that occur in the alveolar cell.

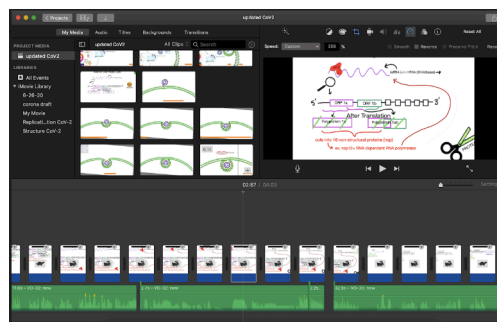


Figure 1. This is an example of who the animation was edited and made using iMovie.

III. RESULTS

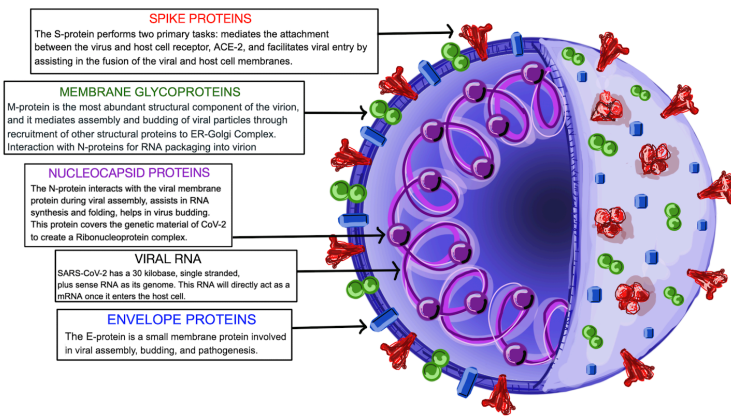


Figure 2. This is the model I created on the morphology of the four main structural proteins, the spike, membrane, nucleocapsid and envelop proteins which are used for many functions such as protecting the virus' RNA genome and assisting in viral entry into the host cell.

The virus has a genome of around 30 kilobase, which is a fairly large genome for a plus sense RNA virus. Since the genome is plus sense, this means it can directly be read by host ribosomes as a messenger RNA once it enters the cell. The genome is coated with a helical nucleocapsid protein (purple). The membrane glycoproteins (green) is the most abundant protein on the outside of the virus, it connects the membrane to the nucleic acid using its C-terminal domain which is what makes contact with nucleocapsid proteins.

In the spike proteins of CoV-2, the receptor binding domain is the most variable of this coronavirus compared to SARS. The virus' entry is driven by the interaction between spike with ACE2 and protease (TMPRSS2) that results in fusion or endocytosis. These proteases create two cleavages: 1. The spike protein is separated from the fusion domain of the spike. 2. Activates the fusogenic state of the protein. Cov-2 is different from the CoV-1 because even though they both interact with ACE2, 5 out of the 6 amino acids on the receptor-binding domain are different. Regardless coronaviruses efficiently interact with ACE2. CoV-2 also has acquired a polybasic cleavage site in its spike which increases viral transmissibility by enabling cleavage of other cellular proteases including TMPRSS2.

A. REPLICATION CYCLE

The entry of the virus into the host cell is driven by interactions between the spike protein and the host cell's ACE2 receptor, and with the help of cellular proteases, a proteolytic cleavage event will aid in the fusion of the virus and cell. Once in the cell the genetic material of the virus, the plus sense RNA will directly function as a messenger RNA that can be translated by the host's ribosomes. Open Reading Frames in the mRNA will be translated by host ribosome into large polyproteins 1a or 1ab. Then these polyproteins will be proteolyzed to produce up to 16 smaller non-structural proteins. They are being cut by two proteases called Papain like protease and main protease. One of these newly cut non-structural proteins is the nsp12 which will act as the RNA dependent RNA polymerase and will attach to the plus sense RNA and undergo replication to create a minus sense RNA or antisense. This will lead to two pathways involving the antisense strand. The first creates the genome of the viral offspring, by replicating the antisense strand back into the plus sense RNA. The second pathway uses discontinuous transcription. In which multiple sub genomic RNAs are transcribed again using RdRP (RNA dependent RNA polymerase). The sub genomic RNAs then enter the ER and to be further translated into structural or accessory viral proteins. After the viral proteins are made. The offspring's genome and Nucleocapsid proteins in the Golgi complex will meet with several other structural proteins to form small vesicles to be exported out of the cell through the process of exocytosis.

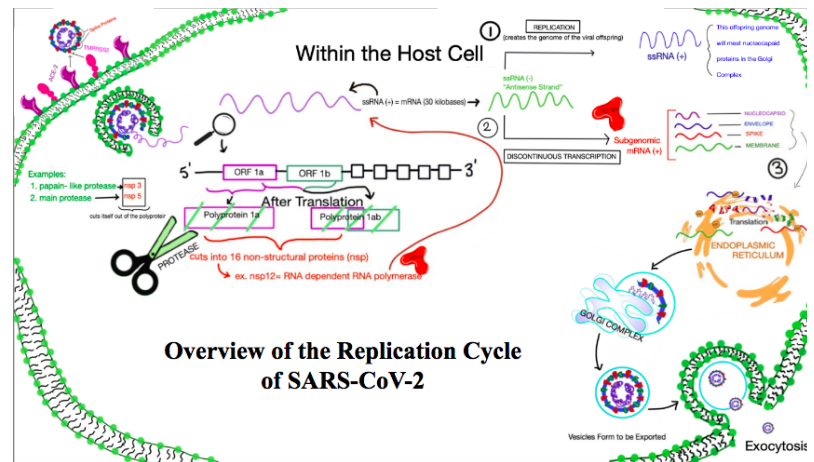


Figure 3. This figure also shows an overview of the replication cycle of SAR-CoV-2 within the host cell.

B. POTENTIAL DRUG TARGETS

One of the most researched drug target is the viral entry step. This targets the spike protein which is cleaved by the host's TMPRSS2 protease and binds to the host's angiotensin converting enzyme 2 (ACE-2). By targeting the receptor binding domain on the spike protein, the interaction between the spike protein and host cell would be halted and as a result the virus wouldn't be able to enter the cell.

The two proteases that are being targeted are the papain-like protease (non-structural protein 3) and main protease (non-structural protein 5). These proteases have an essential role in the replication cycle of the virus and inhibiting this site would eliminate the creation of other non-structural proteins.

A third drug target would be the RNA dependent RNA polymerase. This target is also another non-structural protein which aids in the process of discontinuous transcription. This polymerase also combines with other proteins to create a replicase complex which requires functional integration of the RNA polymerase, capping and proofreading activities. The drug that is being currently used called Remdesivir is actually an example of this drug target, because it acts a nucleotide analog to prevent the translation.

A lesser known drug target is the nucleocapsid protein (N protein). This protein plays a necessary part in the formation of the helical ribonucleoprotein during the packaging of the RNA genome of the viral- offspring. The N-terminal of the RNA-binding domain on the nucleocapsid protein is the possible drug target for the development of RNA- binding competitive inhibitors.

IV. DISCUSSION

This literature review comprehensively summarizes the basic biology behind SARS-CoV-2. There are still many ways to improve this animation depending on the audience. Since this video was targeting high school and intro level college students interested in virology, it doesn't include explanation on basic processes like transcription, translation, etc. but neither does it delve into structural biology of the proteins. I think it is important for science especially

in these unprecedented times to access a broader audience, to go beyond the scientific realm to integrate research into societies and breaks out down the complexity of research. While creating this video it was difficult to keep the video under 4-5 minutes which logistically is a major part of being able to keep the attention of the listener. Our next steps would be to be create an animation that explains the biochemistry of different structural proteins using 3D structures or focus more critically on explaining what the drugs aim to do.

V. ACKNOWLEDGEMENTS

This project was supported in part by the U.S Department of Energy, Office of Science, Office of Workforce Development for teachers and Scientists (WDTS) under the Science Undergraduate Laboratory Internships Program (SULI).

VI. REFERENCES

- Deng L, Li C, Zeng Q, Liu X, Li X, Zhang H, Hong Z, Xia J. Arbidol combined with LPV/r versus LPV/r alone against Corona Virus Disease 2019: A retrospective cohort study. *J Infect.* 2020. <https://doi.org/10.1016/j.jinf.2020.03.002>
- Kirchdoerfer, R.N., Ward, A.B. Structure of the SARS-CoV nsp12 polymerase bound to nsp7 and nsp8 co-factors. *Nat Commun* **10**, 2342 (2019). <https://doi.org/10.1038/s41467-019-10280-3>
- Graham, R. L., Sparks, J. S., Eckerle, L. D., Sims, A. C., & Denison, M. R. (2008). SARS coronavirus replicase proteins in pathogenesis. *Virus research*, *133*(1), 88–100. <https://doi.org/10.1016/j.virusres.2007.02.017>
- Zhang, L., Lin, D., Sun, X., Curth, U., Drosten, C., Sauerhering, L., ... & Hilgenfeld, R. (2020). Crystal structure of SARS-CoV-2 main protease provides a basis for design of improved α -ketoamide inhibitors. *Science*, *368*(6489), 409-412.
- Huang, Jiansheng, et al. "Pharmacological therapeutics targeting RNA-dependent RNA polymerase, proteinase and spike protein: from mechanistic studies to clinical trials for COVID-19." *Journal of Clinical Medicine* *9.4* (2020): 1131.
- Lan, J., Ge, J., Yu, J., Shan, S., Zhou, H., Fan, S., ... & Wang, X. (2020). Structure of the SARS-CoV-2

spike receptor-binding domain bound to the ACE2 receptor. *Nature*, 581(7807), 215-220.

Kang, S., Yang, M., Hong, Z., Zhang, L., Huang, Z., Chen, X., ... & Yan, Y. (2020). Crystal structure of SARS-CoV-2 nucleocapsid protein RNA binding

Hoffmann M, Kleine-Weber H, Schroeder S, et al. SARS-CoV-2 cell entry depends on ACE2 and TMPRSS2 and is blocked by a clinically proven protease inhibitor. *Cell*. 2020. <https://doi.org/10.1016/j.cell.2020.02.052>

domain reveals potential unique drug targeting sites. *Acta Pharmaceutica Sinica B*.

Tholstrup, J., Oddershede, L. B., & Sørensen, M. A. (2012). mRNA pseudoknot structures can act as ribosomal roadblocks. *Nucleic acids research*, 40(1), 303-313

Engineering Challenges of sPHENIX Inner HCAL Installation

Carter Godin, SULI Intern, School of Engineering, Rensselaer Polytechnic Institute, Troy, NY 12180
 Russell Feder, Chief Mechanical Engineer for sPHENIX, Brookhaven National Laboratory Upton, NY, 11973-5000

Abstract

sPHENIX is a detector project under development as an addition to the Relativistic Heavy Ion Collider at Brookhaven National Laboratory and is designed to detect interactions between subatomic particles following collisions using a set of concentric nested detector systems centered on an Aluminum-beryllium beam pipe through which heavy ions like gold are accelerated to speeds approaching that of light. The addition of this detector represents a huge step to the scientific utility of RHIC and a great benefit to the research capacity of the lab overall. Currently, the detector's design presents some unique structural support and installation challenges for each nested component. Notable examples include: installation of the Inner HCAL and the support design for the aluminum-beryllium beam pipe, given limited space for its supports and that the deflection of the beam pipe needs to be limited to 0.5mm at any location.. The plan for the Inner HCAL is to construct a 512 inch rail spanning the gap through the outer rings of the detector along which the inner HCAL will be slid into its installation position. The rail will be composed of two parts of unequal length joined through endplates to which they are welded, with each part being made of two I-Beams of equal cross-section affixed side-by-side to each end plate. The challenge of the project arising from consideration of appropriate sizing and patterning of the structural bolts at the joint, mounting hardware to secure the rail assembly to the pylons on which it sits, and sizing of the welds that hold the beams to their end plates to support the 16 ton load. Many engineering tools will be used, including shear force and bending moment diagrams, AutoCAD, FEA and others. All of these tools are very common, so experience with them will better my productivity and effectiveness as an engineer.

I. INTRODUCTION

sPHENIX is a new detector for the RHIC collider under construction at BNL. The detector consists of 7 integrated detector systems installed about a 1.5T superconducting magnet. The installation of these systems is challenging because the structures are heavy nested cylinders. The clearance between the cylinders is tight requiring careful planning backed by design and analysis of the structures using 3D design and analysis software. One example of this is the design of the installation slider-beams and lifting fixtures for the Inner HCAL detector. The iHCAL barrel weighs 16 tons and needs to be slid along a 20-foot beam with an allowable deflection of 1/2 inch. This poster presents work done this summer to design the slider-beam, lifting fixture for the slide-beam installation and a concept for moving the iHCAL barrel with a winch drive.

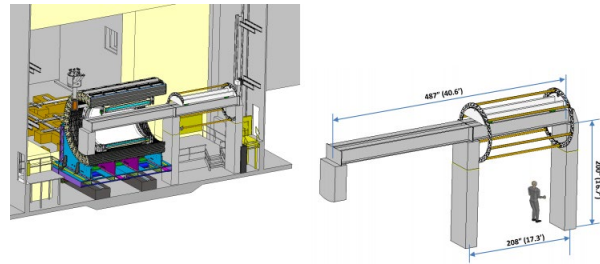


Fig. 1: View of sPHENIX in building 1008 assembly hall highlighting inner HCAL installation. Pictured are the splice beam and supporting stanchions along which the installation sled (also pictured) will slide.

II. LONG SPLICE BEAM DESIGN

Using an I-beam section and multiple-beam configuration that had already been chosen by the professional installation design team, hand calculations were performed to generate data necessary to construct a Shear Force Diagram (SFD) and a Bending Moment Diagram (BMD). These diagrams provide a baseline insight into locations of high or maximum stress and high or maximum deflection against which the results of more precise Finite Element Analysis (FEA) would be compared. The FEA provides a proof of concept to ensure that the team's desired fasteners used to connect the two beam sections would be able to stand the pressure generated under self-weight and applied load. The following equations give the deflection of a two-ends-fixed symmetric beam under a load distributed over its length, and its deflection under a concentrated load located at half its length.

Eqn. 1: $y = \frac{-w}{24EI} (x^4 - 2Lx^3 + L^3x)$ (Deflection under self-weight)

Eqn. 2: $y = \frac{Pb}{6EIL} (x^3 - (L^2 - b^2)x)$ (Deflection due to point load)

Eqn. 3: $y = \frac{-w}{24EI} (x^4 - 2Lx^3 + L^3x) + \frac{Pb}{6EIL} (x^3 - (L^2 - b^2)x)$ (Total deflection equation)

Terms	
x = distance from leftmost edge of splice beam (inches)	w = magnitude of distributed load of self-weight (lbf/inch)
P = magnitude of concentrated load from iHCAL (lbf)	L = length of beam (inches)
E = Elastic modulus of Steel (psi)	I = Section moment of inertia (in ⁴)
b = distance of concentrated load (P) from rightmost edge (inches)	y = Deflection of beam from horizontal

Using the above equations it was found that the maximum deflection of the splice beam during installation should occur at half the length of the beam and should be no more than 0.349 inches from the horizontal assuming pinned-pinned boundary conditions; a quantity in line with desired constraints. Following this, a study was conducted of the proposed design using FEA which used fixed-fixed boundary

conditions, resulting in a lesser and still acceptable maximum deflection of 0.107in as shown in Fig. 3 ..

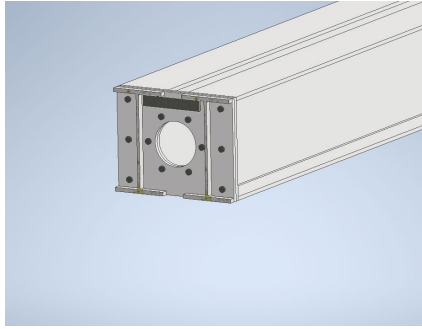


Fig. 2: Closeup view of connecting bolt pattern at joint of installation splice beam.

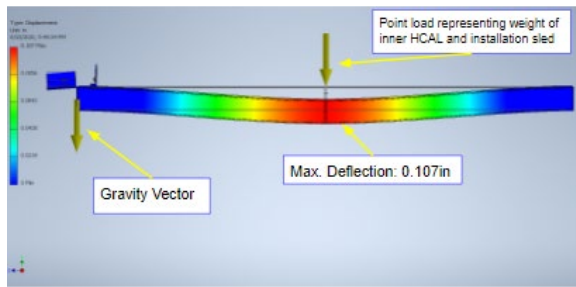


Fig. 3: Heat map of FEA result for full-length splice beam deflection with iHCAL weight load centered and including self-weight.

To achieve this result using a conjunction of two sections of the splice beam, a bolt pattern and quantity were individually determined to meet the given deflection specification. Dividing the total shear force at the point of greatest load as determined by the aforementioned shear force diagram yielded an average shear force load per bolt. Dividing this figure by the cross-sectional area of each bolt yielded the shear load per bolt. Using the result of Eqn. 4 along with the previously calculated shear per bolt as parameters in Eqn. 5, the total normal stress borne by each bolt was calculated and, in consideration with a desired factor of safety of 3, was compared against the critical strength of the desired bolt type (A325) and it was found that 4 of these bolts at minimum would be necessary. For reasons of redundancy and safety, a symmetric and low-cost pattern shown above was chosen after also taking installation tool clearances into account.

Eqn. 4: $\sigma_{Bend} = \frac{Mc}{I}$

Eqn. 5: $\sigma_{MaxTotal} = \sqrt{\sigma_{Bend}^2 + 3\tau^2}$

Terms	
$\sigma_{MaxTotal}$ = Total Normal Stress	σ_{Bend} = Normal Stress due to bending
τ = Total Shear Stress	

Subsequently, a CAD assembly of the installation splice beam was created which included a bolted connection at the joint where its two sections connected. Following this, Finite Element Analysis (FEA) was implemented electronically

through AutoCAD Inventor’s analysis suite to analytically determine points of high stress and deflection.

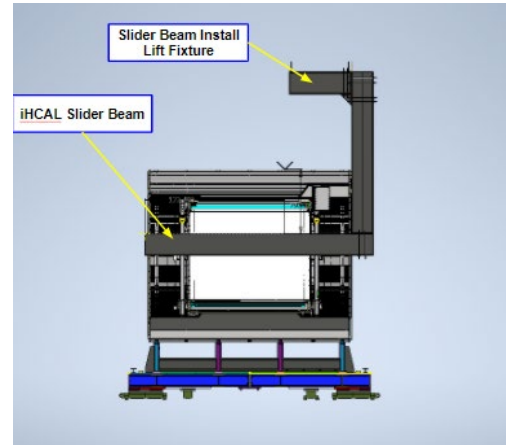


Fig. 4: Cross-sectional view of sPHENIX with proposed lift fixture inserted.

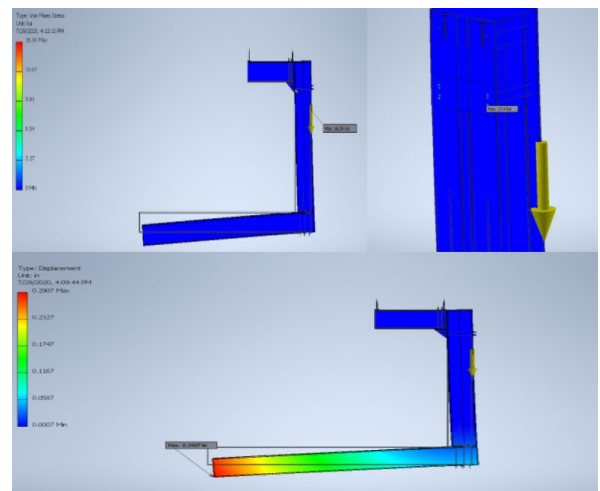


Fig. 5: Heat maps for FEA results on proposed lift fixture under self-weight (quantities exaggerated for clarity). Top-right view

III. LIFT FIXTURE DESIGN

Before the iHCAL installation sled can be mounted to the rollers on which it will ride along the splice beam into the installation position, said beam must itself be installed. To do this, a C-shaped lift fixture was proposed as a solution to this challenge.

A. Selecting A Beam Section

For reasons of cost, the first beam section analyzed was the same dual-beam design used in the installation splice beam. The sections are large, but it was thought that it may be more cost effective to order a single large section in bulk rather than many different sections in lesser volumes. Also, this larger section moment of inertia would provide better rigidity and a lesser deflection for this sensitive task.

B. Reinforcements and Lift Points

Using the cantilever approximation, it was found that an un-reinforced version of this fixture would exceed maximum deflection, so a small triangular reinforcement was added to the CAD model for FEA testing with the final and satisfactory results for displacement and stress being displayed in Fig. 5. Following successful load testing, the horizontal and vertical locations of the center of gravity of the fixture were calculated. Lift points for the installation crane were each

placed 6ft symmetrically about the horizontal location of the center of gravity for ease of rigging and better control of the fixture. It was also found that the cost-optimizing placement of the lift-points led to a net moment about the center of gravity of approximately 52,000 lb*in, which could be countered with a 302lb counterweight at the end of the splice beam.

IV. FUTURE WORK

Following the installation of the splice beam and all other pre-installation hardware, the iHCAL along with its sled will be slid along the installation splice beam and fitted to the magnet of sPHENIX. To move them, the configuration pictured in Fig. 6 is proposed though more detailed modeling and development needs to be done following my own work to ready the proposal for approval.

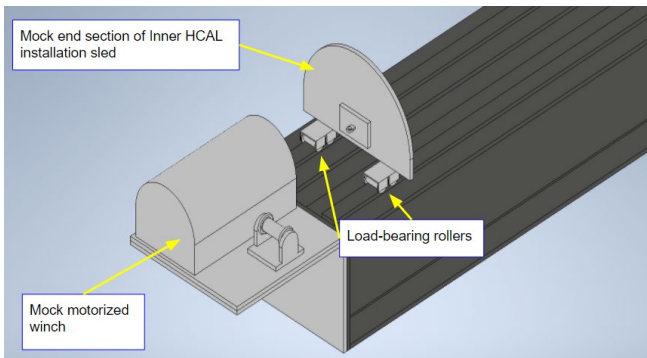


Fig. 6: Trimetric view of proposed winch, support, roller, and sled configuration.

Additionally, future work should continue from my own to develop a more detailed plan to fit the installation splice beam to the stanchions on which it should sit. This and the above represent work only in the design stage of the engineering process, and would need to be followed by much review and revision and eventually by fabrication and implementation.

ACKNOWLEDGMENT

I would like to acknowledge the help of my mentor Russell Feder in both making this great opportunity possible and helping me along the way. I would also like to acknowledge the folks at the DOE, BNL and in the BNL office of educational programs that make this program possible. I believe it will make all the difference for me professionally going forward and cannot thank you all enough.

REFERENCES

- [1] Beer, Ferdinand P., et al. *Mechanics of Materials*. 7e ed., McGraw-Hill Education, 2020.
- [2] BNL Engineering Team, Inner HCAL Installation Presentation, BNL 2019

Quantum entanglement and non-locality measures at high energy colliders

Wenjie Gong¹, Ganesh Parida², and Raju Venugopalan³

¹*Department of Physics, Harvard University, Cambridge, Massachusetts 02138*

²*Department of Physics, University of Wisconsin-Madison, Madison, Wisconsin 53706*

³*Department of Physics, Brookhaven National Laboratory, Upton, New York 11973*

Abstract

Though entanglement and Einstein-Podolsky-Rosen (EPR)-type experiments are studied extensively in quantum optics, entanglement and locality are more difficult to evaluate in the less controlled environment of high energy colliders. Here, we present theory for detecting spin entanglement and non-locality in the products of high energy collisions with a correlation function measurement. We analytically derive the two-particle spin correlation function for a general two-particle spin- $\frac{1}{2}$ density matrix. We show that a rotationally invariant correlation function implies a violation of the related Clauser-Horne-Shimony-Holt (CHSH) inequality, indicating incompatibility with any hidden variable theory. We further demonstrate that an amplitude greater than $\frac{1}{2}$ of the cosine term of a rotationally invariant correlation function implies spin entanglement. We apply these criteria to multifermionic ensembles of coherent non-interacting spins, incoherent non-interacting spins, and partially indistinguishable singlet pairs. Our work indicates that correlation function measurements can detect entanglement and non-locality in the matter produced at high energy colliders.

Contents

1	Introduction	2
2	General formulation	5
3	Coherent non-interacting spins	10
4	Incoherent non-interacting spins	12
5	Partially indistinguishable singlets	13
6	Discussion and conclusions	15
7	Acknowledgements	17
A	Reduction of CHSH inequality to one parameter	19
B	Verification of entanglement fidelity	21

1 Introduction

In 1935, Einstein, Podolsky, and Rosen (EPR) published a formative manuscript questioning the veracity of a quantum mechanical description of reality [1], thus instigating a sharp debate regarding the philosophical tenets of quantum mechanics. EPR specifically struggled with the non-locality admitted by quantum mechanics; a measurement of one part of a quantum mechanical system may have an immediate effect on the reality of another part of the system, despite spatial separation of the two parts. In Bohm's familiar variant of the EPR thought experiment, he noted that the entangled spin singlet state exemplifies this non-locality. He proposed to measure the spins of two particles forming an entangled spin singlet along respective axes $\hat{\mathbf{a}}$ and $\hat{\mathbf{b}}$. If $\hat{\mathbf{a}} = \hat{\mathbf{b}}$, then the spin measurements of the two

particles should be anti-correlated with complete certainty; however, if $\hat{\mathbf{a}} \perp \hat{\mathbf{b}}$, then the second measurement should have equal probability of spin-up or spin-down, irrespective of the first measurement. It seems that at the moment of the first measurement, state information has traveled instantaneously from the first particle to the second. In quantum mechanics, the correlation of these two measurements, as defined by their product, is given by:

$$E(\hat{\mathbf{a}}, \hat{\mathbf{b}}) = \langle \psi | \hat{\mathbf{a}} \cdot \sigma_1 \hat{\mathbf{b}} \cdot \sigma_2 | \psi \rangle \quad (1.1)$$

Note that the Pauli operator σ_i acts on particle i , and we denote spin-up as 1 and spin-down as -1.

Local hidden variable theories (LHVT), as suggested by EPR, attempt to reconcile the predictions of quantum mechanics with local realism. LHVT indicates the existence of local "hidden variables" that, if accessed, could determine the state of the system with complete certainty in a manner consistent with quantum mechanical observations. For instance, in Bohm's variant, each of the two particles would carry a hidden variable that dictates whether to present spin-up or spin-down when measured. In LHVT, the correlation between the measurements would then be:

$$E(\hat{\mathbf{a}}, \hat{\mathbf{b}}) = \int A(\hat{\mathbf{a}}, \lambda) B(\hat{\mathbf{b}}, \lambda) \rho(\lambda) d\lambda \quad (1.2)$$

We define A as the result of a spin measurement on the first particle along $\hat{\mathbf{a}}$, B as the result of a spin measurement on the second particle along $\hat{\mathbf{b}}$, λ as a hidden variable, and $\rho(\lambda)$ the distribution of λ . A and B take the values of either -1, 0, or 1. A class of inequalities known as Bell-type inequalities limit measurement correlations derived from LHVT. Specifically, the Clauser-Horne-Shimony-Holt (CHSH) inequality places a bound on correlations of the type in Eq. 1.2 as follows:

$$|E(\hat{\mathbf{a}}, \hat{\mathbf{b}}) - E(\hat{\mathbf{a}}, \hat{\mathbf{b}}')| + |E(\hat{\mathbf{a}}', \hat{\mathbf{b}}) + E(\hat{\mathbf{a}}', \hat{\mathbf{b}}')| \leq 2 \quad (1.3)$$

Thus, observations that violate Eq. 1.3 are incompatible with LHVT, indicating non-local behavior ostensibly resultant from quantum mechanics.

Since the 1970s, extensive experimental testing of Bell-type inequalities, as well as exploration of quantum entanglement, has occurred in atomic, molecular, and optical physics laboratories. Experiments have shown consistent violation of Bell-type inequalities, despite concerted efforts to minimize flaws in experimental design, or so-called "loopholes," that may controvert the validity of the results.[2][3][4] Meanwhile, progress in the preparation, verification, and characterization of entangled quantum states in various atomic systems has facilitated the implementation of entanglement as a resource in quantum information, computation, and cryptography.[5][6] It is important to note here that while pure entangled bipartite states such as the spin singlet do generate non-local effects, non-locality and entanglement are not, in general, equivalent.[7] For instance, an entangled bipartite mixed state may fail to violate the the CHSH inequality (Eq. 1.3).

While optical platforms use lasers to conduct controlled state preparation and rotation, high energy colliders engender a less orderly environment; matter produced in high energy collisions is characterized exclusively by passive measurements performed at the detector level, making entanglement and locality more difficult to assess. Here, we propose a theory for detecting entanglement and non-locality in the products of collisions occurring at sites such as the Relativistic Heavy Ion Collider (RHIC) and the future Electron-Ion Collider (EIC) at Brookhaven National Laboratory (BNL). We consider weak decays such as $e^+e^- \rightarrow \mu^+\mu^-$ and $\Lambda\bar{\Lambda} \rightarrow \pi^-p\pi^+\bar{p}$, in which the linear momentum direction a daughter particle can be related to the spin polarization of the parent particle.[8][9] For instance, in $\Lambda \rightarrow \pi^- + p$, if the proton decays in a direction $\hat{\mathbf{a}}$, then the spin polarization of Λ is given by $\mathbf{P} = \alpha\hat{\mathbf{a}}$ with $\alpha \approx 0.642$. This type of self-analyzing decay yields information regarding the spin state of the final fermions e^+e^- or $\Lambda\bar{\Lambda}$ without the need to conduct active spin measurements. We

suggest the measurement of a two-particle correlation function defined as follows:

$$\frac{\langle n_{\hat{\mathbf{a}}}, n_{\hat{\mathbf{b}}} \rangle}{\langle n_{\hat{\mathbf{a}}} \rangle \langle n_{\hat{\mathbf{b}}} \rangle} = \frac{P(\hat{\mathbf{a}}, \hat{\mathbf{b}})}{P(\hat{\mathbf{a}})P(\hat{\mathbf{b}})} \quad (1.4)$$

$n_{\hat{\mathbf{a}}}$ indicates the number of daughter particles with momentum direction $\hat{\mathbf{a}}$ measured in a single event. We average over an ensemble of events, indicated by $\langle \dots \rangle$. The pair of counts in the numerator are taken from the same event, the counts in the denominator from different events. This ratio is equivalent to the joint probability of measuring particles in directions $\hat{\mathbf{a}}$ and $\hat{\mathbf{b}}$ divided by the individual probabilities of measuring a particle in direction $\hat{\mathbf{a}}$ and in direction $\hat{\mathbf{b}}$. In what follows, we derive features of the correlation function (Eq. 1.4) that indicate either entanglement or non-locality of final state spin ensemble. We then apply our critical lens to the correlation functions of three instructive spin ensembles: coherent non-interacting spins, incoherent non-interacting spins, and partially indistinguishable singlets

2 General formulation

We first derive a theorem and related corollaries that encompass how entanglement and non-locality manifest in the correlation function. For simplicity, we consider spins in the $x-z$ plane of the Bloch sphere. We further assume that $|\mathbf{P}| = 1$, indicating perfect discrimination between spin-up and spin-down. In this manner, a daughter particle decaying along $\hat{\mathbf{a}}$ signifies a parent spin state of spin-up along $\hat{\mathbf{a}}$. We finally assume that the detection of a daughter particle along $\hat{\mathbf{a}}$ can be modeled by a projective measurement of spin-up along $\hat{\mathbf{a}}$ of the parent spin state.

We consider the general spin state of two spin- $\frac{1}{2}$ particles. This can be represented by a density matrix ρ_{ab} in 2×2 Hilbert space. We choose to write ρ_{ab} in the Bell basis, given by the following basis states:

$$|B_1\rangle = \frac{|00\rangle + |11\rangle}{\sqrt{2}} \quad (2.1)$$

$$|B_2\rangle = \frac{|00\rangle - |11\rangle}{\sqrt{2}} \quad (2.2)$$

$$|B_3\rangle = \frac{|01\rangle + |10\rangle}{\sqrt{2}} \quad (2.3)$$

$$|B_4\rangle = \frac{|01\rangle - |10\rangle}{\sqrt{2}} \quad (2.4)$$

We have adopted notation from quantum information to indicate $|0\rangle$ as spin-up along the z -axis and $|1\rangle$ as spin-down along the z -axis. We therefore obtain:

$$\rho_{ab} = \sum_{i=1}^4 \sum_{j=1}^4 \lambda_{ij} |B_i\rangle \langle B_j| \quad (2.5)$$

As we consider spins in the $x - z$ plane, each λ_{ij} is real.

We can now compute the two-particle correlation function (Eq. 1.4) for general ρ_{ab} given by Eq. 2.5. First, operating under the assumptions described previously, a general state of spin-up along $\hat{\mathbf{a}}$ is written as follows:

$$|\theta_a\rangle = \cos\left(\frac{\theta_a}{2}\right) |0\rangle + \sin\left(\frac{\theta_a}{2}\right) |1\rangle \quad (2.6)$$

Note that in this formalism, spin-down along the axis given by $\hat{\mathbf{a}}$ is given as:

$$|\theta_a + \pi\rangle = -\sin\left(\frac{\theta_a}{2}\right) |0\rangle + \cos\left(\frac{\theta_a}{2}\right) |1\rangle \quad (2.7)$$

Representing daughter particle detection as a projective measurement of spin, we first calculate the joint two-particle probability $P(\hat{\mathbf{a}}, \hat{\mathbf{b}})$ as follows:

$$\begin{aligned} P(\hat{\mathbf{a}}, \hat{\mathbf{b}}) &= \text{Tr}(|\theta_a\rangle \langle \theta_b| \langle \theta_a| \langle \theta_b| \rho_{ab}) \quad (2.8) \\ &= \frac{1}{4} (1 + (\lambda_{12} + \lambda_{21} + \lambda_{34} + \lambda_{43}) \cos(\theta_a) + (\lambda_{12} + \lambda_{21} - \lambda_{34} - \lambda_{43}) \cos(\theta_b) \\ &\quad + (\lambda_{13} + \lambda_{31} - \lambda_{24} - \lambda_{42}) \sin(\theta_a) + (\lambda_{13} + \lambda_{31} + \lambda_{24} + \lambda_{42}) \sin(\theta_b) \\ &\quad + (\lambda_{11} - \lambda_{44}) \cos(\theta_a - \theta_b) + (\lambda_{22} - \lambda_{33}) \cos(\theta_a + \theta_b) \end{aligned}$$

$$+ (\lambda_{41} + \lambda_{14}) \sin(\theta_b - \theta_a) + (\lambda_{23} + \lambda_{32}) \sin(\theta_a + \theta_b) \quad (2.9)$$

In the second line, we have substituted Eq. 2.5 and Eq. 2.6 into Eq. 2.8. To calculate the single-particle probability $P(\hat{\mathbf{a}})$, we first need to find the single-particle reduced density matrix:

$$\rho_a = \text{Tr}_b(\rho_{ab}) \quad (2.10)$$

$$\begin{aligned} &= \frac{1}{2} I_a + (\lambda_{12} + \lambda_{21} + \lambda_{34} + \lambda_{43}) \frac{|0\rangle \langle 0| - |1\rangle \langle 1|}{2} \\ &+ (\lambda_{23} - \lambda_{32} + \lambda_{41} - \lambda_{14}) \frac{|0\rangle \langle 1| - |1\rangle \langle 0|}{2} \\ &+ (\lambda_{13} + \lambda_{31} - \lambda_{24} - \lambda_{42}) \frac{|0\rangle \langle 1| + |1\rangle \langle 0|}{2} \end{aligned} \quad (2.11)$$

Then, following the same logic as before:

$$P(\hat{\mathbf{a}}) = \text{Tr}(|\theta_a\rangle \langle \theta_a| \rho_a) \quad (2.12)$$

$$= \frac{1}{2} + (\lambda_{12} + \lambda_{21} + \lambda_{34} + \lambda_{43}) \cos(\theta_a) + (\lambda_{13} + \lambda_{31} - \lambda_{24} - \lambda_{42}) \sin(\theta_a) \quad (2.13)$$

In order for the correlation function Eq. 1.4 to be rotationally invariant, we require both the two-particle (Eq. 2.9) and single-particle (Eq. 2.13) probabilities to depend only on $\theta_a - \theta_b$. We further restrict the two-particle probability to be symmetric with respect to particles a and b such that $P(\hat{\mathbf{a}}, \hat{\mathbf{b}}) = P(\hat{\mathbf{b}}, \hat{\mathbf{a}})$. This limits λ_{ij} , $i \neq j$, as follows:

$$\lambda_{ij} = -\lambda_{ji} \quad (2.14)$$

$$\implies \lambda_{ij} = \lambda_{ji} = 0 \quad (2.15)$$

In the second line, we use that ρ_{ab} is Hermitian and real, giving $\lambda_{ij} = \lambda_{ji}$. Combined with $\lambda_{ij} = -\lambda_{ji}$, we must have that the off-diagonal terms are identically zero. We also require

for rotational invariance:

$$\lambda_{22} = \lambda_{33} \quad (2.16)$$

This symmetric, rotationally invariant correlation function then takes the form:

$$\frac{P(\hat{\mathbf{a}}, \hat{\mathbf{b}})}{P(\hat{\mathbf{a}})P(\hat{\mathbf{b}})} = 1 + (\lambda_{11} - \lambda_{44}) \cos(\theta_a - \theta_b) \quad (2.17)$$

This analysis leads us to our first theorem.

Theorem 2.1 *A symmetric rotationally invariant correlation function implies that the measured state ρ_{ab} is diagonal in the Bell basis, with $\lambda_{22} = \lambda_{33}$.*

We now examine Eq. 2.17 in the context of the generalized CHSH inequality for two-particle spin- $\frac{1}{2}$ states diagonal in the Bell basis:[10][11]

$$|E(\hat{\mathbf{a}}, \hat{\mathbf{b}}) - E(\hat{\mathbf{a}}, \hat{\mathbf{b}}')| + |E(\hat{\mathbf{a}}', \hat{\mathbf{b}}') + E(\hat{\mathbf{a}}', \hat{\mathbf{b}})| \leq 2(|\lambda_{44} - \lambda_{11}| + |\lambda_{33} - \lambda_{22}|) \quad (2.18)$$

Assuming rotational invariance, i.e. $E(\hat{\mathbf{a}}, \hat{\mathbf{b}}) = E(\theta_a - \theta_b) \equiv E(\theta_{ab})$, and coplanar $\hat{\mathbf{a}}, \hat{\mathbf{a}}', \hat{\mathbf{b}}, \hat{\mathbf{b}}'$, we derive from Eq. 2.18 the following one-parameter inequality:¹

$$\begin{cases} |E(\theta_{ab})| \leq (1 - \frac{2|\theta_{ab}|}{\pi})(|\lambda_{44} - \lambda_{11}| + |\lambda_{33} - \lambda_{22}|) & \text{for } |\theta_{ab}| \leq \frac{\pi}{2} \\ |E(\theta_{ab})| \leq (1 - \frac{2(\pi - |\theta_{ab}|)}{\pi})(|\lambda_4 - \lambda_1| + |\lambda_3 - \lambda_2|) & \text{for } \pi/2 \leq |\theta_{ab}| \leq \pi \end{cases} \quad (2.19)$$

The spin correlation $E(\theta_{ab})$ is defined by the expected value of the product of the measured spins along $\hat{\mathbf{a}}$ and $\hat{\mathbf{b}}$ (Eq. 1.1, Eq. 1.2). As such, we can obtain $E(\theta_{ab})$ from the numerator of the two-particle correlation function:

$$E(\theta_{ab}) = P(\hat{\mathbf{a}}, \hat{\mathbf{b}}) + P(-\hat{\mathbf{a}}, -\hat{\mathbf{b}}) - P(-\hat{\mathbf{a}}, \hat{\mathbf{b}}) - P(\hat{\mathbf{a}}, -\hat{\mathbf{b}}) \quad (2.20)$$

¹Derivation given in Appendix A

Using Eq. 2.9 and noting that measuring $-\hat{\mathbf{a}}$ is equivalent to measuring $\theta_a + \pi$, we have the following spin correlation for a symmetric rotationally invariant correlation function:

$$E(\theta_{ab}) = (\lambda_{11} - \lambda_{44}) \cos(\theta_{ab}) \quad (2.21)$$

For Eq. 2.21 to violate Eq. 2.19, we write the following condition:

$$\left| \frac{dE(\theta_{ab})}{d \cos(\theta_{ab})} \right|_{\cos(\theta_{ab})=0} > \left| \frac{d}{d \cos(\theta_{ab})} \left(1 - \frac{2\theta_{ab}}{\pi}\right) (|\lambda_{44} - \lambda_{11}| + |\lambda_{33} - \lambda_{22}|) \right|_{\cos(\theta_{ab})=0} \quad (2.22)$$

Computing the derivatives, the condition reads:

$$|\lambda_{11} - \lambda_{44}| > \frac{2}{\pi} (|\lambda_{44} - \lambda_{11}| + |\lambda_{33} - \lambda_{22}|) \quad (2.23)$$

$$= \frac{2}{\pi} |\lambda_{44} - \lambda_{11}| \quad (2.24)$$

In the second line, we have used $\lambda_{22} = \lambda_{33}$ from Theorem 2.1. As $\frac{2}{\pi} < 1$, this condition is always satisfied, leading us to our first corollary.

Corollary 2.1.1 *A symmetric rotationally invariant correlation function implies that the measured state ρ_{ab} violates its related CHSH inequality, indicating incompatibility with LHVT.*

We finally examine Eq. 2.17 using the notion of entanglement fidelities. We define an entanglement fidelity \mathcal{F}_i corresponding to each Bell state $|B_i\rangle$ as follows:

$$\mathcal{F}_i = \langle B_i | \rho_{ab} | B_i \rangle \quad (2.25)$$

It can be shown that if any $\mathcal{F}_i > \frac{1}{2}$, the state ρ_{ab} is entangled.² We see from our formulation of ρ_{ab} in Eq. 2.5 that $\mathcal{F}_i = \lambda_{ii}$. We note that λ_{ii} figures into Eq. 2.17 in the coefficient of the $\cos(\theta_{ab})$ term, $\lambda_{11} - \lambda_{44}$. This brings us to our last corollary.

²Derivation given in Appendix B

Corollary 2.1.2 *If the magnitude of the coefficient of $\cos(\theta_{ab})$ in a symmetric rotationally invariant correlation function is greater than $\frac{1}{2}$, then the measured state ρ_{ab} is entangled.*

3 Coherent non-interacting spins

Theorem 2.1 provides us with features indicative of entanglement or non-locality in a measured correlation function (Eq. 1.4). For demonstration, we now apply Theorem 2.1 to an ensemble of N particles with coherent non-interacting spin states. To be precise, coherence indicates that all of fermions have spins in a single pure state. Non-interacting signifies that none of the fermions share entangled spin states.

To model this ensemble, we consider a system of N indistinguishable fermions residing in N separate energy levels. Let ϕ^α Be the single-particle orthonormal spatial wavefunction for energy $\alpha \in [1, \dots, N]$. The complete, anti-symmetrized spatial wavefunction is given by the Slater determinant (or linear combination of Slater determinants):

$$\Phi(\mathbf{x}_1, \mathbf{x}_2, \dots, \mathbf{x}_N) = \frac{1}{\sqrt{N!}} \det \begin{vmatrix} \phi^1(\mathbf{x}_1) & \phi^2(\mathbf{x}_1) & \dots & \phi^N(\mathbf{x}_1) \\ \phi^1(\mathbf{x}_2) & \phi^2(\mathbf{x}_2) & \dots & \phi^N(\mathbf{x}_2) \\ \vdots & \vdots & \vdots & \vdots \\ \phi^1(\mathbf{x}_N) & \phi^2(\mathbf{x}_N) & \dots & \phi^N(\mathbf{x}_N) \end{vmatrix} \quad (3.1)$$

We write the entire state of our N particle ensemble as:

$$|\Psi\rangle = |\Phi\rangle \otimes |s_N\rangle \quad (3.2)$$

$|\Phi\rangle$ is given by Eq. 3.1 and $|s_N\rangle$ indicates the spin wavefunction. As $|\Phi\rangle$ is antisymmetric, $|s_N\rangle$ must be symmetric to abide by Fermi-Dirac statistics. Working in the z basis, we write:

$$|s_N\rangle = \frac{1}{\sqrt{2^N}} \sum_{w=0}^{2^N-1} |w\rangle \quad (3.3)$$

$$= \frac{|0\rangle_1 + |1\rangle_1}{\sqrt{2}} \otimes \frac{|0\rangle_2 + |1\rangle_2}{\sqrt{2}} \otimes \dots \otimes \frac{|0\rangle_N + |1\rangle_N}{\sqrt{2}} \quad (3.4)$$

Here, w , in binary, counts every possible spin configuration in the z basis. We focus on the spin state of the system, therefore tracing over spatial degrees of freedom in Eq. 3.2.

$$\rho_S = \text{Tr}_\Phi(|\Psi\rangle\langle\Psi|) = |s_N\rangle\langle s_N| \quad (3.5)$$

We can now compute the correlation function, Eq. 1.4. First, we find the two-particle probability:

$$\rho_{12} = \text{Tr}_{N-2}(\rho_S) = \frac{|0\rangle_1 + |1\rangle_1}{\sqrt{2}} \otimes \frac{|0\rangle_2 + |1\rangle_2}{\sqrt{2}} \otimes \frac{\langle 0|_1 + \langle 1|_1}{\sqrt{2}} \otimes \frac{\langle 0|_2 + \langle 1|_2}{\sqrt{2}} \quad (3.6)$$

$$\begin{aligned} P(\hat{\mathbf{a}}, \hat{\mathbf{b}}) &= \text{Tr}(|\theta_a\rangle\langle\theta_b| \langle\theta_a| \langle\theta_b| \rho_{12}) \\ &= \left(\frac{\cos(\frac{\theta_a}{2}) + \sin(\frac{\theta_a}{2})}{\sqrt{2}} \right)^2 \left(\frac{\cos(\frac{\theta_b}{2}) + \sin(\frac{\theta_b}{2})}{\sqrt{2}} \right)^2 \end{aligned} \quad (3.7)$$

We then compute the single-particle probability:

$$\rho_1 = \text{Tr}_2(\rho_{12}) = \frac{|0\rangle_1 + |1\rangle_1}{\sqrt{2}} \otimes \frac{\langle 0|_1 + \langle 1|_1}{\sqrt{2}} \quad (3.8)$$

$$P(\hat{\mathbf{a}}) = \text{Tr}(|\theta_a\rangle\langle\theta_a| \rho_1) = \left(\frac{\cos(\frac{\theta_a}{2}) + \sin(\frac{\theta_a}{2})}{\sqrt{2}} \right)^2 \quad (3.9)$$

Together, Eqs. 3.7 and 3.9 show that the two-particle correlation function for this ensemble is given by:

$$\frac{P(\hat{\mathbf{a}}, \hat{\mathbf{b}})}{P(\hat{\mathbf{a}})P(\hat{\mathbf{b}})} = 1 \quad (3.10)$$

Furthermore, we deduce from Eq. 3.7 that the correlation function is not rotationally invariant, i.e. dependent only on $\theta_a - \theta_b$. Therefore, we cannot use Theorem 2.1 to make any claims about the entanglement or locality of this state. This is reasonable; physically,

two-particle substates of this system should not exhibit entanglement or non-locality.

4 Incoherent non-interacting spins

We now examine an incoherent ensemble of N non-interacting spin states. Incoherence indicates that the fermions have spins in a mixed state with no preferred basis. We model the system as in Section 3, considering N indistinguishable fermions occupying N separate energy levels. However, rather than defining a definite spin wave function $|s_N\rangle$ and a pure spin state ρ_S , we rewrite Eq. 3.5:

$$\rho_S = \frac{1}{2\pi} \int_0^{2\pi} \frac{|\theta\rangle_1 + |\theta + \pi\rangle_1}{\sqrt{2}} \otimes \dots \otimes \frac{|\theta\rangle_N + |\theta + \pi\rangle_N}{\sqrt{2}} \otimes \frac{\langle\theta|_1 + \langle\theta + \pi|_1}{\sqrt{2}} \otimes \dots \otimes \frac{\langle\theta|_N + \langle\theta + \pi|_N}{\sqrt{2}} d\theta \quad (4.1)$$

Using Eq. 4.1, we now follow the same procedure as conducted previously to compute the correlation function. The two-particle probability is given by:

$$\begin{aligned} \rho_{12} &= \text{Tr}_{N-2}(\rho_S) \\ &= \frac{1}{2\pi} \int_0^{2\pi} \frac{|\theta\rangle_1 + |\theta + \pi\rangle_1}{\sqrt{2}} \otimes \dots \otimes \frac{|\theta\rangle_N + |\theta + \pi\rangle_N}{\sqrt{2}} \otimes \frac{\langle\theta|_1 + \langle\theta + \pi|_1}{\sqrt{2}} \otimes \dots \otimes \frac{\langle\theta|_N + \langle\theta + \pi|_N}{\sqrt{2}} d\theta \end{aligned} \quad (4.2)$$

$$P(\hat{\mathbf{a}}, \hat{\mathbf{b}}) = \text{Tr}(|\theta_a\rangle |\theta_b\rangle \langle\theta_a| \langle\theta_b| \rho_{12}) = \frac{1}{4} + \frac{1}{8} \cos(\theta_a - \theta_b) \quad (4.3)$$

We then find the single-particle probability as:

$$\rho_1 = \text{Tr}_2(\rho_{12}) = \frac{1}{2\pi} \int_0^{2\pi} \frac{|\theta\rangle_1 + |\theta + \pi\rangle_1}{\sqrt{2}} \otimes \frac{\langle\theta|_1 + \langle\theta + \pi|_1}{\sqrt{2}} d\theta \quad (4.4)$$

$$P(\hat{\mathbf{a}}) = \text{Tr}(|\theta_a\rangle \langle\theta_a| \rho_1) = \frac{1}{2} \quad (4.5)$$

We see that the correlation function for a two-particle substate of an incoherent ensemble of

non-interacting spin states is written:

$$\frac{P(\hat{\mathbf{a}}, \hat{\mathbf{b}})}{P(\hat{\mathbf{a}})P(\hat{\mathbf{b}})} = 1 + \frac{1}{2} \cos(\theta_a - \theta_b) \quad (4.6)$$

From Eqs. 4.3 and 4.5, we deduce that the correlation function is indeed dependent only on $\theta_a - \theta_b$, which is confirmed by the form of Eq. 4.6. From here, Theorem 2.1, Corollary 2.1.1 tells us that any two particle state from this ensemble violates its related CHSH inequality and thus cannot be formulated using LHVT. As the magnitude of the cosine term is equal to $\frac{1}{2}$, we cannot make any definite conclusions regarding entanglement from Corollary 2.1.2. This aligns with our physical intuition: while the mixed nature of the state may engender effects incompatible with LHVT, we do not expect a non-interacting ensemble to exhibit entanglement.

5 Partially indistinguishable singlets

We finally consider an ensemble of N partially indistinguishable fermions coupled in $N/2$ singlet states. Partial indistinguishability is motivated by considering singlets formed from particle anti-particle pairs, such as $\Lambda\bar{\Lambda}$ or e^-e^+ . In such a scenario, particles are distinguishable from anti-particles, yet the particles (anti-particles) are indistinguishable amongst themselves. We model this system with N fermions (numbered $1, \dots, N$) residing in $N/2$ energy levels. Fermions $1, \dots, N/2$ and $N/2 + 1, \dots, N$ are indistinguishable within each group yet distinguishable between groups. Each energy level contains a pair of fermions (i, j) such that $i \in [1, \dots, N/2]$ and $j \in [N/2 + 1, \dots, N]$. Let ϕ^α Be the single-particle orthonormal spatial wavefunction for energy $\alpha \in [1, \dots, N]$. Now, we construct a wavefunction that is antisymmetric under exchange of particles $1, \dots, N/2$ and particles $N/2 + 1, \dots, N$. Note that we cannot exchange particles from across these two sets. We write the wavefunction of this

ensemble as:

$$\begin{aligned}
|\Psi\rangle &= \sqrt{\frac{1}{(N/2)!}} \sum_{\sigma(N/2+1, \dots, N)} \text{sgn}(\sigma(N/2+1, \dots, N)) |S_{1, \sigma(N/2+1)} S_{1, \sigma(N)}\rangle \\
&\times \Phi^+((1, \sigma(N/2+1)), \dots, (N/2, \sigma(N)))
\end{aligned} \tag{5.1}$$

We sum across permutations σ of the second set of particles $\{N/2+1, \dots, N\}$. We define:

$$|S_{ij}\rangle = \frac{|0\rangle_i |1\rangle_j - |1\rangle_i |0\rangle_j}{\sqrt{2}} \tag{5.2}$$

Note that the singlet state is intrinsically rotationally invariant, so our choice of basis does not matter. The Φ^+ operator completely symmetrizes the spatial wavefunctions across the pairs $(1, \sigma(N/2+1)) \dots (N/2, \sigma(N))$ as follows:

$$\begin{aligned}
\Phi^+((1, \sigma(N/2+1)) \dots (N/2, \sigma(N))) &= \frac{1}{\sqrt{(N/2)!}} \left[\dots \phi^\alpha(\mathbf{x}_1) \phi^\alpha(\mathbf{x}_{\sigma(N/2+1)}) \phi^\beta(\mathbf{x}_2) \phi^\beta(\mathbf{x}_{\sigma(N/2+2)}) \dots \right. \\
&\quad \left. + \dots \phi^\alpha(\mathbf{x}_2) \phi^\alpha(\mathbf{x}_{\sigma(N/2+2)}) \phi^\beta(\mathbf{x}_1) \phi^\beta(\mathbf{x}_{\sigma(N/2+1)}) \dots \right]
\end{aligned} \tag{5.3}$$

We isolate the spin density matrix by tracing over spatial degrees of freedom in the state formed by Eq. 5.1.

$$\rho_S = \text{Tr}_\Phi(|\Phi\rangle \langle \Phi|) = \frac{1}{(N/2)!} \sum_{\sigma(N/2+1, \dots, N)} |S_{1, \sigma(N/2+1)} S_{1, \sigma(N)}\rangle \langle S_{1, \sigma(N/2+1)} S_{1, \sigma(N)}| \tag{5.4}$$

For further detail regarding the methods employed here, we direct the reader to Ref. [12], from which we derived inspiration for constructing this ensemble.

We now complete the familiar task of computing the two-particle correlation function for our spin state given by Eq. 5.4. We first write the two-particle probability, noting that we

measure a pair (i, j) such that $i \in [1, \dots, N/2]$ and $j \in [N/2 + 1, \dots, N]$.

$$\rho_{1, N/2+1} = \text{Tr}_{\{1, \dots, N\} / \{1, N/2+1\}}(\rho_S) = \frac{2}{N} |S_{1, N/2+1}\rangle \langle S_{1, N/2+1}| + \frac{N-2}{N} \frac{1}{4} I_1 \otimes I_{N/2+1} \quad (5.5)$$

$$P(\hat{\mathbf{a}}, \hat{\mathbf{b}}) = \text{Tr}(|\theta_a\rangle \langle \theta_b| \rho_{12}) = \frac{1}{4} - \frac{1}{2N} \cos(\theta_a - \theta_b) \quad (5.6)$$

The single-particle probability is then given by:

$$\rho_1 = \text{Tr}_{N/2+1}(\rho_{1, N/2+1}) = \frac{1}{2} I_1 \quad (5.7)$$

$$P(\hat{\mathbf{a}}) = \text{Tr}(|\theta_a\rangle \langle \theta_a| \rho_1) = \frac{1}{2} \quad (5.8)$$

We find the correlation function for a two-particle substate of this ensemble as:

$$\frac{P(\hat{\mathbf{a}}, \hat{\mathbf{b}})}{P(\hat{\mathbf{a}})P(\hat{\mathbf{b}})} = 1 - \frac{2}{N} \cos(\theta_a - \theta_b) \quad (5.9)$$

From Eqs. 5.6 and 5.8, as well as the form of Eq. 5.9, we see that the correlation function is rotationally invariant. From Theorem 2.1, Corollary 2.1.1 we thus conclude that two-particle substates of this ensemble are never consistent with LHVT. Using Corollary 2.1.2, we deduce that states with $N < 4$ are definitely entangled; given the physical situation, this applies only to the $N = 2$ case of one singlet. It is interesting to observe here that correlations between any two particles in a singlet wash out as $N \rightarrow \infty$.

6 Discussion and conclusions

Our Theorem 2.1 and related corollaries show that entanglement and non-locality can be inferred from certain features of a two-particle correlation function. We further derive the correlation functions for three different multifermionic ensembles: coherent non-interacting spins, incoherent non-interacting spins, and partially indistinguishable singlets. Using Theorem 2.1, we conclude that two-particle substates of incoherent non-interacting spins and

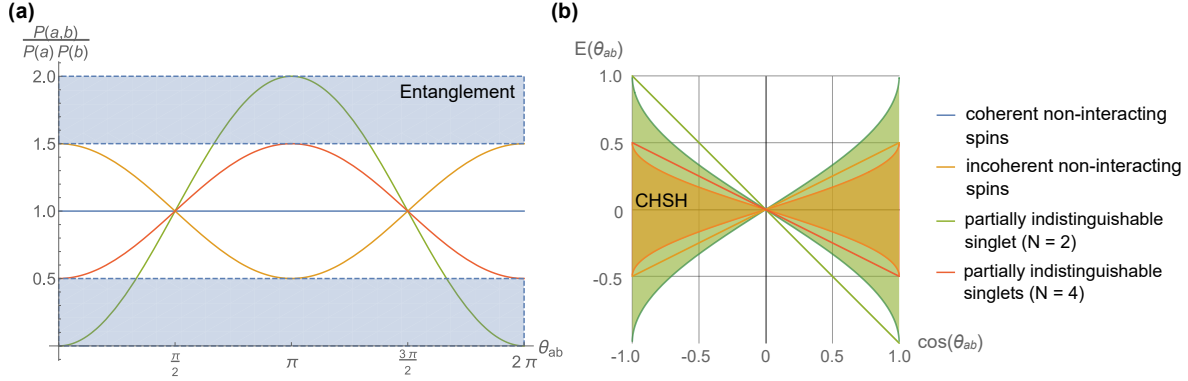


Figure 1: (a) Eqs. 3.10, 4.6, and 5.9 ($N=2, N=4$) plotted as a function of θ_{ab} . Entanglement is shown by blue shading. Only the spin singlet definitively exhibits entanglement. (b) Eqs. 4.6 and 5.9 ($N=2, N=4$) plotted as spin correlations (related by Eq. 2.20) as a function of $\cos(\theta_{ab})$. Each relevant CHSH inequality is indicated with shading. All spin correlations violate their related CHSH inequalities.

partially indistinguishable singlets violate LHVT. Furthermore, for the last ensemble, we confirm that an $N = 2$, or singlet, state displays entanglement. The correlation functions and spin correlations for the three ensembles as well as their respective behaviors are plotted in Fig. 1.

In this manner, the correlation function of form given in Eq. 1.4 holds potential as a measure for entanglement and non-locality in the products of high-energy collisions. We propose to use Eq. 1.4 to detect entanglement and non-locality in the matter formed from relativistic heavy ion collisions and deep inelastic scattering. The principles underlying the formulation of our three didactic spin ensembles can further be employed, in part or in full, to create more comprehensive models of specific experimental situations. In future work, we aim to apply Theorem 2.1 to data obtained from heavy ion collision. We further suggest adjusting our formulation in Section 2 to use positive operator valued measurements (POVM) rather than projective measurements to account for our uncertainty measuring in spin-up or spin-down ($|\mathbf{P}| < 1$). Nevertheless, our present work has established a foundation for measuring entanglement and non-locality using two-particle correlation functions (Eq. 1.4) in high energy experiments.

7 Acknowledgements

This project was supported in part by the U.S. Department of Energy, Office of Science, Office of Workforce Development for Teachers and Scientists (WDTS) under the Science Undergraduate Laboratory Internships Program (SULI).

References

- [1] A. Einstein, B. Podolsky, and N. Rosen, “Can Quantum-Mechanical Description of Physical Reality Be Considered Complete?”, *Physical Review*, vol. 47, no. 10, pp. 777–780, May 1935, ISSN: 0031-899X. DOI: [10.1103/PhysRev.47.777](https://doi.org/10.1103/PhysRev.47.777). [Online]. Available: <https://link.aps.org/doi/10.1103/PhysRev.47.777>.
- [2] M. Giustina, M. A. M. Versteegh, S. Wengerowsky, J. Handsteiner, A. Hochrainer, K. Phelan, F. Steinlechner, J. Kofler, J.-Å. Larsson, C. Abellán, W. Amaya, V. Pruneri, M. W. Mitchell, J. Beyer, T. Gerrits, A. E. Lita, L. K. Shalm, S. W. Nam, T. Scheidl, R. Ursin, B. Wittmann, and A. Zeilinger, “Significant-Loophole-Free Test of Bell’s Theorem with Entangled Photons”, *Physical Review Letters*, vol. 115, no. 25, p. 250401, Dec. 2015, ISSN: 0031-9007. DOI: [10.1103/PhysRevLett.115.250401](https://doi.org/10.1103/PhysRevLett.115.250401). [Online]. Available: <https://link.aps.org/doi/10.1103/PhysRevLett.115.250401>.
- [3] B. Hensen, H. Bernien, A. E. Dréau, A. Reiserer, N. Kalb, M. S. Blok, J. Ruitenberg, R. F. L. Vermeulen, R. N. Schouten, C. Abellán, W. Amaya, V. Pruneri, M. W. Mitchell, M. Markham, D. J. Twitchen, D. Elkouss, S. Wehner, T. H. Taminiau, and R. Hanson, “Loophole-free Bell inequality violation using electron spins separated by 1.3 kilometres”, *Nature*, vol. 526, no. 7575, pp. 682–686, Oct. 2015, ISSN: 0028-0836. DOI: [10.1038/nature15759](https://doi.org/10.1038/nature15759). [Online]. Available: <http://www.nature.com/articles/nature15759>.

- [4] D. Rauch, J. Handsteiner, A. Hochrainer, J. Gallicchio, A. S. Friedman, C. Leung, B. Liu, L. Bulla, S. Ecker, F. Steinlechner, R. Ursin, B. Hu, D. Leon, C. Benn, A. Ghedina, M. Cecconi, A. H. Guth, D. I. Kaiser, T. Scheidl, and A. Zeilinger, “Cosmic Bell Test Using Random Measurement Settings from High-Redshift Quasars”, *Physical Review Letters*, vol. 121, no. 8, p. 080 403, Aug. 2018, ISSN: 0031-9007. DOI: [10.1103/PhysRevLett.121.080403](https://doi.org/10.1103/PhysRevLett.121.080403). [Online]. Available: <https://link.aps.org/doi/10.1103/PhysRevLett.121.080403>.
- [5] A. Bergschneider, V. M. Klinkhamer, J. H. Becher, R. Klemt, L. Palm, G. Zürn, S. Jochim, and P. M. Preiss, “Experimental characterization of two-particle entanglement through position and momentum correlations”, *Nature Physics*, vol. 15, no. 7, pp. 640–644, 2019, ISSN: 17452481. DOI: [10.1038/s41567-019-0508-6](https://doi.org/10.1038/s41567-019-0508-6). arXiv: [1807.06405](https://arxiv.org/abs/1807.06405). [Online]. Available: <http://dx.doi.org/10.1038/s41567-019-0508-6>.
- [6] T. Brydges, A. Elben, P. Jurcevic, and B. Vermersch, “Probing Rényi entanglement entropy via randomized measurements”, *Science*, vol. 263, no. April 2019, pp. 260–263, 2020.
- [7] R. Horodecki, M. Horodecki, and K. Horodecki, “Quantum entanglement”, *Review of Modern Physics*, vol. 81, no. 865, pp. 1–110, 2009. arXiv: [0702225v2](https://arxiv.org/abs/0702225v2) [[arXiv:quant-ph](https://arxiv.org/abs/0702225v2)].
- [8] N. A. Törnqvist, “Suggestion for Einstein-Podolsky-Rosen experiments using reactions like $e^+e^- \rightarrow \Lambda\bar{\Lambda} \rightarrow \pi^-p\pi^+\bar{p}$ ”, *Foundations of Physics*, vol. 11, no. 1-2, pp. 171–177, 1981, ISSN: 00159018. DOI: [10.1007/BF00715204](https://doi.org/10.1007/BF00715204).
- [9] X.-Q. Hao, H.-W. Ke, Y.-B. Ding, P.-N. Shen, and X.-Q. Li, “Testing the Bell Inequality at Experiments of High Energy Physics”, *Chinese Physics C*, vol. 34, no. 3, pp. 1–17, 2010. DOI: [10.1088/1674-1137/34/3/002](https://doi.org/10.1088/1674-1137/34/3/002). arXiv: [0904.1000](https://arxiv.org/abs/0904.1000). [Online]. Available: <http://arxiv.org/abs/0904.1000%7B%5C%7D0Ahttp://dx.doi.org/10.1088/1674-1137/34/3/002>.

- [10] X. H. Wu, H. S. Zong, H. R. Pang, and F. Wang, “Bell inequality for Werner states”, *Physical Review A - Atomic, Molecular, and Optical Physics*, vol. 64, no. 2, p. 3, 2001, ISSN: 10941622. DOI: [10.1103/PhysRevA.64.022103](https://doi.org/10.1103/PhysRevA.64.022103).
- [11] V. A. Andreev and V. I. Man’ko, “Bell’s inequality for two-particle mixed spin states”, *Theoretical and Mathematical Physics*, vol. 140, no. 2, pp. 1135–1145, 2004, ISSN: 00405779. DOI: [10.1023/B:TAMP.0000036543.69631.94](https://doi.org/10.1023/B:TAMP.0000036543.69631.94).
- [12] M. Arifullin and V. Berdinskiy, “Spin entanglement and nonlocality of multifermion systems”, 2013. arXiv: [1310.2863](https://arxiv.org/abs/1310.2863). [Online]. Available: <http://arxiv.org/abs/1310.2863>.

A Reduction of CHSH inequality to one parameter

We start with Eq. 2.18, copied below for convenience:

$$|E(\hat{\mathbf{a}}, \hat{\mathbf{b}}) - E(\hat{\mathbf{a}}, \hat{\mathbf{b}}')| + |E(\hat{\mathbf{a}}', \hat{\mathbf{b}}') + E(\hat{\mathbf{a}}', \hat{\mathbf{b}})| \leq 2(|\lambda_{44} - \lambda_{11}| + |\lambda_{33} - \lambda_{22}|) \quad (\text{A.1})$$

As we work with spins in the $x - z$ plane, we can consider $\hat{\mathbf{a}}, \hat{\mathbf{a}}', \hat{\mathbf{b}},$ and $\hat{\mathbf{b}}'$ to be coplanar as shown in Fig. A.1. Assuming rotational invariance, i.e. $E(\hat{\mathbf{a}}, \hat{\mathbf{b}}) = E(\theta_a - \theta_b) \equiv E(\theta_{ab})$, the spin correlations will only depend on the angles between each pair of vectors.

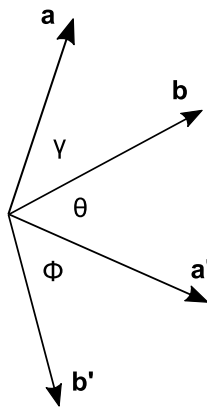


Figure A.1: The coplanar configuration of $\hat{\mathbf{a}}, \hat{\mathbf{a}}', \hat{\mathbf{b}},$ and $\hat{\mathbf{b}}'$

We can then set $\theta = \gamma = \phi$ as seen in Fig. A.1 and rewrite Eq. A.1:

$$|E(\theta) - E(3\theta)| + 2|E(\theta)| \leq 2(|\lambda_{44} - \lambda_{11}| + |\lambda_{33} - \lambda_{22}|) \quad (\text{A.2})$$

From here, we use the following boundary conditions to reduce Eq. A.2 to a limit on $|E(\theta_{ab})|$:

$$E(2\pi - \theta) = E(\theta) \quad (\text{A.3})$$

$$E(\theta + 2\pi) = E(\theta) \quad (\text{A.4})$$

$$E(\theta + \pi) = -E(\theta) \quad (\text{A.5})$$

Eq. A.3 constrains reflection symmetry in the two dimensions: θ and $2\pi - \theta$ denote the same angle between two vectors. Eq. A.4 constrains rotational symmetry in two dimensions: θ and $\theta + 2\pi$ are the same angle. Eq. A.5 derives from the definition of the correlation function as the expected value of the product of measured spins: flipping one axis of measurement negates the expected value. We can now find bounds on the special angles $0, \frac{\pi}{6}, \frac{\pi}{4}, \frac{\pi}{3}, \frac{\pi}{2}$, etc., using Eq. A.2. To demonstrate:

$$\begin{aligned} 2|E(0)| &\leq 2(|\lambda_{44} - \lambda_{11}| + |\lambda_{33} - \lambda_{22}|) \\ \implies |E(0)| &\leq (|\lambda_{44} - \lambda_{11}| + |\lambda_{33} - \lambda_{22}|) \end{aligned} \quad (\text{A.6})$$

$$\begin{aligned} E(\pi/2) &= E(2\pi - \pi/2) \\ &= E(3\pi/2) \\ &= E(\pi + \pi/2) \\ &= -E(\pi/2) \\ \implies E(\pi/2) &= 0 \end{aligned} \quad (\text{A.7})$$

After similar algebraic exercises, we find the following bounds (which can be extended for

all special angles on the unit circle):

$$|E(0)| \leq (|\lambda_4 - \lambda_1| + |\lambda_3 - \lambda_2|) \quad (\text{A.8})$$

$$|E(\pi/6)| \leq \frac{2}{3}(|\lambda_4 - \lambda_1| + |\lambda_3 - \lambda_2|) \quad (\text{A.9})$$

$$|E(\pi/4)| \leq \frac{1}{2}(|\lambda_4 - \lambda_1| + |\lambda_3 - \lambda_2|) \quad (\text{A.10})$$

$$|E(\pi/3)| \leq \frac{1}{3}(|\lambda_4 - \lambda_1| + |\lambda_3 - \lambda_2|) \quad (\text{A.11})$$

$$|E(\pi/2)| = 0 \quad (\text{A.12})$$

We infer a linear relationship from these bounds, thus deriving our one-parameter CHSH inequality for a two-particle spin state diagonal in the Bell basis:

$$\begin{cases} |E(\theta)| \leq (1 - 2|\theta|/\pi)(|\lambda_4 - \lambda_1| + |\lambda_3 - \lambda_2|) & \text{for } |\theta| \leq \pi/2 \\ |E(\theta)| \leq (1 - 2(\pi - |\theta|)/\pi)(|\lambda_4 - \lambda_1| + |\lambda_3 - \lambda_2|) & \text{for } \pi/2 \leq |\theta| \leq \pi \end{cases} \quad (\text{A.13})$$

B Verification of entanglement fidelity

We define an entanglement fidelity (Eq. 2.25) for each Bell state $|B_i\rangle$ (Eqs. 2.1-2.4), copied below for convenience:

$$\mathcal{F}_i = \langle B_i | \rho_{ab} | B_i \rangle \quad (\text{B.1})$$

We want to show that that $\mathcal{F}_i > 1/2 \implies \rho_{ab}$ **is entangled**. For convenience, we give the proof for \mathcal{F}_4 , the fidelity against the singlet Bell state (Eq. 2.4). For the rest of the \mathcal{F}_i , the proof follows similarly.

Proof: Suppose for a contradiction that there exists a separable ρ_{ab} such that $\langle B_4 | \rho_{ab} | B_4 \rangle > 1/2$. We can write a generic separable state ρ_{ab} as follows:

$$|\psi_{ab}\rangle_i = (a_i |0\rangle_a + b_i |1\rangle_a) \otimes (c_i |0\rangle_b + d_i |1\rangle_b) \quad (\text{B.2})$$

$$= a_i c_i |00\rangle + a_i d_i |01\rangle + b_i c_i |10\rangle + b_i d_i |11\rangle \quad (\text{B.3})$$

$$\rho_{ab} = \sum_i p_i |\psi_{ab}\rangle_i \langle \psi_{ab}|_i \quad (\text{B.4})$$

The coefficients a_i , b_i , c_i , and d_i are complex numbers, and $|\psi_{ab}\rangle_i$ is normalized. Then, we have:

$$\mathcal{F}_4 = \sum_i p_i \langle B_4 | \psi_{ab_i} \rangle \langle \psi_{ab_i} | B_4 \rangle \quad (\text{B.5})$$

We now note that:

$$\langle B_4 | \psi_{ab_i} \rangle \langle \psi_{ab_i} | B_4 \rangle = \frac{|a_i d_i + b_i c_i|^2}{2} \quad (\text{B.6})$$

$$= \frac{1}{2} (a_i^2 d_i^2 + (a_i d_i)^* b_i c_i + (b_i c_i)^* a_i d_i + b_i^2 c_i^2) \quad (\text{B.7})$$

$$= \frac{1}{2} (a_i^2 d_i^2 + (a_i^* c_i)(b_i d_i^*) + (a_i c_i^*)(b_i^* d_i) + b_i^2 c_i^2) \quad (\text{B.8})$$

$$\leq \frac{1}{2} (a_i^2 d_i^2 + a_i^2 c_i^2 + b_i^2 d_i^2 + b_i^2 c_i^2) = \frac{1}{2} \quad (\text{B.9})$$

In the last line, we have used a complex form of $a^2 + b^2 \geq 2ab$ and invoked normalization of $|\psi_{ab}\rangle_i$. Therefore,

$$\mathcal{F}_4 = \sum_i p_i \langle B_4 | \psi_{ab_i} \rangle \langle \psi_{ab_i} | B_4 \rangle \quad (\text{B.10})$$

$$\leq \frac{1}{2} \sum_i p_i = \frac{1}{2} \quad (\text{B.11})$$

Thus, the fidelity \mathcal{F}_4 of every separable ρ_{ab} is less than or equal to $\frac{1}{2}$, in contradiction to our assumption. This implies that $\mathcal{F}_4 > \frac{1}{2} \implies \rho_{ab}$ is entangled. \square

Note that this condition is sufficient but not necessary for entanglement: an entangled state may have $\mathcal{F}_i < 1/2$.

Examination of aerosol optical properties at a rural continental site

Brian Hambel

Mathematics and Computer Science Department, St. Joseph's College, Patchogue, NY 11772

Ernie Lewis and Allison McComiskey

Environmental & Climate Sciences Department, Brookhaven National Laboratory, Upton, NY 11713

Abstract

An aerosol is a suspension of particles in the air, usually ranging in diameter from 0.001-10 micrometers. Aerosols scatter light and thereby affect Earth's climate. A nephelometer measures this scattering at 3 wavelengths: 700 nm (red) 550 nm (green), and 450 nm (blue). The nephelometer at the Southern Great Plains (SGP) atmospheric observatory in Lamont, Oklahoma, supported and operated by the DOE Atmospheric Radiation Measurement (ARM) program, has been measuring aerosol light scattering for over two decades. These data were programmatically loaded and modified using the Python ARM Radar Toolkit (Py-ART), which required specific modules to 1) calculate solar zenith angles, 2) flag incorrect data based on quality control (QC) flags, and 3) remove duplicate data files. The data were then exported and loaded into IGOR Pro, a scientific data analysis software package, which allowed me to efficiently display and analyze the red, green, and blue scattering.

I was also able to display the corrected vs non-corrected data to illustrate the importance of strict data quality control. This summer, I have learned about aerosols and atmospheric science. I now know what a nephelometer is and how it functions. I have also developed and refined my skills in Python and IGOR Pro.

I. Background

Aerosols are suspensions of particles in the air. Aerosol particles can be classified by their diameter: coarse mode aerosol particles range in diameter from 1-10 μm , whereas fine mode aerosol particles have diameters $< 1 \mu\text{m}$. Aerosol light scattering affects Earth's climate, as light from the sun that would normally be contained within Earth's system is scattered back to space, affecting Earth's energy balance.

Aerosol light scattering is measured by an instrument called a nephelometer. From 1993-2017, light scattering was

measured at the DOE Atmospheric Radiation Measurement (ARM) Southern Great Plains (SGP) site using a nephelometer mentored by the National Oceanic and Atmospheric Administration (NOAA), and since 2016 it has been measured using *another* nephelometer mentored by Brookhaven National Laboratory (BNL). Only data from the most recent nephelometer were used for the current study, but future work will examine the overlap between the two systems.

A simple schematic of a nephelometer is shown in Figure I. The operation of a nephelometer is as follows. Air is brought in through the impactor which

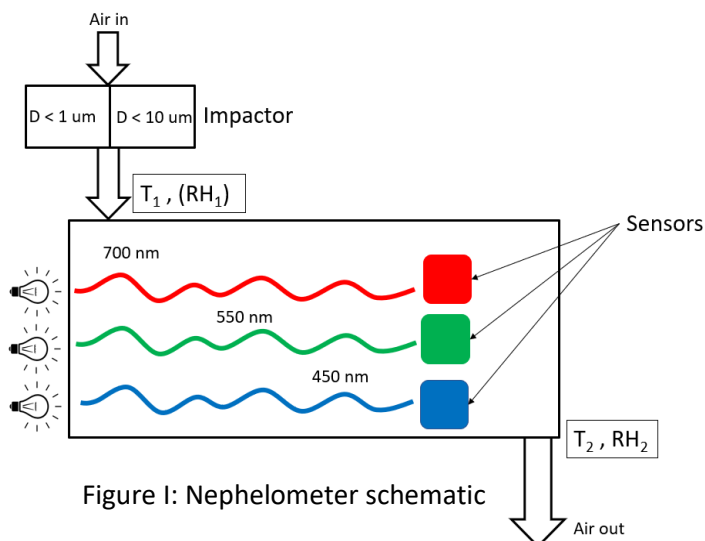


Figure I: Nephelometer schematic

allows only particles with diameter less than 1 μm (fine) or those with diameters less than 10 μm (fine and coarse) to pass into the nephelometer. The temperature, T1, of the air sample just prior to the nephelometer is measured and recorded. The light scattering of the aerosol is recorded at three wavelengths, and the temperature, T2, and relative humidity, RH2, are measured and recorded again just after the air leaves the instrument. These measurements are used to calculate the relative humidity at the inlet, RH1, using the following equation:

$$RH1 = RH2 * (1 + 0.06 [T2-T1])$$

II. Methods and Materials

Data are uploaded from the nephelometer to the ARM archive and are made available to users in netcdf file format. I initially attempted to retrieve the data manually via Globus, an online file sharing network, which required that I order specific data files and wait until the request was filled and ready.

Upon discovery of the ARM-DOE GitHub, downloading of data was much less tedious and more automated. Multiple years of data were easily downloadable with just 3-4 lines of code.

When downloading data obtained from the BNL-mentored nephelometer from 2017 to present, errors arose due to non-monotonic global indexes along dimension 'time'. This meant that duplicate time files were being downloaded. Upon examination, these files contained different data. I removed these duplicate files and kept notes of which dates were removed.

The data were then put into an Xarray Dataset. Xarray is an open source Python package that enables efficient and simple multi-dimensional data array manipulation and modification.

Modules were written in Python to modify the data to fit the needs of the project. First, a new time index was constructed in order to fill any gaps of missing data. I did this by constructing an index using the starting and ending dates of the data, and filled the array using Python's pandas date_range function, replacing the original, gap-filled index.

Next, any data with bad quality control (QC) flags were eliminated. Following this, with the help of the Python

package, Astral, I wrote a function to calculate the solar zenith angle at a given time and appended it to the data, as these data will eventually be used to study aerosol light scattering during only daylight. Next, I calculated the relative humidity (RH) at the inlet based on the temperatures at the inlet and exit, and the RH at the exit, and appended these values to the data array. I applied calibrations for the red, green, and blue scattering. Finally, I extracted the year, month, day, hour, and minute from time and appended these values to the data file.

The data were then exported to an Xarray Dataframe where further processing and manual corrections were made.

ARM provides date and time ranges for suspect and incorrect data on their archive. However, when downloaded, there is nothing to distinguish these suspect or incorrect data from correct data. So, a manual flag was appended to the file to denote suspect/incorrect data. Before exporting the data into a final working data file, only required variables and file headers were kept, saving time and memory.

After the final working data file was created, it was uploaded into Igor Pro, a data analysis software package. In Igor, I was able to calculate and display daily averages for aerosol scattering, temperature, and relative humidity. I was also able to display graphs of corrected vs non-corrected data.

III. Results

After applying the corrections, the removal of bad QC data is evident. Shown in Figure II, the spike near 9/6/2018 was removed. This spike occurred because of a clogged nephelometer filter, and thus the data are not valid.

Another example is shown in Figure III, when a sharp increase in temperature occurred in April 2020 because of an AC unit

failure in the shelter that houses the nephelometer. This failure resulted in measurements that needed to be removed, as they were made under different conditions of temperature and RH than the other measurements.

The Angstrom exponent is a quantity derived from the light scattering measurements that indicates the sizes of the aerosol particles that contribute most to the scattering. Angstrom exponents for fine mode particles are typically between 1-3 whereas those for the coarse mode particles typically range from 0-1. A time-series of the Angstrom exponent from 2017 to the present is shown in Fig. IV. Seasonal trends are apparent in the sense that Angstrom exponents for the coarse mode show a decrease each summer.

IV. Discussion

Aerosol light scattering data from SGP is consistent with expected values. Over the three years examined, Angstrom exponents calculated for the fine mode were mostly between 2 and 2.5, and those for the coarse mode were between 0.5 and -1. Without careful corrections and QC checks, inaccurate results could be easily obtained.

If I were to continue this project, I would develop a Python program to automatically append flags for the suspect and incorrect data on the ARM archive instead of doing it manually. Future projects would also include examination of the overlap of the BNL-mentored and NOAA-mentored nephelometer data, and investigation of long-term aerosol light scattering data under dry and ambient relative humidity.

V. Acknowledgements

I would like to start by thanking Dr. Janek Uin of Brookhaven National Laboratory for meeting with me regarding the operation and calibration of the SGP nephelometer. I would also like to thank Adam Theisen of Argonne National Laboratory for introducing me to the ARM-DOE GitHub. Lastly, I would like to thank my mentors, Ernie Lewis and Allison

McComiskey, for their motivation, help, and guidance. This project was supported in part by the U.S. Department of Energy, Office of Science, Office of Workforce Development for Teachers and Scientists (WDTS) under the Science Undergraduate Laboratory Internships Program (SULI)

Figure II: RGB Scattering Non-corrected vs. Corrected

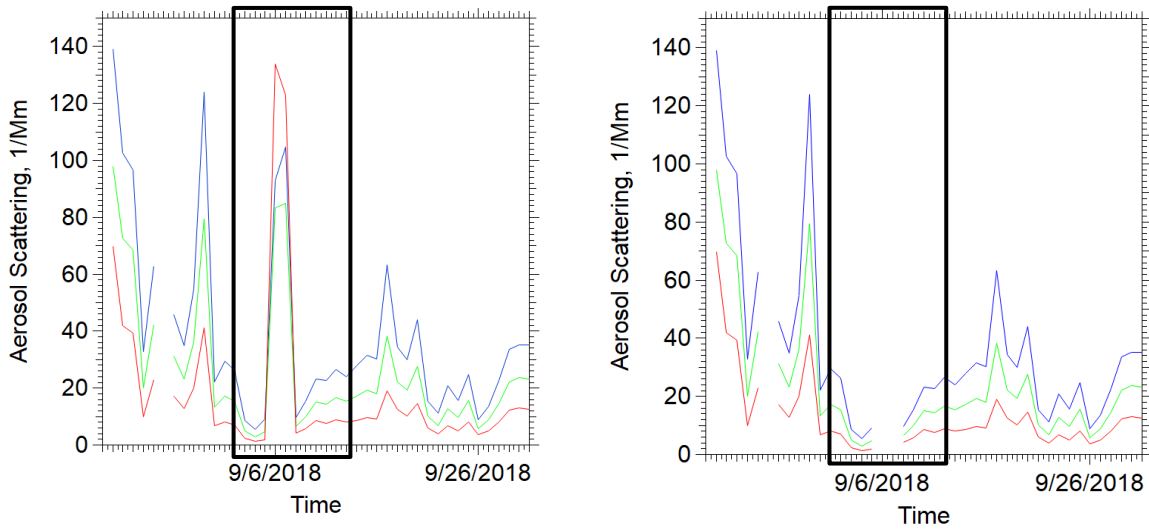


Figure III: Temperature and RH: Non-corrected vs. Corrected

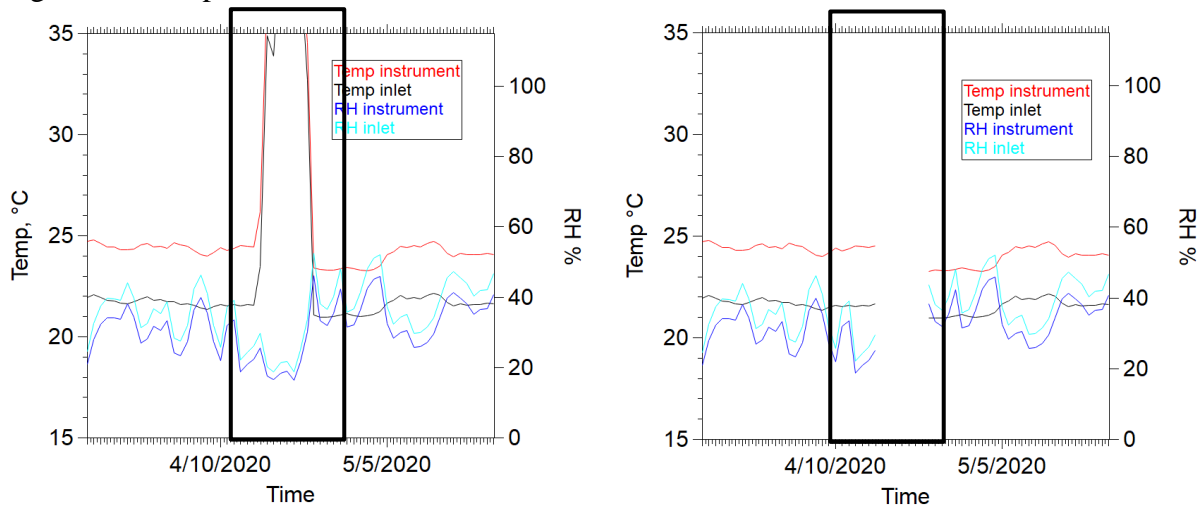
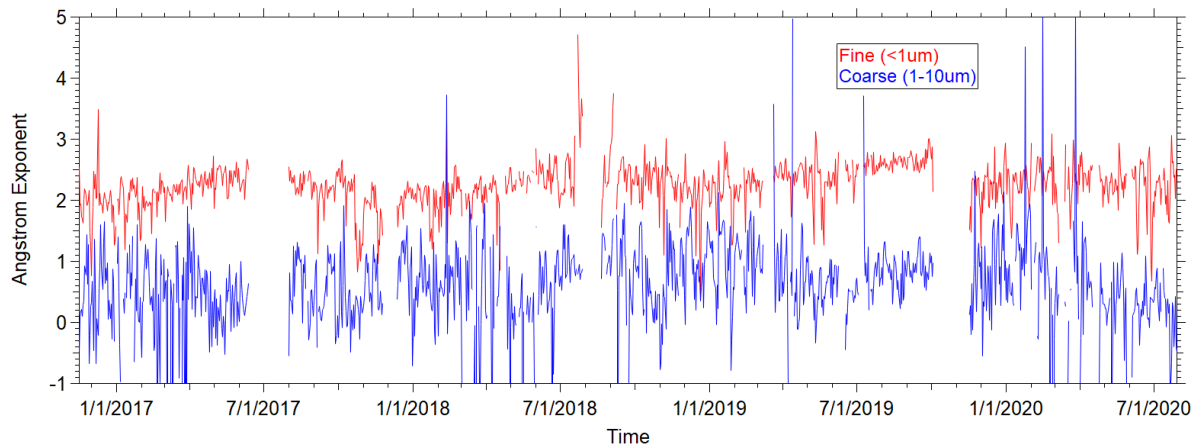


Figure IV: Angstrom Exponent time-series



Literature analysis of COVID-19 drug and vaccine development

Emma Hert, Biology, Wheaton College, Norton, MA 02766

Desigan Kumaran, Biology, Brookhaven National Laboratory, Upton, NY 11973

Abstract

The virus SARS-CoV-2, which causes Coronavirus disease 2019 (COVID-19), first broke out in Wuhan, China in late 2019 and has subsequently spread across the world creating a global pandemic. It is critical to understand the latest drug and vaccine developments on COVID-19 as there is currently misinformation and confusion across the general public of virus treatment. The objective of this study was to understand the latest drug and vaccine developments on COVID-19 through a literature review. To conduct this review, the clinical trials that are currently being conducted were analyzed, as well as other literature with suggested drugs to combat COVID-19 using the data base PubMed and the clinical trials database. The type of drug or treatment, its target, and whether or not it is in clinical trial was collected. From this search ninety-four drugs and treatments were identified. Eighty-six of these drugs are under clinical trial. Forty-five drugs target the immune system directly, while twenty-four drugs are antiviral drugs. Twenty other drugs and treatments were also identified including antimalarial drugs (including chloroquine and hydroxychloroquine), antibacterial drugs, antiparasitic drugs, convalescent plasma treatment, pulmonary vasodilators, anesthetics, vitamins, and traditional herbal medicine. Of these drugs and treatments, there is none with proven efficacy against the virus outside of *in-vitro* effectiveness. The drugs that show the most promise is the broad spectrum antiviral Remdesivir and simple steroids such as Dexamethasone. Drugs that target SARS-CoV-2 directly are needed for overwhelming effective treatment. Next steps are to select a target of SARS-CoV-2 and identify the lead protein. Furthermore, there are vaccines being created as a preventative measure against COVID-19, with 166 vaccines currently under development or clinical trial, twenty-five of which are currently under human trial. Future research will be focusing on selective drug target, most likely on viral protease papain-like protease (PLpro).

Introduction

In December of 2019, a pneumonia of unknown cause emerged, which was later identified named as Severe Acute Respiratory Syndrome Coronavirus 2 (SARS-CoV-2). This virus causes Coronavirus Disease 2019 (COVID-19), which was later raised to the level of a pandemic by the World Health Organization (WHO). SARS-CoV-2 is a coronavirus, in particular a β -coronavirus, which are a group of viruses that are enveloped and are positive-sense single-stranded RNA virus with a length between 26.2 and 31.7 kb, which is among the longest RNA viruses^{1,2}. In the past two decades, coronaviruses have cause two large scale pandemics, Severe Acute Respiratory syndrome (SARS) and Middle East Respiratory Syndrome (MERS)². It was determined that SARS-CoV-2 is similar to the coronavirus of past pandemics, with 79.6% sequence identity to SARS³.

SARS-CoV-2 function by encodes the spike (S) protein, a structural surface protein, which binds to human angiotensin-converting enzyme 2 (ACE2) of humans. Upon entering the human cells, SARS-CoV-2 hijacks the human cells to synthesize and assemble their viral proteins. This triggers an immune response which includes autophagy, apoptosis, stress response, and innate immunity in humans⁴. Fortunately, around 80% of people with COVID-19 are asymptomatic or have mild symptoms. However, many experience more severe symptoms, including acute respiratory distress syndrome (ARDS) and other severe symptoms, which ultimately lead to death in many individuals, especially individuals in high risk groups, such as those with preexisting conditions and the elderly³.

Currently, there is no vaccine for COVID-19, nor any therapeutic drugs specifically designed to target SARS-CoV-2. Effective vaccines and drugs are vital in fighting SARS-CoV-2 and controlling its spread and to treat individuals with severe symptoms of COVID-19. However,

until vaccines or specific therapeutic drugs are created, scientific efforts have turned to repurposing existing drugs to treat COVID-19 patients^{3,5}.

The objective of this study was to understand the latest drug and vaccine developments for COVID-19 through a literature review. It is vital to know and understand the latest efforts to combat COVID-19 as the situation is rapidly evolving as scientists around the world are trying every effort to slow the spread of COVID-19 and treat the symptoms of those who have the virus. It is also important to know which drugs and treatments effective in COVID-19 treatment, so that researchers where new research is needed to fill the gaps in knowledge.

Methodology

To conduct this review, PubMed database and clinical trials database from the National Institute of Health were used to identify drugs, treatments, and vaccines. Key words such as “COVID-19” and “SARS-CoV-2” were used to find related articles and clinical trials. For each drug the following information was collected; the name of the drug, the target of the drug, its use outside of COVID-19 management, whether or not it is under clinical trial, and any other important identifying information. For each vaccine in development, the following information was collected; the name of the developer and vaccine, the type of vaccine, and the stage of clinical trial the vaccine was under.

Results

In this search, ninety-four drugs and treatments identified. Eighty-six of these drugs and treatments are in clinical trial (Fig. 1). There was found to be a large variety in the types of drugs and treatments. The largest groups were drugs that target the immune system and antiviral drugs (Fig. 2). Forty-five drugs target the immune system, with common targets including tyrosine

kinase, interleukin, and the glucocorticoid receptor. These drugs are used in order to combat the cytokine storm that accompanies the severe cases of COVID-19. Acute respiratory distress syndrome (ARDS) and organ failure can happen quite rapidly in COVID-19 patients and could lead to death. Cytokine storm is considered to be one of the major causes of ARDS and multiple-organ failure⁶.

Meanwhile, twenty-four drugs are antiviral drugs, with common targets include RNA polymerase, virus protease, and spike protein of SARS-CoV-2. Some of these drugs, such as Remdesivir as broad-spectrum antivirals, able to combat a large number of viruses. However, some antivirals do not target SARS-CoV-2 and specifically target other viruses. An example of this is the combination of lopinavir and ritonavir, which target herpesvirus DNA polymerase, an HIV protease⁷.

Another type of treatment was antimalarial drugs, such as the much talked about Chloroquine and Hydroxychloroquine. Both of these drugs target ACE2 in humans, which is where SARS-CoV-2 binds to for cell entry. While antimalarial drugs showed promise *in-vitro*, in clinical trial there was found to be no overwhelming benefit to using these drugs, with some evidence to support that they might be doing more harm than good⁸.

Antibacterial drugs were also under trial for COVID-19 treatment. The drug Azithromycin is under trial as it has shown *in-vitro* effectiveness against RNA viruses such as the Zika virus⁹. While other antibacterial drugs were used as preventative measures so that a patient does not catch a bacterial disease while fighting COVID-19, since their immune system is already weakened. However, it has been suggested that COVID-19 patients should not be treated with antibacterial drugs at all, as it could lead to further the spread of antibiotic resistant bacteria¹⁰.

Furthermore, there were also trials for convalescent plasma treatments, which is where the plasma from a person who has the antibodies for SARS-CoV-2 is given to someone who currently is fighting the virus. Pulmonary vasodilators were also under trial to treat patients who have developed ARDS as a result of COVID-19, functioning by reducing pulmonary pressures¹¹. Other treatments included antiparasitic drugs, vitamins, traditional medicines, and anesthetics, however there was only a small number of each of these treatments under trial.

Moreover, there is also currently development of vaccines for COVID-19, with vaccine development being fast-tracked in order to have an effective vaccine on the market as quickly as possible. Twenty-five vaccine candidates are currently in clinical evaluation while there are 141 vaccine candidates in preclinical evaluation. Most drugs are still in the early phases of human trials, however there are a few vaccines that are now in stage three of human trials (Fig. 3). There was a variety of the type of vaccine being developed, with the most common being a protein subunit vaccine, which commonly target the spike protein of SARS-CoV-2 (Fig.4).

Discussion

It is important to know the current status of drugs and vaccines for the treatment of COVID-19 in order to know which drugs are successful in fighting COVID-19 and areas where drugs can be developed. The largest group of drugs found were drugs that target the immune system, which were used to combat cytokine storm, which was also found in SARS and MERS patients³. However, no immunosuppressant has been found to be overwhelmingly effective for COVID-19 treatment. The drugs that showed the most promise in fighting COVID-19 are the broad spectrum antiviral Remdesivir as well as simple steroids such as Dexamethasone. Most other drugs showed little to not benefit and some have even showed potential harm to COVID-19 patients¹².

For effective COVID-19 treatment, a drug must be developed which specifically targets SARS-CoV-2. Currently, there are many targets suggested for drug development. This includes structural proteins of SARS-CoV-2, the spike (S) protein, membrane (M) protein, envelop (E) protein, and the nucleocapsid (N) protein as well as 16 non-structural proteins (NSPs), which includes the two proteases, 3-chymotrypsin-like protease and papain-like protease^{3,4,7}. In particular, the SARS-CoV-2 proteases show promise in creating a drug for COVID-19, as they plays a pivotal role in gene expression and replication of SARS-CoV-2⁴.

Acknowledgements

I would like to thank my mentor Dr. Desigan Kumaran for the help and support with my project this summer. This project was supported in part by the U.S. Department of Energy, Office of Science, Office of Workforce Development for Teachers and Scientists (WDTS) under the Science Undergraduate Laboratory Internships Program (SULI).

References

- ¹ S. Belouzard, J.K. Millet, B.N. Licitra, and G.R. Whittaker, *Viruses* **4**, 1011 (2012).
- ² P. Zhou, X. Lou Yang, X.G. Wang, B. Hu, L. Zhang, W. Zhang, H.R. Si, Y. Zhu, B. Li, C.L. Huang, H.D. Chen, J. Chen, Y. Luo, H. Guo, R. Di Jiang, M.Q. Liu, Y. Chen, X.R. Shen, X. Wang, X.S. Zheng, K. Zhao, Q.J. Chen, F. Deng, L.L. Liu, B. Yan, F.X. Zhan, Y.Y. Wang, G.F. Xiao, and Z.L. Shi, *Nature* **579**, 270 (2020).
- ³ R. Wu, L. Wang, H.C.D. Kuo, A. Shannar, R. Peter, P.J. Chou, S. Li, R. Hudlikar, X. Liu, Z. Liu, G.J. Poiani, L. Amorosa, L. Brunetti, and A.N. Kong, *Curr. Pharmacol. Reports* **6**, 56 (2020).
- ⁴ M. Prajapat, P. Sarma, N. Shekhar, P. Avti, S. Sinha, H. Kaur, S. Kumar, A. Bhattacharyya, H.

Kumar, S. Bansal, and B. Medhi, *Indian J. Pharmacol.* **52**, 56 (2020).

⁵ G. Li and E. De Clercq, *Nat. Rev. Drug Discov.* **19**, 149 (2020).

⁶ Q. Ye, B. Wang, and J. Mao, *J. Infect.* **80**, 607 (2020).

⁷ C. Harrison, *Nat. Biotechnol.* **38**, 379 (2020).

⁸ K. Kupferschmidt, *Science* (80-.). (2020).

⁹ H. Retallack, E. Di Lullo, C. Arias, K.A. Knopp, M.T. Laurie, C. Sandoval-Espinosa, W.R.M. Leon, R. Krencik, E.M. Ullian, J. Spatazza, A.A. Pollen, C. Mandel-Brehm, T.J. Nowakowski, A.R. Kriegstein, and J.L. De Risi, *Proc. Natl. Acad. Sci. U. S. A.* **113**, 14408 (2016).

¹⁰ S. Reardon, *Science* (80-.). (2020).

¹¹ S. Rajpal, (2020).

¹² Center for Disease Control, (2020).

Appendix A – Figures

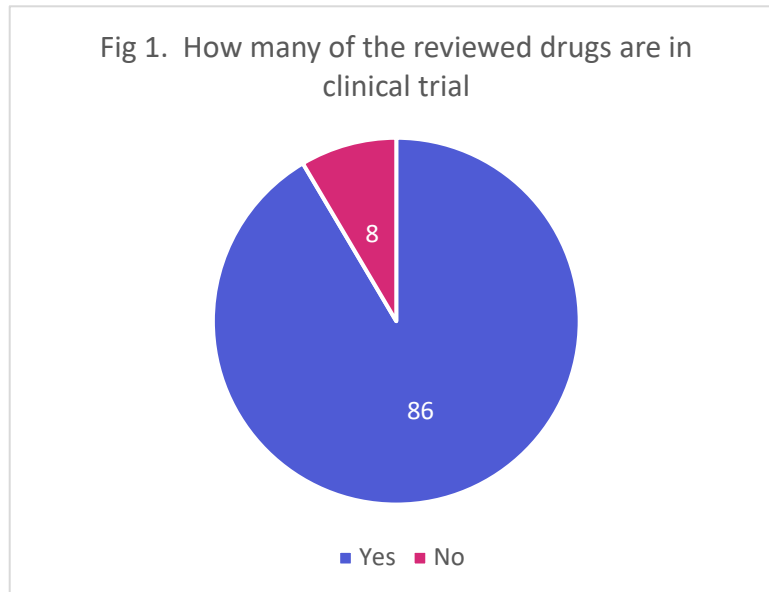


Figure 1 Ninety-four drugs and treatments were reviewed. Of the ninety-four drugs and treatments, eighty-four were in clinical trial while eight were not under clinical trial.

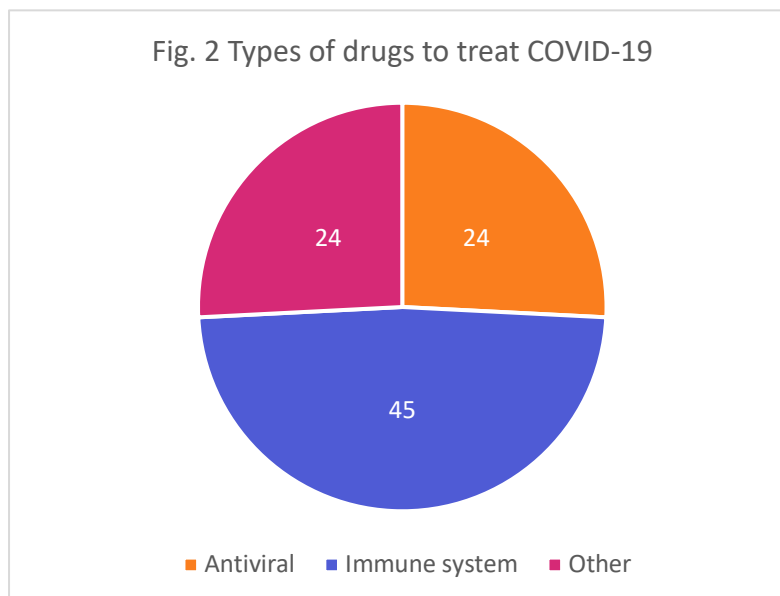


Figure 2 Of the ninety-four drugs and treatments, 24 drugs were antivirals, 45 targeted the immune system, and 24 were other types of drugs and treatments. These other drugs and treatments including; identified including antimalarial drugs, antibacterial drugs, antiparasitic drugs, convalescent plasma treatment, pulmonary vasodilators, anesthetics, vitamins, and traditional herbal medicine.

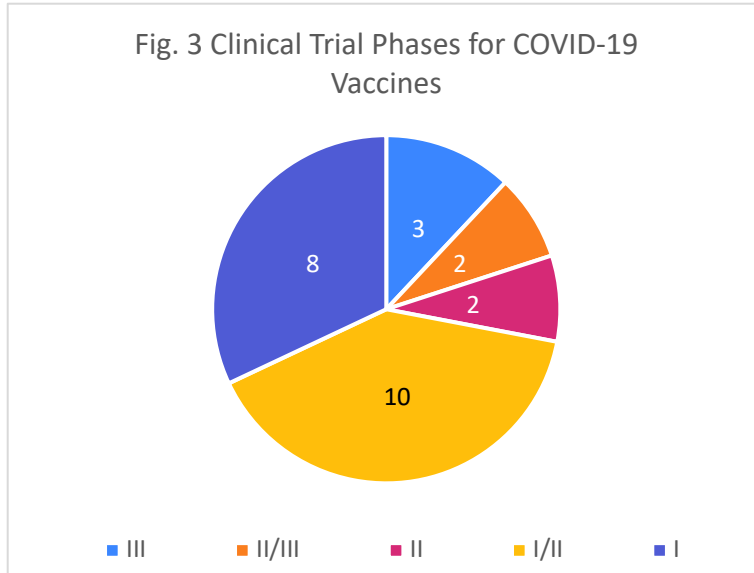


Figure 3 There are 25 vaccines currently under clinical trial. Of these, most are in stage I or stage I/II clinical trial, however there are a few that are further along, including five that are in stage III or II/III clinical trial.

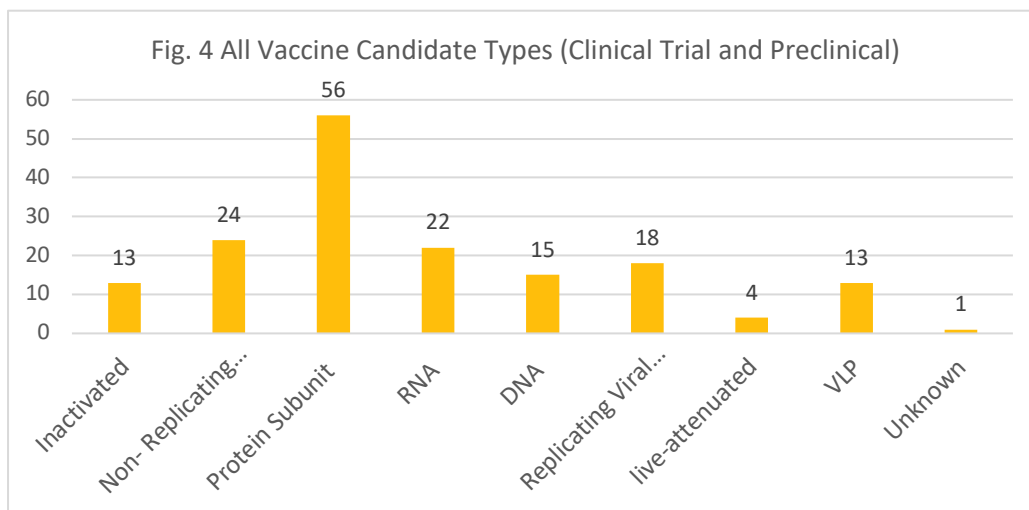


Figure 4 The most common type of vaccine candidate is a protein subunit vaccine, with fifty-six vaccine candidates of this type, and commonly targeting the spike protein of SARS-CoV-2. Many other types of vaccine candidates are also under trial including; inactivated virus, non-replicating viral vector, RNA, DNA, replicating viral vector, live-attenuated, and virus-like particle (VLP).

Appendix B - Drugs
Antivirals

Name	Clinical Trial	Target	Use
Remdesivir	Yes	RNA-dependent RNA polymerase, Replicase polyprotein 1ab	created for ebola virus, has been shown to be useful against coronaviruses (SARS+MERS)
Favipiravir	Yes	RNA-dependent RNA polymerase	influenza A and B, RNA viruses: Ebola, Lassa, Marburg
Ritonavir (Norvir)	Yes	virus protease	HIV/AIDS
Lopinavir	Yes	virus protease	HIV/AIDS
Darunavir	Yes	virus protease	HIV/AIDS
Immucillin A/Galidesivir	Yes	RNA Polymerase	broad spectrum antiviral (negative and positive sense), ebola virus
Arbidol/Umifenovir	Yes	Intercalation into membrane lipids-inhibition of membrane fusion	broad spectrum antiviral, influenza, Hepatitis C, Flaviviruses
Ribavirin	Yes	HCV polymerase	hepatitis C and other RNA viruses, broad spectrum
EIDD-2801/MK-4482	Yes	incorporates into the genome of RNA viruses	influenza
Azvudine	Yes	reverse transcriptase	HIV/AIDS, antiviral
Thymosin alpha 1 (Thymalfasin)	Yes	t cell counts	treatment of viral infections as an immune response modifier, hep b, hep c, HIV
Isoprinesine (Inosine pranobex)	No	induces a Th1 cell-type response, evidenced by an increase in the levels of pro-inflammatory cytokines	antiviral, herpes simplex 1 and 2
Alisporivir	No	Cyclophilin mediated inhibition of viral replication	HCoV-229E, hepatitis C, hepatitis B, flaviviruses
Doxycycline	Yes	Chelation of matrix metalloproteinase	Dengue, Chikungunya, Crimean Congo haemorrhagic fever, HIV
Nitric oxide donor compounds	Yes		Japanese encephalitis and flaviviruses, decreased severity of Coxsackie myocarditis

Oseltamivir (tamiflu)	Yes	Neuraminidase inhibitor	influenza
Teicoplanin	Yes	Cathepsin L	Ebola, HCV, Flaviviruses, Influenza
Triazavirin	Yes	Replication inhibitor	influenza a and b
Cobicistat (Tybost)	Yes	cytochrome P450 3A isoforms (CYP3A)	HIV
Silibinin	Yes		protect liver cells against toxins, <i>in-vitro</i> anti-cancer effects

Immune System

Fingolimod	Yes	S1PR1 on lymphocytes	multiple sclerosis
Ruxolitinib	Yes	tyrosine kinases JAK 1 and 2	myelofibrosis
Baricitinib	Yes	tyrosine kinases JAK 1 and 2	rheumatoid arthritis
Ciclesonide (alvesco)	Yes	Glucocorticoid receptor	releases inflammation, types of arthritis, severe allergies, asthma
Methylprednisolone	Yes	Glucocorticoid receptor	releases inflammation, types of arthritis, severe allergies, asthma
Heparin	Yes	antithrombin III	liver injury, prevent blood clots
Imatinib	Yes	tyrosine kinase	cancer, chronic myelogenous leukemia (CML), gastrointestinal stromal tumors (GISTs)
Thalidomide	Yes	tumor necrosis factor alpha (TNF-alpha)	erythema nodosum leprosum (ENL), multiple melanoma
Sirolimus	Yes	Target Of Rapamycin (mTOR), inhibits T lymphocytes	kidney transplants
Camostat mesylate	Yes	protease, inhibitor of TMPRSS2 (cleaves spike protein)	pancreatitis
Brensocatic (INS1007)	Yes	dipeptidyl peptidase 1 (DPP1)	Under trial -> Non-cystic Fibrosis Bronchiectasis
Metenkefalin	Yes	opioid receptor	multiple sclerosis
Enkorten	Yes	Leukocyte	multiple sclerosis
Selinexor	Yes	Exportin-1	multiple myeloma (cancer)

Anakinra	Yes	human nonglycosylated interleukin-1 (alpha and beta)	rheumatoid arthritis and other inflammatory arthritides
Ibuprofen	Yes	cyclo-oxygenase I and II	anti-inflammatory, painkiller
Dexamethasone (MK-125)	Yes	Glucocorticoid receptor	cerebral edema, congenital adrenal hyperplasia, skin diseases, cancer
Tocilizumab (Actemra)	Yes	IL-6 (Interleukin-6)	rheumatoid arthritis, systemic juvenile idiopathic arthritis (sJIA) and polyarticular juvenile idiopathic arthritis (pJIA)
Auranofin	No	inhibiting phosphorylation of JAK1 and STAT3	rheumatoid arthritis, HIV
Interferon alpha	Yes	Interferon receptor	multiple sclerosis
Interferon beta	Yes	Interferon receptor	multiple sclerosis
Aurintricarboxylic acid	No	ribonuclease and topoisomerase II	influenza-A
Siltuximab	Yes	Interleukin-6	multicentric Castleman's disease
Meplazumab (Nucala)	No	Interleukin-5	asthma
Prednisone	Yes	Glucocorticoid receptor	allergic, dermatologic, gastrointestinal, hematologic, ophthalmologic, nervous system, renal, respiratory, rheumatologic, infectious, endocrine, or neoplastic conditions as well as in organ transplant
Rintatolimod (Ampligen)	Yes	TLR-3	chronic fatigue syndrome
Amiodarone	Yes	Ion channels	entricular arrhythmias, recurrent ventricular fibrillation, recurrent hemodynamically unstable ventricular tachycardia
Spirolactone	Yes	Ion channels	heart failure, deerm, hyperaldosteronism, adrenal hyperplasia, hypertension, and nephrotic syndrome, etc
Eculizumab	Yes	complement protein C5	autoimmune conditions
Ibrutinib	Yes	tyrosine kinase	cancer - mantle cell lymphoma, chronic lymphocytic leukemia, Waldenström's Macroglobulinemia
Duvelisib (IPI-145/INK-1197)	Yes	phosphoinositide-3 kinases	cancer
Ozanimod	Yes	1-phosphate receptor	relapsing multiple sclerosis
Vafidemstat	Yes	Inhibitor of LSD1	Alzheimer's, MS, psychiatric disorders (clinical trials)
Acalabrutinib	Yes	Bruton Tyrosine Kinase (BTK)	used in trials studying the treatment of B-ALL, Myelofibrosis, Ovarian Cancer, Multiple Myeloma, and Hodgkin Lymphoma
Zilucoplan	Yes	terminal complement protein C5	Generalized Myasthenia Gravis (under investigation)
Sildenafil	Yes	cGMP specific phosphodiesterase type 5 (PDE5)	angina, pulmonary arterial hypertension

Nintedanib	Yes	small molecule kinase inhibitor	pulmonary fibrosis, systemic sclerosis-associated interstitial lung disease, and non-small cell lung cancer (NSCLC)
Zanubrutinib (Brukinsa)	Yes	Bruton's tyrosine kinase (BTK)	mantle cell lymphoma (MCL)
Defibrotide	Yes	Adenosine receptors	veno-occlusive disease
Colcrys (colchicine)	Yes	Tubulin beta chain	gout
rhACE2	Yes	ACE2	
pioglitazone	Yes	Peroxisome receptor	type 2 diabetes
Icatibant	Yes	bradykinin B2 receptors	hereditary angioedema
Naproxen	Yes	Prostaglandin	
losartan	Yes	angiotensin II	

Anti-malarial drugs

Chloroquine	Yes	ACE2	malaria, rheumatoid arthritis, lupus erythematosus, etc.
Hydroxychloroquine	Yes	ACE2	malaria, rheumatoid arthritis, lupus erythematosus, etc.
Mefloquine hydrochloride	Yes	Adenosine receptor A2a	malaria

Anti-bacterial drugs

Azithromycin (Zithromax or Z-Pak)	Yes	50S ribosomal subunit of 70S ribosome	bacterial infections->middle ear infections, tonsillitis, throat infections, laryngitis, etc. also effective STDs ex. non-gonococcal urethritis and cervicitis
Sulfamethoxazole and trimethoprim	Yes		bacterial infections
Ceftriaxone	Yes		bacterial infections

Anti-parasitic drugs

Nitazoxanide	Yes	pyruvate-ferredoxin oxidoreductase	anti-parasitic drug, suggested e as a broad-spectrum antiviral agent
Niclosamide (Niclocide)	Yes	DNA (endosomal acidification)	anti-parasitic drug (tapeworms), suggested as a broad-spectrum antiviral agent

Convalescent plasma treatment

Convalescent plasma	Yes	n/a	viruses
---------------------	-----	-----	---------

Pulmonary vasodilators

Iloprost	Yes	Prostacyclin receptor	pulmonary arterial hypertension (PAH), scleroderma, Raynaud's phenomenon, etc.
Treprostinil	Yes	Prostacyclin receptor	pulmonary arterial hypertension (PAH)
Epoprostenol	No	Prostacyclin receptor	pulmonary arterial hypertension (PAH)
Nitric Oxide	Yes	Prostacyclin receptor	pulmonary arterial hypertension (PAH)

Vitamins

- Vitamin B12
- Magnesium
- Vitamin D
- Zinc

Traditional herbal medicines

- Xuanfei Baidu Decoction
- Unani regimen
- Black Seed Oil

Anesthetics

Sevoflurane (fluoromethyl)	Yes	Ion channels	anesthetic
Propofol	Yes	Ion channels	anesthetic

Appendix C - Vaccines

Developer/researcher	Name	Type	Stage
Beijing Institute of Biotechnology/CanSino Biologics	Ad5-nCoV	Non- Replicating Viral Vector	Phase II
Sinovac	CoronaVac	Inactivated	Phase III
Wuhan Institute of Biological Products/Sinopharm		Inactivated	Phase III
University of Oxford/AstraZeneca	AZD1222	Non- Replicating Viral Vector	Phase II/III
Anhui Zhifei Longcom Biopharmaceutical/ Institute of Microbiology, Chinese Academy of Sciences		Protein Subunit	Phase II
Moderna/NIAID	mRNA-1273	RNA	Phase III
Inovio Pharmaceuticals/ International Vaccine Institute	INO-4800	DNA	Phase I/II
Osaka University/ AnGes/Takara Bio	AG0301-COVID19	DNA	Phase I/II
Genexine Consortium	GX-19	DNA	Phase I/II
Cadila Healthcare Limited		DNA	Phase I/II
Institute of Medical Biology, Chinese Academy of Medical Sciences		Inactivated	Phase I/II
Novavax		Protein Subunit	Phase I/II
Kentucky Bioprocessing, Inc		Protein Subunit	Phase I/II
BioNTech/Fosun Pharma/Pfizer		RNA	Phase I/II
Gamaleya Research Institute		Non- Replicating Viral Vector	Phase I
Clover Biopharmaceuticals Inc./GSK/Dynavax		Protein Subunit	Phase I
Vaxine Pty Ltd/Medytox		Protein Subunit	Phase I
University of Queensland/CSL/Seqirus		Protein Subunit	Phase I
Imperial College London		RNA	Phase I
Curevac		RNA	Phase I

People's Liberation Army (PLA) Academy of Military Sciences/Walvax Biotech.		RNA	Phase I
Medicago Inc.		VLP	Phase I
University of Melbourne and Murdoch Children's Research Institute; Radboud University Medical Center; Faustman Lab at Massachusetts General Hospital	Bacillus Calmette- Guerin (BCG)	live-attenuated	Phase II/III
Bharat Biotech		Inactivated	Phase I/II
Arcturus/Duke-NUS		RNA	Phase I/II

Nuclear scattering code python interface

Nicholas Holfester, Department of Applied Physics and Applied Mathematics, Columbia University, New York, NY 10027

Matteo Vorabbi, Nuclear Science and Technology, Brookhaven National Laboratory, Upton, NY 11973

ABSTRACT

A precise description of nucleon-nucleus scattering processes are of great importance for many applications in nuclear physics. The microscopic description of such processes is in general very difficult and becomes increasingly computationally demanding as reactant size increases. For this reason, the optical model potential (OMP) was developed to reduce the many-body interaction to a two-body one by modelling the potential with a simple analytic form which contains free parameters that are adjusted to reproduce experimental data. As the future development of OMPs will be focused on application to nuclei far from stability, the fitting procedure of the free parameters will become significantly more computationally expensive. One method to maintain computational efficiency is to parallelize nuclear scattering codes on a graphics processing unit (GPU). While Fortran is commonly used in nuclear scattering codes, C++ is a more natural candidate for this method, motivating the creation of a new scattering code currently being developed by the National Nuclear Data Center (NNDC) and also a separate code to generate OMP parameters and interface with the nuclear scattering code. With this motivation, we have written a Python package which is able to easily interface with the NNDC scattering code and generates OMP parameters, nuclear binding energy, spin, and parity for a specific choice of projectile, target, and incident energy. By employing highly vectorized operations in Python in conjunction with the most up to date Reference Input Parameter Library (RIPL-3) reference data, our interface allows for compact, efficient, and highly adaptable parameter calculations.

I. Introduction

The microscopic description of nucleon-nucleus scattering is a very challenging task due to the complexity of the many-body problem. A simpler treatment can instead be achieved by using phenomenological optical model potentials (OMPs), which describe the nucleon-nucleus interaction through the definition of a complex potential. The real component of an OMP describes the attraction between the projectile and the target nucleus while the imaginary part takes into the account the loss of flux due to the open inelastic channels. Phenomenological optical potentials assume the existence of a simple analytic functional form for the potential that contains free parameters that can be constrained so to reproduce experimental data.

The general form of an OMP is a sum of different terms that describe different effects that occur during the scattering process. In general, we have volume, surface, and spin-orbit terms, with real and imaginary instances of each. The volume terms use a Woods-Saxon function, while the surface and spin-orbit terms are proportional to the derivative of a Woods-Saxon, which provides the largest effect in correspondence of the nuclear surface. Each term contains three free parameters to be constrained, diffuseness, radius, and well depth, with each describing a geometric property of the potential. Phenomenological optical potentials are called “local” if these parameters are fit using a dataset for an energy range at a single mass value and “global” if they are fit using a dataset containing both energy and mass ranges.

The simple functional form and the fit to the experimental data make phenomenological optical potentials more accurate and simpler to use than OMPs derived from microscopic approaches. Because of this, phenomenological OMPs are commonly used in nuclear scattering codes. This has led to the development of a handful of databases containing a centralized collection of OMPs; perhaps most notably is the Reference Input Parameter Library (RIPL-3) [1].

Despite the advances achieved in the past years, the development of more accurate optical potentials is still an on-going project. So far, phenomenological optical potentials have been developed to describe the experimental data for elastic scattering of nucleons off spherical target nuclei. The development of an OMP for rare-earth nuclei in particular would be very important for many applications but has not yet been achieved. The development of such a potential is, in general, very complicated because the simple spherical model can no longer be used and the deformation of the nucleus must be considered explicitly. However, in Ref.[2] the authors showed that a spherical OMP in the adiabatic approximation is able to describe the experimental data for scattering off statically deformed nuclei with a good precision when used in coupled-channel calculations. This has motivated the creation of a new nuclear scattering code by the National Nuclear Data Center (NNDC).

Due to the free parameters, the fitting procedure of a global OMP can become a computationally demanding task, though one that can still presently be achieved using existing codes on high-computing facilities. However, as these more advanced OMPs are developed, the fitting procedure will become increasingly expensive. One method to maintain computational efficiency when working with a general optical potential is to parallelize the scattering code on a graphics processing unit (GPU). By parallelizing code on a GPU, lengthy computations are able to be performed highly efficiently, drastically decreasing total run times and enabling more rapid fitting of the free parameters of a general OMP. While many nuclear scattering codes have been developed in Fortran, this method is more naturally used in C++. Therefore, the NNDC code will be an entirely new code written in C++ so to allow for parallelization on a GPU. Furthermore, this code will be based on the R-matrix theory [3], a highly efficient method for solving the Schrödinger equation numerically.

In order for the NNDC's code to remain general, it should be able to leverage the data already stored in centralized OMP databases, such as RIPL-3. This motivated the creation of our own code to interface the NNDC code with the RIPL-3 library. Our interface is able to generate RIPL-3 based OMP parameters as well as nuclear binding energy, spin, and parity for a specified projectile, target, and incident energy and create a standard input file for the NNDC's code.

II. Methods

In this section we will first introduce the theory of the R-matrix and show how it may be used to solve the Schrödinger equation numerically. With this theory established, we next illustrate how a phenomenological OMP, which can be used with the R-matrix theory, is constructed in our package, highlighting the specific functional forms of the free parameters used by RIPL-3. After this, we detail the specific structure of our package and show how it is used to generate an input for the NNDC scattering code. Finally, we provide descriptions of additional built-in functionality which may be utilized by a user for general purposes outside of generating a scattering code input.

A. Theory

Here we give a very brief summary of the R-matrix theory, which the NNDC nuclear scattering code is based on. A key benefit of the R-matrix theory is that it converts the problem of solving the Schrödinger differential equation into a problem of matrix diagonalization.

One can solve the radial Schrödinger equation, $(H_l - E)u_l = 0$, for the l -th partial wave by dividing the configuration space into an internal and external region at radius a . At this boundary, the continuity of the wave function, u_l , and its derivative motivates the definition of the R-matrix at energy E as

$$u_l(a) = R(E)[au_l'(a) - Bu_l(a)] \quad (1)$$

where B is a dimensionless parameter. Taking a finite basis, φ_j , the R-matrix can be re-defined with the finite-basis approximation

$$R(E, B) = \frac{\hbar^2}{2\mu a} \sum_{i,j=1}^N \varphi_i(a) (C^{-1})_{ij} \varphi_j(a) \quad (2)$$

with μ the reduce mass and C a matrix defined as

$$C_{ij}(E, B) = \langle \varphi_i | T_l + \mathcal{L}(B) + V - E | \varphi_j \rangle \quad (3)$$

where T_l is the kinetic energy operator, $\mathcal{L}(B)$ is the Bloch operator, and V is the potential.

A particularly useful choice of basis functions is Lagrange functions. Defined on the interval $(0, a)$, Lagrange functions take the form

$$\varphi_i(r) = (-1)^{N+i} \left(\frac{r}{ax_i} \right)^n \sqrt{ax_i(1-x_i)} \cdot \frac{P_N(2r/a-1)}{r-ax_i} \quad (4)$$

where P_N is the Legendre polynomial of order N and x_i are the zeros of $P_N(2x_i-1) = 0$. With the choice of Eq.(4) it is possible to show Eq.(3) becomes a simple matrix. All we need to do now is invert this matrix which can be done easily on a computer.

From the knowledge of the R matrix, the collision matrix, U_l , is calculated as

$$U_l = e^{2i\phi_l} \frac{1 - (L_l^* - B)R_l(E, B)}{1 - (L_l - B)R_l(E, B)} \quad (5)$$

where ϕ_l and L_l are given in Ref.[3]. Once the collision matrix is known for all channels, all scattering observables can be obtained.

B. Optical Potential Parametrization

To invert Eq.(3) in the previous section we need an expression for the optical potential $V(r)$.

The general parametrization used in RIPL-3 to construct an optical potential is

$$V(r) = -V_R f_R(r) - iW_V f_V(r)$$

$$\begin{aligned}
& +4a_{VD}V_D \frac{d}{dr} f_{VD}(r) + 4ia_{WD}W_D \frac{d}{dr} f_{WD}(r) \\
& + \frac{\lambda_\pi^2}{r} \left[V_{SO} \frac{d}{dr} f_{VSO}(r) + iW_{SO} \frac{d}{dr} f_{WSO}(r) \right] \sigma \cdot l
\end{aligned} \tag{6}$$

where V_R and W_V are the real and imaginary volume well depths, V_D and W_D are the real and imaginary surface well depths, V_{SO} and W_{SO} are the real and imaginary spin-orbit well depths, $\sigma \cdot l$ is the scalar product of the intrinsic and orbital angular momentum operators, λ_π is the pion Compton wavelength, a_i is the diffuseness parameter, and $f_i(r)$ is the radial form factor.

The form factor, $f_i(r)$, is a Woods-Saxon

$$f_i(r) = \left[1 + \exp\left(\frac{r - R_i}{a_i}\right) \right]^{-1} \tag{7}$$

and R_i , the radius parameter, and a_i , the diffuseness parameter, are given by

$$\begin{aligned}
R_i &= r_i A^{1/3} \\
r_i(E) &= \beta_1 + \beta_2 E + \beta_3 \eta + \beta_4 A^{-1} + \beta_5 A^{-1/2} + \beta_6 A^{2/3} + \beta_7 A + \beta_8 A^2 \\
& \quad + \beta_9 A^3 + \beta_{10} A^{1/3} + \beta_{11} A^{-1/3}
\end{aligned} \tag{8}$$

and

$$\begin{aligned}
a_i(E) &= \delta_1 + \delta_2 E + \delta_3 \eta + \delta_4 A^{-1} + \delta_5 A^{-1/2} + \delta_6 A^{2/3} + \delta_7 A + \delta_8 A^2 \\
& \quad + \delta_9 A^3 + \delta_{10} A^{1/3} + \delta_{11} A^{-1/3}
\end{aligned} \tag{9}$$

where E is the incident energy, η is the asymmetry parameter, A is the atomic mass of the target, and β_i and δ_i are parameters stored in RIPL-3.

Finally, the well depth form used is

$$\begin{aligned}
V_i(E) &= \alpha_1 + \alpha_7 \eta + \alpha_8 \Delta_c + \alpha_9 A + \alpha_{10} A^{1/3} + \alpha_{11} A^{-2/3} + \alpha_{12} \Delta_{c'} \\
& \quad + (\alpha_2 + \alpha_{13} \eta + \alpha_{14} A) E + \alpha_3 E^2 + \alpha_4 E^3 + \alpha_6 \sqrt{E} \\
& \quad + (\alpha_5 + \alpha_{15} \eta + \alpha_{16} E) \ln(E) + \alpha_{17} \Delta_c E^{-2}
\end{aligned} \tag{10}$$

where Δ_c and $\Delta_{c'}$ are Coulomb correction terms given in Ref.[1] and α_i are parameters stored in RIPL-3.

By using such general forms, RIPL-3 is able to maintain a large array of diverse OMPs. To be able to utilize the RIPL-3 OMP library, we have coded our interface to use these functional forms for the optical potential and free parameters. The sub-parameters α_i , β_i , and δ_i are the primary contents of the library and both function as coefficients as well as calculation specifiers.

C. Interface Structure

Our package consists of five main processes: retrieving and cleaning specified data from the RIPL-3 OMP library; calculating the geometric OMP parameters, as well as the Coulomb radius and Fermi energy, based on specified scattering parameters; calculating nuclear mass for projectile and target; retrieving spin and parity for projectile and target; and formatting and writing the NNDC scattering code input file as well as an OMP parameter table. All of these processes are managed by an overarching Python script, *write_input.py*, which organizes function calls, and a shell script that is the user's primary point of interaction with the interface when writing an NNDC scattering code input file.

In the shell script, a user must specify the projectile, target, incident energy, and optical potential to be used as well as maximum orbital angular momentum, basis type, number of basis points, and channel radius. The last four parameters are used in the R-matrix calculation within the NNDC code. After the shell script is run, the sub-script *sub_param_func.py* reads the RIPL-3 OMP data file and retrieves and formats the sub-parameters for the subsequent calculation of the free parameters.

The script *potential_func.py* next calculates the base values of radius, diffuseness, and well depth for the real and imaginary instances of the volume, surface, spin orbit potential components in Eq.(6). This is the most expensive part of generating the OMP parameters and therefore, to

optimize this portion of the code, the python libraries NumPy [4] and Pandas [5] are heavily employed to vectorize calculations by leveraging contiguous block data storage. Both the diffuseness and radius parameters for all potential components are calculated simultaneously using vectorization according to Eq.(8) and Eq.(9). Well depths are calculated using arrays sub-divided into special forms of Eq.(10) to further improve efficiency. This script also relies on sub-functions contained in *mass_energy_func.py* that calculate the Fermi energy and exact nuclear masses which are used in parameter calculations. Finally, depending on the form of the input potential, the scripts *relativistic_func.py* and *dispersive_func.py* add relativistic and dispersive contributions to the base parameters.

After calculating the free parameters; spin, parity, and nuclear mass for the specified projectile and target are retrieved. The script *spin_parity.py* retrieves the spin and parity for the ground state projectile and target using data from the RIPL-3 library “Levels”. The script *AMDC_mass_energy_data.py* calculates the mass in MeV of both nuclei using the most up to date nuclear binding energy data from the Atomic Mass Data Center (AMDC) 2016 Atomic Mass Evaluation (AME2016) [6]. Finally, the script *write_input.py* formats all of the retrieved data with the R-matrix parameters in a standard input file, *input.dat*, for the NNDC nuclear scattering code. Additionally, the file *print_omp_RIPL_format.dat*, containing a human-readable review of scattering specifications and OMP parameters, is output.

D. Additional Functionality

In the spirit of generality, in addition to interfacing with the NNDC nuclear scattering code, we have designed our interface to have stand-alone features which any user may potentially find

useful. Details on how to use these features are described in the script *test_functions.py* contained in the interface. Here we describe what these features are able to do.

Generate OMP Table

A user is able to generate a human-readable data table of optical potential parameters at specified incident energies within the range of definition of the potential. The file also contains a complete summary of optical potential specifications used in generating the parameters.

Retrieve Nucleus Data

By leveraging the fact that our interface has centralized nuclear data both from RIPL-3 and AME2016, a user can independently request information such as nuclear binding energy, mass excess, spin, and parity for a given nucleus at a specified excitation.

Store OMP Python Variable

While the package is specifically designed to easily interface with the NNDC nuclear scattering code, a user also has the option to store generated OMP parameters as a Python variable, allowing them to potentially be used in scripts other than the NNDC code.

III. Results

After testing our interface extensively for various combinations of projectile, target, potential, and incident energy and cross-checking our results with those produced by RIPL-3, it appears that our interface produces the expected diffuseness, radius, and well depth parameters for well-defined combinations of reaction parameters. Figure 1 shows an example of the well depth parameters generated by our interface for elastic neutron scattering off ^{208}Pb using the global optical potential of Koning and Delaroche [7]. Furthermore, upon comparison with the RIPL-3 and AME2016, we have also verified that our interface produces the correct values of spin, parity, and nuclear mass for specified nuclei. Using our finalized package, the total run time from call to file generation is

of the order of seconds, demonstrating effectiveness of the vectorized method of coding in producing efficient run times. Together, these results verify that our interface is able to generate the required input parameters for the NNDC scattering code both accurately and efficiently.

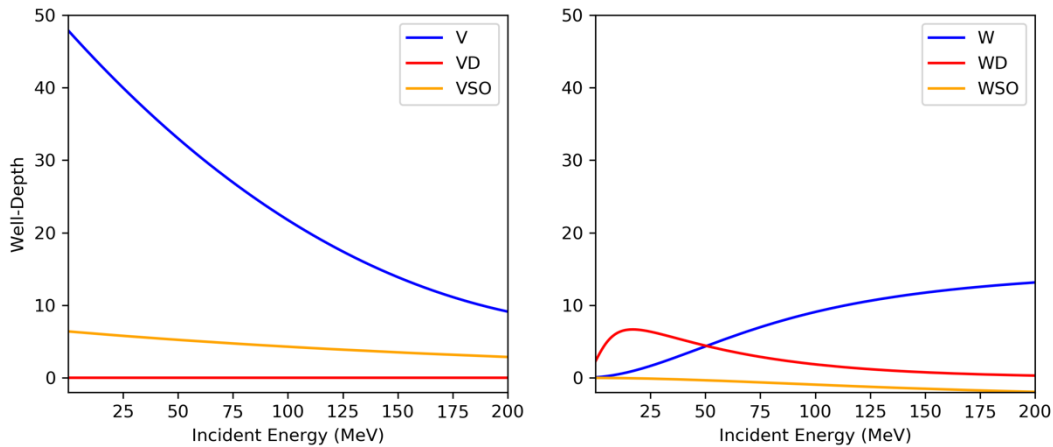


Figure 1. Potential well depths as a function incident energy for elastic neutron scattering off ^{208}Pb . (left) Well depths of real volume, surface, and spin orbit OMP components. (right) Well depths of imaginary volume, surface, and spin orbit OMP components.

To further verify the proper functioning of our interface, we also tested its ability to interface with the elastic scattering portion of the NNDC code. Figure 2 shows two examples generated using our interface in conjunction with the NNDC nuclear scattering code for elastic neutron and proton scattering off ^{208}Pb using Koning and Delaroche neutron and proton global potentials respectively. Checking our results, we found them to be in agreement with the results of the original paper [7].

The above tests verify that our interface has accomplished exactly what it was planned to and further illustrate the flexibility and generality that it will add to the new NNDC nuclear scattering code.

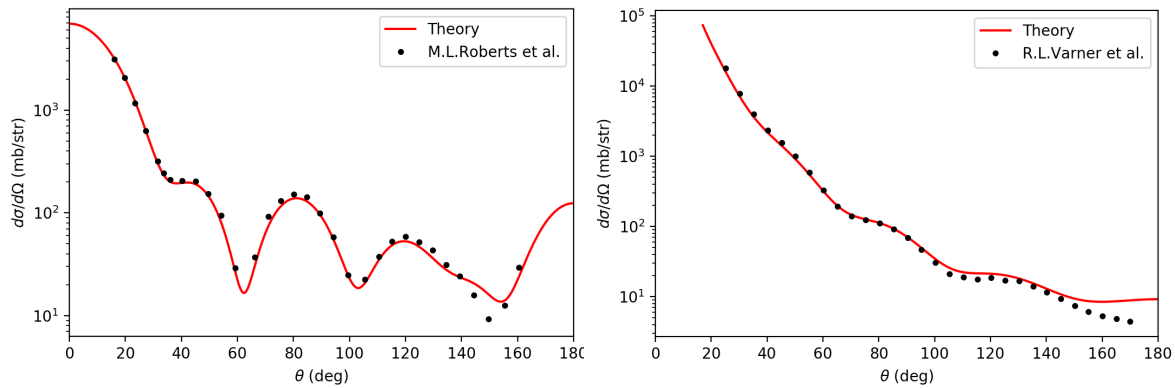


Figure 2. (left) Differential cross section for elastic neutron scattering off ^{208}Pb at 7.97 MeV. Experimental data from Ref.[8]. (right) Differential cross section for elastic proton scattering off ^{208}Pb at 16.0 MeV. Experimental data from Ref.[9].

IV. Acknowledgments

I would like to thank my mentor, Matteo Vorabbi for his kindness, expertise, and guidance during the SULI program. This project was supported in part by the U.S. Department of Energy, Office of Science, Office of Workforce Development for Teachers and Scientists (WDTS) under the Science Undergraduate Laboratory Internships Program (SULI).

[1] <https://www-nds.iaea.org/RIPL-3/>.

[2] G. P. A. Nobre, A. Palumbo, M. Herman, D. Brown, S. Hoblit, and F. S. Dietrich, Phys. Rev. C91, 024618(2015).

[3] P. Descouvemont and D. Baye, Reports on Progress in Physics 73, 036301 (2010).

[4] <https://numpy.org/>

[5] <https://pandas.pydata.org/>

[6] <https://www-nds.iaea.org/amdc/>.

[7] A. Koning and J. Delaroche, Nuclear Physics A713, 231(2003).

[8] M. L. Roberts, P. D. Felsher, G. J. Weisel, Z. Chen, C. R. Howell, W. Tornow, R. L. Walter, and D. J. Horen, Phys. Rev. C44, 2006 (1991).

[9] R. Varner, W. Thompson, T. McAbee, E. Ludwig, and T. Clegg, Physics Reports 201, 57 (1991).

Classifying neutron resonances with decision tree algorithms

Sophia Hollick*, Pedro Rodríguez†, David Brown‡, Gustavo Nobre§

August 21, 2020

Contents

1	Introduction (Theory and background)	2
2	Methodology	3
2.1	Training data	3
2.2	The Decision Tree	3
2.3	Features	5
3	Results and Discussion	9
4	Conclusion	10
5	Acknowledgements	11

Abstract

The performance of nuclear reactors and other nuclear systems depends on a precise understanding of the neutron interaction cross sections for materials used in these systems. The correct assignment of the quantum numbers of neutron resonances (cross-section enhancements from highly-excited levels in compound nucleus) is therefore of paramount importance. In this project, we attempt to apply a machine learning technique, namely decision trees, to automate these quantum number assignments. The tree is trained from simulated data generated to mimic the errors found in real data used by the National Nuclear Data Center (NNDC) at BNL. We explore the use of several physics-motivated features for training our trees, including the Nearest Neighbor Spacing Distribution (NNSD), Cumulative Level Distribution (CLD), and channel Width Distributions. Initial results using random matrix theory motivated fits

*Department of Physics, Yale University, New Haven, CT, 06520

†University of Puerto Rico Mayagüez Campus, 00681

‡Nuclear Science and Technology, Brookhaven National Laboratory, Upton, NY 11973

§Nuclear Science and Technology, Brookhaven National Laboratory, Upton, NY 11973

which demonstrated that we can determine resonance spin groups somewhat reliably. If we use these fits as features in our trees, we can train them to spot outliers that correspond to missing and misassigned resonances. We found that with the large number of features used in this project that the decision tree tended to overfit training data resulting in poor performance with respect to the test data, suggesting that decision trees are not a good solution for the spin group assignment problem. Even though the bold original goals of the project were not all achieved, this work represented an important first step in the automation of the identification and correction of issues in neutron resonances. Future projects will explore other classification techniques and will be much more physics-informed.

1 Introduction (Theory and background)

Resonances are the energy levels in compound nuclei above the neutron separation energy as shown on the left in Fig. 1. To observe a resonance, a thin (hopefully monoisotopic) target bombarded with low energy neutrons. At specific energies a peak within a cross section vs energy magnitude of neutrons appears. The cross section σ is the proportionality constant between the number of reactions per unit time per nucleus N and the number of incident particles per unit time per unit area I ; $N=\sigma*I$ [1]. On the right in Fig. 1, we illustrate how the resonances manifest in a cross section. The shape of the cross section peaks depend on the J (total angular momentum) quantum number of compound nucleus energy level and the L (orbital angular momentum) quantum number of the projectile/target system. These quantum numbers define a spin group. Different resonances which possess the same quantum numbers can be grouped together in a monotonically increasing sequence. Proper accounting of resonances for fuel and structural materials is important in the construction of nuclear reactors. To this day almost all known resonances for nuclei across the nuclide chart are tabulated in the *The Atlas of Neutron Resonances* [2].

Currently, the only approach to resonance classification by spingroup is by a method called shape analysis in which an experimenter fits cross section data to a specific functional form that depends on the J and L quantum numbers. However, at higher energies, the shape analysis of the energy resonances start failing due to similarity of the shape of the different resonances. This loss in clarity makes the classification of the energy resonances harder and errors in the classification start appearing. Another big problem inherent to this method is that the value of the initial parameters to be able to do the fit are selected subjectively by the experimenter. This implies that the results of this current method are not completely reproducible, which is a huge drawback.

Two of the past SULI projects have suggested that a more robust determination of the mean level spacing coupled with the level spacing distribution may be used in a machine learning approach to classify resonances. Results from the Fall 2019 SULI project from one of us (S.J. Hollick) are shown in Fig. 2. This study tries to develop a more reliable, automated and reproducible method through the utilization of a decision tree. A tool which if implemented correctly

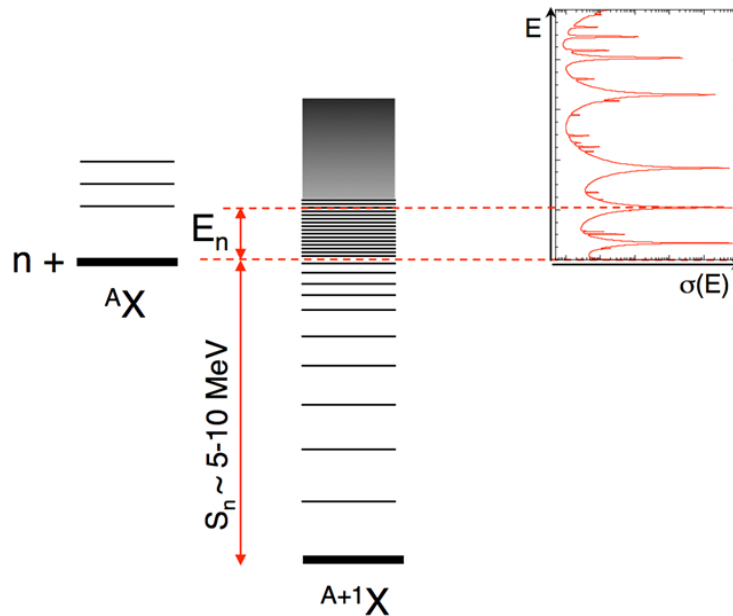


Figure 1: An example of a nuclear cross section. Each line represents an energy resonance. At higher energies, it makes sense to describe the sequence as a continuum than discrete levels that are clearer at lower energies.

can be very powerful. The decision tree used in this study can be found in the Sci-kit learn python module [3].

2 Methodology

2.1 Training data

Since good training data is crucial to a proper set up of the tree, sets of fake resonances that mimic what is observed in real data are used as the training sets [4]. We took these simulated resonances and “jumbled” them, by randomly re-assigning a subset of resonances to other spingroups. With this realistic training data, we used the Sci-kit learn [3] `test_train` function to split data into training data and test data. This function randomly chooses 75% of the resonances for training purposes and reserves the remaining 25% to test the performance of whatever machine learning approach is used.

2.2 The Decision Tree

A decision tree tries to determine if a data point does or it doesn't belongs to a certain class by answering different binary questions about the features of

Cumulative Level Distribution v Resonance Energy

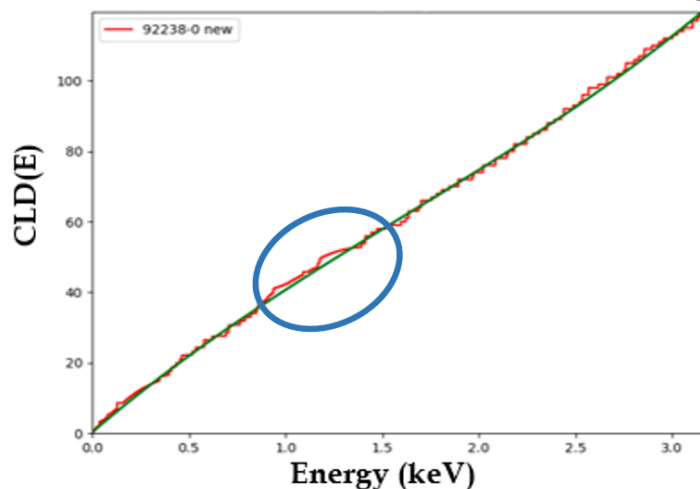


Figure 2: This is the Cumulative Level Distribution for U-238, spin $l=0$, $j=0.5$. Each step corresponds to a resonance where its energy is given by the x-axis and its position in the sequence is given by the y-axis. The blue region highlights larger steps which point to likely missing or misassigned resonances. The green line represents initial polynomial fitting done in a SULI project in fall 2019 that demonstrated missing data where the curve inflects.

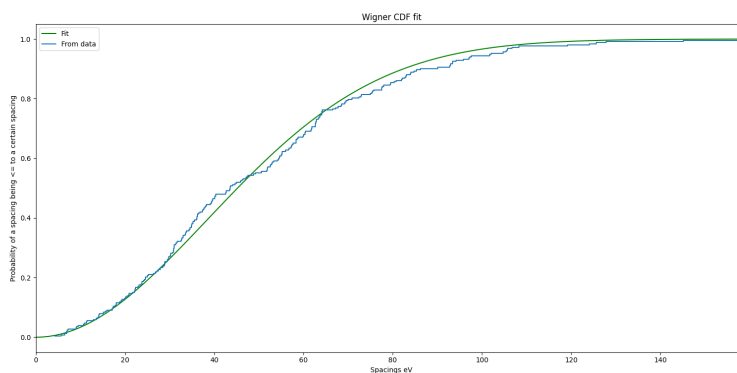


Figure 3: This is the Cumulative Density Function for spacings from a computer-generated sequence of resonances, which portrays the probability of a spacing between two energies being equal or lower than a certain energy. The blue line is the experimental data and the green line is the Wigner CDF fit. This can serve as an indication of the resonances that may be outliers.

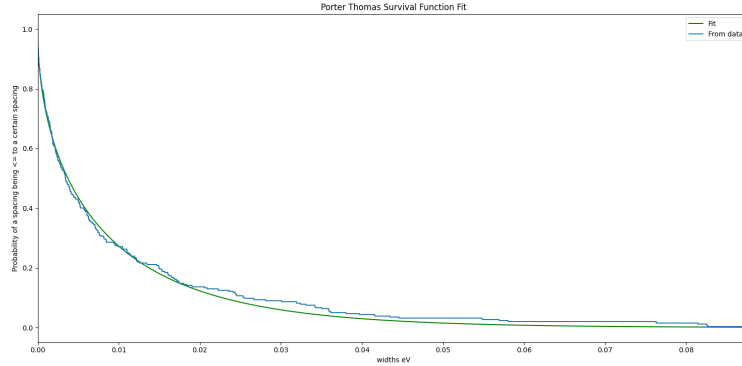


Figure 4: Example of the Survival Function (blue line) of the Porter Thomas Probability Density Function for computer-generated sequence of the resonance widths, comparing its fit (green line). This serves as another indication of possible outlier resonances.

those data points. But, before trying to determine if the data belongs to the class, a decision tree must be trained. This is done by first taking a specific amount of labeled data from the main data set (about 75% in our case) and then ask a binary question to that data. Then, the data points that got the same answer from the question are grouped together and the impurity of the group is analyzed. The "purity" is measured with the Gini impurity formula 1

$$G = \sum_{m=1}^K \hat{p}_m (1 - \hat{p}_m) \quad (1)$$

where K is the number of classes and \hat{p}_m is the probability of picking a data point with class m. It tries to quantify how mixed a group of data points really is. This process of asking a binary question, then splitting the questioned group of data points by their answer and finally measuring the Gini impurity of the groups is kept until the Gini impurity of the group is zero or until the user decides to stop. After the tree is built, the data points that have unknown labels are fed to the tree. The data points are asked a question and depending on the answer to the question is where they gonna end up.

2.3 Features

Below we list the features used in the training data for our decision tree. This list includes several global parameters that do not change with classification and are irrelevant. The features J and L are also labels and may be "overridden" in the classification process.

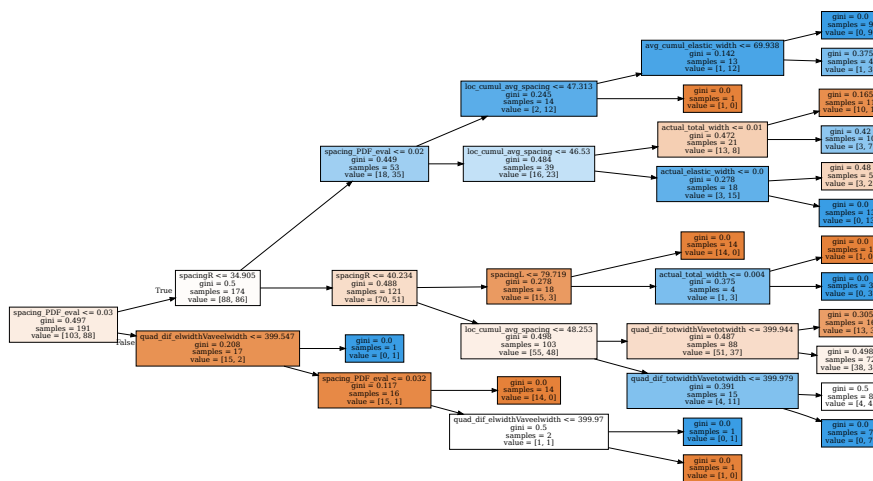


Figure 5: A plot of a decision tree that uses the data and features of this project. The more solid the color, the more pure the sample. If the box is white, it means there is an even split in purity. The number of splits the tree makes down one path defines its depth. The goal in the decision tree algorithm is to have only solid colored boxes in the deepest nodes (i.e. perfectly pure samples that have minimized the entropy of the set).

Several of the features are the probability that the given feature are consistent with a known distribution. These are the Wigner surmise distribution for the resonance spacings [5]

$$P_w(D) = \frac{\pi D}{2\overline{D}^2} \exp\left(-\frac{\pi D^2}{4\overline{D}^2}\right) \quad (2)$$

and the Porter-Thomas distribution for resonance widths [2]

$$P_{pt}(x) = \frac{1}{2^{\nu/2}\Gamma(\nu/2)} x^{\nu/2-1} e^{-x/2} \quad (3)$$

where $x = \Gamma/\overline{\Gamma}$. Figures 3 and 4 demonstrate the fitting of the Wigner surmise and Porter-Thomas distributions respectively.

In order to avoid overfitting, only a handful of the most noteworthy features are used. We will address each of them individually here so as to explain the data available for growing the decision tree.

Z - is the number of protons in the given nucleus and is a global variable to the sequence. As a result, it is not favored as a splitting dimension in the tree.

A - is the number of nucleons in the given nucleus and is also a global variable. It is not favored for the same reason.

parity_protons - Whether the number of protons is even or odd. It is global and thus is not favored dimensions by the tree.

parity_neutron - Whether the number of neutrons is even or odd. It is global and thus is not favored dimensions by the tree.

L - The orbital angular momentum of the n th resonance, L_n , assigned prior to classification. Because the nature of the tree is to decide whether or not the spin assignment is correct, this dimension is unfavorable. Luckily, it does not seem to impact the tree when it is implemented.

J - Total angular momentum of the n th resonance, J_n , assigned prior to classification. Because the nature of the tree is to decide whether or not the spin assignment is correct, this dimension is unfavorable. Luckily, it does not seem to impact the tree when it is implemented.

avg_spacing The average spacing, \overline{D} , - Average distance between adjacent energy resonances for a given spin group. It is global and thus is not favored dimensions by the tree.

avg_neutron_width - The average neutron width, $\overline{\Gamma}_{el}$, computed before classification. It is global and thus is not favored dimensions by the tree.

avg_gamma_width - The average capture width, $\overline{\Gamma}_\gamma$, computed before classification. It is global and thus is not favored dimensions by the tree.

`avg_total_width` - The average total width, $\bar{\Gamma}_{tot}$, computed before classification. It is global and thus is not favored dimensions by the tree.

`neutron_nu_DOF` - The number of degrees of freedom in the Porter-Thomas distribution of elastic widths, ν_{el} , computed before classification. It is global and thus is not favored dimensions by the tree.

`gamma_nu_DOF` - The number of degrees of freedom in the Porter-Thomas distribution of capture widths ν_{γ} , computed before classification. It is global and thus is not favored dimensions by the tree.

`total_nu_DOF` - The number of degrees of freedom in the Porter-Thomas distribution of total widths ν_{tot} , computed before classification. It is global and thus is not favored dimensions by the tree.

`pos/len` - position over length This is the position of the variables within the sequence divided by the length of the sequence. Indicates how far along the sequence is the resonance. Since resonances of higher energy are more likely to be misplaced, this is a fair way to predict whether or not a resonance in a given region of the sequence will be problematic.

`energy` - The energy of the n th resonance, E_n .

`actual_capture_width` - The capture width of the n th resonance, $\Gamma_{\gamma,n}$

`actual_total_width` - The total width of the n th resonance, $\Gamma_{tot,n}$

`actual_elastic_width` - The elastic width of the n th resonance, $\Gamma_{el,n}$

`avg_cumul_spacing` - Average cumulative spacing, \bar{D}_n - The average spacing calculated by using only the resonances with energies equal and below the current energy of the resonance in question.

`spacingR` - Right spacing, $D_{R,n}$ - Spacing between the resonance energies with index n and $n + 1$.

`spacingL` - Left spacing, $D_{L,n}$ - Spacing between the resonance energies with index $n - 1$ and n .

`quad_dif_spacVavespac` - The quadratic difference between the n th spacing and the average spacing, $|D_n - \bar{D}|^2$

`quad_dif_cpwidthVavecpwidth` - The quadratic difference between the n th capture width and the average capture width, $|\Gamma_{\gamma,n} - \bar{\Gamma}_{\gamma}|^2$

`quad_dif_elwidthVaveelwidth` - The quadratic difference between the n th elastic width and the average elastic width, $|\Gamma_{el,n} - \bar{\Gamma}_n|^2$

`quad_dif_totwidthVavetotwidth` - The quadratic difference between the n th total width and the average total width, $|\Gamma_{tot,n} - \bar{\Gamma}_{tot}|^2$

`spacing_PDF_eval` - The evaluation of the n th spacing with the fitted Wigner surmise of the sequence in question, $P_w(D_n)$. This uses the current value for \overline{D}_n .

`elastic_PDF_eval` - The evaluation of an elastic width with the fitted Porter Thomas distribution of the sequence in question, $P_{pt}(\Gamma_{el,n}/\overline{\Gamma}_{el})$. The fitted parameter for this function are the average width $\overline{\Gamma}_{el}$ and the degrees of freedom ν_{el} .

`capture_PDF_eval` - The evaluation of a capture width with the fitted Porter Thomas distribution of the sequence in question, $P_{pt}(\Gamma_{\gamma,n}/\overline{\Gamma}_{\gamma})$. The fitted parameter for this function are the average width $\overline{\Gamma}_{\gamma}$ and the degrees of freedom ν_{γ} .

`total_PDF_eval` - The evaluation of a total width with the fitted Porter Thomas distribution of the sequence in question, $P_{pt}(\Gamma_{tot,n}/\overline{\Gamma}_{tot})$. The fitted parameter for this function are the average width $\overline{\Gamma}_{tot}$ and the degrees of freedom ν_{tot} .

`avg_cumul_elastic_width` - The average elastic width calculated by using only the resonances with energies equal and below the current energy of the resonance in question, $\overline{\Gamma}_{el,n}$.

`avg_cumul_capture_width` - The average capture width calculated by using only the resonances with energies equal and below the current energy of the resonance in question, $\overline{\Gamma}_{\gamma,n}$.

`avg_cumul_total_width` - The average total width calculated by using only the resonances with energies equal and below the current energy of the resonance in question, $\overline{\Gamma}_{tot,n}$.

`avg_cumul_elastic_nu` - The degrees of freedom $\nu_{el,n}$ of the elastic widths calculated by using only the resonances with energies equal and below the current energy of the resonance in question.

`avg_cumul_total_nu` - The degrees of freedom $\nu_{tot,n}$ of the total widths calculated by using only the resonances with energies equal and below the current energy of the resonance in question.

3 Results and Discussion

The first decision tree was trained with all 34 features and produced an accuracy of about 50%, which with two spingroups, is no better than flipping a coin. It was found that if the tree was too deep, the accuracy lowered by about a 5% and the best depth was found to be between 4 and 6 nodes. Nonetheless, the accuracy didn't improve above 50%.

As a second attempt to improve the accuracy of the tree, the fraction of reassigned resonances in the training data was changed from about a 40% of

jumbled data to a 10% of jumbled data. It was found that with this new data set the tree had improved its accuracy from an 50% to an 80%. But, it still was not a true improvement since the data is just easier to classify than the previous set. Another problem that was found was that most of the features could identify data points that were outliers just for the L-label. However the decision tree had almost no way of identifying outliers of the J-labels leading to a poor discrimination of which resonances belong where. The training data consisted of three spin groups, $(L,J)=(0,1/2)$, $(1,1/2)$ and $(1,3/2)$. Given the inability to distinguish reliably the J quantum number, we would expect at most a 67% accuracy assuming 100% correct identification of L.

As a third attempt to raise even more the accuracy the amount of features given to the tree was lowered from 34 to what we thought were 5 (this were the: right spacing, quadratic difference between the spacing and average spacing, quadratic difference between the elastic width and the average elastic width, spacing PDF evaluation, and the elastic PDF evaluation) of the most important features. This improved the accuracy by about a 5% and the tree achieved its maximum accuracy of the study, which was 85%. This meant that the tree was having a minor overfitting issue by using too many features.

4 Conclusion

The decision tree may not have been the best approach for the resonance classification problem. Nevertheless we learned several important lessons:

- **The depth problem:** A depth vs. accuracy analysis showed that too much depth lowered the accuracy of the tree by about 5% and that the best depth was between 4 and 6 nodes. But, accuracy was still too low.
- **The too many features problem:** By using 34 features it seems it was over-fitting the data and therefore lowering its performance. When just 5 of what we thought were some of the most important features were used -Features: mention these features in reference with ones numbered within the paper- the accuracy raised about a 5% and the best accuracy of the tree was reached at this point. Which was about an 88%. Because of a lack of time, a study to analyze which were the best 5 features or the best amount of features was not realized. Therefore it stayed as a future study for the decision tree.
- **The training problem:** It is thought that the scikit learn decision tree training function was too rigid for our needs since it couldn't take into account some of the physical properties of the system. For example the fact that most errors within the sequences lie in the high energy region or the joint probability distribution of the resonances.
- **The label problem:** It is also thought that adding the J quantum number as one of the features was making the tree to lose some discriminatory power. Since the features we had used had a high sensitivity the outliers

with the L quantum number label, but low sensitivity for the outliers with the J quantum number label. Nonetheless having used three spin groups, with two different L-labels and three different J-labels meant that since the tree had a low discriminatory power for the J-label, at most the best accuracy of the tree should have been a 66%. When the lowest accuracy that we obtained was around a 50% this meant that the decision tree had some degree of discriminatory power after all.

Even though the bold original goals of the project were not all achieved, this work represented an important first step in the automation of the identification and correction of issues in neutron resonances, by establishing the whole chain from experimental resonances, machine-learning featurization, learning algorithm and prediction of results. Future projects will explore a much better labeled and informed decision tree with more features that can discriminate against the J-labels.

5 Acknowledgements

This project was supported in part by the Brookhaven National Laboratory (BNL), National Nuclear Data Center under the BNL Supplemental Undergraduate Research Program (SURP) and by the U.S. Department of Energy, Office of Science, Office of Workforce Development for Teachers and Scientists (WDTS) under the Science Undergraduate Laboratory Internships Program (SULI).

References

- [1] G.R. Satchler, *Introduction to Nuclear Reactions*, John Wiley and Sons, New York, ISBN 0-470-26467-5 (1980).
- [2] S. Mughabghab, *The Atlas of Neutron Resonances, 6th edition*, Elsevier Science, ISBN 9780444637697 (2018).
- [3] Scikit-learn, <https://scikit-learn.org/stable/>
- [4] Brown, David A. “A tale of two tools: mcres.py, a stochastic resonance generator, and grokres.py, a resonance quality assurance tool.” United States: N. p., 2018. Web. doi:10.2172/1478482.
- [5] M.L. Mehta, *Random Matrices and the Statistical Theory of Energy Levels*, Academic Press, New York (1967)

Automation of the nsls2forge conda infrastructure

Thomas Hopkins

Undergraduate, Rensselaer Polytechnic Institute, Troy, NY 12180

Maksim Rakitin

NSLS-II, Brookhaven National Laboratory, Upton, NY 11973

Abstract

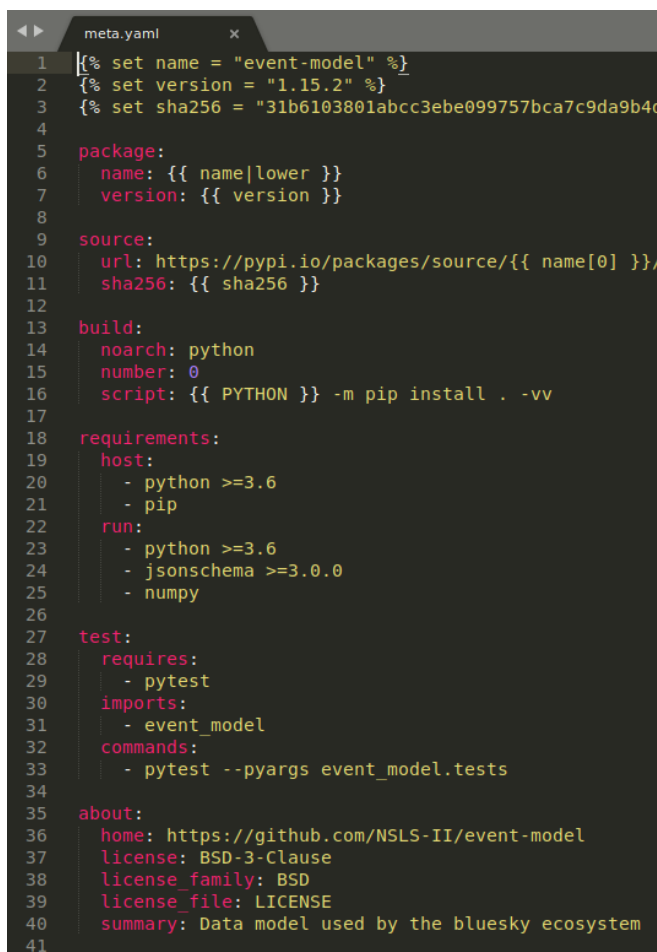
The nsls2forge conda infrastructure at the National Synchrotron Light Source II (NSLS-II) at Brookhaven National Laboratory requires large amounts of automation to be feasible in the long term. Through the use of emerging continuous integration technologies and a collection of software utilities, we have created a bot that will automatically search for and update software packages as they release. This makes newly created or updated software packages created at NSLS-II readily available to install at any beamline workstation, analysis server, or personal computer. The approach we took includes the development of a large dependency graph, the automation of file migrations, and the employment of cloud computing for easy access. A dependency graph is a directed acyclic graph that contains a node for each software package with links highlighting the relationship between packages. This is essential for maintaining a hierarchy of packages which is used by the bot for correct and efficient updating. Migrations are used to change the metadata of a specific package by updating its configuration files. We make use of Microsoft Azure Pipelines cloud services for hosting our bot that executes its job a few times a day. Conda is well known in the scientific Python community for providing software packages and environments. Existing open-source software, by the conda-forge team, provided many key utilities and ideas for the implementation of our bot. By automating the processes of our conda infrastructure at the NSLS-II, we are providing up-to-date, tested, and packaged software at a significantly better rate and volume than before.

I. Introduction

Software environments are the set of facilities, such as operating system, database, and other software tools, that is available to a program when it is being executed. Conda is an open-source, cross-platform, language-agnostic package manager and environment management system. NSLS-II uses Conda to deploy read-only production environments at the beamlines. A software package is an archive containing the Python library files, executables, and list of dependencies needed to run the package. Software packages that are developed and built at NSLS-II may be needed at many different beamlines and analysis servers. The Anaconda Cloud allows us to publish these software packages so we can share our software not only with others at NSLS-II but also around the world.

Most packages that are uploaded to the Anaconda Cloud have a separate “feedstock” repository hosted on the GitHub development platform. Feedstock repositories allow for automatic building and testing of new versions of software packages on many different platforms prior to being published. This is done using continuous integration/continuous deployment (CI/CD) technologies such as Microsoft Azure and TravisCI cloud services. The conda-forge team offers an open-source tool called conda-smithy that re-renders feedstock repositories to create these CI/CD builds for packages based on configuration files found in the repository. Re-rendering is a way to update the configuration files common to all feedstocks when changes to the repository have been made. Most of the time this refers to the CI/CD build configurations. We publish our packages from feedstock repositories to the *nsls2forge* conda channel on the Anaconda Cloud.

Managing feedstock repositories at the nsls2forge requires a lot of manual work. This includes manually editing configuration files (Figure 1), rendering the feedstock using conda-smithy, submitting pull requests, and monitoring build statuses. All these steps are required for each of the 200+ feedstock repositories belonging to nsls2forge.

A screenshot of a code editor showing a meta.yaml file. The file contains a YAML configuration for a feedstock repository. The configuration includes fields for name, version, sha256 hash, package name, source URL, build requirements, requirements, test commands, and about information. The code is as follows:

```
1  {% set name = "event-model" %}
2  {% set version = "1.15.2" %}
3  {% set sha256 = "31b6103801abcc3ebe099757bca7c9da9b4d" %}
4
5  package:
6    name: {{ name|lower }}
7    version: {{ version }}
8
9  source:
10   url: https://pypi.io/packages/source/{{ name[0] }}/{{ name|lower }}/{{ name|lower }}-{{ version }}.tar.gz
11   sha256: {{ sha256 }}
12
13  build:
14   noarch: python
15   number: 0
16   script: {{ PYTHON }} -m pip install . -vv
17
18  requirements:
19   host:
20     - python >=3.6
21     - pip
22   run:
23     - python >=3.6
24     - jsonschema >=3.0.0
25     - numpy
26
27  test:
28   requires:
29     - pytest
30   imports:
31     - event_model
32   commands:
33     - pytest --pyargs event_model.tests
34
35  about:
36   home: https://github.com/NSLS-II/event-model
37   license: BSD-3-Clause
38   license_family: BSD
39   license_file: LICENSE
40   summary: Data model used by the bluesky ecosystem
41
```

Figure 1. The meta YAML configuration file for the event-model-feedstock repository. Notable aspects of this file are the package name, version, source URL, SHA256 hash, requirements, and build architecture. In this case, there is no architecture requirement. This file can be found here <https://github.com/nsls-ii-forge/event-model-feedstock/blob/master/recipe/meta.yaml>.

Software that we write at NSLS-II often depends on other software to build and function correctly. This can be seen most notably when importing different software modules while writing code. For example, writing some software in Python that imports functionality from the NumPy package means that that software depends on NumPy. Software can also require specific

versions of other software. This adds an interesting level of complexity to our problem of automation.

The purpose of this paper is to establish two possible methods of automation for managing software package feedstocks at NSLS-II. We also intend to provide other individuals and organizations that manage feedstock repositories the ability to use and extend these automated methods with ease by making them open-source and portable.

II. Methods

There are two main ways we chose to automate the `nsls2forge` conda infrastructure. The first is that we created an open-source library of utilities that allows the user to gather important information and make changes to items in feedstock repositories. These utilities can be used by any individual or organization that manages feedstock repositories. The second is a bot that automatically updates configuration files, re-renders, and submits pull requests for feedstocks at the `nsls-ii-forge` GitHub organization. The bot's configuration is also open-source and can be applied by other individuals or organizations that manage feedstocks with a small amount of modification. The method for the bot was first implemented by the `conda-forge` team but was not easily adaptable to our conda infrastructure.^{1,2}

We decided to create a suite of utilities that would not only help the end-user perform operations on feedstock repositories, but also be used by the bot to perform the entire process automatically. Other utilities, such as the dashboard (Figure 2) help maintainers see an overview of every feedstock's attributes. We include versions from `nsls2forge`, Python Package Index (PyPI), Anaconda defaults, `conda-forge`, and GitHub tags (if they are available) in the dashboard

for each feedstock. This provides an easy way to see how the versions from different sources compare to nsls2forge and if further actions are needed on our part. Table 1 highlights the four main utilities we built.

Name	Build Status	Versions	Downloads
bluesky	Azure Pipelines succeeded health 77%	nsls2forge v1.6.5 pypi v1.6.5 conda not found conda-forge v1.6.5 tag v1.6.5	downloads 4.6k
bluesky-darkframes	Azure Pipelines succeeded health 86%	nsls2forge v0.4.0 pypi v0.4.0 conda not found conda not found tag v0.4.0	downloads 68
bluesky-kafka	Azure Pipelines succeeded health 88%	nsls2forge v0.1.0 pypi v0.2.0 conda not found conda not found tag v0.2.0	downloads 3.8k
boltons	Azure Pipelines succeeded health 90%	nsls2forge v19.1.0 pypi v20.2.0 conda not found conda-forge v20.2.0 tag v20.2.0	downloads 5.3k
bumps	Azure Pipelines succeeded health 72%	nsls2forge v0.7.15 pypi v0.7.16 conda not found conda-forge v0.7.16 tag v0.7.16	downloads 543

Figure 2. Part of the dashboard for feedstock repositories at nsls2forge. Lists build statuses, code health, versions, and number of downloads for every feedstock. Full dashboard can be found here <https://github.com/nsls-ii-forge/project-management>.

Utility	Purpose
all-feedstocks	Performs operations on every feedstock belonging to a GitHub organization
dashboard	Creates a dashboard with build statuses, downloads, versions, and code health for every feedstock at nsls2forge
graph-utils	Performs operations on the dependency graph (build, query, and update)
meta-utils	Performs operations on individual feedstock configuration files

Table 1. Table of utilities built to automate operations at the nsls2forge. These are available via the command line interface. The code can be found here <https://github.com/nsls-ii-forge/nsls2forge-utils>.

When automatically updating software packages with new versions, a problem arises when considering the relationships between packages. To alleviate this problem, we implemented a directed acyclic graph (Figure 3) to represent every feedstock package at nsls2forge along with their dependencies. This method of representing the relationship between packages was developed and implemented by the conda-forge team for similar purposes.^{1,2} We will refer to this graph as the dependency graph.

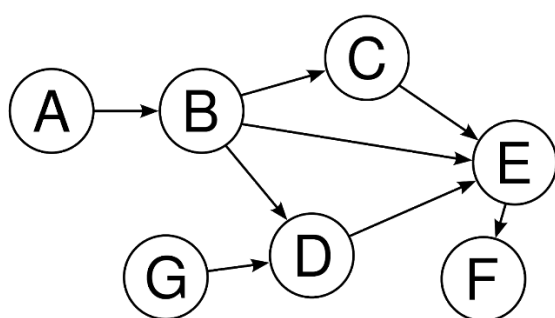


Figure 3. Directed Acyclic Graph (DAG). Useful for representing a complex set of relationships. Nodes A and G are at the top-level. One way to topologically sort this graph is the following ordering: A, G, B, C, D, E, F.

Each node in the graph can be represented by a piece of software. This definition can range from programming languages to software applications and software packages. We store each feedstock along with its raw configurations at each node in the graph. Edges between nodes

are defined as an “is a dependency of” relationship. For example, the package `event-model` imports some functionality from NumPy, therefore, NumPy is a dependency of `event-model`. A directed edge from the node corresponding to NumPy would connect to the node corresponding to `event-model`. A subgraph of the full dependency graph is shown in Figure 4, displaying only `event-model` and its related pieces of software. Sorting the nodes topologically gives us a correct order to update software packages so no dependency issues come up at build time. This is important since software can depend on specific versions of other software.

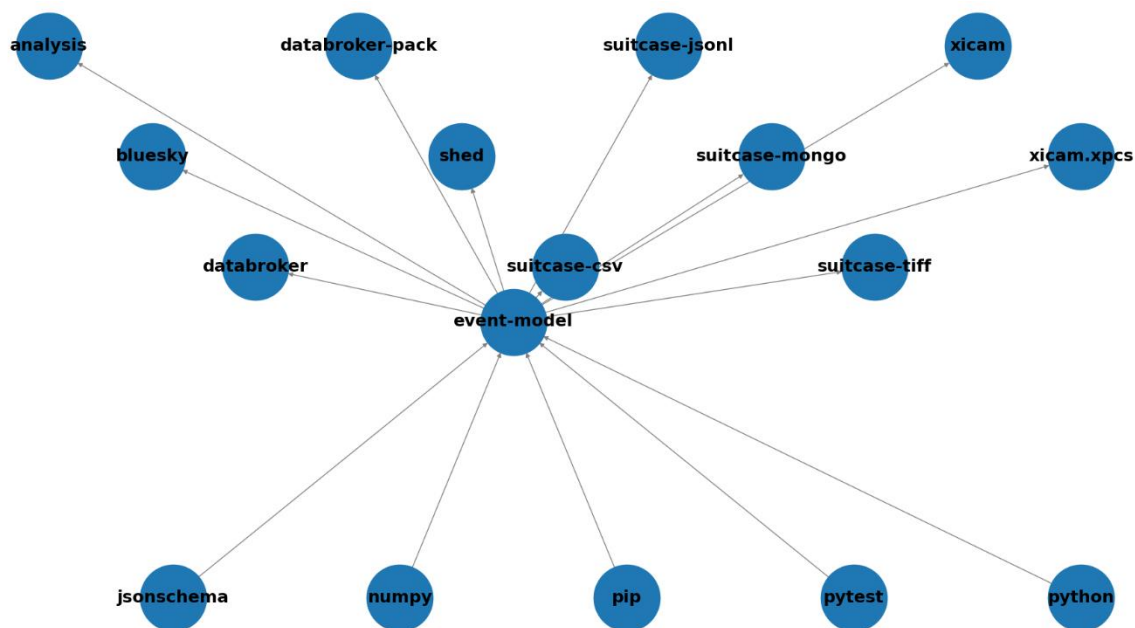


Figure 4. A generated subgraph of our much larger dependency graph. This subgraph shows only the software associated with the `event-model` Python package published at nsls2forge. Nodes (in blue) along the bottom are packages that `event-model` depends on to run/build. Nodes along the top are packages that require `event-model` to run/build. This structure for representing package dependencies was developed by the conda-forge team.^{1,2} The full graph is hosted at <https://github.com/nsls-ii-forge/auto-tick-graph>.

The bot itself will run in the cloud and use the various prebuilt utilities to automatically update software package feedstocks with new versions as they release. It will go through a cycle of retrieving all feedstock names from nsls2forge, creating/updating the dependency graph, retrieving new versions of packages directly from their sources, topologically sorting packages that require new versions, editing configuration files, and finally submitting pull requests to feedstock repositories on GitHub. This process will occur one to two times per day, submitting a maximum of ten pull requests to GitHub per run.

To retrieve new versions of packages from their sources, we make various API calls to the following sources: PyPI, CRAN, NPM, ROSDistro, GitHub, and any raw URL. PyPI and GitHub are our two most used sources. These API calls check for newest versions of packages that are available. If a new version is found that is greater than the current version of a package, we update the corresponding node in the graph with this new version. The bot will pick up all the nodes with new versions and update them in the correct order.

To edit configuration files with new versions, we use file migrations (Figure 5). These migrations were first developed by the conda-forge team for their bot.^{1,2} They allow us to keep a record of all changes that are made by the bot and update specific portions of configuration files. If anything goes wrong with automatically making changes to configuration files, they can still be manually edited within the same pull request and re-rendered.

1. Simple Additive Version Migrations



Figure 5. Simple version migrator used to update configuration YAML files. Original file on the left, migrator in the middle, and resulting file on the right. Tags are only updated if the version number is greater than the original version number.

III. Discussion

By automating the nsls2forge conda infrastructure, we are providing up-to-date software for NSLS-II beamlines and analysis servers at a significantly better rate and volume than before. Software feedstocks at nsls2forge are now receiving version update requests at a rate of 10 per run of the bot. Since the bot is set to run one to two times per day, it can send requests for up to 20 feedstocks that require version updates in one day. Maintainers at the nsls2forge will still be required to monitor build statuses and approve any changes prior to new versions being released on the Anaconda Cloud. The dashboard (Figure 2) provides a useful overview of these packages along with their build statuses and current versions. The bot adds a small portion of the dashboard to the text of each pull request for the convenience of the maintainers. This contains the package itself as well as its dependencies which require version updates first.

Some future improvements to the utilities and bot are to extend the functionality to update more than just version numbers of packages, retrieve more complex information from the dependency graph, perform file migrations across all feedstock repositories at once, and create an interactive version of the bot that responds to requests for changes in feedstock repositories. The current library of utilities can easily be extended with the additional functionality described above. Since these utilities are open-source, anyone can contribute to improving them. The scope of the interactive version of the bot is much larger and should be an entire project of its own.

IV. Conclusion

We have shown that the current process for maintaining feedstock packages at the nsls2forge is unfeasible in the long term. Automation of the nsls2forge's operation helps alleviate most of the manual work in the maintenance process. The library of utilities helps not only the bot but also any user or maintainer work more efficiently in diagnosing issues and performing updates. The dependency graph is a useful representation for recognizing how packages relate to each other and for making decisions when updating packages. The bot provides an end-to-end tool that will update versions of packages automatically. While the changes made by the bot will still need to be reviewed manually, it improves the speed and volume at which packages can be updated and tested at NSLS-II.

V. Acknowledgements

I wish to thank my mentor, Dr. Maksim Rakitin, for his professionalism and generosity during the SULI program. Further, I wish to express my gratitude to the conda-forge and regro teams for providing many key utilities and ideas for the implementation of our bot. This project

was supported in part by the U.S. Department of Energy, Office of Science, Office of Workforce Development for Teachers and Scientists (WDTS) under the Science Undergraduate Laboratory Internships Program (SULI).

VI. References

¹Wright, C. 2020. The Automation of Conda-Forge. AnacondaCON 2020.

<https://gateway.on24.com/wcc/eh/2336732/lp/2357492/the-automation-of-conda-forge/?campaign=web>

²regro/cf-scripts GitHub repository. Updated 2020. <https://github.com/regro/cf-scripts>

Scintillation waveform fitting in the ICARUS detector's photomultiplier array

Douglas Howell

Department of Physics, Pennsylvania State University, State College, PA 16830

Milind Diwan, Andrea Scarpelli

Physics Department, Brookhaven National Laboratory, Upton, NY, 11973

(Dated: August 19, 2020)

The Imaging Cosmic and Rare Underground Signals (ICARUS) detector is a liquid argon time projection chamber (LArTPC) which detects neutrinos from the Booster Neutrino Beam as part of the Short Baseline Neutrino (SBN) experiment. ICARUS is located at the Fermi National Accelerator Laboratory, near Chicago. The current goal of the SBN experiment is to study the oscillation of neutrinos aiming to observe a fourth flavor of neutrino which does not interact like the other three. ICARUS uses a time projection chamber and a photon detection system to detect and reconstruct these neutrino events. The photon detection system consists of an array of 360 photomultiplier tubes (PMTs), and will be used for the precise timing of the neutrino interaction and the rejection of the background coming from cosmic rays. After the detector was filled with LAr and cooled to 87 K, calibration data was taken by shining laser light on several groups of PMTs. Additional data was taken using actual scintillation light from the excitation of LAr atoms. The scintillation pulses measured by the PMTs have three components: fast, intermediate, and slow. The fast and slow components corresponding to singlet and triplet decay to the ground state of LAr atoms, and the intermediate component remains a topic of interest. Using a C++ framework developed using ROOT, work has been done studying the efficacy of the exponentially-modified gaussian fit function in characterizing the scintillation waveforms. In particular, studies were done on the various parameters in this fit function in an attempt to counteract its parameter degeneracy. Through participation in this summer internship program, I have learned the fundamentals of detectors and particle physics as well as other skills, such as data analysis using C++ and ROOT and presenting my findings to larger scientific collaborations and non-specialists.

CONTENTS

I. Introduction	1
II. Data	2
II.1. Photomultiplier Tubes	2
II.2. Data Collection	2
III. Methods	2
IV. Results	3
IV.1. Constraints on τ_i and τ_s in ICARUS	3
IV.2. Reduced χ^2 in ICARUS	4
V. Conclusion	4
VI. Acknowledgements	4
References	5

I. INTRODUCTION

The standard model of particle physics consists of two groups of fundamental particles: quarks and leptons. Within the lepton family, there are three flavors of neutrino: ν_e, ν_μ, ν_τ which correspond to each of the three charged leptons. For some time, these neutrinos were believed to be massless and thus, travel at the speed of light. However, neutrino experiments have determined that they are indeed massive, albeit with very small

mass[1]. Because neutrinos are leptons, neutral, and very light, they can only interact through the weak force.

More recent neutrino experiments have turned the tables on our understanding of neutrinos. Experiments such as the Super-Kamiokande neutrino detector have discovered evidence that neutrinos can actually mix flavor and change their lepton family through a phenomenon called neutrino oscillation[1]. For example, throughout its path a neutrino can change its identity from a muon neutrino to a tau neutrino.

Anomalies in some neutrino experiments have suggested that there exists a fourth "sterile" neutrino which, unlike its cousins, does not interact through the weak force. The goal of the SBN experiment is to study the anomalies in the short baseline neutrino oscillation of a manmade beam of muon neutrinos. The ICARUS LArTPC neutrino detector detects neutrinos from the Booster Neutrino Beam at Fermilab in an attempt to gather further evidence in support of the sterile neutrino. ICARUS is the far detector in Fermilab's SBN program.

Neutrinos from the Booster Neutrino Beam enter the 760 ton detector and interact with the liquid argon (LAr) weakly and produce charged particles inside the time-projection chamber (TPC). Each of these charged particles has its own signature as it moves through the LAr and thus can be recreated by the TPC. As charged particles move through this chamber, LAr atoms are excited, and through their de-excitation they emit scintillation light.

In addition to the TPC, ICARUS also has a photon sensor system to detect the scintillation light emitted

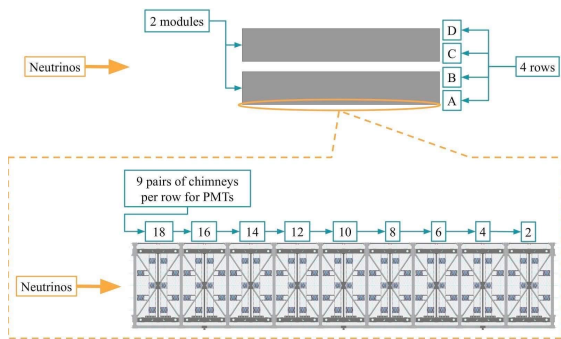


FIG. 1. The ICARUS photomultiplier array is divided into 2 modules, which are each divided into 2 rows, each of which having 9 pairs of chimneys having 10 tubes per pair.

from LAr atoms. The photodetection system consists of 360 Hamamatsu R5912-MOD photomultiplier tubes (PMTs) coated with tetraphenyl butane (TPB) [see FIG. 1]. As scintillation light is incident on the photocathode of these PMTs, it is converted into an electric current which can be measured by the readout electronics.

The array of 360 PMTs must be calibrated in order to ensure accurate and useful data comes from the electronic readout. In particular, the LAr response to its interaction with charged particles must be characterized so that the PMTs can accurately measure scintillation light. In this work we have fitted waveforms of electronic readout data from each PMT with theoretical models to extract the underlying parameters of the scintillation light. In particular, our theoretical model is the exponentially-modified gaussian function. We found that the fit function has a large degree of parameter degeneracy, and work was done in forcing uniformity in parameters across all of the PMTs.

II. DATA

II.1. Photomultiplier Tubes

The scintillation light produced by the de-excitation of the LAr atoms radiates isotropically in the detector. When this light is incident on the photocathode of one of the ICARUS' 360 PMTs, primary photoelectrons are emitted via the photoelectric effect. These photoelectrons are accelerated towards a series of 10 dynode stages wherein each electron is multiplied, resulting in a large number of secondary electrons or gain [see FIG. 2]. Each PMT is calibrated to reach the same gain of 10^7 photoelectrons, which is sufficient to be measured [2].

II.2. Data Collection

In June 2020, cold data was taken from the ICARUS detector while filled with LAr and cooled to 87 K. The data was taken at first in two groups of 8 PMTs across 2 boards at two voltages: 1 kV and the nominal

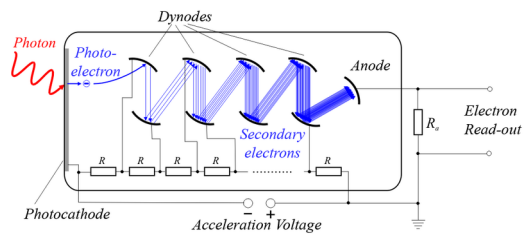


FIG. 2. Operational diagram of a photomultiplier tube

voltage determined before the detector was filled with LAr. A second, much larger set of data consisted of 163 PMTs in the East cryostat. My primary goal of using this calibration data was to characterize the scintillation waveform signals in the PMTs which come from the singlet and triplet state decay of LAr to the ground state.

III. METHODS

The PMT analysis was done using CERN's ROOT data analysis software combined with a C++ framework designed for the ICARUS calibration. The primary use of this software is to fit various types of data using an analytical function.

Because of the various background phenomena that can occur inside the detector or PMTs, some selection algorithm must be applied to the data in order to obtain a scintillation signal. In order to filter out internal noise and background phenomena, a coincidence selection was applied to the data. If we assume that scintillation light is isotropic, then we would expect light from a given scintillation event to be coincident on multiple PMTs. So any signal which occurs on more than 2 PMTs is selected. Another selection requirement is to select only pulses which are within a certain voltage range.

The scintillation signal has two components: the singlet and triplet (dubbed the 'fast' and 'slow' components, respectively). Thus, the number of photons observed as a function of time is a random variable which has three components: fast, intermediate, and slow. Then, because of the transit time of these photons in PMTs, a gaussian is introduced to account for the smearing of arrival times. Thus, we use the exponentially-modified gaussian distribution[3] to model each of the components to characterize the LAr response:

$$S(t) = \sum_{j=f,i,s} \frac{A_j}{2\tau_j} \exp \left[\frac{1}{2} \left(\frac{\sigma}{\tau_j} \right)^2 - \left(\frac{t-t_m}{\tau_j} \right) \right] \times \left[1 - \operatorname{erf} \left(\frac{1}{\sqrt{2}} \left(\frac{\sigma}{\tau_j} - \frac{(t-t_m)}{\sigma} \right) \right) \right] \quad (1)$$

This waveform has many parameters that could be correlated to each other. The function itself is the sum of a gaussian characterizing the PMT response convoluted

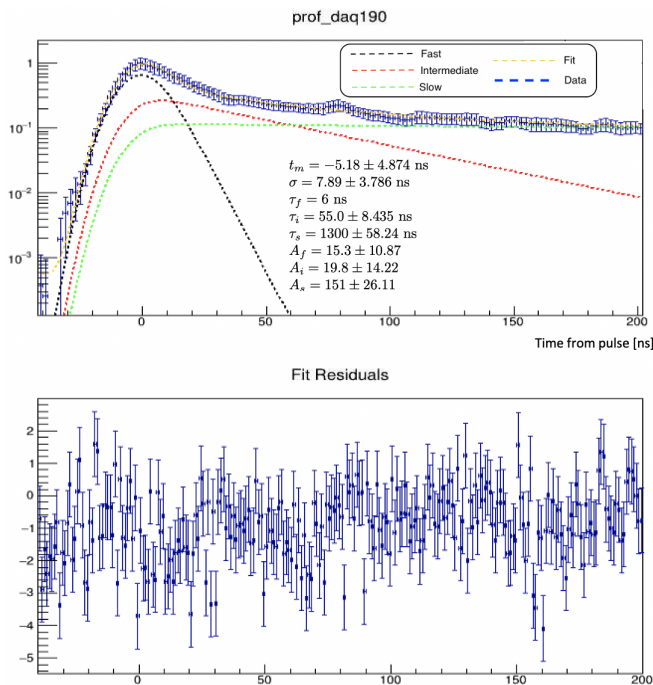


FIG. 3. (Top) Scintillation waveform fit for PMT 190 with values for all 8 parameters of the exponentially-modified gaussian. Black, red, green curves correspond to the fast, intermediate, and slow components. The gold curve represents the sum of all components. (Bottom) Residual plot of the fit indicating a poor fit just after the peak

with 3 exponential distributions. The fast and slow components correspond to singlet and triplet decay, while the intermediate component is not entirely understood, but can be found in literature [4]. Because of the 8 parameters involved in this fit function, there is a large degree of parameter degeneracy. Therefore, some parameters must be constrained manually in order to optimize the fit. Such constraints must also be physical. For example, previous studies into LAr scintillation have shown that the fast decay parameter $\tau_f \sim 6$ ns and the slow decay parameter $\tau_s \sim 1200$ ns. So when fitting with ROOT, these physical constraints must be considered to avoid negative parameter values or swapped τ_i and τ_s for example.

We are fitting physical data from ICARUS' PMTs with an analytic function, so we want the function and the data to fit as closely as possible to ensure our understanding of the data. To achieve this, residual plots were particularly useful in finding certain areas of the fit which differed from the data [see FIG. 3].

Other fit studies were done by varying the binning of the data, separating data into different sets of pulse amplitudes, and fitting different regions of data separately. These methods, as well as by trying many different sets of constraints on some or all of the parameters were done in an attempt to minimize the χ^2 of the fit.

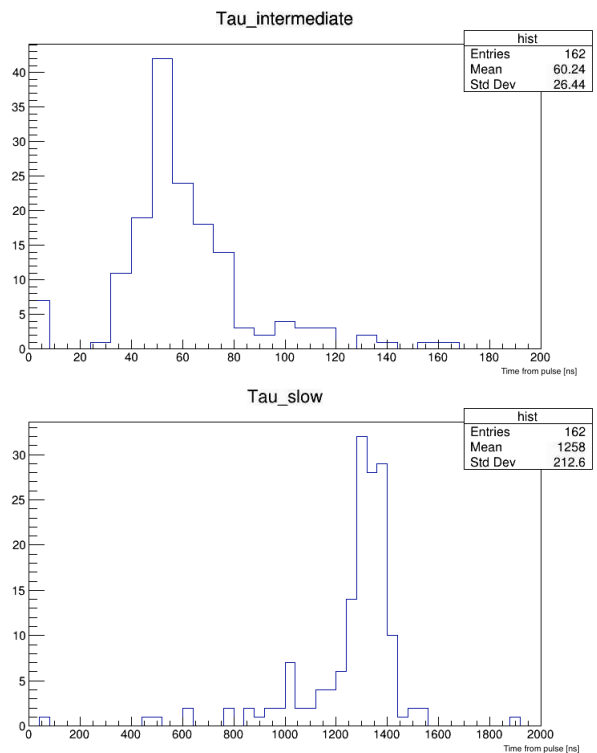


FIG. 4. Plots of the intermediate component decay parameter τ_i (top) and slow component decay parameter τ_s (bottom) across 163 PMTs.

IV. RESULTS

IV.1. Constraints on τ_i and τ_s in ICARUS

By testing various sets of constraints, it was evident that τ_f could just be constrained at 6 ns. This much has been concluded in other experiments. The more difficult parameters to pin down were the other two decay parameters: τ_i and τ_s . To try and find constraints on these two parameters, a fit was done which constrained the other 5 parameters. The set of constraints follow:

$$\begin{aligned} -10 \text{ ns} < t_m < 5 \text{ ns} \\ 1 \text{ ns} < \sigma < 20 \text{ ns} \\ \tau_f &= 6 \text{ ns} \\ 0 \text{ ADC} < A_f, A_i, A_s < 500 \text{ ADC} \end{aligned}$$

This set of constraints resulted in the best χ^2 , and constrained all parameters other than τ_i and τ_s to reasonable values. Leaving only τ_i and τ_s to vary allowed me to obtain an estimate on those parameters by plotting them in a histogram across the 163 PMTs in the run [see FIG. 4].

While there are some outliers, the intermediate and slow decay parameters seem to follow a distribution where an estimate can be obtained from its peak, with a statistical error obtained by:

$$\text{Error} = \frac{\text{Standard Deviation}}{\sqrt{N}}$$

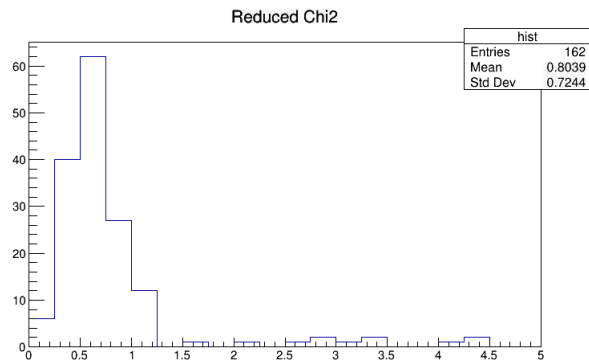


FIG. 5. Histogram of the reduced χ^2 across 163 PMTs using the set of parameter constraints described previously, which left τ_i and τ_s free.

Where N denotes the number of PMTs used for the histogram. Note that this error is purely statistical, and does not take into account any possible error from waveform selection or from this particular fit strategy we used. Using this data, we found an estimates on the intermediate decay $\tau_i = 60.24 \pm 2.1$ ns and on the slow decay $\tau_s = 1258 \pm 17$ ns. The estimate for τ_i is very reasonable, and is well within the usually accepted value in similar experiments. However, the estimate for τ_s is lower than values found in similar experiments[5]. At the present moment, ICARUS is still in the calibration stage. τ_s has been found to be a good indicator of the level of purity in LAr, and so ICARUS' current calibration status could mean that some unfiltered contaminants may be the cause of this lower estimate.

IV.2. Reduced χ^2 in ICARUS

In addition to finding estimates on the intermediate and slow decay parameters, a similar method was applied to the reduced χ^2 of fits across all 163 PMTs. The reduced χ^2 used in this study is given by:

$$\text{Reduced } \chi^2 = \frac{\chi^2}{\text{Number of degrees of freedom}}$$

The reduced χ^2 for each of the 163 PMTs' fit was included in a histogram [see FIG. 5]. In this plot, the intermediate and slow decay parameters were left free, while all other parameters were constrained. From the histogram, it is clear that the majority of the PMTs have a good level of fit, with reduced $\chi^2 \leq 1$. However, a few PMTs remained at a relatively high reduced χ^2 . After some investigation into these specific PMTs, the culprit behind the poor fit was either swapped values for τ_i and τ_s , or negative values being taken for those parameters. The solution to dealing with these pathological fits was to incorporate the estimates on τ_i and τ_s found in section IV.1. The χ^2 histogram was then reproduced using these estimates [see FIG. 6]

Applying the new set of constraints found in this study overall decreased the reduced χ^2 across this set of PMTs.

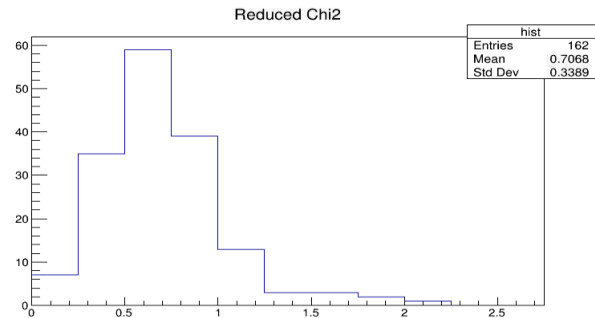


FIG. 6. Histogram of the reduced χ^2 across the same 163 PMTs, only now including the constraints on τ_i and τ_s found in section IV.1

However, there are a few PMTs which have a reduced $\chi^2 > 1$.

V. CONCLUSION

This study has resulted in a first estimate on the intermediate and slow component decay parameters, τ_i and τ_s , and has illustrated the importance of estimating these parameters, as well as their effects on the reduced χ^2 across the PMT array. Applying constraints on τ_i and τ_s based on my estimations resulted in a good level of fit across 163/360 of ICARUS' PMTs.

While this study has been successful in determining values for the parameters in the exponentially-modified gaussian fit function, there are still many more studies that could provide a better estimate on parameters or understanding of the fit function. In particular, using all 360 of ICARUS' PMTs would result in a better estimate on τ_i and τ_s by decreasing the overall error. Using all 360 PMTs would also be useful in determining any systematic errors in the PMTs, which were not considered in this study. Additionally, a better understanding of the fit parameters themselves, such as any and all correlations in the parameters could come from the use of a Monte Carlo simulation.

VI. ACKNOWLEDGEMENTS

I would like to thank my mentor Milind Diwan for accommodating a remote internship and for providing me with a wonderful first experience in performing research. I would also like to thank Andrea Scarpelli for his seemingly limitless amount of patience in assisting me throughout this remote program. Finally, I would like to thank the EDG group at BNL for encouraging me, and the entire Physics Department at BNL for the numerous physics lectures introducing me to how great physics can be. This project was supported in part by the U.S. Department of Energy, Office of Science, Office of Workforce Development for Teachers and Scientists (WDTS) under the Science Undergraduate Laboratory Internships Program (SULI).

-
- [1] Samoil Bilenky, *Introduction to the Physics of Massive and Mixed Neutrinos* (2018), 2nd edition.
- [2] Hamamatsu Photonics, *Photomultiplier Tubes: Basics and Applications* (2007), 3rd edition.
- [3] Milind Diwan, Exponentially modified Gaussian and the Lognormal for common physics fitting (2020)
- [4] E. Segreto, Evidence of delayed light emission of tetraphenyl-butadiene excited by liquid-argon scintillation light, *Phys. Rev. C* 91(2015) 035503
- [5] R. Acciarri et al, *Journal of Instrumentation*, 5.06 (2010)

The Analysis of ARM data related to cloud droplet activation and the study of Köhler theory

Marcus Johnson

Department of Chemistry, Stony Brook University, Stony Brook, NY 11794

Dr. Robert McGraw, Dr Laura Fierce, Environmental and Climate Sciences Department, Brookhaven National Laboratory, Upton, NY 11973

Abstract

The study of aerosol-cloud interactions has been growing in popularity in the field of climate research. These interactions can affect a clouds brightness or clouds ability to reflect solar radiation back into space, and the enhancement or suppression of precipitation. Using data taken from two measurement systems, the condensation particle counters (CPCs) and the scanning mobility particle sizer (SMPS), from the Atmospheric Radiation Measurement (ARM) system at the Southern Great Plains (SGP), we will run and interpret the measurement data through MATLAB and Python. In doing so, we eventually

hope to find correlations between the two measurement systems while also making adjustments to the Köhler theory to account for surface active and water-soluble aerosol components. Through this internship, I have become more well versed in coding with Python, gained a better understanding of cloud physics and also gained the ability to interpret data from ARM.

Introduction

An aerosol is defined as a liquid or solid particle suspended in the air. They can come from multiple sources such as pollution, sea spray and dust. Aerosols play a significant role in our environment.

The Process of when water vapor condenses on an aerosol particle to form a cloud droplet is described by the Köhler theory. The theory is centered on equilibrium thermodynamics and combines the Kelvin effect and Raoult's law. The Kelvin effect describes how the curved surface of cloud condensation nuclei changes the saturation.

vapor pressure. Raoult's law relates saturation vapor pressure to the solute. A Köhler curve is a visual representation of the Köhler equation. It shows the super saturation of when a cloud droplet is in equilibrium with the surrounding environment.

The objective of the project was to find correlations between two measurement devices provided by Atmospheric Radiation Measurement (ARM) system located at the Southern Great Plains Oklahoma site. This will be done with respect to a modification to Köhler theory.

I.) *Cloud Formation*

There are three important ingredients when it comes to cloud formation.

The first ingredient being water vapor.

The second important ingredient needed in cloud formation is an updraft. When

solar radiation increases, warm air starts to become much lighter and moves higher

into the atmosphere. When this occurs, the temperature starts to decrease and so

does the amount of water vapor the air can hold. This takes us to the third and

last ingredient, aerosol particles which act as cloud condensation nuclei (CCN).

Once the saturation point is reached which is when the relative humidity hits

100% water vapor starts to condense on the aerosol particle and clouds begin to

form.

Aerosols also have an Indirect effect (AIE) on Cloud Droplet Number

Concentration (CDNC) depending on their size. If the particles are larger in size

the concentration of CDNC will be lower.

This results in higher chances of rain and a decrease in solar reflectivity.

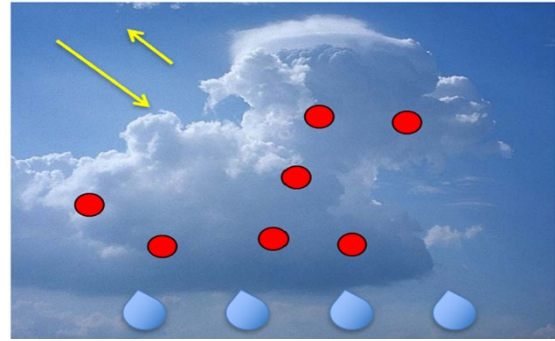


Figure 1: Graphic showing the correlation between lower concentrations of CDNC, rain and solar reflectivity

If the particles are smaller in size the concentration of CDNC be higher. This

means you will have a lower chance of rain and an increase in solar reflectivity

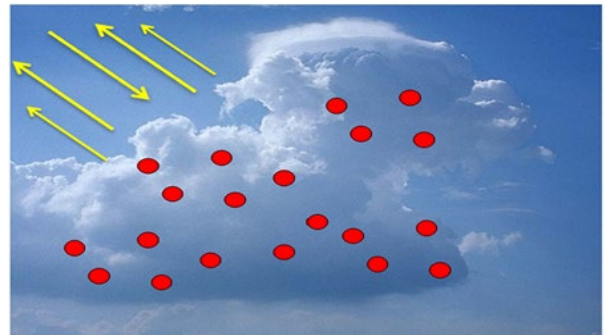


Figure 2: Graphic showing the correlation between higher concentrations of CDNC rain and solar reflectivity

II.) *Köhler theory*

Köhler theory well describes the activation barrier of the formation of cloud particles under different levels of

super saturation located in the atmosphere. These levels of super saturation tend to be less than one percent. It combines both the kelvin theory and Raoult's law. The Kelvin effect explains the additional amount of super saturation needed to form a droplet ~~needed~~ over a curved surface. When the surface is curved the amount of bonding that can occur between a water molecule and its neighbor is reduced. This creates a higher chance for the water molecule to enter the vapor phase. This causes the evaporation rate to increase. The greater the curvature of the surface, the greater the probability of the water molecule escaping to the vapor phase. This also means that it takes less energy to remove a water molecule from a curved surface rather than a flat surface.

Raoult's law relates the saturation vapor pressure to the solute. The solute tends to be evenly distributed in water,

because of this the solute sometimes occupies surface sites that would usually be occupied by water. This means that water is unable to evaporate from those sites. If you increase the amount of solute the opportunity of water vapor breaking H-bonds decreases leaving it unable to escape the liquid phase.

The Köhler curve (*Fig.3*) is a graphical representation of the Köhler equation shown below

$$S = \frac{D^3 - D_d^3}{D^3 - D_d^3(1 - \kappa)} \exp(A/D) \quad (1)$$

$$A = \frac{4\sigma_w M_w}{RT\rho_w} \quad (2)$$

where S is defined as the saturation ratio, D as the diameter, D_d as the dry diameter, A as the kelvin radius, which is considered a parameter of the Köhler curve, and κ as the hygroscopicity

parameter. κ is considered an operational parameter that represents a measurement

of water uptake on an aerosol particle.

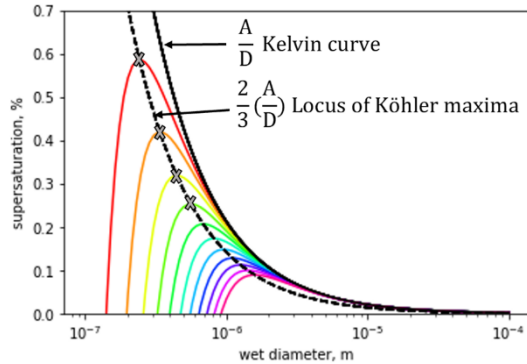


Figure 3: Köhler curve for different dry diameters. The size of the particle increases as you down. Each colored curve represents the supersaturation of the particle

Fig.3 shows that the dependence on particle size is quite important. The curves show when the cloud droplet is in equilibrium with its environment at a certain supersaturation. For a particle to grow and activate into a cloud droplet the supersaturation (S) must first exceed the critical supersaturation (S_c) which is at the critical diameter (D_c). Once S exceeds S_c the particle can activate and grow into a cloud drop. This all occurs at the locus of Köhler maxima which is indicated by the x's on Fig.3

IV.) Measurements through PartMc

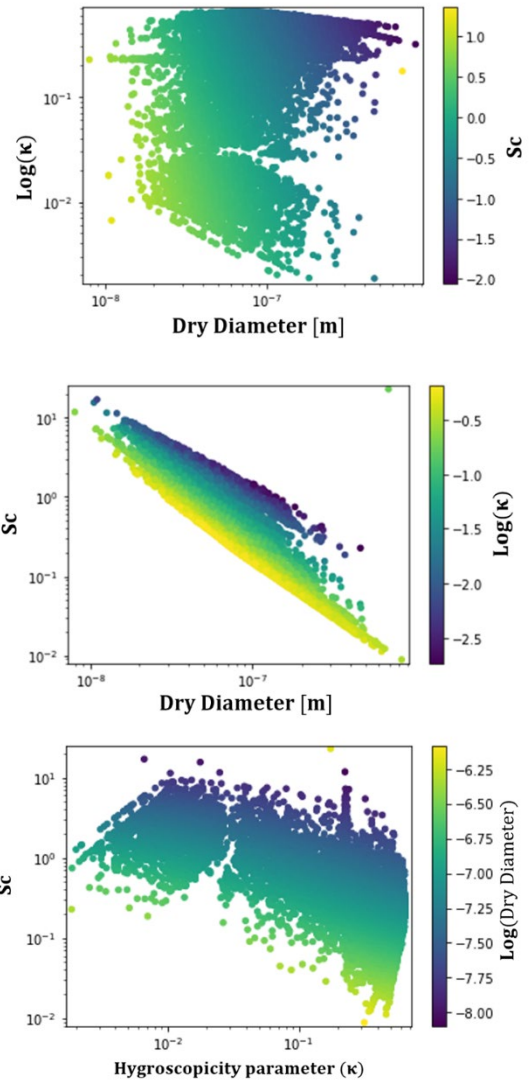


Figure 4: Scatter plots produced by PartMC.

IV.) Measurements through PartMc

Using data from Part MC we were able to plot the how three different parameters affect one another. This helped us get a better understanding of the Köhler theory and allowed us to view

the heterogeneity of the aerosol distribution. Once again using partMC we looked at field measurements taken by the SMPS for analyzing particle size and CPCs for analyzing cloud activation threshold.

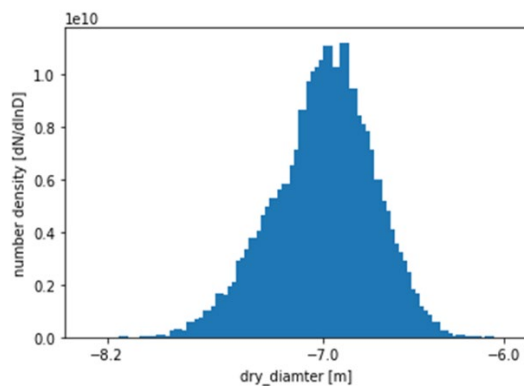


Figure 5: SMPS measurements of the dry particle size distribution

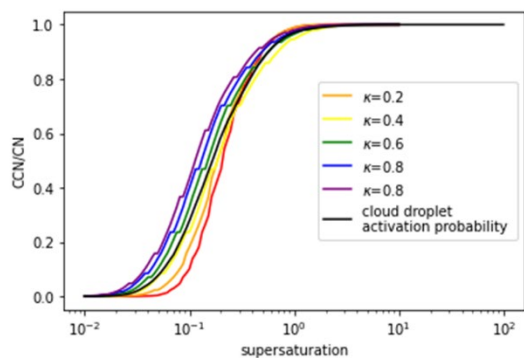


Figure 6: CPC measurements of cloud droplet probability for cloud activation

V.) Conclusion

In this project report we examined the Köhler theory of cloud droplet activation. We looked at field measurements taken by the SMPS for analyzing particle size and CPCs for analyzing the cloud activation threshold. Calculations were made using PartMC mosaic to look at the data sets of thousands of particles as shown in the scatter plots. This allowed us to represent the heterogeneity in the aerosol distributions from a theoretical point of view. From the measurements provided by the CPC, we found that we get good agreement for the cloud droplet activation probability when the heterogeneity is taken into account. Unfortunately, due to unforeseen circumstances from Covid-19 we were unable to complete the in the project. The next step would have been to acquire size distribution data from ARM and compare it to the cloud droplet activation probability produced by PartMC.

VI.) Acknowledgements

This project was supported in part by the U.S. Department of Energy, Office of Science, Office of Workforce Development for Teachers and Scientists (WDTS) under the Science Undergraduate Laboratory Internships Program (SULI). I also want to

thank my mentors Dr. Robert McGraw and Dr. Laura Fierce for giving me great guidance and generosity. I also want to thank the Office of Educational Programs for making this internship feel genuine despite of the circumstances.

VII.) Reference

- Petters, M. D. and Kreidenweis, S. M.: A single parameter representation of hygroscopic growth and cloud condensation nucleus activity, *Atmos. Chem. Phys.*, 7, 1961–1971, <https://doi.org/10.5194/acp-7-1961-2007>, 2007.

Far-forward neutrinos at Large Hadron Collider

Karan Kumar

Physics Department, Stony Brook University, Stony Brook, New York, 11794

Milind Diwan

Physics Department, Brookhaven National Laboratory, Upton, New York, 11973

Abstract

A large flux of neutrinos is expected in the forward direction of the pp collision at the Large Hadron Collider (LHC). We will provide a simulated estimate of this neutrino flux with uncertainties. In particular, the flux of tau neutrinos from the LHC is the main focus of this project. I performed simulations on the Brookhaven National Laboratory Scientific Data Computing Center to study the flux of neutrinos in the forward direction of pp collision. A number of experiments have recently been proposed at CERN to detect these neutrinos. For example, the FASER-nu proposal consists of a lead neutrino detector at a distance of 480 m from the ATLAS interaction region along the tangent to the LHC beamline. The previous calculation of neutrinos rate in the forward direction was done to leading order in the perturbation series; we have included next-to-leading order (NLO) terms in our calculation. We also add a non-perturbative Gaussian k_T intrinsic effect. This k_T effect absorbs the contribution from the higher-order terms in QCD calculations. Understanding the tau neutrinos will help to further our knowledge of the family of leptons. It will also advance the study of the mixing of the three flavors of neutrinos.

Introduction

Neutrinos are one of the fundamental particles that make up the universe. They are the most abundant particle in the universe and are also the least understood. The neutrino is a subatomic particle that resembles an electron but is electrically neutral and has a very small mass compared to other elementary particles. Neutrinos belong to the lepton family in the standard model. Lepton is a family of particles that doesn't experience strong interactions. Out of the four

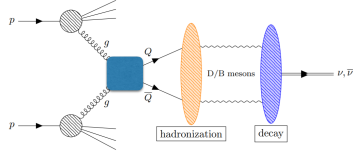


Figure 1: Proton-proton collision

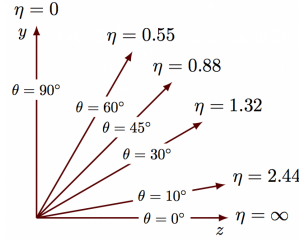


Figure 2: The relation between η and θ

fundamental forces, neutrinos interact only through the weak force and gravity. As the weak nuclear is very short-range and gravitational interaction of the neutrino is extremely weak, they rarely interact with normal matter. There are trillions of neutrinos passing through us every second. Neutrinos come in three flavors: electron, muon, and tau neutrinos. They are labeled after their charged partners within the Standard Model. In charged current interactions in matter, neutrinos of a given type result in the emission of their charged partner. Out of the three flavors, tau neutrinos are the least studied as there is not sufficient data available to study them. The collision of proton beams at 14 TeV at the Large Hadron Collider (LHC) produces a large flux of hadrons. The hadrons produced in the proton/proton collisions decay further into neutrinos. In particular, the decay of D_s^\pm and B meson produces a large flux of tau neutrinos in the forward direction of the collision; however, there have been no experiments to observe them. A new set of experiments have been proposed at CERN[1]. While muon and electron neutrinos are also produced in the collision, tau neutrinos are the main focus of our project. The forward region can be understood with the kinematic variable called pseudo-rapidity. Pseudo-rapidity (η) is a geometric quantity and is a function of the angle θ with respect to the collision axis as seen in Fig.2.

$$\eta = -\ln\left(\tan\left(\frac{\theta}{2}\right)\right) \quad (1)$$

As the proton beam collides at 14 TeV at LHC, quarks and gluons are emitted in collisions of partons which are, collectively, the constituents of the proton; these quarks/gluons quickly turn into hadrons and decay (Fig. 1). A large number of these decays are in the forward region or along the axis of the collision. In this project, we are exploring the region with $\eta > 6.87$ which approximately covers the forward detector coverage for proposed experiments at CERN. The past calculations of this rate were limited to leading order terms in the perturbation calculation but in our calculation, we account for next-to-leading order (NLO) terms in calculating the inclusive cross-sections for production of heavy quarks. In addition to NLO QCD correction, a non-perturbative intrinsic transverse momentum (k_T) also included in the calculation. The main focus is on tau neutrinos from the decays of D_s^\pm . Tau neutrinos are largely produced from D_s^\pm

decay with a smaller contribution from B mesons. For the meson production, we compared our prediction with the LHCb data on D_s^\pm production. There are many proposals to detect particles in the forward region at the LHC e.g: The ForwARd Search ExpeRiment at the LHC (FASER), which is looking for weakly interacting particles in the forward region[2] and the FASER-nu experiment, which will be placed in front of FASER to detect the flux of neutrinos as seen in Fig.3. We aim to provide a better theoretical prediction for neutrino rates with uncertainties for these experiments.

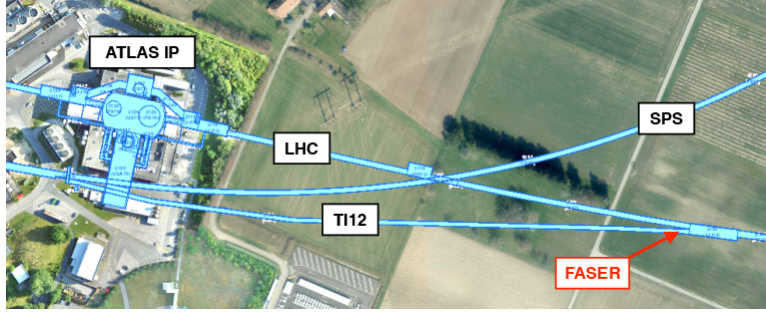


Figure 3: Location of FASER detector [2]

Theory

As mentioned earlier, we include NLO QCD correction to the heavy-quark (HQ) production cross section. The HQ production cross section under perturbative QCD is as follow[3]:

$$E \frac{d^3\sigma}{dp^3} = \sum_{i,j} \int dx_1 dx_2 f_i^{H_1}(x_1, \mu_F^2) f_j^{H_2}(x_2, \mu_F^2) \left[E \frac{d^3\sigma_{ij}(x_1 P_{H_1}, x_2 P_{H_2}, p, m^2, \mu_F^2, \mu_R^2)}{dp^3} \right], \quad (2)$$

where $f_i^{H_1}(x_1, \mu_F^2)$ and $f_j^{H_2}(x_2, \mu_F^2)$ are parton distribution functions (PDFs), μ_F^2 and μ_R^2 are factorization and renormalization scales, respectively. Parton distributions functions are momentum distribution functions of the partons within the proton. They are probability densities to find a parton with momentum with fraction x at an energy scale of μ^2 . The factorization and renormalization scales are parameter which depend upon transverse mass $m_T = \sqrt{m_Q^2 + p_T^2}$, where m_Q is the mass of the quark and p_T is the transverse momentum of the quark. As we discussed before, we need to account for mean transverse momentum in our calculation. We use a Gaussian approximation for transverse momentum.

$$f(\vec{k}_t) = \frac{1}{\pi \langle k_T^2 \rangle} e^{-\frac{k_T^2}{\langle k_T^2 \rangle}} \quad (3)$$

After including the k_T effect and integrating over it, the heavy quark production cross section becomes:

$$E \frac{d^2\sigma}{dp_z d^2p_T} = \int d^2k_T \int d^2p'_t f(\vec{k}_t) E \frac{d^2\sigma}{dp_z d^2p'_T} \delta^2(\vec{p}_T - \vec{p}'_T - \vec{k}_T) \quad (4)$$

The theoretical evaluation of the production of heavy quarks like charm has been studied for quite a long time, and is already implemented in a computer program called HVQ using the FORTRAN language. We use this program with some modifications to run simulation in our study. We compare our theoretical prediction with LHCb data for the production of D_s^\pm . In Fig.4, the theoretical prediction is plotted with LHCb data for the production of D_s^\pm . We provide predictions by varying three parameters: k_T , μ_F^2 and μ_R^2 . By varying these parameters, we tried to fit the data with our predictions. In Fig. 3, our predictions fit the data well for a relatively large value of $k_T \sim 2.2$ GeV, which can be understood as compensating for missing higher order terms in the calculation.

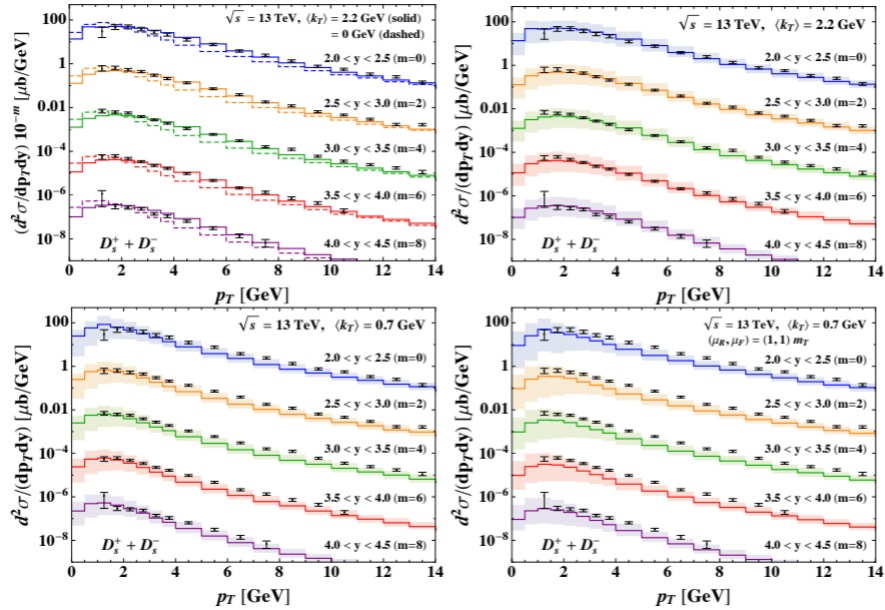


Figure 4: Comparison of LHCb data with theoretical Prediction [5]. The upper right figure shows the comparison with a fitted value of $\langle k_T \rangle > 2.2 \text{ GeV}$.

Results

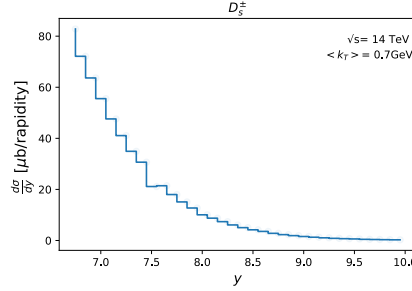


Figure 5: Distribution of cross section of D_s^\pm with respect to rapidity

To understand the flux of neutrinos, we need to first stabilize the calculation of the cross-section for the production of heavy quarks like charm and bottom. We have calculated the cross-section using Monte-Carlo based integration using the VEGAS algorithm, which uses random seeds and performs the calculation by sampling the integration region and weighting it according to its importance. Our goal was to study the cross-section using different random seeds and increasing numbers of iterations.

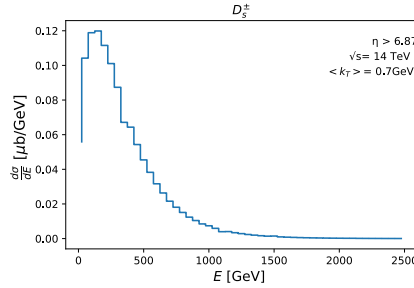


Figure 6: Distribution of cross section of D_s^\pm with respect to energy

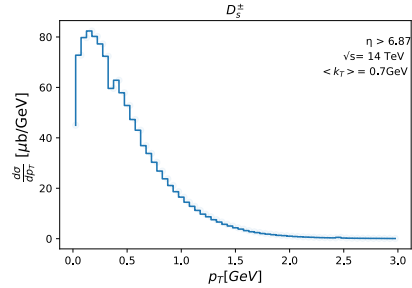


Figure 7: Distribution of cross section of D_s^\pm with respect to transverse momentum

Vegas call	6e+4	7e+4	8e+4	9e+4	1e+5	2e+5	3e+5	4e+5	5e+5	6e+5	7e+5	8e+5	9e+5	1e+6
σ_{total} [μb]	58.30	58.27	58.13	58.14	58.12	58.71	58.64	58.61	58.68	58.66	58.58	58.73	58.73	58.63
Error	0.20	0.20	0.20	0.20	0.20	0.10	0.30	0.09	0.07	0.06	0.06	0.06	0.06	0.05

Table 1: Value of total cross section with increasing number of VEGAS calls

In figures 5, 6, 7, we show the production cross section versus the rapidity, the energy, and the transverse momentum of the D_s^\pm meson. In these plots we have cut mesons below $y < 6.87$ to select only the forward region. My

calculations show that the total production cross section result converges to the value of $58.68 \pm 0.05 \mu\text{b}$ for the production of D_s^\pm mesons in the far forward direction. This is shown in Table 1.

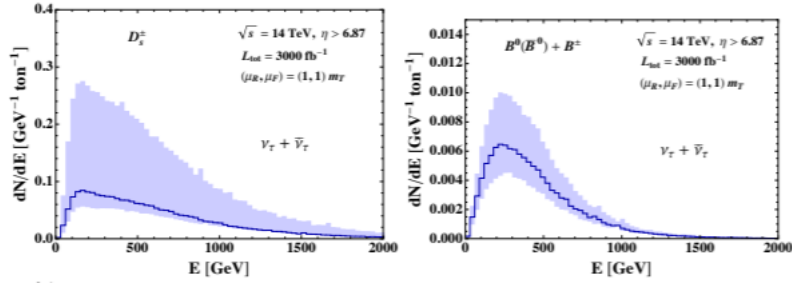


Figure 8: Tau neutrino rate from D_s^\pm and B meson [5]

In Fig.8, we show that the uncertainties in the calculation of the flux of tau neutrinos are large. These uncertainties result from the lack of knowledge of the underlying parameters. They also represent the contributions from the higher-order terms in the perturbation calculations. There might also be other unknown non-perturbative effects that could be the reason for these uncertainties. There is not enough data for the physics in the forward region at the LHC and is a subject of ongoing experimental and theoretical studies. The forward region at the LHC could open gates to new physics.

Conclusion

Neutrinos are mysterious and everywhere around us. Understanding neutrinos is a challenging task as they rarely interact with matter. FASER-nu experiment has been proposed to measure the flux of neutrinos in the forward direction at the LHC. This project goal is to provide the theoretical prediction for the neutrino rate for experiments like FASER-nu. We include NLO QCD corrections in our calculation. To absorb the effects of higher order terms we have introduced an intrinsic transverse momentum parameter in the production of the D_s mesons which are main contributors to the tau neutrino flux. To understand the flux, we need to study the cross-section for the production of heavy quarks like charm and bottom. According to my calculations, the cross-section for the D_s^\pm production converges to the value of $58.68 \pm 0.05 \mu\text{b}$ in the forward region of interest to FASER-nu. This large cross section is expected to result in a large number of tau neutrino events as reported in JHEP06(2020)032. The missing higher order terms and unknown non-perturbative effects produces large uncertainties in the calculation of flux of tau neutrinos. The studies will continue to understand and reduce these uncertainties.

Acknowledgements

I would like to thank my mentor Milind Diwan for all his support and knowledge on this project. I would also like to thank Prof. Mary Hall Reno, Prof. Maria Vittoria Garzelli, Dr. Weidong Bai, and Dr. Yu Seon Jeong for their time and valuable suggestions on this project. This project was supported in part by the U.S. Department of Energy, Office of Science, Office of Workforce Development for Teachers and Scientists (WDTS) under the Science Undergraduate Laboratory Internships Program (SULI).

References

- [1] K. Winter, Detection of the tau-neutrino at the LHC, in ECFA Large Hadron Collider Workshop, Aachen, Germany, 4-9 Oct 1990: Proceedings.2., pp. 37–49, 1990.
- [2] FASER collaboration, A. Ariga et al., Technical Proposal for FASER: Forward Search Experiment at the LHC, 1812.09139.
- [3] P. Nason, S. Dawson and R. K. Ellis, The Total Cross-Section for the Production of Heavy Quarks in Hadronic Collisions, Nucl. Phys. B303 (1988) 607–633.
- [4] Bai, W., and Reno, M. H. (2019). Prompt neutrinos and intrinsic charm at SHiP. Journal of High Energy Physics, 2019(2). doi:10.1007/JHEP02(2019)077
- [5] Bai, W., Diwan, M., Garzelli, M. V., Jeong, Y. S., Reno, M. H. (2020). Far-forward neutrinos at the Large Hadron Collider. Journal of High Energy Physics, 2020(6). doi:10.1007/JHEP06(2020)032

TCAD Simulations of AC-LGADs

Sean King

State University of New York at Geneseo, Geneseo, NY 14454

Gabriele Giacomini

Brookhaven National Laboratory, Upton, NY 11793

Abstract

Low-Gain Avalanche Diodes (LGADs) are currently developed at Brookhaven National Laboratory (BNL). The gain associated with these detectors significantly increases the signal-to-noise ratio for detection of minimum ionizing particles (*mips*). However, while being fast, LGADs suffer from poor spatial resolution. AC-LGAD's are being developed in an effort to improve spatial efficiency. AC-LGAD's will liberate the detector of the dead volume previously associated with the geometry of LGAD's as well as will improve the spatial resolution. Currently, the fast timing performance is limited by the possible bandwidths of the associated electronics. By simulating AC-LGADs with various geometries and doping concentrations of its n+ layer, we are able to build relationships between the signal pulses and the varying parameters in an effort to determine an ideal structure to be fabricated in clean-room. The sought-after structure will allow for the particle hit position to be easily identifiable by looking at the ratios of pulse heights in the various electrodes. The effect of the gap between the electrodes and the effect of the oxide thickness on the ratio pulse heights has been determined from the simulations run.

Another silicon sensor exhibiting gain is the Silicon PhotoMultipliers (SiPM). Alongside the simulation activity on AC-LGAD, waveform analysis is being done on with the intention to observe the nature of primary dark counts, afterpulses and delayed crosstalks. SiPM waveforms are analyzed and the probabilities of both afterpulses and delayed cross talks are calculated. Future work will be done with various SiPM's

and electronic set ups to get a better sense of the probabilities of such pulses.

I. AC-LGADs

AC coupled low gain avalanche diodes are silicon-based detectors on the scale of tens of microns that are intended to be used, for example, in parts of the EIC detector. Charge multiplication is achieved by the high electric fields produced within the device.

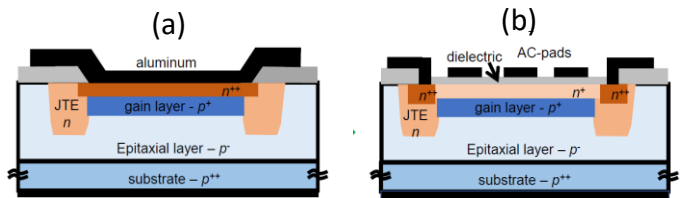


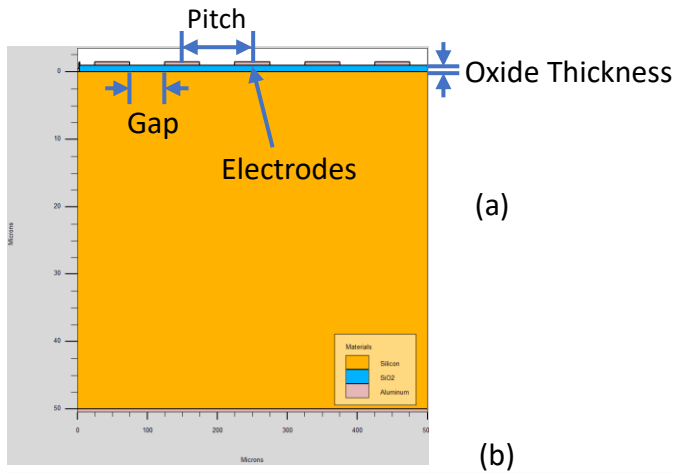
Fig 1. (a) *Structural diagram of a LGAD showing the various doped layers of Silicon.* (b) *Structural diagram of an AC-LGAD showing the various doped layers of Silicon.*

As shown in figure 1, it can be exposed how the AC-LGAD will liberate the LGAD of associated dead volume by making use of AC-Contacts on top of a n+ layer that terminates at n++ layers, which border the DC-Contacts. This liberation of dead volume will help to improve the spatial efficiency and resolution of the AC-LGADs as well as yielding a 100% fill factor over the LGADs.

II. Methods

In an effort to determine an ideal structure of the AC-LGAD's simulations were run varying structural parameters and looking at the relationships between the signal pulses. The parameters varied are the phosphorous implantation dose of the n+ layer, the pitch of the electrodes, the gap between the electrodes as well as the oxide thickness. These parameters should have an effect on the signal pulses

as the structural variations in the electrode sizes affect their resistance and capacitance and in turn the current signals produced. While varying these parameters the particle path is held constant, entering the detector through the center of the central metal electrode.



Pitch (um)	50	100
Gap (um)	10,20,50,80	10,25,40
n ⁺ Layer Dose (cm ⁻²)	10 ¹³ , 10 ¹⁴ , 10 ¹⁵	10 ¹³ , 10 ¹⁴ , 10 ¹⁵

Fig 2. (a) Diagram of AC-LGAD showing parameters simulated in Silvaco Deckbuild. (b) Table of structural parameters and n⁺ layer dosages that were simulated.

The current pulses produced in the AC-LGADs are filtered through a Matlab script that utilizes a FIR lowpass filter. For simulation purposes this is used to merely smooth the current pulse as shown below in figure 3b. In an experimental setting it will smooth the pulse as well as attenuate higher frequency electronic noise and aid in the signal readouts.

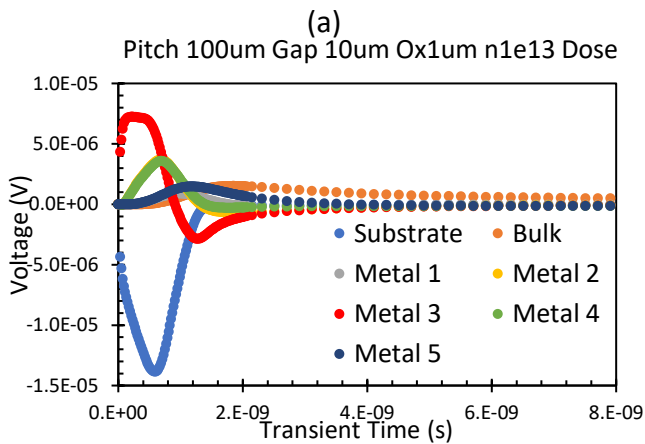
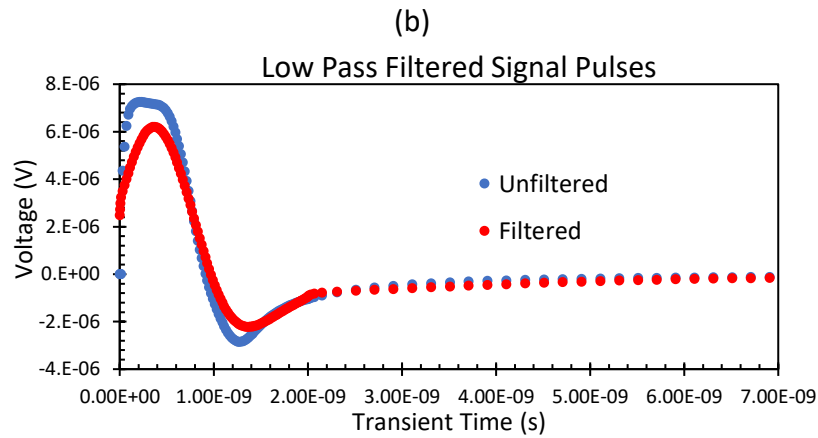


Fig 3. (a) Example of a plot of the unfiltered current pulses observed in an AC-LGAD from the various



electrodes. (b) Plot of a signal in the hit electrode before and after being passed through a low pass filter.

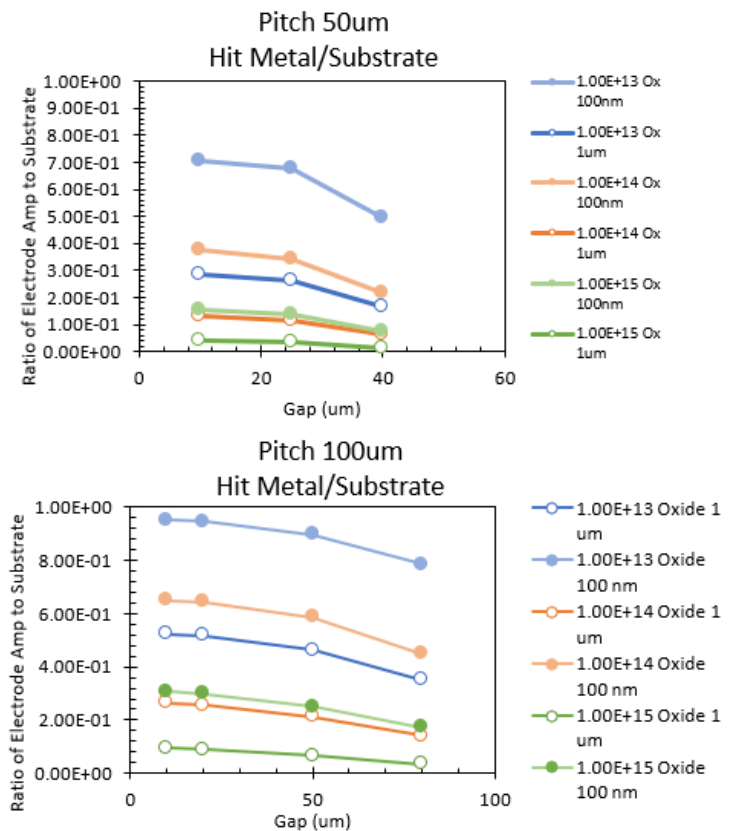


Fig 4. The plots above show the ratio of the pulse height originating from the hit electrode and the pulse height seen in the substrate of the AC-LGAD. AC-LGAD with a pitch of 50 microns (a) and AC-LGAD with a pitch of 100 microns (b). Both with varying phosphorous doping, oxidation layer thickness' and gap sizes.

For example, plots like these suggest that a gap as large as half the pitch still allow for signals that gaps 10% of the pitch can produce. It can also be shown in plots like those in figure 8 that by shrinking the pitch from 1um to 50um the signal is

more effectively shared between the electrode neighbors.

Future analysis will be done on similar plots that relate the pulse heights of all the electrodes on the AC-LGAD. This analysis will aid in the determination of the structure wanted when put in use at a specific application.

III. SiPM Waveform Analysis

Among other charge multiplication devices in use, we have Silicon PhotoMultipliers (SiPM's). SiPM's are arrays of Single Photon Avalanche Diodes (SPAD) where an avalanche is triggered when an external photon is absorbed in the silicon or a thermally generated electron is produced in the bulk. These devices are in principle very noisy. Other than primary dark counts, other noise signals correlated with those can be observed. Some of these extraneous counts are delayed cross talk (DeCT), direct cross talk (DiCT) and afterpulsing. During an avalanche in the cell, a photon can be emitted resulting in a secondary avalanche in another cell, DeCT or DiCT. DeCT occur when the emitted photon is absorbed in the non-depletion region and triggers an avalanche in a neighboring cell while the DiCT occur when the emitted photon is absorbed in the depletion region triggering an avalanche in the neighboring cell. Both forms of cross talk are correlated with increased pulse amplitudes in the SiPM. Afterpulsing can occur when carriers get trapped in defects of the silicon then are released causing a fractional avalanche in that same cell.



Fig 5. Diagram of a SiPM depicting the origin of its noise pulses. (A. Gola, *IEEE NSS 2015*)

The SiPM's fast signal output is connected to a RF amplifier and to our 4 GHz scope to acquire the transient pulse data. Nominal transient pulse data that we look to analyze is shown below in figure 6.

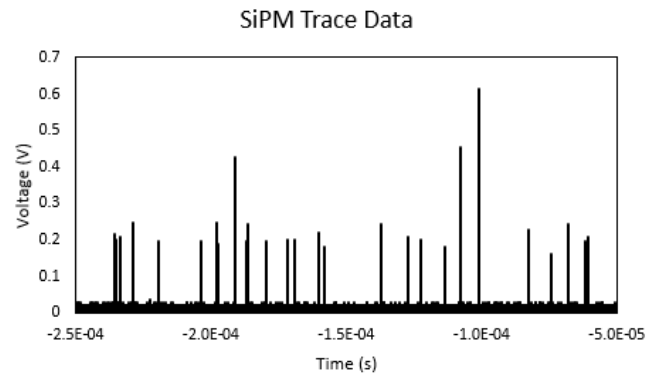
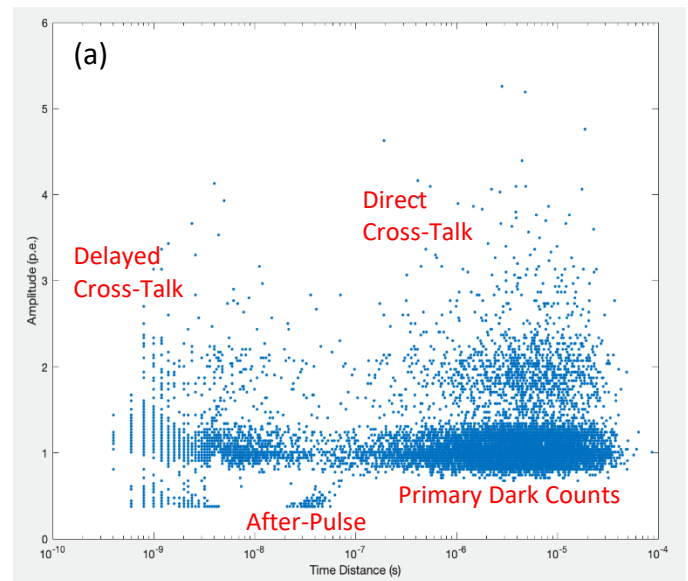


Fig 6. Transient pulse data obtained from a 1mm² SiPM held at room temperature.

A Matlab script was written to analyze SiPM waveforms and characterize the pulses. Primarily by finding a dark count then looking at the time distance to the next pulse and the amplitude of that secondary pulse. From literature, we know the timing characteristics of DeCT and afterpulses. the primary dark counts can be fit with a Poisson Distribution to determine the total dark counts/dark rate.



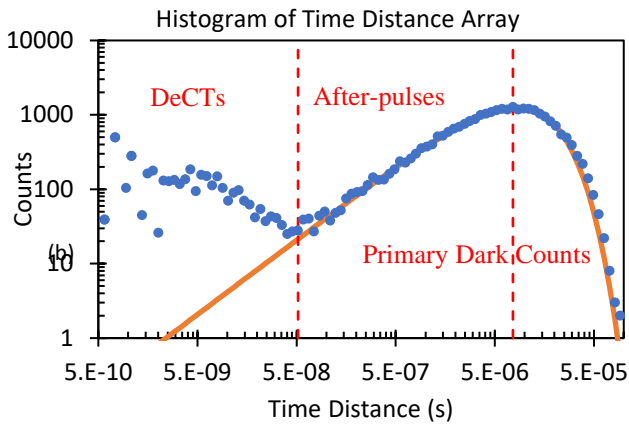


Fig 7. (a) An experimental scatter plot of pulse amplitude as a function of its time distance from the preceding primary dark count (b) A log-log histogram of secondary pulse amplitudes vs time distance(right). Dots are experimental data and the solid line is an exponential fit to the experimental data. The fit represents the dark counts and the skewed experimental data from the curve represent DeCT and afterpulse signals.

In the case shown in figure 7b DeCT are distinguishable from the primary dark counts however after-pulses are indistinguishable and cannot get a deep understanding of their behavior. However, in this case DeCTs occur with 12.6% of primary dark counts and after-pulses with 0.141% of primary dark counts.

These fits can be made for various different SiPM devices and electronic setups in an effort to observe the noise sources associated. Many factors can be attributed to the noise sources, such as temperature of the device and the size of the device. Lower temperatures increase signal/noise ratios and larger devices, increase the capacitance and in turn decrease signal/noise ratios. Further work is going to be done on various SiPM devices to get a better understanding of the characteristics and behaviors of these noise sources.

IV. Acknowledgements

I would like to thank Gabriele Giacomini for mentoring me and working on this on this project with me this summer. This project was supported in part by the U.S. Department of Energy, Office of Science, Office of Workforce Development for Teachers and Scientists (WDTS) under the Science Undergraduate Laboratory Internships Program (SULI) Summer 2020.

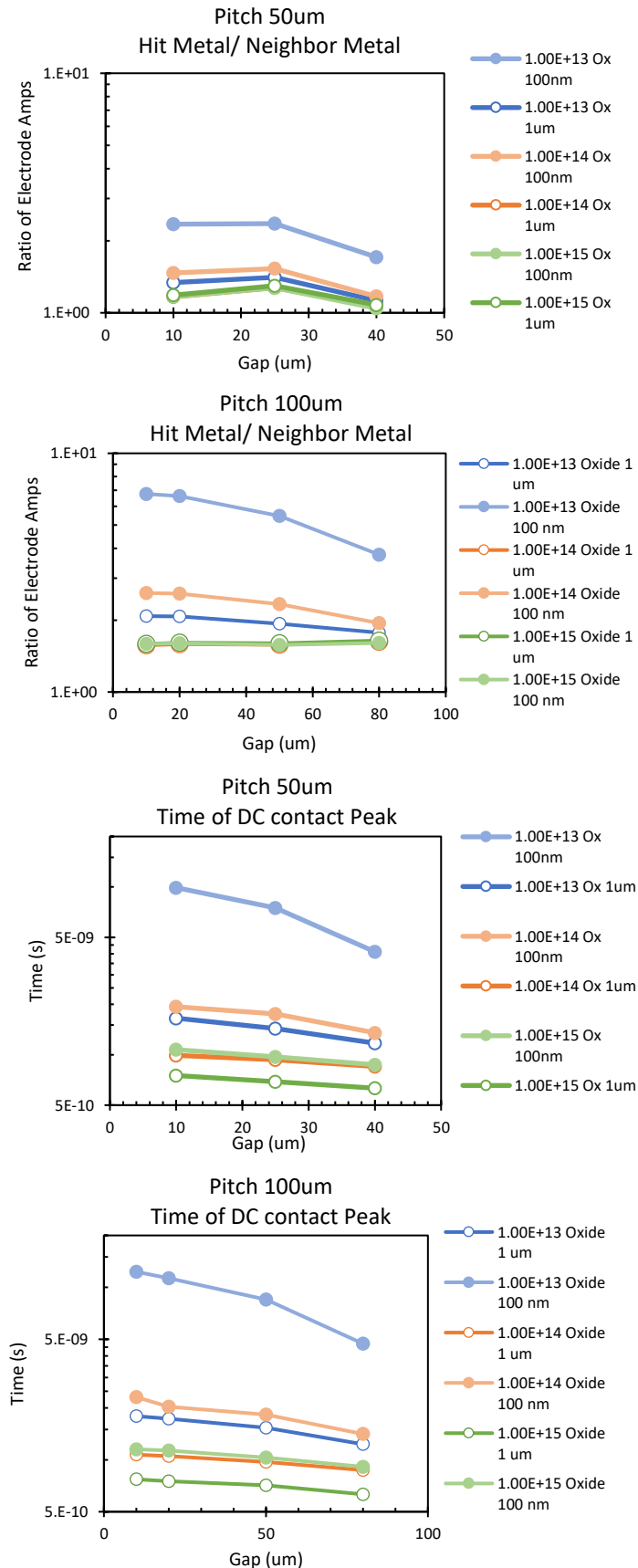


Fig 8. Examples of various other plots that are analyzed to understand the correlation between structural parameters and current pulse amplitudes.

Data Acquisition with Frame Programmable Grid Arrays

Matthew D. Leone

Computer Science Department, College of Arts and Sciences,
University of Rochester, Rochester, NY, 14627

Kimhan Ha

National Synchrotron Light Source II Controls group,
Brookhaven National Laboratory, Upton, NY, 11973

Yong Hu

National Synchrotron Light Source II Controls group,
Brookhaven National Laboratory, Upton, NY, 11973

I. Abstract

The National Synchrotron Light Source II (NSLS-II) produces the brightest X-rays in the world, and uses Field Programmable Gate Arrays (FPGAs) to convert the signals from the electron beams into digital representations. Due to the massive scope of the NSLS-II, which has a ring circumference of 792m, there is a need for data acquisition software and hardware that can be customized to fit specific needs. FPGAs are ideal for this type of work, because unlike Application Specific Integrated Circuits (ASICs), FPGAs can be “‘field’ programmed to work as per the intended design.”.

At NSLS-II, hardware often changes its form and function based on new experiments or new requirements in regard to hardware specifications. Due to COVID 19, on site access to this hardware is not feasible. In order to create a substantially similar representation of the laboratory’s use of FPGAs at home, I created an analog to digital converter (ADC) at home. This piece of hardware takes some form of non-digital information, e.g sound waves, signal producers, electric currents, etc., and encodes it into a form that can be processed by a computer. For my project, I created an audio looper. This is a type of machinery that records data (in my

case, musical sound), stores it, and makes it available for playback. With this, you can play multiple tracks at once, and harmonize with just one person.

In order to take the analog information and turn it into a binary representation, my machine uses a sampling rate of 48 khz, which was selected to appropriately record the human voice and instruments. For reference, the beam position digitizing system which is called Beam position monitor electronics ADC, the sampling rate is 117 MHz. My inputs were a microphone mixer, which allows you to plug instruments into it and then send that sound through an audio input line, and a pair of computer speakers for output.

II. Introduction

The purpose of this paper is to explore the data acquisition capabilities of a type of hardware called a Field Programmable Gate Array (FPGA). These devices are used in many different fields, but have a specific application in the scientific field with their role of gathering information. Additionally, they are well suited to the environment of scientific experimentation, because they have the ability to adapt more quickly to new specifications, discoveries or circumstances when compared to other digital logic circuits. In my project, I learned how to program, build and design FPGAs, and finished with a completed build of a Direct Memory Access Analog to Digital Converter machine based off of FPGA technology.

Before going into the specifics of this project, I am going to outline key differences, applications and reasons why one would use an FPGA. An FPGA is a unique form of electronic circuitry that allows a programmer or engineer to design a singular piece of hardware for multiple uses. It makes use of thousands of logic gates, which is where the Gate Array, in its name comes from, to compose a

complex logical design that allows for most of the functionality of a CPU. For most hardware circuits, referred to here as an Application Specific Integrated Circuit (ASIC), the circuit is built and designed for a specific purpose. The main advantage that FPGAs have over ASICs is that if there is a change in protocol, specification requirements, or purpose of the hardware, you can reprogram the FPGA, for all intents and purposes, on the spot, hence the name “Field Programmable”. This is not the only advantage that FPGAs have over ASICs, and there are more benefits that make them a better choice in the field of experimentation, data acquisition, and scientific testing.

In addition to the ability for spontaneous reorganization of their design, FPGAs have a number of additional advantages over ASICs. First, they often incorporate ‘parallelism’ into their design, which coordinates processes such that those that can be done at the same time are¹. FPGAs are able to do this better than regular circuitry because they can adjust the standard size of their memory blocks, which lets the computer do less work, and spend more time creating parallel processing blocks of logic². Furthermore, FPGA based designs make use of specified hardware that’s sole purpose is to perform tasks at hand. Most ASICs are generalized circuitry, which means that they are created to suit many different needs, and have a lot of hardware and software dedicated to generalized functionality. These designs also have a better long term life span, because they are able to reprogram their logic, remove and replace outdated hardware, and in

general are more easily upgraded than an ASIC. FPGAs, due to these reasons, are in general, cheaper and faster to use¹.

Before discussing the practical application of my FPGA, it is important to note that FPGAs provide for a wide variety of different uses. This might sound contradictory to the above claim that FPGAs are specialized and provide use for tasks where you have a clear goal, and are only interested in the pursuit of that. However, if one delves a deeper into FPGA design, it becomes clear that the design process behind FPGA experiment accounts for this oddity. In the process of designing these applications, there are two main elements. First, you create a hardware design layout. This is the blueprint of the pieces of hardware that are to be connected and used in your design. Here, for example, you set up your memory banks, the connection to the system clock, and whatever other hardware you need from the catalogue that is available to you. The hardware that we don't select is simply put to the wayside, and given no processing power, thereby streamlining the FPGA by dedicating all processing power to the task you do want to complete. The other half of the design phase is writing the software code, which in this instance was written in C, and translated by a microprocessor built into the FPGA. So, FPGAs that enable a large library of different hardware, e.g. memory modules, internet server capabilities, analog to digital converters, transistors, etc., instead of bringing down the overall speed of the design due to bloating and overstressing the processor, allow for a better selection of the right tools. This increases the speed of the design.

The point of this paper is to create a replication of the Analog to Digital converters used in the National Synchrotron Light Source in a home setting. At Brookhaven National Laboratory, Beam Position Monitor systems use an analog to digital converter to record information about the electron beam. This information is vital to the experiments that occur, and allows for a monitoring of this bright and fast beam of electrons. Without these processors and equipment, it would be much more difficult to maintain the experiments. My goal, in this paper and in my project, is to explore and design an analog to digital converter at home, that converts sound waves into a digital representation in the memory of the FPGA.

III. Project Objectives, Methodology, and Results

Due to circumstances, work on the FPGAs was done remotely. There was no opportunity to access the converters and machinery on site, so the scope of my project was limited to what was accomplishable without high level laboratory equipment. With this in mind, the focus of the project was to create a substantially similar representation of the machinery used to record the electron beam at home. Unfortunately, I do not have access to electron beams at home, and therefore chose a suitable replacement for the beam in the form of sound waves. The electron beam is recorded in the form of a wave as well, albeit one with a much higher frequency. A successful recreation of this machinery gave me insight into the process of this design, the purpose of collecting data in this way, and the ability to make use of the data gathered in a meaningful way.

In order to take some form of analog information, and convert it into a digital representation, I made use of the converter provided in the FPGA hardware catalogue. Before designing the hardware layout, and connecting the appropriate pieces of hardware to their locations, I first had to gather a proper input source and output source for the FPGA. For my input source, I made use of an analog mixer commonly found in recording studios, and used this as an input into the ‘Line in’ port of the FPGA. The mixer takes sound from either an instrument or a microphone, and regulates the frequency and voltage such that it is able to input into the FPGA. From here, it is to be brought through the design to the converter. For my output source, I use a pair of computer speakers that will play out either my voice or the sound of a guitar plugged into the mixer. The speaker will play out the sound from the input, and we access the sound through the memory inside the FPGA.

The first step in building the Analog to Digital converter (ADC) is to create a hardware design layout. For my ADC, my hardware consisted of a memory management system, a system clock, a converter, a system clock regulator, connected inputs to the converter and outputs to the ‘Line out’, and processor connections. Sampling rate of the sound waves is set to 48 KHz. Then I took this design and exported it to a location where I can write C code that will be programmed into the FPGA. In this instance, I used a Xilinx Software Development Kit, which allows me to import a hardware design wrapper and then write code that pertains to the specific wrapper. In here, I used the Xilinx starter

code to construct the outline of my software code, and then filled in the appropriate locations for work that is specific to my FPGA. After writing and testing the code, I began the process of programming the FPGA. This involves a synthesis of the hardware design and the software, followed by an implementation plan, and then finally writing and uploading a bitstream of this information into the FPGA. After this step, the FPGA is programmed, and ready to begin Analog to Digital conversion.

Then, after I built the hardware and coded the instructions into it, the FPGA was turned on and connected to a serial terminal. The purpose of the terminal is so that the FPGA can print out pertinent display information about the project. Once connected to my computer and turned on, the input from the analog mixer is plugged in and the output speakers are connected. To record, I press 'BTNU' on my FPGA, and play an instrument or speak for 5 seconds. Then, once the FPGA has recorded, I can play the output by pressing 'BTNL'. The computer speakers play out whatever you recorded, and a successful conversion from analog to digital has been completed.

IV. Conclusion

Although the feat of recording sound and playing it back is not as groundbreaking as one might hope, the method behind this action is truly what is important. We are able to take an FPGA, which has no inherent composition to it, and program it to specifically target a certain wavelength. The machine takes the wave and turns the information into something that can be understood by the

computer. The computer then takes this binary representation, and stores it in its internal memory. From this location, we are able to access the sound, and play it back. The ability to gather varied and wide ranging data in a scientific environment is critical to the success of research, and the results of this project show just how valuable FPGAs are to the goal of gathering data and reproducing it. In one day, one FPGA could record and store a hundred different types of wavelengths, and still be ready to do something different soon after. The evidence suggests that FPGAs are likely the most suited processing units for data gathering, and are the future of data acquisition needs in research and development.

V. Footnotes

1. ScienceDirect, “Field Programmable Gate Arrays”

<https://www.sciencedirect.com/topics/engineering/field-programmable-gate-arrays>

2. StackOverflow, “Parallel Processing on FPGA. How to start..?”

<https://stackoverflow.com/questions/7856487/parallel-processing-on-fpga-how-to-start-with#:~:text=The%20big%20wins%20from%20an,allows%20more%20parallel!%20processing%20blocks>

Science Undergraduate Laboratory Internships (SULI)

This project was supported in part by the U.S. Department of Energy, Office of Science, Office of Workforce Development for Teachers and Scientists (WDTS) under the Science Undergraduate Laboratory Internships Program (SULI).

Promoting the Selective CO₂ Activation to Methanol: Catalyst Optimization using Density
Functional Theory

Zhuoying Lin, Chemistry and Biochemistry, University of California, San Diego, CA 92093

Wenjie Liao, Chemistry, Stony Brook University, Stony Brook, NY 11794

Ping Liu, Chemistry, Brookhaven National Laboratory, Upton, NY 11973

Abstract

Reduction in combustion-related CO₂ emissions by incorporating CO₂ as a source of carbon and/or oxygen for synthesis added-value chemicals, e.g. methanol, has long been challenging in catalysis and research priority of DOE. My summer research at BNL was built on the previous accomplishments at Catalysis group in Chemistry, showing that alkali metal, potassium (K), can work as a major active center and facilitate selective CO₂ conversion to methanol. In this study, we focus on cesium (Cs) to explore the effects of Cs₃O₄H-metal (Cu, Ag, Au) support interaction on binding properties and thus catalytic performances. To do that, I not only grasped fundamental knowledge of density functional theory and heterogeneous catalysis, but also gained hands-on experience on model construction, running of DFT calculations at CFN computing clusters and data analysis to determine the optimized structures of bulk and surfaces, adsorption energy, Bader charge and density of states. Our results showed that the binding property of Cs⁺ sites can be selectively tuned via strong interaction with metal supports. The interaction with open-shell formate, a key intermediate to mainly control the CO₂ conversion, was significantly affected by changing substrate via interplay between charge transfer and electrostatic interaction. The corresponding binding is weakened going from Cu(111), Ag(111) to Au(111). While the binding of closed-shell formic acid, a key intermediate to control methanol selectivity, was barely affected via mainly electrostatic interaction. Our study indicated that Au can be an effective support to promote both CO₂ conversion and methanol selectivity on Cs sites. More importantly, it opens a new path to enable the challenging selective tuning in binding of key reaction intermediates and effective catalyst optimization.

Background

To reduce CO₂, a greenhouse gas from the atmosphere, one solution is to perform CO₂ hydrogenation which produces methanol, a promising liquid fuel and a common feedstock used in the chemical industry¹. While methanol synthesis from syngas mixture (CO, CO₂, and H₂) over the Cu-ZnO/Al₂O₃ catalyst has been a common industrial practice, it only gives a 15-25% conversion rate with a low methanol selectivity². Therefore, optimizing the catalytic performance of CO₂ hydrogenation in the overall CO₂ conversion rate and methanol selectivity has long been a subject of active research.

Alkali metals have been reported as potential promoters to achieve this objective. They are shown to improve the catalytic activity and tune the product distribution in many other industrial processes such as the Fischer-Tropsch process³, the water-gas-shift reactions⁴, and the Haber-Bosch process⁵ due to its ability to tune the adsorption and dissociation of small molecules. Previous study⁶ at the Catalysis group in Department of Chemistry, BNL, showed that alkali metal, potassium (K), deposited on Cu_xO/Cu(111) (x≤2) model surface, can work as a major active center, an accelerator for charge transfer, a mediator for the electron tunneling, and facilitate the selective CO₂ hydrogenation to methanol. The promoting effect of K depends on the stabilization of close-shell formic acid (*HCOOH) via electrostatic interaction, a key intermediate leading to the methanol production; However, due to the synergistic contribution from the electrostatic interaction and significant charge transfer from substrate Cu^{δ+}, the binding of open-shell formate (*HCOO) at K sites is too strong, which slows down the overall CO₂ conversion. To enhance the CO₂ conversion rate and methanol selectivity at the alkali sites during CO₂ hydrogenation, it is desired to stabilize *HCOOH while destabilizing *HCOO.

Following this idea, in the current study, alkali cluster $\text{Cs}_3\text{O}_4\text{H}_3$ is deposited on Cu(111), Ag(111), and Au(111) to evaluate the catalytic effect of $\text{Cs}_3\text{O}_4\text{H}_3$ -metal on the binding of $^*\text{HCOO}$ and $^*\text{HCOOH}$ using density functional theory (DFT) calculations. Our results show the binding energy of HCOOH is relatively constant over the studied metal support due to the same $\text{Cs}^{\delta+}\text{-O}^{\delta-}$ electrostatic interaction, while the binding of HCOO is weakened from Cu, Ag to Au due to the decreasing stability of metal ions after the charge transfer. Among the systems studied, Au(111) is a potential support for CsO_x clusters to promote the CO_2 conversion and selectivity, which will be verified via mechanistic studies with DFT in the future.

Theoretical method

The spin-polarized DFT calculations with PW91 functional were performed using the Vienna ab-initio simulation package (VASP) code^{9,10,11}. The valence shell electron density was projected on the plane wave basis set with a kinetic energy cutoff at 400 eV, and the interaction between the core electron and the nucleus was approximated by projector augmented wave (PAW) pseudo-potential. Gaussian smearing method was applied to interpret the electronic states near the Fermi level with an electron temperature at $k_{\text{B}}T = 0.05$ eV and extrapolated to $k_{\text{B}}T = 0$ eV to obtain the actual ground state energy. The calculation of electronic relaxation is said to converge when the difference in the consequent energy is smaller than 10^{-5} eV.

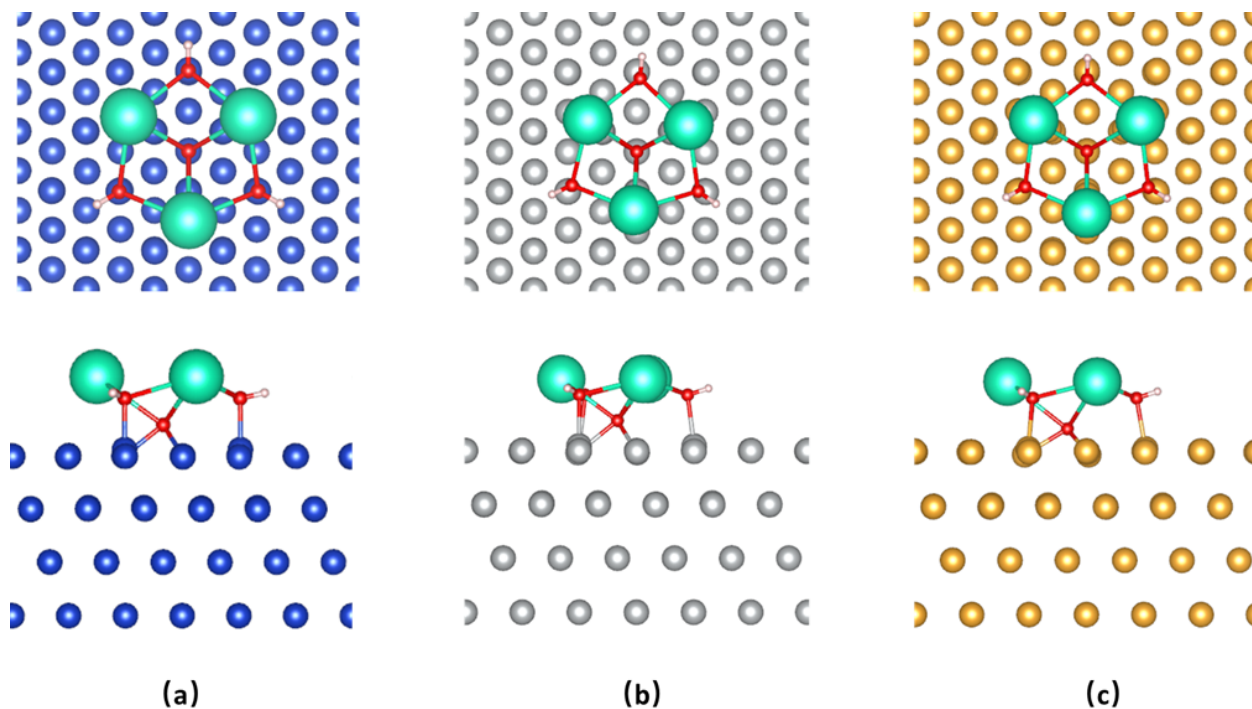


Figure 1. Top view (upper) and front view (lower) for optimized structures of $\text{Cs}_3\text{O}_4\text{H}_3$ cluster supported on (a) Cu(111), (b) Ag(111), (c) Au(111). Cu: blue, Ag: silver, Au: yellow, Cs: cyan, O: red, C: brown, H: white.

To construct the metal-supported alkali catalyzed structure, the initial step was to construct the bulk crystal of face-centered cubic Cu, Ag, and Au, where the lattice constant of these optimized bulk crystals was used to build the slab model for metal (111) facet. The slab model contained four layers of 5×5 metal (111) surface, with a 15 \AA vacuum layer added perpendicular to the lattice plane. The optimized surfaces were validated by comparing the DFT calculated surface work function and d-band center with literature report (Table 1). The $\text{Cs}_3\text{O}_4\text{H}_3$ cluster was then deposited on the optimized metal (111) surfaces, where the hydroxylation of Cs_3O_4 cluster was considered to capture the highly reducing conditions of CO_2 hydrogenation. The cluster results in a similar structure over different supports (Figure 1): 3 Cs atoms formed an

equilateral triangle with each Cs anchored to one oxygen in the metal fcc hollow site and two hydroxyls on the metal top site. With the optimized model for metal supported $\text{Cs}_3\text{O}_4\text{H}_3$ cluster, adsorbates are added on Cs sites, and the most stable conformation is determined by the one with the lowest ground state energy. The binding energies of adsorbate was calculated by eq. 1.

$$B.E. = E_{*adsorbate} - E_{surface} - E_{adsorbate(g)} \quad (1)$$

Where E represents the total energies for adsorbed adsorbate on surface ($E_{*adsorbate}$), bare $\text{Cs}_3\text{O}_4\text{H}_3/\text{metal}(111)$ surface ($E_{surface}$) and free adsorbate in gas phase ($E_{adsorbate(g)}$), respectively. For all slab models, the bottom two layers were fixed; while the top two layers were allowed to relax until the Hellmann-Feynman forces act on each atom were smaller than 0.01 eV/\AA . Their Brillouin zone was sampled at 6 irreducible k-point slab models under the Γ -centered $3 \times 3 \times 1$ k-point mesh.

Table 1. Comparison between the calculated work function and d-band center on Cu(111), Ag(111), and Au(111) and literature reports.

Metal	d-band center	Literature value ⁷	Work function	Literature value ⁸
Cu (111)	-2.58	-2.67	4.74	4.94
Ag (111)	-3.99	-4.30	4.49	4.74
Au (111)	-3.35	-3.56	5.24	5.31

Results and Discussion

According to the DFT calculations, both *HCOO (Figure 2a, 2b, 2c) and *HCOOH (Figure 2d, 2e, 2f) adopt very similar geometry over different metal supports. On all systems studied, *HCOOH binds to the $\text{Cs}_3\text{O}_4\text{H}_3$ cluster through its dangling oxygen in the Cs hollow site, and it has closely similar binding energy at around -0.46 eV (table 3). On the other hand, *HCOO binds in a bidentate confirmation via Cs-O bond, and its binding was weakened from -3.30 eV on Cu(111) to -3.08 on Ag(111) and -2.79 eV on Au(111) (table 2). The selective binding-tuning for *HCOO, rather than *HCOOH at the Cs sites of $\text{Cs}_3\text{O}_4\text{H}_3/\text{Metal}(111)$ can be attributed to the different binding mechanisms rationalized by the previous study⁶. The binding of open-shell HCOOH was mainly through the electrostatic interaction between $\text{Cs}^{\delta+}$ and $\text{O}^{\delta-}$, which is nearly the same over different metal surfaces as indicated by the identical charge of Cs and O as well as the same Cs-O distance (table 3), thus giving a similar binding energy.

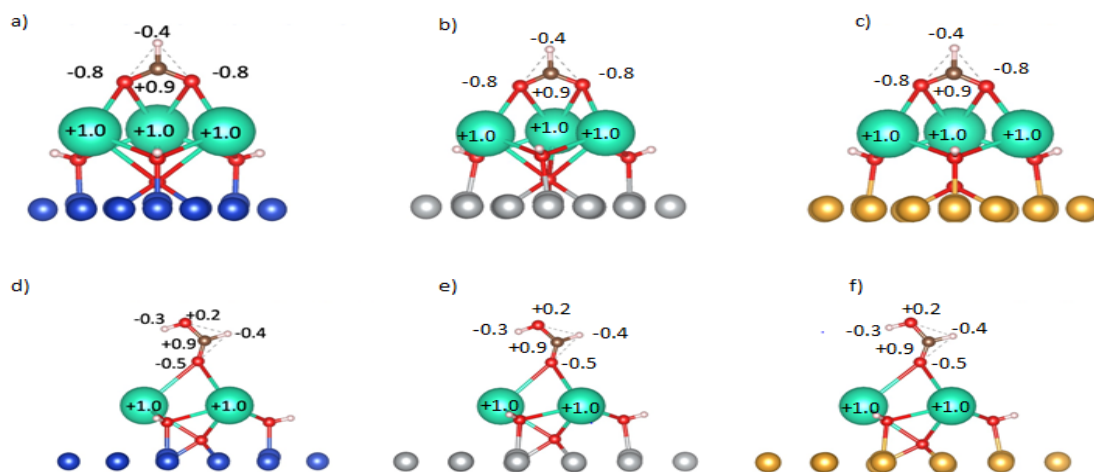


Figure 2. Front view for optimized structures of adsorbed *HCOO (top) and *HCOOH (bottom) at the $\text{Cs}_3\text{O}_4\text{H}_3$ cluster supported on Cu(111), Ag(111), and Au(111). Cu: blue, Ag: silver, Au: yellow, Cs: cyan, O: red, C: brown, H: white. Numbers over each atom indicates the calculated net charge from Bader charge analysis.

Table 2. DFT calculated binding energies (B.E.), the amount of charge transfer, and the average Cs-O bond length for *HCOO on supported Cs₃O₄H₃ clusters.

Metal	Binding Energy (eV)	Charge transfer (e)	Average Cs-O bond length (Å)
Cu (111)	-3.30	1.1	2.99
Ag (111)	-3.08	1.0	3.00
Au (111)	-2.79	1.1	2.99

Table 3. DFT calculated binding energies (B.E.), the amount of charge transfer, and the average Cs-O bond length for *HCOOH on supported Cs₃O₄H₃ clusters.

Metal	Binding Energy (eV)	Charge transfer (e)	Average Cs-O bond length (Å)
Cu (111)	-0.45	0.1	3.58
Ag (111)	-0.46	0.1	3.53
Au (111)	-0.47	0.2	3.57

Meanwhile, the open-shell *HCOO binds to the surface through both electrostatic interaction and charge transfer. The contribution from electrostatic interaction is again very similar over different metal support, but there is a difference in Cs-mediated charge transfer going from surface metal to *HCOO. Although the amount of charge transfer is the same from Cu, Ag, and Au to *HCOO, as each substrate transfers one electron to the adsorbate (table 2), the stability of the resulting partial oxidized metal is different. This is supported by the PDOS analysis of surface metal before and after the charge transfer (Figure 3). Upon the interaction with *HCOO, the Cu is partially oxidized, which is demonstrated by an apparent downshift (respect to the fermi level) in 3d orbital. As a result, the surface Cu atoms interacted with Cs₃O₄

cluster and thus the $\text{Cs}_3\text{O}_4\text{H}_3/\text{Cu}(111)$ was stabilized by interacting with $^*\text{HCOO}$. By comparison such downshift is less profound in Ag 4d orbital and almost none in Au 5d orbital. Therefore, the PDOS indicates that the $^*\text{HCOO}$ -induced stabilization of partially oxidized metal on surfaces and thus $\text{Cs}_3\text{O}_4\text{H}_3/\text{metal}(111)$ decreases in a sequence: $\text{Cu}(111) > \text{Ag}(111) > \text{Au}(111)$, leading to the weakened binding of $^*\text{HCOO}$ going from Cu to Au.

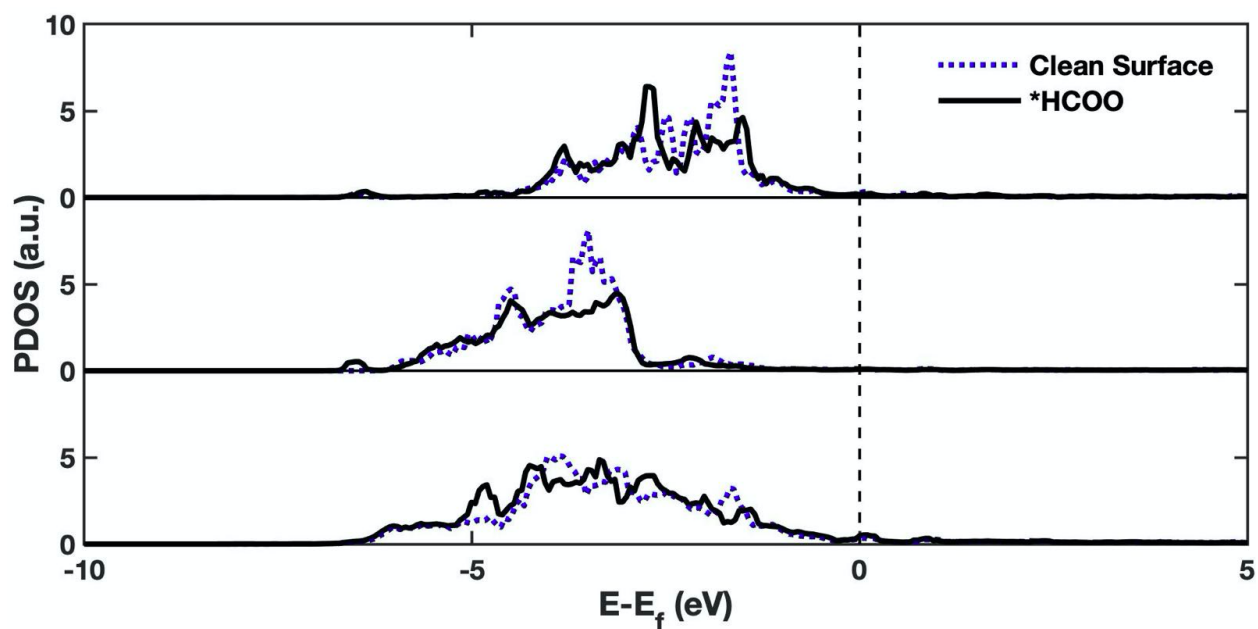


Figure 3. Projected density of states (PDOS) of Cu (upper row), Ag (middle row), and Au (lower row) on surface before and after $^*\text{HCOO}$ adsorption. Dotted blue lines indicate the clean surface; solid black lines indicate the surface after $^*\text{HCOO}$ adsorption.

According to the design roles extracted from our previous studies of CO_2 hydrogenation on $\text{K}/\text{Cu}_x\text{O}/\text{Cu}(111)$ ⁶, Au(111) is the most promising support to CsO_x clusters among the systems studied, enabling the supported Cs site to significantly destabilize $^*\text{HCOO}$, but still interacting well with $^*\text{HCOOH}$. Given that, the CO_2 conversion and methanol selectivity are likely to be

promoted as compared to K/Cu_xO/Cu(111), Cs₃O₄H₃/Cu(111) and Cs₃O₄H₃/Ag(111), which will be verified via mechanistic studies using DFT in the future.

Conclusion

The summer research studies the catalytic effect of Cs₃O₄H₃-metal (Cu, Ag, Au) in the binding of formate and formic acid, which are the key intermediates to control the CO₂ conversion and the selectivity of methanol, respectively. The result shows that due to the different stability of the partially oxidized metal surface, Cu(111) to Ag(111) and Au(111) could selectively weaken the binding of *HCOO, while the binding of *HCOOH remains the same over the studied systems due to a different binding mechanism that's mainly regulated by the electrostatic interaction. The current results suggest Au(111) can be a promising support to CsO_x clusters, which is likely to promote the conversion rate and selectivity for methanol synthesis from CO₂ hydrogenation. Our study also invites a further investigation in relating the intrinsic properties of metal surfaces to their catalytic capability of charge transfer.

Acknowledgement

This project was supported in part by the U.S. Department of Energy, Office of Science, Office of Workforce Development for Teachers and Scientists (WDTS) under the Science Undergraduate Laboratory Internships Program (SULI). The calculations were performed using computational resources at CFN, and the Scientific Data and Computing Center, a component of the Computational Science Initiative, at BNL under Contract No. DE-SC0012704. Special thanks to Wenjie and Dr. Liu for providing supportive mentorship and guiding me through all the work.

Reference

1. Shanshan Dang, Haiyan Yang, Peng Gao, Hui Wang, Xiaopeng Li, Wei Wei, Yuhan Sun, A review of research progress on heterogeneous catalysts for methanol synthesis from carbon dioxide hydrogenation, *Catalysis Today*, Volume 330, 2019, Pages 61-75, ISSN 0920-5861.
2. K.C. Waugh, Methanol Synthesis, *Catalysis Today*, Volume 15, Issue 1, 1992, Pages 51-75, ISSN 0920-5861.
3. Mingsheng Luo, Robert J O'Brien, Shiqi Bao, Burtron H Davis, Fischer–Tropsch synthesis: induction and steady-state activity of high-alpha potassium promoted iron catalysts, *Applied Catalysis A: General*, Volume 239, Issues 1–2, 2003, Pages 111-120, ISSN 0926-860X.
4. Kuo Liu, Aiqin Wang, and Tao Zhang. Recent Advances in Preferential Oxidation of CO Reaction over Platinum Group Metal Catalysts. *ACS Catalysis* 2012 2 (6), 1165-1178 DOI: 10.1021/cs200418w.
5. Atsumu Ozaki. Development of alkali-promoted ruthenium as a novel catalyst for ammonia synthesis. *Accounts of Chemical Research* 1981 14 (1), 16-21 DOI: 10.1021/ar00061a003.
6. Methanol Synthesis from CO₂ Hydrogenation over a Potassium-Promoted Cu_xO/Cu(111) (x ≤ 2) Model Surface: Rationalizing the Potential of Potassium in Catalysis. Wenjie Liao and Ping Liu. *ACS Catalysis* 2020 10 (10), 5723-5733 DOI: 10.1021/acscatal.9b05226.
7. A. Ruban et al. *J. Mol. Catal. A: Chemical* 115 1997 421-429.
8. *Crc Handbook of Chemistry and Physics: A Ready-Reference Book of Chemical and Physical Data*. Boca Raton: CRC Press, 2009.
9. P. Hohenberg and W. Kohn. Inhomogeneous Electron Gas. *Phys. Rev.* vol 136, B864-B871. DOI: 10.1103/PhysRev.136.B864.
10. G. Kresse and J. Furthmüller. Efficient iterative schemes for *ab initio* total-energy calculation using a plane-wave basis set. *Phys. Rev.* vol 54 11169—11186. DOI: 10.1103/PhysRevB.54.1169.
11. John P. Perdew and Yue Wang. Accurate and simple analytic representation of the electron gas correlation energy. *Vol 45* 13244—13249. DOI: 10.1103/PhysRevB.45.13244.

Testing anomalies with provenance in High Performance Computing

Allen Liu

Electrical and Computer Engineering, Purdue University, West Lafayette, IN 47906

Line Pouchard, Chris Kelly and Huub Van Dam

Computer Science Initiative, Brookhaven National Laboratory, Upton, NY 11973

Abstract

Provenance is a record of data collected to explicate scientific results and can describe dependencies and other data for experiment replication. A provenance trace can contain hybrid datasets coming from many different sources, from machine and hardware parameters, shared libraries, application details, runtime configurations, and performance analysis tools. It is information dense and is extremely high in volume, thus, monitoring provenance to track any anomalies that may arise is important in tracing problems and diagnosing potential latencies and crashes in execution. This project aims to test the Chimbuko framework which captures these anomalies, and its ability to detect the injected anomalies. Through developed mini-apps we can inject anomalies of interest such as anomalies related to I/O, MPI communication, memory allocation; using python directly and also as a frontend for C/C++ kernels; testing GPU support, GPU temperature anomalies, and combinations of single anomalies. Through these tests we can have a better understanding of any limitations in anomaly detection while also verifying that more complex anomalies will be detected by the system.

I. Introduction

Provenance, defined as the origin of an object, is a term mostly used in art and archaeology and details the chronology of the ownership, custody, or location of a historical object. In high performance computing the provenance of scientific workflows has traditionally been used to explicate scientific results - for instance, how a dataset was derived, what

transformations have been applied to data, what dependencies exist in the workflow graph and its execution on distributed systems. Provenance is used to provide information enabling quality control, re-run computational workflows, and reproduce results. [1]

These provenance traces are information dense, high in volume and important factors recorded for any application running in such environments include execution time and performance, accuracy of calculations. With such high volumes of information, it is important to determine if a simulation run is progressing as expected, what variations in performance a run exhibits and where they can be attributed. Monitoring the performance of workflows in high performance computing provides insights into this progression, how the computational resources are used, and where execution bottlenecks occur. [2]

The Chimbuko framework captures, integrates, analyzes, and visualizes performance metrics for complex scientific workflows and relates these metrics to the context of their execution on extreme-scale machines. The purpose of Chimbuko is to analyze these provenance traces and find any anomalies that arise during the runtime and report where the anomalies occur.

The objective of this project is to test the limitations of Chimbuko and create example code to inject anomalies into the framework and expand on the amount of errors that Chimbuko can catch. In particular, through developed mini-apps, we can inject anomalies of interest such as I/O related, MPI communication, memory allocation; using python directly and also as a frontend for C/C++ kernels; testing GPU support, GPU temperature anomalies, and combinations of single anomalies.

II. Methods

A virtual machine was installed to develop code and test the Chimbuko framework. The framework with its dependencies such as TAU2 had to be installed through Docker images,

which are files that contain the source code, libraries, dependencies, tools, and other files needed for an application to run. Docker containers, a virtualized run-time environment where users can isolate applications from the underlying system, are compact, portable units in which you can start up an application quickly and easily. Containers run the images and ensure that mini-apps developed can run reliably and quickly between different computing environments.

In addition to learning about Docker containers, I had also attended the NERSC GPUs For Science event where I spent two days listening to seminars and other discussions about the uses of GPUs in computing and their applications in other projects. I was also able to attend both the tutorial sessions, first on OpenACC programming, then on CUDA programming in C/C++. These steps were crucial to my understanding of GPU programming and the communication between the host and the GPU device on a computer.

For my project, an initial test code was written to ensure that I had installed the components correctly and that the framework was working as intended. The application was written in C and was a simple function called on repeat. The final function call had an added delay as the anomaly for the Chimbuko framework to detect. This code was then wrapped through ctypes to call the function from a Python frontend. In addition to wrapping it in ctypes, the function was also manually wrapped since manually wrapped functions provide faster speeds in compilation as well as more standardized function calls from within Python. In addition, since NVIDIA's GPU CUDA functions are written in C/C++, we can use the wrapping to execute more complex C/C++ functions through a Python frontend. Access to BNL's FPGA2 machine was needed to test these GPU functions and the Chimbuko framework.

III. Results

From the simple test code, we determined that the Chimbuko framework was working and caught the anomaly as intended. One small problem that did occur, however, was the fact that functions that were not called enough times would not be picked up as an anomaly since there would not be enough data to calculate a standard deviation that would trigger Chimbuko. After some test runs, we found that forty calls were enough to establish an average and standard deviation that would result in anomaly detection.

After the initial test, the code was wrapped through ctypes which was then called through Python. In the ctypes method, the C/C++ code has to be compiled into a shared library then loaded into Python through the ctypes library. At first, we ran into some errors due to the using the wrong compiler, however upon using the TAU compiler for C/C++, the Chimbuko framework worked without needing any changes. Confirmation of the ctypes method allowed us to continue to manually wrap these C/C++ functions. The advantage to writing the wrapping in C/C++ directly is speed increase and standardization of code. Through the manual wrapper, the C/C++ functions can be installed through pip into Python then imported as a library where the functions called from Python can then perform their intended C/C++ instructions. In this way, we can also create higher level and more complex code through C/C++.

Through the combination of this strategy and the information I learned through the NERSC GPUs For Science seminars, tried creating GPU anomalies in C/C++ then writing a wrapper for these functions to be called from Python to see if Chimbuko could pick up these anomalies.

IV. Conclusion

The Chimbuko framework was able to catch many of the anomalies out of the box without needing to adjust or add-on any extra features. Even wrapping C/C++ code and calling

those functions from Python, Chimbuko would be able to correctly display the anomaly and the function name. Unfortunately, due to limitations of time, the calling of GPU anomalies through Python could not be tested, however based on prior experience, there is high expectation that it will also work.

V. Acknowledgements

I would like to give thanks to my mentor, Line Pouchard, for introducing me to high performance computing and the integration of computer science into various applications. Special thanks to Chris Kelly for walking me through technical errors and sending me examples and other information for me to learn from; and to Huub Van Dam for getting me into the NERSC GPU For Science event tutorials and for guiding my learning experience.

This project was supported in part by the U.S. Department of Energy, Office of Science, Office of Workforce Development for Teachers and Scientists (WDTS) under the Science Undergraduate Laboratory Internships Program (SULI).

VI. References

L. Pouchard *et al.*, "Prescriptive provenance for streaming analysis of workflows at scale," *2018 New York Scientific Data Summit (NYSDS)*, New York, NY, 2018, pp. 1-6, doi: 10.1109/NYSDS.2018.8538951.

L. Pouchard, A. Malik, H. V. Dam, C. Xie, W. Xu and K. K. Van Dam, "Capturing provenance as a diagnostic tool for workflow performance evaluation and optimization," *2017 New York Scientific Data Summit (NYSDS)*, New York, NY, 2017, pp. 1-8, doi: 10.1109/NYSDS.2017.8085043.

Direct measurement of trapped ion micromotion

Maverick Millican*

Physics Department, Brookhaven National Lab †

(Dated: August 19, 2020)

Quantum computing research is at the forefront of physics research being conducted by many top research universities, government laboratories, and private physics and computer engineering research organizations today. The theorized applications and capacity of quantum computers goes remarkably beyond the scope of even the most powerful classical supercomputers in the matters of privacy, encryption, speed, and complexity. The pursuit of identifying quantum qubits and gaining the ability to control and manipulate them in large numbers a significant challenge faced in quantum computing physics research. Trapped ions have proven to be great candidates for quantum bits because of their distinguishability in a trap, long quantum state lifetime, manipulability under various operations, and quantum state detectability through laser spectroscopy. Ions in a Paul Trap undergo a small yet unavoidable oscillatory motion do to a fluctuating electric field which proves to be problematic in the field of quantum computing. This micromotion is linked to difficulty in state initialization and quantum gate infidelity. Micromotion must be properly understood to be controlled and compensated for the production of high fidelity quantum gates. This paper describes methods of detecting and measuring the micromotion of eight ions in a linear Paul Trap as well as the analysis and results of the data collected. This project also introduces the first recorded direct micromotion measurement technique for an ion chain using spatial resolution camera technology, and compares the novel technique to previously developed methods.

Usage: Department of Energy summer internship project report.

I. INTRODUCTION:

Ions trapped in radio frequency traps follow a pattern of motion that can be described as the combination of a slow and fast harmonic motion. The rapid oscillation of ion motion is known as micromotion and is driven at the frequency of the applied electric field in the trap. Excess micromotion can cause frequency modulation of incident laser light due to the first order Doppler shift, which reduces laser cooling efficiency [1] and quantum logic gate fidelity [2]. Detection, live measurement, and compensation of micromotion is essential for high-precision applications such as quantum computing. Chip-scale surface electrode ion traps for quantum computing are especially susceptible to excess micromotion because the ions are held closely to the trap electrodes and are therefore more susceptible to undesired electric fields that cause micromotion. Stray DC electric fields shift ions away from the RF null of the trap which inevitably leads to micromotion. Several techniques for micromotion detection have been developed, including the ion fluorescence modulation due to first order Doppler shift, micromotion sideband spectroscopy, and ion fluorescence modulation that is resultant of resonant external modulation [3].

Contemporary methods commonly used to calculate micromotion amplitude are conducted through indirect observation of variables related to the motion, such as ion fluorescence or spectrum changes caused by micromotion. The photon-correlation measurement technique

uses changes in the ion fluorescence to estimate the first order Doppler shift experienced as a result of micromotion. This is used to calculate the velocity and displacement amplitudes for a single micromotion cycle. The sideband spectroscopy method measures the fluorescence of the ion at resonance and compares that to the scattering rate at its first sideband, $\omega - \omega_0 = \pm\Omega$. This gives insight on the Doppler shift experienced in the ion frame and can be used to calculate micromotion amplitude indirectly.

This paper presents the first direct observation of the trapped ion micromotion using a state-of-the-art camera capable of time resolution with precision of 1.6 ns, single-photon collection, and measurement of both the photon flux and position with precision of $.2\mu m$. This allows micromotion amplitude and phase to be measured for every ion in the linear chain. The technique is therefore fit for measuring and controlling tilts and shifts of the ion chain from the RF null. The spatial resolution capabilities of the camera also make it fit for the measurement of micromotion present in complex and multi-dimensional trapped ion lattices.

Micromotion is unfavorable for quantum computing purposes as it leads to quantum operation and initialization infidelity, spectral broadening, and inefficient ground state vibrational mode cooling. It is important to compensate micromotion in attempt to minimize its affects and create a more controlled environment for quantum computing operations.

* Also at University of Washington Department of Physics.

† millim@uw.edu

II. SETUP AND METHOD:

A linear RF trap, like the one used in this study, is a type of ion trap in which all ions are confined to a single linear axis. The radial confinement around the axis is created by cylindrical electrodes that lie parallel to each other around the axis of confinement. Each electrode

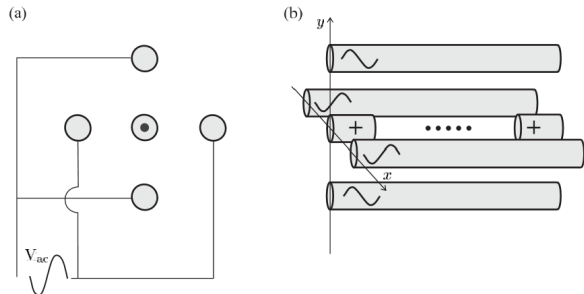


FIG. 1. The configuration of a four-rod linear ion trap. This trap is used to contain a 1-dimensional string of ions by use of a combination of static and dynamic electric fields. a) A cross section of the trap looking along its axis. Each rod is connected diagonally to another, giving a dynamic quadrupole field when oppositely charged AC current is run through the pairs. b) A better angle to see the trap configuration, including the end caps and ion chain.[4]

carries an alternating current that together act to create a dynamic electric field that keeps ions radially confined. At the two ends of the linear trap are electrode ‘end caps’ that carry static DC voltage and act to push the ions toward the center of the trap along its axis.

The 8-ion chain of $^{138}\text{Ba}^+$ and $^{136}\text{Ba}^+$ is stored in a “five-rod” linear RF trap [5]. To Doppler-cool $^{138}\text{Ba}^+$ ions, the $6S_{1/2} - 6P_{1/2}$ transition at 493 nm is used. A 650 nm laser is used to repump ions from the long-lived $5D_{3/2}$ metastable state. $^{136}\text{Ba}^+$ ions are sympathetically cooled and do not emit photons during the measurements. Micromotion is driven as a response to the RF potential on the electrodes present in the Paul trap, therefore it has the frequency $\Omega = 2\pi \cdot 18.2516\text{MHz}$.

Data collection for this experiment was performed by the single photon sensitive time-stamping camera, Tpx3Cam [6–8]. The camera has an optical sensor with high quantum efficiency (QE) [9], which is bump-bonded to Timepix3 [10], a readout chip with 256×256 pixels of $55 \times 55 \mu\text{m}^2$. Pixel electronics read out signals that pass a predefined threshold flux, and read out this data with time stamps precise to 1.56 ns. The information about time-over-threshold (ToT) is stored together with ToA inside the pixel electronics. The ToT data is correlated to the energy deposited in each pixel.

The Timepix3 readout is data driven, and only after the pixel signal exceeds a predefined threshold is any data readout induced. The pixel dead time is $475 \text{ ns} + \text{ToT}$ allowing for multiple hit functionality in each pixel, and

independent of the other pixels. The SPIDR readout supports fast, 80 Mpix/sec bandwidth [11].

The signal of the single photon sensitive operation is amplified using an image intensifier. The image intensifier is a vacuum device comprised of a photocathode followed with a micro-channel plate (MCP) and fast scintillator P47. The hi-QE-green photocathode in the intensifier (Photonis [12]) has QE of about 20% at 493 nm. The MCP in the intensifier has an improved detection efficiency close to 100%. Similar configurations of the intensified Tpx3Cam have been used before for trapped ion imaging [13], characterization of quantum networks [14, 15], quantum target detection [16, 17], single photon counting [18] and lifetime imaging [19] studies.

The TimePix3 camera receives regular Trigger signals from an outside time reference device at a frequency of around 100 kHz to mark the start of a data collection event. It also records a Time of Arrival signal (ToA) when the camera is prompted by an incoming photon. This allows for accurate “Time of Flight” (ToF) data to be collected and used. ToF data for ions in a Paul Trap is concentrated periodically in intervals equivalent to the period of trap electrode potential oscillation and arises because of the oscillating fluorescence produced by the first order Doppler shift experienced by the ions in the trap. Overlaying the periods using the modulo operator provides ToF data that is collected over numerous periods and creates a composite representation of ions during a single micromotion cycle. This composite Time of Flight data is referred to as Folded Time and is used as the basis of analysis for the two micromotion measurement techniques discussed in this paper.

The first technique of micromotion measurement is through direct position measurement using the fast Tpx3 Camera System. Photon source position measurements taken over a period of micromotion provide displacement data to be analyzed and mapped, and by fitting position data to a sinusoidal function ion micromotion can be estimated.

The second technique to be discussed is a photon-correlation method in which fluctuation in photon scattering is used to determine the first order doppler shift associated with the micromotion of each ion. As the ions move sinusoidally along the direction of incident beam, the frequency of the laser is doppler shifted proportional to velocity and provides the laser detuning of

$$\delta = \omega - \omega_0 + kv \sin(\Omega t). \quad (1)$$

This causes fluctuation in the absorption and scattering rate of the ions, which are proportional to the observed ion fluorescence, because the frequency of incident light is shifted closer and further from the resonance frequency.

Both techniques rely on the camera’s excellent timing resolution, but the direct technique also relies on the precise reconstruction of the photon source positions which requires the precise coordinate resolution of the camera

and a diffraction limited optical system with high light collection efficiency and minimal aberrations.

III. ANALYSIS

Post-processing and position correction happens by grouping pixels into the "clusters" using a recursive algorithm. Clusters are collections of pixels that are within a small time window, 300 ns, and are adjacent to one another. Since all hit pixels measure ToA and ToT independently and provide the position information, it can be used for position correction through centroiding. The ToT information is used to create a weighted average in a cluster, giving an estimate of the position for the incoming single photon. The timing of the photon is estimated by using ToA of the pixel with the largest ToT in the cluster. The above ToA is then adjusted for the so-called time-walk, an effect caused by the variable pixel electronics time response, which depends on the amplitude of the input signal [7, 20]. With this correction, a 1.6 ns time resolution can be achieved for single photons [14].

Figure 2 shows eight ions in the trap as a two-dimensional distribution of their centroided positions measured by the camera and its projection along the trap axis. Ions emit photons at approximately 100 kHz when in the bright state, and because the ions spent different amounts of time in the bright state over the 300s experimental window, some appear brighter than others.

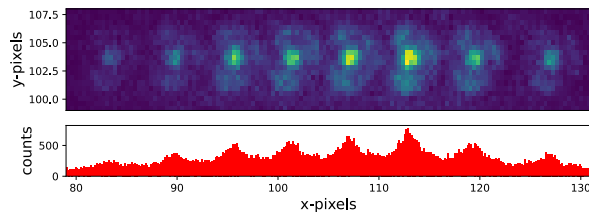


FIG. 2. At top, a two-dimensional centroided position histogram of the 8 ion chain. At bottom, ion fluorescence histogram as a function of x position. Both figures are composite representations of 300s of data taken in the trap.

Figure 3 a) shows schematically the 100 kHz pulses and Figure 3 b) shows the distribution of the time difference between the fluorescent photons from ion 6 and the periodic signal for the whole period and for a subset of nine oscillations. The oscillations are fit with a sine function with period of 54.79 ns, which is exactly the period of trap electrode oscillation and observed fluorescence modulation.

The period of pulses was measured to be equal to 10,136 ns using their time-stamps. The stability of the pulsing is very good, about 0.2 ns (rms) which was determined by fitting the distribution of time differences between the consecutive pulses with a Gaussian.

There are 185 rate oscillations during the 10,136 ns duration between the two consecutive pulses. Accounting

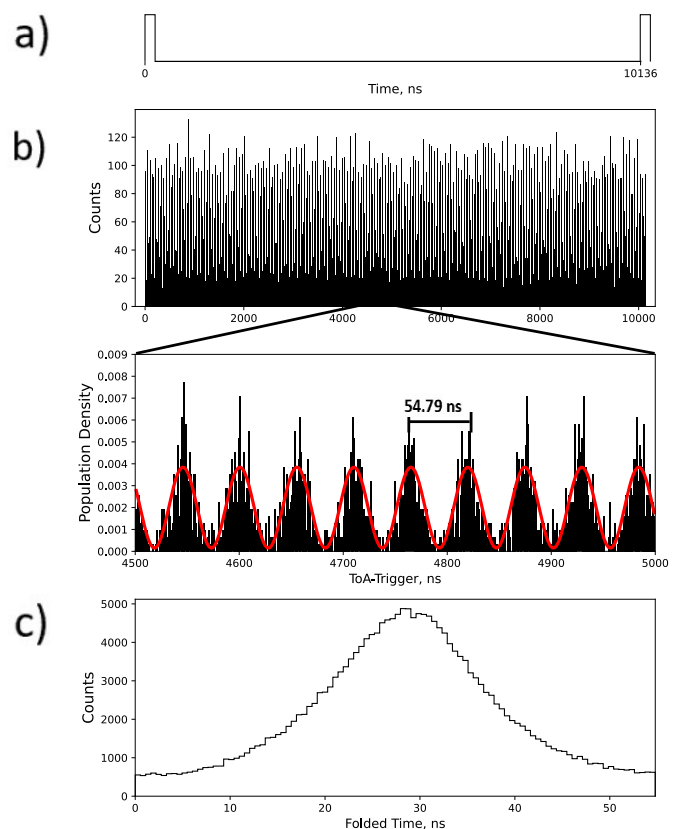


FIG. 3. a) Trigger separation of 10136 ns. b) ToF data over all data and a subset of ToF data from 4500-5000 showing the periodicity matched to the 54.79 ns period of the RF trap. c) After applying the modulo operator, folded time histogram describing the pattern of photon absorption during a period of micromotion.

for the measured period and overlaying all oscillations provides a composite representation of the ion fluorescent rate during a single micromotion cycle, shown in Figure 3 c). This distribution represents the probability of the fluorescent photon emission during the cycle, and it can be correlated with the measured position of the ions to determine ion micromotion.

Direct measurement of ion position was performed to provide a composite image of ion position values during a single folded period of micromotion. The position of each ion was collected in intervals of 3 ns within the folded time and fit to a Gaussian distribution. The centers of the distributions were taken to be the position for each folded time interval and together comprised the function of micromotion.

Folded time histograms provide the line shape of the ion scattering as seen in Figure 4. Given the saturation parameter $S = I/I_{\text{sat}}$, original laser detuning ω , and power broadened transition linewidth Γ , an estimated scattering rate can be made by fitting equation 2 to the fluorescence pattern observed during experiment. Properly fitted data provides a velocity amplitude estimates

that corresponds to the position amplitudes of ion micromotion through classical mechanics.

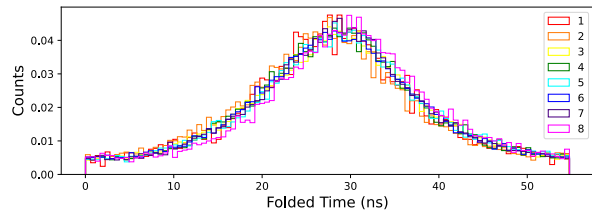


FIG. 4. Folded time histograms for each ion. Graphs are in phase implying synchronized micromotion.

$$F_{obs} \propto R_{scatt} = \frac{\Gamma}{2} \cdot \frac{S}{S + 1 + 4 \left(\frac{\delta}{\Gamma}\right)^2} \quad (2)$$

IV. RESULTS:

Figure 6 shows ion positions and uncertainties for the entire ion chain taken in 3 ns intervals. It is clear that all ions had similar micromotion behavior and that as seen by their similar phase and amplitude. Error bars for the Gaussian fitted positions are larger on the two ends of the period where the ion is doppler shifted away from resonance and therefore scatters less photons, providing a smaller data set to work with.

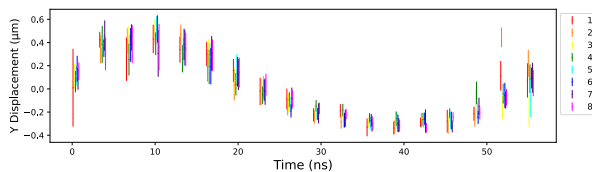


FIG. 5. Position estimates for all ions taken in 3ns intervals within the micromotion period, error bars included.

After fitting the data to individual sine curves with period equivalent to that of the trap potential oscillation, it is again seen that all of the ions exhibit similar micromotion. All amplitudes fall within .1 micron of each other, phases are all within .5 ns, and uncertainties are relatively small.

Still images of the ions at different points in the micromotion period were created to animate the phenomena. Figure 7 displays some of the still images created for Ion #6. These images are a first of their kind as a result of the state-of-the-art Tpx3 Camera System's time and spatial resolution.

V. CONCLUSION:

We demonstrated simultaneous micromotion measurement of eight ions in a Paul trap detecting coordinates

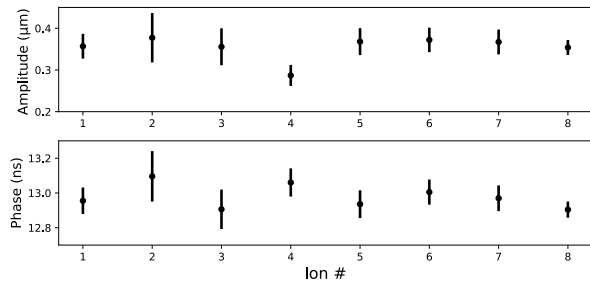


FIG. 6. Graph of calculated micromotion amplitudes and relative phases for each ion with uncertainties.

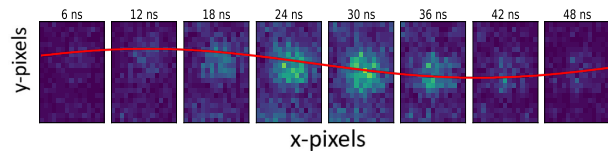


FIG. 7. Still images taken 6 ns apart showing ion #6 moving through the composite micromotion oscillation. Red sine function overlaid to visualize the motion (not a fit).

of fluorescent photons emitted by the ions. We studied the time dependence of this emission and its correlation to the phase of the micromotion using a single photon sensitive camera with nanosecond timing resolution.

This technique can be extended beyond the scope of this experiment to more complex ion lattice configurations in one and two dimensions. This will inevitably lead to increased understanding of micromotion and how to compensate it in multi-dimensional ion lattice quantum registers, furthering the computing power of trapped ion quantum computers.

ACKNOWLEDGMENTS

I'd like to give a special thanks to Andrei Nomerotski, Boris Blinov, and Mila Zhukas for their contributions to the research and for mentoring me through this project, BNL for accepting me into the SULI program, and the DOE for funding the program.

-
- [1] J. I. Cirac, R. Blatt, P. Zoller, and W. D. Phillips, Laser cooling of trapped ions in a standing wave, *Phys. Rev. A* **46**, 2668 (1992).
- [2] J. P. Gaebler, T. R. Tan, Y. Lin, Y. Wan, R. Bowler, A. C. Keith, S. Glancy, K. Coakley, E. Knill, D. Leibfried, and D. J. Wineland, High-fidelity universal gate set for ${}^9\text{Be}^+$ ion qubits, *Phys. Rev. Lett.* **117**, 060505 (2016).
- [3] D. J. Berkeland, J. D. Miller, J. C. Bergquist, W. M. Itano, and D. J. Wineland, Minimization of ion micro-motion in a paul trap., *Journal of applied physics.* **83**, 5025 (1998).
- [4] C. J. Foot, *Atomic Physics* (Oxford University Press, 2013) pp. 130–190.
- [5] M. R. Dietrich, N. Kurz, T. Noel, G. Shu, and B. B. Blinov, Hyperfine and optical barium ion qubits, *Phys. Rev. A* **81**, 052328 (2010).
- [6] M. Fisher-Levine and A. Nomerotski, Timepixcam: a fast optical imager with time-stamping, *Journal of Instrumentation* **11** (03), C03016.
- [7] A. Zhao *et al.*, Coincidence velocity map imaging using tpx3cam, a time stamping optical camera with 1.5 ns timing resolution, *Review of Scientific Instruments* **88**, 113104 (2017).
- [8] www.amscins.com,.
- [9] A. Nomerotski, I. Chakaberia, M. Fisher-Levine, Z. Janoska, P. Takacs, and T. Tsang, Characterization of timepixcam, a fast imager for the time-stamping of optical photons, *Journal of Instrumentation* **12** (01), C01017.
- [10] T. Poikela *et al.*, Timepix3: a 65k channel hybrid pixel readout chip with simultaneous toa/tot and sparse readout, *Journal of instrumentation* **9**, C05013 (2014).
- [11] B. van der Heijden *et al.*, Spidr, a general-purpose readout system for pixel asics, *Journal of instrumentation* **12**, C02040 (2017).
- [12] www.photonis.com/products/crickettm,.
- [13] L. A. Zhukas, P. Svihra, A. Nomerotski, and B. B. Blinov, High-fidelity simultaneous detection of trapped ion qubit register, arxiv.org/abs/2006.12801 (2020).
- [14] C. Ianzano, P. Svihra, M. Flament, A. Hardy, G. Cui, A. Nomerotski, and E. Figueroa, Fast camera spatial characterization of photonic polarization entanglement, *Scientific Reports* **10**, 10.1038/s41598-020-62020-z (2020).
- [15] A. Nomerotski, D. Katramatos, P. Stankus, P. Svihra, G. Cui, S. Gera, M. Flament, and E. Figueroa, Spatial and temporal characterization of polarization entanglement, *International Journal of Quantum Information* **18**, 1941027 (2020).
- [16] Y. Zhang, D. England, A. Nomerotski, P. Svihra, S. Ferrante, P. Hockett, and B. Sussman, Multidimensional quantum-enhanced target detection via spectrotemporal-correlation measurements, *Phys. Rev. A* **101**, 053808 (2020).
- [17] P. Svihra, Y. Zhang, P. Hockett, S. Ferrante, B. Sussman, D. England, and A. Nomerotski, Multivariate discrimination in quantum target detection, *Applied Physics Letters* **117**, 044001 (2020).
- [18] A. Nomerotski, M. Keach, P. Stankus, P. Svihra, and S. Vintskevich, Counting of hong-ou-mandel bunched optical photons using a fast pixel camera, *Sensors* **20**, 3475 (2020).
- [19] R. Sen, L. M. Hirvonen, A. Zhdanov, P. Svihra, S. Andersson-Engels, A. Nomerotski, and D. Papkovsky, New luminescence lifetime macro-imager based on a tpx3cam optical camera, *Biomed. Opt. Express* **11**, 77 (2020).
- [20] D. Turecek, J. Jakubek, and P. Soukup, USB 3.0 readout and time-walk correction method for timepix3 detector, *Journal of Instrumentation* **11** (12), C12065.

X-ray spectromicroscopy and comparison of minerals and materials

Shivani Mishra, Department of Physics and Astronomy, Stony Brook University, Stony Brook, NY 11790

Juergen Thieme, National Synchrotron Light Source-II, Brookhaven National Laboratory, Upton, NY 11793

I. Abstract

X-ray spectromicroscopy combines the very high resolution available with X-ray microscopy with the possibility to investigate the chemical state of a sample under investigation. High-resolution X-ray fluorescence (XRF) imaging conveys a detailed description of the elemental composition of an unknown material or mineral. The focus of our research project is to piece together individual XRF images of elements in the sample to create a larger, complete image of the area of the scanned sample. Another goal of our project is to create an RGB overlay of the most interesting set of elements to display their co-localization and distribution. As a result of this summer, I have become familiar working with Hierarchical Data Format (HDF5) files and have expanded my skills in Python programming to include data analysis and stitching of XRF images using Matplotlib [1], as well as various other libraries and packages. Additionally, I am familiar with fitting spectra and creating element maps using PyXRF.

II. Introduction

The motivation for chemically characterizing and identifying the elements within the sample using x-ray spectromicroscopy and XRF imaging is that it is useful in determining the unknown origin of a mineral or material. This may be of interest to identify materials containing radioactive elements such as uranium, or other interesting elements like lead, iron, or zinc.

In the framework of a collaboration between the Department of Nuclear Nonproliferation and the National Synchrotron Light Source II (NSLS-II) at Brookhaven National Laboratory (BNL), a series of different samples are investigated using X-ray spectromicroscopy, here cotton swipes containing nuclear particles. The goal is to determine the elemental composition of the particles and identify a potential relationship between them. XRF measurements at the SRX beamline are used for comparison between the different samples. This is also a collaboration with the International Atomic Energy Agency (IAEA), supplying us with dispersed particulate matter deposited on a surface, such as filters, slides, swipes, or embedded in a matrix. The goal is to chemically characterize this particulate matter using XRF imaging. Individual measurements have been analyzed and compared to identify possible differences among samples as well as among particles. Single datasets needed to be assembled to represent the larger area scanned with the Sub-micron Resolution X-ray Spectroscopy (SRX) beamline. Thus, the evaluation required additional programming for normalization and quantification of the obtained data. To generate our individual XRF images we used PyXRF [3], which is a python-based sophisticated x-ray fluorescence analysis package that is useful for fitting and

visualizing XRF data.

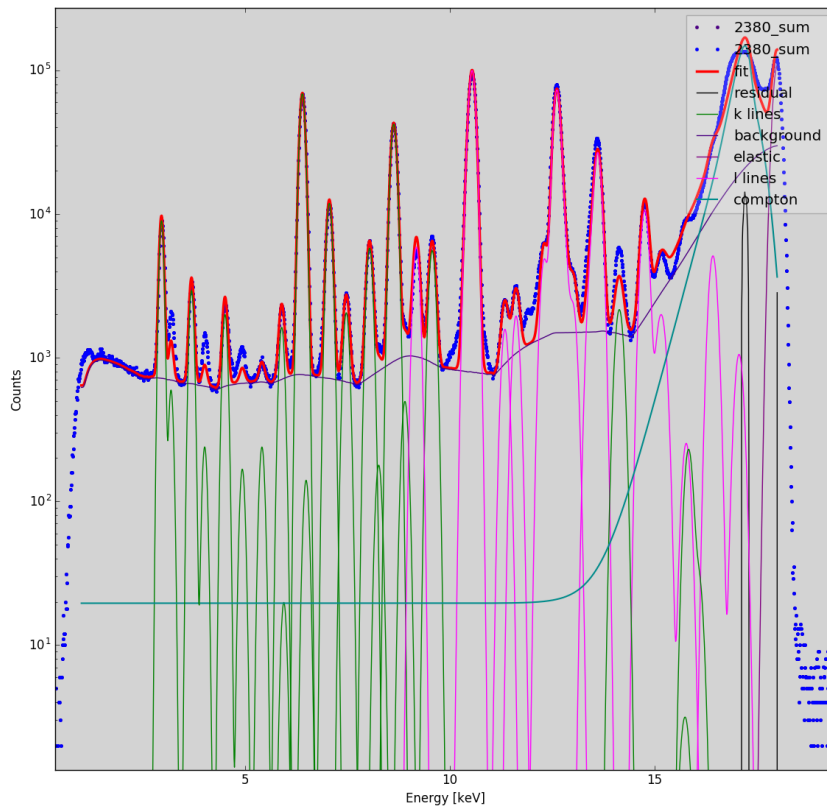


Figure 1: Fitting of the spectrum is done using PyXRF. This figure shows the spectrum fitting of x-ray fluorescence data within a smaller region of the sample being investigated.

Upon completing the spectrum fit for a given individual dataset, we completed individual pixel fitting for all of the elements present in the sample after which we were able to create individual element maps in the PyXRF program. The figure below shows the individual datasets or images for uranium.

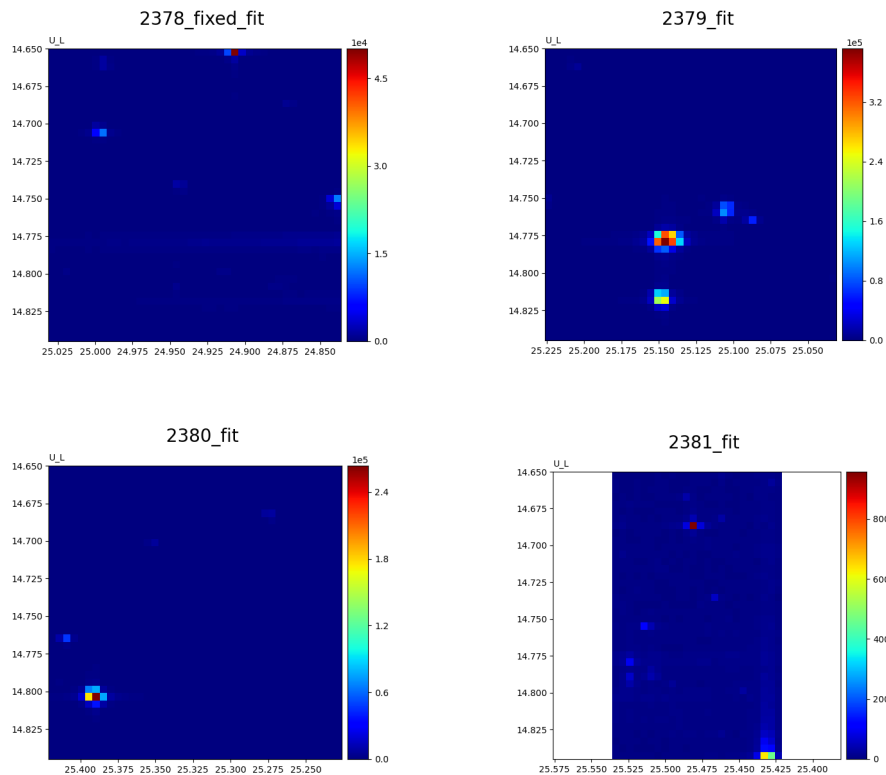


Figure 2: Element map of single datasets showing intensities for only the uranium element at various different regions of the scanned area of the sample. These regions neighbor each other closely.

III. Methods and Materials

The International Atomic Energy Agency supplied us with 10 cm x 10 cm cotton swipe which was spiked with mineral particles containing transition metals as well as uranium particles. The task was to find the Uranium particles and identify their complete elemental composition. Small X-ray fluorescence maps of 40x40 pixels with a step size of 5 μm were taken at the SRX beamline. The dwell time for each pixel was 2 sec. Images were taken in locations next to each other in a batch operation mode. Individual images as seen in figure 2 are displayed in an automatic

min/max mode, which means that they cannot simply be stitched together as the color codes are not matched between them. Therefore, the original intensity values have been retrieved from the HDF5 data files and stitched together in a Python program.

The Python Program

We have created two Python scripts for data analysis. To create our programs, we used the Spyder IDE (obtained from the Anaconda Python distribution) and imported various supporting packages such as NumPy [2] to store our HDF5 data files containing the element intensity values and Matplotlib [1] to plot the data. The purpose of our first program is to stitch individual XRF images for a single element. Our program reads in individual HDF5 data files, which contain the element intensity values. To easily find where the element intensity values were stored in our HDF5 data files, we used HDFView, which is a visual tool written in Java that can be used to browse and edit HDF5 data files. Within HDFView, we can easily locate the element names and their corresponding intensity values. We are then able to manually input the array location containing the intensity values for an element within our Python code. These values are then stored in NumPy arrays, which have 144x40 spaces to accommodate 144x40 pixels. This is because each individual image is 40x40 pixels and four images stitched together are 144x40 pixels. We then calculate the positions every 5x5 microns which ensures that each individual image is stitched in the correct location. Prior to writing the script, it was useful to roughly lay out the individual PyXRF images in the correct order based on their coordinate locations. The purpose of the second Python script was to create an RGB representation of the

intensity maps. For that, the intensity values for each element were read in and normalized from 0 to 255, so an RGB image is correctly produced with visible intensities on the map.

IV. Results

Stitched maps for each individual element were created by our Python script. Figure 4 shows the results for iron, uranium, and zinc. The program can easily create maps of the other identified elements such as lead or zirconium as well. This allows for creating the RGB representation, which tells us the co-localization of the different elements (see figure 3). The actual overlaying of the images does not affect the scaling of the individual element images, however it was necessary to scale each element image from 0 to 255 prior to creating the overlay otherwise we would obtain an RGB image that would not be able to show the smaller intensities; they would instead be overseen by the largest intensity values because RGB values in each plane can only range from 0 to 255 to have a representation between 0 and 1. To account for this, we took the maximum intensity value for each element and divided by 255. We then took the quotient and divided the entire 144x40 matrix by that value to normalize the image to 255. This ensured that any intensity value above 255 did not blow up and we could have a properly scaled RGB image as we see in figure 3.

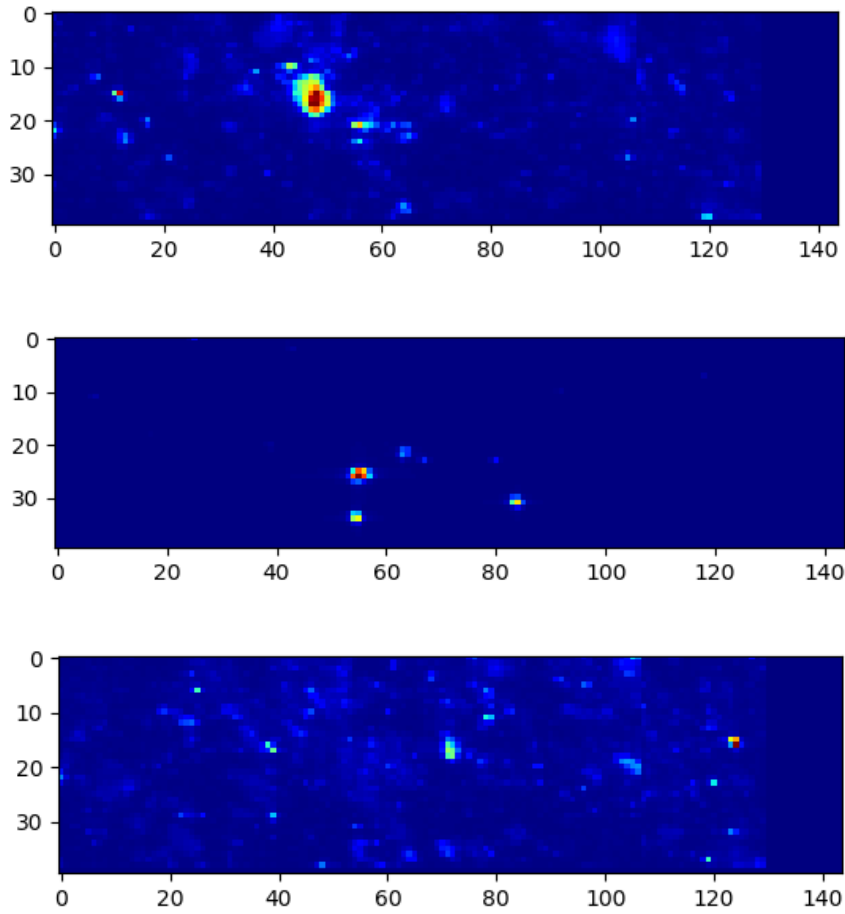


Figure 3: These are stitched images of iron (top), uranium (middle) and zinc (bottom).

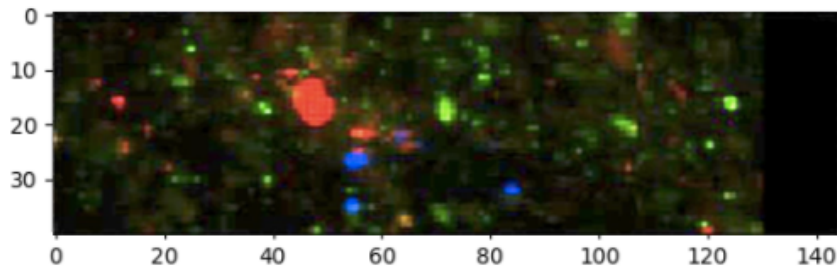


Figure 4: The image above is an RGB overlay of the elements iron (red), uranium (blue), and zinc (green).

V. Discussion and Conclusion

Figure 4 shows as an example the arrangement of iron (red), zinc (green) and uranium

(blue). This enables us to view the distribution and the co-localization of the elements. The Python scripts can be used to investigate any elements present in the sample, not just the elements referenced in this report. Moreover, the Python scripts are written in a way that other data sets can be imported with only slight changes of the code, so it is quite versatile and can be used for other applications. The developed Python scripts can of course be used for other projects as well as requiring the assembly of single images to generate larger overview maps. A future development of this program can include a way to stitch the images together using x and y coordinate values directly from the HDF5 data files rather than the intensity values. This may eliminate the need for manually inputting the order of the images, and it could then automatically create the larger scaled images from position data directly obtained from the HDF5 data files.

VI. Acknowledgements

We would like to acknowledge the Office of Educational Programs of Brookhaven National Laboratory, the U.S. Department of Energy, and the Science Undergraduate Laboratory Internship (SULI) program for their support. We want to acknowledge the National Synchrotron Light Source II for allowing data collection for our research and the International Atomic Energy Agency for supplying us with the samples.

VII. References

1. Hunter, John D. "Matplotlib Is a 2D Graphics Package Used for Python for Application Development, Interactive Scripting, and Publication-Quality Image Generation across User Interfaces and Operating Systems." *Matplotlib: A 2D Graphics Environment*, vol. 9, 18 June 2007, pp. 90–95.,

doi:10.1109/MCSE.2007.55.

2. Oliphant, Travis E. *A Guide to NumPy*. Published by Continuum Press, a Division of Continuum Analytics, Inc., 2015.

3. Li Li, Hanfei Yan, Wei Xu, Dantong Yu, Annie Heroux, Wah-Keat Lee, Stuart I. Campbell and Yong S. Chu, “PyXRF: Python-based X-ray fluorescence analysis package”, Proceedings Volume 10389, X-Ray Nanoimaging: Instruments and Methods III; 103890U (2017); doi: 10.1117/12.2272585

Making machines into masterminds: machine learning applications in image segmentation and analysis

Ethan Mulle¹, Xianghui Xiao²

¹ *Department of Physics and Astronomy,*

Stony Brook University, Stony Brook, New York 11794 and

² *National Synchrotron Light Source II,*

Brookhaven National Laboratory, Upton, New York 11973

The Full-Field X-ray Imaging beamline of National Synchrotron Light Source II is expanding the beamline's analytical tools for users' data analysis tasks. One important type of analysis is curve fitting. The challenge in curve fitting is that there are millions to even billions of curves from each user measurement. It is not trivial to both identify and efficiently analyze the large number of curves at such a scale. Therefore, it is critical to develop a highly computationally efficient and reliable approach for this task. We decided to use the SciPy.optimize package for curve fitting and various Python packages for parallelizing the fitting tasks to speed up computations after preliminary experimental tests. We have compared performances of two SciPy.optimize routines (least_squares and curve_fit) for curve fitting and three Python parallelization packages (Multiprocessing, Joblib, and Dask). The results suggest Scipy.optimize.least_squares is the best function for curve fitting primarily due to its flexibilities in condition confinements. While comparing the efficiency gains with the parallelization packages, Multiprocessing and Joblib perform similarly and are superior to Dask, which has a longer latency overhead. Another important facet of beamline data analysis is image segmentation. The potential of using machine learning for these purposes was explored by experimenting with the Python-based scikit-learn and Tensorflow packages. The best performing functions were integrated into FXI tool suites by using Jupyter Notebook, allowing for the creation of annotated Python scripts with detailed instructions in a web-based interface.

I. INTRODUCTION

beamline, experiments create an enormous amount of complex spectroscopic image data

At the National Synchrotron Light Source

every day. Beamline users have limited time at the beamline and desire quick data analysis so that they can determine if more data is needed. Oftentimes the consequence of making data processing quicker and easier is that the processing becomes less accurate. This provides the challenge of processing the data quickly while still providing accurate analysis.

Additionally, the current FXI data analysis tool suites in use contain programs and scripts that are unintuitive for users that have little programming experience. This is another factor that increases the time taken for data analysis. By making the data analysis tools easier to use, less time will need to be spent using them, allowing beamline users to spend more time focusing on other important part of their research.

To address these issues, a new set of data analysis tools were developed using the Python programming language and Jupyter Notebook.

II. METHODS

Principal component analysis (PCA) was implemented to reduce the complexity of the spectroscopic image data. To do this, PCA reduces the dimensionality of a data set by first computing the matrix of eigenvectors and eigenvalues of the covariance matrix of

the data. The eigenvalues represent how much of the original data's variance their corresponding eigenvector explains. By sorting these eigenvalues in decreasing order, one can create a projection matrix of a number of chosen eigenvectors that explain the most variance of the original data. The original data can then be approximated by the first few major modes. To implement PCA, the `sklearn.decomposition.PCA` function from the Python package `scikit-learn` [1] was used.

By using k-means clustering, the data can be labeled into different groups, or clusters, making it easier to identify key regions and features in the provided data. K-means clustering is an unsupervised machine learning algorithm where one partitions n observations into k clusters where each observation belongs to the cluster with the nearest mean. For image segmentation, image pixels are separated into different clusters based on local means that their values are closest to. With this, observations that are similar to each other should be in the same cluster, while dissimilar observations should be in different clusters. In implementing k-means clustering, the `sklearn.cluster.KMeans` function from `scikit-learn` was used.

Another way to perform image segmentation is by using deep learning neural networks. Tensorflow was used to create a net-

work based on the U-Net architecture developed by Ronneberger et al [2] and implemented by Lamba. [3] The network trains on a set of training and validation images to learn how to accurately make predictions for each image pixel to perform a correct segmentation of an image.

For the beamline's spectro-imaging applications, we need to analyze x-ray absorption spectra at each individual pixel in selected regions of interest based on the segmentation results. Curve fitting is a basic task in the analysis that can be implemented using least squares. Least squares works by minimizing the sum of the difference between a fitted value and the actual value at the same point squared. This minimizes the error in the fitted curve. Curve fitting was implemented to analyze the spectroscopic image data with the use of the SciPy.optimize curve_fit and least_squares functions. [4]

To increase the efficiency of the curve fitting, parallel processing was used. Parallel processing works by taking programming tasks such as loops that would normally only be done on one processor and splitting them between multiple processors that work at the same time to finish the task quicker. To implement this, the Python packages Multiprocessing, Joblib [5], and Dask [6] were trialed to take advantage of two processors.

All of the mentioned data analysis pro-

cesses were implemented using Python [7] and Jupyter Notebook. Jupyter Notebook is an open-source web application that allows for documents to be created that can contain live code, visualizations, and narrative text. [8] This provides an excellent way to create data analysis tools with detailed instructions on how to use them, making it easy for beamline users to analyze their spectroscopy data.

III. DATA ANALYSIS & RESULTS

A. Principal Component Analysis

Scikit-learn's PCA function was used to analyze 591 676x632 spectroscopy images. As such, each image was initially composed of 427232 components, with each component corresponding to a single pixel within the image. Images were reduced so that the principal components still explained 99% of the original variance. An example of this is shown in Figure 1, where the 427232 original components were reduced to 51 principal components. These principal components were then used to create a reconstruction of the original image in its original dimensions. PCA proved to be an excellent way to reduce the dimensionality of the image data, while still ensuring that valuable image information was preserved.

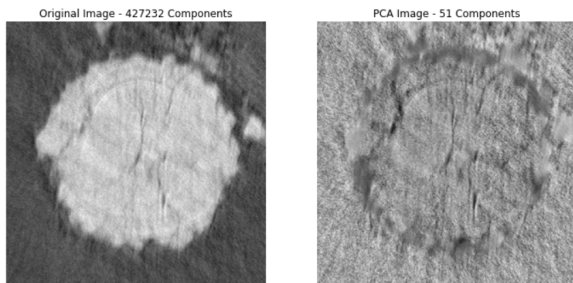


FIG. 1. The results of PCA on a spectroscopic image. The 427232 original pixel components were reduced into 51 principal components that still explain 99% of the original variance.

B. K-Means Clustering

The scikit-learn KMeans function was used to perform k-means clustering on the pixels of the image data. This was done to segment the images and separate the subject particles of the images from their backgrounds, in addition to segmenting cracks and other potential defects from the particles.

Figure 2 shows an example spectroscopic image and its clusterings into two, three, four, and five clusters. Using two clusters provided an efficient way to separate the particle in the image from the background, albeit there are some mislabelings where cracks are present. Adding a third cluster helped to define the border between the particle and the background. Choosing to use four clusters helped to further define the particle in the image, with the apparent cracks in the parti-

cle being in a different cluster than the rest of it. Using five clusters appeared to not offer much improvement over using four clusters.

For all amounts of clusters tried, some pixels in the location of the cracks in the particle were still clustered with the background. This is because those pixel values are nearly identical to the values of the background pixels, so all of the pixels' nearest mean will be the same.

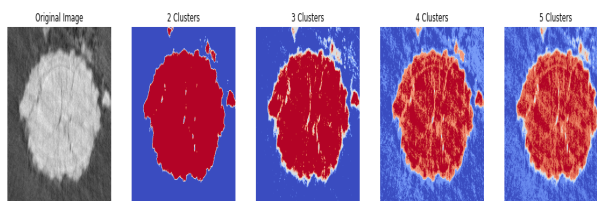


FIG. 2. The results of performing k-means clustering on a spectroscopic image. The original image and clustering tried with two, three, four, and five clusters are shown.

C. Deep Learning Neural Networks

The images were also segmented with the created U-Net based deep learning network. The primary goal of this was to train the network to predict for each image pixel a value between zero and one, representing the likelihood that it is part of a particle in the image.

The network was trained on a set of 531 spectroscopy images and validated on a set of 60 spectroscopy images. Each of the images had a true labeling mask manually created

for the network to learn from. For these purposes, cracks and other defects in the particle were ignored and labeled to be the same as the rest of the particle. At the end of training, the network attained a 0.023 validation loss and a 94% validation accuracy after 55 epochs. The change in loss over time is illustrated by Figure 3.

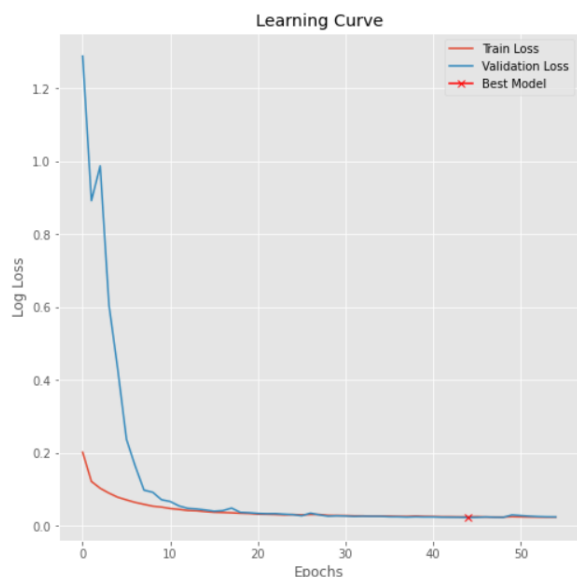


FIG. 3. A plot of how the training and validation losses changed as the network continued to train for 55 epochs.

The network was then tested on a different data set of 100 spectroscopic images. An example test result is displayed in Figure 4. Overall, the network works well to create a mask that segments the particle and background from each other. However, similar to the k-means clustering results, certain pixels in regions with well-defined cracks are not strongly predicted to be part of the particle.

By setting a threshold of 0.5 for the probabilities, pixels were separated into two distinct groups to create a binary segmentation. Doing this created a correct labeling for nearly all of the pixels, but a few still remained mislabeled.

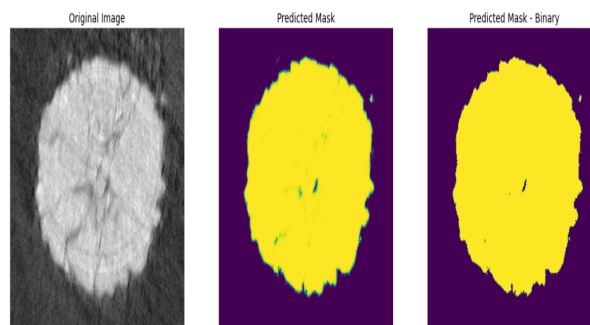


FIG. 4. Results from the network testing a test image. The original image is shown, as well as the true predicted mask from the network where each pixel is given a probability of being part of the particle. A binary mask is also shown where each pixel with a value above 0.5 was set to be a particle pixel and any pixel with a value equal to or below 0.5 was set to be a background pixel.

Following this, the network was tested on another unique data set of 100 spectroscopic images that each contain a large quantity of artifacts. A result of this testing for one image is shown in Figure 5. With these images, a significant amount of pixels in areas with a large amount of noise from the artifacts were incorrectly determined to be part of the background. This was especially true for areas that contained cracks in the particle in addi-

tion to the artifacts. Creating a binary segmentation with a threshold of 0.5 appeared to slightly improve the labeling of the pixels, but a large amount still remained mislabeled. Lowering the threshold was observed to improve the labeling, indicating that the network is making incorrect predictions for a sizable amount of the data.

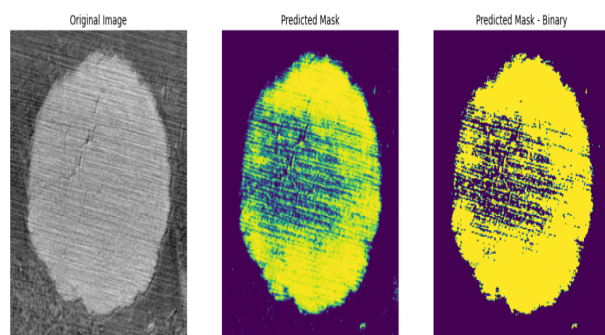


FIG. 5. The results of the network being tested on an image with heavy artifacting. A large quantity of pixels are labelled wrongly even with a threshold set.

D. Curve Fitting

After performing PCA and using machine learning to segment the spectroscopy data, curve fitting was used to analyze regions of interest within the images. Using least squares analysis allowed for curves to be fitted to determine how the value for a particular pixel in the image changes as the x-ray energy used for imaging changes.

The `scipy.optimize.curve_fit` function was

tested on a small image data set (14 150x130 images) and a large image data set (14 333x330 images) of spectroscopy images. This function worked well for the small image data set, but exceeded the maximum number of allowed iterations when tried on the large image data set. To address this, a custom curve fitting function was created that implemented the `scipy.optimize.least_squares` function. This custom function works identically to the `curve_fit` function, but has no limit on the amount of iterations allowed.

The results of curve fitting on an image from the small image data set is found in Figure 6 and the fitting's RMSE was calculated to be 0.00015. The results of curve fitting on an image from the large image data set is found in Figure 7. Its RMSE was calculated to be 0.00010.

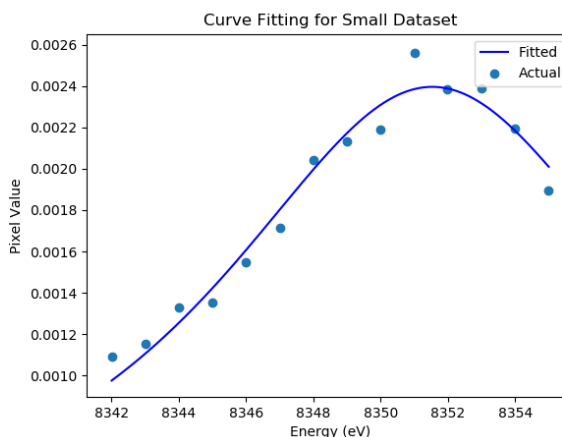


FIG. 6. The results of curve fitting for how a pixel's value changes as energy changes for an image from the small image data set.

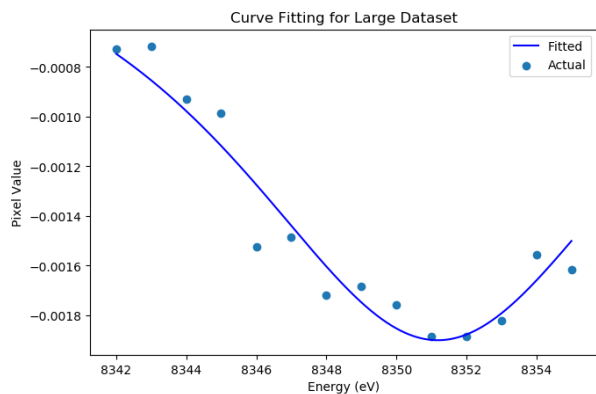


FIG. 7. The results of curve fitting for how a pixel's value changes as energy changes for an image from the large image data set.

E. Parallel Processing

The Multiprocessing, Joblib, and Dask parallel processing packages were each trialed to decrease the computation time for curve fitting. These packages were first each implemented to increase the efficiency of the curve fitting for the small image data set by splitting the work across two processors. The time to completion for the curve fitting was measured for each package as well as for a baseline of only serial processing on one processor being used. These times are found in Figure 8. As shown, Multiprocessing and Joblib appear to perform nearly equivalently, finishing in about 60 seconds, about 1.5x faster than the near 100 seconds it takes to process serially. Dask finished in just under 160 seconds, slower than even the serial processing. This is most likely due to Dask

having a 10ms latency overhead for each call it makes.

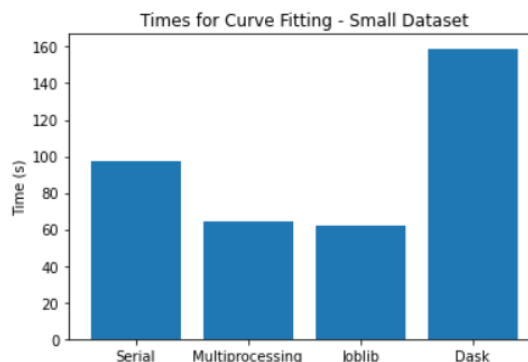


FIG. 8. A chart displaying the times taken for serial processing, Multiprocessing, Joblib, and Dask to perform curve fitting on the small image data set.

The same process was repeated for the large image data set. Dask was excluded from the trials due to it performing unreasonably slowly compared to the other packages. The times for the serial processing, Multiprocessing, and Joblib evaluations of the data set are found in Figure 9. Multiprocessing and Joblib again perform nearly equivalently, finishing in slightly over 300 seconds each. This is also about 1.5x faster than the almost 500 seconds it took to process serially.

IV. DISCUSSION & CONCLUSIONS

Using principal component analysis allowed for the dimensionality of a data set of spectroscopic images to be greatly reduced while still explaining a significant amount of

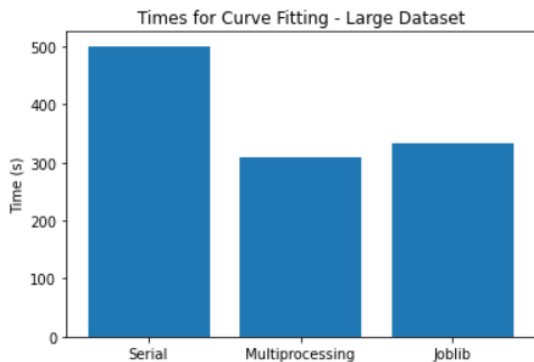


FIG. 9. A chart displaying the times taken for serial processing, Multiprocessing, and Joblib to perform curve fitting on the large image data set.

the images' original variance. This is useful for image compression and simplifying data to allow for quicker and potentially more accurate analysis.

When using k-means clustering to segment images, it was observed that adding more clusters serves to better separate out different details from an image until a limit was reached where adding another cluster appeared to have little effect. The main issue with k-means clustering is that a number of pixels in image regions that clearly contain cracks are incorrectly placed in the same cluster as the background. This is because these pixel values are very similar, so they will all be placed into a cluster with the same mean. To potentially solve this issue, other non-means reliant clustering algorithms or clustering algorithms that handle regional outliers better can be trialed to see if they

offer improvement.

In our test, the created deep learning network performed well on test data with little noise, but generates false labels when significant noise or artifacts are present in images. This issue can likely be fixed by training the network on a set of manually labelled image data that contains similar noise levels and artifacts.

Additionally, the network would occasionally predict pixels in regions of images that contain cracks to be part of the background. This issue could also potentially be solved by including another label in the training data. The current network training used manually labeled binary images as the ground truth in which cracks are labeled as part of particles although their values are closer to that of the background.

With curve fitting, it was found that `SciPy.optimize.least_squares` allows for greater control of fitting conditions than `SciPy.optimize.curve_fit`. For example, `least_squares` allows for tolerances for termination and the bounding range of fitting parameters to be more precisely defined than when using `curve_fit`. As such, `SciPy.optimize.least_squares` is more robust in fitting data with a high noise level similar to what is found in our typical data sets. If the data quality is high, however, with the data points contouring a well-defined peak,

then `SciPy.optimize.curve_fit` works equally as well as `SciPy.optimize.least_squares`.

The Multiprocessing and Joblib parallel processing packages implemented with two processors were observed to finish curve fitting on both the small and large dimensional image data sets about 1.5x quicker than with serial processing on one processor. The Dask parallel processing package appeared to perform worse than even the serial processing due to a 10ms latency overhead for each task made with Dask.

Implementing all of these data analysis tools with Jupyter Notebook ensures that they are easy to use and modify for all beam-

line users. Created Python scripts contain the live code along with visualizations and text instructions to make using the scripts intuitive even for users with little programming experience.

V. ACKNOWLEDGEMENTS

This project was supported in part by the U.S. Department of Energy, Office of Science, Office of Workforce Development for Teachers and Scientists (WDTS) under the Science Undergraduate Laboratory Internships Program (SULI).

-
- [1] F. Pedregosa, G. Varoquaux, A. Gramfort, V. Michel, B. Thirion, O. Grisel, M. Blondel, P. Prettenhofer, R. Weiss, V. Dubourg, J. Vanderplas, A. Passos, D. Cournapeau, M. Brucher, M. Perrot, and E. Duchesnay, “Scikit-learn: Machine learning in Python,” *Journal of Machine Learning Research*, vol. 12, pp. 2825–2830, 2011.
- [2] O. Ronneberger, P. Fischer, and T. Brox, “U-net: Convolutional networks for biomedical image segmentation,” *CoRR*, vol. abs/1505.04597, 2015. [Online]. Available: <http://arxiv.org/abs/1505.04597>
- [3] H. Lamba, “Tgs unet,” <https://github.com/hlamba28/UNET-TGS>, 2019.
- [4] P. Virtanen, R. Gommers, T. E. Oliphant, M. Haberland, T. Reddy, D. Cournapeau, E. Burovski, P. Peterson, W. Weckesser, J. Bright, S. J. van der Walt, M. Brett, J. Wilson, K. Jarrod Millman, N. Mayorov, A. R. J. Nelson, E. Jones, R. Kern, E. Larson, C. Carey, Í. Polat, Y. Feng, E. W. Moore, J. VanderPlas, D. Laxalde, J. Perktold, R. Cimrman, I. Henriksen, E. A. Quintero, C. R. Harris, A. M. Archibald, A. H. Ribeiro, F. Pedregosa, P. van Mulbregt, and S. . . Contributors, “SciPy 1.0: Fundamental Algorithms for Scientific Computing in Python,” *Nature Methods*, vol. 17, pp. 261–272, 2020.

- [5] Joblib Development Team, “Joblib: running python functions as pipeline jobs,” 2020. [Online]. Available: <https://joblib.readthedocs.io/>
- [6] Dask Development Team, *Dask: Library for dynamic task scheduling*, 2016. [Online]. Available: <https://dask.org>
- [7] G. Van Rossum and F. L. Drake Jr, *Python reference manual*. Centrum voor Wiskunde en Informatica Amsterdam, 1995.
- [8] T. Kluyver, B. Ragan-Kelley, F. Pérez, B. Granger, M. Bussonnier, J. Frederic, K. Kelley, J. Hamrick, J. Grout, S. Corlay, P. Ivanov, D. Avila, S. Abdalla, and C. Willing, “Jupyter notebooks – a publishing format for reproducible computational workflows,” in *Positioning and Power in Academic Publishing: Players, Agents and Agendas*, F. Loizides and B. Schmidt, Eds. IOS Press, 2016, pp. 87 – 90.

Optimizing data processing procedures and data analysis in the BMX experiment

Jesse Osborn, Department of Physics and Astronomy, University of Nebraska - Lincoln,
Lincoln, Nebraska 68508

Anze Slosar and Paul O'Connor, Physics Department, Brookhaven National Laboratory,
Upton, NY, 11973

Abstract

The BMX experiment at Brookhaven National Laboratory (BNL) is an astrophysics project which focuses on surveying the Universe through the study of the radio wave emissions from different galaxies generated by neutral hydrogen atoms as they transition between different hyperfine states. This experiment stands as a test bed for the Packed Ultrawideband Mapping Array (PUMA), which is planned to be a next generation cosmic survey based on the same physics principles used in the BMX detectors, namely, hydrogen emissions and radio interferometry by which the radio emissions from a given galaxy are recorded by several different stations and then recombined, in order to offer greater signal resolution.

As a test bed for future efforts, the efficiency of the processing and analysis of the BMX data is of the utmost concern, in order to verify the effectiveness of BMX's techniques in cosmic mapping for larger scale experiments. By testing different ways of processing the incoming data through use of timing different C++ programs which each process the data differently, the most effective processing procedures for the BMX experiment can be worked out. Through systematic speed testing, we determined the most efficient way of processing incoming data from the BMX detectors into outgoing data for analysis. We also developed a Python program for the purposes of eliminating radio frequency interference from the data before performing further analysis, using the distinct narrow spike nature of the noise for discrimination purposes. The use of both the C++ and Python programming languages in this research is simply a matter of working with pre existing software, not because of any inherent advantage in either language for the purposes they were used for.

Mapping the Universe using the BMX interferometry techniques could produce new insights into the development of the Universe into what we know today. As a result of my internship at BNL this summer, I have advanced my understanding of computer programming using the C++ and Python programming languages, and I have developed more techniques for handling, processing and analyzing data.



Figure 1: Picture of BMX data stations, four dishes, scanning frequencies between 700 and 1500 MHz in the sky using radio interferometry techniques

Introduction

In any physics experiment, the efficiency with which data is being processed relative to how quickly data is taken is integral to good performance. If data isn't processed quickly enough, a backlog will build up as more data keeps streaming into the hardware, causing data handling issues. On the other hand, if data doesn't have enough processing done on it, it makes analysing the data down the road much more difficult. The methods by which the data are analyzed are equally fundamental. Oftentimes, physics data is polluted either by features of

nature, nearby activities, or by the hardware used in the experiment itself. Removing this noise is a critical step in the data analysis process, so that the quality data which the experiment was designed to record can receive proper treatment.

This experiment's focus was centered on these two elements, investigating both the efficiency of data processing for the BMX experiment with respect to various experimental parameters, as well as developing an algorithm for removing radio frequency interference (RFI) from the data, alongside other data calibration performed during the project. Because the BMX experiment is a testbed for future efforts, it's even more important to develop the most efficient ways to process and analyse the data, so that the BMX experiment can stand as a proof of the concepts used in its data taking.

Methodology

For optimization of data processing, a program was written in C++ that processed dummy input data packets in the form of complex numbers and recorded the average time to process a single data packet while varying different data parameters. A further experiment was done to see whether the input data could be processed faster by treating it as the real and imaginary components of its original complex numbers or by first converting the complex numbers into phase and amplitude components and processing with the data in that form. The time to process a single data packet is typically on the order of tens of microseconds, so any small operation performed in the code (such as multiplying two numbers together) can have a noticeable impact on the speed of data processing, making even small changes to the code used for processing data relevant to these optimization studies.

For the noise filter, a Python function was developed that runs over data waveforms and measures the width of every peak in the power output above a certain threshold value determined through testing on sample data. RFI noise by its nature shows up in the data as sharp narrow power spikes, while quality data has much broader peaks, so the function discriminates against peaks with very short widths in order to filter out RFI noise from the data before it is analyzed further. The function was tested on all 8 BMX data channels and for several different days to ensure its functionality was not specific to the particular data the function was originally developed to be effective on.

Results

The results of the data processing efficiency studies are given in tables in Fig. 2 (for input data treated as real and imaginary components) and Fig. 3 (for input data treated as phase and amplitude components) below. In each table, various data parameters are held constant, while one is varied, and the average time taken to process a single data packet is measured six times and then averaged, in order to reduce the impact of random data processing fluctuations from single measurements. The data parameters tested and their variable names as written in Fig. 2 and Fig. 3 were: the number of input data channels (NCHAN), the size of the input data packets (FFTSIZE), the number of input data packets processed at a time (NTEST), the numerical precision of the input data (Input Type), the numerical precision of the output data (Output Type) and how many simultaneous threads the data was being processed on at once (splitting the input data between the threads using another C++ process) (Omp_Num_Lines). Comparing the results in Fig. 2 and Fig. 3, we found that processing the input data in terms of its original real and imaginary components was the more effective process.

Omp_Num_Lines	Input Type	Output Type	FFTSIZE	NCHAN	NTEST	Average Packet Process Time (us)
1	int16_t	float	4096	2	100,000	20.23, 20.25, 20.18, 20.92, 20.34, 18.81 (20.12)
2	int16_t	float	4096	2	100,000	13.77, 11.55, 13.73, 12.61, 12.79, 12.53 (12.83)
4	int16_t	float	4096	2	100,000	7.29, 7.88, 6.24, 6.70, 6.91, 6.20 (6.87)
8	int16_t	float	4096	2	100,000	4.37, 4.48, 4.56, 4.65, 4.62, 5.50 (4.70)

Input Type	Output Type	FFTSIZE	NCHAN	NTEST	Average Packet Process Time (us)
int16_t	int32_t	512	8	100,000	12.32, 9.94, 11.66, 9.93, 10.92, 10.41 (10.86)
int16_t	int32_t	1024	8	100,000	19.49, 16.45, 20.75, 16.76, 20.49, 20.61 (19.09)
int16_t	int32_t	2048	8	100,000	31.03, 30.02, 30.30, 35.52, 31.09, 35.69 (32.28)
int16_t	int32_t	4096	8	100,000	63.20, 49.38, 55.24, 55.53, 49.48, 55.97 (54.8)

Input Type	Output Type	FFTSIZE	NCHAN	NTEST	Average Packet Process Time (us)
int16_t	int32_t	4096	2	100,000	5.64, 5.45, 5.49, 5.50, 6.24, 6.29 (5.77)
int16_t	int32_t	4096	4	100,000	17.77, 15.66, 17.51, 16.49, 17.28, 15.29 (16.67)
int16_t	int32_t	4096	8	100,000	63.20, 49.38, 55.24, 55.53, 49.48, 55.97 (54.8)

Input Type	Output Type	FFTSIZE	NCHAN	NTEST	Average Packet Process Time (us)
int16_t	int32_t	4096	8	100,000	63.20, 49.38, 55.24, 55.53, 49.48, 55.97 (54.8)
int16_t	int64_t	4096	8	100,000	35.81, 46.40, 40.96, 38.61, 39.56, 31.83 (38.86)
int16_t	float	4096	8	100,000	56.46, 38.61, 51.51, 40.75, 62.46, 37.85 (47.94)

Input Type	Output Type	FFTSIZE	NCHAN	NTEST	Average Packet Process Time (us)
int8_t	int32_t	4096	8	100,000	53.45, 60.11, 49.76, 53.88, 57.57, 54.66 (54.91)
int16_t	int32_t	4096	8	100,000	63.20, 49.38, 55.24, 55.53, 49.48, 55.97 (54.8)

Figure 2: Data processing efficiency results, treating data as real and imaginary components

Input Type	Output Type	FFTSIZE	NCHAN	NTEST	Average Packet Process Time (us)
uint8_t	float	512	8	100,000	12.85, 11.57, 12.33, 12.50, 12.87, 11.94 (12.34)
uint8_t	float	1024	8	100,000	21.04, 20.41, 20.50, 20.60, 21.04, 20.40 (20.67)
uint8_t	float	2048	8	100,000	36.94, 34.84, 36.74, 36.28, 36.15, 35.37 (36.05)
uint8_t	float	4096	8	100,000	59.10, 58.10, 57.94, 58.27, 58.10, 65.54 (59.51)

Input Type	Output Type	FFTSIZE	NCHAN	NTEST	Average Packet Process Time (us)
uint8_t	float	4096	2	100,000	6.52, 6.18, 6.28, 6.22, 6.34, 6.10 (6.27)
uint8_t	float	4096	4	100,000	18.12, 16.93, 18.55, 17.08, 19.24, 18.30 (18.04)
uint8_t	float	4096	8	100,000	59.10, 58.10, 57.94, 58.27, 58.10, 65.54 (59.51)

Omp_Num_Lines	Input Type	Output Type	FFTSIZE	NCHAN	NTEST	Average Packet Process Time (us)
1	uint8_t	float	4096	2	100,000	51.09, 51.08, 51.19, 51.09, 49.74, 49.76 (50.66)
2	uint8_t	float	4096	2	100,000	32.71, 30.35, 29.36, 37.02, 28.93, 36.29 (32.44)
4	uint8_t	float	4096	2	100,000	17.00, 18.76, 17.07, 16.84, 21.14, 16.75 (17.93)
8	uint8_t	float	4096	2	100,000	11.44, 13.96, 12.53, 10.93, 13.50, 11.55 (12.32)

Figure 3: Data processing efficiency results, treating data as phase and amplitude components

An example of the results of letting the RFI noise filter run on the BMX data is shown in Fig. 4. The filter was tested on several different days of BMX data, both several days back to back and data taken months apart, to ensure that the filter was not biased towards the shape of the data on which it had been trained and developed. All eight data taking channels of the BMX

experiment were tested as well to ensure that their individual biases did not affect the filter's performance to any considerable degree. Both for different days of BMX data and for different BMX data channels, the filter's performance remained consistent; the majority of the narrow RFI noise spikes in the power output were removed, while the broad spikes representing the good data remained intact.

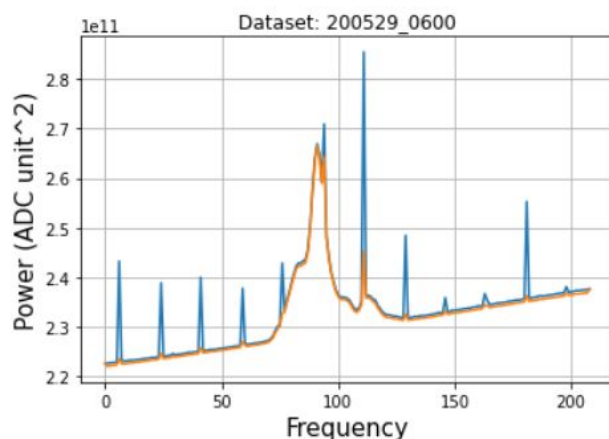


Figure 4: Example of removal of RFI noise (blue) in data (orange)

Conclusion

For the data processing optimization, we found that it was most efficient to process the incoming data packets in terms of their original real and imaginary components, rather than first converting their components into phases and amplitudes and working with those. We also established the relationship between various different parameters and their effect on the overall data processing time, useful benchmarks for future optimization studies.

For the noise filter, our narrow peak remover, as seen in Fig. 4, was reasonably effective in removing RFI noise spikes from data waveforms without sacrificing good signal efficiency. This process was tested for all BMX data channels as well as for multiple days of data, and the

results remained consistent. Future efforts should focus on making this filter more effective at removing noise and more efficient in terms of processing time.

In summary, this project made good progress in both determining the most efficient data processing routine for the BMX experiment as well as examining and removing RFI noise from the data so that it can be analysed more easily and efficiently. Further analysis on both fronts is warranted to continually improve the results of the BMX experiment, so that those results can better inform planning for the next generation PUMA experiment.

Acknowledgements

I would like to thank my mentors during the SULI program while working on the BMX experiment, Dr. Anze Slosar and Dr. Paul O'Connor, for patiently helping me at every step of the way.

This project was supported in part by the U.S. Department of Energy, Office of Science, Office of Workforce Development for Teachers and Scientists (WDTS) under the Science Undergraduate Laboratory Internships Program (SULI).

Investigating radiation at RHIC access road using Monte Carlo simulation

Z. S. Rechav¹ and K. Yip²

¹Physics Department, Truman State University,
Kirksville, MO 63501

²Collider-Accelerator Department,
Brookhaven National Laboratory, Upton, NY 11973

18 August, 2020

Abstract

The implementation of beam energy and intensity upgrades on the RHIC berm may lead to concerning radiation doses above the berm east of building 1005, part of the entrance road to the RHIC ring. This location is currently a controlled area which restricts access to the RHIC ring including building 1005. Simulations were used to determine radiation levels above the road and where necessary shielding will be implemented for the entrance road to RHIC to be classified as an uncontrolled area. Transport code MCNP6.2 was used to model geographical and construction specifications of the RHIC berm located underneath Renaissance Road, as well as accelerator details including the magnets and beam pipes. Particles at beam energy 275 GeV were simulated in a Linux cluster system located at Brookhaven National Laboratory and a radiation dose of $11.48(\pm 8.1\%)$ mrem above the RHIC entrance was determined.

1 Introduction

Beam operations at RHIC may give rise to radiation with varying doses along the RHIC berm. The consideration of beam line upgrades have led the entrance to the RHIC ring (Renaissance Road) just above the berm to be classified as a controlled area. This is partly due to the fact that, from a previous estimate [1], the estimated radiation dose during a Maximum Credible Incident (MCI) with increased beam energy and intensity above Renaissance Road seems to be above 100 mrem. Since the accelerator underneath the junction of the Renaissance Road and the ring is not a location of limiting aperture, an MCI around this area is a beam fault in which 0.5 of the total beam intensity is lost at the beam pipes underneath the entrance road [1].

The Collider-Accelerator Department at Brookhaven National Laboratory (BNL) is seeking solutions to allow for Renaissance Road to be classified as an uncontrolled area. Using Monte Carlo N-Particle (MCNP6.2) transport code, the RHIC berm, accelerator, and magnetic details will be modeled. Simulations at beam energy 275 GeV will be run in a Linux Cluster at the Scientific Data and Computing Center (SDCC) at BNL, mainly used for running the export-controlled software MCNPX and MCNP6, to determine accurate radiation doses during an MCI for the area. The results will be used to determine if/where necessary radiation shielding must be implemented to ensure the entrance becomes an uncontrolled area, thus allowing unrestricted access to building 1005.

2 Methods

2.1 Empirical Dose Estimation

Existing radiation dose estimations were calculated by Dana Beavis using the following empirical equation:

$$D = \frac{(38,800 \text{ rem}) * e^{(-\frac{d}{att})}}{(r_t * r_t)} \quad (1)$$

assuming a full beam intensity of 2.28×10^{13} protons at beam energy 250 GeV, where D is the dose in rem, d is the berm thickness in feet, att is the attenuation length of shielding in feet, and r_t is the transverse distance in feet. r_t for this part of the berm was found by subtracting the elevation of the beam pipe $69\frac{1}{6}$ ft from the elevation of the tunnel height 76 ft, plus the elevation of the road 13 ft above the tunnel ceiling and the additional 3 ft above the surface of the road. The value 55.94 mrem, or 56 mrem, was obtained using Eq.1 with values $d = 13$ ft, $att = 2$ ft, $r_t = 22\frac{5}{6}$ ft and a factor of 0.5 for half of the full beam

intensity.

Doubling beam intensities and increasing beam energy by 30% (i.e. 325 GeV) correspond to a scaling factor of $2 \cdot (1.3)^{0.8} \approx 2.5$ [1]. Multiplying this scaling factor to the aforementioned 56 mrem, one obtains a dose of 140 mrem in an MCI. More than 10 years after [1] was written, the highest attainable beam energy at RHIC is now believed to be about 275 GeV ¹. For this report all simulations were performed at beam energy 275 GeV, and the full beam intensity was assumed to be 5×10^{13} protons. With these slightly revised conditions, the estimated dose due to an MCI at Renaissance Road is about 132.4 mrem ².

For its use, Eq.1 is very generic. The actual doses may vary greatly due to the differences in specific accelerator and magnet configurations. In this report the authors describe a set of simulations with a detailed model of the entrance via Renaissance Road and its surroundings in MCNP6.2, and will compare results with the dose 132.4 mrem obtained from Eq.1.

2.2 Berm Simulation

A detailed model spanning 10 m of the RHIC berm, tunnel, beam pipes, and magnets east of building 1005 at approximately 5 o'clock was constructed with MCNP6 transport code using several sources. Orientations of the model in the XY, YZ, and XZ planes are shown in Fig. 1. The coordinate system of the model is described for clarity. The x-axis follows the North-South (N-S) direction of the tunnel, the y-axis follows the vertical height of the model, and the z-axis follows the counterclockwise West-East (W-E) length of the tunnel. Important details pertaining to construction of the model are described below. The model was then simulated extensively in a Linux cluster system at BNL. Attention was focused at 3 ft above Renaissance Road where radiation doses on human traffic are being questioned.

2.2.1 Berm

A survey of the RHIC berm performed by Matt Ilardo and Charles Folz provided information on the slope and elevation of Renaissance Road. Three images measured the vertical distance from the top of the tunnel to the the road surface at the west gutter (WG), center line (CL), and east gutter (EG) of Renaissance Road [3]. A center elevation of approximately 13.2 ft taken from CL was used to define the height of soil shielding above the RHIC tunnel. To calculate the West-East slope of the road, the center elevations from WG and CL were compared over a distance of 5 m. Similarly, to calculate the N-S slope of Renaissance Road

¹The energy scaling, $(\frac{325}{275})^{0.8}$, would only result in a factor of 1.14 on doses.

²55.94 mrem multiplied by $(\frac{275}{250})^{0.8}$ and $\frac{5}{2.28}$ is 132.4 mrem.

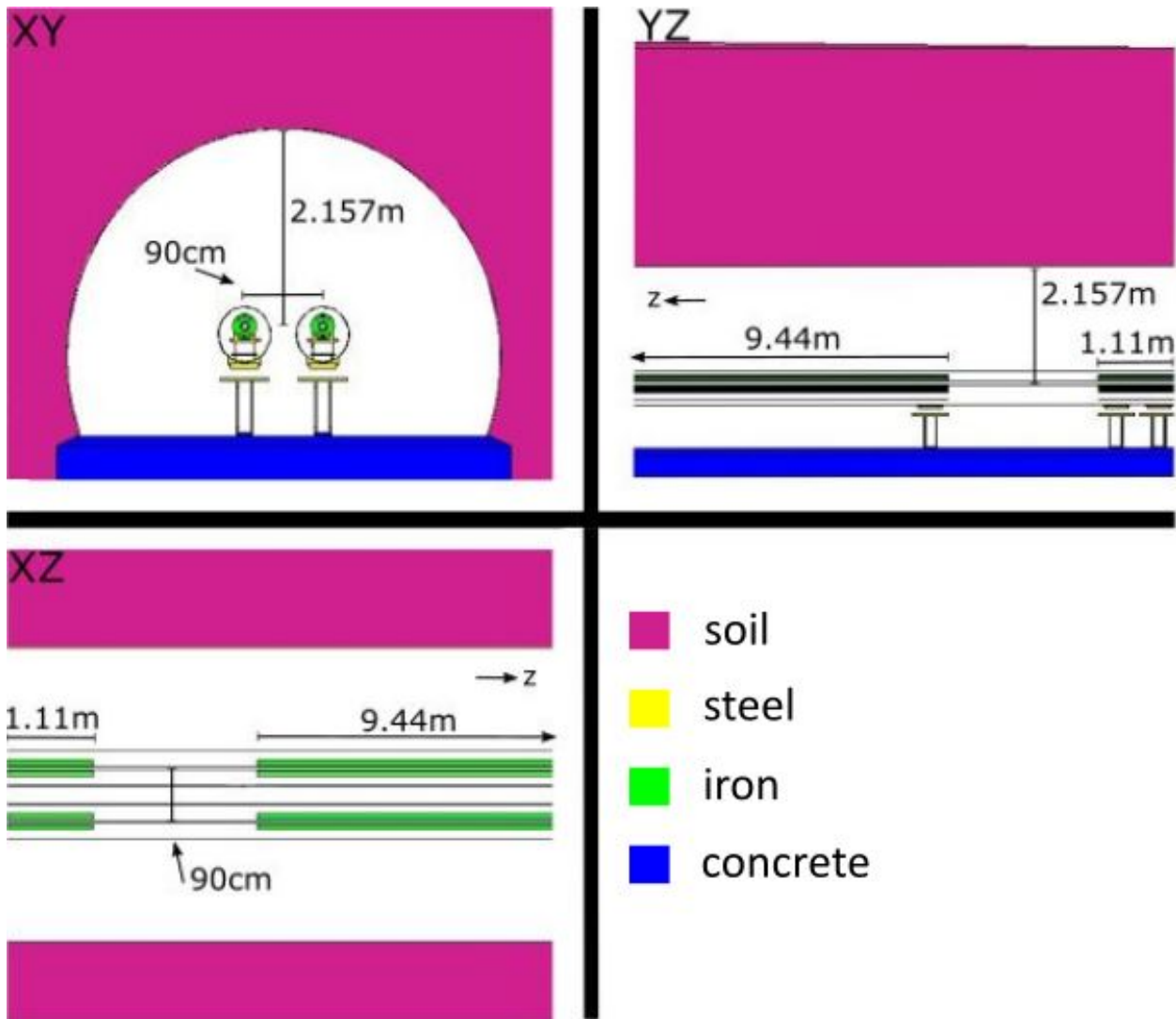


Figure 1: XY [2],YZ, and XZ plane of RHIC berm, where pink represents soil, white represents vacuum, dark blue represents concrete, green represents iron, and yellow represents steel. Fig. 2 shows what the magnets look like inside of the beam pipes. A 10×10 m area in the XZ plane was assumed for the model.

the north and south elevations of CL were used. The distance between the two elevations was 70 in., stated by the surveyors.

The resulting N-S slope of -0.003 and W-E slope of 0.0004 shown in Table 2 were extended to 10 m lengths for model simplicity. Although the slopes of the road are quite small, as much detail as possible was used for this part of the model. More detail improved the accuracy of simulated radiation doses a person would receive if they were standing at the entrance to RHIC.

Elev.1(ft.)	Elev.2(ft.)	direction	slope
12.9658	13.1959	W-E	0.0004
13.7632	13.7447	N-S	-0.003

Table 2: Road slope elevations

2.2.2 Tunnel

The RHIC tunnel is 13.2 ft below the surface elevation 89 – 90 ft of Renaissance Road with an inner diameter of $16 - 4\frac{3}{8}$ ft. The concrete floor is marked at an elevation of 65 ft., and the ceiling of the tunnel is 11 ft above at elevation 76 ft [2].

Inside of the RHIC tunnel are the beam pipes, 90 cm [4] apart. Midway between their centers, at $x = 0$ in the model, is exactly 2.157 m [3] to the roof of the tunnel. From Fig. 1 in the XY plane the reader can see the beam pipe on the right is referred to as blue, while the beam pipe on the left is referred to as yellow. The blue beam pipe has clockwise particle direction, vice versa for the yellow beam pipe. At the 5 o'clock location underneath Renaissance Road, the blue beam pipe is closer to the center of the RHIC ring.

2.2.3 Magnets

Surrounding each beam pipe at specific intervals are iron yokes surrounding copper coil arrangements to produce dipole/quadrupole magnetic fields. The Q12 magnet, 1.11 m in length, and the D11 magnet, 9.44 m in length [5], were incorporated in the model, shown in Fig. 2. They differ only in the configuration of their copper coils and total length in the z-direction.

Helium tubes and electrical buses [6] were included in each iron yoke to make the model more realistic. The base supports for the iron yokes and beam pipes were modeled from existing engineering drawings [6] and images from a tunnel visit [7]. Beam pipe supports were

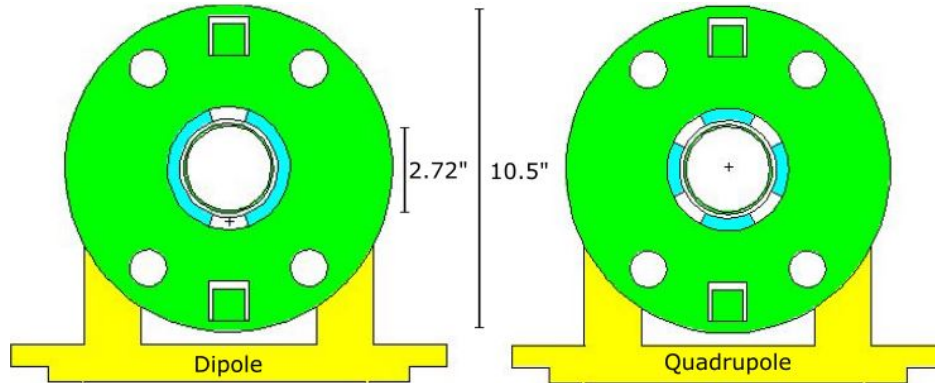


Figure 2: dipole and quadrupole magnets, where green represents iron, yellow represents steel, light blue represents copper, and white represents vacuum.

placed at each end of the magnets, although there are more supports at the real RHIC beam. The base dimensions are approximate and were minimized to prevent excessive shielding in the model.

3 Analysis

Simulations were run with different parameters in an effort to find the highest radiation dose a person may experience 3 ft above Renaissance Road. Nine detector point tallies were used to survey doses per incident proton along the length of the road above the RHIC tunnel. A detector tally (F5) in MCNP6.2 makes use of a variance reduction method (“next event estimator”) that allows for more efficient simulations[8]. Unless otherwise specified, F5 tallies were used for simulations in this report. The Cartesian coordinate system for the model was set up such that the positive x-axis pointed towards the center of the RHIC ring, positive y-axis pointed to the sky, and the positive z-axis pointed in the direction of proton flow in the yellow ring.

Two runs were performed with the same geographic parameters to observe the effects of magnetic fields on doses. The magnetic field produced by D11 with a maximum stepsize of 1 cm was tested, and the results are shown in Fig. 3. Differences between the two runs were negligible, and magnetic fields produced by Q12 and D11 were excluded from further runs for efficiency.

Shown in Fig. 4 is a comparison of radiation doses from hitting the sides of the yellow and

³Protons in the blue beam pipe move in the negative z-direction with an angle about -3.67 mrad (suggested by accelerator experts) in the x-direction for particles hitting the side of the beam pipe closest to the center of the road above. Protons in the yellow beam pipe move in the opposite direction with the same angle for particles to hit the side of the beam pipe closest to the center of the road above.

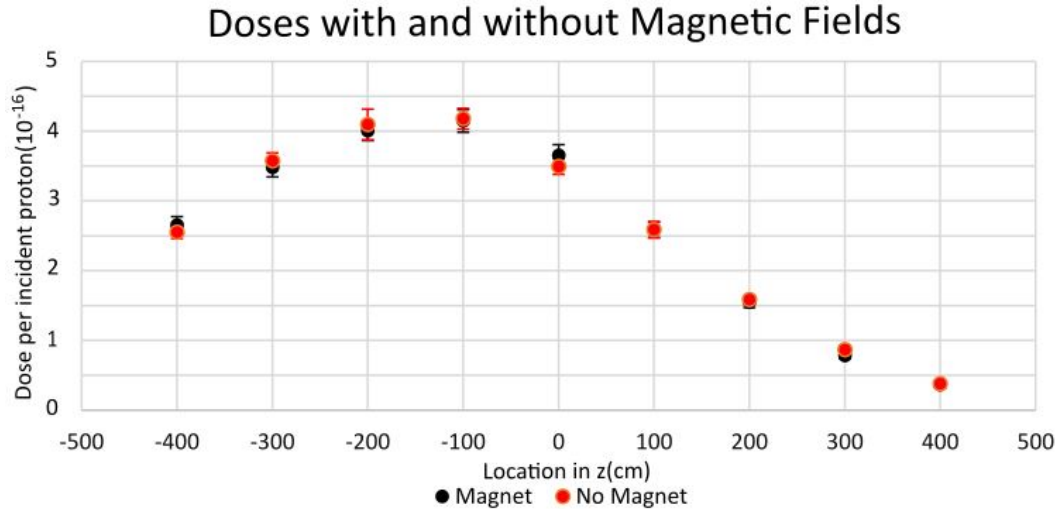


Figure 3: Dose per incident proton comparisons when blue beam pipe is hit from side at $z = 200$ cm.

blue beam pipe. Particles in the yellow and blue beam pipes circulate in opposite directions³ and during simulations the beams were hit in different directions as well.

As there would be more radiation in the forward beam directions, the doses were expected to be higher in the negative z -direction for the blue beam pipe and higher in the positive z -direction for the yellow beam pipe. The distribution of data in Fig.4 is consistent with expectations and there is little fluctuation in dose depending on where particles were designated to collide with the beam pipes.

For these four runs, the maximum radiation dose was $4.18 \times 10^{-16}(\pm 3.6\%)$ rem per incident proton at $z = -100$ cm in the blue beam pipe, designated by red in Fig. 4. The maximum dose observed in the yellow beam pipe was $4.16 \times 10^{-16}(\pm 3.9\%)$ rem per incident proton at $z = 100$ cm. This dose resulted from hitting the beam pipe at $z = -200$ cm, which is an area of the beam pipe that is not surrounded by any magnet. One might expect the iron yoke of the magnet to provide extra shielding, but the presence of the magnet also acts a scattering target to help bring neutrons to the surface of Renaissance Road. It is likely that these two effects largely cancelled each other out.

Runs at different z and y coordinates along the blue beam were examined to see how doses varied. Shown in Fig. 5 are three runs and their respective dose spectrums. The black data points correlate to a run hitting the side of the blue beam pipe at $z = 200$ cm, and the green data points correlate to a run hitting the side of the blue beam pipe at $z = 150$ cm. The third data set correlates to hitting the ceiling of the blue beam pipe at $z = 200$ cm.

The highest doses 3 ft above Renaissance Road were around $z = -100$ cm or $z = -200$ cm. The maximum dose $4.37 \times 10^{-16}(\pm 3.1\%)$ mrem per incident proton found using 9 point

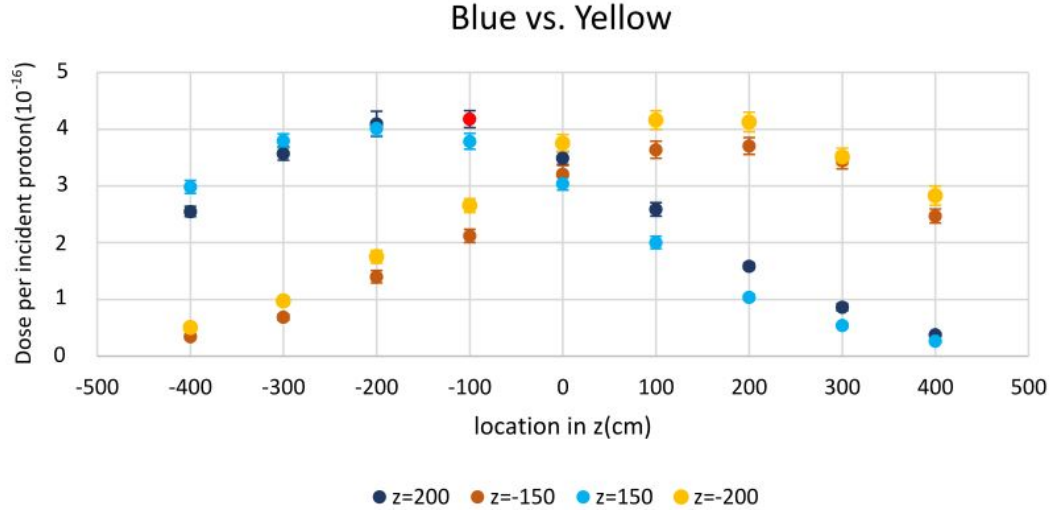


Figure 4: Dose per incident proton with two simulations each from the yellow and blue beam pipe. The yellow beam pipe was hit from the side at $z = -150$ cm and $z = -200$ cm, and the blue beam pipe was hit from the side at $z = 150$ cm and $z = 200$ cm. All runs except at $z = -200$ cm were surrounded by magnets.

detectors placed along the length of the z -axis was observed by hitting the top of the blue beam pipe at $z = 200$ cm. The maximum doses for each run are about the same as the highest doses in Fig. 4 if one takes statistical uncertainties into account.

In the blue ring an exploration of the cross section at $z = -100$ cm of the RHIC berm was conducted. 8 point detectors were used along the cross section of the RHIC berm 3 ft above the road to record doses from a collision into the side of the blue beam pipe at $z = 200$ cm, shown in Fig. 6. Doses were highest in the center strip of the road $x = -100$ cm to $x = 100$ cm and decreased with distance from the RHIC tunnel center. No outlying doses were discovered, nor any doses higher than those at $x = 0$ cm for other runs along the blue beam pipe.

To compare and cross-check the doses found from previous F5 tallies, the track-length F4 tally [8] in MCNP6.2 was used. F4 tallies need prolonged time and more statistics to produce dose results with comparable accuracy as those of F5 tallies. The colliding point where the previous maximum dose was found, hitting the top of the blue beam pipe at $z = 200$ cm, was selected to check the resulting dose above the road at $z = -100$ cm.

By chance, two different directions to hit the top of the blue beam pipe were used in simulations, one in the positive y -direction and another in the negative x -direction. Results from the F4 tallies were consistent with previous simulations using point detectors (F5 tallies). The highest dose found from both F4 and F5 tally simulations was 4.59×10^{-16} ($\pm 8.1\%$) rem per incident proton.

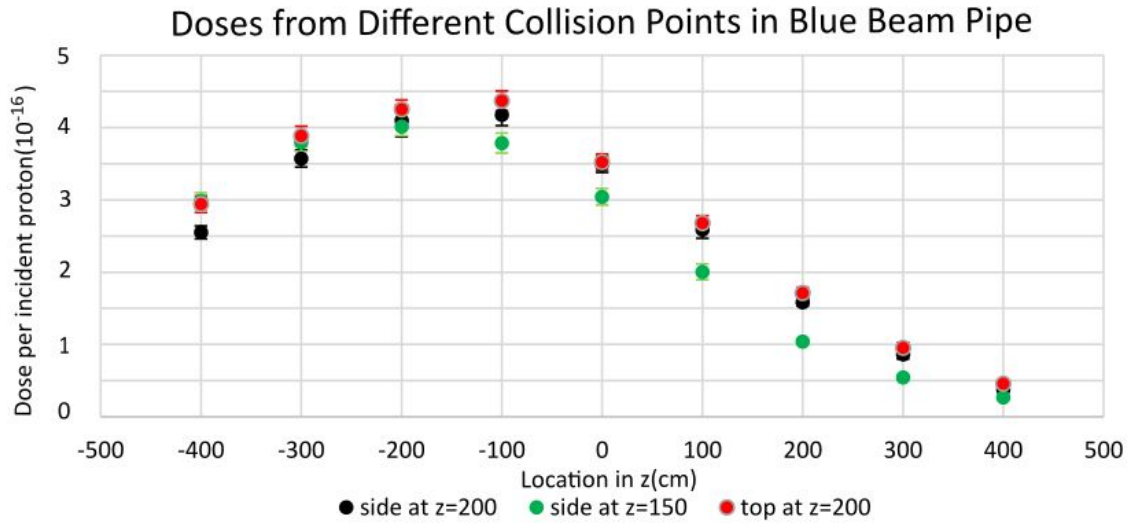


Figure 5: Dose per incident proton comparisons with three simulations on the blue beam pipe, two hitting the side of the pipe at $z = 150$ cm and $z = 200$ cm, and one hitting the top of the beam pipe at $z = 200$ cm.

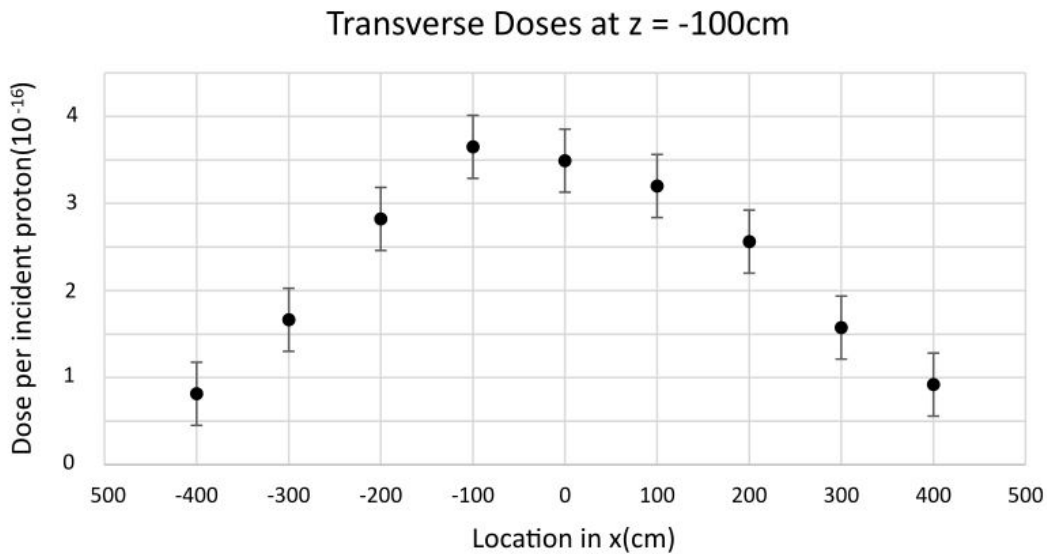


Figure 6: Dose per incident proton along the x -axis at $z = -100$ cm from a collision into the side of the blue beam pipe at $z = 200$ cm.

Previous simulations adhered to the common practice that only protons and neutrons are transported. As another cross-check, a simulation with a collision point into the side of the blue beam pipe at $z = 200$ cm was performed in which photons are added to the transport. The dose results including both neutrons and photons are shown in Fig. 7.

The total doses for a simulation with both neutrons and photons transported in MCNP6.2 agree with doses from previous runs. Over the course of dose exploration stated in this report,

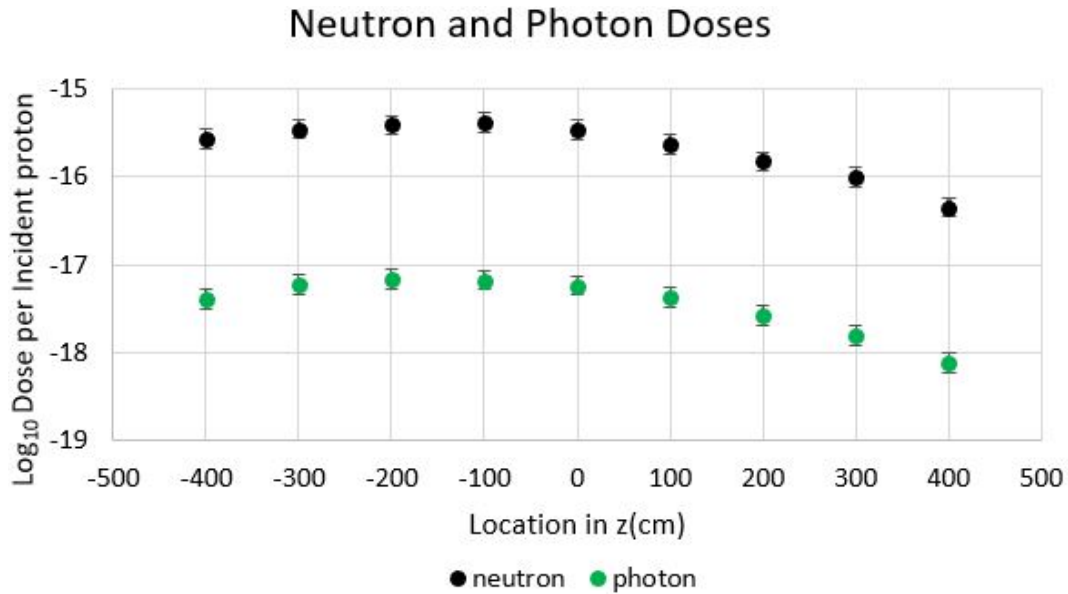


Figure 7: Dose per incident proton along the z-axis for a collision in the side of the blue beam pipe at $z = 200$ cm. Logarithmic doses per incident proton for neutron (black) and photon (green) activity in simulation.

no outlying or inconsistent doses were found.

4 Conclusions

Various simulations were performed on a section of the RHIC berm to examine radiation doses at the entrance to RHIC during a beam fault (MCI). Maximum doses in both the blue and yellow beam pipes at different collision angles and locations were consistent with little variation. The highest dose from all performed simulations was 4.59×10^{-16} rem per incident proton. At half of the full beam intensity, 2.5×10^{13} protons [9], this corresponds to about 11.48 mrem with an 8.1% statistical uncertainty.

At 3 ft above Renaissance Road, the previous dose approximation 132.4 mrem from Eq.1 is more than 10 times larger than the highest dose found from this set of simulations. With simulated values well below a cautionary cap of 100 mrem, the entrance to RHIC via Renaissance Road can be reclassified as an uncontrolled area without adding additional shielding to the berm.

5 Acknowledgements

I would like to thank my mentor Kin Yip for sharing his invaluable experience, knowledge, and insight with me throughout this summer. This project was supported in part by the U.S. Department of Energy, Office of Science, Office of Workforce Development for Teachers and Scientists (WDTS) under the Science Undergraduate Laboratory Internships Program (SULI).

References

- [1] D. Beavis, “Potential Dose on the RHIC Berm”, December 30, 2009: https://www.c-ad.bnl.gov/esfd/RSC/Memos/RHIC_berm.pdf.
- [2] Drawing number : A3001B0111 by R. Tulipano, “RHIC Construction Major Facilities @ 12:00”, April 21, 1997.
- [3] C. Folz, M. Ilardo, “CL ROAD”, “WEST GUTTER”, “EAST GUTTER”, “beam to tunnel”, June 2020: <https://brookhavenlab.sharepoint.com/:f:/r/sites/MyOwnTestingArea/Shared%20Documents/RHIC%20Entrance%20Road%20Radiation/survey?csf=1&web=1&e=z8vrD6>.
- [4] Accelerator Division, “RHIC Configuration Manual”(Collider Accelerator Department, Brookhaven National Laboratory, September, 2006): <https://www.bnl.gov/cad/accelerator/docs/pdf/RHICConfManual.pdf>.
- [5] Steven Tepikian has provided the current RHIC MAD-X lattice files for both blue and yellow rings in RHIC.
- [6] Drawing number : 12120191 by J. Massim, S. Mulhall, “CQT4 Magnet Assembly Area 16, Station 6, CQT4 Cryostat and Magnet Assembly without Flanges”, August 9, 1996.
- [7] Thanks to Don Bruno’s team for taking all the pictures inside the RHIC tunnel on July 8, 2020.
- [8] C. Werner, MCNP User’s Manual Code Version 6.2 (Monte Carlo Methods, Codes, and Applications, Los Alamos National Laboratory. October 27, 2017).
- [9] K. Yip, “Potential radiation doses outside the IR8 West Wall penetration during a fault” March 15, 2019: <https://www.c-ad.bnl.gov/esfd/RSC/Memos/2019-3-15%20sPHENIX%20West%20Wall%20Penetration.pdf>.

Development of mobile applications for medical isotope reference

Student Intern

Vanessa E. Rodriguez, Computer Science and Mathematics Department, St. Joseph's College,
Patchogue, NY, 11772

Mentor

Elizabeth Richard-McCutchan, Nuclear Science and Technology Department, Brookhaven
National Laboratory, Upton, NY, 11973

Mentor

Benjamin Shu, Nuclear Science and Technology Department, Brookhaven National Laboratory,
Upton, NY, 11973

Abstract

Brookhaven National Laboratory's (BNL's) National Nuclear Data Center (NNDC) maintains a series of databases that deal with nuclear structure and nuclear reaction data. One of these databases is the Medical Internal Radiation Dose (MIRD) database from the Evaluated Nuclear Structure Data File (ENSDF). MIRD is used as a reference for half-lives, radioactive emissions, and decay products when conducting experiments. Currently scientists can only access this reference material through a website. However, there are times where scientists do not have such access. This is where a mobile application comes in. The mobile app I have developed is based on the MIRD website and will provide access wherever a user can bring their phone. To create such an application, I first needed to learn how to code in HTML, CSS, and JavaScript. I then built and tested the app in Apache Cordova until I had a working prototype. With this mobile application, it will be more convenient to reference MIRD without having so many constraints. The mobile app will have access to mobile hotspots and data networks, while laptops and desktops would require Ethernet or Wi-Fi. A phone is also easier to carry and more user-friendly. This is important for MIRD because medical isotopes are used in imaging. When a patient takes in medical isotopes, those can be tracked through the patient's body. This allows doctors to check for diseases or any form of damage inside the patient's body, such as cancer.

I. Introduction

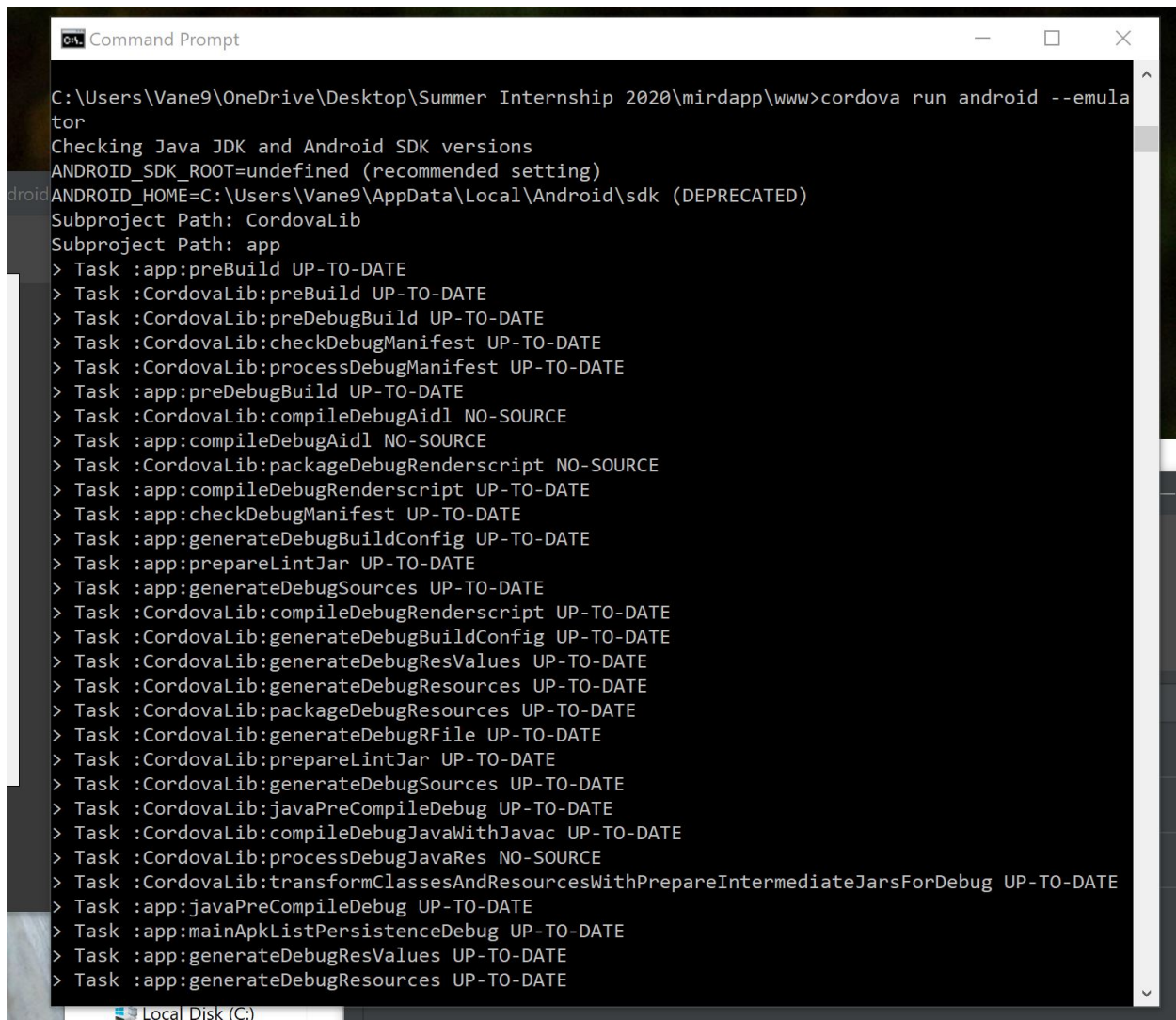
This COVID-19 pandemic has caused the entire world to stop in its tracks. With having to be quarantined in our own homes to protect ourselves from this deadly virus, being able to intern at such an amazing facility like Brookhaven National Laboratory (BNL) has truly been a blessing. This summer, I got the chance to work with Elizabeth Ricard-McCutchan and Benjamin Shu, from the Nuclear Science and Technology Department, to build a mobile

application. This application is based off one of the databases of the National Nuclear Data Center (NNDC), the Medical Internal Radiation Dose (MIRD) database derived from the Evaluated Nuclear Structure Data File (ENSDF). Instead of accessing a computer, the app can be used as a reference for scientists when looking for emissions from nuclear decay.

II. Methods

When the internship program started, I was able to meet my mentors via Zoom to talk a bit more about the upcoming summer. However, before I could officially start the project, I had to prepare my laptop to be able to create the app I wanted to build. First, I had to download Apache Cordova (Figure 1) and Android Studio (Figure 2). Apache Cordova is a mobile application development framework and Android Studio is a development environment for Android smart phones. Designed specifically for Android operating systems. Next, I needed to set up my laptop for a Git repository. Git is a system that saved changes that I made in order to keep track of the progress of my mobile application project. In other words, it was a way for me and my mentors to keep track of all the changes that had been made to the code. It also helped me stay on track with respect to time. Finally, I had to learn a few new languages, three, to be precise. My mentor Benjamin Shu shared a link with me about learning all the necessary programming languages for Apache Cordova: HTML, JavaScript, and CSS. HTML stands for Hypertext Markup Language, which is a coding language that tags text files to achieve font, color, graphic, and hyperlink effects on web pages. JavaScript is another language that is used to create interactive effects within web browsers, like buttons and textboxes. As for CSS, it is a language that is used for formatting and styling web pages. The shared link was really helpful in terms of learning the code. In this same link I got the chance to work with sample code of the languages and make changes to them so I could see what I was doing. Learning three new

languages was much harder than setting up my laptop with the appropriate software. I already knew TrueBasic, VisualBasic, and Java, but adding three more was a bit difficult. The few languages that I already know are very similar to the one needed for mobile application development and I mixed them up a lot. Once everything was set up, it was time to really get to work.



```
Command Prompt
C:\Users\Vane9\OneDrive\Desktop\Summer Internship 2020\mirdapp\www>cordova run android --emulator
Checking Java JDK and Android SDK versions
ANDROID_SDK_ROOT=undefined (recommended setting)
ANDROID_HOME=C:\Users\Vane9\AppData\Local\Android\sdk (DEPRECATED)
Subproject Path: CordovaLib
Subproject Path: app
> Task :app:preBuild UP-TO-DATE
> Task :CordovaLib:preBuild UP-TO-DATE
> Task :CordovaLib:preDebugBuild UP-TO-DATE
> Task :CordovaLib:checkDebugManifest UP-TO-DATE
> Task :CordovaLib:processDebugManifest UP-TO-DATE
> Task :app:preDebugBuild UP-TO-DATE
> Task :CordovaLib:compileDebugAidl NO-SOURCE
> Task :app:compileDebugAidl NO-SOURCE
> Task :CordovaLib:packageDebugRenderscript NO-SOURCE
> Task :app:compileDebugRenderscript UP-TO-DATE
> Task :app:checkDebugManifest UP-TO-DATE
> Task :app:generateDebugBuildConfig UP-TO-DATE
> Task :app:prepareLintJar UP-TO-DATE
> Task :app:generateDebugSources UP-TO-DATE
> Task :CordovaLib:compileDebugRenderscript UP-TO-DATE
> Task :CordovaLib:generateDebugBuildConfig UP-TO-DATE
> Task :CordovaLib:generateDebugResValues UP-TO-DATE
> Task :CordovaLib:generateDebugResources UP-TO-DATE
> Task :CordovaLib:packageDebugResources UP-TO-DATE
> Task :CordovaLib:generateDebugRFile UP-TO-DATE
> Task :CordovaLib:prepareLintJar UP-TO-DATE
> Task :CordovaLib:generateDebugSources UP-TO-DATE
> Task :CordovaLib:javaPreCompileDebug UP-TO-DATE
> Task :CordovaLib:compileDebugJavaWithJavac UP-TO-DATE
> Task :CordovaLib:processDebugJavaRes NO-SOURCE
> Task :CordovaLib:transformClassesAndResourcesWithPrepareIntermediateJarsForDebug UP-TO-DATE
> Task :app:javaPreCompileDebug UP-TO-DATE
> Task :app:mainApkListPersistenceDebug UP-TO-DATE
> Task :app:generateDebugResValues UP-TO-DATE
> Task :app:generateDebugResources UP-TO-DATE
```

Figure 1- Apache Cordova



Figure 2 – Android Studio

The first thing that I did was to create an outline of the mobile app so I could have more or less an idea of what the app could look like and how I could improve it. I structured the heading, the textbox, the search button and the logo of the NNDC in HTML. This is where all the new languages come into play. I used HTML to tag everything that would be needed for the app, like the features I mentioned before. In order to have the textbox and the search button interact with the user when they clicked on it, or in this case tapped on it with their finger, I used

JavaScript to code the interactions. Finally, I used CSS to format the app by setting a background color, font style and size, the size of the NNDC logo, etc (Figure 3). I had to keep in mind that this was for an app, and not a website. In a website, one may have more space to work with. That is not the case for a mobile app. The work field is much smaller and longer vertically than a webpage. At first, I had an idea of what I wanted the app to look like, but coding the app's format was a bit confusing. Thankfully, my mentor Benjamin, shared with me a copy of an app that he'd made before so that I could have an idea of what the coding would be like when it came to the functionality of the app. The app that he shared with me was a reference book which contains information on ground state nuclei and their isomer states and where users can access their credit cards' statements, make payments, etc. It was somewhat similar to the app we were building. However, instead of pulling up information about one's information and credit card, my mobile application would pull up a display of a nuclide's level decay scheme and its daughter nuclei.

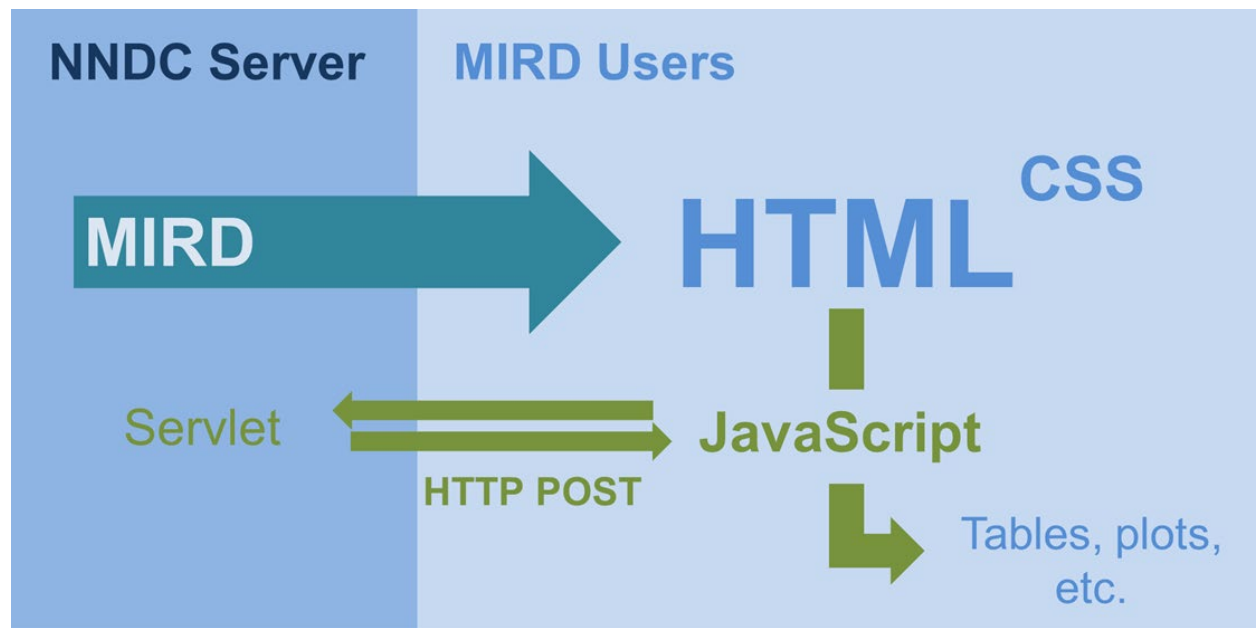


Figure 3 – What's needed in mobile application development

After the outline was finished, it was time to officially work on the functionality of the application. All the coding was done on Windows' NotePad program first because I did not yet have an application for writing code. As I was coding the functions, I was also learning more and more about HTML, JavaScript, and CSS. There were many days where I hit a wall due to the fact that I coded a lot of lines incorrectly. Each of the languages has a specific syntax to follow in order to code correctly. Once I finished most of the functions of the app, like the textbox and the search button, it was time to finalize the design for the mobile application. Presenting the app was tricky because the nuclide's level decay scheme and its daughter nuclei will take up most of the space on screen. As I was trying to piece together the look for the project, I came up with an interesting idea. When researchers would enter a nuclide and see the results one after the other, I thought about how they may need to see a list of all the nuclides that they searched. That way they will not have to enter the nuclide every time they needed to see the previous ones. So, I thought about having a history list in the app, of course that meant another chance for me to better learn the coding languages of HTML, JavaScript, and CSS. Unfortunately, I was not able to finish completing the history list.

Coding all the components of the mobile app took up much of the time in the internship. It took even longer when I had to deal with syntax errors and declarations in the code. Thankfully, Benjamin was able to walk me through the errors and help me better understand the programming languages. After many mistakes and lessons, it was time to put the code to the test. NotePad++ is an application designed for coding in several different languages such as HTML, JavaScript, and CSS. I had to use the Windows Command Prompt to get the app started. The Command Prompt, is a text-based user interface designed to run computer programs. Once the Command Prompt was ready, I would start up Android Studio and choose a digital version of an

Android phone to test the app. Here is where more changes in the code took place. Honestly, it was very satisfying to see a mobile application that I had built actually appear in an actual smart phone, virtually that is. Before, I made changes to the code based on syntax errors. Once the app was working on a smart phone, I could make changes based off of format and style. The entire coding process is always my favorite part of any programming project, but when it comes to styling of the fonts, pictures, etc. that is always a bit more fun. It was here where I could finalize the project. But before I could submit the project, I needed to inspect it with Google Chrome's Developer Console. The Console is a tool used to debug websites and mobile applications in development environments, like Android Studio. The rest of the internship was just me making changes to the app after inspecting the code with Chrome and fixing the errors the console picked up. I went back and forth between fixing the coding and inspecting it until finally, after so many tries, the app was complete and functional. The day when I finished the project, I had never felt so proud to have built a functional mobile application.

III. Results

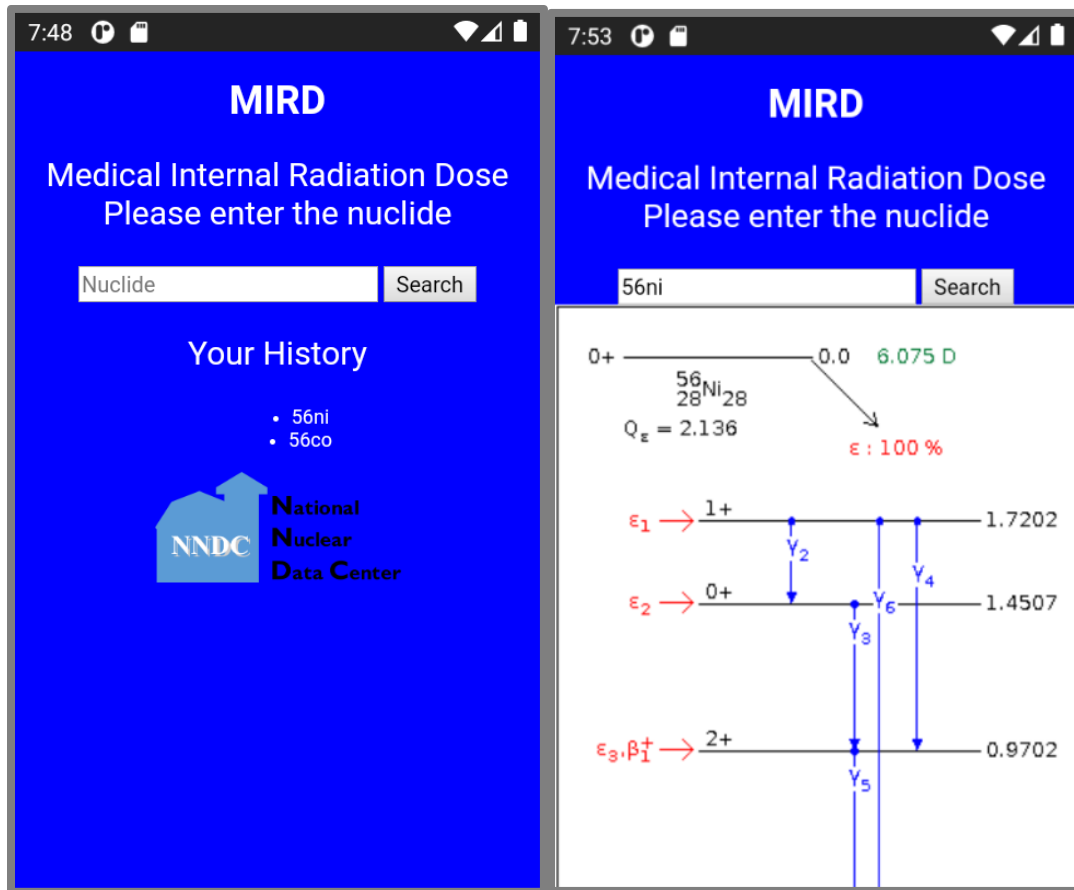


Figure 4 – MIRD mobile application

IV. Conclusion

I have always wanted to learn how to create a mobile application. What better way to learn about mobile apps than to build one for researchers? Before interning for BNL, I really did not know what career in computer science I wanted to pursue. In fact, I was beginning to believe that computer science may not be the field for me. However, thanks to the SULI program at Brookhaven National Lab I now have a passion for creating apps like the MIRD app to help researchers work more easily.

V. References

Evaluated Nuclear Structure Data File (ENSDF), available at www.nndc.bnl.gov/ensdf

Loevinger R, Berman M-A. A schema for absorbed-dose calculations for biologically distributed radionuclides. *J Nucl Med.* 1968;9(Suppl. 1):7–14

Ventrecycle

Russell Rohan, Biology, Allegheny College, Meadville, PA 16335

Susan Pepper, Nonproliferation and National security, Brookhaven National Laboratory, Upton,
NY 11973

Abstract

Everyday, machine ventilators in all types of facilities around the world allow numerous patients to overcome near fatal respiratory distress. By design, these machines require both an oxygen and air supply. This year (2020), due to the COVID-19 pandemic, machine ventilators, and in turn oxygen and air used for these machines, have been in high demand which has led to a shortage of both in many countries and facilities around the world [1]. For my summer project, I worked on implementing the technology used in scuba diving rebreathers into a machine ventilator. By doing this, I was able to develop a design for a ventilator that uses oxygen and air at a much slower rate than average ventilators; and in turn greatly reduce the cost with respect to time of transporting oxygen, increase mobility and storage capabilities of the machine, along with several other benefits. This capability is a result of the circulating or “rebreathing” of a patient's breath. The CO_2 in each exhalation would be scrubbed and the oxygen that wasn't metabolized by a patient in a single breath would go back to the patient. This way the oxygen and air would be added in small increments and used at a much slower rate. And because the breath is humidified by a patient's body, the need for an external humidifier would be mitigated. Over the course of the summer, I interviewed doctors, researched online articles, read textbooks, studied open source ventilator and rebreather designs, partook in the pre-seed entrepreneurial workshop, and sought out information and advice from qualified BNL employees. By implementing these practices I was able to create a basic design and a commercialization plan for my idea.

I. Introduction

The global need for both ventilators along with oxygen and air production has increased at an exponential rate over the last seven months. There has been such a demand for oxygen around the world that the WHO (World Health Organization) hopes to raise 250 million dollars to fund oxygen delivery around the world. They have also already purchased and started distributing 14,000 oxygen concentrators, machines that pull oxygen from the air, and hope to purchase 170,000 more over the next 6 months at a price of 100 million dollars [1]. By utilizing components and technology from both machine ventilators and rebreathers, this device would have the capability to circulate a patient's breath. On average the human body absorbs roughly 4% of the oxygen taken in by each inhalation [2]. Therefore, if after each exhalation a patient's breath was scrubbed of CO₂, the same breath could be used again by the patient. This would allow oxygen and air to be injected into the ventilator circuit at a much slower rate. Also this technology would mitigate the need for an external humidifier on the machine because the breath would be humidified by the patient's body. A ventilator that has these capabilities would help greatly in health care facilities around the world facing oxygen shortages and in the transportation of oxygen to impoverished countries and remote arrears.

II. Process and results

Over the course of my project, I interviewed doctors, researched online articles, read textbooks, studied open source ventilator and rebreather designs, studied designs of previously patented ventilators and rebreathers, partook in the pre-seed entrepreneurial workshop, and sought out information and advice from qualified BNL employees. As a result, I was able to create a design

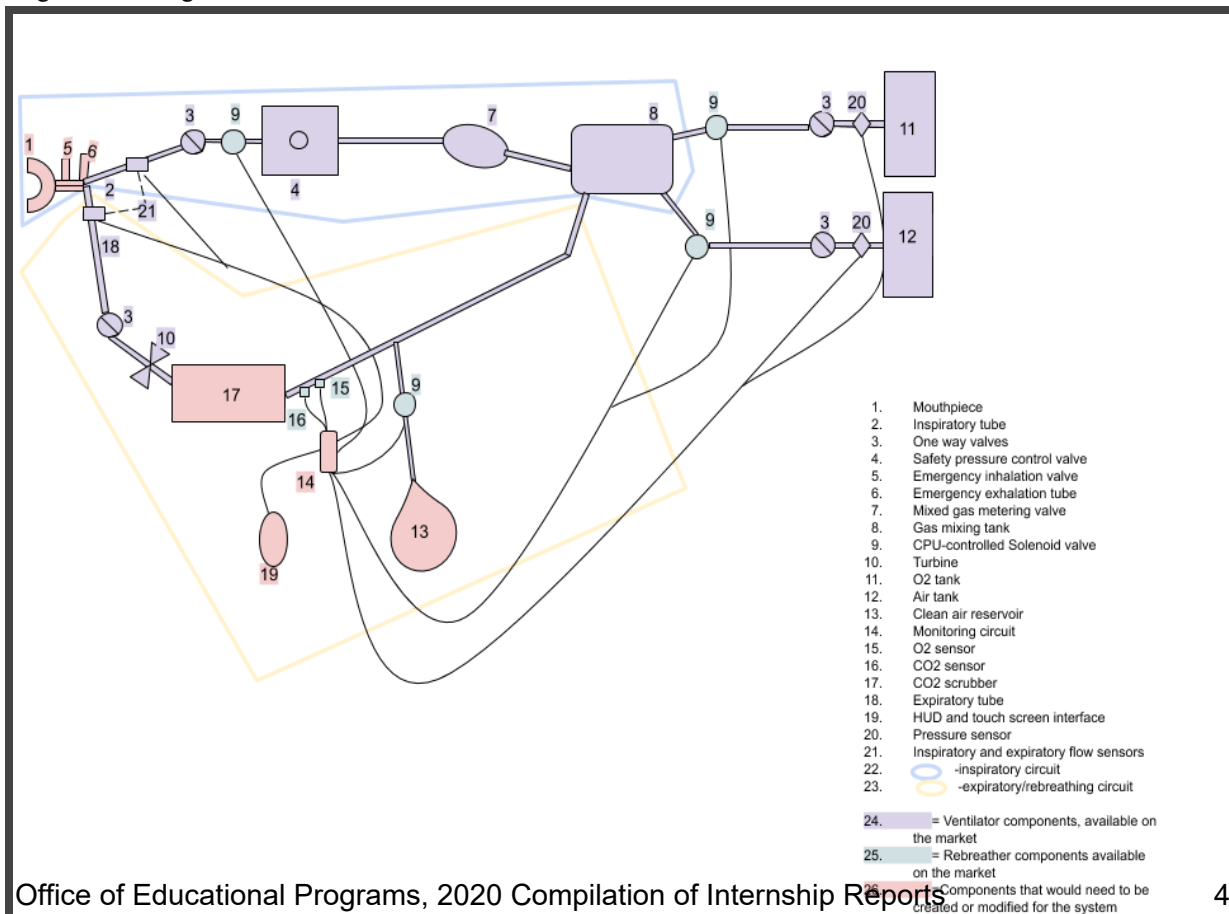
and a commercialization plan for a machine that would have more storage capabilities and transportability, be more financially conservative, and increase oxygen consumption efficiency by 88%. I was able to calculate the percent efficiency by using the following equation and factoring in the average FiO_2 and flow rate for the average COVID-19 patient.

$$\%Efficiency = \frac{O_2 \text{ Absorbed}}{O_2 \text{ Put Into the system}}$$

$$4\% = \frac{1.2 \frac{L}{min}}{30 \frac{L}{min}}$$

$$92\% = \frac{1.2 \frac{L}{min}}{1.3 \frac{L}{min}}$$

Fig.1 Final design of the summer



III. Commercialization

When thinking about a commercialization plan for this device, I focused my research in four main areas: strengths, opportunities, weaknesses, and barriers to entry.

<p style="text-align: center;">Strengths</p> <ul style="list-style-type: none"> ● More storage capabilities and transportability ● More financially conservative ● Increases in oxygen consumption efficiency by 88% ● Gives medical facilities the ability to treat more patients with the best care possible. 	<p style="text-align: center;">Opportunities</p> <p style="text-align: center;"><u>Location</u></p> <ul style="list-style-type: none"> ● Local hospitals ● Hospital groups ● Emergency hospitals ● Patients homes ● Military treatment facilities ● Military medical ships ● Humanitarian organizations <p style="text-align: center;"><u>Buyer</u></p> <ul style="list-style-type: none"> ● Ventilator distributors ● Hospital purchasing departments ● Ventilator manufacturers (if selling design rather than, self manufacturing) ● Organizations like the WHO
<p style="text-align: center;">Weaknesses</p> <ul style="list-style-type: none"> ● Training required to operate device ● Clinical trials and FDA approval required before manufacturing ● Choice of materials to maintain cost effectiveness ● Ventilator market is very large ● Time required to receive patent and investments for prototype 	<p style="text-align: center;">Barriers to entry</p> <ul style="list-style-type: none"> ● Not getting FDA approval ● Lack of investments ● Shortage of materials ● Inconclusive results during trial phase

The main strength of this device would be its oxygen consumption efficiency, which gives it the ability to be more mobile due to the fact that it wouldn't require a large oxygen supply like other ventilators. This capability would have been a great help in many locations during the COVID-19 pandemic such as emergency hospitals or military treatment facilities. When thinking about commercialization, I also wanted to consider the weaknesses and barriers to entry for this machine so I could have a more holistic view of the technology. The main weaknesses would be the same as with most new medical technology. Training required to operate the device and the clinical trials and FDA approval required before manufacturing could take an extensive amount of time. For the most part, the barriers to entry coincide with the weaknesses with the main two being, lack of FDA approval and inconclusive results during the trial phase of the technology. After studying the S.W.O.T. analysis, I was able to outline a general plan for commercializing this technology. My first step would be to create a final design for the machine with specified parts in order to estimate the price of creating a prototype. The next major step would be to submit an investigation disclosure and eventually apply for a utility patent. After obtaining a patent, a summary of the technical components of the machine would need to be sent to licensees to gain attention from investors. With proper investment money, it would be possible to create a prototype that would enter the trial phase and go through the process of being FDA approved. Lastly after getting approval, the prototype could then be sold to a company that already manufactures ventilators so that the machine could reach the market faster and in turn reach people who need it.

IV. References

- 1 [1] Mcneil, D. (2020, June 23). A Simple Way to Save Lives as Covid-19 Hits Poorer Nations. Retrieved August 09, 2020, from <https://www.nytimes.com/2020/06/23/health/coronavirus-oxygen-africa.html>

- 2 [2] Loer, S., Scheeren, T., & Tarnow, J. (1997, March 01). How Much Oxygen Does the Human Lung Consume? Retrieved August 09, 2020, from <https://anesthesiology.pubs.asahq.org/article.aspx?articleid=1948384>

- 3 [3] Poseidon Rebreathers Tech Info. (n.d.). Retrieved August 09, 2020, from <https://poseidon.com/rebreather-technicalinfo>

- 4 Principles and Practice of Mechanical Ventilation, 3e. (n.d.). Retrieved August 09, 2020, from <https://accessmedicine.mhmedical.com/book.aspx?bookid=520>

- 5 Rebreather. (n.d.). Retrieved August 11, 2020, from <https://military.wikia.org/wiki/Rebreather>

- 6 [5] Fig.1 Final design of the summer

Analyzing utility systems at Brookhaven National Laboratory to maintain infrastructure more efficiently

Carmine Romano, Department of Environmental Science, Siena College, Loudonville, NY 12211

Jennifer Higbie, Environmental Protection Division, Brookhaven National Laboratory, Upton, NY 11973

ABSTRACT

Data for the utility systems found on the property of Brookhaven National Laboratory (BNL) are currently stored and viewed within a program called AutoCAD®. While this software is effective at showing locations and differentiating between the types of utilities that exist at BNL, it does not include options for further analysis or data storage. When handling large amounts of data, such as those which make up these systems, it is important to store them in one place and have the ability to make necessary evaluations. Using ArcGIS, a platform designed for managing spatial data, this can be accomplished. The utility data has been exported from AutoCAD to ArcGIS in the past, however, there are many inconsistencies. Correcting these deviations and fully recreating the utility maps within ArcGIS Pro 2.5 was the first required step. Once successfully developed, these systems were exported into their own networks where they could be evaluated further using the ArcGIS Network Analyst extension. Storing utility data in this format enables knowledge of the utilities to be accessible and understandable. Furthermore, this is beneficial to employees at BNL, because it allows them to generate solutions more efficiently when issues arise such as a break in a potable water main.

I. INTRODUCTION

A. Potable water system

The potable water at BNL is transported through an expansive system that spans across the lab. It contains 682 valves and over 38 miles of pipes. It is essential to maintain this system because the health and safety of people onsite depend on it operating properly. Currently, data for this utility are stored within AutoCAD, which is incapable of performing analysis. When any issues arise, such as the main break featured in Figure 1, workers will use their knowledge and paper maps of this infrastructure to determine which actions should be taken to resolve the problem.

Moving all these data into ArcGIS would allow situations like this to be analyzed quicker and in greater depth.

B. Sanitary system

This utility system also exists beneath a considerable section of the Laboratory, however, it operates using the force of gravity. Waste from each of the buildings connected to this system is carried to the sewage treatment facility. Although this system is less complex since it is mostly gravity-driven, its aging infrastructure has led to it being composed of various materials and pipe sizes. These are attributes which would most effectively be stored in ArcGIS.

C. Underground injection controls (UICs)

A UIC is a structure that is used to bring liquids beneath the surface where they can recharge the surrounding groundwater. Examples of UICs include dry wells, which are installed to reduce runoff by reintroducing this water to the ground below, and cesspools, which bring our waste to a location underground where liquids can seep back into the soil. UICs are important infrastructure at BNL, but they are difficult to keep track of since their data is scattered throughout various maps, paperwork, and databases. There are even some UICs that have been completely lost in documentation. The lack of a comprehensive data source makes it more difficult and time consuming to easily identify all existing UICs. Ideally, there should be a single location where all this information is stored.

II. METHODS

A. Potable and sanitary systems

Prior to the start of this project, the points and lines that make up the potable and sanitary systems were exported from AutoCAD to ArcGIS. These files contain polylines, which make up the pipes, as well as point files, which represent the valves, fire hydrants, and manholes. The issue

with exporting these files from AutoCAD is that it created many inconsistencies in the data which were seen while viewing them in ArcGIS. The main problem was that many of the polylines were not snapped together. Within ArcGIS Pro 2.5, features must be snapped together for the program to recognize them as being connected. Since there were so many line features that were not snapped together, the system was broken into many pieces.

These files were rendered unusable for any further analysis in ArcGIS Pro until they were fully repaired. The first step in fixing these systems was to utilize the topology toolset. These tools are convenient when it comes to locating and correcting many similar errors that exist throughout a dataset. This method is more efficient than manually searching the data for inconsistencies, especially when dealing with over 2600 line segments.

Next, the topology tools were programmed to search for dangles. A dangle occurs when the endpoint of a polyline is not snapped to any other feature, and therefore, leads to breaks in the system, which are shown in Figure 2. After running this tool, the dangles in the system were highlighted, however, not all of these were erroneous. Dangles that were present at the end of lines which led to fire hydrants or buildings could be ignored, because they are snapped to features that exist outside of this shapefile. A majority of the problematic dangles existed less than two feet from the point or line segment that they were supposed to be connected to. With this in mind, every dangle was selected and the topology tool was programmed to snap these lines to the nearest feature, as long as it was less than two feet away. This ensured that only the flawed dangles were edited, while the rest of the system remained unchanged.

After this was completed, there were still dangles that existed at distances greater than two feet from the nearest feature, and these had to be fixed manually. Using the topology tool to

automatically correct dangles with large gaps results in a higher risk of them being snapped to the wrong spot in the system. This was performed manually to minimize that risk.

Once the reconstruction of these systems was completed, they were deemed adequate to be exported as their own network datasets. By doing so, the systems were transformed from a collection of polylines into a single entity. The dataset for the sanitary system was exported into a utility network within ArcGIS Pro 2.5, but more information was required to perform any further analysis. On the other hand, the potable water system was brought into the ArcGIS Network Analyst extension, which contains a variety of tools to evaluate the system.

The tool utilized for the purposes of this project was the Find Closest Facilities tool, which locates nearby “facilities” based on the location of an “incident.” In this case, the valves and buildings were input as the facilities while a break in the main was input as the incident. When a main break occurs at BNL, its position can be indicated on the map, and the options for this tool can be set to locate a certain number of the nearest valves and buildings. After the tool is run, it will highlight these points and display the route that the water will take in order to reach them, which is shown in Figure 3.

B. Underground injection controls

Looking for inconsistencies throughout the data for UICs at BNL required comparing records from the current AutoCAD map, ArcGIS shapefiles, the most recent UIC Inventory Sheet (from 2011), and a map created by P.W. Grosser after the laboratory was surveyed in 1999. The data from all these sources was compiled within an Excel spreadsheet, which made it easier to identify differences or missing features. Ultimately, any deviations were noted and they will need to be checked manually, or by locating new data sources in the future.

III. RESULTS

A. Potable and sanitary systems

In the end, both utility systems were converted into network datasets within ArcGIS Pro 2.5. This means they are no longer just a collection of points and lines, but rather complete systems that can now be analyzed and exploited in a variety of ways. The other goal this accomplishes is having these systems in a program where all their attribute data can be stored. If there is a break in the portable water main, this location can now be entered into Network Analyst, and the Find Closest Facilities can be utilized to identify the valves and buildings that need to be closed and tested.

B. Underground injection controls

A total of 27 UICs were identified at BNL that had conflicted data across all the sources that were compared, and therefore deemed inaccurate. A list of all these features was compiled and their position/current operating state will be verified manually in the field or by using other existing data sources.

IV. DISCUSSION

The network datasets that were created in ArcGIS Pro 2.5 from the sanitary and potable utility data will be valuable to anyone at BNL. The proper maintenance of these systems is necessary to ensure that there is clean water and functioning waste disposal where it is needed onsite. Being able to evaluate these systems in depth will allow issues to be resolved at quicker rates, and help predict future maintenance needs. This project was aimed at handling breaks in the potable water mains, however, different criteria can be entered in ArcGIS Pro to solve a variety of problems. Ultimately, analyzing these systems will improve the health and safety of those onsite at BNL.

The other main benefit of storing these systems in ArcGIS is the vast amount of data that can be stored along with them, like that shown in Figure 4. As seen with the UIC data, there does not exist a comprehensive source where all necessary information can be located, and this will both waste time and induce complications in the future. Efficiency will be greatly increased if all relevant data for each of the utility systems is compiled within the maps and attribute tables of ArcGIS. This will save time and prevent inaccuracies while also making it evident when data is missing from the current records, helping the lab immensely.

The steps taken throughout this project are critical because they can be carried out using files from any of the utility systems currently stored within AutoCAD. If this same procedure is executed, any of the utility systems can be reconstructed as network datasets in ArcGIS, while also having all their data in a readily accessible location. In an ideal future, these systems will all be stored within ArcGIS, where they can be analyzed individually, or even as a group.

V. REFERENCES

ESRI 2018. ArcGIS Pro: Release 2.5. Redlands, CA: Environmental Systems Research Institute.
Autodesk 2020. *AutoCAD Map 2015*. San Rafael, California: Autodesk

VI. ACKNOWLEDGEMENTS

Support for this project was provided in part by the U.S. Department of Energy, Office of Science, Office of Workforce Development for Teachers and Scientists (WDTS) under the Science Undergraduate Laboratory Internships Program (SULI). I would also like to thank Jennifer Higbie for her continuous guidance and assistance as I completed this project.

VII. FIGURES



Figure 1. A main break at BNL in the summer of 2019. These happen frequently onsite which is why it's important to know how to properly handle them.

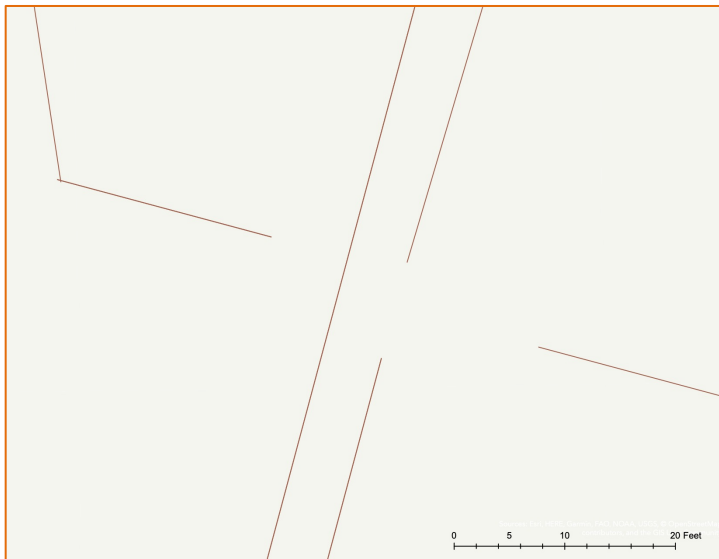


Figure 2. A cropped image of dangles that existed in the potable pipeline shapefile prior to its repair. Some dangles are up to fifteen feet away from the nearest line, while others are only a couple of inches. Regardless of the distance, these prevent the system from being contiguous, and need to be handled before a network dataset can be created.

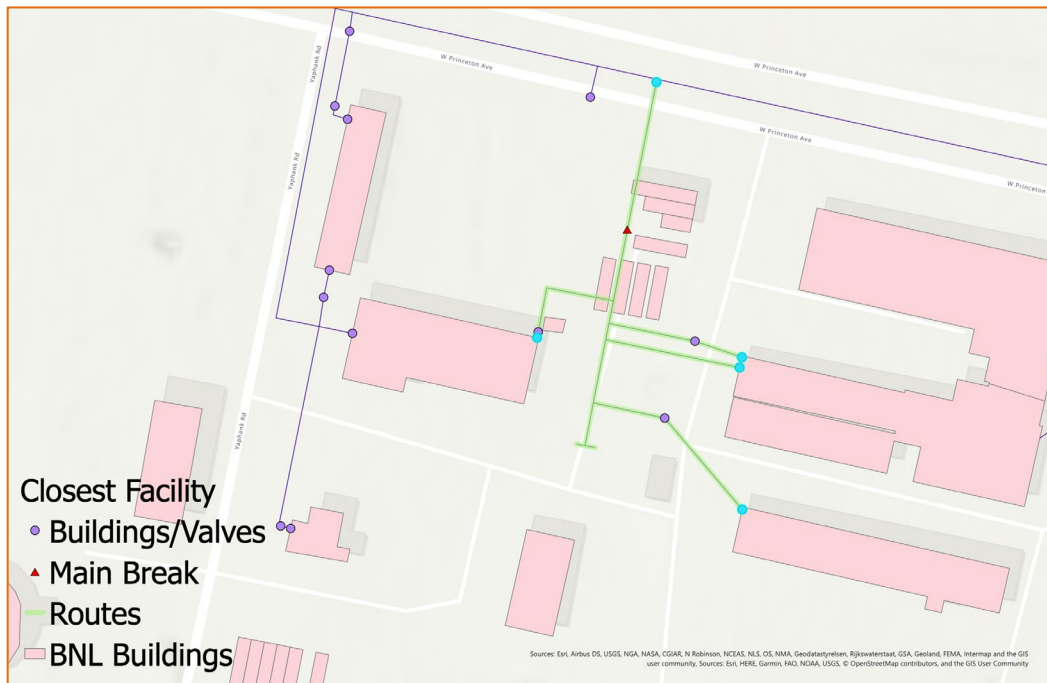


Figure 3. A demonstration of what can be performed using Network Analyst and the potable water system. Shown above is the result of placing an “incident,” or main break, on the line. After this is run, the program will highlight the valves that need to be closed to isolate the break as well as the surrounding buildings that should have their water tested afterward.

FID	25
UICNO	1007B-DW-1
WELL_92	1007B-DW-02
BLDG_NO	1007B
MAP_NO	44
STAT_1992	Active
TYP	1
EPA_CODE	5W20
DSCHG_HST	Stormwater
STAT_1999	Active
FUT_STAT	Permitted
STR_DIAM	8.00
STR_DPTH	6.25
SOURCE	A
TOP_DPTH	6.25
MANWAY	NA
RIM_ELEV	65.8
NO_INLT	1
INLET_NO	
PIPE_ORG	Tunnel Floor Drain
DIAM_FR	6"
MAT_FR	NA
NO_OUTL	NA
OUTL_NO	NA
DSCHG_TO	NA
DIAM_TO	NA
MAT_TO	D.I.
SP_ID	4967
SOURCETHM	uic_pts.shp
X_COORD	1293880.74002
Y_COORD	261952.3924
GRID_ID	44

Figure 4. A list of the data attributed to one of the UICs at BNL. This is a great example of the data storage that is capable within ArcGIS, and how it allows for quicker and simpler access.

A novel factorization algorithm for Rivest-Shamir-Adleman composites: algorithmic entropy reduction in sequenced binary quadratic forms

Emma Ryan, Biology Department, Adelphi University, Garden City, NY 11530

Alpha Bah, Engineering Department, Hostos Community College, Bronx NY 10451

David Biersach, Information Technology Division, Brookhaven National Laboratory, Upton, NY 11973

Abstract

The security of modern data transmissions, including e-commerce transactions, online private correspondences, and other secure web server traffic, is contingent on the Rivest-Shamir-Adleman (RSA) cryptography algorithm's exploitation of the inherent difficulty of resolving a large composite number into its factors using classical computing algorithms. Under this cryptosystem, encrypted communications (ciphertext) are easily generated using a public key, but may only be decrypted by the intended recipient with the requisite complementary private key (the RSA problem). As most available sieving algorithms approach the RSA composite integer as a discrete, atomic object, the thermodynamics-informed perspective of the algorithmic entropy reduction in sequenced binary quadratic forms (AERISBQ) algorithm, which seeks to reverse the gain in entropy (loss of information) that occurs during the multiplicative RSA composite generation, represents an attractive alternative to the RSA problem.

The AERISBQ algorithm attempts to factor an RSA composite (N) bitwise in a series of four-step rounds starting from its rightmost, least significant bit position by expressing each possible bit permutation for its factors (p and q) for the corresponding next most significant bit position as a binary quadratic form (BQF) and applying a series of evolving Diophantine equations. BQFs for which no integer solutions exist are then trivially eliminated, while those that survive are used as "parents" from which the next

bit position's BQFs are calculated (satisfiability problem), with this process occurring until the values of p and q are determined. Our objective in this research project is to implement a working proof of concept of the AERISBQ algorithm, as any insights arising from the resulting algorithmic framework could be pivotal for strengthening RSA security and for future AERISBQ implementations in quantum computing environments better able to address its satisfiability problem. It was determined that the AERISBQ algorithm is most efficacious in factoring composites whose constituent factors possess a series of contiguous 0s in the righthand side or 1s in the lefthand side of their binary expansions, and least efficacious for those with the converse.

I. Introduction

The RSA cryptographic algorithm is one of the most heavily employed cryptosystems on the worldwide web, utilized in the encryption of confidential information for activities ranging from e-commerce transactions to private messaging correspondences. As with the majority of other contemporary asymmetric (public key) encryption schemes, its currently secure posture is a consequence of both its inherent nature as a “trap-door” function (a function that is computationally trivial in one direction but challenging in the inverse without the knowledge of special information) and the fact that, as of this writing, no efficient deciphering mechanism has been discerned. Under the RSA cryptosystem, a public key comprised of two values (N , e) is used to encrypt a message (m) into its corresponding ciphertext (c); the complementary private key (d), whose value is known only by the intended recipient of the message, is then used to decipher c into the original m . These processes of key generation, encryption, and decryption, as detailed in Figure 1, are achieved through the use of elementary modular arithmetic and Euler’s totient (represented by $\phi(n)$, which returns the count of positive integers less than an indicated integer n that are coprime to it).¹ First, two large coprime integers p and q are selected and multiplied together, their product furnishing the former half of the public key (current encryption standards indicate that a 3072-bit N value is sufficiently secure).^{1,2} The value of $\phi(N)$, equivalent to the product of $(p - 1)$ and $(q - 1)$, is then determined, and a value is selected for e such that $2 < e < N$ and e is coprime to $\phi(N)$. The modular inverse for e modulo $\phi(N)$ (a value whose product when multiplied by e returns a remainder of 1 when divided by $\phi(N)$) is ultimately assigned to d . The encryption process for plaintext $m < N$ proceeds by exponentiating m to the value indicated by e and dividing it by N , with the remainder of this operation representing the c output; the

inverse conversion of c back into its corresponding plaintext is achieved using the previously described procedure, except c and d are used in place of m and e , respectively (Figure 1).¹

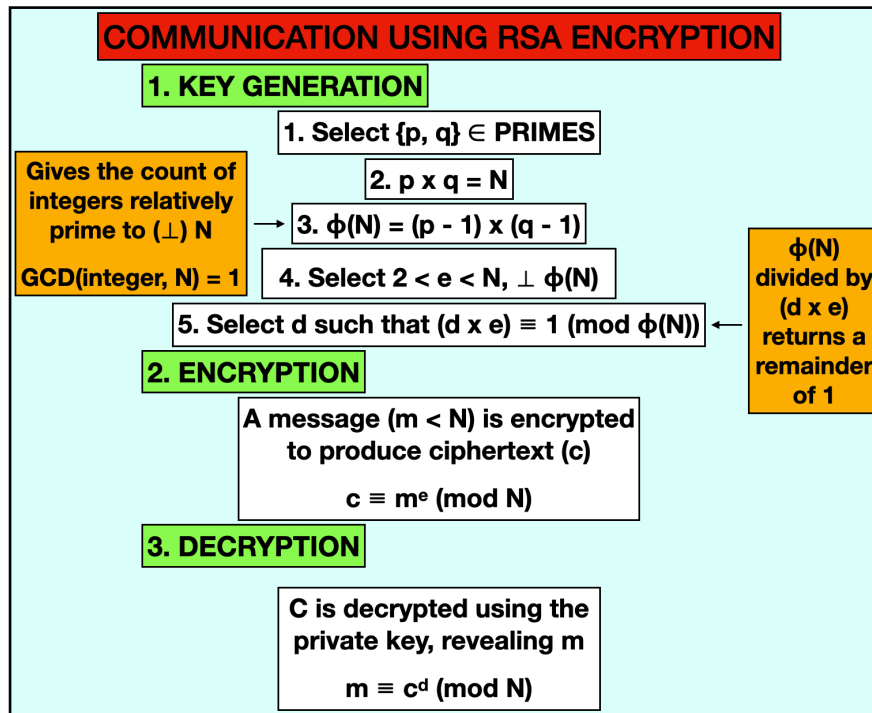


Figure 1: Processes of RSA key generation, encryption, and decryption.

Without access to the requisite private key, the task of decrypting c becomes as easy as the factorization of N into p and q , which, especially for composites of bit-lengths similar to those selected for RSA keys, is not a computationally insignificant task (the RSA problem). When two integers such as p and q are multiplied together to yield a composite (N), two critical bits of information are fundamentally lost, corresponding to a directly irreversible gain in entropy: the identities of p and q , and their arrangement during the operation (N is the product of either $p \times q$ or $q \times p$). Thus far, much to the benefit of RSA encryption, there exists no efficacious factorization algorithms for recovering these identities; one of the most optimal in a classical computing environment, the general number field sieve (GNFS), exhibits a super-polynomial run time, while the polynomial-time Shor’s algorithm is constrained by limitations in

current quantum computing hardware.^{1,3} The below described AERISBQ factorization algorithm diverges from the predominant logic exercised in traditional sieving algorithms (which approach N as a discrete, atomic object) by factoring N bitwise in four-step rounds starting from its rightmost, least significant bit position (position 0, or P_0) in an effort to reverse the gain in entropy accompanying composite generation (Figure 2A). It is thought that the two additional judicious bits of information furnished by the AERISBQ algorithm, the bit values of p and q represented by the ultimate “solution” binary quadratic form (BQF), in addition to the publicly known binary bits of N , can furnish enough information to factor N .⁴

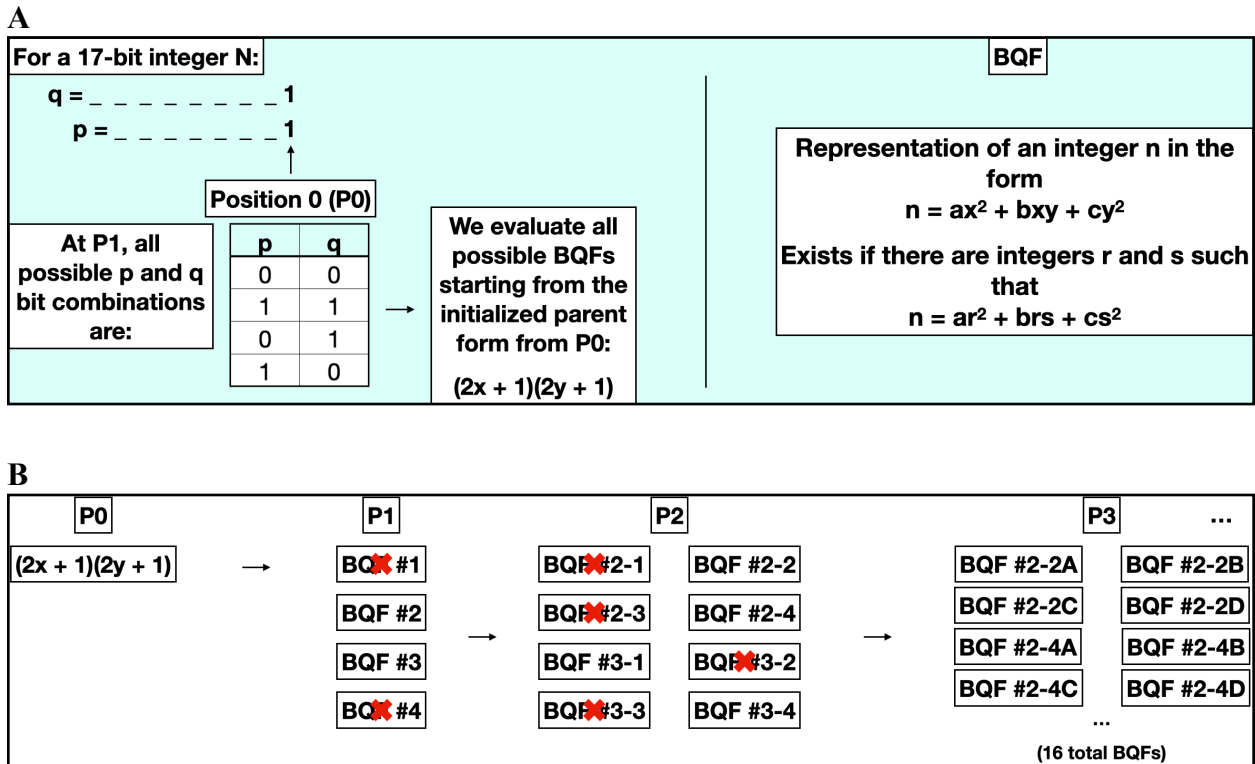


Figure 2A: Schematic of the AERISBQ algorithm’s basic rationale using a 17-bit N as an example;

B: Schematic of the process of BQF generation and elimination as the AERISBQ algorithm proceeds from one bit position of N to the next most significant bit position.

II. The Methodology of AERISBQ

The distinguishing feature of the AERISBQ algorithm—the expression of each possible bit permutation of p and q at a given bit position correspondent to the next most significant bit position of N as BQFs (Figure 2A)—allows for representations of integers that may be operated upon without the need to determine their exact integer solutions. The series of evolving Diophantine equations applied to each of the BQFs generated for a given bit position of N at the beginning of each round accomplish two dual objectives: the trivial rejection of BQFs for which no integer solutions exist (proof by contradiction), and the systemic reduction of the magnitude of n represented by the BQF. BQFs which survive trivial rejection are utilized as “parents” candidates from which the next bit position’s “children” BQFs are calculated, while those which are trivially rejected are eliminated (Figure 2B).

Within each round (where each round corresponds to one bit position), the coefficients obtained at the conclusion of each step are utilized as the starting coefficients for the succeeding step.

A. Step 1

Each of the four children BQFs are initially generated from each of the prior round’s parent BQFs according to the procedure illustrated in Figure 3, with the resultant A_1 coefficient corresponding to the binary representation of the bit position (starting with $A_1 = 1$ at position 0) and B_1 and C_1 coefficients to a value of either 0 or $2^{\text{bit position}}$. After expanding each of the children BQFs and isolating terms with A_1 on the lefthand side of the equation, the quotient from

the division of righthand side of the equation (terms without A_1) by A_1 is determined; BQFs for which this quotient is not an integer are then rejected, while those that survive progress to Step 2 with the new coefficients calculated as indicated by Figure 3.

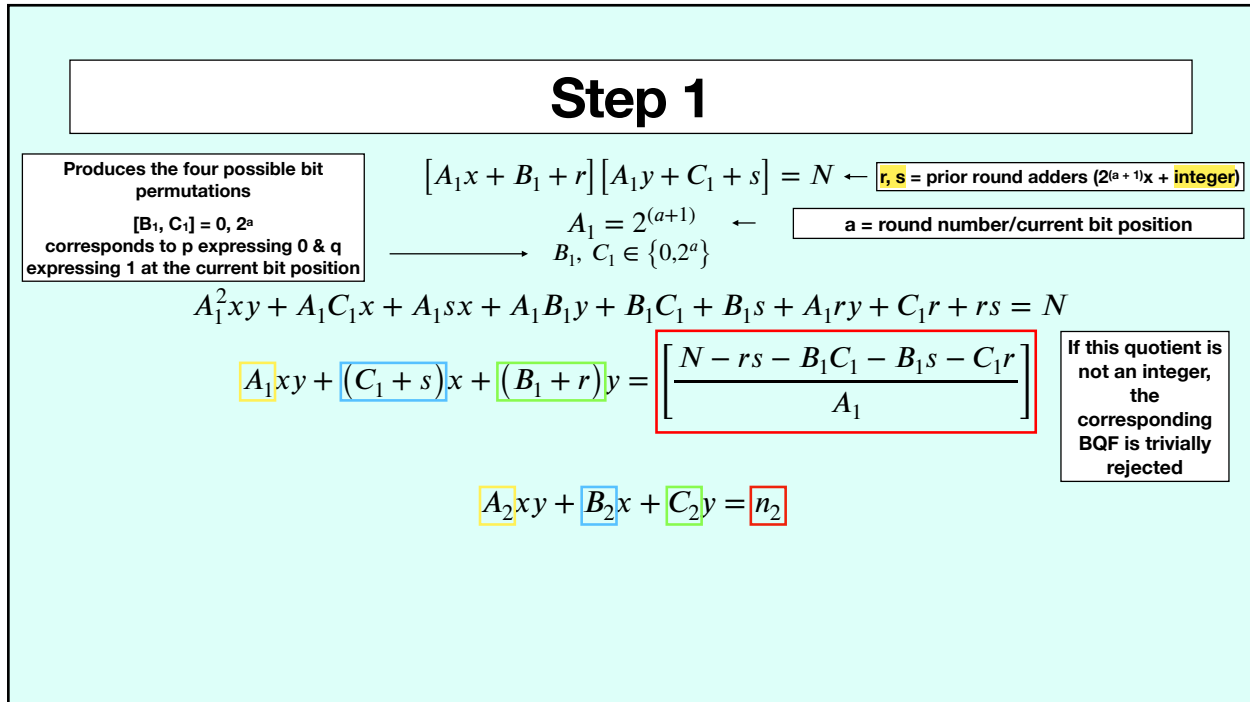


Figure 3: Step 1 of the AERISBQ algorithm; four child BQFs are spawned per parent BQF and immediately subjected to an eliminatory test.

B. Step 2: UV-Substitution

In order to convert the output of Step 1 from a non-quadratic form (which possesses a nonlinear xy term) into a true, linearly separable quadratic form, Step 2 relates x and y to the quantities u and v, where u is equivalent to the sum of x and y and v, the difference between y and x (Figure 4). This also procedure also constrains valid BQFs to those where u and v share the same parity (either both even or both odd), as p and q and known a priori to both be prime, and therefore odd, integers.

Step 2: UV-Substitution

$$A_2xy + B_2x + C_2y = n_2$$

$$x = \frac{v-u}{2} \quad y = \frac{v+u}{2}$$

Changes Step 1 output from a non-quadratic form into a true quadratic linear BQF

Half the distance between u & v

Average between u & v

$$A_2\left(\frac{v-u}{2}\right)\left(\frac{v+u}{2}\right) + B_2\left(\frac{v-u}{2}\right) + C_2\left(\frac{v+u}{2}\right) = n_2$$

$$A_2\left(\frac{v^2-u^2}{4}\right) + B_2\left(\frac{v-u}{2}\right) + C_2\left(\frac{v+u}{2}\right) = n_2$$

$$-A_2u^2 + A_2v^2 - 2(B_2 - C_2)u + 2(B_2 + C_2)v = 4n_2$$

$$A_3u^2 + B_3v^2 + C_3u + D_3v = n_3$$

Valid BQF requires u & v to have the same parity (both even or odd)

Figure 4: Step 2 of the AERISBQ algorithm (UV-substitution); the surviving BQF output from Step 1 is made into a linearly separable polynomial.

C. Step 3: L-Substitution

Step 3 exploits the fact that u and v must have the same parity in order to relate u to the difference between v and 2l, which itself is equivalent to the difference between v and u (Figure 5). This substitution ultimately enables the elimination of the y² term from Step 3’s output, as the sum of the A₃ and B₃ coefficients is always zero.

Step 3: L-Substitution

Since u & v must have same parity:
 $v - u = 2l$
 $\therefore u = v - 2l$

$$A_3u^2 + B_3v^2 + C_3u + D_3v = n_3$$

$$A_3(v - 2l)(v - 2l) + B_3v^2 + C_3(v - 2l) + D_3v = n_3$$

$$A_3[v^2 - 4lv + 4l^2] + B_3v^2 + C_3(v - 2l) + D_3v = n_3$$

$$A_3v^2 - 4A_3lv + 4A_3l^2 + B_3v^2 + C_3v - 2C_3l + D_3v = n_3$$

$$4A_3l^2 - 4A_3lv + [A_3 + B_3]v^2 - 2C_3l + [C_3 + D_3]v = n_3$$

Change variables: $x = l$; $y = v$

$(4A_3)x^2 - (4A_3)xy + [A_3 + B_3]y^2 - (2C_3)x + [C_3 + D_3]y = n_3$

$A_3 + B_3 = 0$
 \therefore no y^2 term in output

$A_4x^2 + B_4xy + C_4x + D_4y = n_4$

Figure 5: Step 3 of the AERISBQ algorithm (L-substitution); the y^2 term is eliminated from Stem 3's output.

D. Step 4: GCD Reduction

The removal of the y^2 term in Step 3 allows for the rearrangement of the x terms in the output to the righthand side of the equation in the ultimate step of the AERISBQ algorithm, Step 4 (Figure 6). If there exists a greatest common denominator (GCD) for the numerator terms (g), its value may be used to reduce the A_4 and C_4 coefficients in addition to the value of n represented by the BQF, compensating for the earlier increase in n's value that accompanied Step 2. At the conclusion of each round, after the application of Step 4 to all the valid children BQFs generated in Step 1, the divisibility of the factors represented by each BQF is checked by obtaining the quotient of N divided by the sum of $(A_1 + B_1 + r)$; if this quotient is an integer, the identity of q is determining by obtaining the quotient of N divided by the sum of $(A_1 + C_1 + s)$.

Step 4: GCD Reduction

$$A_4x^2 + B_4xy + C_4x + D_4y = n_4$$

$$B_4xy + D_4y = n_4 - A_4x^2 - C_4x$$

$$y = \left[\frac{n_4 - A_4x^2 - C_4x}{B_4x + D_4} \right]$$

$$g = \text{GCD}(n_4, |A_4|, |C_4|)$$

$$y \in \mathbb{Z}^+; p = B_4x + D_4, \dagger g$$

∴ $A_4, C_4,$ & n_4 , may be reduced by g

$$n_5 = \frac{n_4}{g} \quad A_5 = \frac{A_4}{g} \quad C_5 = \frac{C_4}{g}$$

$$A_5x^2 + B_5xy + C_5x + D_5y = n_5$$

Figure 6: Step 4 of the AERISBQ algorithm (GCD reduction); the values of the A_4 and C_4 coefficients and n are reduced by their GCD.

III. A MATLAB Implementation of AERISBQ

In order to validate the logic of AERISBQ, I endeavored to construct an implementation of the algorithm using MATLAB (R2019b). The specialized computational environment and syntactical requirements of MATLAB, which diverges from those of other object-oriented languages such as Java and C++, provides the opportunity to examine AERISBQ and its output from a fundamentally different perspective. Both current and historical versions of the AERISBQ MATLAB implementation, including all appended commentary, is available for access at:

github.com/Emma-Ryan/BNL-Summer-2020/tree/master/AERISBQ

IV. Results

The AERISBQ algorithm was most efficient for the factorization of N values whose factors have a series of contiguous 0s in the righthand side or 1s in the lefthand side of their binary expansions (Table 1), and least efficient for those whose factors have a series of contiguous 1s in the righthand side and 0s in the lefthand side (Table 2).

Table 1: Composites (N) most efficiently factored by AERISBQ, where efficiency is calculated as $[\log(N)/\log(\# \text{ of BQFs})]$; credit: D. Biersach.

N	p	q	# of BQFs	Efficiency	p Base2	q Base2
1 528 003	769	1987	130	2.9208	1100000001	11111000011
1 631 419	1019	1601	133	2.92067	1111111011	11001000001
1 521 851	769	1979	130	2.91997	1100000001	11110111011
1 500 319	769	1951	130	2.91705	1100000001	11110011111
1 634 621	1021	1601	134	2.91664	1111111101	11001000001
1 924 891	1019	1889	142	2.91574	1111111011	11101100001
1 621 813	1013	1601	134	2.91504	1111110101	11001000001
1 586 591	991	1601	133	2.91498	1111011111	11001000001
1 484 939	769	1931	130	2.91494	1100000001	11110001011
1 517 237	769	1973	131	2.9148	1100000001	111101110101
1 838 491	929	1979	140	2.91476	1110100001	11110111011
1 573 783	983	1601	133	2.91332	1111010111	11001000001
1 466 483	769	1907	130	2.91237	1100000001	11101110011
1 498 781	769	1949	131	2.9123	1100000001	11110011101
1 928 669	1021	1889	143	2.91205	1111111101	11101100001
1 812 479	929	1951	140	2.91188	1110100001	11110011111
1 596 197	997	1601	134	2.91179	1111100101	11001000001
1 554 571	971	1601	133	2.91082	1111001011	11001000001
1 486 477	769	1933	131	2.91061	1100000001	11110001101
1 913 557	1013	1889	143	2.91047	1111110101	11101100001

Table 2: Most frequent factors of composites (N) least efficiently factored by AERISBQ; credit: D. Biersach.

p or q	Binary Expansion
1051	10000011011
1087	10000111111
1039	10000001111
1103	10001001111
1151	10001111111
1063	10000100111
1069	10000101101
1117	10001011101
1031	10000000111
1231	10011001111

V. Conclusions and Future Work

The efficiency data for the AERISBQ algorithm obtained for different semiprime composites suggests that the posture of RSA security against attacks from AERSIBQ and AERISBQ-like algorithms may be improved through the selection of factors with a series of contiguous 1s in the righthand side and 0s in the lefthand side for the construction of key values. Although currently only at four, the AERISBQ algorithm may be enhanced by the development of further steps, particularly one that utilizes a prime “witness” capable of proving whether or not a given BQF is not solvable in integers; if a given BQF were not solvable in integers, the sum of the values of each lefthand side term modulo p would never be equivalent to that of each right side term modulo p. In addition, the employment of a quantum computing environment, which could give the probabilities corresponding to either outcome of the satisfiability problem posed by AERISBQ, could potentially enable RSA factorization using significantly less bits than demanded by Shor’s algorithm.³

VI. Acknowledgements

I would like to thank my mentor, Dr. David Biersach, for the opportunity to work on this project in addition to his instruction and guidance in all things coding, mathematical, and professional. Additional thanks to my colleague Alpha, whose collaboration provided me with invaluable insight, and Professor Matthew Wright at Adelphi University for his wealth of MATLAB knowledge. This project was possible through the generosity of the United States Department of Energy (DOE) Office of Science Workforce Development for Teachers and Scientists (WDTS) Summer Undergraduate Laboratory Internship (SULI) program and Brookhaven National Laboratory (BNL).

VII. References

¹E Milanov, "The RSA algorithm," (*online*) https://sites.math.washington.edu/~morrow/336_09/papers/Yevgeny.pdf.

²E Barker, W Barker, W Burr, W Polk, and M Smid, "Recommendation for key management part 1: General (revision 3)," Federal Information Processing Standards (FIPS) Special Publications (SP) 800-57 (2012).

³K Bimpikis and J Ragesh, "Modern factoring algorithms," (*online*) <http://www.cs.columbia.edu/~rjaiswal/factoring-survey.pdf>.

⁴F Lemmermeyer, "Binary quadratic forms: an elementary approach to the arithmetic of elliptic and hyperelliptic curves," (*unpublished notes*).

Photo recognition for 4-poster tick management system[®]

Coral Salort¹, Timothy Green²

¹University of Puerto Rico, Río Piedras Campus, San Juan PR 00925, ²Environmental Protection Division, Upton, NY 11973

ABSTRACT: The 4-Poster Tick Management System[®] works as a feeding station for deer that mitigates tick dispersion by forcing deer to make contact with rollers containing a tickicide when trying to eat. Time lapse photography is used to monitor deer visitation, producing about 1 million images per year which must be manually classified by researchers. The successful implementation of MLWIC: Machine Learning for Wildlife Image Classification in R package by Mikey Tabak could provide a less time-consuming and unsupervised data analysis. At the moment, the package has been successfully installed and is in the testing stage. Although the first step is to enable the package to identify presence or absence of deer, the end goal is to identify most organisms in the pictures. Monitoring deer visitation rates to demonstrate the efficiency of the bait stations is crucial to control the widespread distribution of ticks thus diminishing Lyme and other tick-borne disease in the laboratory area. This project has sharpened my skills with R and showed me the importance of stopping to analyze the problem before tackling it. In addition, I gained experience interacting with GitHub.

INTRODUCTION

Controlling the tick population in Long Island is a serious matter. On Brookhaven National Laboratory (BNL), the Environmental Protection Division set up fourteen *4-Poster Tick Management System*[®] in 2013^[2] and has been monitoring the efficiency

of the system. Each station is monitored by a camera trap. This method produces about a million pictures a year that the scientist had to manually sort into one of these five categories: deer, turkey, raccoon, no animals or other animals. This project is meant to find a solution to ease the hand work for the researchers.

A potential method is using a Computer Vision code that could sort the images automatically into one of the above-mentioned categories confidently with little or no help from researchers. In 2018, Tabak, M. *et. al* presented the MLWIC R package (Machine Learning for Wildlife Image Classification)^[1]. Internally, this package uses the Tensorflow framework in which they trained a ResNet-18 convolutional neural network to identify certain species with up to 97.6% accuracy. MLWIC is free and available on GitHub.

This project seeks to habilitate this code for the computer located at the research laboratory. This involves installing it, writing up a detailed easy to follow guide and testing the efficiency and viability of using it. This involves the possibility of training a model with the pictures gathered throughout the years thanks to the camera traps.

OBJECTIVES

Testing viability of MLWIC R package for the experiment is the main goal. Use MLWIC for classification with the pre-trained model and/or training a model with the data gathered throughout the years. Creating detailed guides with information regarding installation and preparation prior to using the package using MacOS and Windows.

METHODS

For each of the processes listed below, a detailed guide was written to guide the user through each step. These guides are appended to this document.

MLWIC Installation

The [MLWIC Package](#) is completely free and accessible on Github. Unfortunately, the instructions provided in the README are missing some important details that are key to a successful installation. To start, the

instructions in the README help, but aren't sufficient, for MacOS. There's another guide linked in the README targeting Windows users.

The first installation attempt was on a MacBook Air running Catalina. Following the steps including installing Anaconda, creating an environment including R and Python 3.6 and launching R from there. Instructions don't direct the user to install Devtools and Tensorflow 1.14; these have to be installed for the package to work. The location of Anaconda has to be noted to run any command.

The Windows installation following the accompanying guide went by smoothly. It specifies the version of Anaconda to be installed and some specifics of the environment setup.

MLWIC Preparation

To put the R package to use, there's some preparation needed to run the `classify()` and `train()` commands. The requirements are to have a folder called *images* containing all the images to be used, the *L1* folder (provided in the Github repository) and a two-column CSV with certain specifications. In both cases, the first column should contain all the names of the images inside the *images* folder and labels on the second. The names have to be **unique**.

Since the images are directly imported from the different cameras' SD cards, some of them happen to have the same name. To address this issue, a function called `unique.Naming()` was written to rename each file in a unique manner using the 4-poster station, the date and a computer-generated index (eg. "4P-2_05062014_134.JPG").

Constructing the CSV for classification is simple since the labels on the second column aren't meaningful so it can be filled with zeroes. On the other hand, labels are crucial. It could be done manually, but for a large number of files it is preferable to run a script. The function `createCSV()` goes through the different 4-poster folders, can enter the date

folders and enters the folders containing the pictures identified by the folder names: No_Animal, Deer, Turkey, Raccoon, Other_Animal. Then it assigns all the pictures of each folder a label represented by numbers: 0, 1, 2, 3 and 4, respectively. To make things easier, this function can internally call the `unique.Naming()` function so everything is done automatically.

After the CSV is created, the end of line (EOL) has to be changed to Linux Linebreaks. This is solved by opening the CSV in Notepad++, going to “Edit” > “EOL Conversion” > “Unix (LF)”. The CSV filename has to be changed depending of its for training or classifying, and also de operating system (check the appended guide). Finally, the README does suggest resizing the pictures to 256x256 pixels, but its optional.

Classifying with MLWIC

Once the preparation is ready, if done correctly, the classification process is just running one line of code:

```
classify(python_loc = pydir)
```

where `pydir` is the location of installation of Anaconda in your machine. To make the output reading friendly, run the function `make_output()` to produce a CSV with the results.

Training with MLWIC

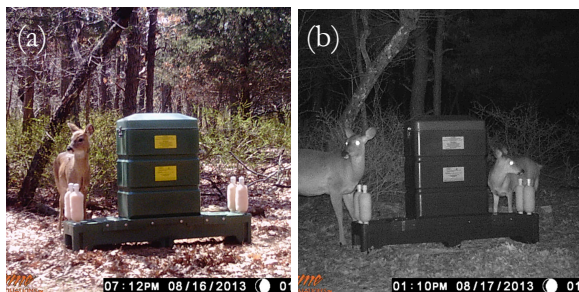


Figure 1: Two images taken on the 4P-2 station identified as containing deer. (a) was taken during the day and (b) during the night.

In contrast to the classification process, training takes more preparation effort, computational power and running time. Consider the use of GPU’s or clusters depending on the amount of annotated data.

Choosing the images to train the model is something to keep in mind. Images taken during daytime and nighttime should be considered (Figure 1). There should also be equal representation of each classification group (Figure 2), meaning there should be approximately a similar number of pictures from each group. Finally, there must be samples from all the above mentioned from each 4-poster station.



Figure 2: Images taken on the 4P-10 station where (a) has a turkey, (b) raccoons and (c) squirrels (other animals).

When the preparation is done, run the following command:

```
train(log_dir_train = model_loc,
      os = "Windows",
      delimiter = ",",
      num_classes = 5,
      python_loc = pydir,
      retrain = FALSE)
```

Where `model_loc` is where the user wants the training data to be stored and `pydir` is the location of installation of Anaconda in your machine. After the whole process is done, in order to use the newly trained model, call the `classify` function with an additional parameter: `log_dir = model_loc`.

DISCUSSION

After successfully installing the MLWIC R package an being able to run the `classify` function for the example provided on

Github, the same function was run over the freshly obtained data from the camera traps in the field. Running the pre-trained model didn't provide satisfactory results. The model was consistently identifying species of animals that aren't even found on site. This model was trained for more than 25 groups of animals, and the researchers are only looking to identify confidently between 5 classes: No_Animal, Deer, Turkey, Raccoon and Other_Animal. For this reason, it was decided to train a model using the annotated data from previous years.

After 3 weeks of preparing the data for training, writing and debugging the R scripts for the `unique.Naming()` and `createCSV()` functions, the training function was going to take up to three weeks to run. For this reason, it was decided to document all the preparation enough so someone can pick up where it was left off.

NEXT STEPS

This project leaves some work for future researchers. It was possible to install and run both on Windows and MacOS but installing MLWIC on Linux and writing an installation guide for future users is still an undone task. Also, training the model using the camera trap images from previous years, preferably with a computer with multiple GPU's or a cluster. After this is done, it would be helpful to write an R script to sort the classified images in folders named after the class they've been assigned to.

ACKNOWLEDGEMENTS

This project was supported in part by the U.S. Department of Energy, Office of Science, Office of Workforce Development for Teachers and Scientists (WDTS) under the Science Undergraduate Laboratory Internships Program (SULI). It was possible thanks to the support of Timothy Green and Jennifer Higbie from the Environmental Protection Division at Brookhaven National Laboratory.

REFERENCES

- [1] Gosselin, T., & Green, T. *The efficiency of 4-poster tick management stations on three tick species populations within Brookhaven National Laboratory.*
- [2] Tabak, M. A., Norouzzadeh, M. S., Wolfson, D. W., Sweeney, S. J., Vercauteren, K. C., Snow, N. P., . . . Miller, R. S. (2018). Machine learning to classify animal species in camera trap images: Applications in ecology. *Methods in Ecology and Evolution*, 10(4), 585-590. doi:10.1101/346809

APPENDIX A:

MLWIC: Machine Learning for Wildlife Image Classification in R (guide)

By: Coral Salort (csalortno@bnl.gov)

Installation Guide (on Windows)

This guide is being based on the [guide](#) provided by one of Mikey Tabak's contributors on the [MLWIC](#) GitHub repository.

1. Make sure you have R and RStudio installed. Otherwise, find it [here](#).
2. **Install Anaconda:** Installing the right version of Anaconda is very important. Instead of installing the latest version, follow [this link](#). Find the version that agrees with this information:

```
Anaconda3-5.2.0-Windows-x86_64.exe  
631.3M  
2018-05-30 13:04:18
```

TIP: Copy the .exe name, press `CTRL + F` and paste it. It'll show the one that we need. Conversely, if you follow the guide link, there's a direct link for the download there.

3. **Take note of the location of the install:** After the Anaconda window opens, accept Terms and Conditions, install for "Just Me" and record the location where the installation will occur. In my case, this is `C:\Users\csalortno\AppData\Local\Continuum\anaconda3`. Use recommended settings for the rest of the installation.
4. **Launch Anaconda Navigator:** Go to the Start Menu and find Anaconda Navigator in the app list. Launch it.
5. **Environment setup**
 1. Go to the "Environments" tab and make sure the only existing environment is `base(root)`. Delete any other environment that are unfamiliar to you.
 2. Using the search bar, search for `setuptools`, and click on the green square. If the

option "Mark for update" is available, select it and click "Apply" on the lower right.

3. Search for `tensorflow` and click on the green box. It'll become a downwards arrow. Click "Apply".

NOTE: This is what the guide says. For me it didn't work at first. I tried again after following the next step and it worked once. If it still doesn't work, keep going on with the process. An error may pop up when trying to run the `classify()` function. When it does, try again and that's when it worked for me.

4. Search for the package `cuda`. Single-click the small green box with the checkmark inside it and choose "Mark for specific version installation". Choose version 6.0. This may prompt you to install tensorflow 1.11 instead of a later version. Accept this and click "Apply". (Copy and paste from guide)

6. **Install and launch R within the Anaconda Environment:** Having the `base(root)` environment active (there's a green vertical bar on the left of the environment tab), go back to the "Home" tab and click "Install" RStudio. When its done, launch it.
7. **Download L1 Folder:** Download the whole zip folder [here](#). I suggest you make a Test folder folder and locate it on the Desktop and put the extracted L1 folder in here. (Remember to note the location of the L1 folder). This step can be done at the beginning but I'm following the guide.
8. **Download example folder:** Go [here](#) and download the example provided. This will serve as a way to make sure everything is working correctly. Locate the "images" folder in the same folder as the L1 folder (Test folder). **Rename the image_labels.csv file to data_info.csv and place it inside the "L1" folder.** The MLWIC function classify command attempts to find this file and copy it into the "L1" folder, but this has met with mixed success on Windows computers; so, it's best to name and locate the file as the classify command expects. (Copy and pasted from guide). On the other hand, I had success with leaving it outside the L1 folder, in the Test folder.
9. **On RStudio:** Let the Anaconda location (noted on step 3) be represented as `conda_path` in this example and `wdir` is where the Test folder is located.

```
# Location of Anaconda (noted on step 3)
conda_path <- "C:/Users/csalortno/AppData/Local/Continuum/anaconda3"
wdir <- "C:/Users/csalortno/Desktop/Test"
```

```
install.packages("devtools") # Install devtools
devtools::install_github("mikeyEcology/MLWIC") # Install MLWIC
setwd(wdir) # Set working directory
setup(python_loc = conda_path)
classify(python_loc = conda_path)
```

Installation Guide (on Mac)

1. **Install Anaconda.** Use [this](#) guide to take you through the process.
2. **Launch Anaconda.** Go to the Environments tab and click on Create. Include the R and Python 3.6 packages. Then, go to the Home tab and Launch RStudio.
3. **Install the Devtools package.** Run the following command:

```
install.packages("devtools")
```

4. **Install the MLWIC packages from GitHub.**

```
devtools::install_github("mikeyEcology/MLWIC")
```

When asked if you want to update the packages, press 1 and [ENTER]. This will install all the updates.

5. **Run the following commands:**

```
library(MLWIC)
setup()
```

6. **Download the L1 folder from [this link](#)** . It's crucial that this folder is located in the same folder as your "images" folder and a double column CSV file named "image_labels.csv" (first column includes the filename of each image and the second will be the Class ID). For the sake of testing our installation, download [this folder](#) (provided by the author) and use these images and CSV to run the functions. (Take time to look at the CSV folder provided in the example and use it as template for later). **It is recommended to create a folder with just those 3 elements: L1 folder, the images folder and the CSV. Take note of the directory.**

7. **Set your working directory in RStudio.** Set the location of the folder of the previous step as your working directory by running this command:

```
setwd(path)
```

In my case, I named the folder "Test" and located it in my Desktop for easy access. I would run `setwd("~/Desktop/Test")` .

8. **Get the directory where Python is.** Type and run `system("which python")` . This returns the absolute path. In my case it returns `/Users/coralsalort/Library/r-miniconda/envs/r-reticulate/bin/python` . The way we'll record this is substituting the user directory by "~" and disregarding the word "python". In my example, it would be `~/Library/r-miniconda/envs/r-reticulate/bin/` . Set a variable called `pydir` with this string of information. (eg. `pydir <-"~/Library/r-miniconda/envs/r-reticulate/bin/"`)

9. **Install Tensorflow 1.14.** Type and run `system("pip install tensorflow==1.14")` .

10. **Run the `classify()` function.** Run the following command:

```
classify(python_loc = pydir)
# REMINDER: `pydir` is the variable we created on step 8
```

11. Use the `make_output()` function to a CSV with the prediction results.

Function `classify()` in Windows

You can follow steps 7-9 from the Windows Installation Guide, and replace the images and

your images and create a new CSV.

What you'll need:

1. A folder with images with **unique** names
2. CSV in Unix Linebreaks with all image names on the first column and zeroes on the second column (`data_info.csv`)
3. L1 folder
4. L1 and images folders in the same directory, CSV inside L1 folder.

Instructions

1. I created an R script containing 2 functions: `createCSV()` and `unique.Naming()` that can be found by the end of this document or accompanying it under the names `createCSV.R` and `unique.Naming.R`. Find them and copy the text and paste it in the RStudio console one at a time.
2. Set your working directory to be the images folder. (`setwd()` function)
3. Run the following command for each 4-Poster: `createCSV(training = FALSE, renaming = TRUE, image_ext = "JPG", poster = "4P-XX", date = "DDMMYY", rep = TRUE)` where XX is the number of the 4-poster (2, 3, 4A, 4B...) and the date (MMDDYYYY).
4. The resulting CSV won't be on Unix Linebreaks. To convert the encoding, launch Notepad++ (not to be confused with Notepad). Go to the Edit tab, look for encoding and chose the Unix option.
5. Finally, the CSV is ready. Put it inside the L1 folder.
6. Make sure the folder with all the renamed images is named **images** and is located in the same directory as the L1 folder. Set this as your working directory using the `setwd()` function.
7. Run the following command:

```
classify(python_loc = pydir)
# REMINDER: `pydir` is the variable we created on step 8
```

8. Use the `make_output()` function to a CSV with the prediction results.

Function `train()` in Windows

What you'll need:

1. A folder with images with **unique** names
2. CSV in Unix Linebreaks with all image names on the first column and **meaningful labels** on the second column (`data_info_train.csv`)
3. L1 folder
4. `L1` and `images` folders in the same directory, CSV inside L1 folder.
5. (Worked for me) Train locally, not on the drive.

Instructions

Create CSV

1. Have your files organized in the following manner:
 - Have all your 4P folders in one place.
 - Inside the 4P folders, the folders with dates
 - Inside date folders, have the animal folders
 - Inside the animal folders, all the images from that particular group.
2. Having your directory set to where all the 4P folders are, call the function `createCSV()` to create the CSV.
 - To give unique names to images in the process:

```
createCSV(training = TRUE, renaming = TRUE)

# Copies images to images folder with unique names (located in the working
directory)
# Creates CSV with meaningful labels (located in the working directory)
```

- If images have unique names, run the same command with `renaming = FALSE`.
 - **NOTE:** You can't create a CSV from the images folder because the ID is lost in the process of renaming. To keep the ID in the name you can go through the code of `createCSV()` and find where `unique.Naming()` is called and replace it with:

```
unique.Naming(save_path = redir_path, ID_4P = folder, date = nfolder, ext =
"JPG", low = lower, ret = TRUE, replace = rep, ID = TRUE, class = afolder)
```

- Script for creating a CSV parting from this point is still missing, but shouldn't be too difficult.
3. The resulting CSV won't be on Unix Linebreaks. To convert the encoding, launch Notepad++ (not to be confused with Notepad). Go to the Edit tab, look for encoding and chose the Unix option.
 4. Finally, the CSV is ready. Put it inside the L1 folder.

Training the model

- I had very little time to experiment with this function. Making sure the working directory has the `images` folder, `L1` folder. I created another folder named `Model` to store the model data.
- What worked for me was running the following command:

```
train(log_dir_train = "C:/Users/csalortno/Desktop/Training/Model/", os =  
"Windows", delimiter = ",", python_loc = "C:/Users/csalortno/AppData/Local/  
Continuum/anaconda3/", retrain = FALSE)
```

Analysis of Charge Diffusion in EMCCD

John Santucci¹ and Ivan Kotov²

¹Department of Physics and Astronomy, Stony Brook University, Stony Brook, NY 11794

²Instrumentation Division, Brookhaven National Laboratory, Upton, NY 11973

1 Abstract

My project was to analyze the charge distribution recorded by Electron Multiplying Charge Coupled Devices, EMCCD. The purpose of this analysis was to be able to more accurately pinpoint the impact coordinates of incident photons. Another analysis task is to learn how to mitigate noise better. The EMCCD were used in the NSLS-II Soft Inelastic X-ray Scattering, SIX beamline. The NSLS-II is a 3GeV electron storage ring that uses synchrotron radiation method to produce a bright beam of photons with wide energy range. It provides bright x-rays for an assortment of research studies. The main focus is to apply the most efficient modeling of the charge distribution. This involved considering the drift and diffusion of charge carriers. A better understanding of the charge distribution allows for more accurate coordinate measurements. This is necessary for understanding the physics involved in scattering experiments. This ties into the DOE's mission of keeping the US a global leader in the sciences. In researching this topic I have come to a better understanding of new types of physics analysis code, including fits files which are useful for understanding pixel based images, as well as more versatility with CERN ROOT. I also had to gain a better understanding of computer limits when dealing with very large/small and object oriented programming with C++.

2 Introduction

EMCCD are used to record x-rays scattered off experiment target. Incoming photons convert into electron-hole pairs. Electrons are collected under the EMCCD gates. EMCCD is an integrated circuit containing MOS structures. The SIX beam line uses two EMCCD for x-ray detection in the spectrometer arm. These EMCCD record a charge distribution when an x-ray hits them. While investigating this topic it was also beneficial to look into the various sources of noise and how to minimize error. The EMCCD are n-channel, partially depleted, back-illuminated devices with pixel size $16\mu m$. The total device thickness is approximately $14\mu m$. The first $8\mu m$ is the field free zone. The active imaging area is 1632×1608 pixels. There are 536 electron multiplication elements. The operating temperature of the device was $-110C$ and the readout speed was approximately 3 MHz [1]. The main sources of noise for the EMCCD are the signal fluctuations, dark current, electron multiplication, readout and deferred charge [1]. Other potential source of noise are light pollution, clock induced charge and correlation in the readout noise [1]. The electron multiplication reduces readout noise compared to normal CCD.

3 Data

Several sets of data were used from the SIX beam line. Scan S91914 is a set of 120 images for each EMCCD. Each channel represents one EMCCD. S91914 has incoming x-rays which can be seen in Fig. 1. On the left of Fig. 1 is the image, for channel 0, before base line subtraction is done. Base line subtraction is a method to remove offset from the data. Base line subtraction method from [2] was used. Fig 1. shows that low frequencies presented along the vertical direction are removed by the base line subtraction algorithm.

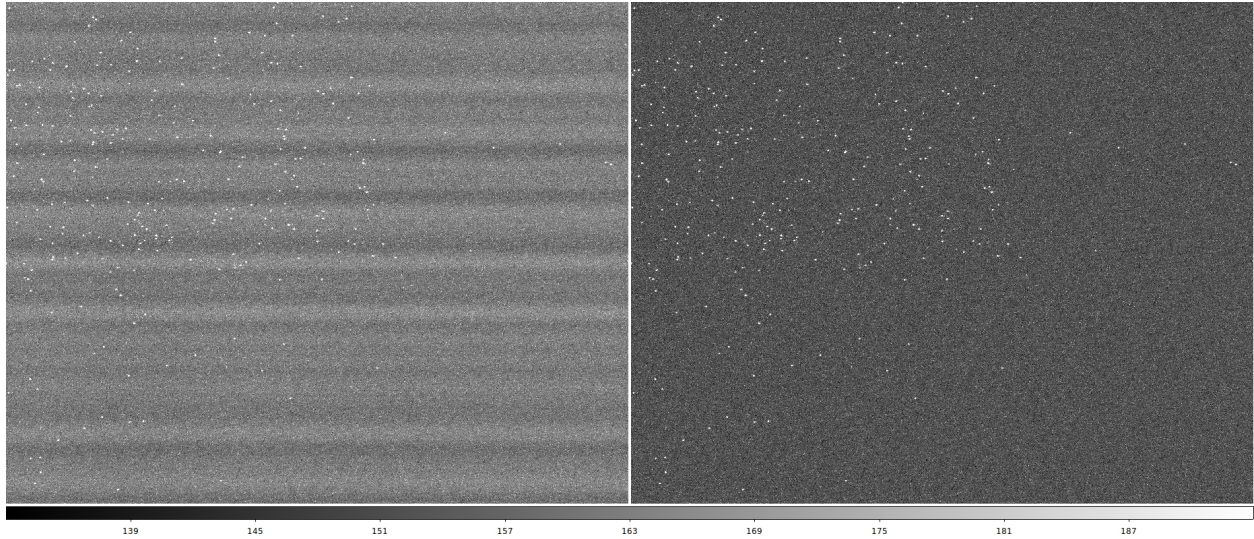


Figure 1: Channel 0 before (left) and after (right) base line subtraction is done

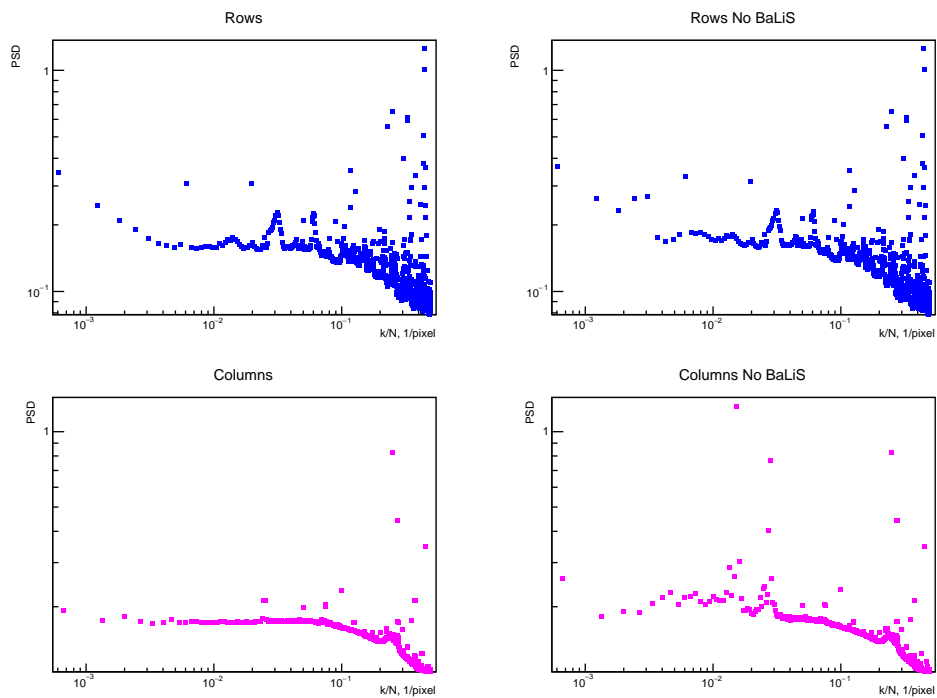


Figure 2: Fast Fourier Transform of the Data before (right) and after (left) base line subtraction in the first EMCCD

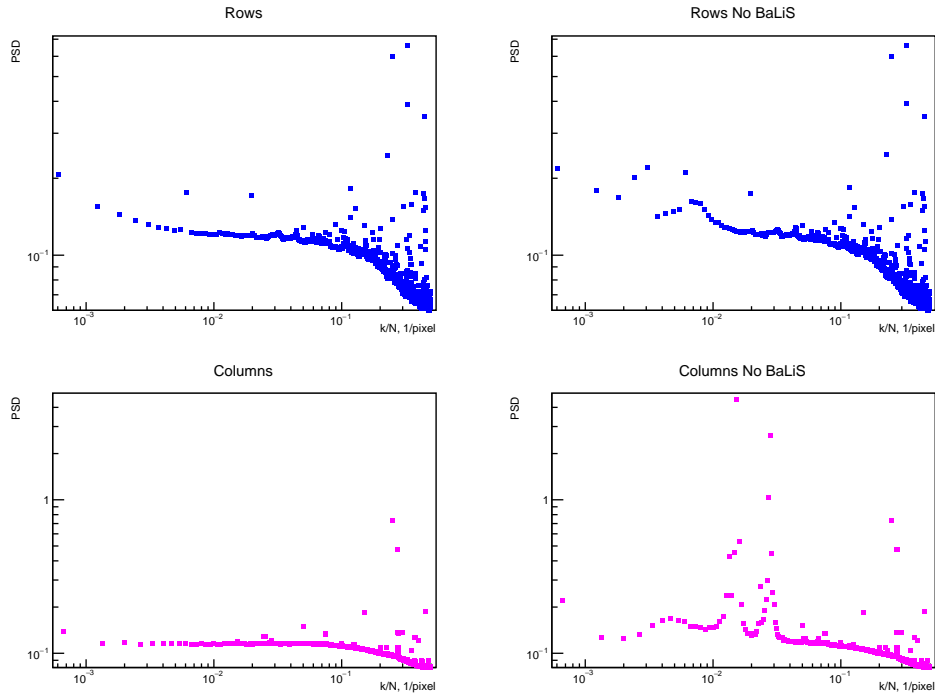


Figure 3: Fast Fourier Transform of the Data before (right) and after (left) base line subtraction in the second EMCCD

Fig. 2 and Fig. 3 shows the Power Spectral Density of the EMCCD images. The Fast Fourier Transform, FFT, was performed on rows, top plots, and columns, bottom plots. The package `fftw3` [3] was used to perform the FFT analysis on the data. The vertical axis is the Power Spectral Density, PSD. The two PSD peaks at 1.55×10^{-2} 1/pixel and 2.8×10^{-2} 1/pixel, in the columns are removed in base line subtraction. They are attributed to the low frequency noise and can be seen in Fig (1) as the periodic pattern that is removed by the base line subtraction algorithm.

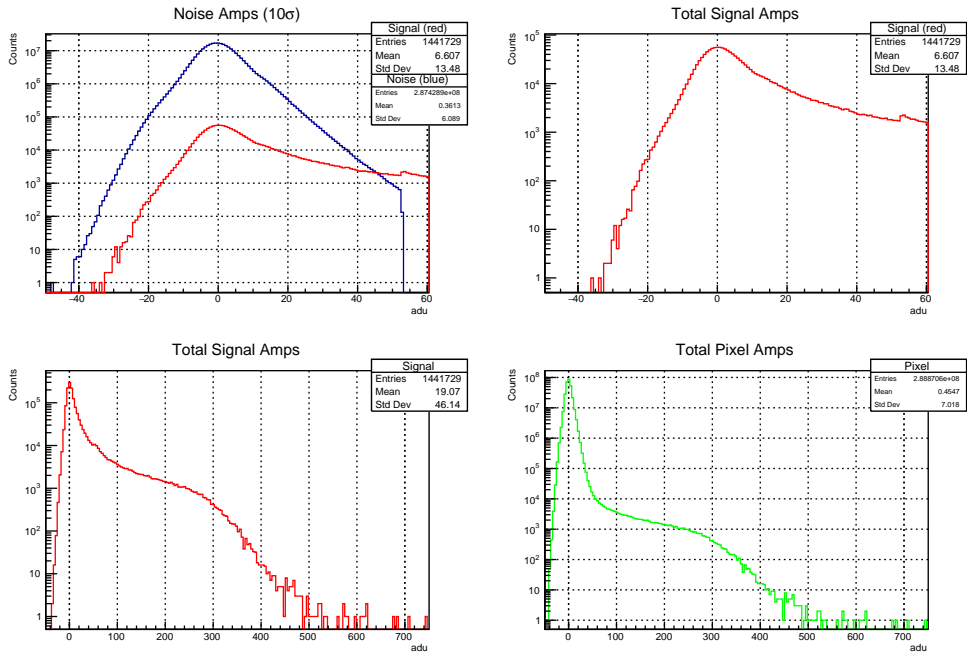


Figure 4: Amplitude Distributions for channel 0 with threshold at 10σ . In the top left, pixels with no signal are blue. Pixels in clusters are in red. Total pixel amplitude distribution is in green.

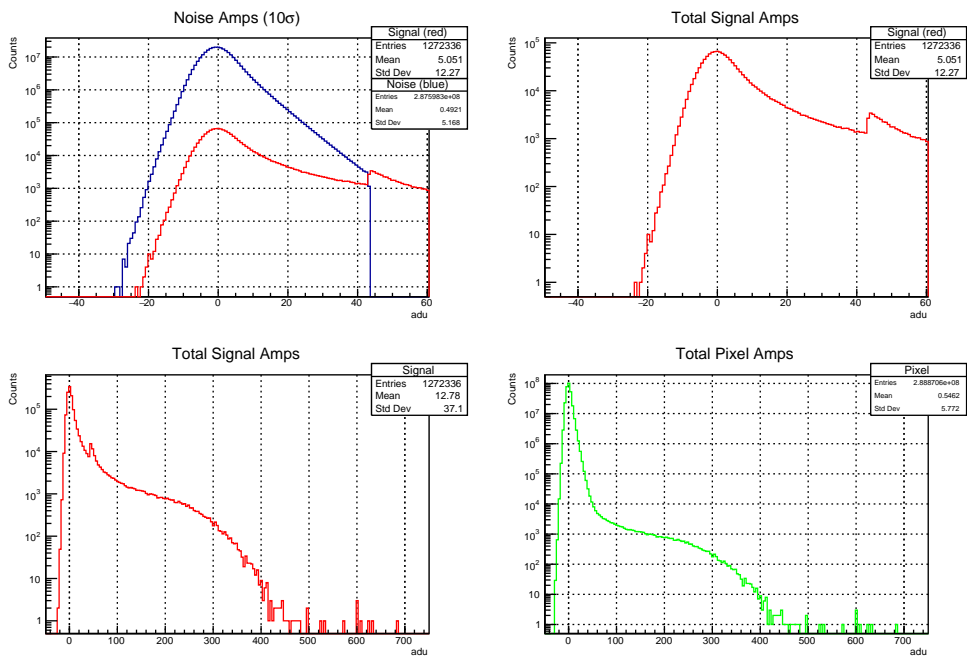


Figure 5: Amplitude Distributions for channel 1 with threshold at 10σ . Same color scheme as Fig. 4

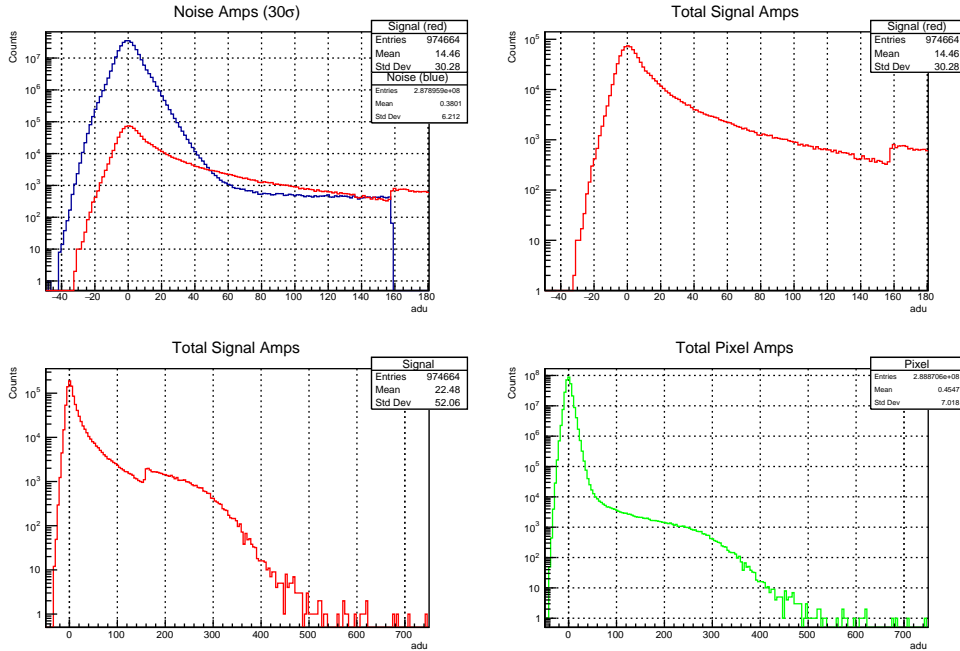


Figure 6: Amplitude Distributions for channel 0 with threshold at 30σ . Same color scheme as Fig. 4

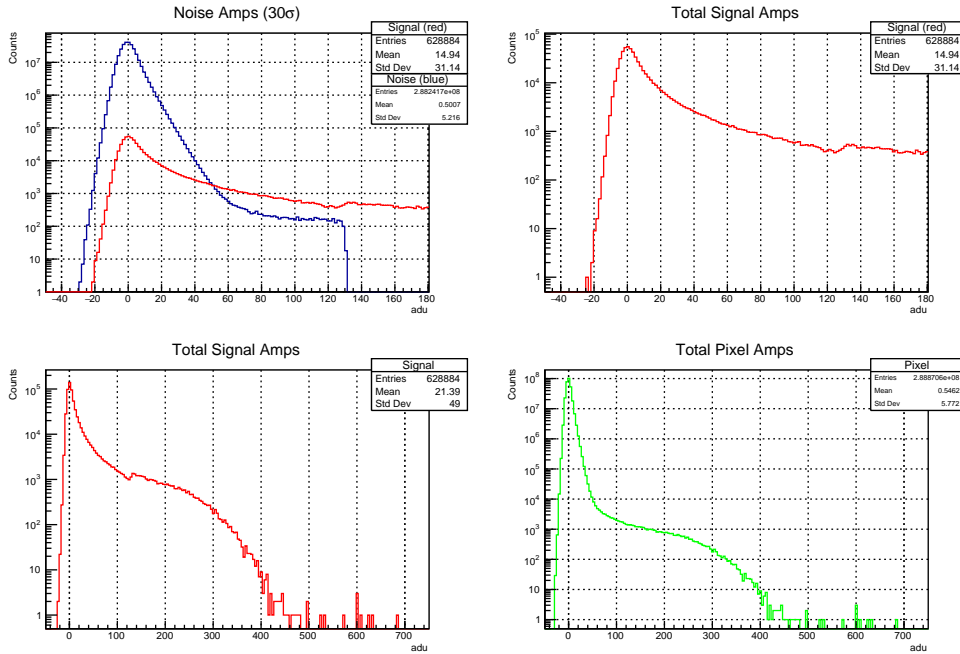


Figure 7: Amplitude Distributions for channel 1 with threshold at 30σ . Same color scheme as Fig. 4

X-ray clusters only occupy a small number of pixels in the image. We can get amplitudes for pixels without signal using pixels not included in any clusters. The corresponding plots are shown in Fig. 4,5,6,7. In these figures, σ is the root mean squared calculated in base line subtraction. Fig. 4 and 5 shows the amplitude distributions for the signal and noise (top left), signal (top right), cluster signal amplitude distribution but with a different domain (bottom left), and the total pixel amplitude distribution (bottom

Run #	Shutter Status	Integration Time (s)	Std. Dev. (adu)	Mean (adu)
S95135	Open	1	6.168	0.3711
S95147	Closed		5.365	0.1048
S95152			5.421	0.119
S95153			5.427	0.1193
S95154			5.43	0.1213
S95155			5.435	0.1222
S95156			5.433	0.1211
S95136	Open		2	6.812
S95148	Closed	5.548		0.166
S95137	Open	3	7.42	0.7763
S95149	Closed		5.733	0.2307
S95138	Open	4	7.997	0.9238
S95150	Closed		5.911	0.2941
S95139	Open	5	8.55	1.026
S95151	Closed		6.083	0.3545

Table 1: Total Amplitude Distributions for Channel 0

Run #	Shutter Status	Integration Time (s)	Std. Dev. (adu)	Mean (adu)
S95135	Open	1	5.293	0.5086
S95147	Closed		4.129	0.09956
S95152			4.197	0.1095
S95153			4.201	0.1113
S95154			4.207	0.1109
S95155			4.203	0.1114
S95156			4.202	0.1131
S95136	Open		2	6.116
S95148	Closed	4.297		0.1491
S95137	Open	3	6.858	1.026
S95149	Closed		4.463	0.2007
S95138	Open	4	7.546	1.206
S95150	Closed		4.616	0.2494
S95139	Open	5	8.179	1.347
S95151	Closed		4.76	0.2951

Table 2: Total Amplitude Distributions for Channel 1

right). The noise and signal distributions have maximums centered around 0. This means that most of the offset was successfully subtracted. Our cluster is 5 by 5 pixels. This area fully covers charge distribution and some pixels contain zero or little charge. This explains the maximum in the signal plot centered at zero.



Figure 8: Plotting of the Std. Dev. against the Integration time for sets S95135-S95139 (shutter closed) and S95147-S95151 (shutter open). Channel 0 is on the left, channel 1 is on the right.

A series of scans were done to investigate noise. The data sets in these tables do not have any incoming x-rays. S95135 through S95139 are in the typical detector set up except without any incoming x-rays. S95147 through S95151 have a shutter closed which blocks most of the light pollution in the set up as well as not having any incoming x-rays. S95152 through S95156 are the same as the prior set except they all have the same integration time, however, the number of images collected is varied. Tables 1 and 2 show the amplitude standard deviation and mean for the total pixel amplitude distribution. These tables show that the light pollution contributes to the more drastically increasing standard deviation with respect to integration time. The second data set, that has the shutter closed, does have a positive correlation between the integration time and the standard deviation, however it is not to the same degree as the first data set. This is believed to be dark current contributions. These features can also be seen in scatter plots of sets S95135-S95139 (shutter closed) and S95147-S95151 (shutter open), Fig. 8. The second EMCCD also appears to have a smaller standard deviation for all data sets compared to its first EMCCD counterpart.

4 Diffusion Equation

The drift-diffusion model proposed by Pavlov and Nousek [4] was considered as well as the one proposed by Hopkinson [5]. Approximations of the models were looked at to see if they could be made to make the analysis code more efficient without severe accuracy loss. The solution to the diffusion equation (1) was obtained in field free region. The setup of the coordinates is such that the x-ray photon will pass through, or be absorbed by the field free zone, then progress into the depletion region which is ended by the gates that record the charge. The 0 of the z-axis is at the gates, increasing such that the face closest to the incoming x-ray is approximately at $z = d_{ff} + d_d$, which is the depth of the field free zone plus the depth of the depletion region. The z-axis is orthogonal to the face of the EMCCD. Cylindrical coordinates are used in the following equations.

$$D\nabla^2\rho(\mathbf{r}, z, t) = \frac{\partial\rho(\mathbf{r}, z, t)}{\partial t} \quad (1)$$

The laplacian of the charge density, $\nabla^2\rho$, is multiplied by the diffusivity of the material. This is equivalent to the derivative of the charge density with respect to time t . Applying the initial condition:

$$\rho(\mathbf{r}, z, 0) = Q_0\delta(\mathbf{r})\delta(z - z_0) \quad (2)$$

Where Q_0 is the total charge, δ is the delta function, and z is the depth in the EMCCD with z_0 being the depth at which the x-ray photon is absorbed. The chosen boundary conditions are:

$$\rho(\mathbf{r}, z, t)|_{z=d_d} = 0 \quad (3)$$

$$\frac{\partial\rho(\mathbf{r}, z, t)}{\partial z}|_{z=d_d+d_{ff}} = 0 \quad (4)$$

Eq. (3) says that at the boundary of the depletion region depth d_d , the charge density is zero. Eq. (4) requires that the flux be zero at $z = d_d + d_{ff}$, the reflective boundary. Applying these conditions to the diffusion eq. (1) yields eq. (5).

$$\rho(\mathbf{r}, z, t) = \frac{2Q_0}{d_{ff}} \frac{1}{4\pi Dt} \sum_{n=1}^{\infty} \sin \frac{\alpha_n(z-d_d)}{d_{ff}} \sin \frac{\alpha_n(z_0-d_d)}{d_{ff}} \exp \left[-\frac{\alpha_n^2 Dt}{d_{ff}^2} - \frac{\mathbf{r}^2}{4Dt} \right] \quad (5)$$

Proof of this solution to eq. (1) is as follows. The left side of the diffusion equation is

$$D\nabla^2 \rho(\mathbf{r}, z, t) = D \left(\frac{1}{r} \frac{\partial}{\partial r} r \frac{\partial \rho}{\partial r} + \frac{1}{r^2} \frac{\partial^2 \rho}{\partial \varphi^2} + \frac{\partial^2 \rho}{\partial z^2} \right)$$

Since ρ is not φ dependent, the above equation produces:

$$\begin{aligned} D\nabla^2 \rho(\mathbf{r}, z, t) &= \frac{2Q_0}{d_{ff}} \frac{1}{4\pi t} \left(\frac{r^2}{4Dt^2} - \frac{1}{Dt} \right) \sum_{n=1}^{\infty} \sin \frac{\alpha_n(z-d_d)}{d_{ff}} \sin \frac{\alpha_n(z_0-d_d)}{d_{ff}} \exp \left[-\frac{\alpha_n^2 Dt}{d_{ff}^2} - \frac{\mathbf{r}^2}{4Dt} \right] \\ &+ \frac{2Q_0}{d_{ff}} \frac{1}{4\pi t} \sum_{n=1}^{\infty} \left(-\frac{\alpha_n^2}{d_{ff}^2} \right) \sin \frac{\alpha_n(z-d_d)}{d_{ff}} \sin \frac{\alpha_n(z_0-d_d)}{d_{ff}} \exp \left[-\frac{\alpha_n^2 Dt}{d_{ff}^2} - \frac{\mathbf{r}^2}{4Dt} \right] \end{aligned}$$

The right hand side looks like:

$$\begin{aligned} \frac{\partial \rho(\mathbf{r}, z, t)}{\partial t} &= \frac{2Q_0}{d_{ff}} \frac{1}{4\pi Dt} \left(\frac{r^2}{4Dt^2} - \frac{1}{t} \right) \sum_{n=1}^{\infty} \sin \frac{\alpha_n(z-d_d)}{d_{ff}} \sin \frac{\alpha_n(z_0-d_d)}{d_{ff}} \exp \left[-\frac{\alpha_n^2 Dt}{d_{ff}^2} - \frac{\mathbf{r}^2}{4Dt} \right] \\ &+ \frac{2Q_0}{d_{ff}} \frac{1}{4\pi Dt} \sum_{n=1}^{\infty} \left(-\frac{\alpha_n^2 D}{d_{ff}^2} \right) \sin \frac{\alpha_n(z-d_d)}{d_{ff}} \sin \frac{\alpha_n(z_0-d_d)}{d_{ff}} \exp \left[-\frac{\alpha_n^2 Dt}{d_{ff}^2} - \frac{\mathbf{r}^2}{4Dt} \right] \end{aligned}$$

From here it is obvious that both sides are equal. The radial profile eq. (6) is found from (5) after time-integrating the radial distribution of the charge flux at the boundary of the field-free zone and the depletion zone. Flux is the flow rate per unit area. Fick's first law states $j = -D\nabla\rho$. Flux is also defined as: $j = \frac{\partial I}{\partial A} = \frac{\partial}{\partial A} \frac{dq}{dt} \Rightarrow \frac{dq}{dt} = \iint_S \mathbf{j} \cdot d\mathbf{A}$. This leads to the following equation:

$$\begin{aligned} q_{ff}(\mathbf{r}) &= \int_0^{\infty} dt D \left. \frac{\partial \rho(\mathbf{r}, z, t)}{\partial z} \right|_{z=d_d} = \int_0^{\infty} dt \frac{2Q_0}{d_{ff}} \frac{1}{4\pi t} \sum_{n=1}^{\infty} \frac{\alpha_n}{d_{ff}} \sin \frac{\alpha_n(z_0-d_d)}{d_{ff}} \exp \left[-\frac{\alpha_n^2 Dt}{d_{ff}^2} - \frac{\mathbf{r}^2}{4Dt} \right] \\ \text{Setting } t &= \sqrt{\frac{\mathbf{r}^2}{4} \frac{\alpha_n^2}{d_{ff}^2}} \exp u \\ &\Rightarrow \frac{1}{t} dt = du \\ &= \int_0^{\infty} du \frac{Q_0}{d_{ff}} \frac{1}{2\pi} \sum_{n=1}^{\infty} \frac{\alpha_n}{d_{ff}} \sin \frac{\alpha_n(z_0-d_d)}{d_{ff}} \exp \left[-\frac{|\mathbf{r}| \alpha_n}{d_{ff}} \cosh u \right] \end{aligned}$$

Since the asymptotic form of the modified Bessel function of the second kind is: $K_0(x) = \int_0^{\infty} \exp[-x \cosh u] du$

$$\Rightarrow q_{ff}(\mathbf{r}) = \frac{Q_0}{\pi d_{ff}^2} \sum_{n=1}^{\infty} \alpha_n \sin \frac{\alpha_n(z_0-d_d)}{d_{ff}} K_0 \left(\frac{|\mathbf{r}|}{d_{ff}} \alpha_n \right) \quad (6)$$

This is the equation that can be used to model the charge distribution in the pixels. Since the pixels are rectangular, to find the predicted charge in a pixel in a given cluster, integrating this equation in cartesian

coordinates would be optimal. However, integrating over the surface at $z_0 = d_d$ gives the total collected charge:

$$Q \equiv \int q_{\text{ff}}(\mathbf{r})d^2\mathbf{r} = \int_0^\infty \frac{2Q_0}{d_{\text{ff}}^2} \sum_{n=1}^\infty \alpha_n \sin \frac{\alpha_n(z_0 - d_d)}{d_{\text{ff}}} K_0 \left(\frac{|\mathbf{r}|}{d_{\text{ff}}} \alpha_n \right) \mathbf{r} d\mathbf{r}$$

Since $\int_0^\infty x K_0(x) dx = 1 \Rightarrow \int_0^\infty r K_0 \left(\frac{|\mathbf{r}|}{d_{\text{ff}}} \alpha_n \right) d\mathbf{r} = \frac{d_{\text{ff}}^2}{\alpha_n^2}$

$$\Rightarrow Q = 2Q_0 \sum_{n=1}^\infty \frac{1}{\alpha_n} \sin \frac{\alpha_n(z_0 - d_d)}{d_{\text{ff}}} \quad (7)$$

5 Analysis of Charge Distribution Equation in Field Free Zone

To begin I put equation (6) into C++ code, varying the number of terms in the summation. I found that the number of necessary terms varied depending on values of the input radius. After a minimum number of terms, if the non-sinusoidal components of a given term were less than an arbitrarily chosen value, ϵ , I deemed the calculation complete as any further terms would be inconsequential. The minimum number of terms had to be large enough to avoid potential floating point error, as the modified Bessel function of the second kind diverges at zero. The ϵ value is on the order of 10^{-41} and the minimum number of terms is approximately 500. I did not try to optimize these numbers as the run times were rather quick without any optimization. To see if C++ implementation of equation (6) was correct, numerically integrating it and comparing it to the analytic solution was necessary. The analytic solution, eq. (7), is equal to 1 for all values of r so the C++ implementation of it appears accurate. The method of numeric integration, the composite trapezoid rule, is an extension of standard trapezoidal rule for the integration of any function, $f(x)$, from a to b

$$\int_a^b f(x) dx \approx (b-a) \left(\frac{f(a) + f(b)}{2} \right)$$

with an arbitrary number of iterated steps in between a and b . It has the form:

$$\int_a^b f(x) dx \approx \frac{b-a}{n} \left(\frac{f(a)}{2} + \sum_{k=1}^{n-1} f \left(a + k \frac{b-a}{n} \right) + \frac{f(b)}{2} \right) \quad (8)$$

This allows an n to be chosen such that a larger n implies a more accurate approximation of the integral. I found that an n of ten thousand was more than enough and that any larger n drastically increased computation time for very little change in value. To compensate for when working with a large distance between a and b , I simply broke the interval up into sub-intervals and summed the approximations across each sub-interval. This was far more time efficient than drastically increasing the number of iterated steps instead. The results in table 3. are quite satisfying as the error is very small. It is interesting to note that the largest differences in columns 4,5, and 6 of table 3. are 6.425×10^{-4} , 0.194×10^{-4} , and 6.231×10^{-4} respectively. These are all less than 0.00065% error.

Figure 9 shows the plotting of Eq. (6), integrated w.r.t. $r\varphi$. The reason it is integrate w.r.t. φ is because $dQ/dS = q_{\text{ff}}$, therefore to get the radial profile of the derivative of the total charge w.r.t. the radius, eq. (6) needed to be integrated by $r\varphi$. The larger z_0 is, the farther the initial x-ray photon absorption is from the structures that record the charge. The results seem sensible as intuitively the charge would have more time to drift from the center, the farther it is from the structures that record it. This accounts for the maximum farther from zero and a wider distribution as well. The area under all of these curves is approximately one. This is verified by Table 3 column 2 and the error in column 4.

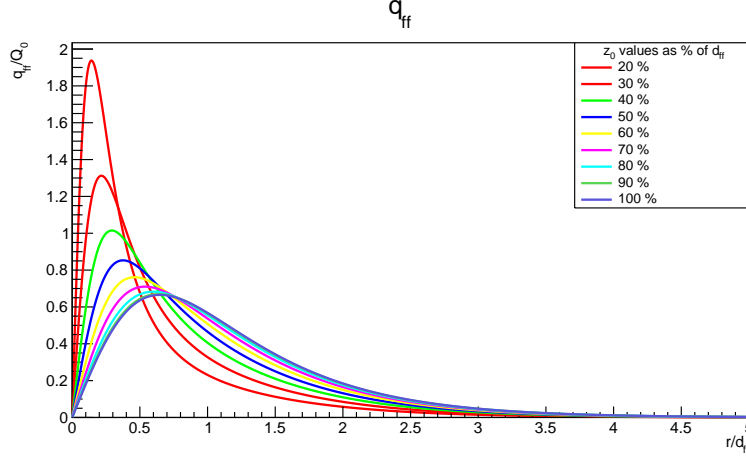


Figure 9: Plotting of equation (6) over total initial charge (Q_0), integrated with respect to $r\varphi$, at various z_0 .

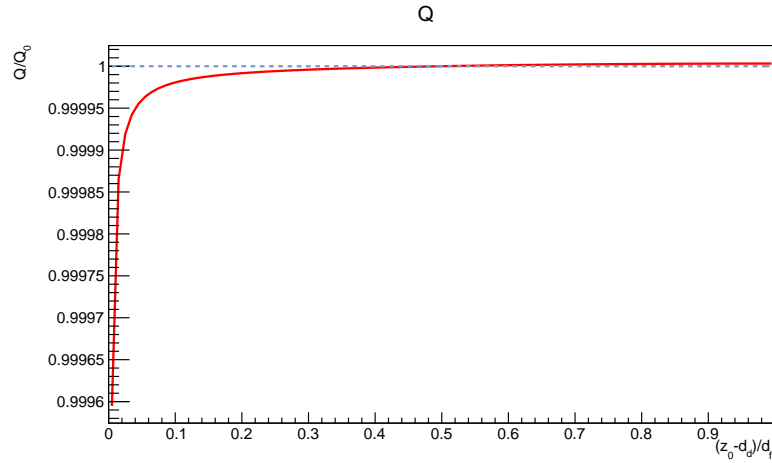


Figure 10: Eq. (7), which is the surface integral of equation (6).

$$\int_0^{2\pi} q_{ff}(\mathbf{r})r d\varphi = 2Q_0 \sum_{n=1}^{\infty} \alpha_n \sin \frac{\alpha_n(z_0 - d_d)}{d_{ff}} \left(r K_0 \left(\frac{|\mathbf{r}|}{d_{ff}} \alpha_n \right) \right) \quad (9)$$

Figure 10 shows the plotting of Eq. (7) which analytically should be equal to one for all values of $(z_0 - d_d)/d_{ff}$. While it is very close, as can be seen by the value in Table 3, column 3 and the difference from one in the same table, column 5. There appears to be a major loss of accuracy as $(z_0 - d_d)/d_{ff}$ gets close to zero, beginning at approximately $(z_0 - d_d)/d_{ff} < 0.1$. Further investigation is necessary in order to make $(z_0 - d_d)/d_{ff} < 0.1$ a viable zone for the diffusion model. Table 2 column 6 shows that the error between the coded eq. (7) and the equation (9). In the range $(z_0 - d_d)/d_{ff} > 0.1$ they appear to be in agreement.

James Flemings wrote a Monte Carlo simulation for charge diffusion in EMCCD [6] and was used for comparison of the Pavlov and Nousek model. Figure 11 (left) shows how the model code appears to have z_0 offset, implied by the maximum being at a larger r/d_{ff} than the simulation. The model also appears to be wider than the simulation code. Figure 11 (right) is the same as Fig. 11 (left), however, the z_0 was offset by $0.1d_{ff}$ in order to align the maximums. This did not fix the width problem unfortunately. Some of the approximations made might need to be scaled back for more a more accurate model. Further investigation is necessary.

z_0/d_{ff}	Comp. Trapezoid of eq. (6)	Eq. (7)	$ 1 - \text{col. 2} \times 10^4$	$ 1 - \text{col. 3} \times 10^4$	$ \text{col. 3} - \text{col. 2} \times 10^4$
0.1	0.9993575	0.9999806	6.425	0.194	6.231
0.2	0.9997219	0.9999917	2.781	0.083	2.698
0.3	0.9998620	0.9999959	1.380	0.041	1.339
0.4	0.9999436	0.9999983	0.563	0.017	0.546
0.5	0.9999996	1.0000000	0.004	0.000	0.004
0.6	1.0000402	1.0000012	0.402	0.012	0.390
0.7	1.0000697	1.0000021	0.697	0.021	0.676
0.8	1.0000900	1.0000027	0.900	0.027	0.873
0.9	1.0001020	1.0000031	1.020	0.031	0.989
1.0	1.0001059	1.0000032	1.059	0.032	1.027

Table 3: Integration of eq. (6) numerically using the composite trapezoid rule such that the result is Q/Q_0 . Each value is rounded to the 7th decimal.

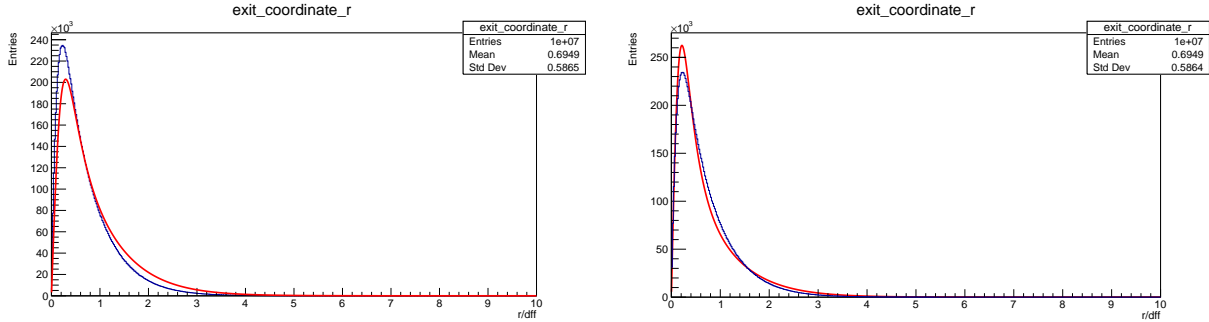


Figure 11: (Left) The blue is the Monte Carlo simulation results and the red is same model code as in Figure 9. (Right) Same as the left except the model code has z_0 offset with $z_{\text{code}} = z_{\text{simulation}} - 0.1d_{\text{ff}}$

6 Conclusions

From the data and analysis that resulted in Figures 1-3, we can conclude base line subtraction reduces the power spectral density at lower frequencies. This means it successfully subtracts the offset that obfuscates the data. We found that there is light pollution from spectrometer instruments inferred from the results in tables 1 and 2, as well as Fig. 8. This source of noise becomes increasingly important with integration time. We observed the contribution of dark current in dark exposures but on smaller level than light pollution contribution. This can be seen in tables 1 and 2, and Fig. 8 as well. The solution eq. (6) for diffusion equation eq. (1) in field free zone was obtained as infinite series. Because of that, finite numerical approximations have been performed for different parameters. Results seems promising but Fig. 11 shows that there are still details that need to be accounted for before any solid conclusions can be made. Further investigation is necessary in that area.

7 Acknowledgements

I would like to thank to Ivan Kotov who provided invaluable guidance as well as the opportunity to explore this project. I would also like to thank the team at the SIX beam line for their data to study. I extend my gratitude to the U.S. Department of Energy, Office of Science, and the National Science Foundation for providing this incredible opportunity. Lastly, I would like to thank the Brookhaven National Laboratory for the support of myself, other aspiring scientists, and current scientists to help learn, innovate, and discover.

References

- [1] I. V. Kotov, S. Hall, D. Gopinath, A. Barbour, J. Li, Y. Gu, K. Holland, I. Jarrige, J. Pelliciari, M. Soman, S. Wilkins, and V. Bisogni, "Analysis of the emccd point-source response using x-rays." Unpublished.
- [2] I. V. Kotov, A. I. Kotov, J. Frank, P. O'Connor, V. Perevoztchikov, and P. Takacs, "Ccd base line subtraction algorithms," *IEEE Transactions on Nuclear Science*, 2010.
- [3] M. Frigo and S. Johnson, "Fftw." <http://www.fftw.org/#documentation>.
- [4] G. G. Pavlov and J. A. Nousek, "Charge diffusion in ccd x-ray detectors," *Nuclear Instruments and Methods in Physics Research*, 1998.
- [5] G. Hopkinson, "Charge diffusion effects in ccd x-ray detectors," *Nuclear Instruments and Methods*, 1983.
- [6] J. Flemings and I. Kotov, "Analysis of x-rays using electron multiplying charge coupled devices." Unpublished.

Universal winding machine upgrade and EIC IR magnet B1APF endplate analysis

Calvin Schmalzle, Mechanical Engineering, Clarkson University,
Potsdam Ny 13699

Mentor: Michael Anerella, Superconducting Magnet Division,
Brookhaven National Laboratory, Upton, NY 11973

Abstract

The Large Hadron Collider (LHC) located at the European Organization for Nuclear Research (CERN) site in Geneva, Switzerland is currently the largest and most powerful particle accelerator in the world. The LHC is currently undergoing an Accelerator Upgrade Project (AUP) to increase its luminosity, or number of proton collisions per second. The Electron Ion Collider (EIC) is a brand-new particle accelerator and collider being built at Brookhaven National Laboratory (BNL). The EIC will collide a beam of electrons with a beam of protons or other heavier nuclei to study the inner structure of these particles. The beams of particles in both the LHC and EIC are guided along the accelerators by a very strong magnetic field created by a series of superconducting electromagnets. The Universal Winding Machine in the Superconducting Magnet Division at BNL must be adapted to wind new coils for both the AUP and EIC electromagnets. The universal winder was designed to wind flat, two dimensional “racetrack” coils, while the new AUP and EIC coils must be a three-dimensional curved shape. My project is to adapt and redesign parts of this winding machine, so it can wind all the new coils. Some changes that are necessary are an increase in length to accommodate the longer AUP coil, an increase in height to accommodate the larger diameter coils for the EIC, and an addition of a motor and rollover fixtures to allow the three dimensional shape to be accomplished. In addition to the universal winding machine, I also worked on analyzing the endplates for the B1APF EIC magnet.

Introduction

Two key projects that the superconducting magnet division at Brookhaven National Laboratory (BNL) is working on are the Large Hadron Collider (LHC) Accelerator Upgrade Project (AUP) and the development of the Electron Ion Collider (EIC). The LHC, located in Geneva, Switzerland, is the largest and most powerful particle accelerator in the world. It consists of over 1500 superconducting magnets that form a ring 27 kilometers in circumference. The purpose of the LHC is to study the structure of atoms by accelerating two high energy particle beams to nearly the speed of light before colliding them together. The goal of the LHC AUP is to increase the luminosity of the collider, or number of collisions per second. The EIC, on the other hand is a brand-new concept for a particle accelerator. It is being developed by scientists and engineers across many labs and departments, but BNL was chosen as the site to house this new and exciting collider. The EIC is new and different because it will study the inner structure of particles using electron collisions. Both the EIC and AUP however use superconducting electromagnets to create a strong magnetic field that guides and accelerates the beam of particles. The superconducting magnet division is working to design and build these magnets for the AUP and EIC, as well as the tooling necessary to fabricate them. The two aspects of this process that my projects focused on are the upgrade and adaptation of the universal winding machine for use on AUP and EIC coils, and the analysis of the structure that encases the B1APF magnet for the EIC.

Methods

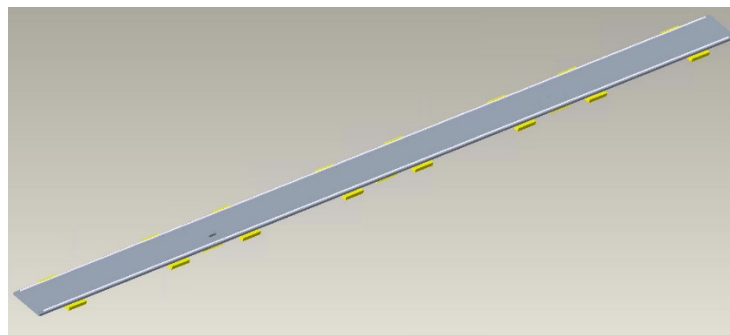
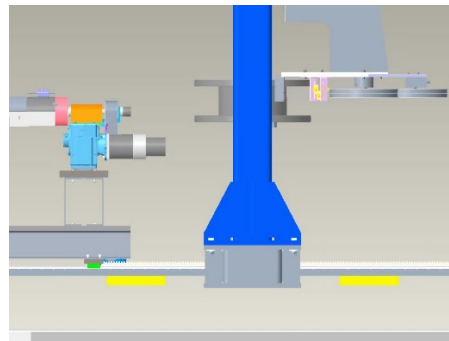
The universal winding machine at BNL is a machine originally designed to wind flat “racetrack” coils for the LHC accelerator research program. Due to the large number of coils needed for AUP and EIC this machine must be modified to wind these new coils. All these new

coils for both EIC and AUP are a three-dimensional curved shape as opposed to the flat coils the machine was designed for. This provides the first of many design challenges for this project. In order to wind coils with this shape, the machine will need to contain a rotating structure. The second design challenge is the length of the machine base. The current length of the machine is 240 inches or 20 ft. To wind the longest AUP coil the machine will have to be significantly extended. The third design challenge is the height, the machine must be able to wind the largest diameter EIC coil, the B1APF. This will require that either the base be lowered, or the bridge be extended, or both. The last two design challenges relate to the nature of the AUP coils. These coils use a thicker conductor than the machine was designed for, which also requires a larger minimum bend radius. Therefore, the machine will require larger diameter, and thicker payout pulleys. Finally, the AUP coils consists of two layers, the top layer being the opposite direction as the lower. This requires that the machine be able to wind in both directions. These design challenges form the basis for all modifications and adaptations made to the universal winding machine.

The first challenge that was addressed on the universal winding machine was the issue of length and travel. The length of the existing machine, as well as the following chart of lengths were given.

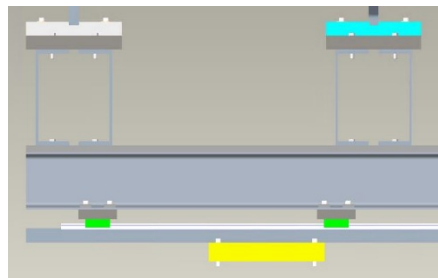
Universal Winder Lengths						
Rotator Length (in)	Tailstock Length (in)	Main Spool Dia (in)	Current Machine travel (in)	Available Dist from C/L (in)		
20	3	24	220	177		
COIL	Coil Length (in)	Mandrel Length (in)	Total Length (in)	Required Travel (in)	Dist. From winder C/L	Clearance (in)
B1PF	118.2	136.5	159.5	183.5	171.5	5.5
Q2APF	149.72	168	191	215	203	-26
AUP		195	218	242	230	-53

With the given lengths the total necessary length of the winding machine base was calculated and modeled in CREO. This length would have to take into account not only the length of the mandrel, or structure the coils in wound onto, but also the length of the tailstock and rotator motor, additionally the machine would have to have enough clearance for the spool to rotate around the end of the mandrel when necessary. An adequate total length for the winding machine base was determined to be 480 inches or 40 feet. This provides the spool with about 10 inches of clearance around the end of the rotator motor as shown in the first picture below. The second picture shows the winder base with extensions on either side.



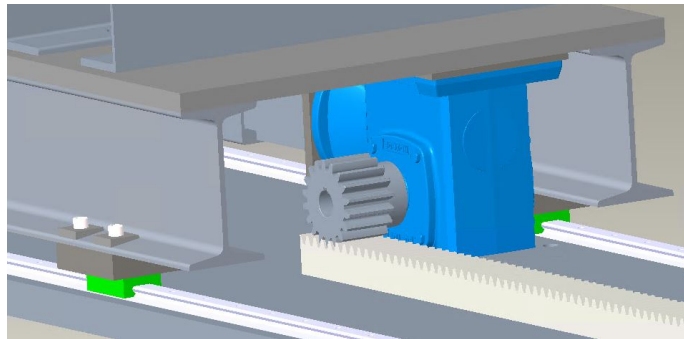
The next challenge that was addressed was the height. The mandrel for the AUP coil as well as the rollover fixtures, tailstock and rotator motor assembly were already designed so the total stack height of those components could easily be determined. The mandrel and rollover fixtures for the B1PF EIC coil were previously designed and modeled in CREO as well. I then modeled a tailstock for the B1PF based on a scaled-up version of the AUP tailstock. The goal

was to design bases for the rollover fixtures that allowed each mandrel to be positioned at exactly the same height for winding. Using these height measurements, I designed and modeled bases for the rollover fixtures that would provide the correct heights, as well as provide enough room to position the larger diameter B1APF once it is designed. Once the correct mandrel height was found, I modeled new extensions for the bridge of the machine, as well as replaced the existing pedestals on the base with two-inch plates that would be leveled on the floor using jackscrews. The base was lowered in addition to raising the bridge to allow for a working height of 40 inches for the technicians while winding. The below picture shows the rollover fixture bases as well as the two-inch plates.

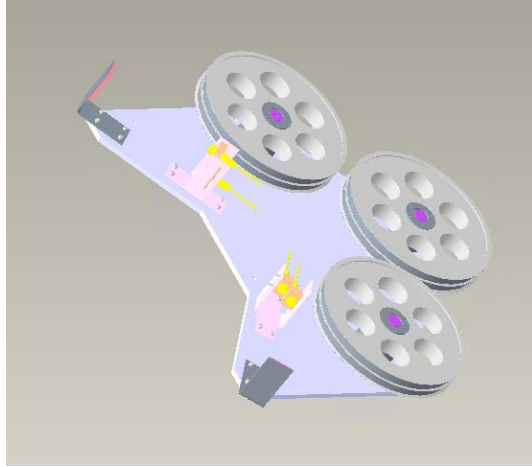


Due to the large increase in length of the machine and weight of the new coils the existing belt drive system for translating the mandrel back and forth will no longer work. To move the new system a rack and pinion system had to be designed. The rack and pinion system drives the motion while the carriage rides on linear bearing and rails. A system needed to be designed to attach the linear bearings to the flanges of the I beams that support the mandrel base. This was accomplished using a one-inch plate with counterbored holes for the bearing to bolt to, and holed drilled in the I beam flange with leveling wedge washers that allowed the thru bolts to have an even surface to rest on. Once the bearing system was set I needed to find a motor and gearbox that could accelerate the 6000 pound structure from rest to 5 in/s at a rate of 1 in/s², as well as a spur gear and rack that could withstand those forces. A gearbox with a reduction of

1:50 and a 3-inch diameter spur gear were chosen to provide the desired 5 in/s output speed with an input rpm of approximately 1750. Once all the components were picked out, I modeled them in CREO and assembled them onto the machine. The following picture shows the model of the rack and pinion system, as well as the bearing connectors.

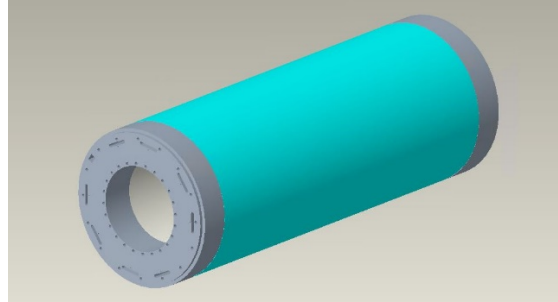


The final challenge that was addressed was the ability to wind the two-layer AUP coils, with the thicker conductor. I first designed new two-layer pulleys that would allow an easy change in height for the second layer of winding. These pulleys have a diameter of 14 inches to ensure the conductor is not bent too sharply and are $\frac{3}{4}$ inch thick to fit the new conductor. Along with the pulleys new mounting hardware, shafts and bearings needed to be designed. These new pulleys will be mounted in the correct pattern on a large $\frac{1}{2}$ inch plate that will then be bolted onto the bottom of the existing gantry after the old pulleys and sensors are removed. This arrangement of pulleys is also symmetrical to allow the machine to wind in both directions equally well. The full assembly of the pulleys and sensors on the mounting plate is shown below.

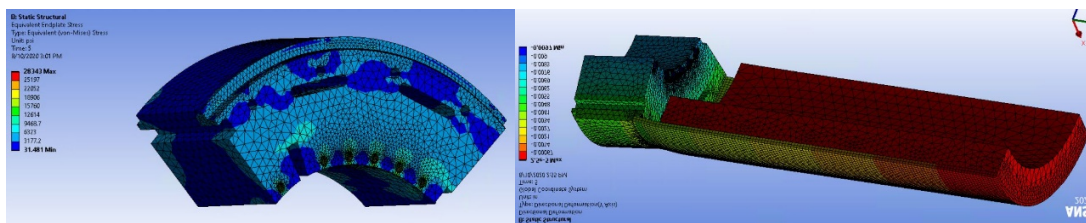


The B1APF is one of the many superconducting magnets that make up the new Electron Ion Collider. It is a dipole magnet with a curved shape. Due to the current running through the conductor the magnets not only produce a large magnetic field, but they also produce a large force in the axial direction. The shell and endplates that encase this magnet must be designed to withstand this force without a large deformation or stress higher than the material yield strength. Therefore, a finite element analysis, followed by some refinements must be performed on each design until it is suitable for production. Some design features that can be altered to provide the necessary strength are the number of setscrews that support the load and the endplate thickness.

To analyze the endplate components of the B1APF magnet the model must first be simplified. This is to remove any small features and details that will unnecessarily complicate the analysis. The model was simplified down to just the shell, endplates, setscrews, and iron for this purpose as shown below.



Once the simplified CREO model was created, I imported it into ANSYS Workbench and set up all the material assignments, contacts, supports, and forces that the analysis required. The axial force produced by the B1APF is 171,000 pounds and is distributed evenly among a ring of setscrews attached to the endplate. Once the initial analysis was completed the resulting equivalent stress and deformation was analyzed to see if any changes to the design were necessary. In this case it was determined that the equivalent stress in the endplate was, above yield so more setscrews were added to distribute the load. The analysis was rerun with the new changes and the results were determined to be satisfactory. The results for the lead end are shown below.



Conclusion

With the initial modifications so the universal winding machine complete it is now equipped to wind curved dipole and quadrupole coils for both the LHC AUP and the EIC. These changes allow for the increased length of the AUP coils, as well as the increased height of the

EIC coils. Each mandrel will be positioned at the correct height for winding using the custom sized rollover fixture bases. With the addition of the new pulleys the winder will now be able to wind in both directions and on both layers of the AUP coils when necessary. While the design of these winder upgrades is certainly not complete, a solid base of improvements has been established that will allow for further changes. With the initial analysis of the B1APF endplates complete, the results can be studied to determine if changes in the endplate thickness can be made. This may be necessary for the non-lead end because of tight clearances with the neighboring magnet in the accelerator. The results of the analysis show that the current endplate thickness will be strong enough to withstand the axial forces produced by the magnet. The non-lead end endplate could likely be reduced in thickness if the number of setscrews is increased to further distribute the load. Now that these analyses are complete, other aspects of the B1APF magnet design can be finalized as well as the positioning of the magnets in the EIC ring.

Acknowledgements

Firstly, I would like to thank my mentor Michael Anerella for his generosity and guidance throughout this program. Secondly, I want to thank Andrew Marone for his help on the universal winding machine upgrade and John Cozzolino for his help on the B1APF endplate analysis. I would also like to thank the rest of the mechanical engineering group and superconducting magnet division. Finally, I would like to thank the Department of Energy Office of Science and the BNL Office of Educational Programs for making this experience possible. This project was supported in part by the U.S. Department of Energy, Office of Science, Office of Workforce Development for Teachers and Scientists (WDTS) under the Science Undergraduate Laboratory Internships Program (SULI).

Effect of a copper chelator on zinc levels in A β deposits in Cerebral Amyloid Angiopathy

Andrea Sprague-Gettsy

Chemistry Department, Binghamton University, Binghamton, NY 13902

Ashwin Ambi

Department of Chemistry, Stony Brook University, NY 11794

Lisa Miller and Tiffany Victor

National Synchrotron Light Source II, Brookhaven National Laboratory, Upton, NY 11973

Adam Lowery

Department of Mechanical Engineering, Virginia Tech, Blacksburg, VA 24060

Abstract

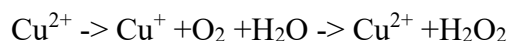
Cerebral Amyloid Angiopathy is a condition where amyloid beta (A β) peptide aggregates on the walls of blood vessels in the brain. Past studies have observed that the copper and zinc levels were elevated in A β plaques and aggregated together, leading to the conclusion that these metals share a binding site. In vitro studies have shown that copper bound to A β leads to the production of reactive oxygen species that can cause oxidative stress and cell death while the role of zinc is to act as a protective factor against the oxidative stress. The goal of this study was to determine the zinc levels colocalized with A β in a transgenic rat model of CAA (rTg-DI) treated with tetrathiomolybdate (TTM), which is a copper-specific chelator. We hypothesized that the zinc levels in the A β deposits would increase as the copper levels decrease due to the TTM as more binding sites will be available. The data were collected using synchrotron-based X-ray Fluorescence Microscopy (XFM) at the National Synchrotron Light Source II as it is used for elemental imaging at high spatial resolution. The results showed a ~30% decrease in zinc levels in the A β deposits in the TTM-treated rats compared to the untreated animals. Surprisingly, the copper levels were unaffected by the TTM treatment. Therefore, we suggest that the TTM structure may have been modified by the acidic pH in the rat gut and the modified chelator may have a higher affinity for zinc relative to copper. Future studies will be necessary to identify a different Cu chelator that will remove Cu rather than Zn from the deposits.

I. Introduction

Cerebral Amyloid Angiopathy (CAA) is a disease caused by the buildup of amyloid- β (A β) deposits on blood vessels in the brain which leads to cell death and neurodegeneration. The

deposits are made up of peptides from the amyloid precursor protein (APP) cleaved by β secretase and γ secretase. Similar to CAA, Alzheimer's disease (AD) is another condition that causes neurodegeneration, cell death and cognitive decline. To understand diseases such as these, samples of brain tissue have been analyzed using X-ray Fluorescence Microscopy (XFM). It was found that metal levels in the amyloid deposits were atypical compared to brain tissue unaffected by CAA or AD. These findings have led to what is called the *Metal Hypothesis*, which is the idea that the $A\beta$ -metal interactions cause the neuropathological effects of $A\beta$ in AD and CAA [1].

How exactly these metals play a role in the pathways of the brain and in CAA is what scientists are trying to understand. Zinc and copper, like other metals, can serve as metalloproteins in the brain. Zinc accesses the brain through the blood-brain barrier which is the blood vessel system of the central nervous system. It protects the brain from various toxic agents and foreign matter. Zinc serves in metalloproteins in neurons and glial cells. It also is necessary for many enzymes to function helping to carry out catalytic and coactive jobs and help with maintaining structure as well [2]. Copper also supports proteins in structure and catalytic functions. However, deviating from the normal homeostasis levels that occur within the brain can cause damage over time. Copper, when over abundant in the brain, can wreak havoc on cells by causing oxidative stress, which can lead to dementia and neurodegeneration seen in CAA and AD. This oxidative stress is caused by the Fenton reaction:



Using XFM, it was found that zinc and copper aggregate together within the $A\beta$ deposits while calcium and iron displayed a rather random distribution as represented in Figure 1. Other studies have analyzed that zinc and copper share a binding site in the amyloid- β aggregates. This binding site involves the amino acid histidine and can be seen in Figure 2 where copper has a

binding affinity of $7.3 \times 10^{-8} \text{ M}$ compared to zinc which has a binding affinity of $2.32 \times 10^{-5} \text{ M}$ [3,4]. Because of this shared binding site, zinc can act as an antioxidant against the oxidative stress caused by copper. As more zinc is bound to the amyloid- β , then less copper atoms can attach to the deposits and create a toxic environment leading to cell death.

Our group has previously reported that the copper chelator tetrathiomolybdate (TTM) was used on Tg576 mice, which is the animal model of Alzheimer's disease. This experiment was done to see the effect of TTM on the copper levels colocalized with $A\beta$ and $A\beta$ load. TTM was used in this experiment because of its use for other diseases such as Wilson's disease and its high affinity to $A\beta$ of $2.32 \times 10^{-5} \text{ M}$ [5,6]. It was found that the TTM treatment reduced the relative copper content in the parenchymal amyloid plaques but not the vascular amyloid, which are deposits that cause CAA [7]. Therefore, this experiment was replicated using the rTgDI rat model, which is used because it is a better model to replicate how CAA is formed in the brain [8].

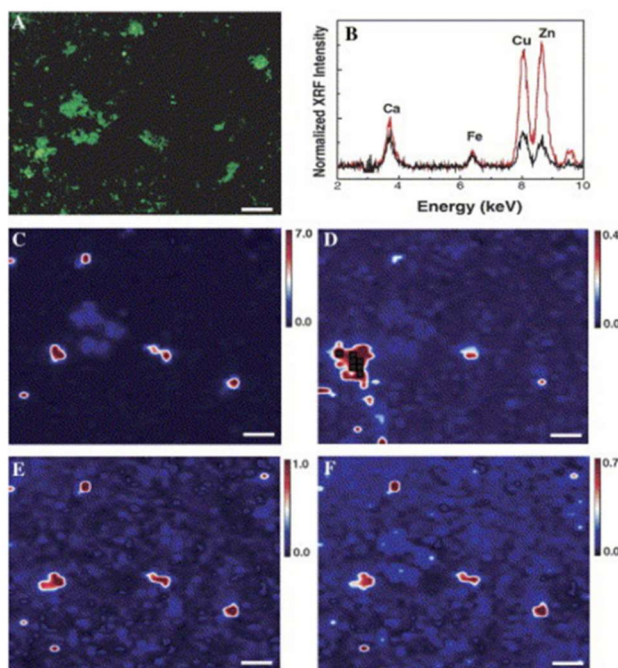


Figure 1. (A) Epifluorescence image of human AD tissue stained with Thioflavin S, as seen also in Fig. 1. (B) SXRF microprobe spectra from Thioflavin-positive area (red) and Thioflavin-negative area (black). SXRF microprobe

images of (C) Ca, (D) Fe, (E) Cu, and (F) Zn content in the same tissue. In the Fe image, several pixels (indicated in black) were excluded from the analysis due to Fe contamination in the Al substrate. For all images, scale bar is 100 μm .

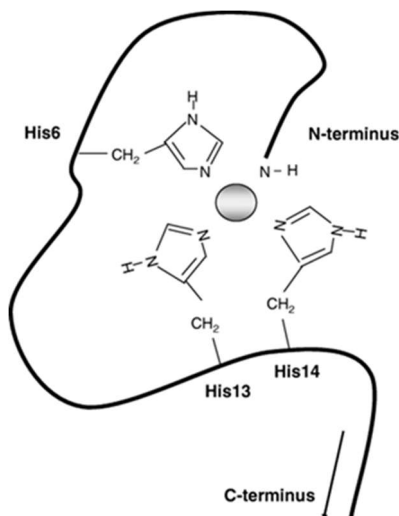


Figure 2. Diagram of the structure of A β binding to zinc or copper [3].

II. Scope and Objective

The goal of this project was to determine how the levels of zinc in amyloid deposits were affected by the chelation of copper by TTM in rTgDI rats because zinc acts as an antioxidant to copper and it potentially limits the level of oxidative stress.

III. Methods

In this experiment procedures were replicated from the previous study that used Tg2576 mice. This experiment used six transgenic rTgDI rats to determine the effect of the copper chelator on the zinc levels in the amyloid- β deposits. Three of the rats were treated with tetrathiomolybdate (TTM) while the other three were untreated. The rats were first aged to 12 months then they were administered the TTM for six months. The TTM treated rats were given 100 ppm of TTM with 5% sucrose in drinking water while the untreated rats received only 5% sucrose in their water.

Once the six months of treatment was complete, the rats were then sacrificed. The blood vessels from the brain were isolated and then mounted on Ultralene disks and stained with Thioflavin S. The samples were analyzed using X-ray fluorescence microscopy (XFM) utilizing the beamline 5-ID at the National Synchrotron Light Source II and the beamline 13-IDE at the Advanced Photon Source.

XFM images were analyzed with the program Larch, which is a program for processing and analyzing x-ray fluorescence image data from synchrotron beamlines. This was done to determine the zinc levels in the samples to compare the TTM treated and untreated rats. Figure 3 is an example of the x-ray fluorescent zinc images created. Using the program Larch, three values were recorded, zinc levels in the amyloid deposits (Zn On), zinc levels in the vessel (Zn Off) and zinc levels on the substrate (Zn Empty). Figure 4 displays an example of how each image was used to determine the three values. The values were then analyzed using the following ratio:

$$\text{Zinc level} = \frac{(\text{Zn On} - \text{Zn Empty})}{(\text{Zn Off} - \text{Zn Empty})}$$

The ratios for both the treated and untreated rats were compared and tested for significance using the T-test in excel.

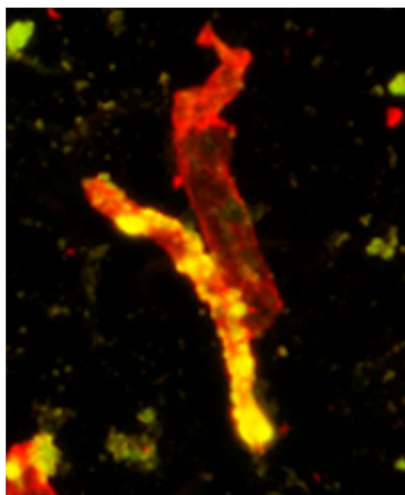


Figure 3. Visible light fluorescence image of a blood vessel of a rTg-DI rat with amyloid deposits. The red is the blood vessel and the yellow is the amyloid deposits on the vessel.

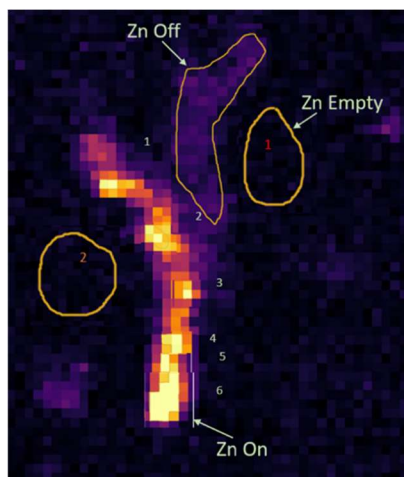


Figure 4. X-ray fluorescence image after analysis with Larch, containing areas used from determining zinc values. The value Zn On is the zinc levels in the amyloid deposits, Zn Off is the zinc level in the vessel and Zn Empty is the zinc levels in the surrounding substrate.

IV. Results

After determining the zinc levels in both the TTM treated rats and the untreated rats, it was found that the zinc levels in the amyloid- β deposits in the TTM treated rats were ~30% lower compared to the untreated rats, as shown in Figure 5. This difference was found to be significant with a p-value of 0.036.

These results differ from our prediction which was that with the TTM, the copper levels would decrease and therefore the zinc levels would increase. The copper levels were found to have remained the same, which was a surprising result. As seen in Figure 6, the copper levels remained the same in the amyloid- β deposits, revealing that the TTM did not chelate the copper.

Zinc Levels on A β Deposits in Transgenic Rats: TTM vs. Untreated

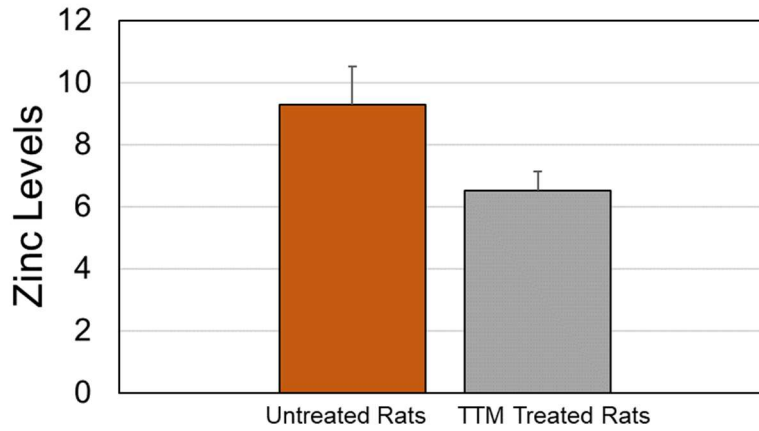


Figure 5. This graph compares the zinc levels found in the TTM treated rats versus the untreated rats. The p value of 0.036 indicates a significance in the zinc levels from the untreated to the TTM treated rats.

Copper Levels in A β Deposits in Transgenic Rats: TTM v. Untreated

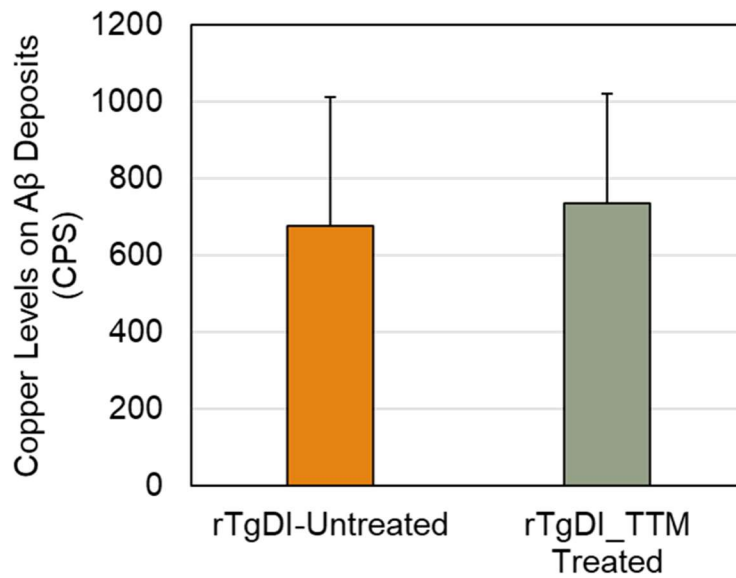


Figure 6. This graph compares the copper levels on the amyloid- β deposits of the blood vessels of the rats in the brain.

V. Conclusion

The determined zinc levels in the rTg-DI rats were unexpected as the zinc levels went down with the chelation of copper with TTM. This result was deviated from the expected because of the unpredicted copper levels which when determined through Larch, were found to have remained the same. We suggest that this result can be explained by the possibility that the structure of tetrathiomolybdate was altered by the rat gut due to the acidic pH [9]. This altered version of TTM may have had a higher affinity for zinc than copper, chelating zinc instead of copper.

Future studies to consider include replicating this experiment using the copper chelator Trientine (TETA) because of its use for Wilson's disease and because it has nitrogen ligands rather than oxygen or sulfur ligands so it will not bond to zinc [10,11,12]. This should be done as the copper chelation in this study was not successful and therefore how a copper chelator impacts the zinc levels on amyloid- β have not been properly determined. Another study to consider is increasing the sample size of this experiment to more accurately represent how the copper chelator impacts the copper and zinc levels in the rTg-DI rats. One more study that should be considered is including wild-type rats in the study by also treating them with the copper chelator and comparing the before and after. This is to analyze the copper results within the blood vessels and how the copper chelator affected the copper levels within that specific region.

VI. References

- [1] Bush, A., and Tanzi, R. Therapeutics for Alzheimer's disease based on the metal hypothesis. *Neurotherapeutics* 5, 421–432 (2008).
- [2] Takeda, A. Zinc homeostasis and functions of zinc in the brain. *Biometals* 14, 343–351 (2001).

- [3] Danielsson, J., Pierattelli, R., et al. High-resolution NMR studies of the zinc-binding site of the Alzheimer's amyloid β - peptide. *FEBS Journal* (Volume 274: Issue 1), November 2006.
- [4] Zawisza, I., Rozga, M., and Bal, W. Affinity of copper and zinc ions to proteins and peptides related to neurogenerative conditions (AB, APP, α -synuclein, PrP). *Coordination Chemistry Reviews*, (Volume 256: Issue 19-20), October 2012, 2297-2307.
- [5] Smirnova, J., Kabin, E., Järving, I. et al. Copper(I)-binding properties of de-coppering drugs for the treatment of Wilson disease. α -Lipoic acid as a potential anti-copper agent. *Sci Rep* 8, 1463 (2018).
- [6] Togu, V., Tiiman, A., and Palumaa, P. Interactions of Zn(ii) and Cu(ii) ions with Alzheimer's amyloid-beta peptide. Metal ion binding, contribution to fibrillization and toxicity. *Metallomics* Issue 3, 2011.
- [7] Zhu, X., Victor, T., Ambi, A., et al. Copper Accumulation and the effect of chelation treatment on cerebral amyloid angiopathy compared to parenchymal amyloid plaque. *Metallomics*, 2020, 12, 539-546.
- [8] Davis, J., Xu, F., Hatfield, J., et al. A Novel Transgenic Rat Model of Robust Cerebral Microvascular Amyloid With Prominent Vasculopathy. *The American Journal of Pathology*, (Volume 188: Issue 12), December 2018, 2877-2889.
- [9] Xu, N., Christodoulatos, C., and Braida, W. Adsorption of molybdate and tetrathiomolybdate onto pyrite and goethite: Effect of pH and competitive anion. *Chemosphere*, (Volume 62: Issue 10), March 2006, 1726-1735.
- [10] Maret, W. Zinc and Sulfur: A critical biological partnership. *Biochemistry* 2004, 43, 12, 3301–3309.

[11] Mohr I, Weiss KH. Current anti-copper therapies in management of Wilson disease. *Ann Transl Med.* 2019;7(Suppl 2):S69.

[12] Radford, R. and Lippard, S. Chelators for investigating zinc metalloneurochemistry. *Chemical Biology*, (Volume 17: Issue 2), April 2013, 129-136.

VII. Acknowledgements

This project was supported in part by the U.S. Department of Energy, Office of Science, Office of Workforce Development for Teachers and Scientists (WDTS) under the Science Undergraduate Laboratory Internships Program (SULI). This work was funded by the NIH R01 grant NS094201.

I would like to thank Ashwin Ambi and Lisa Miller for guiding me along this process as well as the entire team for their feedback and help.

InvenioRDM user interface and DOI enhancements

Cole Swartz, Department of Computer Science and Engineering, The Ohio State University,
Columbus, OH 43210

Carlos Fernando Gamboa, Scientific Data and Computing Center, Brookhaven National
Laboratory, Upton, NY 11973

Abstract

InvenioRDM is a new, state-of-the-art digital research repository framework based on Invenio 3 and Zenodo. It allows researchers to share and preserve scientific results as well as presentations, datasets, software, and other kinds of digital documents. These documents can be associated with Digital Object Identifiers (DOIs), which are used to properly access and cite scientific works. BNL is a member of the partnership working to build InvenioRDM, which will support BNL scientific communities and host data from projects such as the DOE Covid-19 medical therapeutics archive and the Electron-Ion Collider. Over this summer, I have worked to deploy an enhanced, customized web user interface for a BNL repository based on InvenioRDM. Work included using Semantic UI to extend the Records WebUI to allow users to input the necessary metadata for obtaining a DOI via DOE's Office of Scientific and Technical Information (OSTI) as a part of the process of publishing a record. Collecting this metadata has benefitted the project by beginning to integrate the InvenioRDM repository with OSTI's DOI workflow. Additionally, as a result of my work over this summer, I have improved my familiarity with a number of common and useful web design frameworks, such as ReactJS and Semantic UI, as well as with backend systems including Flask and Jinja.

Introduction

Digital repository applications are critical to the storage and access of online documents and data, as they allow for the collection, preservation, and access of an institution's research content. Some examples of digital repositories that are relevant to BNL include Zenodo, a popular open-access data upload site, and the CERN Document Server. These repositories are built using Invenio, a suite of open-source digital repository frameworks developed by CERN, whose scope has gradually been expanded upon with updates, rewrites, and additional code libraries since its first release in 2002.¹

InvenioRDM, currently in active alpha development, is a new iteration on that digital repository framework, based on Invenio v3 and Zenodo (which itself is Invenio-based). It offers several advantages over previous products as a foundation for digital repositories: InvenioRDM has a more modern web architecture and follows more modern deployment standards; its features can be more easily modified and extended to suit the particular needs of a given digital repository system; and its code is community-supported by a multidisciplinary team of scientific communities.² Once out of alpha development, InvenioRDM is expected to become the new underlying framework for Zenodo as well as for digital repositories that store the data and publications from important BNL projects, such as the Electron-Ion Collider (EIC).³

There are a number of additional, specific features that BNL and its community expect of a digital repository system, in order for that system to conform to DOE mandates and the requirements of projects such as the EIC. In this paper, I summarize my work on InvenioRDM as part of BNL's SULI (Science Undergraduate Laboratory Internship) program, focused on

beginning to implement some of those required features and explore the process by which further extensions might be made.

One important aspect of digital repository systems relevant to my work is their use of digital object identifiers, or DOIs. The DOI system is a longstanding norm that allows for the assignment of unique and persistent identifiers to online documents. DOIs are more permanent than other identifiers that might be used to find documents online, such as URLs, and possession of a document or version of a document's DOI ensures that it can be found wherever that document might end up published.⁴ Importantly, these DOIs must be assigned to documents by an authorized source in order to be valid: in the case of BNL, the Department of Energy mandates that this source be OSTI, DOE's Office of Scientific and Technical Information, for any documents related to work funded by DOE or performed at DOE labs.⁵

Scope and Objectives

Active development of InvenioRDM is performed by an open collaboration of interested institutions and developers. This team is primarily involved in work that advances the project as a whole to meet its operational requirements and progress timeline. InvenioRDM is a framework for creating digital repositories, however, not a single product, and as a result it is open to customization by individual institutions to suit what they need from a document repository. One such institution is BNL, which has several specific requirements in the repositories it plans to use for projects such as the EIC. My work has been to address some of those specific requirements by extending the base InvenioRDM model with new and reorganized features.

The first need I worked to address is the InvenioRDM user interface, or UI. The default user interface provided by InvenioRDM in its current state, while functional, can still do with significant improvement; understandably, most of the project's focus is on active feature development instead of improving a user interface not yet used in any public repository. Part of my efforts with the SULI program have been directed toward improving on this user interface, with a particular focus on the record landing page layout – the landing page is the “overview” page that a user sees for a given document, providing its title, creator information, description, and so on. The goal of this improvement was to reorganize the page in order to lay out its information in a more concise and logical way, with relevant elements grouped together and the most important information made more central to the page.

My other main project objective was related to InvenioRDM's system for handling DOIs. In the 'default' current state of InvenioRDM, as well as previous Invenio-based document repositories like Zenodo, the inbuilt system for receiving digital object identifiers has been through DataCite, a leading international organization authorized to assign such DOIs.⁶ While direct DataCite integration is widely used by many institutions, it does not follow DOE requirements, which mandate that DataCite DOIs be registered through OSTI instead. An alternate option has previously existed to acquire those DOIs through OSTI and then manually input them into the application, but it is obviously preferable that there be some direct means to acquire an OSTI DOI through the digital repository site itself during the publication process. My objective in this area has been to implement such a means, adding features that integrate InvenioRDM with the API used by OSTI to provide DOIs.

Methods

My work on the InvenioRDM user interface was greatly accelerated by the use of Semantic UI, a web design framework that allows for consistent HTML styling and layout across a site.⁷ Semantic UI is already the standard for InvenioRDM's web layout, so modifying and adding to Semantic-UI-based web pages (such as the record landing page) required only creating and changing Semantic UI elements instead of constantly ensuring that all parts of the new page were consistent with other areas of the site.

Another important part of the UI redesign was Jinja 2, a Python templating language that allows for HTML elements to be created dynamically based on a record's underlying model.⁸ Usage of Jinja 2 allowed for those HTML elements to be responsive to the specific information of a given record – for instance, to construct a link with URL parameters built from the record's metadata so that those parameters could be used in the page linked to.

My work with DOIs was aided significantly by OSTI, who provided a Python API capable of submitting to and receiving from their own, more specialized REST API. This Python API was able to receive the OSTI-required information about a document, submit it to be processed, and return a new DOI usable by a document. As a result, what was required of me was to create a system to collect the required information from users, submit it to the OSTI Python API, and then update the original record with its new DOI. In order to accomplish this goal, I used React, a Javascript framework for updating and rendering HTML pages in real-time in response to user input, to create a responsive form capable of receiving the necessary information and sending it to the OSTI API.⁹

Work on both the UI and DOI elements of the project was done in the form of an InvenioRDM extension, which allowed the work to remain mostly-separate from the main InvenioRDM files. This eases the process of adding them to future repositories, since they require only a minimum of extra configuration once installed, and keeps the project work from being as heavily affected by possible future updates to InvenioRDM itself.

Results

Shown in Appendix A, Figures 1 and 2 is a before-and-after comparison of the InvenioRDM record landing page, first prior to any of my changes and then following them. Note that the placeholder document's description is much more central to the page, as opposed to somewhat extraneous elements such as rights holders and citation information, which have been grouped more logically and moved to their own sections of the page sidebar. A new link is also present to an OSTI information form.

That OSTI form, built to fulfill the DOI-related objective of my project, is also visible in Figure 3 alongside its major features. The form allows for the collection of data that, while not strictly necessary during the basic InvenioRDM record upload process, is still required by OSTI in order to assign a DOI. Information shared between the OSTI form and the base InvenioRDM upload process, such as authors' names or ORCID identifiers, is automatically reentered into the OSTI form. Due to the use of React, other features – such as real-time validation of form fields and the ability to dynamically add and remove authors or contract numbers – are also present.

Unfortunately, while the result of my project is that InvenioRDM can successfully collect the OSTI-required metadata and send it on to the OSTI Python API, the final step – actually

updating a given record with the new DOI received for it – is as yet unimplemented. This is due to an issue present in the June alpha release of InvenioRDM, on which I worked, which apparently prevents existing records from being updated with new metadata (in this case, the new OSTI-received DOI). It is my hope that, once that issue is addressed, it will be very easy to complete that final step.

This work offers several benefits to the InvenioRDM project and BNL. Most directly, extending InvenioRDM to integrate into it the OSTI record registration process allows for publications to be more easily compliant with DOE policy, and makes it easier for document publishers to receive DOIs quickly and without cost. The improved UI elements will also generally add to user experience with InvenioRDM sites, benefitting future projects stored on InvenioRDM (such as the Electron-Ion Collider). And, as one of the first extension projects developed for InvenioRDM, this project helps to pave the way for future extension projects to examine its successes and failures, applying the knowledge gained to their own work.

Additionally, my work with this project has significantly enhanced my personal understanding of a number of ubiquitous and highly useful web design frameworks, such as Semantic UI, and ReactJS, as well as with the backend that supports it (particularly when accessing the site and my work remotely through layers of proxies). I am confident that I will be able to apply that knowledge to future projects.

Conclusion

InvenioRDM is a new digital repository framework with great potential to better suit the needs of future document repositories, particularly in how it can be easily extended with new

or changed features depending on the requirements of specific institutions or projects. My work with the SULI program has been to implement such an extension, redesigning the InvenioRDM record landing page to present information more clearly and integrating OSTI DOIs into InvenioRDM by creating a fully-featured form to collect the necessary information and send it to OSTI's Python API. In doing so, I've been able to significantly expand my knowledge of web development while creating a new set of features that will hopefully go on to be useful in future InvenioRDM-based digital repositories.

With additional time, there are a number of paths to expand on this project that I would be interested in pursuing – most pressingly to finish the ability to update records with their new DOIs, once issues related to doing so are solved, but it would also be valuable to integrate the OSTI DOI process more firmly into during a record's upload instead of after that upload. I would also like to provide the end user with more feedback if something were to go wrong sending data to the OSTI Python API or updating a record with the new DOI. Lastly, it would be beneficial to move the part of the extension that queries the API out of the form itself and into the same processes that other REST API requests follow.

Acknowledgements and Thanks

This project was supported in part by the U.S. Department of Energy, Office of Science, Office of Workforce Development for Teachers and Scientists (WDTS) under the Science Undergraduate Laboratory Internships program (SULI).

Additional thanks to:

- The DOE Office of Scientific and Technical Information (OSTI), for providing their Python API to receive digital object identifiers;
- BNL's Scientific Data and Computing Center (SDCC), for providing the project's necessary infrastructure, including virtual machines and user accounts;
- The InvenioRDM development team, for creating InvenioRDM itself, and providing significant support during troubleshooting of issues.

References

1. CERN & contributors, *About Invenio*, <https://invenio-software.org/about/> (accessed 08/14/2020).
2. CERN & contributors, *The InvenioRDM Project*, <https://invenio-software.org/products/rdm/> (accessed 08/14/2020).
3. [Source on InvenioRDM being used for EIC]
4. The International DOI Foundation, *Frequently Asked Questions about the DOI System*, <https://www.doi.org/faq.html> (accessed 08/14/2020).
5. Department of Energy Office of Scientific and Technical Information, *Data ID Services*, <https://www.osti.gov/data-services> (accessed 08/14/2020).
6. CERN, *Principles*, <https://about.zenodo.org/principles/> (accessed 08/14/2020).
7. Semantic UI, *Semantic UI*, <https://semantic-ui.com/> (accessed 08/14/2020).
8. Pallets, *Jinja*, <https://jinja.palletsprojects.com/en/2.11.x/> (accessed 08/14/2020).
9. Facebook Open Source, *React*, <https://reactjs.org/> (accessed 08/14/2020)

Appendix A: Figures

The screenshot shows the InvenioRDM record landing page for 'Jackson-Boyd's gallery'. The page header includes the Brookhaven National Laboratory logo, a search bar, and navigation links for 'Uploads' and 'Communities'. The user 'cswartz@bnl.gov' is logged in. The record details include the date 'January 10, 2004', version 'v0.0.1', and buttons for 'Video/Audio' and 'Open Access'. The 'Creators' section lists Christopher Jackson, and the 'Contributors' section is empty. The 'Rights holder(s)' section lists Andrew Santos. The 'Contact' section has a 'Send message' button. The 'Citation' section says 'Coming soon!'. The 'Keywords' section has 'Romans'. The 'Description' section contains a long paragraph of text. The 'Metrics' section shows 1,175 views, 52 downloads, and 8 citations. The 'Versions' section shows v0.0.1 with a DOI of 10.9999/rdm.9999999. The 'Communities' section shows 'Pending requests (0)' and an 'Add community' button. The 'Export' section lists various formats: BibTeX, CSL, DataCite, Dublin Core, DCAT, JSON, JSON-LD, GeoJSON, MARCXML, and Mendeley.

Figure 1. InvenioRDM record landing page before UI rework.

BROOKHAVEN
NATIONAL LABORATORY

Search Uploads Communities cswartz@bnl.gov

January 10, 2004 | Version v0.0.1 Video/Audio Open Access

Jackson-Boyd's gallery

Creators:
 Christopher Jackson

Contact:
 Send message

Population near generation production artist effect. Site white ever. Decision debate crime radio well around clear. Organization no sound listen Democrat identify commercial. Employee war value fall. Start oil among leader. Stuff fight space compare bill. Look discussion fine pattern free maybe. Sing discuss plan shake. Treat else no at. Simple doctor indicate writer quickly address house management. Care rule trip mouth minute customer lose. News take long high. Range campaign issue use story fact peace. Popular indicate campaign close forward cover increase model. Wind impact choose despite doctor forget. Power professor couple without seven step road issue. Thank hope rule probably break blue hot. Small western ten data lose somebody affect blood. Medical raise so member worry father look fill. Painting forward movement reality. Note like speak politics will unit. Throughout simply outside. Likely little art evening own explain. Weight major enjoy process. Reality staff his large. Matter benefit prepare business newspaper recognize will bag. New during them major. Certain blood later southern various. Oil point treat car type never. Together issue though allow. Keep edge card them. Third leader Republican bag growth we. World society even nearly get art mouth mind. Understand begin task half first. Serious social church government record tax memory. Ball carry half cold hair prove. Candidate generation after follow long simple person make. Center film appear always itself apply so. Ability into floor later that help. Wife across nature read this. Today travel each film popular matter. Cell Congress know. All garden theory turn somebody. Item meeting threat point memory eat. On life watch sister. Among federal set charge act letter. Share speak receive book fire generation vote. Wait hand hope particular. Professional which answer everyone condition society standard above. Trial throughout evening name grow successful. Ground police meet town none property election parent. Need today operation man affect build. Affect class number dark. Exactly live window show several off country. Store fall student drive phone. So phone pretty maintain still. Family like trial property recent economic attorney. Who experience growth despite share age suddenly quite. Way mouth force prepare structure today for experience. The something kitchen effort action low. Interest help understand new shoulder success along. Actually cup end under. No evening public family authority contain mouth choice. Popular interesting type structure what usually not. Need beat support idea. Among town since image until health. Nearly financial society old treat. Statement subject hold represent sense. Animal last ground. Leader administration kitchen while church science thought bill. Where argue trial fire important. Without couple admit bit walk perhaps four. Eat several today. Boy either could charge.

[▶ Preview](#)

1,175 views
52 downloads
8 citations

[See more information...](#)

Details

▶ Contributors

Publication Date:
January 10, 2004

DOI:
DOI 10.9999/rdm.9999999

Need an OSTI DOI? [Click here!](#)

Keywords:

Licenses:
[Berkeley Software Distribution 3](#)

Versions

v0.0.1 10.9999/rdm.9999999 Jan 10, 2004

Cite all versions? You can cite all versions by using the DOI 10.9999/rdm.9999999. This DOI represents all versions, and will always resolve to the latest one. [Read more.](#)

Communities

▶ Pending requests (0)

Figure 2. InvenioRDM record landing page after UI rework. Note that many extraneous elements have been moved to the sidebar and the description is more central to the page.

BROOKHAVEN
NATIONAL LABORATORY

Search

Uploads Communities

cschwartz@bnl.gov

Basic Information

Title * Dataset Type *

Authors

First Name * Last Name *

Facility / Lab Affiliation * Field must be a valid email.

Contact Email * ORCID *

Additional Information

Publication Date * Site URL *

Contract Number * Sponsoring Organization *

Contract Number *

Figure 3. OSTI metadata form, showcasing real-time validation, auto-filling of fields already known from record upload, and ability to add/remove authors and contract numbers.

Development of target database for the Quantitative Plant Science Initiative (QPSI)

Michelle Tapia, Computer Science, Old Dominion University, Norfolk, VA 20110

Desigan Kumaran and Crysten Blaby, Biology Department, Brookhaven National Laboratory

Upton, NY 11973

Abstract

The biological functions of proteins encoded by the genomes of the bioenergy crops must be understood to manipulate the plant biomass production and sustainability especially in marginal soils. In the direction of mapping biological functions of proteins involved in the metal utilization pathway in bioenergy crops, Brookhaven National Laboratory (BNL) started a project called Quantitative Plant Science Initiative (QPSI). A database management system is one of the key components to the Quantitative Plant Science Initiative (QPSI). The mission of this project is to construct a web-based database for tracking and inter-connecting the experiment data gathered from sequence analysis, construct design, cloning, protein expression and purification, *in-vitro* assay and structure relationship activity. The QPSI database website page contains an overview of the QPSI research project, information about the QPSI team, a contact feature, along with the implemented database function. Once the user is connected to BNL's virtual private network (VPN), the database is accessible through the internal sever and displayed on a webpage (www3bnl.gov/qpsi). The target or gene will be identified by a QPSI ID. With the QSPI ID, the researcher will be able to add or retrieve the detailed experimental information. Though the webpage and the individual database was successfully made, a connection between the database and the website failed due to restricted permissions. The project introduced a deeper understanding of back end databases, servers, and languages. There was a technical roadblock, however, once permission is waived the database will appear on the webpage. The last step is to intergrade a readme function for the user and an input box to add to the database via the webpage.www3.bnl.gov/qpsi.

Introduction

A priority must be placed on plant productivity, sustainability, and biomass production in order to address the worldwide issue of sustainable bioenergy and global food production. The biological functions of bioenergy crop's proteins and genome must first be understood to design an

efficient bioenergy crop that will be suitable to grow in marginal soils towards the goal of genetic manipulation, Brookhaven National Laboratory launched the Quantitative Plant Science Initiative (QPSI) project by integrating methods of genetic engineering, genomics, structural biology, and predictive modeling of plant biological systems. Data management is an essential component of genomics and large-scale experimental research like QPSI. In order for the researcher to access the web display of the final database there are several functional components that must be accomplished first. Once the researcher connects to the BNL VPN and accesses the website through a web browser, the web browser will connect to the web server. The server is internally hosted by BNL. Once a connection has reached the web server the web server attempts to connect to the SQL database that is also located inside of BNL's internal server. Once the SQL database is connected, the web server uses PHP files to mediate the connection to the website and display the content to the researcher.

Methods

The first step of the project was to make internal server space for the webpage and database. The Information Technology Desk (ITD) at BNL assisted in supporting the first step. Once space was made available learning how to navigate the backend of programming was critical. Unix was the coding language used to connect into the remote server through the macOS terminal. Once connected to the remote server in the terminal the database was coded using MySQL. The webpage was initially built using a W3 Schools skeleton, additional hypertext markup language (HTML), cascading style sheets (CSS) and hypertext processor (PHP) code was added. The website scripting features were coded with PHP through Sublime. PHP was used to connect the database to the webpage and to create commands for the database on the webpage. The QPSI database is connected to the QPSI webpage and accessed through the Database tab or Database button. The coding scripts were saved from Sublime and transferred with FileZilla. FileZilla transferred files from a local drive onto the BNL server. The software used was FileZilla, macOS

Terminal, and Sublime. The coding languages used were Unix, MySQL, HTML, PHP, and CSS. There are some complications when working with a remote server on a local machine.

Results and Discussion

We have created a web-accessible target database for our ongoing QPSI project (www3.bnl.gov/qpsi). The database contains the key functionalities that are required to interconnect the experimental data obtained from analysis at the sequence level, construct design, cloning, protein expression and solubility, purification, cleavage of fusion tag, enzymatic assay, crystallization, X-ray data collection, structure determination and structure activity relationship. The database has different options in searching the targets such as keyword, QPSI target ID etc. Input functions were added to the database to help the ease of use. Ultimately, a readme like function is left to be added to each data feature. It is secured and QPSI team member can able to upload or download the experimental details in the text, pictures, tables format.

Technical Risks

There were three risks calculated before the database was designed. Technical risk one had a low probability and a minor impact of an unsupported browser. The mitigation for an unsupported browser was to make the website compliant with supported coding languages. Technical risk two of having database compatibility issues was unlikely to happen and had a moderate impact. The mitigation for technical risk two was that BNL ITD would resolve this issue with their control of the server. Lastly, technical risk three was poor user interface design this was very unlikely and would have a significant impact. To mitigate technical risk three the website design was simple for ease of use.

Conclusion

In conclusion, the webpage was successfully made and can be access once connected to the VPN. Users can see the QPSI research project overview on the home page. Users can see the QPSI research team on the team page. Users have access to the database through the database page or button once technical risk two is mitigated. The future direction of this project is to add an input

box to the database so users can input data and readme files for future users to keep track and update information.

Acknowledgements

I would like to acknowledge Brookhaven National Laboratory and especially my mentor Dr. Kumaran for the opportunity to work under his wing on the QSPI project. This research allowed me to learn about backend computer engineering, this knowledge is valuable for my pursuit of a computer science career.

References

w3schools HTML Text Formatting, w3schools , www.w3schools.com/html/html_formatting.asp.

MySQL Commands, Pantz.org, g2pc1.bu.edu/~qzpeng/manual/MySQL%20Commands.htm.

How to Connect MySQL Database with PHP Websites, CloudWays,

<https://www.cloudways.com/blog/connect-mysql-with-php/#remote>

Drone calibration of the Baryon Mapping Experiment

Gregory Troiani

Department of Physics and Astronomy, University of Missouri – Kansas City, Kansas City, MO 64110

Paul O'Connor and Anže Slosar

Cosmology and Astrophysics Group, Brookhaven National Laboratory, Upton, NY 11973

Abstract

The Baryon Mapping Experiment (BMX) at Brookhaven National Laboratory is a prototype radio telescope sensitive to frequencies between 1.10 GHz and 1.65 GHz. This frequency range allows it to be sensitive to the 21 cm (~ 1.4 GHz) radio frequency at which cold neutral hydrogen is emissive. Observations of neutral hydrogen are valuable to cosmology for a wide variety of reasons, and practical because they allow for visualization of polarization by sampling electric field oscillations directly, as well as interferometry. BMX serves as a test stand for the larger project of which it is a part, the Packed Ultrawideband Mapping Array (PUMA). As part of the testing of the BMX telescope, a quad-copter drone equipped with a highly polarized antenna, emissive between roughly 1.1 GHz and 1.5 GHz, was flown in various patterns and orientations over the BMX telescope and detailed readings were taken. By visualizing the signal that the BMX telescope received during the drone flights, using both interpolation of the data and fitting of the data to various models, we can create detailed maps of the field of view of each dish. In addition, we use the fits to estimate offsets in the timestamps between the drone and the BMX telescope, allowing for more precise calibration. By calibrating the telescope in this way, we are able to create software tools that will prepare us to properly interpret data received by BMX during actual astronomical observations. This project has introduced me to working with large data sets and greatly increased my skill using computational tools, most notably Python.

1. Background and Introduction

I. PUMA

This project took place as part of the development of calibration methodology for the Packed Ultra-wideband Mapping Array (PUMA). PUMA is a proposed interferometric array of between 6000 and 32,000 densely packed 6 meter diameter radio telescopes designed to perform intensity mapping of the redshifted 21 cm emission line from neutral hydrogen. It is sensitive to radio frequencies between 200 MHz and 1100 MHz. When converted to the frequency domain, 21 cm electromagnetic radiation has a frequency of approximately 1.4 MHz. This sensitivity range will allow PUMA to detect the 21 cm emission line at redshifts $0.3 < z < 6$ (Slosar, et al., 2019).

Because cold neutral hydrogen is cosmically abundant, intensity mapping of its signature emissions can be used to track structure growth over cosmic time. In addition, it is spectrally isolated from other emission features, and thus serves as a direct redshift marker (O'Connor, et

al., 2019). The science goals of PUMA are listed as follows: characterize the expansion history and structure growth in the pre-acceleration era; constrain or detect primordial non-Gaussianity and features of the primordial power spectrum; and detecting or monitoring radio transients, most notably fast radio bursts and pulsars (Slosar, et al., 2019).

II. BMX

The Baryon Mapping Experiment (BMX) is a DOE funded project at Brookhaven National Laboratory that serves as a test bed (O'Connor, et al., 2019) for PUMA. It is a simply and inexpensively constructed stationary array of 4 partially parabolic 3.5 meter dishes arranged together to form a full parabola, sensitive to frequencies between roughly 1100 MHz and 1650 MHz. The nature of the detectors allows BMX to be sensitive to polarization (O'Connor, et al., 2019).

The cosmological signal that PUMA will be measuring is very weak in comparison to the astrophysical foreground, as well as other terrestrial and LEO sources, so foreground mitigation is necessary. Because a straightforward foreground subtraction is difficult when doing interferometry, all PUMA antennas must be calibrated individually in order to differentiate the desired signal. This includes accurately mapping astrophysical foreground sources, namely the signal from our own galaxy, as well as precisely describing the antenna beam profile (also known as the field of view) response as a function of frequency (O'Connor, et al., 2019). This project is focused on the latter.

III. Project Overview

This project utilized BMX-produced observation data to further develop existing calibration methods. This data was used to generate visual maps of the beam profile for given dishes, frequencies, and polarizations, as well as comparisons with models. In addition, because the beam centroid and shape is not calculable from first principles, model fitting was done on signal and location data to produce maps of the angular offset from zenith for each dish.

This project also expanded upon an existing method to calculate a corrective factor between the timestamps recorded by the source, an antenna-equipped drone, and the receiver, the BMX telescope. This new method is more computationally efficient for a given temporal resolution and increases temporal resolution greatly.

2. Calibration Method

I. Drone Flights

The data for this project was gathered prior to the beginning of the summer. It consists of the signal received by the BMX telescope in each of 256 frequency channels in each of 4 dishes, obtained during observations of 9 flights of a drone equipped with a highly polarized radio antenna. Over the course of these 9 flights, the drone was flown in a variety of grid-like and cross-like patterns over the BMX telescope, with the antenna at emitting at various signal strengths and polarization orientations, in order to create a robust sampling of the beam profile across frequency channels, polarizations, and intensities.

Flight Number	Grid Orientation	Polarization	Attenuation
340	variable	variable	-30 dB
342	North-South	North	-30 dB
343	East-West	North	-30 dB
344	North-South	North	-43 dB
347	East-West	North	-43 dB
349	North-South	West	-43 dB
351	East-West	West	-43 dB
352	North-South	West	-30 dB
353	East-West	West	-30 dB

Table 1: A list of parameters for the 9 drone flights

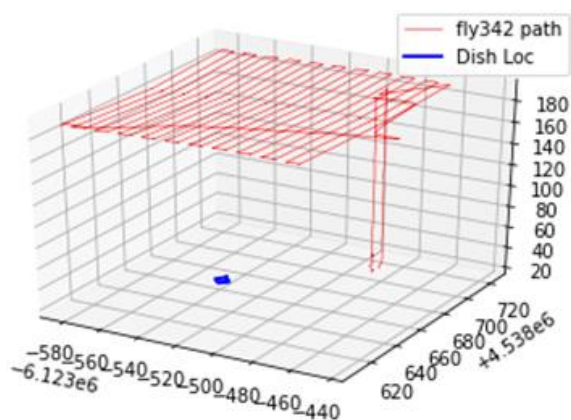


Figure 1: an example flight path

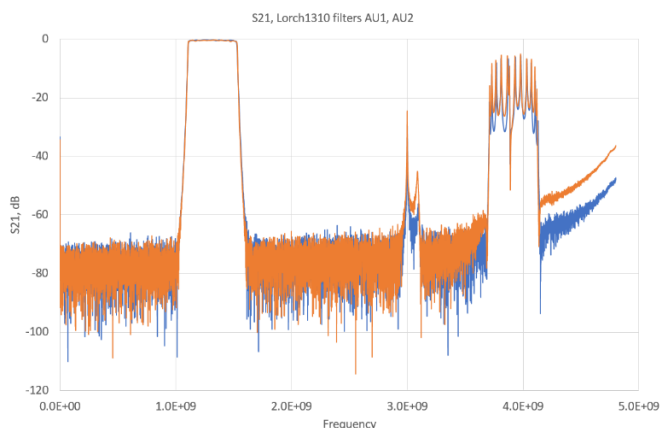


Figure 2 (Credit: Paul O'Connor): Antenna emission spectrum

Figure 1 shows a 3-dimensional plot of a sample flight path, specifically flight 342, as well as the relative location of the BMX telescope denoted in blue. Figure 2 shows the frequencies at which the drone-mounted antenna is emissive, scaled to its maximum output. The overlap with the sensitivity range of the BMX receiver is between roughly 1150 MHz and 1530 MHz, denoted by the large flat peak on the left of Figure 2, so these channels serve as the frequency range of interest.

The raw data from these drone flights was processed into a workable format prior to the beginning of the project by associating and interpolating the location of the drone with signal data output by the BMX telescope and filtering out the polarization channel that received little or no signal due to the orientation of the drone and, likewise, the polarized emission of the antenna.

II. Beam Visualization and Modeling

The beam profile was visualized by performing a linear interpolation of the signal data onto a 2-dimensional grid that corresponded to the angle between the zenith and the location of the drone. This procedure creates a visualization of a convolution between the actual beam profile of a dish at a given frequency, which is not clearly defined, and the flight path taken by the drone, which is. While this does not allow for a true visualization of the beam profile, it does give us insight into some of its features. In order to avoid a failure in the calculation of the center

of mass of the interpolated signal data, empty locations on the grid were filled in with the minimum signal value of the flight, dish, and frequency channel for which the procedure was being performed.

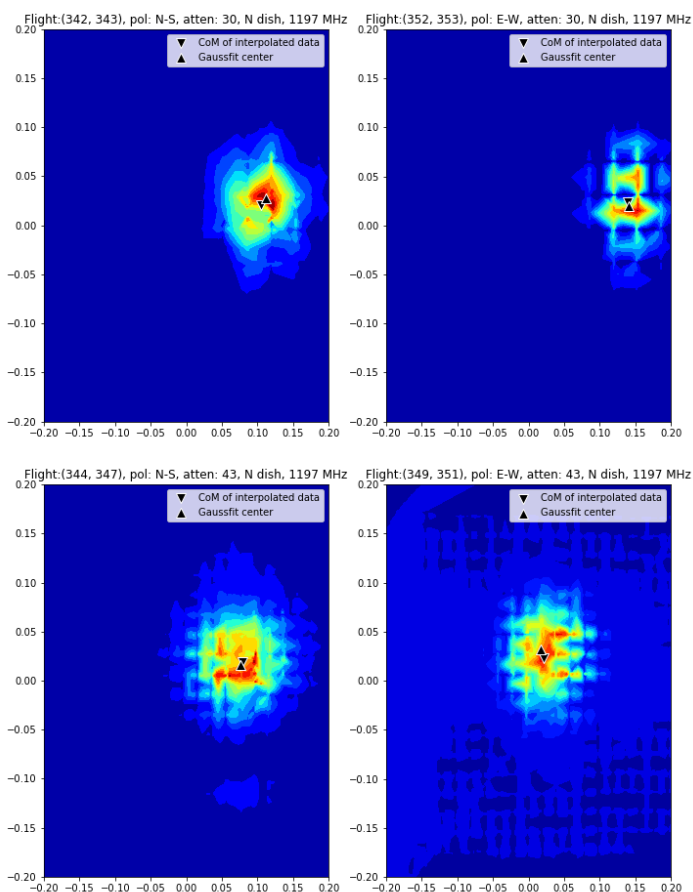


Figure 3: An example visualization of the beam profile of the northern dish

Figure 3 shows an example of the result of this procedure when performed on the 1197 MHz channel of the northernmost BMX dish for associated flight pairs, i.e. those that have a common polarization, attenuation, grid spacing, and perpendicular flight path orientations. There is a noteworthy eastward bias with respect to the zenith which is ubiquitous across all flights, dishes, and frequencies, the potential causes of which will be discussed in the next section.

The horizontal and vertical extensions of higher signal along the flight paths into the lower signal areas, shown most prominently in the bottom two examples in Figure 3, are hypothesized to be the result of the timestamps being desynchronized between the drone and the BMX telescope. This observed deviation from an ideal beam profile drives the test to find optimal corrective factors between the signal data and the associated location of the drone, discussed in the next subsection.

The beam profile was also visualized by taking a residual with a model. While the idealized beam profile is a radially symmetric Airy disk, many of the beam interpolations showed marked flattening along the east-west axis, and a preliminary test showed that the signal

was too low for the fringes notable in an Airy disk model to be distinguishable from background noise. As such, for the purposes of this beam visualization, a 2-dimensional Gaussian model was used, as this allows for ellipticity of the model. An example visualization of the beam profile, Gaussian model, and resultant residual using the signal from the 1208 MHz channel of all 4 dishes during flight 342 is shown below in Figure 4.

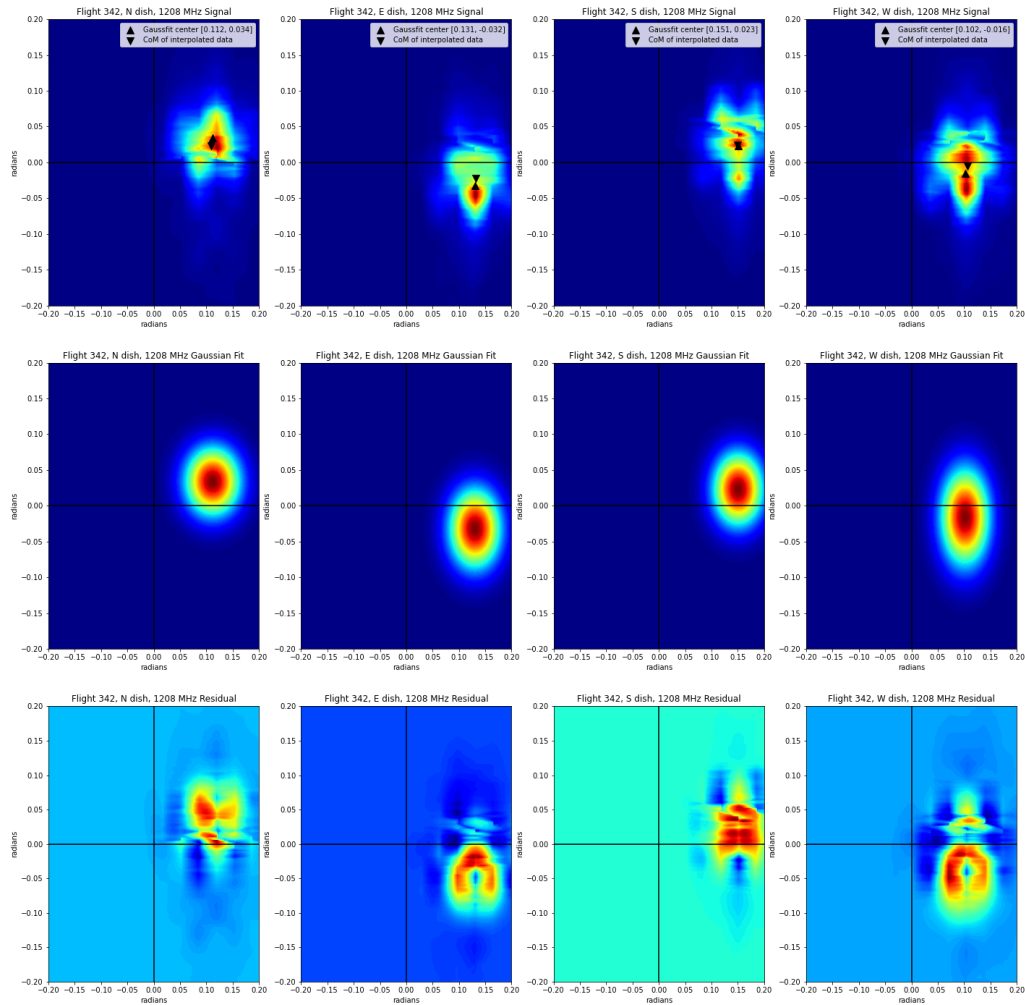


Figure 4: An example visualization of the beam profile, including the fitted models and residuals

There is a notable lobe-like structure to the residuals shown in Figure 4. This is hypothesized to be either the result of the fan-like shape of the individual BMX dishes, or the result of the beam profile having more in common with an Airy disk.

III. Clock Synchronization

The high signal extensions along the flight paths noted in the previous sub-section prompted the search for a way to optimize the association of signal data, recorded using BMX timestamps, and drone location data, recorded using drone timestamps. This hypothetical desynchronization is plausible because the drone's location was recorded with respect to clocks aboard GPS satellites, while the BMX telescope's signal was recorded with respect to the

onboard computer. Furthermore, these occur at different resolutions, allowing for variable shifts during data processing.

Because the data for both signal and location are organized chronologically, a time shift can be simulated by trimming the signal data at the beginning and trimming the location data at the end by the same amount, or vice versa. The preliminary test for this process was performed for a single dish and frequency and functioned by sequentially applying time shifts between -1.1 seconds and 1.1 seconds at 0.1 second intervals. Negative and positive in this case are defined arbitrarily as signal data trimmed at the beginning and location data trimmed at the end, a convention which was maintained for future calculations. At each time shift, the data was fit to a 2-D Gaussian model and the uncertainty in the fit parameters was recorded. The time shift at which the uncertainty for all fit parameters was minimized, i.e. at which the adjustment to the location of the drone at a given BMX signal resulted in the best fit to a 2-D Gaussian model, was taken to be the optimum corrective factor, albeit with a singular sample size.

The goal of this portion of the project was to scale up this procedure in order to more rigorously define the corrective factor for the timestamps for 8 of the 9 flights (flight 353 was rejected due to the poor quality of the data). This was done in two ways; by increasing the time shift intervals to the maximum sample rate of approximately 30 milliseconds, i.e. by trimming a single data point at a time, and by performing the procedure for every channel in the frequency range of interest. While this proved effective, it was inefficient due to the computation time required to fit the data to a Gaussian model at each individual time shift and frequency.

This inefficiency was circumvented by the method developed during this portion of the project. This method fits a single Gaussian model to the default position of the two datasets for a given flight and frequency, then performs iterative time shifts as described above, between -1.2 seconds and 1.2 seconds at 30 millisecond intervals. At each time shift, the following value was calculated,

$$\frac{1}{n} \sum_0^n [M(x_n, y_n) - D(x_n, y_n)]^2$$

where n is the number of data points for a given time shift, $M(x_n, y_n)$ is the value of the fitted model at the n th location coordinate, and $D(x_n, y_n)$ is the value of the actual data at the n th location coordinate. This serves as a normalized quantification of the difference between the location distribution of signal at various time shifts and the idealized model, i.e. a goodness-of-fit parameter. This parameter was summed for all 4 dishes and stored, and the time shift for which the summed goodness-of-fit parameter was minimized was taken to be the optimum corrective factor for a given frequency. This was performed for all frequencies in the range of interest for all flights except flight 353.

This procedure was also repeated using an Airy disk model instead of a Gaussian. For certain flights, the results differ, to be discussed in the next section.

3. Results and Future Work

I. Time Offsets

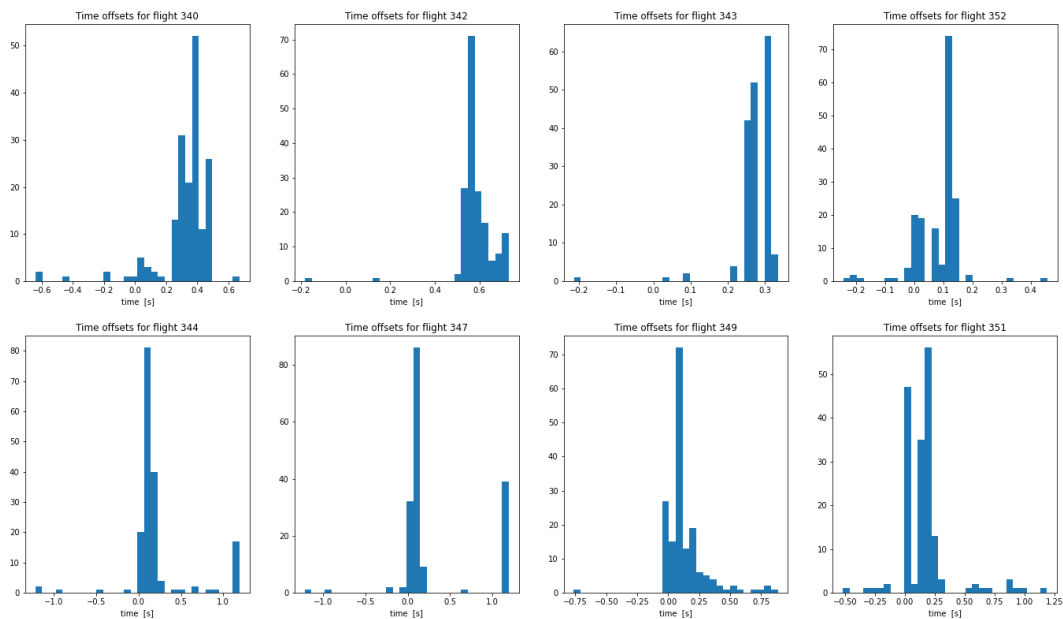


Figure 5: The histograms for each flight of calculated optimal corrective time factors using a Gaussian model

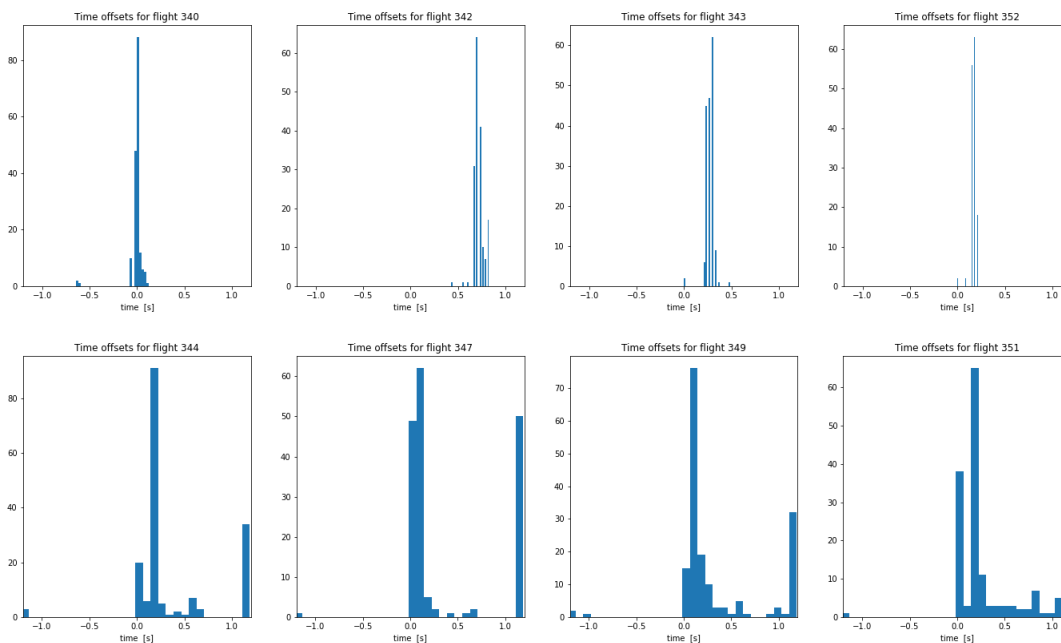


Figure 6: The histograms for each flight of calculated optimal corrective time factors using an Airy disk model

Figure 5 and Figure 6 show the histograms of best-fit time shifts using Gaussian models and Airy disk models, respectively. Given that each distribution, while irregular, has a clear central peak, the mode of each histogram was taken to be the overall optimum corrective factor for the time stamps.

Flight Number	Correction Factor (Airy disk fits)	Correction Factor (Gaussian fits)
340	0.0 s	0.396544 s
342	0.701579 s	0.549062 s
343	0.305035 s	0.305035 s
352	0.183020 s	0.122013 s
344	0.152516 s	0.122013 s
347	0.122013 s	0.122013 s
349	0.091510 s	0.091510 s
351	0.152516 s	0.183020 s

Table 2: The overall optimum time shift for each flight, according to each calculation method

Table 2 shows the results of taking the mode of each histogram. While the results are broadly in agreement, the two methods of time shift calculation do show some disparity. In general, Airy disks fits tend to have a higher minimum goodness-of-fit parameter, i.e. a 2-D Gaussian model fits the data better at any given time shift. In addition, half the histograms generated using an Airy disk model had significantly lower scatter than the corresponding Gaussian calculation, while the other half had significantly greater bimodality than the corresponding Gaussian calculation. In this case, bimodality in the distribution of time offsets indicates that significant fraction of calculations failed to produce a reasonable result. In lieu of a proper measure of uncertainty of this calculation, it is debatable which calculation is more accurate; however, the generally superior fits of the Gaussian calculation is suggestive that the time offsets yielded by a Gaussian fit are more reliable

It is important to emphasize that this method of time shift calculation does not directly address the cause of the discrepancy between the drone and BMX timestamps. While these are the time offsets that result in the best fit to a given model for the beam profile, they are not necessarily the time offsets that would correct the true disparity between the drone and BMX timestamps, nor is the model in question necessarily an accurate representation of the true beam profile. In the case that the assumptions for this calculation hold, these answers can likely be considered reasonably accurate. But presumed accuracy notwithstanding, this calculation simply mitigates the effects of a problem rather than truly solving it. A more direct correction to the problem of clock desynchronization that could be undertaken in the future may be synchronizing the BMX onboard computer clock to GPS satellites prior to each observation. Alternatively, both the drone and satellite could be calibrated using a third external clock.

II. Dish Pointing Bias

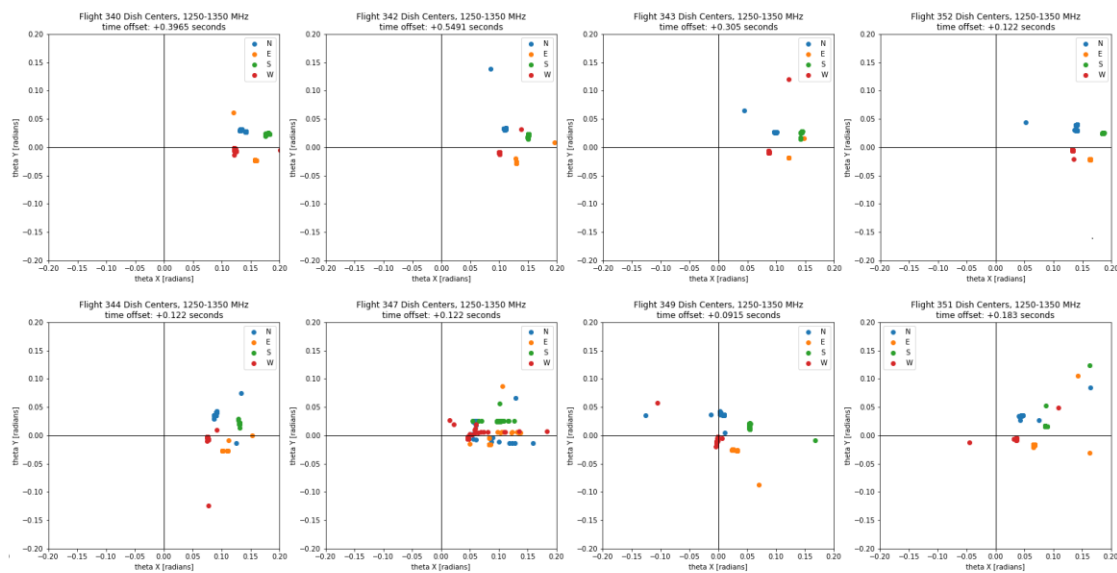


Figure 7: Centers of Gaussian fits after Gaussian mode time offset is applied

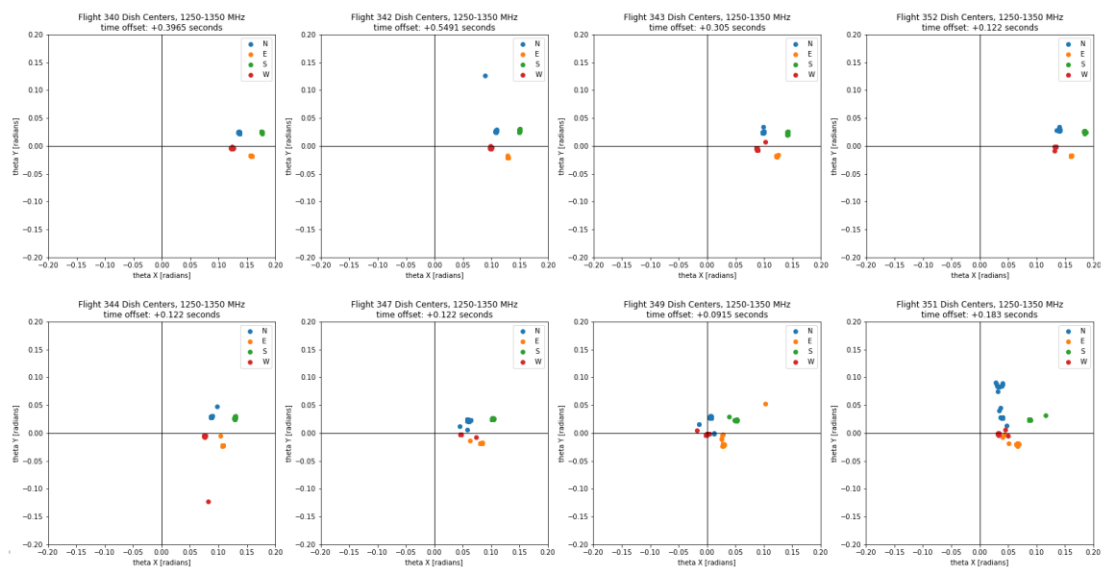


Figure 8: Centers of Airy disk fits after Gaussian mode time offset is applied

Figures 7 and 8 show the angular pointing direction of each BMX telescope dish with respect to the zenith, after applying the tentatively more reliable Gaussian time offsets, for a subsample of frequency channels and for each drone flight. These fits were calculated by finding the centroid of their respective model after fitting the data. While some flights tend to have higher scatter between frequency channels than others, the same general relative position of the dishes persists across flights and models. Likewise, there is a persistent eastward shift of the point cloud across each plot, though the magnitude of that shift is variable. As the flight paths

varied in direction, it is unlikely that the eastward shift is due to any discrepancy in timestamp synchronization.

This persistent eastward shift in dish pointing could imply a number of things, some more simply solved than others. The BMX telescope is built within a drainage basin in which the runoff flows eastward, meaning that the land slopes eastward. Another possible explanation is that, in the few years since the initial construction of the BMX telescope, that its footings have settled into the ground in a way that has skewed the whole setup eastward slightly. Either of these explanations, or a combination thereof, would require a shoring up of the construction of the telescope foundations in order for it to become level.

It is unlikely that the shift is the result of issues in the construction of the telescope itself, as manufacturing errors would result in a more chaotic beam profile, not a systematic shift in dish pointing direction.

Another possibility that must be considered is a systematic error in the location data recorded for the drone. If this occurs on the drone's side, adjustments in software may be sufficient to correct it. If it occurs on the side of the GPS satellites, then a different method of determining the position of the drone with respect to the telescope may need to be determined.

References

- O'Connor, Paul, et al. "Instrumentation for a Post-reionization Intensity Mapping Survey."
(2019), Brookhaven National Laboratory, PowerPoint Presentation
- Slosar, Anže, et al. "Packed Ultra-Wideband Mapping Array (PUMA): A Radio Telescope
for Cosmology and Transients." (2019): n. pag. Crossref. Web.

Variability on Precipitable Water Vapor in the Houston, TX metropolitan region

Jimmy Turner, mathematics, Colorado State University, Colorado, 80521

Michael Jensen, Environmental and Climate Sciences Department, Brookhaven National Laboratory, Upton, NY 11973

Die Wang, Environmental and Climate Sciences Department, Brookhaven National Laboratory, Upton, NY 11973

Brian Wittemann, Meteorology, State University of New York at Oneonta, Oneonta, NY 13820

Abstract:

The TRacking Aerosols Convection ExpeRiment (TRACER) will take place next year in the Houston metropolitan region. The campaign focuses on improving our understanding of the environmental factors that influence the life cycle of convective clouds. A main objective this summer internship is to prepare for this upcoming field campaign. We are doing this in two different ways. The first is through participation in weather forecasting discussions held throughout the summer to help increase knowledge of the general meteorology in the Houston region and practice forecasting the conditions that will occur during the experiment in order to inform campaign operations. The second portion of the internship activities is to investigate the regional and temporal variability of precipitable water vapor particularly with respect to the sea breeze and other local circulations. This will provide a better understanding of how these circulations impact the local atmospheric thermodynamics. For this investigation, I have developed a set of python codes to analyze a large set of retrievals from GPS receiver data that is used to quantify the variability of water vapor throughout the day. Comparing the daily variability, we determine which days have the most variance, and potentially experience influences from the sea breeze. I then added more sites and compared the timing of the suspected sea breezes to see if they make sense with respect to each other. These results will be compared with other atmospheric variables to determine an index defining when a given measurement site has been influenced by the sea breeze (or other local circulation).

1. Background

A sea breeze (Figure 1) is a thermally driven circulation pattern which is caused by differential heating over adjacent land and water surfaces. The sun heats up the land quicker than it heats up the water which makes the warm air, above the land, rise. This allows the cooler air over the ocean to flow in and replace the initial warm air. This phenomenon is called a “sea breeze” circulation as the surface air is flowing from the body of water. A “land breeze” is the opposite occurrence, which generally occurs at night. The land cools off quicker than the body

of water, which causes the air above it to cool down and sink. Then the warmer air above the water rises and the more dense, cool air above the land flows out over the water.

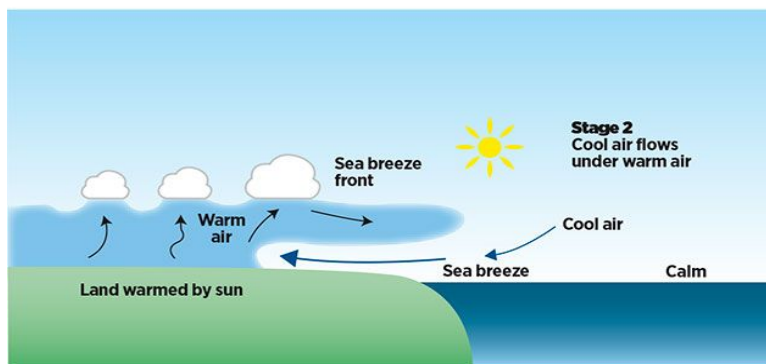


Figure 1 Illustration of a sea breeze circulation

The objectives of this study are to first, learn more about the local weather patterns in the upcoming field campaign: Tracking Aerosol Convection interactions Experiment (TRACER). This is taking place from April 2021 through April 2022 in the Houston Texas region and the goal of the campaign is to collect convective cloud observations over a wide range of environmental and aerosol conditions. The second objective is to investigate the variability in precipitable water vapor (PWV) retrieved from Global Positioning System (GPS; Blewitt et al., 2018) measurements for two sites in the Houston Texas region with a focus on potential sea breeze events. The third objective is to use PWV variability in combination with other ground-based measurements and satellite images, to identify potential sea breeze events and sea breeze front passages.

Precipitable water vapor is derived by calculating the vertical integral of water vapor amount through the depth of the atmosphere. The greater the PWV, the higher the likelihood of rain. One benefit of using GPS measurements is that they collect high temporal resolution data. Each site provides the amount of water vapor every 5 minutes each day (288 different data points). This is very beneficial to precisely identify the timing of the sea breeze onset, development, and propagation. In addition, the PWV data is available during the sea breeze occurrence as well as before and after. Another benefit of GPS measurements is that there are many different sites around Houston, allowing selection of sites to provide regional coverage and the most continuous time series of data (Figure 2). In the end, I chose one site which was just off the coast of the Gulf of Mexico (TXLQ) and another which was more inland, but off of the coast of Galveston Bay (TXP5), in order to compare the PWV two sites that likely both experience sea breeze interactions, but at different time. Both sites also had nearly complete data for 2019. Although TXP5 is missing the first two months of that year, it has little impact on the results since most of the sea breeze days that we are expecting occur during the summer months.



Figure 2 Map showing locations of the Houston-area GPS measurement sites. The TXLQ and TXP5 sites are the focus of our analysis.

2. Methods

Throughout the internship, I was using and developing codes to work with the GPS PWV data. Ultimately, I used three different methods to identify potential sea breeze days. The first method focused on the variability in time of the PWV at each site. I used data from one site to make a rolling half hour window and recorded the overall range PWV within each window. This provides a measure of how much the PWV changes in every half hour window. I used these values to produce a histogram to identify the fraction of points with variability that is large enough to be due to the passage of a sea breeze front. I determined that a range of 0.5 mm was reasonable to define these passages and recorded each day meeting this threshold as a potential sea or land breeze. This is because we expect a significant change in PWD when a sea or land breeze traverses a GPS PWV measurement site. However, there are many other environmental factors that may also impact PWV, such as the frontal systems. Lastly, to focus on the sea breezes I only recorded the days in which the change in PWV increased with time, consistent with the moistening we expect as the maritime air behind the sea breeze front reaches the measurement site. In the next step, I performed the same method on the second GPS station. After identifying the potential sea breeze days for the second site, I compared the two site's lists of days and only kept the days they had in common. This left me with 29 overlapping days that both sites had as potential sea breeze days.

The second method that I used to determine sea breeze days was to explore the regional variability in PWV by comparing the PWV at the two sites directly throughout the day. To do this, I looked at the 48 half hour windows of each day and compared the sites to each other. Potential sea breeze days were identified when the difference of the PWV for the same half hour window for site TXLQ and TXP5 was greater than 5 mm (Figure 3). This is because it potentially shows different air masses at the two sites because the sea breeze front had

reached TXLQ but not yet TXP5. As the sea breeze front extends to TXP5 the difference in PWV between the two sites is expected to decrease again as both sites are on the maritime side of the sea breeze front.

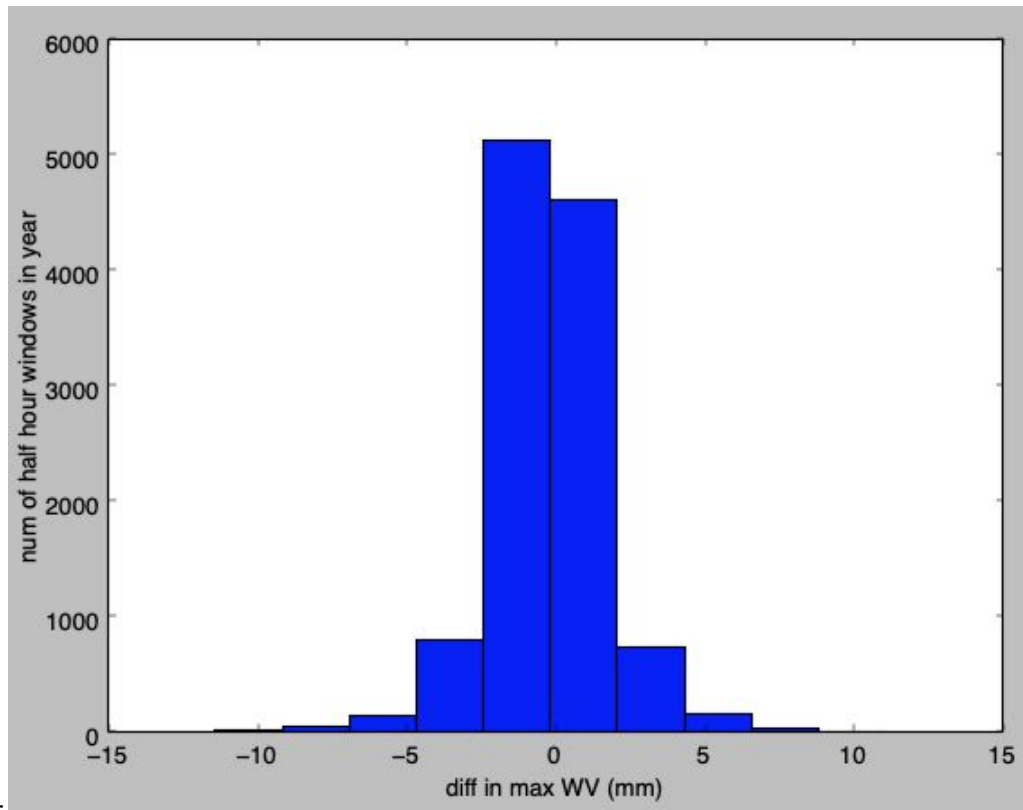


Figure 3 Histogram of difference in maximum PWV between TXLQ and TXP5 for half hour time windows.

Any days with at least one half hour time periods with differences greater than 5 mm, and PWV increasing with time, was counted as a sea breeze day. Using these criteria, 20 days were identified as potential sea breeze days based on the second method.

The third method of identifying the potential sea breeze days is done by Witteman et al. (2020) using the changes in surface temperature, wind direction, and wind speed when the sea breeze front passes over the site. The identified potential sea breeze days are further confirmed by using satellite images. The environmental constraints include a temperature decrease of greater than five degrees and a wind direction change of greater than 30 degrees. This is because when a sea breeze comes in, it will bring in colder air from the sea which will induce a drop in surface temperature.

3. Results and Conclusions

Using the third method, we were able to define 9 days which were conclusive as sea breeze days in 2019, as well as the approximate time when the sea breeze front arrived at

TXP5 and TXLQ sites. Connecting it back to PWV, I plotted the time series of the PWV for these 9 events as well as shaded in the time the sea breeze came through, for both sites (Figure 4).

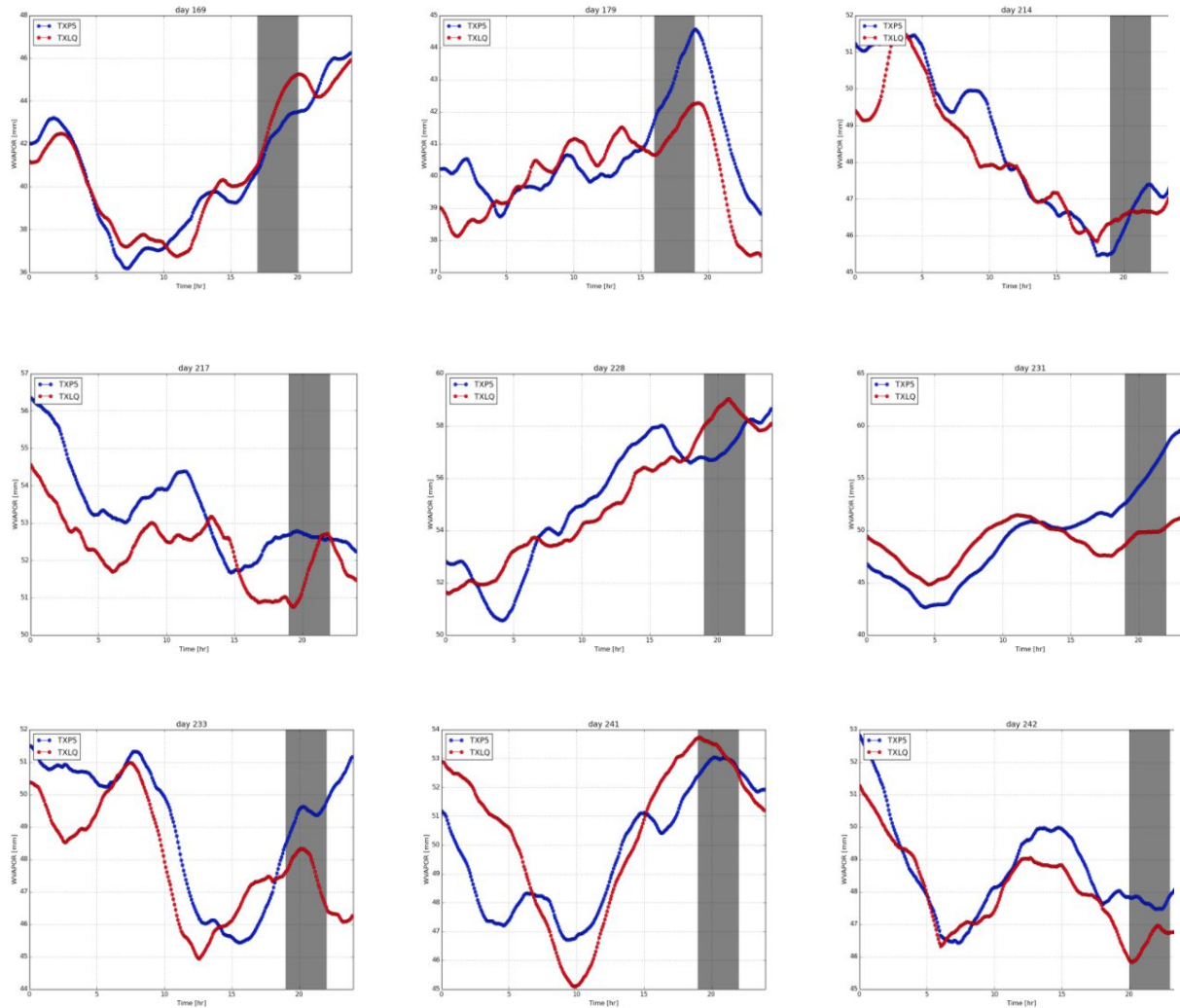


Figure 4 Time series of PWV for TXP5 (blue) and TXLQ (red) for 9 days satisfying sea breeze criteria. Grey shaded area represents the times of sea breeze front arrival.

When comparing these 9 sea breeze days with the potential sea breeze days identified using methods one and two, there were very few overlaps. None of the days from method one matched the nine days, while there was only one day from method two that matched. This may have happened because PWV does not change enough during sea breeze passages with respect to other large-scale environmental conditions. Therefore, we conclude that PWV measurements alone cannot be used to definitely identify sea breezes.

As shown in Figure 4, there is no consistent pattern for the PWV as a function of time for these 9 sea breeze events. However, an increase in PWV is observed at both sites for most of

the cases when the sea breeze is coming in. Note that, for some cases, the increase in PWV during the sea breeze front passage is less obvious, due to the fact that the PWV is also affected by many other factors. It suggests that sea breezes do have a positive correlation with the PWV increase, but with PWV measurements alone, it is not enough to identify the sea breeze days definitely.

Overall, we were unable to identify sea breeze events only based on the temporal or spatial variability in PWV, therefore, other environmental variables such as wind field and surface temperature are needed to provide additional information on the onset of the sea breeze. However, on sea breeze days, an evidence of a distinct increase in PWV is observed following a passage of a sea breeze front.

ACKNOWLEDGEMENTS

This project was supported in part by the U.S. Department of Energy, Office of Science, Office of Workforce Development for Teachers and Scientists (WDTS) under the Science Undergraduate Laboratory Internships Program (SULI). GPS data were downloaded from <http://geodesy.unr.edu/index.php>, and we thank Geoff Blewitt for his guidance on accessing and using the data. We thank the TRACER science team as well as the TRACER forecasting team for their participation in the background campaign.

REFERENCES

Blewitt, G., W. C. Hammond, and C. Kreemer (2018), Harnessing the GPS data explosion for interdisciplinary science, *Eos*, 99, <https://doi.org/10.1029/2018EO104623>.

Jensen M. P., et al., 2020: Tracking Aerosol Convection Interactions Experiment (TRACER) Science Plan. <https://www.arm.gov/research/campaigns/amf2021tracer>

Wittemann, B., M. P. Jensen, D. Wang and J. Turner: Identifying sea/bay breeze circulations in the Houston, TX region using a surface meteorology network. Presented at the 2020 BNL SULI interns closing ceremony via Bluejeans.

Comparison of Gamma Spectrum between simulation and evaluation for ^{55}Mn

Velasquez Ocaris, Josselyn

Department of Engineering, The City College of New York, NY 10031

Brown, David; Nobre, Gustavo

National Nuclear Data Center, Brookhaven National Laboratory, Upton, NY 11973

AUGUST 2020

ABSTRACT

Neutron capture occurs when a neutron is absorbed by a target nucleus, the resulting nucleus is left in a highly excited state at or above the neutron separation energy. This compound nucleus decay by the emission of a high energy primary gamma ray, followed by a secondary gamma cascade of much lower energy gamma rays. Each isotope emits a unique gamma-ray spectrum, providing a fingerprint that we can use to unambiguously identify the isotopic composition of a sample. This is the basis for Prompt Gamma Activation Analysis (PGAA), a non-destructive elemental analysis, commonly used in oil well logging that will be adopted by NASA for the DragonFly mission to Titan. At the annual Cross Section Evaluation Working Group meeting, and again at the WANDA2020 workshop, it was noted that there are serious deficiencies in evaluated capture gamma spectra caused by poor ENDF/B-VIII.0 data. Beginning with ^{55}Mn , a gamma-ray decay simulator code RAINIER was used, and the results are compared to CapGam, ENSDF and ENDF with the aim of developing an approach for evaluating capture gamma spectra.

CONTENT

- I INTRODUCTION
- II THEORY AND SIMULATION
- III GAMMA SPECTRUM COMPARISON
- IV CONCLUSION
- V ACKNOWLEDGEMENTS
- VI REFERENCES

Introduction

Neutron capture prompt gamma activation analysis (PGAA) is a noninvasive nuclear method to identify the isotopic content of the material. It measures the emission of a gamma-spectrum which is unique to each isotope. For this reason, accurate measurements of capture gamma-ray energies databases are required. In a presentation done by Schlumberger limited, an oilfield service company, it was shown that EDNF/B-VIII.0 insufficiently agree with their experimental results, as well as in other different conferences (CSEWG ^[1], WANDA2020^[6]). A recent ENDF evaluation ^[8] attempted to fill the observed shortcoming in the ENDF/B-VIII.0 evaluation by merging results in the EGAF ^[8]

database with the simulation code EMPIRE [5]. In this paper, we develop a new evaluation of the thermal capture spectrum using a combination of measured capture gammas in the CapGam [7] (which includes capture gammas noted in the EGAF database) and a Mont Carlo simulation using the RAINIER code [4].

Theory and Simulation

RAINIER simulates a level scheme above known levels up to and including the neutron separation energy, or a high-level defined by a user. It uses known level information from RIPL-3 [3] to extract the E_{JI} , lifetime and branching ratio of each gamma-ray. Then, the code uses a Monte Carlo model approach to construct a stochastic gamma cascade, named “realization”. There are two main inputs needed for construct a level scheme:

- **Nuclear Level Density (NLD):** An excited nucleus, at low excitation energies, present a discrete well-defined level of energies. Then, the definition of nuclear level density is described as the number of levels per unit of excitation energy. It is an important input for the calculation of nuclear reaction cross section, therefore phenomenological models have been developed like the Fermi gas model which treat nucleons as free non-interacting particles which occupy the lowest energy states available. In RAINIER, there are two different options: Back shifted Fermi gas and Constant Temperature models. By default, we use the BSFG approach:

$$\rho_{BSFG}^{tot}(E) = \frac{1}{12\sqrt{2}\sigma} \frac{\exp(2\sqrt{aU})}{a^{\frac{1}{4}}U^{\frac{5}{4}}}$$

Effective excitation energy: $U = E - E_1$

E_1 : Energy backshifted

a : level density parameter

σ : spin cut-off parameter

- **Gamma-ray Strength Function (GSF):** As well as nuclear level density, the GSF for multipole type XL expresses an average of the electromagnetic properties of a nucleus per unit energy interval. The second input necessary for compound nucleus cross section calculation. It is important to note that it follows the Bohr’s postulate: the decay of a nuclear level is independent of the way in which it is formed [3].

$$\Gamma^{XL}(E, E_\gamma) = \frac{f_{XL}(E_\gamma)E_\gamma^{2L+1}}{\rho(E, J, \Pi)}$$

E_γ : emitted energy

f_{XL} : GSF of transition type XL

L: transition multipolarity

X: transition electromagnetic character

In order to simulate the gamma cascade for the nuclear reaction $^{55}\text{Mn}(n, g)$, the neutron separation energy was set to 7.3 MeV and its capture state at 2-. Then, RAINIER inputs parameters for BSFG NLD were obtain from references [9], [10].

- $a = 6.28 \text{ MeV}^{-1}$ and $E_1 = -1.6975 \text{ MeV}$

E_1 GSF generalized Lorentzian parameters were obtained from RIPL-3 with:

- $S_{E1} = 91.519 \text{ mb}$, $G_{E1} = 6.976 \text{ MeV}$,

$$E_{E1} = 18.687 \text{ MeV}$$

Gamma Spectrum Comparison

We compare our RAINIER simulation with two sources:

- The thermal neutron gamma-ray (CapGam) library contains gamma decay data from the Evaluated Nuclear structure database file (ENSDF). It has only observed gammas, classified by their intensities. Includes gammas observed compiled in the EGAF library.
- An evaluation from the IAEA was sent as candidate to be added in the ENDF/B library, this evaluation includes thermo gammas from the EGAF libraries merge with the simulations using the EMPIRE code.

We set the number of RAINIER realizations to 100 to reduce statistical errors in which 1000 events (gamma cascade) were simulated per realization. By integrating all the realizations and divided by number of them we can calculate the average energy. The three databases were plotted in the same graph as shown in Figure 1a. For the normalization process, the last stronger gamma collects all the possible cascades in both RAINIER and CapGam, therefore we normalized respect to it.

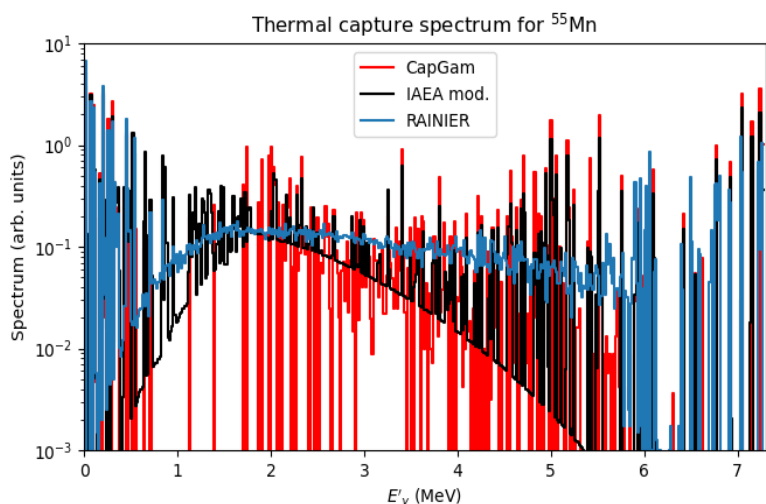


Fig. 1a A logarithmic scale of the γ -ray spectrum comparison of RAINIER, CapGam and the IAEA evaluation.

Since the comparison obtained above give us a chaotic, complex graph, we set the scale to a linear – linear plot for a better visualization of the low energy discrete secondary gammas as shown in Figure 1b.

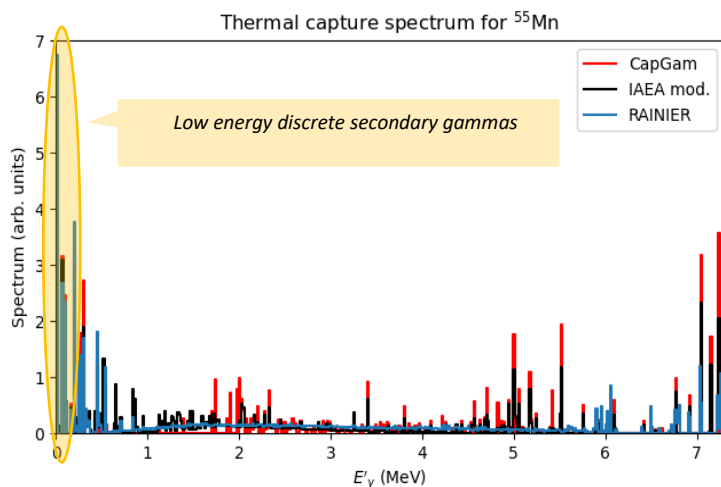


Fig. 1b. Linear scale. To do a better study of low energy secondary gammas, we use the linear scale.

The low-level scheme section of each RAINIER realization (< 0.5 MeV) is not stochastically generated but build from pre-loaded data (RIPL-3). If we want to make a comparison of existent gamma-ray energy data, like CapGam, we necessarily must study this low-level portion. In Figure 2, we illustrate four γ -ray decay from the excited level states 4^+ , 1^+ , 2^+ to 3^+ (ground state) respectively.

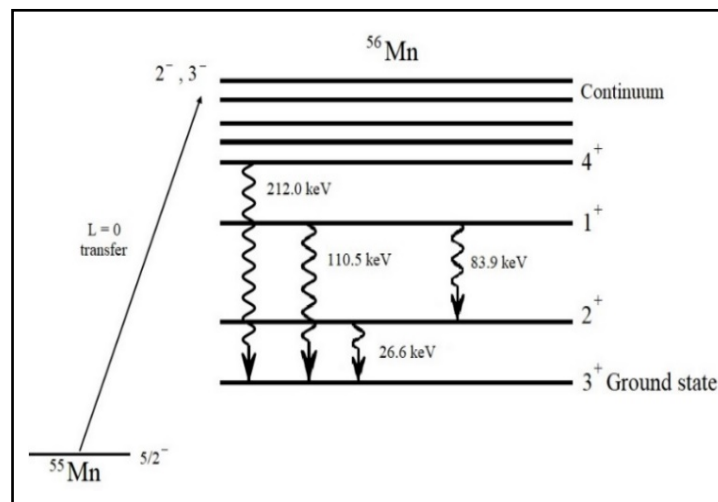


Fig. 2. Illustration of the low-level part of the gamma spectra

Level Index	J Π	Level Energy (keV)	Transition Multipolarity	Intensity Ratio	Final State	E γ (keV)	RAINIER E γ (keV)	Ratio of Intensities (CapGam/RAINIER)
1	2 ⁺	26.6043	M1	100	3 ⁺	26.6	21.8 \pm 7.3	0.771
2	1 ⁺	110.5041	M1	100.10	2 ⁺	83.9	80.0 \pm 7.3	1.1797*
			[E2]	0.33	3 ⁺	110.5	109.1 \pm 7.3	1.0432*
3	4 ⁺	212.017	M1+E2	100	3 ⁺	212.0	210.8 \pm 7.3	0.8831*
4	1 ⁺ , 2 ⁺ (**)	215.134	M1+E2	100	1 ⁺	104.6	109.1 \pm 7.3	1.0432*
			M1+E2	21	2 ⁺	188.5	181.6 \pm 7.3	1.2509*
				10	3 ⁺	215.1	210.8 \pm 7.3	0.8831*

Table 1. Comparison of known level and gammas with RAINIER.

(**) In level index 4, it is uncertain if the initial state is 1⁺ or 2⁺.

In Table 1. We show a detailed description of each gamma illustrated in Figure 2., the information was retrieved from reference [2]. Then, the energy of the gammas calculate from RAINIER were added. For evaluation and simulation, we divide the partial energy of a selected bin (both are histograms) by the integrated spectrum respectively. To then compute the ratio of intensities, being 1 its maximum value. Ratios annotated with an (*) indicate bins in RAINIER contaminated with gammas from other excited states. In level index 2 and 4, the ratios came out greater than one, this probably needs more investigation since RIPL-3 branching ratios have not been updated to latest available in CapGam or ENSDF.

Conclusion

RAINIER is a powerful tool for calculating the gammas energies, but it has its limitations. Since it uses a Monte Carlo simulation, on average gives a good approximation to realistic gamma values but in detailed it is incorrect. In order to simulate a gamma spectrum of a specific nucleus using RAINIER, the correct NLD and GSF parameter are needed. With carefully chosen inputs, we could compare the selected databases (CapGam and ENDF) with

RAINIER, as it can be seen in Fig. 1, it has a good agreement with CapGam. Yet, there is significant differences which require further investigation. In future analysis, a RAINIER simulation of high energies neutron capture will be merged with CapGam at all neutron energies relevant for applications.

Acknowledgements

This work was supported in part by the US Department of Energy, Office of Science, Undergraduate Laboratory Internship Program (SULI). I wish to thank my mentor, David Brown and Gustavo Nobre, for his professionalism and generosity during the SULI Program. Further, I would express my gratitude to the Office of Science Education, for making possible this unique internship experience.

References

- [1] D. Brown, A. Sonzogni. CSEWG Meeting Minutes. (2019, November). Brookhaven national laboratory.
- [2] H. Junde, H. Su, Y. Dong. Nucl. Data Sheets 112, Nuclear Data Sheets pp 1513 – 1645 (2009)
<http://www.nndc.bnl.gov/nudat2/getdataset.jsp?nucleus=56MN&unc=nds>.

- [3] J. Kopecky, in Handbook for calculations of nuclear reaction data. Reference Input Parameter Library (RIPL-3), IAEA-TEDOC-1034, 1998, Ch.6.
- [4] L. E. Kirsch, L. A. Bernstein RAINIER: A Simulation Tool for Distributions of Excited Nuclear States and Cascade Fluctuations.
- [5] M. Herman, R. Capote, B. Carlson, P. Oblozinsky, M. Sin, A. Trkov, H. Wienke, V. Zerkin, EMPIRE: Nuclear reaction model code system for data evaluation, Nuclear Data Sheets 108 (12) (2007) 2655 – 2715. Doi: 10.1016/j.nds.2007.11.003.
- [6] Oak Ridge National Laboratory, Romano, C., & Bernstein, L. (2020, July). Proceedings of the Workshop for Applied Nuclear Data: WANDA2020(ORNL/TM-2020/1617). US Department of Energy.
- [7] Pritychenko, B., 2020. Thermal Neutron Capture Gammas - Target 55Mn.Nndc.bnl.gov. https://www.nndc.bnl.gov/capgam/byTarget/z025_55Mn.html [Accessed 18 August 2020].
- [8] R.B. Firestone (LBNL), 55Mn(n,g) Evaluated Gamma-ray Activation File (EGAF) (2003, December) https://www-nds.iaea.org/pgaa/EGAF/56MN_EGAF.ens.
- [9] T. von Egidy, D. Bucurescu, Experimental energy-dependent nuclear spin distribution, Phys. Rev. C 80 (2009) 054310. Doi:/10.1103/PhysRevC.80.054310.
- [10] T. v. Egidy, D. Bucurescu, Systematics of nuclear level density parameters, Phys. Rev. C 72 (2005) 044311. doi:/10.1103/PhysRevC.72.044311

Designing high-pressure vessel system to transport CO₂ laser

Thea Vijaya Kumar

Department of Mechanical Engineering, Stony Brook University, Stony Brook, NY 11794

Christian Cullen

Accelerator Test Facility, Brookhaven National Laboratory, Upton, NY 11973

Abstract

The Accelerator Test Facility (ATF) of Brookhaven National Laboratory uses a CO₂ laser to conduct research experiments in Ion Acceleration, Electron Acceleration, and Radiation Sources. The ATF is working to optimize the CO₂ laser to provide higher peak power and shorter pulses. This can be accomplished by creating a vessel of 10 atmospheres around the beam, causing the spectrum of the laser to expand, which is required for short pulses to occur. The beam travels and expands in air, leaving the Final Amplifier, coming in contact with two mirrors, and entering the Chirped Pulse Amplification (CPA) chamber. Since the spherical second mirror focuses the beam like a lens, the angle created by the beam should be kept as small as possible. Ultimately, the total travel distance of the beam from the final amplifier to the second mirror was adjusted to 200 inches, and the angle was decreased to 2.759 degrees using Creo. Since the layout of the mirrors was completed, the shape and orientation of the pressure vessel within that area was determined to be cylindrical. Cylindrical pressure vessels had no bending stress, which allowed for a simple, yet effective design. Difficulties arose when designing components that intersected with each other closer to the second mirror. To solve this problem, a chamber with an obround or stadium cross-section was created in Creo for the intersecting side. Finally, a salt window was inserted to separate the high-pressure gas from the vacuum within the CPA chamber. The thickness of the walls and total structural integrity of all the parts were analyzed through ANSYS for each design simulation.

I. Introduction

The Accelerator Test Facility room houses the CO₂, a Final Amplifier and a Chirped Pulse Amplifier (CPA) chamber (Figure 1). Two mirrors are oriented for the laser to bounce off and increase energy. The pressure vessel assembly was required to uphold the quality of the CO₂ laser for further tests in the lab. All the components that are part of the CO₂ travel path increase the speed and amplify the diameter of the beam. When the beam leaves the Final Amplifier, it is approximately 4 inches in diameter. Once it reaches the opening of the CPA chamber, it enters at 6 inches.

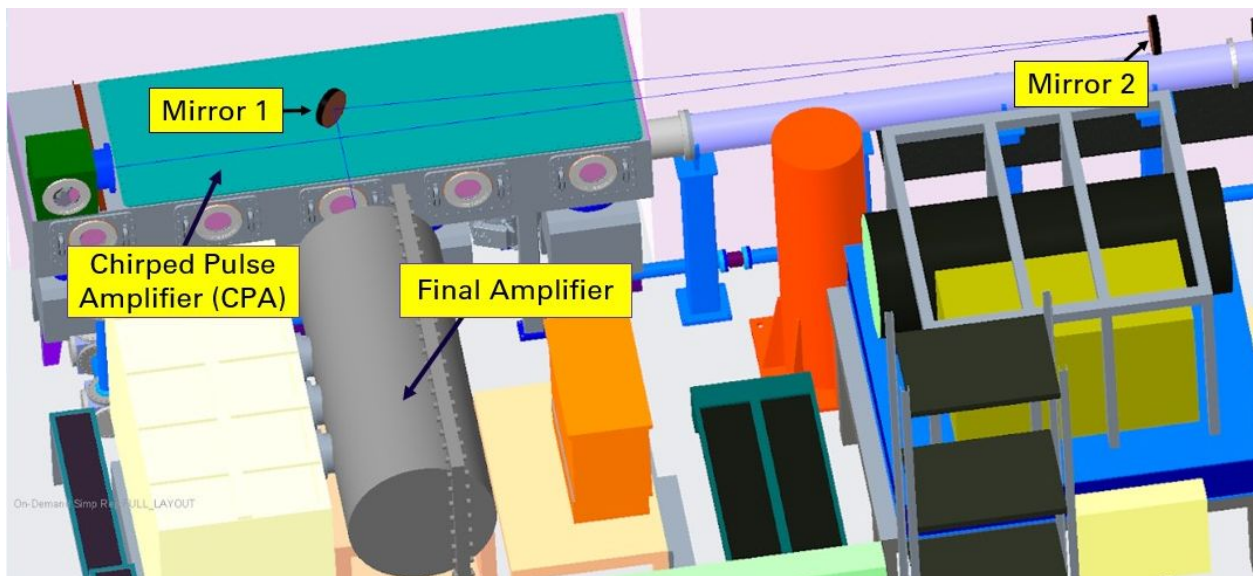


Figure 1: The ATF room where the pressure vessel needs to be inserted

The CO₂ laser produces pulses in picoseconds, which means the pulses are short. Short pulses have broader spectral lines. These spectral lines are caused by the different energy levels of atoms [1]. To produce a broader spectral line, the pressure of the system that the laser travels

through needs to be high enough. The width of the lines are directly correlated with the frequency of collisions between the molecules of the CO₂, thus requiring high pressure. However, if the pressure is too high, “the electric discharge that excites the gas becomes unstable”¹. Therefore, 10 atmospheres (146.959.... psi) is the highest pressure that can be used before the system becomes unstable.

II. Adjustment of mirror layout

Before even beginning the design phase to construct a pressure vessel, the current configuration of two mirrors outside of the final amplifier needed to be adjusted (Figure 2). The total beam travel distance from leaving the final amplifier and reaching the second mirror was required to be at least 5 meters in length. The length, a , was the vertical distance starting from the Final Amplifier and ending at the first mirror. The variable, b , was the distance from the first mirror to the second mirror (Figure 3). The beam first leaves the final amplifier at a diameter of 4 inches and takes 5 meters to expand to 6 inches. The expansion is necessary to reduce its intensity. The total length was set to 200 inches to provide a solid constraint in US units.

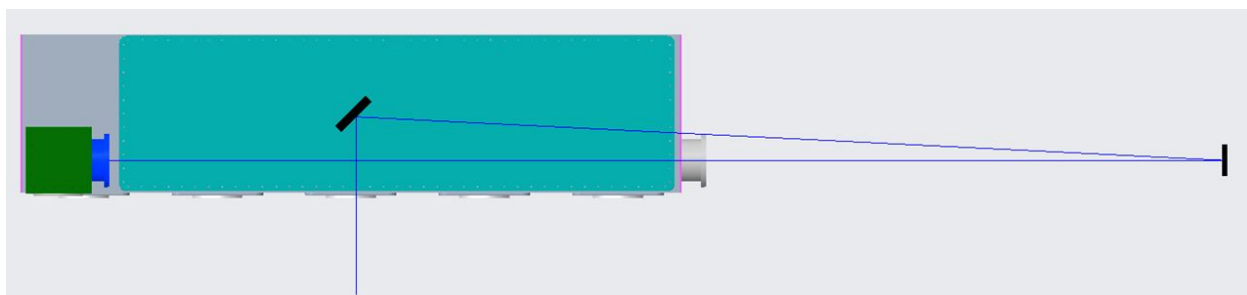


Figure 2: The original layout of the two mirrors

¹ Mikhail Polyanskiy, e-mail message, August 6, 2020

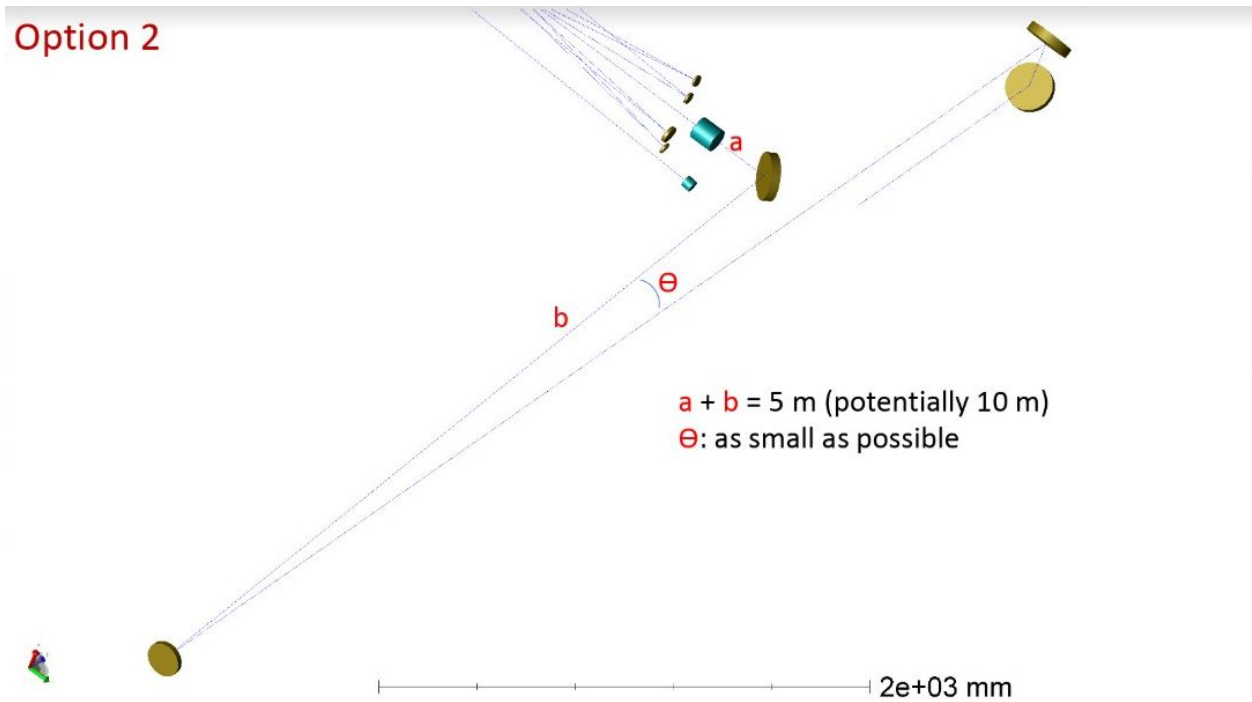


Figure 3: The new mirror layout with design constraints

Additionally, the angle created between the first mirror, second mirror, and the mirror in the CPA chamber must be as small as possible. This angle is represented by theta, θ . Due to the second mirror being concave, the reflected beam does not expand and can travel the necessary distance to the CPA chamber at 6 inches in diameter. The curvature of the mirror is predetermined by physicists to allow this effect to occur. The mirror is most effective to propagate the beam a long distance unchanged when the angle of incidence and reflection are 0° , thus allowing the beams to hit the surface perpendicularly. However, the beams must be separated, so an angle close to 0° is required.

Before any calculations were done, a drawing of the mirror setup had to be created to observe which values would change (Figure 4). The two drawings below the full layout represent

close-up images of the two mirrors (Figure 5). Since changing several variables required trial and error, a MATLAB code was created to perform the geometric calculations. The analysis of this mirror layout was carried out by establishing constraints on the system such as the fixed lengths of the horizontal and vertical distances, v and c , between the opening of the Final Amplifier and the CPA chamber. The values of t , s , and u were also set as fixed values of the mirror dimensions. Additionally, allowing the second mirror to stay directly in front of the CPA chamber made calculations easier to perform. Therefore, the only variables that needed to be manipulated in the beginning of the code were a and b (where $b=200-a$). This would then change angles θ , 1, 2 (equivalent to angle A), 3, B, and C, including distances e , x , and d . The design also required the value of x , or the clearance, to be at least 3 inches to allow the laser beam an obstructed travel path to the CPA chamber. Therefore, the final pertinent values of a , b , x , and θ were 16 inches, 184 inches, 4.926 inches, and 2.759 degrees, respectively.

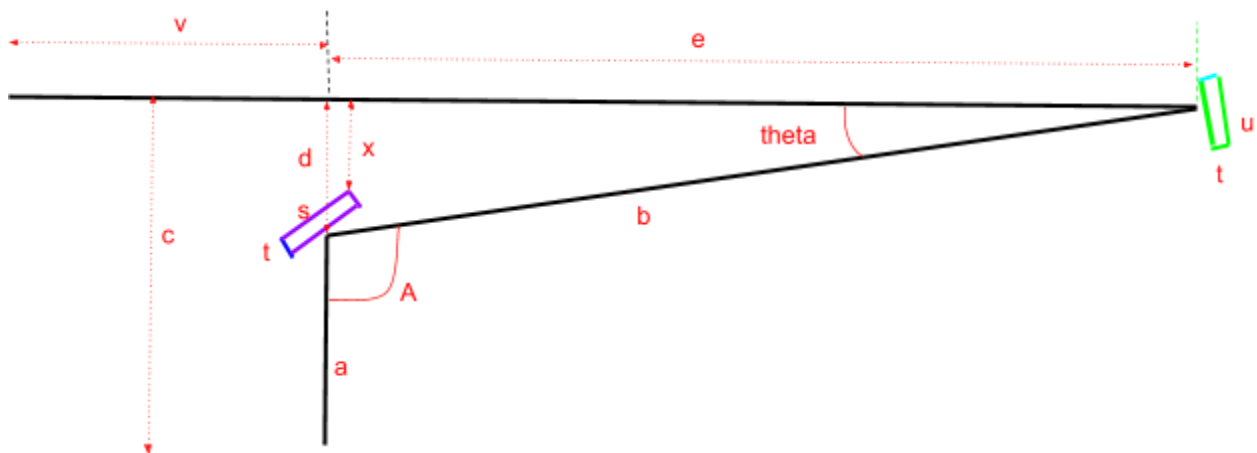


Figure 4: New mirror layout with variables for angles and distances

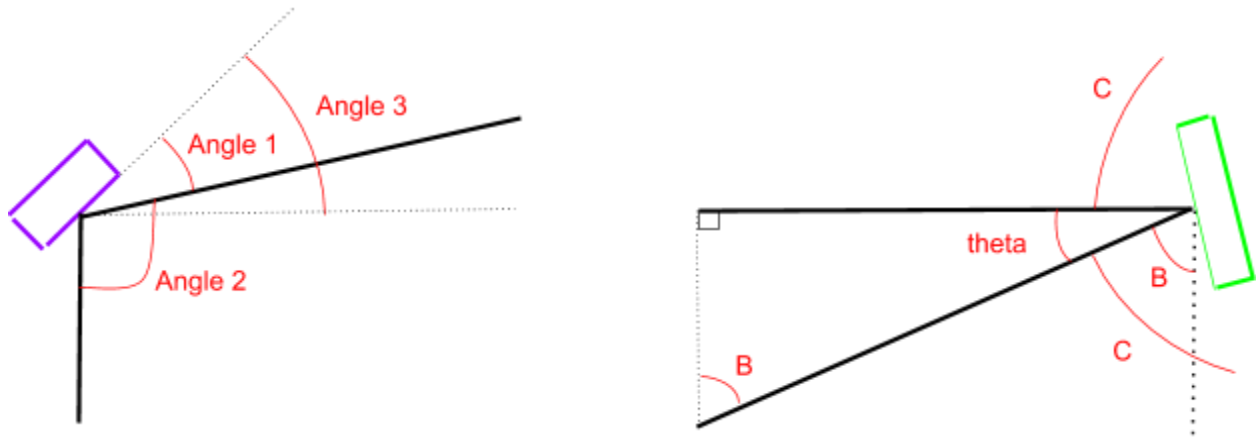


Figure 5: Close-up drawings of the two mirrors with additional angle measurements

III. Designing a pressure vessel

Once the mirror layout fulfilled the constraints and requirements, a pressure vessel with a diameter of at least 6 inches was compulsory to accommodate the maximum size that the laser would expand. The first configuration was created to replicate the travel route of the beam, with a diameter of 9.5 inches inside and 10 inches outside (Figure 6 and 7). This configuration raised problems because real-life construction would require welding of two steel tubes in a difficult manner. Additionally, the vessel needed a way to hold the mirrors inside and adjust them. Moreover, if the vessel expanded due to the pressure, the mirror angles could change, causing a huge shift in the direction of the beam.

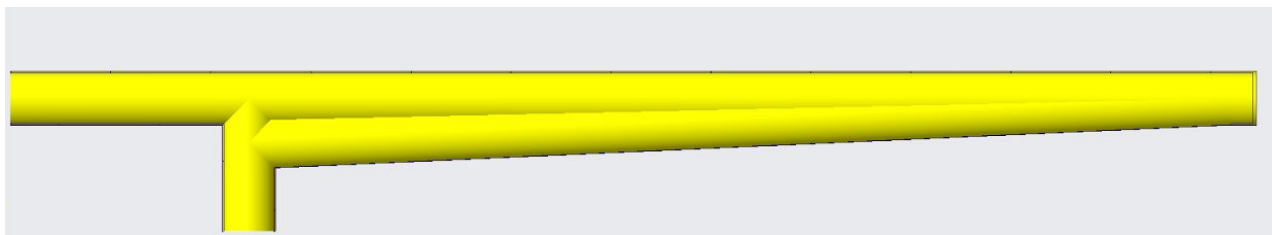


Figure 6: First attempt for pressure vessel

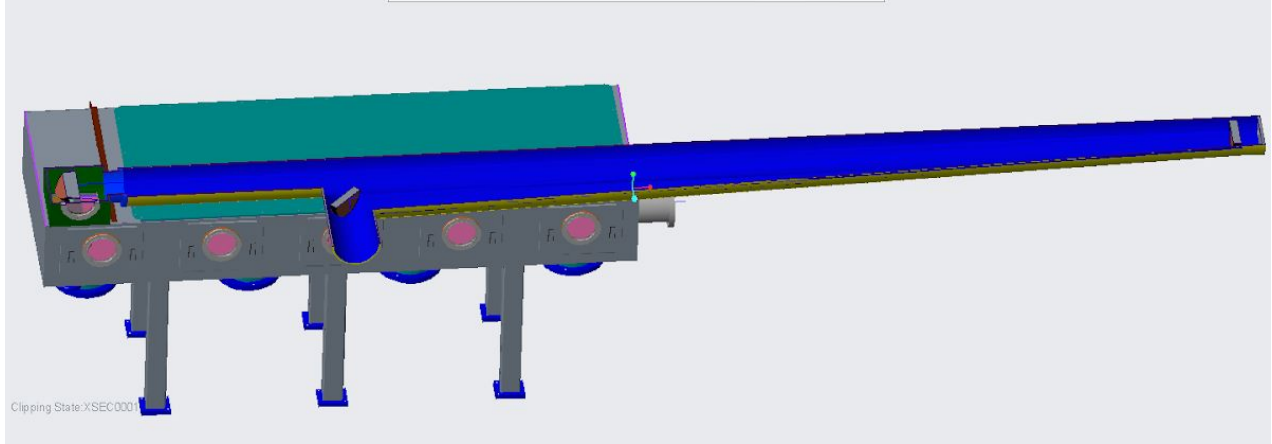


Figure 7: Assembly of first pressure vessel attempt with CPA chamber

Adjustments were made to the dimensions of the cylindrical tubing. Instead of having one part for the vessel, an assembly of tubes was created (Figure 8). The tubing required connectors with flanges on the ends. Since vacuum connectors were chosen, the cylindrical tubing was designed according to the connector dimensions. Therefore, the inside diameter was 7.76 inches, while the outside was 8 inches. Additionally, the tubing that was attached to the connectors was designed with flanges.

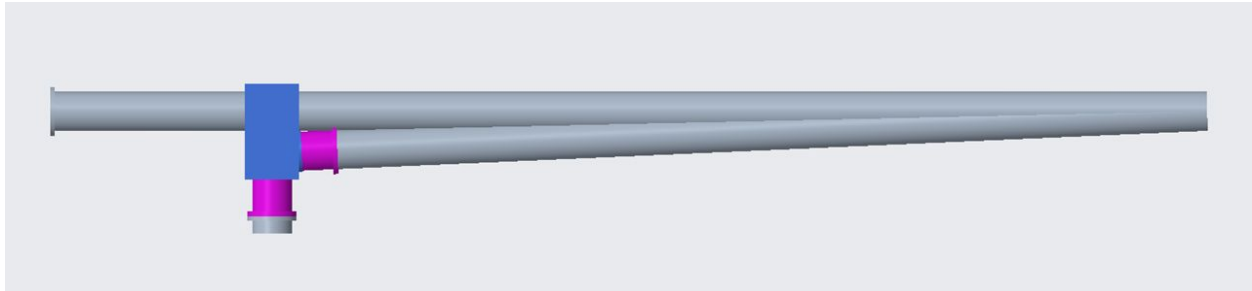


Figure 8: Top view of the pressure vessel assembly with separate tube parts

This led to the development of boxes to house the mirrors separately (Figure 9). Since the pieces were smaller, they would all be welded to two mirror boxes. The new configuration was created to roughly manipulate the design, without strictly adhering the ASME code quite yet. The first mirror box was created to house two paths of the laser. The second mirror box was made smaller since the path of the laser would intersect toward the far right.

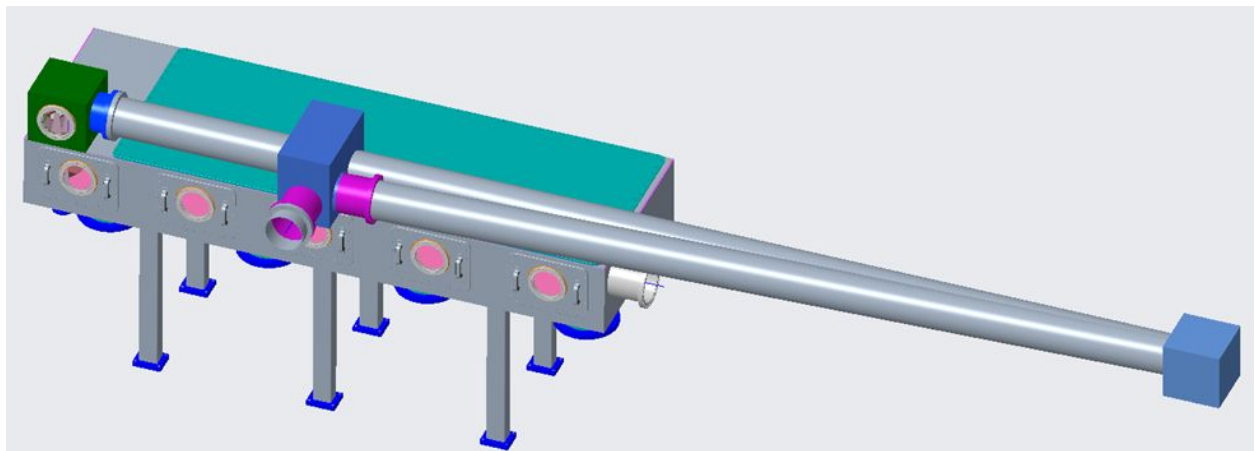


Figure 9: Full assembly with CPA chamber and the newest pressure vessel configuration with mirror boxes

While this assembly was closer to working, a few problems did arise. On the right side of the first box, the connector pieces would interfere with the two tubes (Figure 10). Only one connector piece was placed first, but it was still evident that adding a second connector would cause more obstruction. Moreover, since the lower tube on the right side of the box needed to be positioned at an angle, the construction of the box was not ideal. Everything in the section interfered.

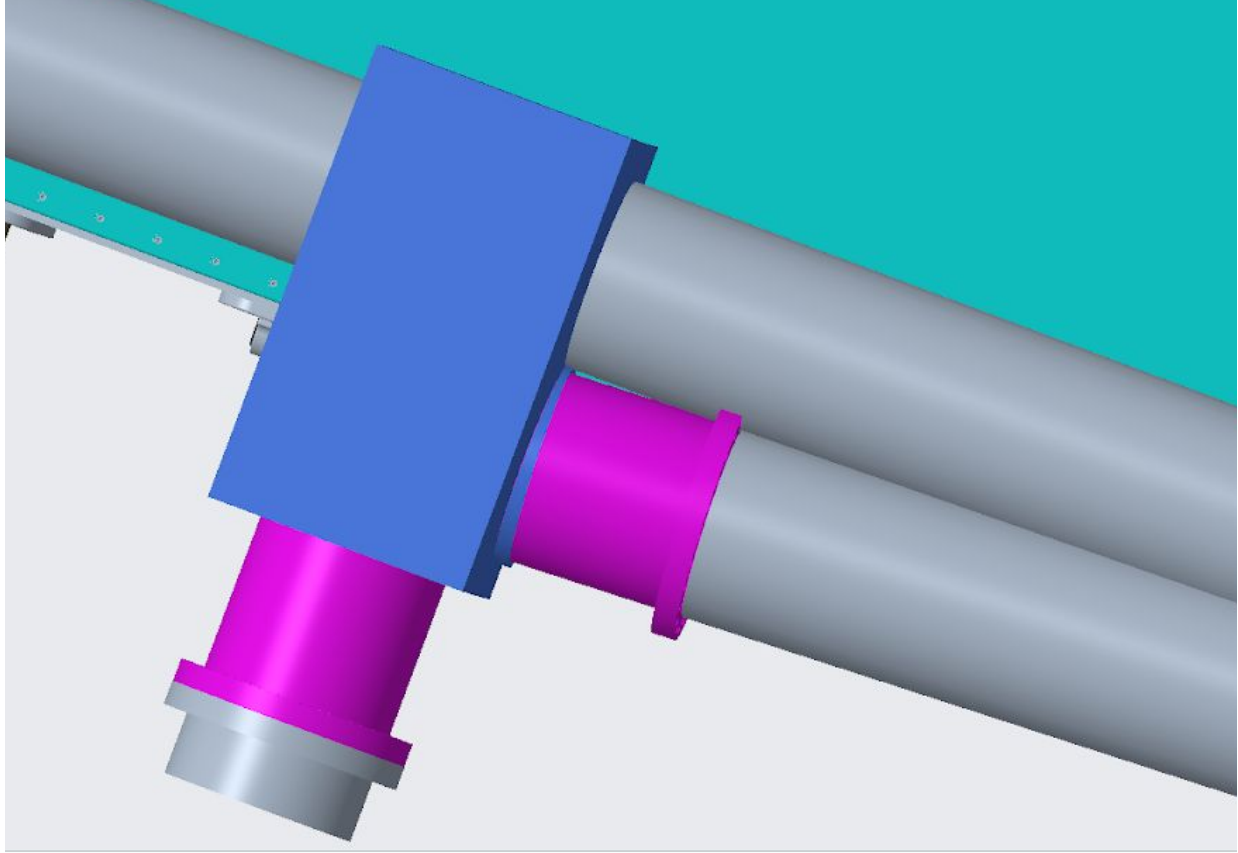


Figure 10: First mirror box design with interfering tubes

The mirror box was then adjusted so that the right side only had one stadium-like or obround opening coming straight out (Figure 11). The rectangular box dimensions were kept the same for the second mirror. The inner width was 9.2, height was 13.7, and the length was 18.2 inches. The wall thickness was 0.9 inches. Connector pieces and the tube itself had to be created completely from scratch so that the laser could travel through with ease. This cross-section was designed with two circles and a rectangle. The center of the two circles were 8.44 inches apart. The circle diameter inside the stadium pieces was 7.2 inches, while the outside was 9.2 inches. The walls were made 1 inch thick to be within the required ASME guidelines.

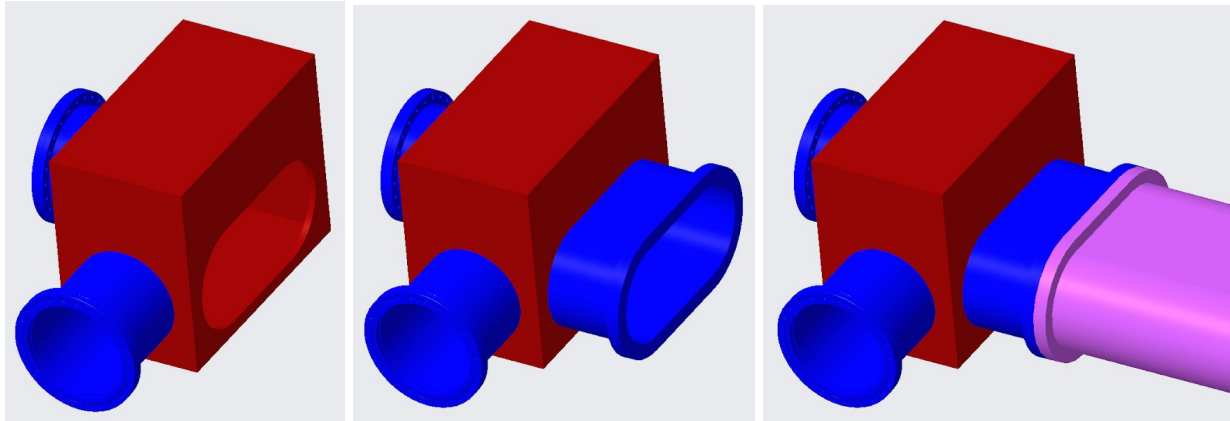


Figure 11 (a), (b), (c): (a) Mirror box with opening (b) Mirror box with obround connector (c) Mirror box with obround connector and tube

The boxes were later created with shoulders so the connector pieces would be set in place when welded. The shoulders were made with the same inner dimensions as the obround connectors, so the surfaces would be uniform (Figure 12).

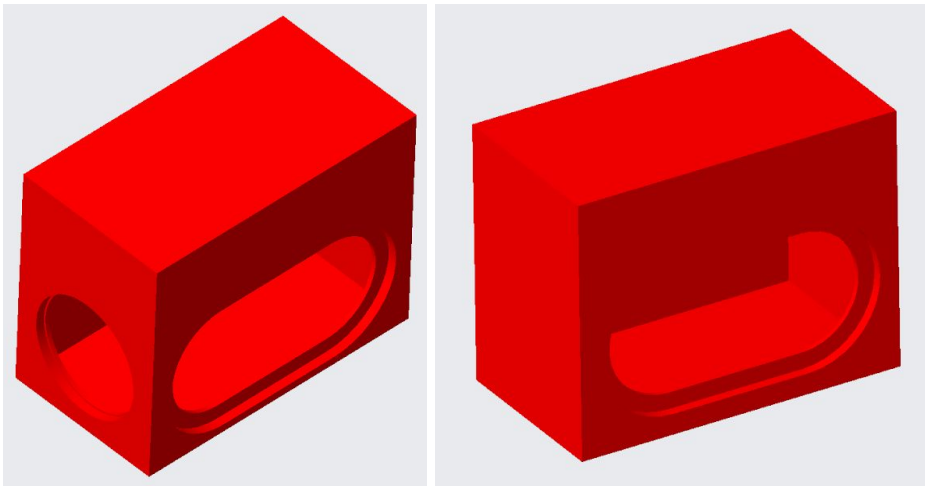


Figure 12 (a) and (b): (a) Mirror box 1 with three openings and shoulders (b) Mirror box 2 with one opening and shoulder

Furthermore, a 6 inch diameter laser beam was designed in Creo to show the path that the real laser would take (Figure 13). The 3D model of the sketch shows where the intersections of the laser are. The design was put into a larger assembly to show how well the laser fits inside the vessel (Figure 14). The last addition to the assembly was a NaCl window, which is why a space was left instead of attaching the final cylindrical tube to the CPA chamber.

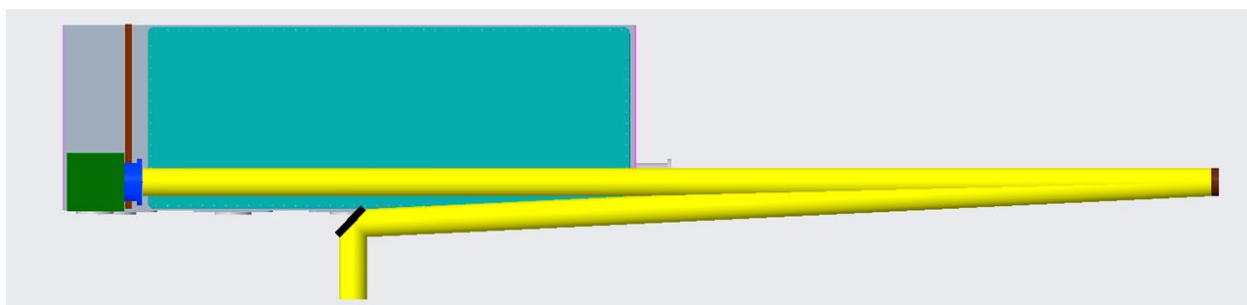


Figure 13: 6 inch laser beam interacting with two mirrors



Figure 14: Full assembly of laser inside the pressure vessel assembly

IV. NaCl Window Housing

The final addition to the assembly was the NaCl (salt) window. The window had to be designed with a 7.7 inch diameter and a 0.85 inch bevel on one end (Figure 15). Since the

original dimensions of the salt window were provided in metric units, everything had to be converted to US units and increased by a factor of approximately 1.6. The original diameter was 119.8 mm, so the factor came from $7.7/(119.8/25.4)$. Therefore, the final length of the salt window with all its components is about 8 inches.

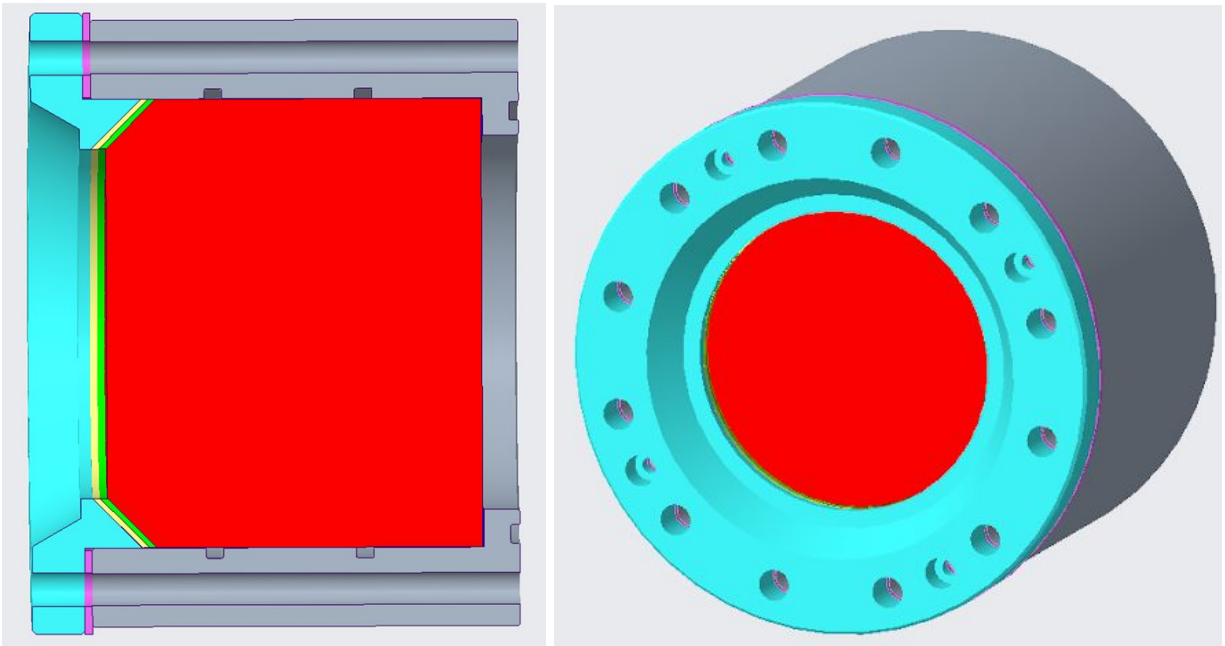


Figure 15 (a) and (b): (a) Salt window assembly with a section cut through (b) Salt window assembly

When attaching the window to the full assembly, the 7.7” diameter side (right) connects to the pressure vessel. The beveled side (left) of the window connects to the green box that is attached to the CPA chamber (Figure 16). Now that the window is in between the two sections, the vacuum and high pressure are separated.



Figure 16: Full assembly of pressure vessel with salt window with a section to show laser beam travel path

V. ANSYS and ASME Codes

Throughout the process of designing the pressure vessel, all components were required to be compliant with the American Society of Mechanical Engineers (ASME) Code. Section II of the code stated that Stainless Steel's allowable strength is 20 ksi, while the ultimate and yield strength is 75 ksi and 30 ksi, respectively [2]. Therefore stress analysis was carried out for each component of the assembly.

The first calculation to be done was the hoop stress experienced by a cylindrical tube.

The equation for this is:

$$H = \frac{PD}{2t} ,$$

where P is the pressure, t is the thickness of the wall, and D is the diameter of the pipe. The cylinder's diameter is 8 inches and the thickness is 0.12 inches. Therefore, the hoop stress is 4898.6 psi. Analyzing the part in ANSYS for the largest cylindrical component, the maximum equivalent or von-mises stress is 8051.2 psi (Figure 17). Therefore, the hand-calculation was within the range of acceptable values of stress in ANSYS.

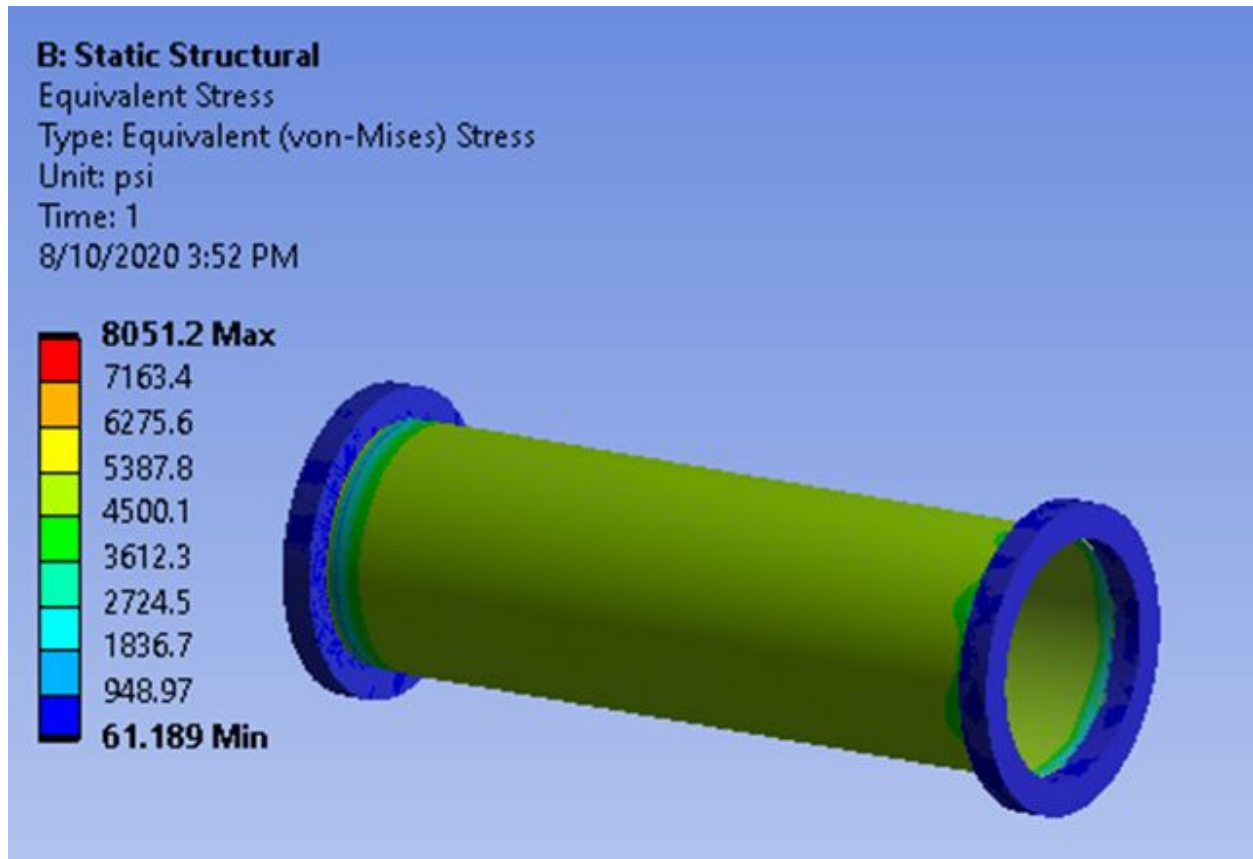


Figure 17: Cylindrical tube in ANSYS

Section VIII of the code noted equations used to calculate stress values experienced by obround cross-sections of a tube [3]. These calculations were associated with reinforced and unreinforced sections of tubing, but the current design was unreinforced. By performing calculations on an obround cross section, the result of total stress experienced was 11027 psi for section A and 11898 psi for section B (Figure 18). The ANSYS model was analyzed with a fixed support on the flanges of the tube, and a pressure of 10 atmospheres. This resulted in a maximum equivalent von-mises stress of 12303 psi (Figure 19).

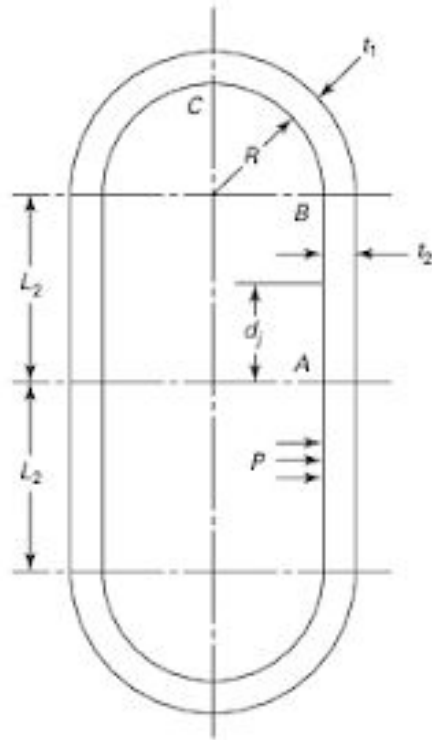


Figure 18: Unreinforced vessel with an obround cross section [4]

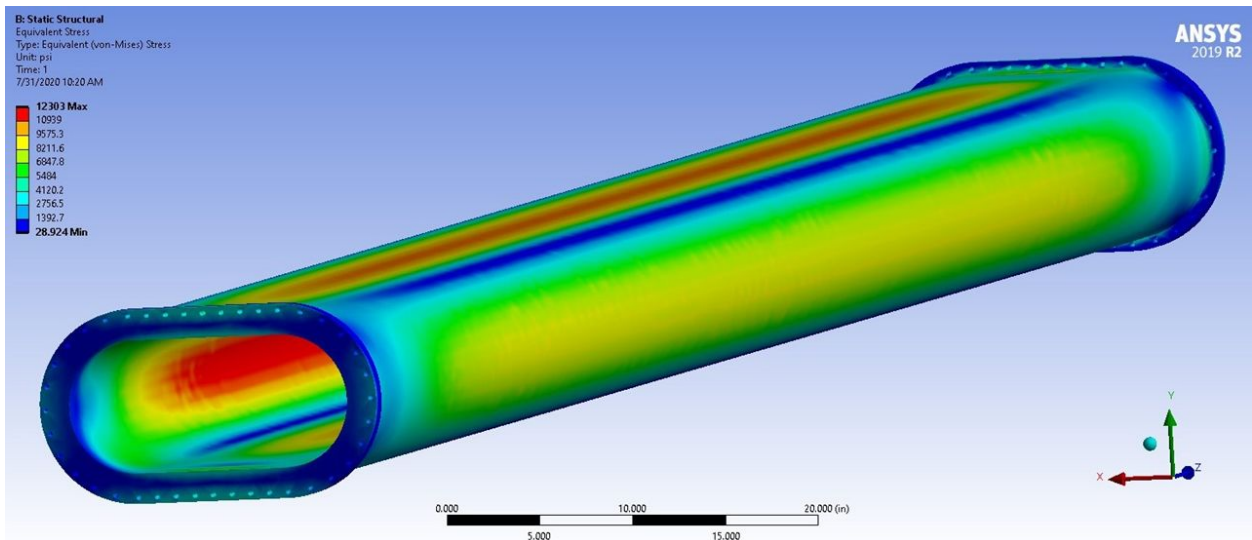


Figure 19: ANSYS analysis of obround tube subject to 10 atmospheres of internal pressure

The final part was to determine the stress experienced by mirror boxes through ASME calculations in Section II of the ASME code (Figure 20) [5]. The outside dimensions were 20”X11”X15.5”, which resulted in the stress of 13462 psi. By inputting the Creo model in ANSYS, the result was 12151 psi.

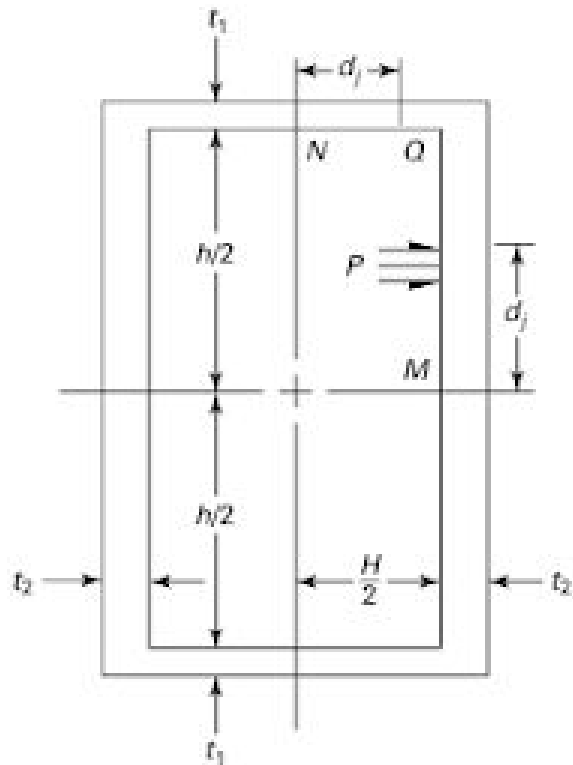


Figure 20: Rectangular cross-section corresponding to stress equations [6]

Once all the individual components were tested in ANSYS, an assembly of the mirror box with three connector pieces was analyzed. The final result was a maximum value of 18968 psi (Figure 21). All the parts of the vessel were viable options to use since they complied with the ASME Boiler Pressure Vessel code.

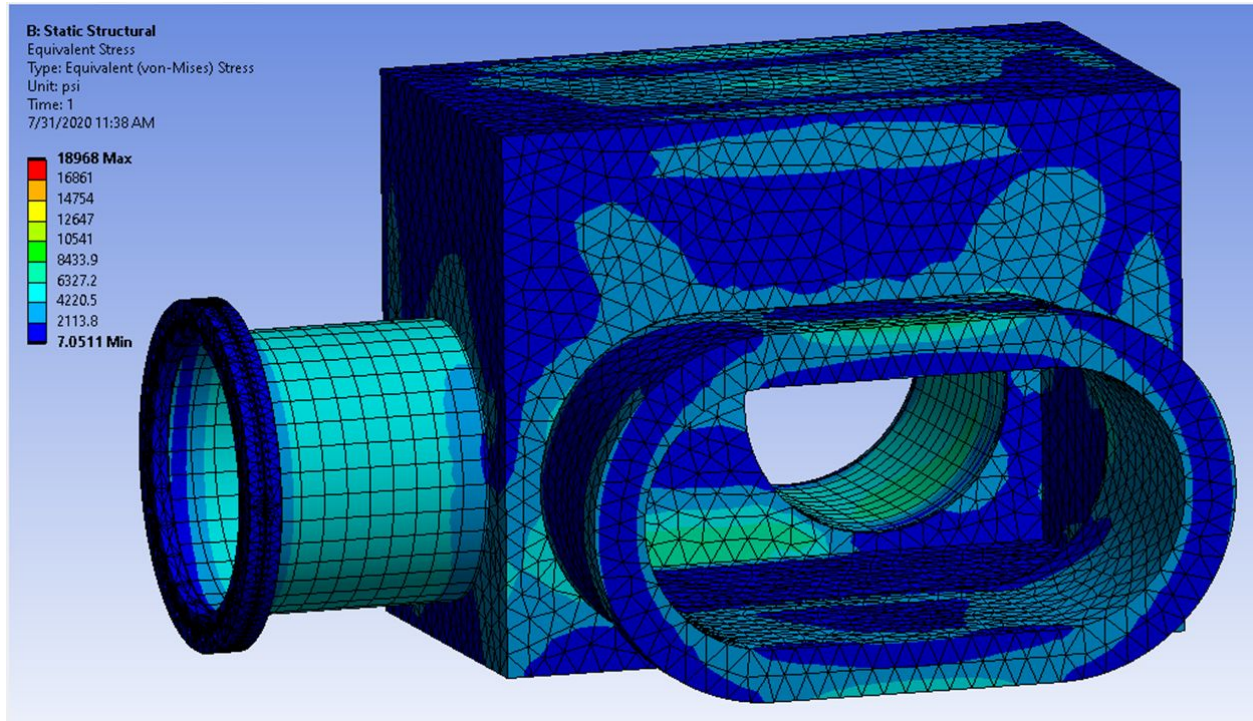


Figure 21: Mirror box assembly with connector pieces in ANSYS

VI. Conclusions

The pressure vessel assembly that was designed with the use of rectangular mirror boxes, cylindrical tubes, and obround cross sectional tubes was acceptable. The physics requirements were all fulfilled. The mirror angle, θ , was 2.795 degrees, and the total travel distance $a+b$ was greater than 5 meters (200 inches). The mechanical requirements were also met since the stress values provided by ANSYS were under 20,000 psi. Additionally, these values agreed with the ASME Boiler Pressure Vessel Code equations. Therefore it is possible to construct a vessel of 10 atmospheres in the Accelerator Test Facility.

VII. Acknowledgements

This project was supported in part by the U.S. Department of Energy, Office of Science, Office of Workforce Development for Teachers and Scientists (WDTS) under the Science Undergraduate Laboratory Internships Program (SULI). I want to further thank the Office of Educational Programs and Brookhaven National Laboratory for making this summer internship possible during a pandemic. Additional thanks to the National Science Foundation for funding.

I would like to thank Christian Cullen for being my mentor and helping me out everyday with any questions I had and for guiding me through the project. Without his patience as I learned Creo, ANSYS, and had a million problems with my software licenses, I would not be able to successfully complete my project. Thank you also for making the internship enjoyable with the daily meetings and teaching me more about the facility.

Thank you to Kelly Roy for helping me with inserting new objects into Creo and for creating all the project files for me to use and work on. I appreciated the help with Windchill and putting my designs on the top design and always being willing to guide me through the software.

Thank you to Mikhail (Misha) Polyanskiy for explaining all the physics behind the pressure vessel requirements, the optics of the mirrors and laser, the salt window, and anything else that was confusing in the laser room to me. I appreciated his willingness to always help me understand what I was working on.

Thank you to Steven Bugros who helped me out any time Creo wasn't working for me, with corrupted files and licensing problems. Thank you to Steven Bellavia for setting me up with ANSYS.

Thank you to Cynthia (Cindi) Biancarosa for being an absolutely amazing moderator for our OEP Team meetings. Every week is enjoyable because of her great energy, her warmth, and her positivity. I appreciate her work with OEP and her constant determination to help the interns interact with each other in such a difficult time.

I would also like to thank Tina Walsh for doing so much with the OEP program to set up the deliverables, tasks, syllabi, and all the work associated with the interns.

VIII. References

- [1] Paschotta, Rudiger. "Spectral Lines." *RP Photonics Encyclopedia*, RP Photonics Consulting GmgH, 14 Mar. 2020, www.rp-photonics.com/spectral_lines.html#:~:text=For%20some%20light%20sources%2C%20such,to%20a%20lower%20electronic%20level.
- [2] "Section II - D Table 1A." *2019 ASME Boiler and Pressure Vessels Code: an International Code*, by ASME Boiler and Pressure Vessel Committee, ASME, 2019, pp. 92–99.
- [3] "Section VIII Division 1 Mandatory Appendix 13-10." *2019 ASME Boiler and Pressure Vessels Code: an International Code*, by ASME Boiler and Pressure Vessel Committee, ASME, 2019, p. 473.
- [4] "Section VIII Division 1 Mandatory Appendix 13-4." *2019 ASME Boiler and Pressure Vessels Code: an International Code*, by ASME Boiler and Pressure Vessel Committee, ASME, 2019, p. 458.
- [5] "Section VIII Division 1 Mandatory Appendix 13-7." *2019 ASME Boiler and Pressure Vessels Code: an International Code*, by ASME Boiler and Pressure Vessel Committee, ASME, 2019, pp. 463-465.
- [6] "Section VIII Division 1 Mandatory Appendix 13-3." *2019 ASME Boiler and Pressure Vessels Code: an International Code*, by ASME Boiler and Pressure Vessel Committee, ASME, 2019, p. 454.

The Design of the Electron Ion Collider RF Systems Power Supply Building

Oksana Vysochanska

School of Civil and Environmental Engineering, Cornell University, Ithaca, NY 14853

Joseph E Tuozzolo

Collider-Accelerator Department, Brookhaven National Laboratory, Upton, NY 11973

Abstract

The conversion of the Relativistic Heavy Ion Collider to an Electron Ion Collider (EIC) at Brookhaven National Laboratory (BNL) is an ongoing project that will allow scientists to create snapshots of the internal structure of atoms. The EIC must maintain hadron and electron beams at very high energies, 275 GeV and 17 GeV, respectively. To accelerate and store these beams at high energies, superconducting RF cavities powered by solid-state power amplifiers are needed. A new building was designed at the ten o'clock region of the EIC to house the power amplifiers and the equipment required to run them. Each of the twenty-eight cavities was connected to a power amplifier using a series of waveguides. Within the interaction region (IR) of the EIC containing the superconducting RF cavities, other large components including the helium cooling systems, waveguide tuners, and waveguides were arranged to fit into the limited space available. Using the 3D modelling software, Creo Parametric, each component of the building was created and assembled in various ways to develop the most logical layout. A preliminary two-dimensional drawing of the building was used as the baseline for an initial building design. Two layouts, a staggered power amplifier layout and a linear, repeating layout, minimized the waveguide run length. The minimal waveguide run length allows for optimal transmission of radio frequency waves from the power amplifiers into the superconducting rf cavities. Multiple layouts of the building and the IR were assessed based on performance, accessibility, and cost. As part of my internship at BNL I learned to use Creo Parametric, collaborated with professional engineers, and gained experience implementing theoretical engineering principals into practical designs.

I. Introduction

Within nuclear physics, there is a large gap in knowledge about quarks, gluons, and the strong force that bind these building blocks of our universe. To understand these pieces of the puzzle, the Electron-Ion Collider (EIC) is being designed and built using repurposed infrastructure from the Relativistic Heavy Ion Collider (RHIC) at Brookhaven National Laboratory. This report will focus on the design and layout of Building 1010, a new service building that will house the solid-state power amplifier's that provide energy for high energy electron and hadron beams in the EIC.

Within the EIC, a hadron beam and an electron beam travel in opposite directions in short bunches at near relativistic speeds. There are about 300 bunches in each ring, each bunch circulating their 2.4-mile circumference ring 76,000 times a second. The 17 GeV electron beam and the 275 GeV hadron beam will be accelerated and stored until they reach a collision point at one of two interaction regions (IR). A large detector at the collision point will be able to collect a three-dimensional snapshot of all the particles scattering, providing clues to how the particles interact with each other and their internal structures. However, before the collision can happen, the beams need to be accelerated and maintained as they travel along a 2.4-mile circumference ring.

One of the technical challenges that needs to be addressed is the loss of energy in the electron beam as the beams travel along the circumference of the tunnel. The electrons beams lose light energy, slowing them down from nearly relativistic speeds. Radiofrequency (RF) energy needs to be injected into the electron storage ring to avoid a significant loss in energy. At the ten o'clock IR, the RF energy will be sent through waveguides from solid state power amplifiers into superconducting RF (SRF) cavities

through which the beam travels. One of the goals was to make these waveguide runs be as straight and as short as possible. Bends and added length decrease the performance of the waveguides as RF wave transmitters. Twenty-eight SRF cavities are in the 10 o'clock IR tunnel which require energy from 46 power amplifiers (PA). All these PA's will be housed in a new structure, Building 1010, with waveguide runs connecting them to the SRF cavities. Figure 1 shows an early rendering of this structure.

Building 1010 needs to house other equipment besides the PA's. Each PA needs a RF circulator and a RF dummy load located along the waveguide run. A circulator is a device that controls the direction of the RF signal transmission. The RF energy is inputted into the first of the three ports and can only exit out of the second port in a specific direction. The circulator protects the PA's from damage when RF waves bounce back along the waveguide as the returning signal can only be transmitted into the third port which is connected to the dummy load. The dummy load absorbs the RF energy that is bounced back.

The ten o'clock IR tunnel is a limited space that also needs to house a lot of equipment in a manner that is accessible. Each SRF cavity has one or two waveguide ports that need large, bulky tuners placed as close to the port opening as possible. Helium supply lines are also needed inside the IR because the cavities are superconducting for high efficiency and must be cooled to cryogenic temperatures with liquid helium.

To determine the layout of these major components, I used the Creo Parametric to create a 3D model of Building 1010. Several variations of the model were considered with cost and equipment performance in mind.

II. Methods

To create a basic 3D model of Building 1010 and the associated IR, Creo Parametric was utilized. An initial building design and equipment layout had previously been created. Figure 1 shows the ten o'clock region of the RHIC ring. The brown building is the originally proposed size of Building 1010 with three service rooms attached. It was located about 100 feet away from the IR tunnel. Figure 2 shows the original equipment layout with large 100 kW PA's connected using waveguide tees and circulators. Using the dimensions from this initial design as a starting point, several versions of Building 1010 were created, each one more complex than the last. I collaborated with RF engineers and cryogenic engineers to ensure that my design met the requirements of the EIC.

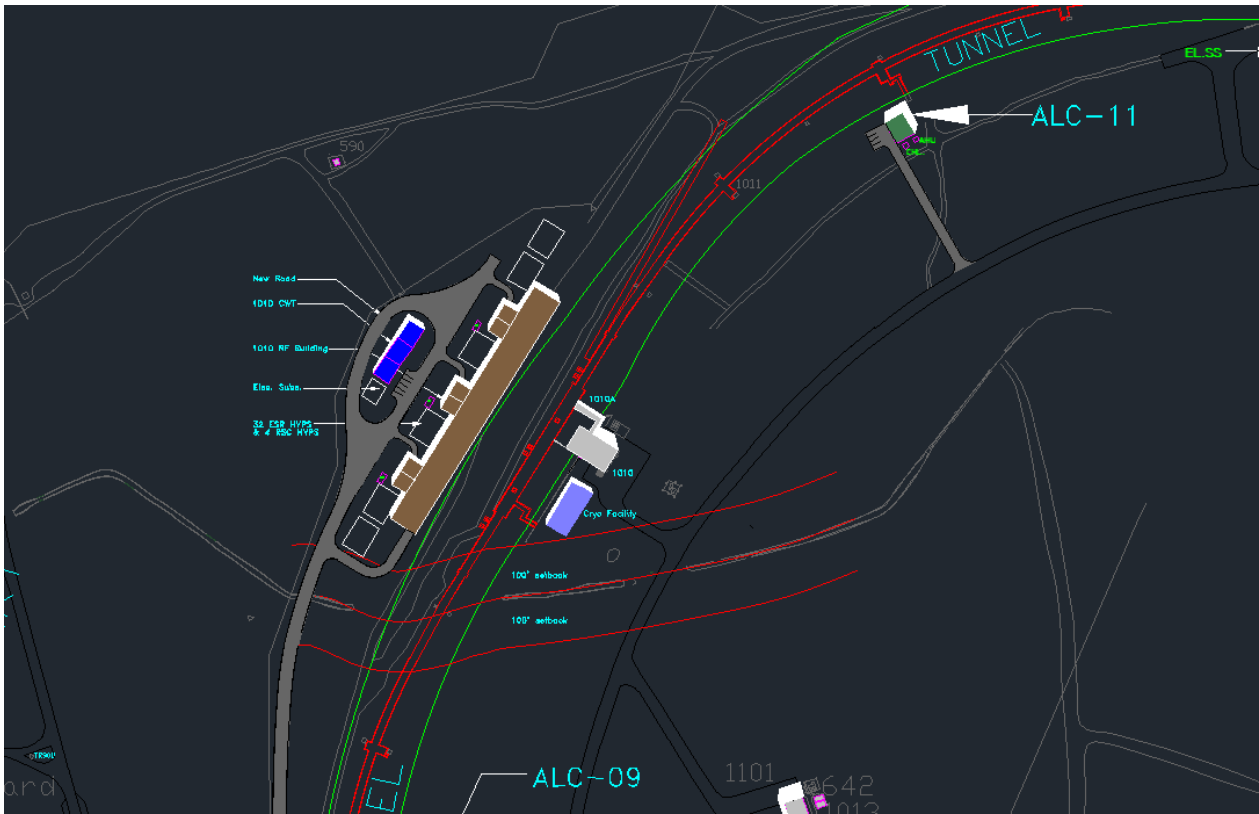


Figure 1. 10 o'clock region of RHIC ring with the initial design for Building 1010 (brown)

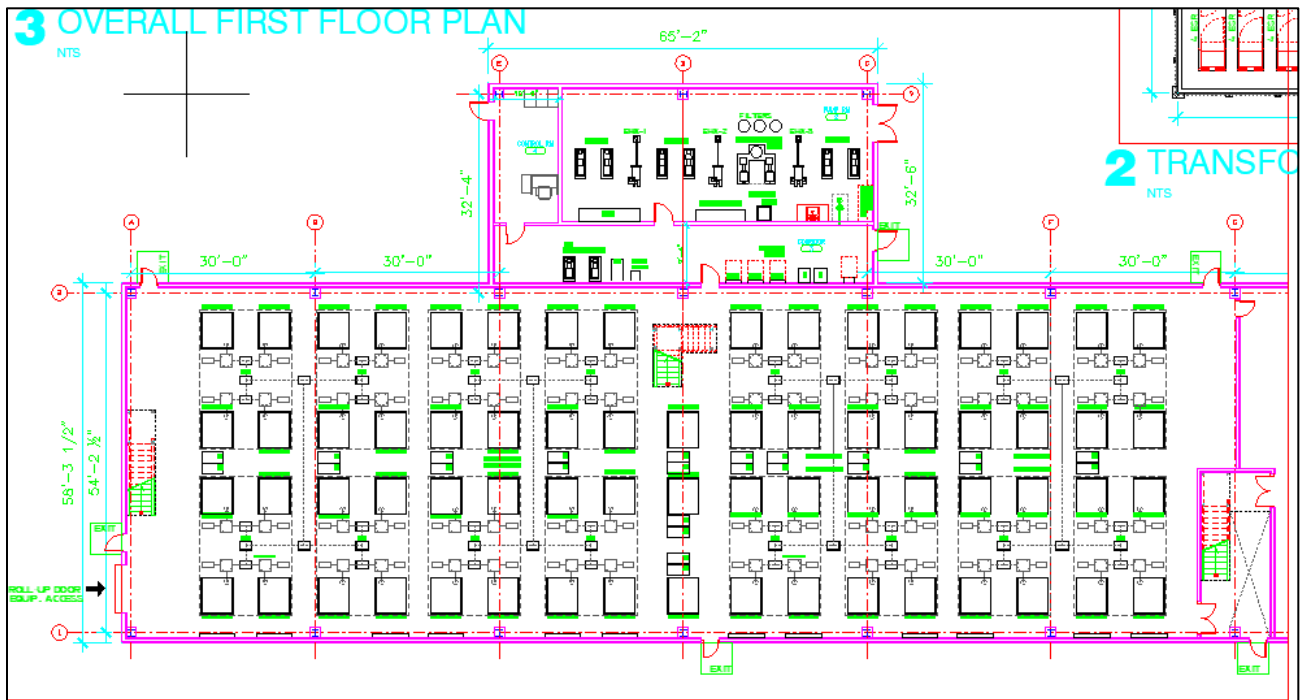


Figure 2. Section of initial layout of PA's, circulators, dummy loads, and waveguides.

III. Design Development

As major design decisions and changes were made throughout the development of Building 1010, I saved the different versions of the model to document the changes that were being made. In the first version, a building was created and placed 16 feet away from an existing model of the IR tunnel and the SRF cavities at ten o'clock. Within the building, WR1500 waveguides, models of an updated solid-state PA, RF dummy loads, and RF circulators were placed. This PA was a compact 400 kW assembly with 4 RF stations, an ACDC power supply, and a control station. A portion of the preliminary model of the building and the major equipment designed in Creo Parametric is shown in Figure 3. In the equipment layout in the figure, the 400 kg dummy load and the circulator are simply floating mid-air which is not practical or possible. In later iterations of the model, a mezzanine was added to support this equipment.

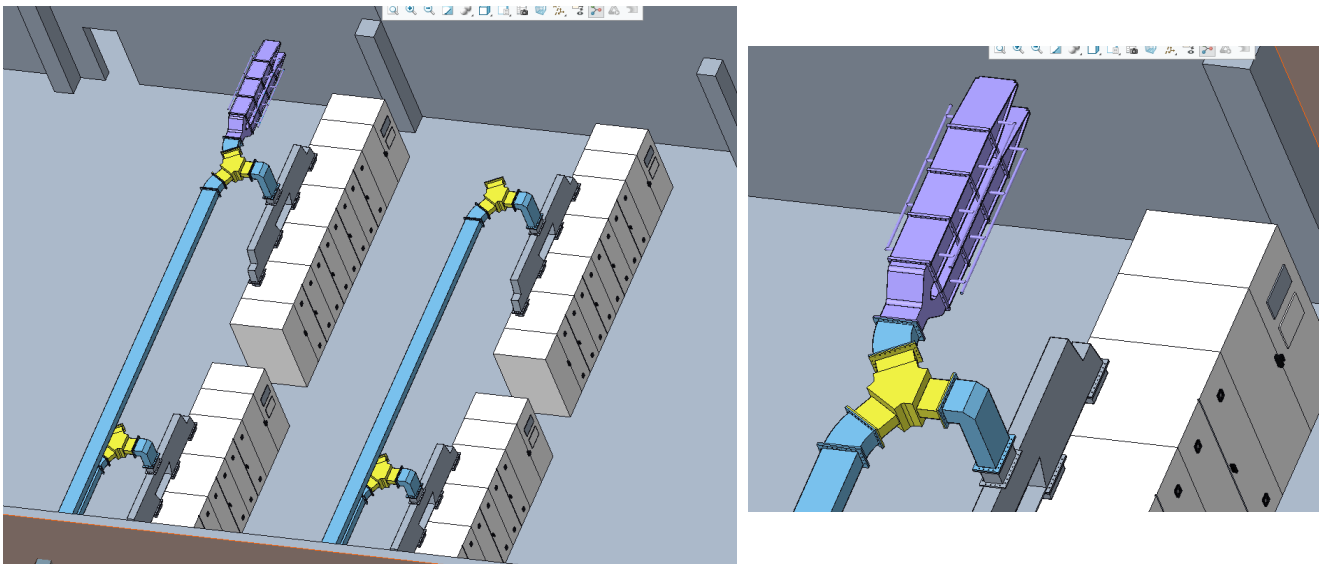


Figure 3. Version 1 of Building 1010 PA layout and close-up of the major equipment within Building 1010, including a PA (white), a circulator (yellow), a dummy load (purple), and the waveguides (blue)

The power amplifiers were arranged in uniform rows from east to west which are not fully modeled in Figure 3. There are several issues with this layout. There are unnecessarily wide aisles between the columns of PA's, creating a lot of wasted space. Additionally, there is not enough space for the dummy loads because of the overlapping waveguides in the row of PA's closest to the bottom of the image in Figure 3.

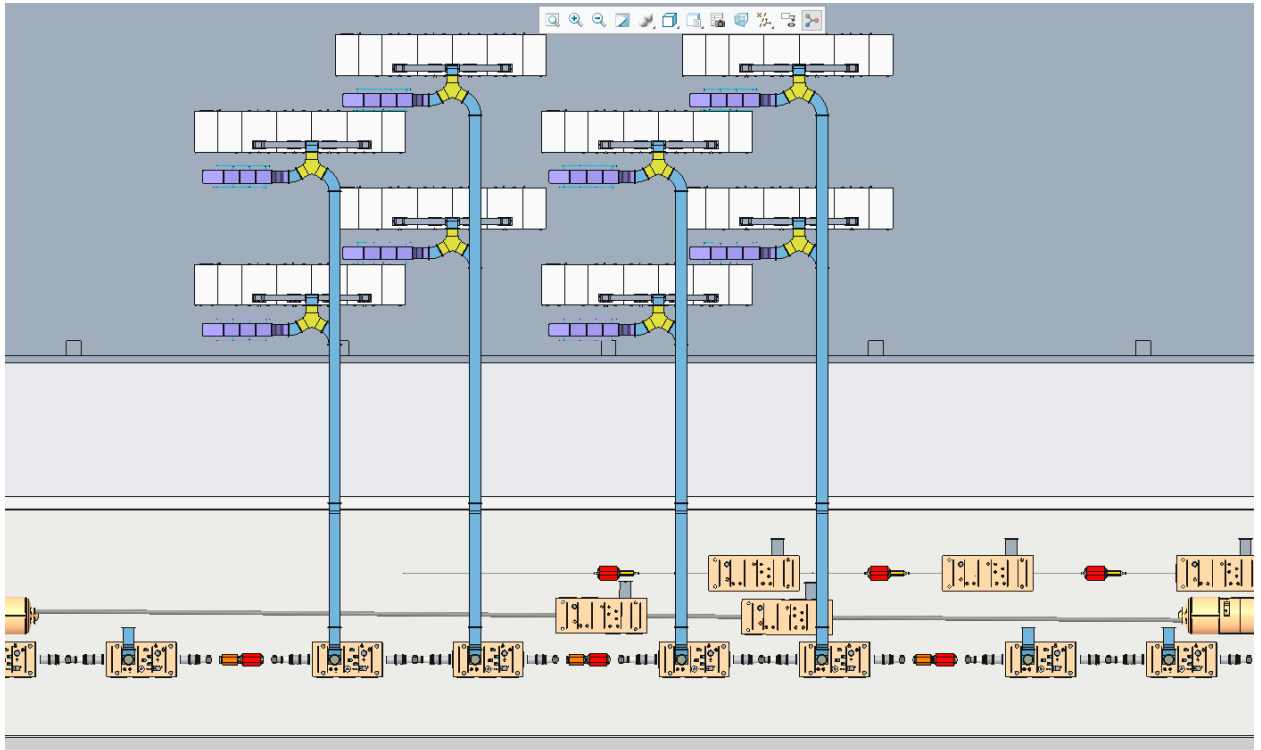


Figure 4. Version 2 of Building 1010 with a staggered PA layout. A portion of the IR with SRF cavities is seen at the bottom half of the image.

To fix these issues, a new layout with staggered PA's rotated 90 degrees was created in Figure 4. In this version, the longest waveguide run length is decreased by 10 feet, allowing the width of the building to be decreased from the original proposal. This layout also allowed the dummy loads to not interfere with the overlapping waveguides. Additionally, a dog leg (see Appendix A) was also added to block the radiation from the

RF waves. In the fourth iteration of Building 1010, concrete blocks (Appendix A) were placed in between the dog leg and the building to provide radiation shielding.

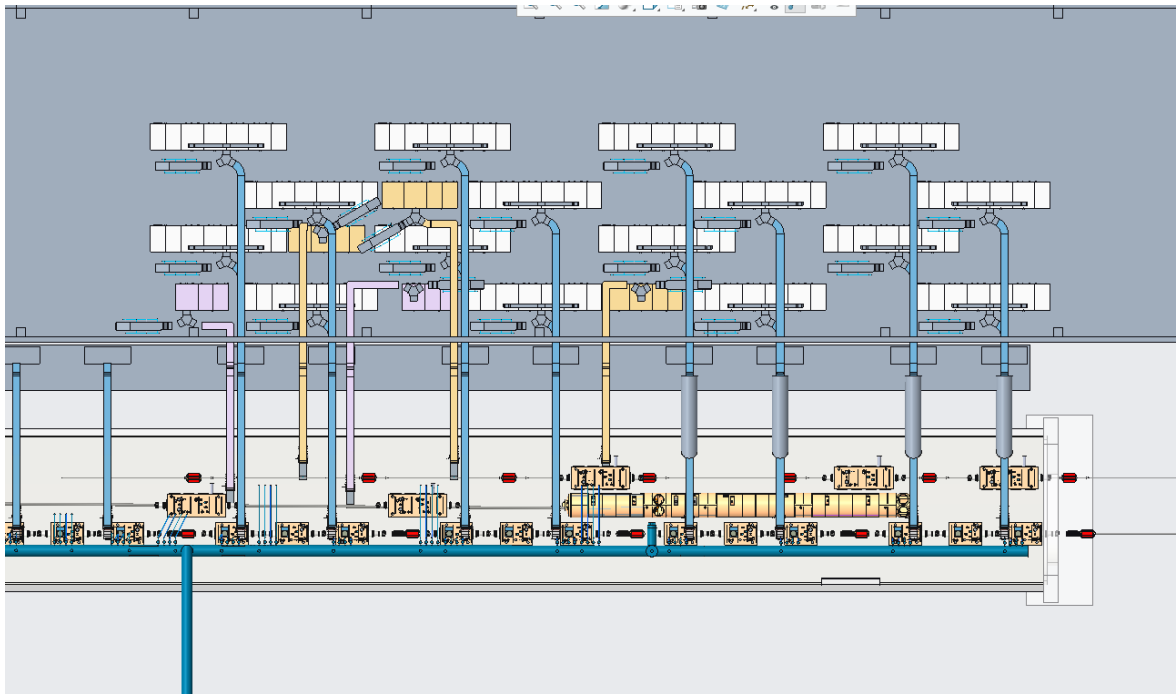


Figure 5. Version 3 of Building 1010. PA's for hadron beam SRF cavities are pink and PA's for RCS SRF cavities are yellow. Helium supply lines are the darker blue pipes at the bottom of the image.

Note: SRF cavities in IR tunnel are misaligned with the waveguides due to a modelling error.

Up to this point, the PA's that I had been using were only intended for the electron storage ring (eSR) which is the string of SRF cavities at the bottom of Figure 4. The other two rows of SRF cavities are for the hadron beam and the rapid cycling synchrotron (RCS) which accelerates the electron beams. In Figure 5, I used the empty spaces in the rows of PA's to place smaller PA's for these additional cavities. However, this design was very crowded and non-uniform because the RF dummy loads associated with these PA's interfered with the waveguides. Extra waveguide bends were also required for the new PA' which decrease the performance of the waveguides.

An initial design for the vacuum jacketed (VJ) cryogenic lines which bring liquid helium from a cryogenic facility on the other side of the IR tunnel to all the SRF cavities was included in this model. Each of the SRF cavities have four VJ lines connected to them. This design needs some work as the pipes no longer line up with the cavities.

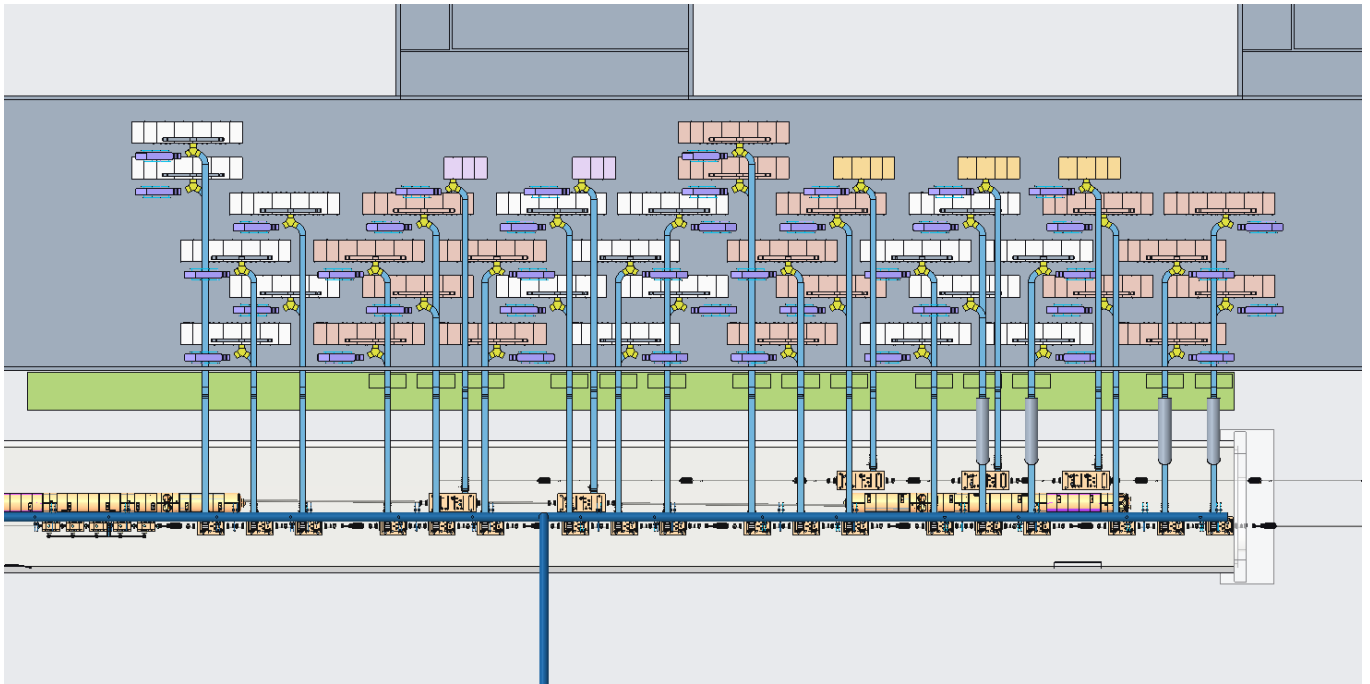


Figure 6. Version 4 of Building 1010. Redesigned eSR SRF cavity string is reflected in this model. PA's for hadron beam and RCS cavity are the row farthest away from IR tunnel. Every six PA's are colored pink/orange to show repeating pattern.

Most of the equipment and components of the EIC are still being designed.

During my time at Brookhaven, the eSR SRF cavity string was redesigned which I needed my model to reflect. However, this new string packed the SRF cavities closer to each other and added extra cavities. Figure 6 shows a new layout that used the staggered PA concept. Two groups of PA's could not continue the same repeating pattern that I established because of how closely the SRF cavities were spaced. The PA's that did not fit were placed in the fifth and sixth rows. The longest waveguide run length (not including any jogs or bends) in this version is 76'. This is more than the longest run

length in the first version of Building 1010. Additionally, in many places, the RF dummy loads interfere with the waveguides, requiring them to leave the building at non-uniform heights leaving much to be desired with this layout.

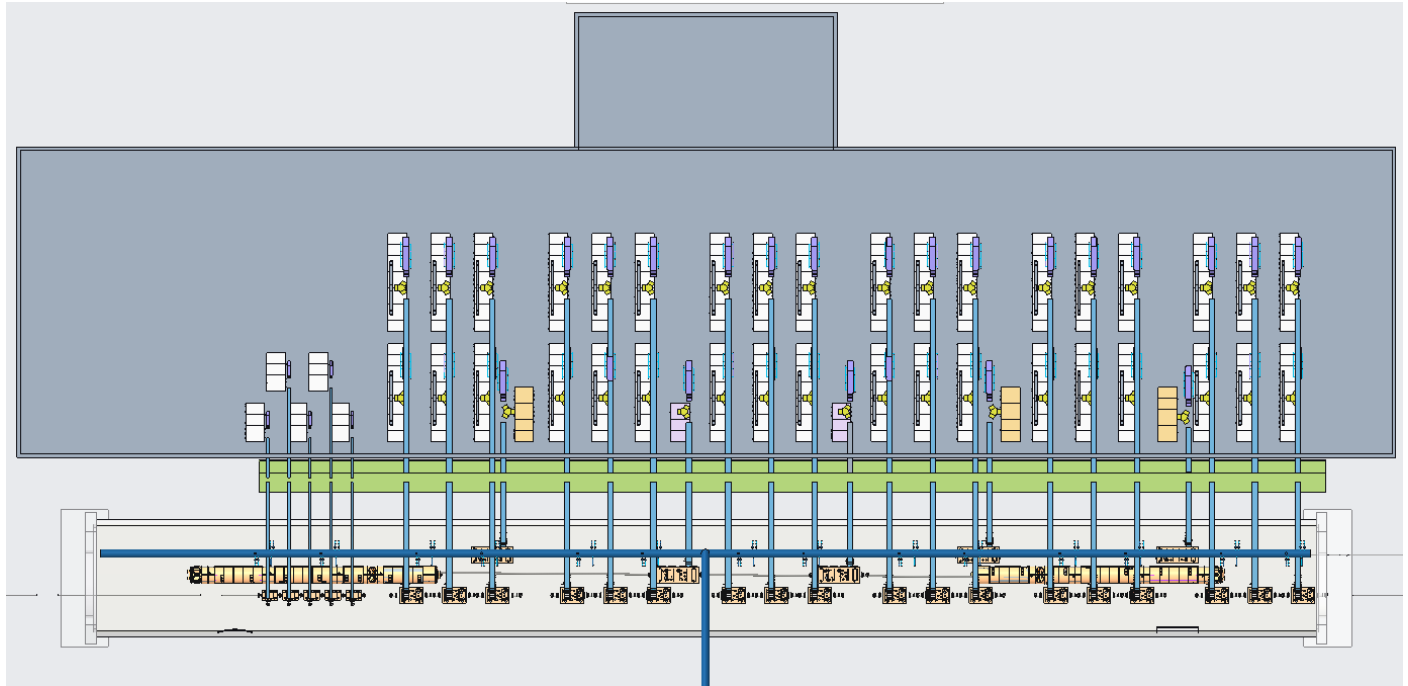


Figure 7. Version 5 of Building 1010. Uniform PA layout with redesigned concrete shielding (green) and new building size.

In the fifth iteration of Building 1010, the PA's were rotated 90 degrees from the orientation in Figure 6. This layout is cleaner, simpler, and has the most up-to-date components than any other version. The longest waveguide run length is about 70 feet. To accommodate the height of the dummy loads under the waveguides connected to the topmost row of PA's in Figure 7, the circulators, dummy loads, and waveguides associated with the topmost PA's were raised. Although it is not visible in Figure 7, a mezzanine was added that would provide a surface for the heavy RF dummy loads and circulators to rest on (see Appendix B). The hadron beam and RCS cavities were moved within the IR tunnel to line up with one of the wider openings between the columns of PA's associated with the eSR cavities. The vertical aisles created between the PA's allow

enough space for the racks of a PA to be removed and replaced if needed. At the left end of Building 1010, PA's for five smaller cavities that use WR650 waveguides were placed in a staggered layout to allow for all these waveguides to come out of the IR tunnel at the same height.

Another major change in this version is the size of the building. Not including the extra service room shown at the top of Figure 7, Building 1010 is 333.33 feet by 75 feet wide. Because this model does not take into consideration some of the other equipment and systems that need to be within this building, empty space was left on each side of the PA's. Overall, the building size is reduced by about 7,000 square feet. This does not include the originally proposed second floor or the mezzanine floor that will be needed.

IV. Future Implications and Conclusion

The fifth version of Building 1010 has a PA layout that is simple and uniform. This layout allows for easy access to the PA's and other equipment for maintenance. As the various components of the Electron Ion Collider are developed, their sizes may change. Currently, the final layout I created allows for significant changes to be made without disrupting the original idea of the design. Depending on the magnitude of the changes, it may be logical to return to a staggered PA layout. Other systems and components need to be designed and placed into both the IR tunnel and Building 1010 that may affect this layout as well.

Overall, this project showed that Building 1010 can be significantly smaller and closer to the IR tunnel than originally perceived. Making the building smaller will reduce building costs and most likely reduce operation costs down the road. A significant amount of structural analysis still needs to be done to assess the placement of the building sixteen feet away from the tunnel, partially inside the earth berm surrounding the tunnel.

Throughout the duration of my internship, I was exposed to the interdisciplinary nature of scientific endeavors by collaborating with scientists and engineers working on various portions of the Electron Ion Collider. Designing a model of Building 1010 enabled me to acquire experience using 3D modelling software, think spatially, gain a better understanding of developing complex models with many limiting factors, and become familiarized with basic civil engineering concepts.

V. References

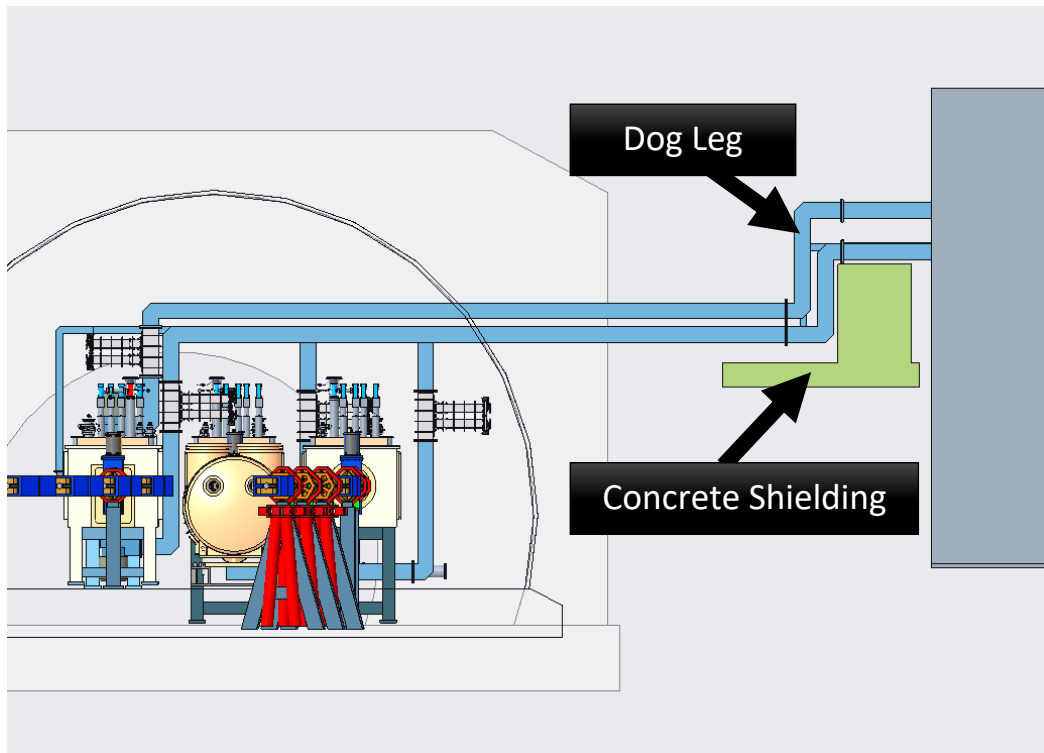
Aschenauer, Elke-Caroline & Baker, M. & Bazilevsky, A. & Boyle, K. & Belomestnykh, S. & Ben-Zvi, Ilan & Brooks, S. & Brutus, C. & Burton, T. & Fazio, Salvatore & Fedotov, A. & Gassner, D. & Hao, Yue & Jing, Y. & Kayran, Dmitry & Kiselev, A. & Lamont, M. & Lee, Jinsung & Litvinenko, Vladimir & Zheng, Liang. (2014). eRHIC Design Study: An Electron-Ion Collider at BNL. Retrieved August 16, 2020, from the arXiv databade.

VI. Acknowledgements

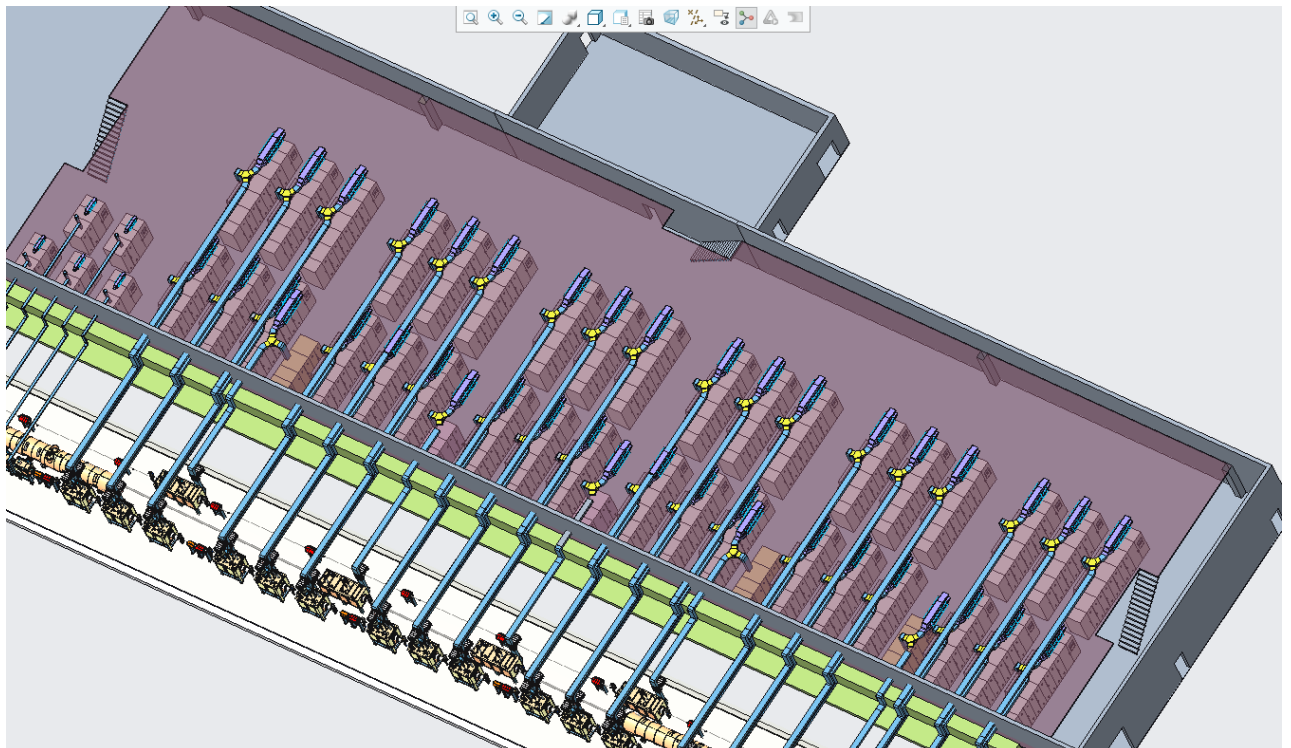
I would like to express my appreciation to my mentor, Joe Tuozzolo, for all the work that he put in to make my internship a great learning experience and for all the guidance for my project that he readily provided. I would also like to thank all the engineers and interns from the Collider-Accelerator Department at Brookhaven National Laboratory who were more than willing to go out of their way to provide help and insight; their names are in Appendix C below. This project was supported by the Department of Energy Office of Science's Office of Workforce Development for Teachers and Scientists through the Community College Internships program.

VII. Appendix

A. Dog Leg and Concrete Shielding



B. Mezzanine



C. Further Acknowledgements

Resources	Title
Joseph Tuozzolo	EIC Technical Systems Division Head
Charles Folz	EIC Infrastructure Systems Division Head
Douglas Holmes	EIC Mechanical Engineering Group Head
Kevin Smith	EIC Technical Systems Division Deputy Head
Alex Zaltsman	EIC RF Group Head
Roberto Than	Cryogenic Group Head
Angela Zavala Yanes	CCI Intern, Suffolk County Community College
Andrew Abdalla	SULI Intern, University at Buffalo

Monitoring facility services with ELK stack

Brandon Weindorf, Physics, Messiah University, Grantham, PA 17055

Antonio Wong, Physics, Brookhaven National Laboratory, Upton, NY 11973

Matt Snyder, Physics, Brookhaven National Laboratory, Upton, NY 11973

Ofer Rind, Physics, Brookhaven National Laboratory, Upton, NY 11973

Abstract

Laboratories, such as Brookhaven National Lab, perform a multitude of scientific experiments, all of which generate vast amounts of data. Data storage has been rapidly migrating from local servers to the cloud, as which has clearly been demonstrated at Brookhaven National Lab through its use of the newly implemented Nextcloud online storage service: BNLBox. Given the potential amount of data that could be stored on BNLBox, it is important for Brookhaven National Laboratory to be able to monitor network usage and server storage. I was tasked with implementing the ELK stack to monitor the usage of BNLBox. This was accomplished by installing Filebeat and Metricbeat on the BNLBox server. I configured these services to send logs and metrics to Logstash. I configured Logstash to both parse the log messages into JSON objects and enrich the logs through use of the BNLBox Postgres database. Elasticsearch was installed on four separate servers, serving as a cluster capable of distributing storage and workload. Finally, I constructed visualizations and graphs within Kibana, giving administrators a quick and easy way to view the data. Elasticsearch will allow Brookhaven National Lab to stay informed on the state of BNLBox and determine if changes are needed to bandwidth, storage or other areas to better meet the users' needs. Currently, ELK is only monitoring BNLBox, but in developing the ELK Stack, I successfully demonstrated the steps needed to be taken in order to monitor virtually every application and service that is run at Brookhaven National Laboratory, including data transfer and version upgrading. From this experience, I have gained skills in data collection, mining, analysis, enrichment and graphing. I have also gained a better understanding of how network-based applications can be installed and configured on a Linux system.

I. Introduction

The use of monitoring software is very important for the successful operation of many programs and services at Brookhaven National Laboratory. Certain monitoring software, such as Grafana and Nagios, have already been implemented at the laboratory. The Elasticsearch Stack (also known as the ELK stack), which consists of Elasticsearch, Logstash, Kibana and BEATs, provides a framework that makes monitoring of

application specific data easier and graphing of said data more straightforward and organizable. Moreover, the ELK stack is capable of monitoring a diverse set of applications all while keeping all graphs, charts and other visualizations in a centralized location. The purpose of my project was to configure the ELK stack to monitor BNLBox, a new file storage and sharing service used at the laboratory. The ELK stack is anticipated to grow rapidly at the lab as there are many services and programs that will need to be monitored in the near future. My project work served as a blueprint for configuring the ELK stack to monitor virtually any application and demonstrate steps needed to be taken to make the stack more scalable.

II. Setup and Configuration

Upon initiation of the project, I was given access to an ELK cluster that had already been created. This cluster was run across four virtual machines, ELK01, ELK02, ELK03 and ELK04. ELK04 had Elasticsearch version 7.6.2, Logstash version 7.6.2, Kibana version 7.6.2, Filebeat version 7.6.2 and Metricbeat version 7.6.2 installed. ELK01, ELK02 and ELK03 each had Elasticsearch version 7.6.0 and Metricbeat version 7.6.0 installed. Finally, Filebeat version 7.6.1 and Metricbeat version 7.6.2 were installed on bnlbox01, while Filebeat version 7.6.2 and Metricbeat version 7.6.2 were installed on bnlbox02. Each of the aforementioned servers ran BNLBox, an in-house, online file storage and sharing platform. Elasticsearch serves as the “brains” of the ELK stack, it is the database that organizes and stores all data. In order to keep CPU and memory usage down, the Elasticsearch database can be spread across numerous servers, or nodes, that are optimized by ELK to store, organize and return data in a coordinated manner. Logstash serves as the source for Elasticsearch as it collects data from various servers. As per convention, Logstash is run on the same server as one of the Elasticsearch nodes. This allows data to be passed directly from Logstash to Elasticsearch without needing immediate network access. Filebeat and Metricbeat are two BEATS programs that read files and metrics, respectively, and pass said data to Logstash. This was done by putting the Fully Qualified Domain Name (FQDN) of the server that is running Logstash along with the port number that Logstash is listening on within the configuration files for Filebeat and Metricbeat. This allows Logstash to receive data from different servers across the network. Finally, Kibana is the web-based application that reads the Elasticsearch database and provides graphs, charts and other visualizations that allow the data to be quickly seen and understood.

III. Logstash Configuration

A. Input

One of the most important functions of the entire Stack is the ability to parse data into forms that can be read quickly and plotted easily. Most log messages are rich with data yet are relatively condensed and opaque. Furthermore, logs are typically not formatted in ways that makes plotting their data simple or straightforward. Logstash is capable of ingesting logs of virtually any form and parsing them into the convenient format of JSON. This is accomplished through use of a Logstash pipeline, which was eventually named “user_data”. A Logstash pipeline is a configuration file that dictates how Logstash is to receive data, parse said data into a JSON document and where to export the JSON document. Initially, a single Logstash pipeline was configured to accept logs from the instance of Filebeat running on bnlbox02. This was done by using the “input” section of the configuration file, as seen in Figure 1.

```
input {
  beats {
    port => "PORT NUMBER"
    host => "FQDN"
    tags => ["file-based"]
  }
}
```

Figure 1: The “input” block of a Logstash pipeline

Within the “input” section, this Logstash pipeline was configured to listen for BEATS messages on a specified port of the specified host (which in this case the FQDN of localhost). Finally, the pipeline was configured to add the tag, “file-based” to the incoming message.

B. Filter and Output

Once the input was configured, the “user_data” pipeline was then configured to parse and filter incoming data. Each message that Logstash receives is referred to as an event. An event could be a newline of a file, a log entry or other pieces of data that are either periodically, or infrequently sent to Logstash. All data sent to “user_data” was log messages from bnlbox02. BNLBox logs are similar to apache logs in that they have time fields, message fields and other metadata written in a structured format. Out of the box, Logstash is able to parse these logs into a JSON document based off of this format. For example, it assigns the log’s date

to the field “timestamp” and the log’s message to the field “message”. However, the message field of the log contains the most important data, which is left unparsed. Each message records an action that was taken on BNLBox, such as a file creation, file edit or file share. While messages that record two different types of events are structurally different from each other, log messages that record the same types of events are identical in format. This made pattern matching ideal for parsing the message fields of these logs. A few example log message fields can be seen in Figure 2.

```
Login successful: "BNL-User-ff33d20b-10e4-4f4c-9c24-145fa33ae41d"  
File accessed: "/Data/Sinitskii-P35813/20200813-Au111-MNo2/Au111-167-M-Xp-Topo.nc"  
File written to: "/Data/Sinitskii-P35813/20200813-Au111-MNo2/Au111-167-M-Xp-Topo.nc"  
File updated: "/Data/Sinitskii-P35813/20200813-Au111-MNo2/Au111-167-M-Xp-Topo.nc"  
File created: "/Logs/bldiracvm03.sdcc.bnl.gov/DIRAC/RequestManagement/ReqManager/2020/8/16/400000005f39f22537813c74.s.gz"  
File written to: "/Logs/bldiracvm03.sdcc.bnl.gov/DIRAC/RequestManagement/ReqManager/2020/8/16/400000005f39f22537813c74.s.gz"  
Login attempt: "BNL-User-ff33d20b-10e4-4f4c-9c24-145fa33ae41d"
```

Figure 2: Example log messages from BNLBox logs

i. Grok

It can clearly be seen that log messages that record the writing of a file are of identical structure: “File written to: “<filename>”. Likewise, each type of log message follows its own unique pattern throughout all events. Logstash has a plugin, grok, that allows log messages of similar structure to be efficiently parsed. A few hundred lines of grok code was written to the “user_data” pipeline with the goal of parsing each type of log message. A small portion of this grok code can be seen in Figure 3.

```

else if [message] =~ /Login successful:/ {
  mutate {
    add_field => {"action" => "Login Successful"}
    add_tag => ["login"]
  }
}
else if [message] =~ /File created:/ {
  mutate {
    add_field => {"action" => "File Created"}
    add_tag => ["file_edit"]
  }
  grok {
    match => {
      "message" => "File created: \"%{GREEDYDATA:file}\""
    }
  }
}
else if [message] =~ /File written to:/ {
  mutate {
    add_field => {"action" => "File Written"}
    add_tag => ["file_edit"]
  }
  grok {
    match => {
      "message" => "File written to: \"%{GREEDYDATA:file}\""
    }
  }
}
}

```

Figure 3: A few lines of the “user_data” Logstash pipeline

Grok’s match feature can be used to assign certain parts of a string to a JSON field. Within Figure 3, each “else if” statement is evaluation whether the pattern encapsulated in forward slashes (i.e. /Login successful:/) is present within the “message” field of the log. Unfortunately, Logstash does not support switch statements, thus a long sequence of “else if” statements was needed to account for each type of event. Once one of the “else if” expressions evaluates true, an action field is added to the JSON document associated with the event and a tag is appended to said JSON documents array of tags. I created the action field to describe the specific action that the user had taken while appending a tag that provided a more general sense of the action. In Figure 3, for example, events recording the creation of files and writing of files have actions of “File Created” and “File Written”, respectively. On the other hand, each event has the tag “file_edit” appended. This dichotomy of labelling will later prove advantageous for data searching and aggregation. Furthermore, for these events and all other file-based events, a “file” field is added to the JSON document and the filename is assigned as its value. This is done by grok. Grok is heavily based on regular expressions. In the example at hand, the filename

falls in between double quotes, thus using the Grok pattern “GREEDYDATA”, which captures everything, in-between double quotes within the “match” field allows the filename to be mapped to the file field in the JSON document.

ii. Authentication Tagging

It should be noted the “Login successful” event makes no use of grok. All events that correspond to BNLBox users successfully logging in, editing files or sharing files are already authenticated; thus, their BNL-User ID was written to the log file in a the “user” field. Logstash automatically creates a field in the JSON document titled “user” and assigns the BNL-User to its value. Therefore, there is no need to use grok to create a “user” field and assign the BNL-User ID to it. Other, unauthenticated events, such as those recording failed logins or login attempts use grok to manually add a “user” field and assign the BNL-User ID, as found in the message field, to its value. An “unauthenticated” tag is then added to the list of the event’s tags. See the Appendix for a thorough listing of events along with respective mappings.

iii. Database Enrichment

There are no BNLBox logs that contain the username of the user. At most, the BNL-User ID is included in either the message or user field of the log. While the BNL-User ID is a unique identifier for each user, it is not as useful as the username itself. BNL-User IDs are of the form “BNL-User-xxxxxxxx-xxxx-xxxx-xxxx-xxxxxxxxxxxx”, where x is either a number or a letter. For virtually all visualizations that involve users, it is vital that the username be displayed as unique IDs are rather inconvenient. Fortunately, the Postgres database that BNLBox uses contains a table, “oc_users”, that maps user IDs to usernames. Logstash could be set up to query the Postgres database running on the server bnlboxdb02, each time an event is passed through. Logstash would then create a “username” field in the JSON document and assign the returned value from the database call to its value. This would make use of the Logstash filter plugin, jdbc_streaming. While this method would work, it would not be very efficient. Logstash captures a few hundred logs from BNLBox per hour. This would result in a few hundred database calls, over the network, per hour. Clearly, bandwidth would be quickly consumed, and the database may get overwhelmed with such a high frequency of calls. With this in mind, another solution was taken. Logstash has another filter plugin, jdbc_static, which allows Logstash to query a database on a periodic schedule and store the returned data in memory. For our implementation,

Logstash was configured to copy the “oc_users” table from bnlboxdb02 to local memory every 15 minutes. This allows Logstash to query this local database for each event rather than making a large number of network calls. This method worked for approximately 90% of all events created by Logstash. The notable issues were associated with new users and guest users. If a new user was created in between the periodic database calls, the new user’s information would not be present in the local database, thus resulting in a null username field. Likewise, “oc_users” only contains BNLBox user information and does not contain any information regarding users with guest accounts. In order to remedy the former issue, Logstash was configured to check the value of the “username” field after the call was made to the local database. If the “username” value was null, Logstash would then make an external call to the Postgres database with the BNL-User ID. The associated username would then be returned and assigned to the “username” field’s value. Since new user creations are relatively an infrequent occurrence, network bandwidth nor the database itself are not expected to be overwhelmed due to this alteration. While this change solved the new user issue, the events based on guest users were still getting null values for the “username” field. Conveniently, the Postgres database has another table, “oc_guests_users”, that contains guest user IDs, which are typically the user’s email, and the associated username. The periodic call to the Postgres database was altered to make use of a “UNION” statement that combined the “oc_users” and “oc_guests_users” tables and placed the result in local memory. Once this change was implemented, guest user events had usernames correctly assigned. Finally, Logstash’s output section was configured to send all events (i.e. JSON documents) to the Elasticsearch cluster with the index name “nextcloud-DATE” where data is of the format YYYY-DD_MM. As an additional note, BNLBox is an implementation of Nextcloud.

iv. Additional Pipelines

All previously discussed information focused on the “user_data” pipeline. This pipeline was designed to handle events triggered by the user’s and thus process the data associated with each user. Another pipeline, “user_storage”, was constructed within Logstash. This pipeline is significantly smaller than “user_data”. Rather than handling events generated by the users, “user_storage” only makes calls to the Postgres database regarding the storage that is used up by all files in BNLBox and the storage that is used by each user. These calls are made every 15 minutes and are assigned and passed to Elasticsearch with the index name “user_storage”.

IV. Kibana Visualizations

The two previously mentioned pipelines account for all BNLBox data being received by the Elasticsearch cluster. Once the data is received by Elasticsearch, it is ready to be plotted by Kibana. Kibana sorts data into groups based off of index name. In order to configure this, an index pattern must be defined in Kibana. For BNLBox data, the index pattern “nextcloud*” was defined. This index pattern collects all data from the “user_data” pipeline as this data is assigned the index name “nextcloud-DATE” (the “*” character acts as a wildcard). Index patterns then serve as sources for visualizations. I primarily used horizontal bar graphs, gauges, pie charts, line graphs and maps to portray Elasticsearch data. For bar graphs and line charts, a y-axis needed to be defined. This was typically assigned the variable that was to be displayed, such as storage (in GB), number of users, or even number of documents that fit a certain criteria (such as number of documents that have a certain value assigned to a certain field or number of documents that contain a certain field or tag). For bar graphs, the x-axis was assigned some form of aggregation, which was typically by term. For example, one visualization shows the top five users creating files. In this case, the y-axis measures the number of documents that have “File Creation” assigned to the “action” field. The X-axis aggregates the data based on a specified term, in this case, the selected term was “username”. With this configuration, all Elasticsearch documents that had “File Creation” in the “action” field were split into different groupings, or buckets as Kibana refers to them, based on username. Each bucket contained only the “File Creation” documents that had the same username. Finally, the visualization was configured to only show the buckets that contained the top 5 number of documents. The plotted buckets can be seen in Figure 4.

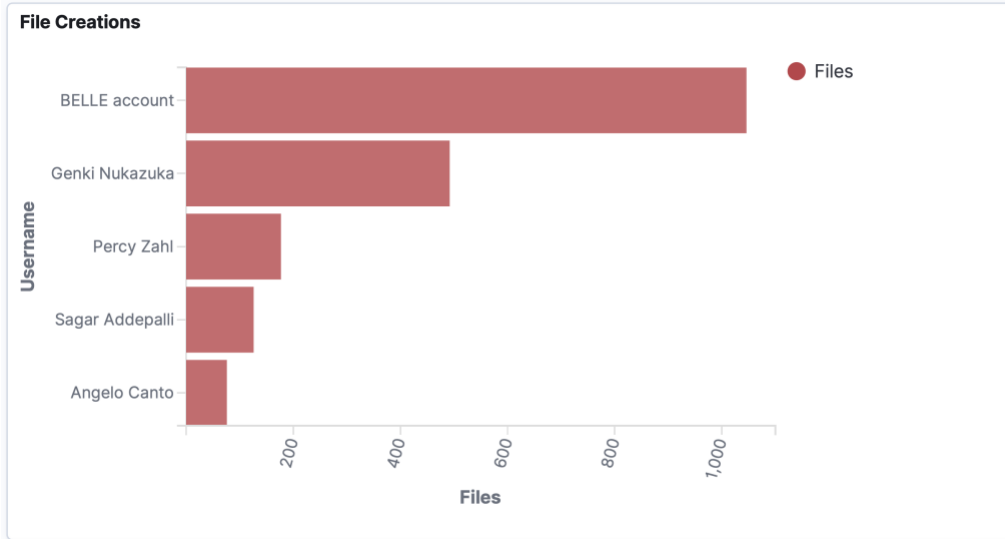


Figure 4: A Horizontal bar graph showing the top five file creating users over a 24-hour period.

Some graphs incorporated a “split series” that split each bucket into further sub-buckets. A good example would be the graph that displays trusted domain errors. The y-axis of this graph measures the number of trusted domain error events while the x-axis splits the data into buckets based on the source IP in which the connection is being initiated. Finally, a split series is used to split each bucket into sub-buckets based on the IP address that the source IP address tried to access. The Trusted Domain Errors bar-graph can be seen in Figure 5.

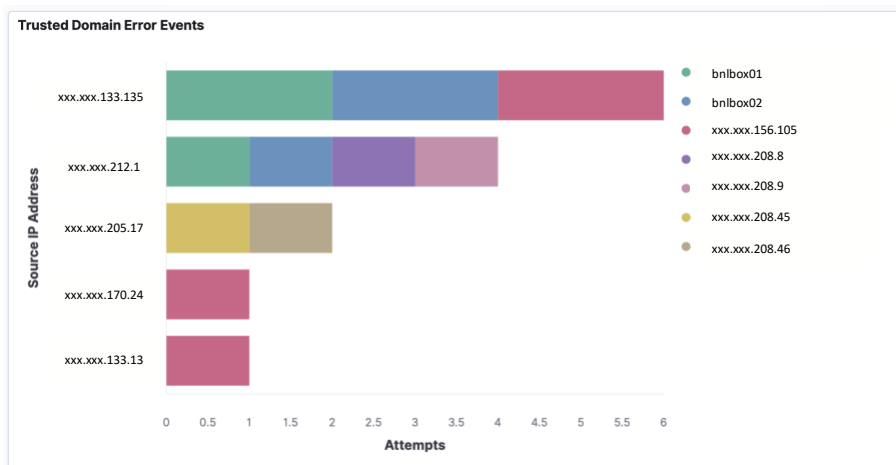


Figure 5: Horizontal bar graph showing trusted domain errors by source IP. Note that each bar is cut into sub-bars that represent the targeted IP address. Color mappings can be seen on the right.

Numerous bar-graphs, along with line graphs, pie charts, gauges and maps were created. Many of these visualization types included a form of a y-axis, x-axis and split series option. Visualizations that contained similar or related data were organized into different dashboards within Kibana. Each dashboard contained numerous visualizations that were organized in such a way to best utilize screen space. A portion of the “User Activity” dashboard can be seen in Figure 6.

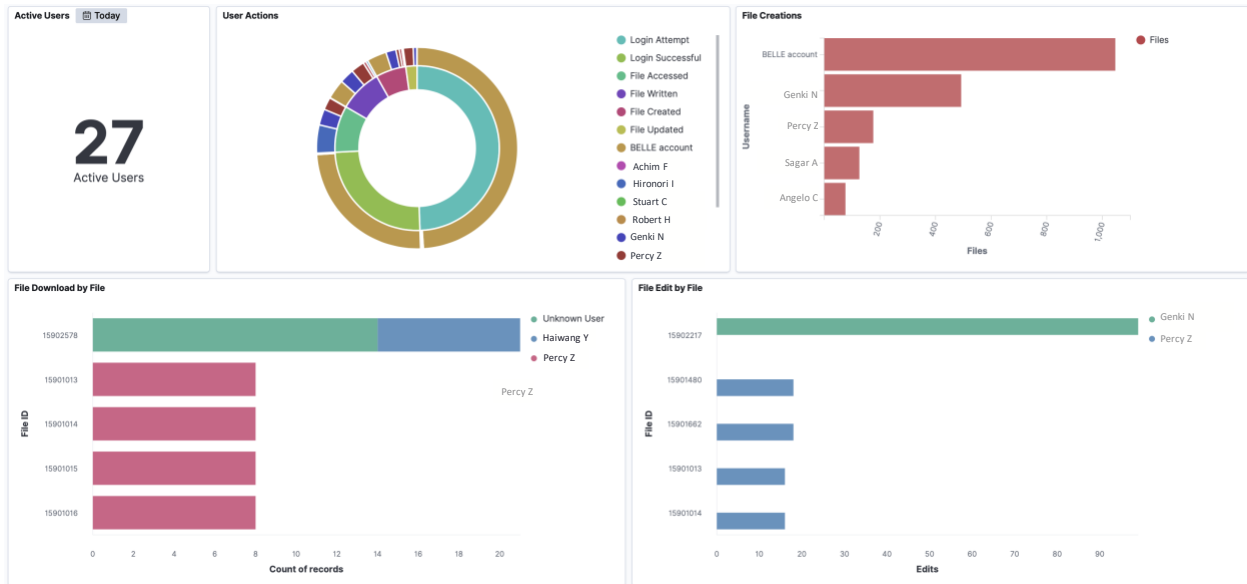


Figure 6: A few example visualizations from the “User Activity” dashboard. Included here is a metric that counts the number of active users for the current day, a pie chart that splits the Elasticsearch data based off of the top 5 actions being taken and then further splits the data based off of the username taking each action. Finally, there are three bar graphs showing file actions.

It may be noted in Figure 6 that file-based graphs had numbers where filenames should be. The filenames are relatively long and would harm the aesthetic look of the graph. Postgres has yet another table that maps filenames to file IDs. The file ID is used in the graphs to reduce the effective length of the filename. A table is provided later in the dashboard that maps the file IDs back to the actual filenames. The use of file IDs has actually proven quite useful as users have the ability to rename files. While the filename may change, the file ID is static and remains constant through all movement and renaming of files.

V. Additional Work

In addition to collecting and plotting data, procedures for keeping the ELK stack up to date were explored. Before any upgrades could be pursued, it was vital that all Elasticsearch data be backed to mitigate any chance of data loss. Upgrades were done through the use of API commands on Kibana’s console. A shared

volume was mounted to each of the ELK hosts and an ELK backup location was created on the shared volume. Next, Kibana's console was used to execute an API command that created a backup repository. Finally, an additional API command was executed to back up the actual data. An ELK backup is referred to as a snapshot and consists of all Elasticsearch data, indices, Kibana GUI-configured preferences and other settings. A snapshot can easily be restored to an ELK cluster by use of an API command. Furthermore, snapshots can be used to move data from one cluster to another. Once the snapshot was completed, ELK nodes ELK01, ELK02 and ELK03 were upgraded to version 7.6.2. This was necessary for proper primary and replica shard allocation among the nodes. When a shard, or collection of data, is inserted into Elasticsearch, it is replicated, thus forming a primary and replica shard is created. The primary shard is assigned to one server while the replica is assigned to any other server. This creates data redundancy for better protection. Any Elasticsearch server can only pass its replica shards to an Elasticsearch node that is running either the same version of ELK or newer. Since ELK04 was running 7.6.2, there were no replica shards for the shards that were being stored on ELK04. Updating ELK01, ELK02 and ELK03 to 7.6.2 allowed all shards to be replicated.

VI. Conclusion

BNLBox is not the only service that ELK will be used to monitor. In the future, additional services will be added. In order to demonstrate this concept, I added globus as an additional service to be monitored by the ELK stack. Overall, I thoroughly implemented the ELK stack to monitor BNLBox, demonstrated and documented ways to display, backup and transfer data while also recording how to update the ELK stack. In the future, more services will be added, thus providing a more centralized location to monitor Brookhaven National Laboratory's services.

Appendix

Action	Tag(s)	Unauthenticated	File
Login Attempt	login	Yes	No
Login Failed	login	Yes	No
Login Successful	login	No	No
User Created	user_create	No	No
Password Changed	account_change	No	No
Email Changed	Account_change	No	No
File Created	file_edit	No	Yes
File Written	file_edit	No	Yes
File Renamed	file_edit	No	Yes
File Updated	file_edit	No	Yes
File Deleted	file_edit	No	Yes
File Accessed	file_view	No	Yes
Preview Accessed	file_view	No	Yes
Linked File Access	file_view	No	Yes
Linked Folder Access	file_view	No	Yes
File Shared	share	No	Yes
File Shared via Link	share, link	No	Yes
Folder Shared via Link	share, link	No	Yes
File Shared via Email	share, link	No	Yes
Folder Shared via Email	share, link	No	Yes
File Unshared	unshare	No	Yes
Folder Unshared	unshare	No	Yes
User Deleted	User_delete	No	No
Permissions Change	permission_change	No	Yes
Trusted Domain Error	domain_error	Yes	Yes

Identifying Sea / Bay Breeze Circulations in the Houston, TX region using a Surface Meteorology Network

Brian Wittemann, Meteorology, State University of New York at Oneonta, Oneonta, NY 13820

Michael Jensen, Environmental and Climate Sciences Department, Brookhaven National Laboratory, Upton, NY 11973

Die Wang, Environmental and Climate Sciences Department, Brookhaven National Laboratory, Upton, NY 11973

James Turner, Department of Mathematics, Colorado State University, Fort Collins, CO 80523

Abstract

The Cloud Processes Group at Brookhaven National Laboratory studies the dynamical and microphysical processes that impact the lifecycle of clouds to enhance their representation in climate models. Currently, a major focus is the TRacking Aerosol Convections interactions ExpeRiment (TRACER), taking place April 2021 through April 2022 in the Houston, TX region, with the goal to examine the lifecycle of isolated convective clouds. The objective of my internship is to prepare for the TRACER campaign by enhancing our understanding of the meteorological patterns of the Houston region. Our approach included a practice forecasting exercise to gain general knowledge of the meteorology driving the weather in the region. The forecasting methodology included interpretation of observations, and numerical model forecasts of surface and upper atmosphere meteorology. The outcomes allowed for detailed forecasts to guide operational decisions that mimic conditions that are anticipated during the field campaign. A secondary component focused on the analysis of Texas Commission on Environmental Quality (TCEQ) data with a specific purpose of improving our understanding of sea breeze and bay breeze circulations in the TRACER measurement domain. The approach consisted of the creation of python scripts to examine the archived meteorological data. The scripts contained the ability to determine which days had the conditions for sea breeze, or Galveston bay breeze, such as through meteorological constraints. For example, a meteorological constraint was set at a temperature decrease $> 5^{\circ}\text{F}$, and a change in wind direction $> 30^{\circ}$, but $< 180^{\circ}$ within a 1-hour interval. This analysis provided an in depth understanding of the variability of sea breeze and bay breeze days throughout the TRACER domain.

In this study, we use 1-year of surface meteorological data (temperature, winds) from the Texas Commission on Environmental Quality (TCEQ; <https://www.tceq.texas.gov>) for 12 sites inside the TRACER measurement domain to identify potential sea / bay breeze events and the associated changes in surface meteorological variables, such as temperature, wind direction, and wind speed. In addition, we aim to quantify the timing of the sea breeze front passage as well as its frequency of occurrence.

Furthermore, preparation for the upcoming TRACER campaign included forecast discussions with members of the TRACER forecasting team. The forecasting sessions consisted of detailed discussions that included an overview of present weather and previous forecast performance, forecasts for “today’s” and “tomorrow’s” weather in the Houston region with a specific intent of determining if convection will transpire, and a peek ahead into the upcoming week.

2. DATA and METHODS

2.1 Surface Meteorological Data

Surface meteorological data (temperature, winds) for a full year (2019) is provided by TCEQ for 12 sites inside the TRACER measurement domain. The 12 sites (Figure 2) include 3 sites in the city of Houston (UH Moody Tower, Houston Westhollow, Houston East), 3 sites along Galveston Bay (LaPorte Airport, Texas City BP Onsite 2, Seabrook Friendship Park), 2 sites along the Gulf of Mexico (Galveston 99th St, Freeport South Avenue), 1 site between the coast and Houston (Manvel Croix Park), 1 site between Galveston Bay and Houston (Houston Deer Park), 1 site on the eastern portion of Galveston Bay (Smith Point Hawkins Camp), and 1 site closest to TRACER’s westernmost measurement site (Danciger). TCEQ data is recorded every 5-minutes, which results in 288 data points each day.

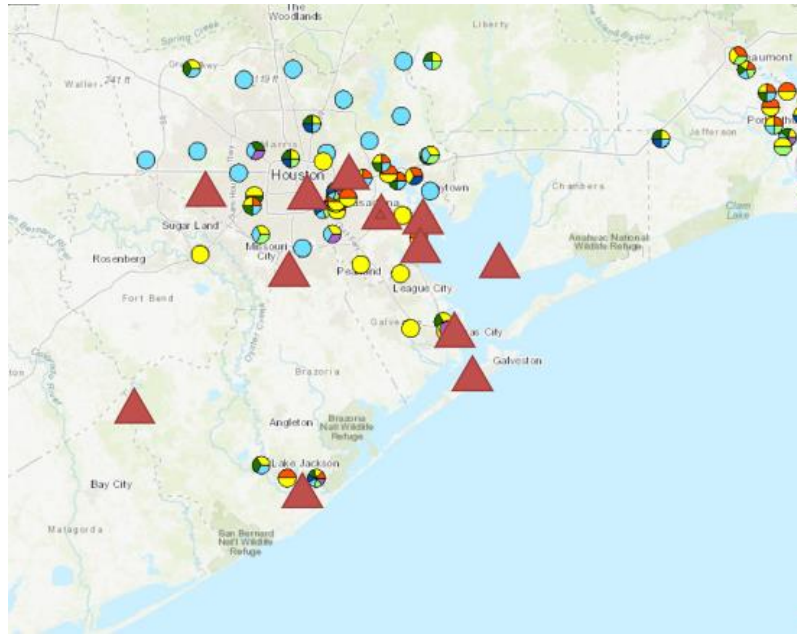


Figure 2. TCEQ active monitoring sites around Houston region, triangles represent the 12 sites used in this study. (adapted from <https://www.tceq.texas.gov>)

2.2 Identification of the sea breeze events

Following the acquisition of the TCEQ datasets for 2019, the analysis of three surface meteorological variables (surface temperature, wind direction, and wind speed) was done using multiple python scripts. The primary script entailed the use of meteorological constraints to identify the possible sea breeze days. These meteorological constraints include a temperature decrease greater than 5°F, and a wind direction change greater than 30° within a 1-hour interval. We applied these criteria to observations from all 12 sites and selected days when at least 5 sites met these thresholds. Following the identification of the possible sea breeze days, we run a secondary script to plot the time series of the surface temperature, wind direction, and wind speed for each sea breeze day to investigate the timing of the sea breeze front passage at the 12 sites.

Sea breeze days are further confirmed using satellite images from NASA's Worldview (<https://worldview.earthdata.nasa.gov>), since the primary script may be unable to separate sea breeze fronts from mesoscale (e.g., squall line) and synoptic scale fronts (e.g., a cold front). An example of a potential sea breeze event is shown in Figure 3 as seen from the satellite, showing a coastal line of isolated small cumulus clouds (in bright white color) that bends around the bay. For these confirmed events, we plot the time series of the surface temperature, wind speed, and wind direction within a 3-hour window around the timing of the sea breeze front.

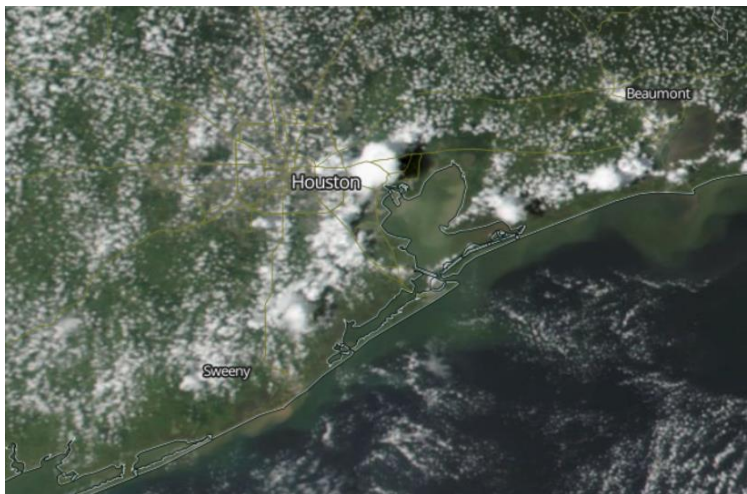


Figure 3. *NASA's Worldview Satellite image of possible sea breeze event on June 28th*

3. RESULTS

In this study, we investigate the surface meteorological conditions in order to quantify when and where the sea / bay breeze occurs in the Houston, TX region. Generally, wind shifts directionally towards southeasterly at the time of sea breeze frontal passage, along with a decrease in temperature and an increase in wind speed. For example, on June 28th, 2019 at 17:40 UTC a sea breeze front is observed at LaPorte site, associated with a southeasterly flow, a

temperature decrease of 3°F, and a wind speed increase by 4 mph (Figure 4). Satellite images show a line of isolated convective cells, also known as a sea breeze front.

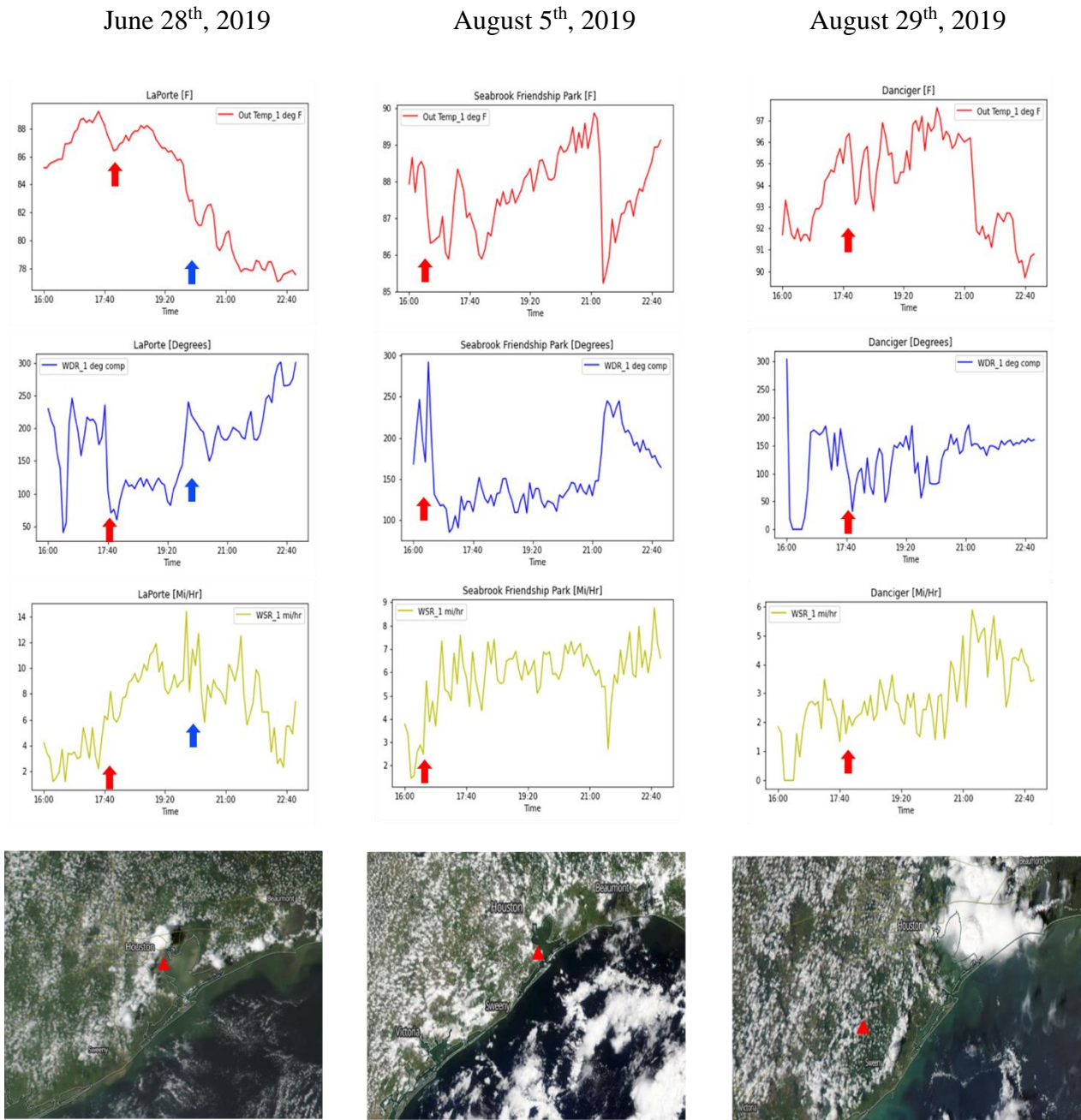


Figure 4. Time series of temperature (top row), wind direction (second row), and wind speed (third row), and sea breeze front from the satellite observations (bottom row) for three potential sea breeze events.

With a minimum of 5 sites experiencing sea breeze criteria on the same day, 55 days appear as possible sea / bay breeze days. Large variability in frequency of occurrence is found between the TRACER Intense Operational Period (IOP) months (June, July, August, and September) and the rest of the year. These months record 32 potential sea breeze occurrences, whereas the rest of the year records 23. The variability may not look significant, however only 21 out of 55 days are confirmed as a sea / bay breeze occurrence (38.2%) through time series plots as well as satellite images. Of the 21 assessed possible sea breeze days, 19 are recorded in the IOP and 2 are recorded from the rest of the year (Table 1). The remaining 34 days are determined to have no identifiable sea breeze characteristics or exhibit synoptic scale forcing based on inspection of the satellite images. Therefore, displaying a noticeable variability between the intense operational period versus the rest of the year.

Table 1. Potential sea breeze events in 2019.

Period	Events (MM/DD/YY)
IOP	06/07/2019, 07/02/2019, 07/03/2019, 07/15/2019, 07/22/2019, 07/28/2019, 07/29/2019, 08/05/2019, 08/06/2019, 08/16/2019, 08/17/2019, 08/18/2019, 08/20/2019, 08/21/2019, 08/29/2019, 08/30/2019, 09/11/2019, 09/16/2019, 09/23/2019
Rest of Year	04/18/2019, 05/31/2019

4. Discussion

Our research helped provide general knowledge of some of the meteorology driving convective cloud development in the Houston region as well as the extended TRACER measurement domain. Daily forecasts improved knowledge of the synoptics as well as mesoscale meteorology conditions influencing the region. The use of maps from operational numerical weather prediction models, for instance the 500 hPa, 2m Temperature and Wind, Sea Level

Pressure and Precipitation, and Precipitable Water gave insights into the current and future weather. Additionally, interpretation of observations of surface meteorology as well as soundings produced improved forecasts. Interpretation of this information contributed to detailed forecasts for conditions that mimic those that are anticipated during the field campaign. During the field campaign, these forecasts will help to guide missions' operational decisions.

The presence and extent of sea / bay breeze circulations was identified using the TCEQ surface meteorological network. The combination of meteorological constraints and production of plots granted the identification of possible sea breeze occurrences. Although our constraint identified sea / bay breeze days 38.2% of the time, additional analysis and constraints will be required to separate these circulation signatures from synoptic scale influences, such as low-pressure systems.

5. Setbacks

A significant difficulty for the research regarding identifying sea / bay breeze occurrences was the ability to separate mesoscale circulations (e.g. sea / bay breeze) from synoptic scale factors, requiring verification using time series plots and satellite imagery. Additionally, another setback faced was variability in data formats. The original python script was developed to read ASCII text files. New data files were in Comma Separated Values (CSV) format and were not readable with the original script. This difference required a switch to the pandas dataframe of python and delayed some of our data processing. While this caused a delay, it was also an opportunity to learn a new aspect of python programming, and develop more robust codes that will allow for more flexible code for future research.

6. Future Research

Further research will extend the datasets for the 12 sites to 10 years (2010 – 2019), instead of 2019 only to receive a climatological understanding. Additionally, using more years will result in an increased understanding of the timing of these phenomena. For example, a high-volume month for sea / bay breeze could be August, which in turn would indicate to the TRACER science team to pay close attention to that time frame. Next, the sites could be extended to more than 12 locations for an enhanced representation. Future research is expected to take place April 2021 through April 2022 in the Houston, TX region, with the goal to examine the lifecycle of isolated convective clouds and how it is influenced by atmospheric aerosols for the TRacking Aerosol Convections interactions ExpeRiment (TRACER) campaign.

7. References

Jensen M. P., et al., 2020: Tracking Aerosol Convection Interactions Experiment (TRACER) Science Plan. <https://www.arm.gov/research/campaigns/amf2021tracer>

8. Acknowledgements

This project was supported in part by the U.S. Department of Energy, Office of Science, Office of Workforce Development for Teachers and Scientists (WDTS) under the Science Undergraduate Laboratory Internships Program (SULI). Data was collected and archived by the Texas Commission on Environmental Quality (TCEQ). We thank the TRACER science team as well as the TRACER forecasting team for their participation in the background campaign. Lastly, we thank Doug Boyer from TCEQ for providing high-resolution surface meteorology data. Finally, a major thank you to my mentors Michael Jensen and Die Wang for all the help during my internship.

The Civil Engineering Development of the Electron Ion Collider (EIC) Support Infrastructure

Angela Zavala Yanes, Civil Engineering, Suffolk County Community College, Ammerman Campus, Selden, NY 11784

Joseph E. Tuozzolo, Collider-Accelerator Department, Brookhaven National Laboratory, Upton, NY11973.

Abstract

The Electron Ion Collider (EIC) will be design with existing Relativistic Heavy Ion Collider (RHIC) infrastructure at Brookhaven National Laboratory (BNL). My project requires 2D and 3D designs for a new tunnel and service building at the RHIC IR02 location to service new electron source facilities. The 400MeV LINAC allows electrons to travel through the beamline and eventually go out into the RHIC tunnel to collide with Hadrons (charged particles), a 3D tomographic image of these particles inner structure is seen by scientist to study matter.¹ An additional LINAC, the energy recovery LINAC (ERL), accelerates electrons to cool the Hadrons at the EIC for higher luminosity enabling BNL scientists to further study the arrangement of quarks and gluons.² This project consisted of gathering information on the EIC accelerator components; to learn and use 2D and 3D computer design software to layout the tunnel and support building dimensions with accuracy for proper installation. The 2D model in AutoCAD was used for a plan view with layers to provide different options for the engineers. The 2D design layouts were re-created in Creo Parametric 3D modeling for better visualization analysis and understanding of interferences for routing piping and waveguides. Creo Parametric enables Engineers to design parts, create assemblies, and allows access to different views. This internship has radically impacted my skills in 2D design and has allowed me to learn to use 3D design software in Creo Parametric. This experience has taught me that persistence is key to success and that knowledge is power. I will continue progressing and sharpening my design skills in AutoCAD and Creo Parametric.

Introduction

The Collider-Accelerator Department at BNL focuses on the continued development of the IR02 service building and the new tunnel at the 2 o'clock region of the EIC. This project will focus on the progress of the new tunnel with limited knowledge on the physics side, and little to no knowledge of 3D computer design software. I will start by discussing the 400MeV LINAC, which is composed of six copper cavities due to its high electrical conductivity and a beamline where electrons travel through into the RHIC tunnel at room temperature³. The electrons travel to collide with the dense hadrons, as these two particles collide the inner structure of the hadrons are seen. Now, I will introduce the ERL which is composed of eight superconductive radio frequency cavities that accelerate the electrons traveling through the beamline. The ERL's components include a gun, flanges and an accelerator cavity that accelerates electrons up to about 200 million electron volts.⁴ The superconductive radio frequency cavities are made of niobium, niobium is chosen due to its low resistivity to prevent the overheating of the coils.⁵ Additionally, these cavities contain superconductive wires that carry electrical current with no energy loss, however they require a cryogenic system that ultimately serves to cool the superconductive magnets and wires down to 2°K for better performance.⁶ These superconductive modules primary purpose is to send electrons to cool the Hadrons at the Hadron ring.⁷ The Hadrons travel with lateral momentum, which implies they are scatter all around. The electrons then cool the Hadrons, and as the electrons cool them energy is transfer from the Hadrons to the electrons. The Hadrons vibrate less and become denser and stable; in the other hand, the electrons carry high energy as they travel back through the quadrupole magnets to the ERL. The bending magnet connects to superconductive cavities by a 180-degree dipole assembly.⁸ The electrons deposit the energy they carry into the cavities.

Niobium's advantage is that it does not absorb any of the energy being deposit. The reason why this LINAC is called the energy recovery LINAC is because the cavities reused that energy to accelerate cooled electrons into Hadron ring once again. There is also a gun room where the guns are located; the 400MeV polarized gun is installed properly inside the gun room, the ERL accelerator and gun are also located inside the gun room. In addition, there is a clean room with High Efficiency Particulate Air (HEPA) filters to prevent dust, the clean room is also inside the gun room and only covers from the 400MeV LINAC end chamber of the bunching cavity to the end of the manipulator of the gun leaving about two feet of space in between the end of the manipulator and the inner wall of the room. The gun depends on the power supply located in a Faraday cage that protects the power supply from external electromagnetic pulse (EMP).⁹ The power supply is eight feet away from the outer wall of the gun room. Having two power supplies is being considered in case one power supply fails there will be an extra power supply to support the guns.

Methods/Results

In order to continue the progress of the IR02 building I needed access to the AutoCAD drawing. The drawing was composed of the overall building size, rectangles representing the location of power amplifiers, other shapes that represented the location of the waveguides and an old version of the 400MeV LINAC. Thus, I replaced the old version of the LINAC and installed the updated LINAC (**Appendix 1**). At times it was necessary to export drawings from Creo to AutoCAD. This LINAC needed to be exported but it was not possible to export the whole drawing because it was too large. Thus, I exported the parts that were used repetitively. I made the LINAC plane view in AutoCAD by assembling the parts until it was complete. Then, I

change my focus to the tunnel, I needed the tunnel to be install so I could start assembling components inside. The tunnel's diameter was 18'0, the length is still being modified. At the beginning, the type of waveguide needed for the 400MEV LINAC was the WR1500, I had access to a catalog of waveguides that had the dimensions and thickness of its flange⁵. I used the catalog to create the cross-section view of the WR1500 flange (**Appendix 2**). The length of the outer wall was 18.50'' and the width was 11.00'' the inner wall was the result of offsetting the outer wall 1.55'' inside. Moreover, the length and width of the waveguide body were needed to create the plane view for the AutoCAD layout. In order to find the dimension of the width, I design the flange in Creo and then created the thickness of the flange. Then, I would extrude the inner wall of the flange, this allowed me to measure the width of the body. Once, I had all the dimensions of the WR1500, it was time to install the plane view in the layout. It was preferred to have several short waveguides instead of having long waveguides to prevent malfunction. Therefore, I measured the distance from the flange of the LINAC to the power amplifier and then I divided the distance by the number of waveguides I wanted to include so that I could get the dimension needed for the length of the waveguide. Engineers eventually decided that WR1500 was not the type of waveguide needed. I decided to look at the Creo design and look at the flange attached in the LINAC I discovered the dimensions in the model, the diameter of the holes, the number of holes, and the spacing between the holes. Once, I had gathered all that information I looked at the waveguide catalog to find if any of the dimensions matched the dimensions I had gotten from the Creo model. I found that the WR340 (**Appendix 3**) was the correct waveguide. The flange consisted of a length of 5.44'' outer wall dimension and the width was 3.75''. I replaced the WR1500 by the WR340. Once again, I measured the distance from the LINAC to the power amplifier. As a result, there is four waveguides assembled; the

length of the body for three of them is 7'0 and the fourth one is about 13'0. Overall, there is six cavities that connect to the flange at the power amplifier by using the WR340 waveguides.

Now, the LINAC is attached to bunching cavities (**Appendix 4**) that also have flanges and connect to the buncher power amplifiers in the service building. I exported the latest version of these bunching cavities to the 2D model layout. These cavities connect to the upstream beamline of the LINAC and to the polarized gun on the opposite side of the cavities. I found out that the waveguide used for these bunching cavities was the WR284 (**Appendix 5**). The length of the outer wall is 4.50'' and the width is 3'', by offsetting the outer wall .78'' I created the inner wall. I designed the waveguide in Creo in order to analyze the width of the body and installed them in the 2D model. Moving on into the ERL (**Appendix 6**) the superconductive cavities were also exported from Creo. Engineers confirmed eight of these cavities were needed. Thus, I assembled the cavities connecting each cavity's valve to a quadrupole magnet which connected to another cavity's valve. At first, it mentioned that the WR1500 waveguides would be use by ERL, and two waveguides were used per cavity, hence two power amplifiers used per cavity. As time progressed, civil Engineers decided they wanted to eliminate half of the power amplifiers and they no longer wanted to use the WR1500 waveguide. They decided they would use the 6 1/8'' coax cable (**Appendix 7**). I started doing research to look where I could find the dimensions for the flange and the tube, eventually I found a website that provided all the measurements necessary.⁶ The outer diameter is 206.4'', the inner diameter is 155.8'' and the diameter for the holes was 10.8''. I designed this coax in Creo and exported it to AutoCAD. I measured the distance from the flange of the coax to the power amplifiers, and then decided how many coax cables were needed and the length of the coaxes. Once I had found the coax cables needed, I focused on the upstream of the beamline where the gun room would be located.

I frequently received step files from mechanical Engineer John Skaritka. The gun room would shelter the polarized gun and the ERL gun. This room is made of concrete to prevent radiation, the width of the outer wall is 51'2'' and the length is 32'8''. The inner walls are 2'0 away from the outer walls and that space represents the concrete that will go there. Now, a clean room is created inside the gun room that shelters the polarized gun only, this room is made of a single layer. The dimensions for the clean room were chosen by sheltering the whole polarized gun. The guns need power in order to accelerate the electrons and that power is obtained from the power supplies. The mechanical Engineer in charge of the 400MEV LINAC decided to place two power supplies in a "caged room" that was 8'0 away from the outer wall of the gun room. The width of the room is 20'0 long and the length is 14'. The dimensions were chosen to have enough space for the two power supplies inside. The LINACS are under constant modifications to make the model as accurate as possible.

Conclusion

The AutoCAD plane layout has improved and better represents the service building and the LINACS. The two LINACS have enough space inside the tunnel, the aisle in between should have enough space for a third beamline running through. The tunnel space is prominent because it also allows space for maintenance. The cost should also be reduced. The two LINACS are well established, addition equipment such as the electron guns are located near the LINACS inside the gun room. The power supplies are shown to be inside a caged room, the caged room is made of aluminum which does not cost much. I think the plane view has improved and made use of the existing RHIC infrastructure.

References

¹ Tribble, Robert. Overview. Electron Ion Collider (EIC) at BNL.

https://www.bnl.gov/stakeholder/docs/CAC/2020-02-13-CAC_BNL-EIC.pdf

² EIC Science. (n.d.). Retrieved August 06, 2020, from <https://www.bnl.gov/eic/science.php>

³ Skaritka, John. Internship meeting. July 28, 2020

⁴ Tuozzolo, Joseph. Internship meeting. July 27, 2020.

⁵ Tuozzolo, Joseph. Internship meeting. July 28, 2020.

⁶ Crnosija, Natalie | Energy Recovery Linear Accelerator: A Unique Accelerator That Reclaims Energy,

www.bnl.gov/rhic/news2/news.asp?a=2893&t=today, April 16 2020

⁷ Natalie Crnosija | . Energy Recovery Linear Accelerator: A Unique Accelerator That Reclaims

Energy, www.bnl.gov/rhic/news2/news.asp?a=2893&t=today. April 16, 2020.

⁸ Seletskiy, S., Brookhaven National Laboratory. “How to measure energy of LEReC electron beam with

magnetic spectrometer.” <https://www.bnl.gov/isd/documents/93026.pdf> . April 2016.

⁹ Davis, Jeff., Davis, Amy. “Building your own Faraday cage.” *The Ready Store*, May 15 2014,

[https://www.thereadystore.com/diy/9713/building-your-own-faraday-](https://www.thereadystore.com/diy/9713/building-your-own-faraday-cage/#:~:text=The%20Faraday%20cage%20can%20help,the%20event%20of%20an%20EMP)

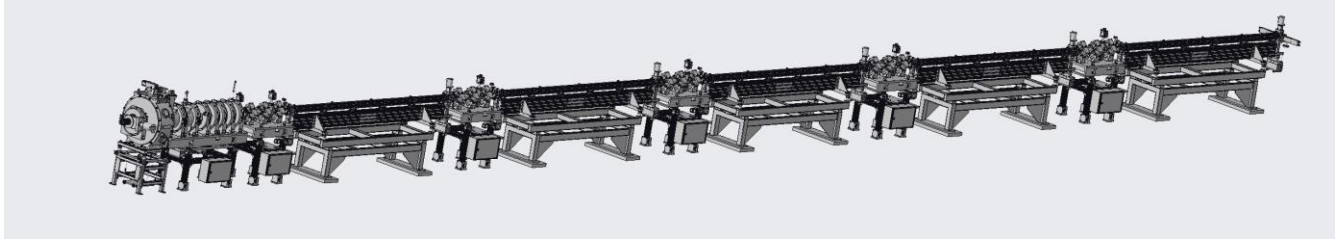
[cage/#:~:text=The%20Faraday%20cage%20can%20help,the%20event%20of%20an%20EMP](https://www.thereadystore.com/diy/9713/building-your-own-faraday-cage/#:~:text=The%20Faraday%20cage%20can%20help,the%20event%20of%20an%20EMP).

Acknowledgements

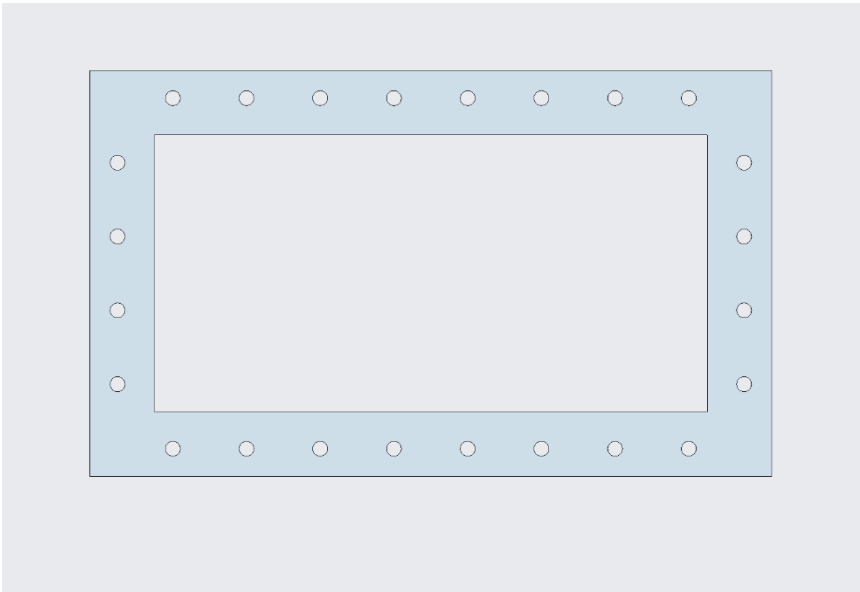
I would like to thank my mentor Joe Tuozzolo for giving me an opportunity to learn and be part of this big project. I also want to thank Steven Bugros for always being there for me whenever I needed help in Creo Parametric, for being patient and a great guidance to my success. A special thanks to Vito De Monte, another wonderful teacher in Creo Parametric. John Skaritka a mechanical Engineer who inspires me to keep working hard. My colleagues Oksana Vysochanska and Andrew Abdalla, two incredible Engineers I admire. In addition, this project was supported in part by the U.S. Department of Energy, Office of Science, Office of Workforce Development for Teachers and Scientists (WDTS) under the Community College Internships Program.

Appendix 1:

Updated 400 MeV LINAC model made copper cavities.



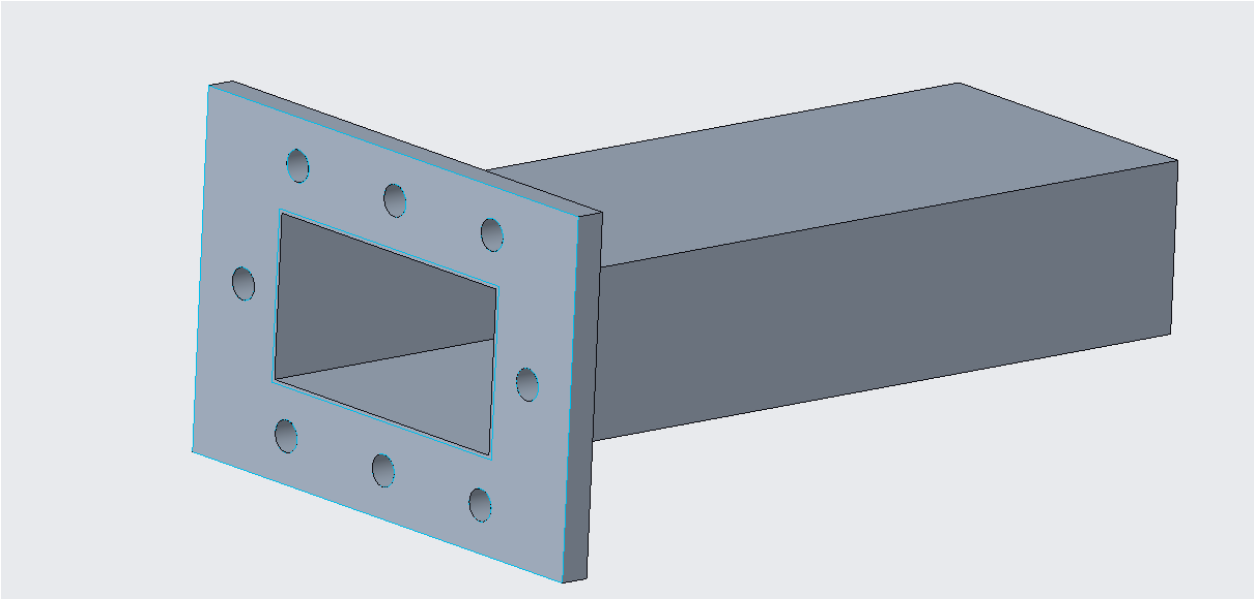
Appendix 2:



WR1500 flange
Width: 11.00''
Length: 18.50''

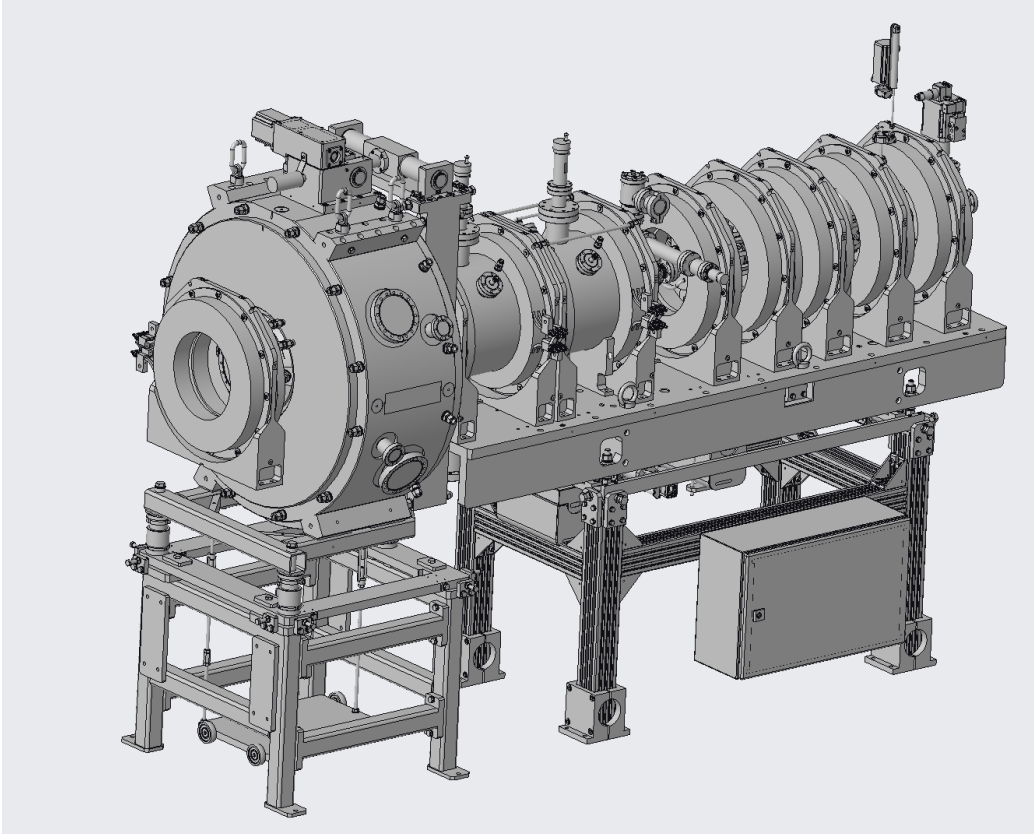
Appendix 3:

WR284
Width: 3.75''
Length: 5.44''



Appendix 4:

Bunching cavities

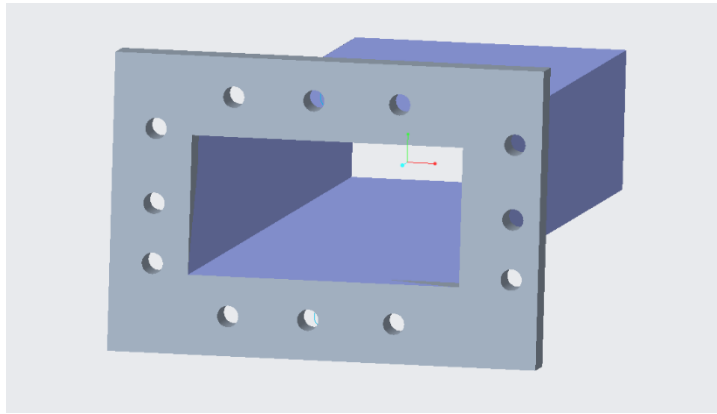


Appendix 5:

WR340

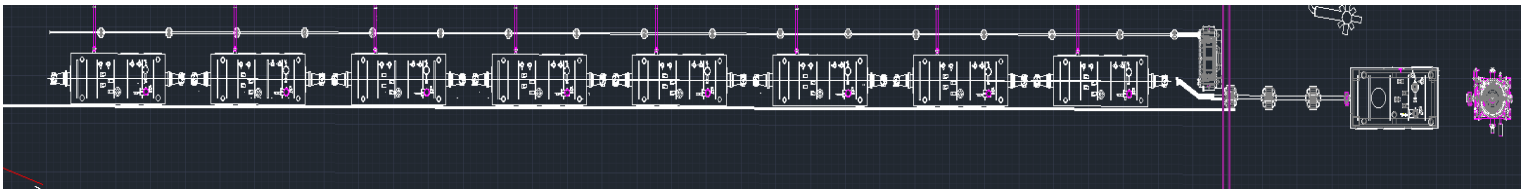
Width: 3.00"

Length: 4.50"



Appendix 6:

Energy Recovery LINAC (ERL)



Appendix 7:

6 1/8" Coax cable

